THE DETRITAL MINERAL RECORD OF CENOZOIC SEDIMENTARY ROCKS IN THE CENTRAL BURMA BASIN: IMPLICATIONS FOR THE EVOLUTION OF THE EASTERN HIMALAYAN OROGEN AND TIMING OF LARGE SCALE RIVER CAPTURE

Cynthia Anne Brezina

A Thesis Submitted for the Degree of PhD
at the
University of St Andrews

2015

The detrital mineral record of Cenozoic sedimentary rocks in the Central Burma Basin: implications for the evolution of the eastern Himalayan orogen and timing of large scale river capture

Cynthia Anne Brezina

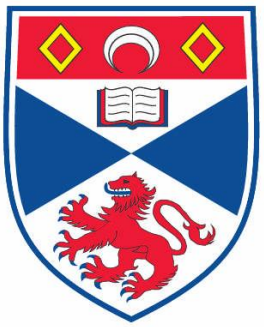

This thesis is submitted in partial fulfilment for the degree of PhD

at the University of St Andrews

July 2014

Declarations

1. Candidate's declarations:

I, Cynthia Anne Brezina, hereby certify that this thesis, which is approximately XXXX words in length, has been written by me, and that it is the record of work carried out by me, or principally by myself in collaboration with others as acknowledged, and that it has not been submitted in any previous application for a higher degree.

I was admitted as a research student in January, 2009 and as a candidate for the degree of PhD in January, 2009; the higher study for which this is a record was carried out in the University of St Andrews between 2009 and 2014.

Date: signature of candidate

2. Supervisor's declaration:

I hereby certify that the candidate has fulfilled the conditions of the Resolution and Regulations appropriate for the degree of PhD in the University of St Andrews and that the candidate is qualified to submit this thesis in application for that degree.

Date: signature of supervisor

3. Permission for electronic publication:

In submitting this thesis to the University of St Andrews I understand that I am giving permission for it to be made available for use in accordance with the regulations of the University Library for the time being in force, subject to any copyright vested in the work not being affected thereby. I also understand that the title and the abstract will be published, and that a copy of the work may be made and supplied to any bona fide library or research worker, that my thesis will be electronically accessible for personal or research use unless exempt by award of an embargo as requested below, and that the library has the right to migrate my thesis into new electronic forms as required to ensure continued access to the thesis. I have obtained any third-party copyright permissions that may be required in order to allow such access and migration, or have requested the appropriate embargo below.

The following is an agreed request by candidate and supervisor regarding the electronic publication of this thesis:

PRINTED COPY

No embargo on print copy

ELECTRONIC COPY

Embargo on all of electronic copy for a period of two years on the following ground(s):

- Publication would preclude future publication

Date: signature of candidate

Date: signature of supervisor

Abstract

This study contributes to the understanding of major river evolution in Southeast Asia during the Cenozoic. In order to trace the evolution of a hypothesized palaeo-Yarlung Tsangpo-Irrawaddy River, this work undertakes the first systematic provenance study of detrital minerals from Cenozoic synorogenic fluvial and deltaic sedimentary rocks of the Central Burma Basin, employing a combination of high precision geochronology, thermochronology, and geochemistry analytical techniques on single grain detrital zircon and white mica. The dataset is compared to published isotopic data from potential source terranes in order to determine source provenance and exhumation history from source to sink.

A Yarlung Tsangpo-Irrawaddy connection existed as far back as ca. 42 Ma and disconnection occurred at 18–20 Ma, based on provenance changes detected using a combination of U-Pb ages and εHf(t) values on detrital zircons, and $^{40}Ar/^{39}Ar$ dating on detrital micas. During the Eocene and Oligocene, units are dominated by U-Pb age and high positive εHf(t) values, characteristic of a southern Lhasa Gangdese magmatic arc source. An antecedent Yarlung Tsangpo-Irrawaddy River system formed the major river draining the eastern Himalaya at this time. A significant change in provenance is seen in the early Miocene, where detritus is predominantly derived from bedrock of the eastern Himalayan syntaxis, western Yunnan and Burma, a region drained by the modern Irrawaddy-Chindwin river system characterized by Cenozoic U-Pb ages and negative εHf(t) values. This is attributed to the disconnection of the Yarlung-Irrawaddy River and capture by the proto-Brahmaputra River, re-routing Tibetan Transhimalayan detritus to the eastern Himalayan foreland basin. Re-set zircon fission track ages of 14-8 Ma present in all units is used to infer post-depositional basin evolution related to changed in the stress regime accommodating the continued northward migration of India. The early Miocene initiation of the Jiali-Parlung-Gaoligong-Sagaing dextral shear zone and the continued northward movement of the coupled India-Burma plate aided in focusing deformation inside the syntaxis contributing to the disconnection of the Yarlung Tsangpo-Irrawaddy system, linking surface deformation and denudation with processes occurring at deeper crustal levels.

Acknowledgements

Completing this doctoral thesis has been both a long, challenging, but rewarding experience. I would not have been able to get this far if were not for the valuable support of others.

Firstly, I would like to thank Dr. Ruth Robinson for her excellent supervision, support in more ways that I can count and eternal patience. It's been an epic journey and it has been a privilege to work with you.

I would like to gratefully acknowledge fellow researchers that provided technical and analytical support without which this project would not have been possible. To Dr Nay Win Oo of the Department of Geography, University of Pyay, Burma and Professor Myint Thein of the Department of Geology, University of Mandalay, Burma that aided in sampling, Professor Randy Parrish, Dr. Matt Horstwood and others at the NERC Isotope Geoscience Laboratory for zircon geochronology and geochemistry analysis, Dr. Dan Barfod and Dr. Darren Mark at the SUERC Argon Isotope Facility, Professor Andy Carter for conducting fission track dating, Dr. Bruno Dhuime at the Bristol Isotope Group for zircon Lu-Hf analysis and Donald Herd and Angus Calder at the University of St. Andrews Department of Earth Sciences for their technical support during mineral preparation, BS/CL imaging, random questions and general banter.

To the research community and colleagues in St. Andrews, it has been a privilege and a pleasure.

To my friends and family, especially Dad, Louis, Ben, Jennifer, Monica, Janie, Christina, and Jamie, I am eternally grateful for your unending support – I love you so much.

And lastly, to Mom, Jeff and Lincoln- you are with me, always.

Table of Contents

List of Figures

Chapter 1. Introduction

1.1. Thesis statement and objectives

This work focuses on the little studied Central Burma Basin sedimentary archive which may represent the best preserved and accessible record of early erosion from the eastern Himalayas. Although several authors have suggested a Yarlung Tsangpo-Irrawaddy connection, provenance investigations of the Cenozoic sedimentary rocks of the Central Burma Basin, which would record evidence of the duration of this system and timing of disconnection, are virtually non-existent. Additionally, the existing stratigraphy is based on poorly resolved biostratigraphic age controls. This study presents the first high precision geochronological, thermochronological and geochemical analyses on a sequence of Eocene, Oligocene and Miocene synorogenic sedimentary rocks of the Central Burma Basin in order to 1) identify the source regions for the sedimentary sequences, 2) test the existence of a long-lived longitudinal Yarlung-Tsangpo-Irrawaddy river system, 3) if proven, determine the timing of river capture and disconnection and, 4) identify the mechanisms driving river disconnection. In conducting this research, the study will provide more precise depositional ages than currently exist. The outcomes of this research will have major implications for geodynamic models of the early Himalayan orogeny and the interaction between crustal deformation, exhumation, surface uplift and major drainage capture. There is a gap in our knowledge because the eastern Himalayan syntaxis and the Namche Barwa region, drained by the Yarlung Tsangpo-Brahmaputra rivers, is one of the most rapidly exhuming areas globally (Booth et al., 2009; Booth et al., 2004; Enkelmann et al., 2011; Finnegan et al., 2008; Stewart et al., 2008; Zeitler et al., 2001), yet the Eocene and Oligocene history of these two river systems is not fully understood and how the evolution of the orogen reflects the coupled feedback between tectonics, exhumation and riverine erosion.

It is hypothesized that if the Yarlung Tsangpo-Irrawaddy formed a single longitudinal river, this would have been the major river draining the eastern Himalayas at this time and sediment derived from bedrock that was exposed in the modern Yarlung Tsangpo drainage within southern Tibet would be present within the Cenozoic deposits

of the Central Burma Basin. If the Irrawaddy was not involved in a river capture event, the sediment preserved in the basin should be representative of the bedrock exposed in the modern Irrawaddy catchment. The headwaters of the Irrawaddy River are located near the eastern Himalayan syntaxis and it is hypothesized that progressive uplift and exhumation of this region led to the breakdown of the Irrawaddy-Tsangpo system and establishment of the modern Yarlung Tsangpo-Brahmaputra and Irrawaddy river systems (Figure 1.1, Figure 1.2). The signal of this exhumation should be reflected in the increasing metamorphic grade and decreasing lag times of the detritus through time; lag times are expected to increase when exhumation rates reduce (Bernet and Spiegel, 2004; Carrapa et al., 2009; Carrapa et al., 2004; Hodges et al., 2005; Ruiz et al., 2004; Szulc et al., 2006). A change in provenance will reflect a change in the source region being eroded and geochronological and thermochronological data can help constrain the timing of river disconnection. The identification of specific tectono-thermal events in both the source terranes and detrital mineral grains allows the coupling of palaeo-river and tectonic evolution during the progressive collision of India into Eurasia since ca. 50 Ma to be confirmed and further understood. In documenting the evolution of the Irrawaddy River using these data, this thesis presents new insights into the tectonic evolution of the west Burma block during the Eocene to Miocene (Figure 1.1).

The objectives of the project are to compare the ages and geochemical characteristics of potential source terranes and detrital mineral grains in order to determine detrital mineral provenance, and associate changes in provenance with changes in the sediment pathways. The exhumation of source areas through time is determined using geochronology, thermochronology, and geochemistry on single detrital grains, and these are compared to published thermochronology data for all potential source terranes. Specifically, the objectives are to:

(1) Provide a new stratigraphic framework on sediments with previously limited age control to better constrain the tectonic and sedimentation history of the basin
(2) Determine the provenance of the sediments using a multi-proxy approach of high precision age dating and isotopic analysis of single detrital grains and comparing the characteristics to that of published bedrock data in the proposed

catchments to interpret the exhumation and erosion history in context of specific geographical regions and tectonics events

(3) Link the observed changes in sediment provenance of the detrital record through time with the loss or gain of specific source areas in order to reconstruct the palaeogeography through time

(4) Use low temperature $^{40}Ar/^{39}Ar$ dating of muscovite mica, U-Pb and fission track dating of detrital zircon combined with Lu-Hf isotope analysis to resolve source provenance and exhumation history, constrain the timing of capture of the Yarlung Tsangpo from the Irrawaddy River by the Brahmaputra River and determine the role of focused deformation and exhumation in the eastern syntaxis in driving river capture events.

In this work, the Cenozoic evolution of the Irrawaddy River system is investigated through a detailed provenance study of the heavy mineral record of Eocene, Oligocene and Miocene sedimentary rocks of the Central Burma Basin deposited by the Irrawaddy River, utilizing combined U-Pb and fission track age dating and Lu-Hf isotopic analysis of detrital zircons, as well as $^{40}Ar/^{39}Ar$ dating of detrital white mica. This data is then compared with similar datasets in published literature for bedrock within potential source regions in the modern Yarlung Tsangpo catchment (Lhasa terrane), Parlung River catchment (eastern Himalayan syntaxis region) and Irrawaddy River catchment (western Yunnan and Burma).

This works seeks to address hypotheses involving the evolution of the major river systems draining the eastern Himalaya and specifically allows for testing of a palaeo-Yarlung Tsangpo-Irrawaddy connection and subsequent capture of the Yarlung Tsangpo by the proto-Brahmaputra during the Late Cenozoic (Brookfield, 1998; Clark et al. 2004; Liang et al., 2008). The timing of river capture may be inferred from a change in provenance in the Central Burma Basin, providing a temporal constraint to the development of the modern drainage systems observed today, where the Irrawaddy River now drains a region south and east of the eastern Himalayan syntaxis, including western Yunnan and Burma, and the Brahmaputra River, linked with the antecedent Yarlung Tsangpo, drains a large area encompassing southern Tibet, the eastern syntaxis and the eastern Himalayan front (Figure 1.1).

If the Yarlung Tsangpo-Irrawaddy formed a single longitudinal river, this would have been the major river draining the eastern Himalayas at this time, and sediment derived from bedrock that was exposed in the modern Yarlung Tsangpo drainage within southern Tibet would be present within the Central Burma Basin. If the Irrawaddy was not involved in a river capture event, the sediment preserved in the basin should be representative of the bedrock exposed in the modern Irrawaddy catchment. Therefore, identification of detritus derived from bedrock that was exposed in the modern Yarlung Tsangpo drainage within southern Tibet within Cenozoic syn-orogenic sedimentary rocks of the Central Burma Basin and changes in sediment provenance through time may potentially document the evolution of the large river systems draining the eastern Himalaya during the early stages of orogenesis, which may have major implications for geodynamic models involving the interaction between crustal deformation, exhumation, surface uplift and major drainage capture in the eastern syntaxis region.

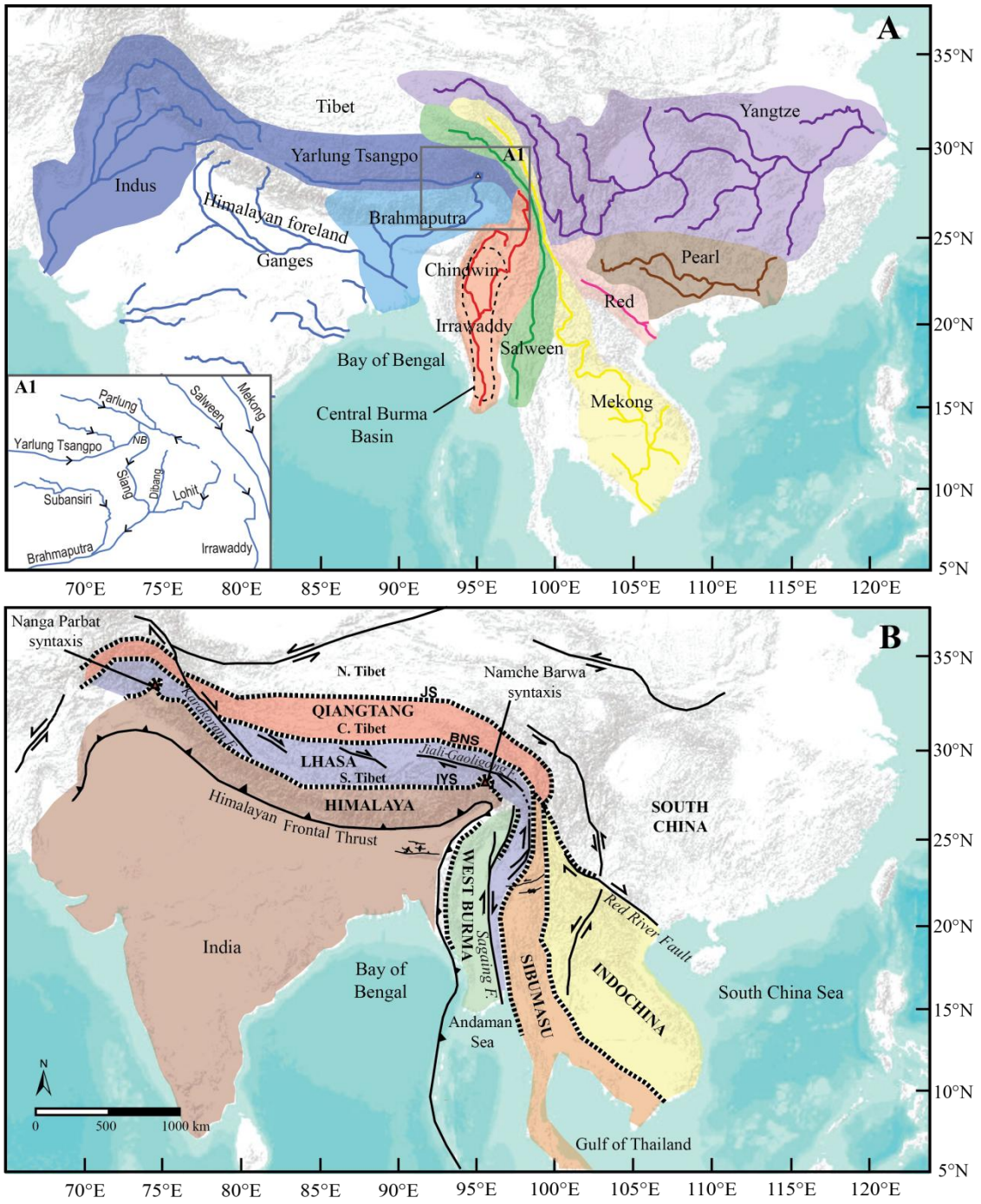

Figure 1.1 Simplified map showing the geological terranes and major structures of Southeast Asia and modern catchments of major rivers draining this region. A) Map of Asia showing the modern drainage catchments of the major Asian river systems: Yarlung Tsangpo, Brahmaputra, Irrawaddy, Chindwin, Salween, Mekong, Red, Pearl and Yangtze. Insert map A1 shows modern rivers draining the eastern Himalayan syntaxis region. B) Simplified geological map showing the major tectonic features (modified from Lee et al., 2003) and divisions of Southeast Asia after Metcalfe (1996) and Morley (2012), separated by remnant Tethyan ocean ophiolitic suture zones (dotted line). JS – Jinsha suture (Palaeotethys); BNS - Bangong-Nujiang suture (Mesotethys); IYS – Indus Yarlung suture (Neotethys).

1.2. Background

1.2.1. Geological evolution of river systems

The eastern region of the Himalayas is a complex geological collision zone where uplift, deformation and river capture have all influenced landscape evolution throughout the Cenozoic, making it an ideal region to test hypotheses involving coupled surface and crustal processes. The eastern syntaxis has experienced some of the highest rates of exhumation since the Late Miocene to Pliocene (Booth et al., 2009; Booth et al., 2004; Burg et al., 1998; Ding et al., 2001; Stewart et al., 2008) and Cenozoic-aged detritus deposited by river systems draining this area offer an opportunity to study the feedback between tectonics, exhumation, erosion and climate through time. Geodynamic modelling (Beaumont et al., 2001; Koons et al., 2002), thermochronology and geochronology record the progressive evolution of this region and reveal the potential for surface erosion to influence metamorphism and exhumation in active orogenic settings (Booth et al., 2009; Booth et al., 2004; Ding et al., 2001; Enkelmann et al., 2011; Finnegan et al., 2008; Koons et al., 2002; Stewart et al., 2008; Zeitler et al., 2001). Thus, an understanding of the drainage evolution of the Yarlung Tsangpo, Brahmaputra, and Irrawaddy river systems is important because their sedimentary records potentially contain information on the onset of significant deformation and surface uplift in the early eastern Himalayas, critical to evaluating models of the early evolution of the Himalayan orogeny and the landscape response to continued convergence.

The unusual geometry of the major eastern Himalayan drainage systems has been attributed to crustal shortening and shear zone development along the eastern Tibetan Plateau, accommodating the northward movement of India into Asia (Hallet and Molnar, 2001; Wang and Burchfiel, 1997). In this scenario, long-lived antecedent river systems record strain, becoming more attenuated with progressive indentation of the north-eastern corner of India and the clockwise rotation of crustal blocks around the eastern syntaxis (Brookfield, 1998; Chen et al., 2000; Hallet and Molnar, 2001; Wang and Burchfiel, 1997). Alternatively, the drainage patterns of Southeast Asia have been attributed to tectonically induced river capture and drainage re-organization. The modern Yarlung Tsangpo flows eastward along the Indus Yarlung Suture Zone before

making an anomalous 180 degree bend around the eastern Himalayan syntaxis before joining with the Brahmaputra River, connecting the Lhasa terrane of southern Tibet to the Bay of Bengal (Figure 1.1). The origin and evolution of this system is widely debated, although most researchers consider the present-day catchment to be the result of Late Cenozoic drainage re-organization (Brookfield, 1998; Chirouze et al., 2012b; Cina et al., 2009; Clark et al., 2004; Liang et al., 2008; Najman et al., 2012; Zeitler et al., 2001).

Several palaeogeographic reconstructions on the rivers of Southeast Asia depict the longitudinal Yarlung Tsangpo in southern Tibet as formerly draining into the palaeo-Red River (Figure 1.2), with progressive uplift and eastward tilting of the Tibetan Plateau driving successive westward capture of the upper reaches of the Mekong, Salween, and the Irrawaddy Rivers (Brookfield, 1998; Clark et al., 2004; Clift et al., 2006a). Previous studies have suggested the Yarlung Tsangpo flowed into the palaeo-Irrawaddy River prior to capture by the Brahmaputra, although the timing of this event is not well constrained (Brookfield, 1998; Clark et al., 2004; Liang et al., 2008). Localized deformation around the eastern syntaxis may have led to one of the last capture events of the Cenozoic, where the ancestral Yarlung Tsangpo-Irrawaddy was truncated by the Brahmaputra River through headward erosion, via the Lhuit, Dibang, and/or Siang Rivers, which is tentatively dated as late Miocene (<10 Ma) (Booth et al., 2009; Booth et al., 2004; Ding et al., 2001), or Pliocene (ca. 4–3 Ma) (Figure 1.2) (Brookfield, 1998; Burg et al., 1998; Clark et al., 2004; Stewart et al., 2008). However, because these studies are based on geomorphologic evidence, the timing of this capture event is unconstrained. Evidence for this capture event in the sedimentary record is under-explored, with investigations into the sediment repositories of the eastern Himalayas utilizing high precision geochronology, thermochronology and geochemistry only recently coming into play. If the characteristics of the source rocks are known and can be linked to those of single grain detrital minerals, it is possible to deduce the timing of major river capture by using provenance methods on the ancient sedimentary record because drainage capture results in the addition or removal of source terranes, changing the composition of the sediment load. Knowledge of the timing of river capture involving, and development of, the modern Yarlung Tsangpo-Brahmaputra

system has implications in modelling tectonic-exhumation-erosion interactions in the eastern syntaxis where either an antecedent system was deformed by development of the Namche Barwa antiform (Burg et al., 1998; Lang and Huntington, 2014; Seward and Burg, 2008) or surface and crustal processes are coupled in a "tectonic aneurysm" model where river incision drives rapid focused exhumation of deeper crustal levels (Stewart et al., 2008; Zeitler et al., 2001).

Figure 1.2 Cenozoic drainage evolution of major rivers in Southeast Asia from pre-Miocene to present day in response to the Himalayan orogeny after Seward and Burg (2008) (Model A) and Clark et al. (2004) (Model B). A) Model A invokes an antecedent Yarlung Tsangpo-Brahmaputra system that experienced progressive distortion within the eastern Himalayan syntaxis region during northward migration and exhumation of the Namche Barwa massif (Lang and Huntington, 2014; Seward and Burg, 2008). A) Dual antecedent systems consisting of the Yarlung Tsangpo-Brahmaputra and the Parlung-Irrawaddy with a hypothesized Early-Middle Miocene capture of the Parlung River from the Irrawaddy River by the Lohit River, a tributary to the Brahmaputra. B, C) Northeastward migration of deformation within the eastern syntaxis led to the anomalous 180° bend observed in the modern Yarlung Tsangpo-Brahmaputra system, and not river capture. Model B attributes the anomalous drainage patterns of SE Asian river systems to river capture and reversal in response to regional surface uplift, with one of the last river capture events involving the loss of the Yarlung Tsangpo from the Irrawaddy River via headward erosion and capture by a tributary to the Brahmaputra during the Late Cenozoic (Brookfield, 1998; Clark et al,. 2004; Liang et al., 2008). D) Pre-Miocene proposed river connections for the Yarlung Tsangpo in Tibet and the upper reaches of the Salween and Mekong as tributaries to the Red River, which formed a single, southeast flowing system empting into the South China Sea (after Clark et al., 2004). E, F) Late Miocene to present day palaeo-river reconstruction of Yarlung Tsangpo-Parlung-Irrawaddy river, and its disconnection and subsequent capture by the Lhuit and the Brahmaputra (after Clark et al., 2004; Brookfield, 1988; Liang et al., 2008). C, F) Present day orientation of the major river systems of the eastern Himalayan syntaxis region, where Burma is internally drained by the Irrawaddy River. Modified from Clark et al. (2004), Lang and Huntington (2014), Liang et al. (2008) and Seward and Burg (2008).

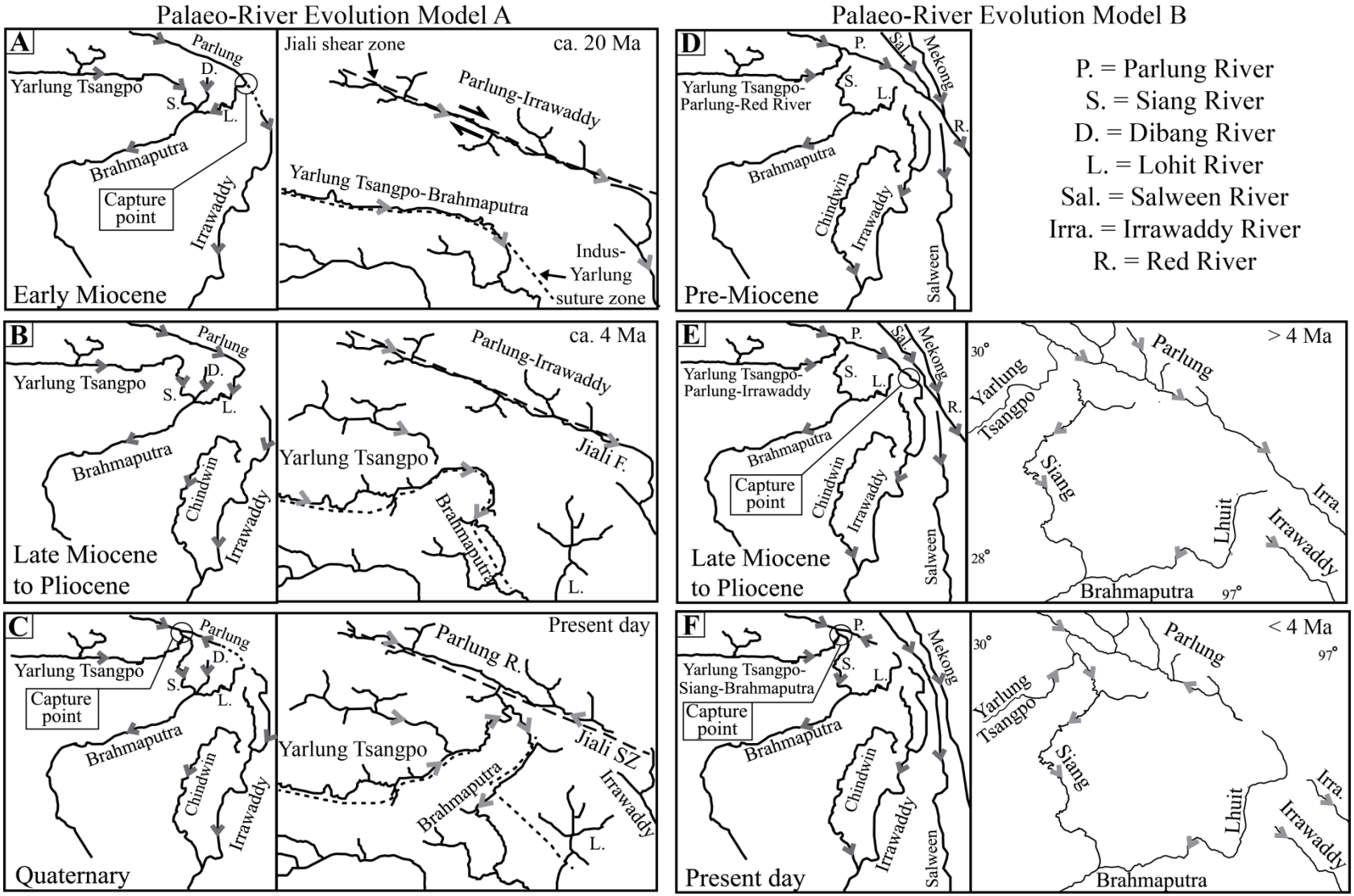
Palaeo-River Evolution Model A
Palaeo-River Evolution Model B
A
Parlung
D.
Yarlung Tsangpo
S.
L.
Brahmaputra
Capture point
Irrawaddy
Early Miocene
Jiali shear zone
ca. 20 Ma
Parlung-Irrawaddy
Yarlung Tsangpo-Brahmaputra
Indus-Yarlung suture zone
D
P.
Sal.
Mekong
Yarlung Tsangpo-Parlung-Red River
S.
L.
R.
Brahmaputra
Chindwin
Irrawaddy
Salween
Pre-Miocene
P. = Parlung River
S. = Siang River
D. = Dibang River
L. = Lohit River
Sal. = Salween River
Irra. = Irrawaddy River
R. = Red River
B
Parlung
D.
Yarlung Tsangpo
S.
L.
Brahmaputra
Chindwin
Irrawaddy
Late Miocene to Pliocene
ca. 4 Ma
Parlung-Irrawaddy
Jiali F.
Yarlung Tsangpo
Brahmaputra
L.
E
P.
Sal.
Mekong
Yarlung Tsangpo-Parlung-Irrawaddy
S.
L.
R.
Brahmaputra
Capture point
Chindwin
Irrawaddy
Salween
Late Miocene to Pliocene
> 4 Ma
30°
Parlung
Yarlung Tsangpo
Siang
Lhuit
Irra.
Irrawaddy
28°
Brahmaputra
97°
C
Parlung
D.
Yarlung Tsangpo
S.
Capture point
L.
Brahmaputra
Chindwin
Irrawaddy
Quaternary
Present day
Parlung R.
Jiali SZ
Yarlung Tsangpo
Brahmaputra
Irrawaddy
L.
F
P.
Mekong
Yarlung Tsangpo-Siang-Brahmaputra
S.
L.
Capture point
Brahmaputra
Chindwin
Irrawaddy
Salween
Present day
< 4 Ma
30°
97°
Parlung
Yarlung Tsangpo
Siang
Lhuit
Irra.
Irrawaddy
Brahmaputra

1.2.2. The use of sedimentary provenance studies in the Himalayas and Southeast Asia

Provenance research is fundamental for understanding palaeo-drainage evolution in the Himalayas since the collision of continental India with Eurasia at the generally accepted age of ca. 55–50 Ma (Brewer et al., 2003; DeCelles et al., 2004; DeCelles et al., 1998; Hodges, 2000; Najman et al., 2010; Najman et al., 2005; Rowley, 1996; Zhu et al., 2005), although ages as old as ~70–65 Ma (Chung et al., 2009; Lee and Lawver, 1995; Mo et al., 2007; Yin and Harrison, 2000; Zhu et al., 2011) and as young as ~35 Ma (Aitchison et al., 2002; Aitchison et al., 2011; Ali and Aitchison, 2008; Davis et al., 2004; Davis et al., 2002) have also been proposed for the timing of India-Asia collision. The latter hypothesis invokes the collision of India with an intra-oceanic arc at ~55 Ma, initial contact of the plate edge with Burma from the Eocene onwards (~55–45 Ma), followed by hard continental collision during the latest Eocene-early Oligocene (Ali and Aitchison, 2008; Davis et al., 2004; Davis et al., 2002; Lee and Lawver, 1995). Provenance studies of the foreland and remnant ocean basin deposits have been used to reconstruct the source to sink pattern of erosion in the Himalayas using high precision geochronology and geochemical analyses (Chirouze et al., 2012a; Chirouze et al., 2012b; Cina et al., 2009; Copeland and Harrison, 1990; Copeland et al., 1990; DeCelles et al., 1998; Garzanti et al., 2007; Henderson et al., 2010; Najman, 2006; Najman et al., 2012; Najman et al., 2008; Najman et al., 2000; Najman et al., 2009; Najman et al., 2005; Najman and Garzanti, 2000; Najman et al., 2003; Najman et al., 2004; Najman et al., 2001; Najman et al., 2002; Najman et al., 1997; Szulc et al., 2006; Uddin et al., 2010; Uddin and Lundberg, 1998b; van der Beek et al., 2006; White et al., 2001; White et al., 2002). Where source rocks have distinct geochronological and geochemical signatures, detrital mineral studies can be used to identify provenance between catchments and record temporal and spatial changes in source area, providing information for palaeo-geographic reconstructions. In recent years, work has focused on understanding the evolution of the Himalayan orogenic belt through studies utilizing thermochronological techniques on rocks in the hinterland to constrain exhumation rates of the different lithotectonic units (DeCelles et al., 2000; Gehrels et al., 2011; Najman, 2006). Early tectono-thermal events may not be preserved in the present-day outcrops of the exhumed orogen due to erosion or over-printing by younger deformation events

and therefore the sedimentary archive may be the only, albeit catchment-integrated, record of exhumation. While numerous studies have focused on characterizing the Cenozoic sedimentary rocks of the Himalayan foreland basin and the sediment routing systems of the western and central Himalayas (Clift and Blusztajn, 2005; Clift et al., 2001; DeCelles et al., 1998; Henderson et al., 2010; Najman, 2006; Najman et al., 2003), relatively little work has been done on characterizing early Himalayan erosion and sediment deposition in the eastern Himalayas.

The single grain geochronometers used in this study record the timing of zircon crystallization at high temperatures (~750^{o}C; zircon U-Pb), cooling at mid-crustal levels (~350^{o}C; ^{40}Ar/^{39}Ar white mica), and exhumation-related cooling at shallow crustal levels (240^{o}C; zircon fission track) in order determine the geodynamic evolution of the source region(s) and assess what controls drainage development. Illite crystallinity is used in conjunction with zircon fission track dating to determine post-depositional re-setting during sedimentary burial in the basin. Using a multi-mineral method ensures a reduction in bias from an interpretation based on a single chronometer.

Chapter 2. Regional geology and evolution of SE Tibet and Burma

The Central Burma Basin consists of a forearc (Western Trough) and backarc (Eastern Trough) region (Figure 2.1, Figure 2.2) formed during northeastward subduction of the Bengal oceanic crust beneath Burma and is comprised of Eocene-Quaternary sedimentary and volcanic rocks (Mitchell, 1993). Seismic reflection data reveal that the basin is composed of a Western Trough with up to fifteen kilometres of Eocene-Pliocene sedimentary rocks, while less than eight kilometres of primarily Miocene-Pliocene rocks overlie the basement rocks of the Burma plate in the Eastern Trough (Bertrand and Rangin, 2003; Pivnik et al., 1998). The Kabaw Fault bounds the Central Burma Basin on the west (Figure 2.1, Figure 2.2) and separates it from the Late Mesozoic-Neogene carbonate and flysch forearc-accretionary prism and plutonic rocks of the Indo-Burman Ranges (Allen et al., 2008; Bender, 1983; Mitchell, 1993). The Mogok Metamorphic Belt and Sibumasu Block border the basin to the east, and south of Mandalay this boundary is clearly defined by the right-lateral Sagaing Fault (Figure 2.1, Figure 2.2). The Mogok Metamorphic Belt occurs as narrow deformational zones (30–40 kilometres wide) between the Central Burma Basin and the Shan Plateau of the Sibumasu block and is bounded by the Slate Belt in northeast Burma (Mitchell et al., 2007). These regions contain intrusive rocks that are part of the Late Jurassic-Eocene magmatic arc which can be traced north through the eastern Himalayan syntaxis and into the Transhimalayan rocks of Tibet (Barley et al., 2003; Chiu et al., 2009; Chu et al., 2006; Liang et al., 2008; Mitchell et al., 2012; Mitchell et al., 2007; Searle et al., 2007; Xu et al., 2012). All of the magmatic arc rocks have similar chronologies, but differing geochemistry: the Gangdese is an I-type batholith, whereas the intrusive rocks of the eastern Transhimalayan, Mogok Metamorphic Belt and western Thailand are predominately S-type (Bertrand et al., 1999; Chiu et al., 2009; Ji et al., 2009a; Mitchell et al., 2007; Searle et al., 2012). The geological history, and geochronological and isotopic signatures, of all the rocks in the Yarlung Tsangpo and Irrawaddy River catchments, and in the Sibumasu Block, will be described in detail below in order to link the regional geology to potential source areas.

2.1. Gangdese Batholith, Southern Lhasa terrane

The generation of latest Triassic to Cretaceous Gangdese arc magmatism is linked to the long-lasting northward subduction of Neo-Tethyan oceanic lithosphere beneath the southern Lhasa terrane prior to the collision of India with Asia (Figure 2.1) (Debon et al., 1986; Ji et al., 2009a; Ji et al., 2009b; Mo et al., 2005; Mo et al., 2009; Wen et al., 2008b; Xu et al., 1985; Yin and Harrison, 2000). Mesozoic magmatism in an Andean-type arc setting occurred in two main stages in the Gangdese Batholith, driven by the northward subduction of Neo-Tethys oceanic lithosphere beneath the southern margin of Eurasia, during the Late Triassic to Late Jurassic (215–150 Ma) and middle Early to middle Late Cretaceous (120–78 Ma) (Chu et al., 2011; Chu et al., 2006; Ji et al., 2012; Ji et al., 2009a; Ji et al., 2009b; Wen et al., 2008a).

The later stage of Mesozoic magmatism is coeval with, and slightly younger than, peak magmatism in the northern Lhasa magmatic belt (ca. 135–100 Ma) that has been attributed to either crustal thickening (Chu et al., 2011; Chu et al., 2006) or back-arc extension (Zhu et al., 2011, 2009b) following the Lhasa-Qiangtang continental collision, and regional crustal shortening on the scale of 47–60% (Kapp et al., 2007b; Murphy et al., 1997). This led to significant thickening of the crust and elevation gain via a southward propagating thrust-and-fold belt in the northern Lhasa terrane (Kapp et al., 2005) and a northward propagating thrust-and-fold belt in the central-southern Lhasa terrane, the retro-arc region of the Gangdese Batholith (Kapp et al., 2007; Pullen et al., 2008; Leier et al., 2007a,b). The duration of thrusting in the retro-arc region is constrained by the maximum depositional age of the Takena Formation (ca. 90–80 Ma), which was likely incorporated into the fold-and-thrust belt (Leier et al., 2007; Pullen et al., 2008).

Late Cretaceous granitoids with adakitic geochemical features recorded in the southeastern Gangdese arc accompanied the waning stages of Mesozoic magmatism, and coeval high temperature, medium pressure granulite-facies metamorphism (ca. 90 Ma) has been attributed to the upwelling of asthenosphere following subduction of a mid-ocean ridge segment that created a tear in the subducting slab (‘slab window’) (Zhang et al., 2010b; Zhang et al., 2010c), or from roll-back of the subducted Neo-Tethyan slab (Ma et al., 2013). This is followed by a ~10 Ma magmatic quiescence in

the Gangdese Batholith, attributed to the flattening of the angle of the subducting Neo-Tethys oceanic slab (Wen et al., 2008a; Wen et al., 2008b). Flab slab subduction may have driven, or enhanced the crustal shortening observed in the Lhasa terrane during this magmatic gap (ca. 80–70 Ma) (Murphy et al., 1997; Wen et al., 2008a; Yin and Harrison, 2000), as evidenced by the folding of the Cretaceous Takena Formation, with a maximum depositional age of ca. 90–80 Ma (Leier et al., 2007a), uplift and erosion prior to deposition of the widespread, flat-lying Palaeogene Linzizong volcanic succession from ~69 Ma to at least 43 Ma (Figure 2.1) (He et al., 2007; Lee et al., 2009; Mo et al., 2008; Zhou et al., 2004).

2.2. Mesozoic Gangdese magmatism recorded in the Xigaze forearc basin

Cretaceous to earliest Palaeocene (ca. 116–65 Ma) sedimentary rocks of the Xigaze Group, consisting mainly of turbiditic volcaniclastic sandstones, were deposited in an east-west trending forearc basin that developed along the southern margin of Eurasia during the northward subduction of Neo-Tethys oceanic crust, prior to the collision of continental India (Figure 2.1, 2.3) (Aitchison et al., 2011; Dürr, 1996; Wu et al., 2010). Detrital zircon data from this strata reveals a wide range of ages from 3,184 ± 10 Ma to 72 ± 2.1 Ma (Aitchison et al., 2011; Wu et al., 2010), but primarily middle Early to middle Late Cretaceous (130–80 Ma) and subordinately Jurassic (190–150 Ma) ages. Zircons are characterized by high, positive εHf(t) values, and are interpreted to be sourced from the Gangdese arc that experienced significant uplift, denudation and erosion during the time of fore-arc deposition (Wu et al., 2010). Overall, Mesozoic ages dominate (75% of total population) and older Proterozoic to Palaeozoic ages make up only a quarter of the total population. The main stage of deposition (~107–84 Ma) in this region is marked by an increase in detritus with a northern Lhasa provenance after ~101 Ma, where the number of zircons of Palaeozoic to Proterozoic age, and those of Mesozoic age associated with negative εHf(t) values (from Palaeozoic cover strata, Cretaceous back-arc foreland basin sedimentary rocks and Mesozoic granitoids in the back-arc region) are observed. This is possibly due to the development of south-ward flowing river systems that cut across the uplifted Gangdese arc, linking the northern Lhasa terrane to the Xigaze fore-arc basin (Wu et al., 2010).

The Gangdese arc formed a topographic high (at least locally) separating the fore-arc (south) and retro-arc (north) basins, and the Takena Formation was deposited in the retro-arc basin until ca. 90–80 Ma, primarily sourced from the Gangdese arc. This supports the proposition that the arc was actively undergoing erosion during Cretaceous to earliest Palaeogene time (Aitchison et al., 2011; He et al., 2007; Leier et al., 2007a; Leier et al., 2007b; Pullen et al., 2008; Wu et al., 2010).

2.3. Geodynamic setting for Palaeocene-Eocene Gangdese magmatism

Continuous magmatism in the southern Lhasa terrane occurred during Palaeocene to Eocene time (ca. 65–34 Ma), with increasing neodymium and hafnium enrichment of source melts, expressed in the bimodal distribution of εNd(t) and εHf(t) isotopic values observed in Early to Middle Eocene-aged granitoids (Chu et al., 2011; Chu et al., 2006; Ji et al., 2012; Ji et al., 2009a; Ji et al., 2009b; Mo et al., 2005; Mo et al., 2009; Wen et al., 2008b; Zhang et al., 2010a) and the majority of zircons display εHf(t) values greater than +6.

Following approximately 10 Ma of magmatic quiescence, the Gangdese Batholith experienced continuous magmatism from ca. 65 to 35 Ma (Chu et al., 2011; Chu et al., 2006; Guan et al., 2012; Ji et al., 2012; Ji et al., 2009a; Ji et al., 2009b; Mo et al., 2009; Mo et al., 2005; Wen et al., 2008b; Zhang et al., 2010a). The most voluminous period of magmatic activity in the Gangdese Batholith occurred during earliest Palaeocene to middle Eocene time (ca. 65 to 41 Ma), with a peak age at ca. 50 Ma, as determined by zircon U-Pb dating of igneous rocks of the southern Lhasa terrane (Chu et al., 2011; Chu et al., 2006; Guan et al., 2012; Ji et al., 2012; Ji et al., 2009a; Ji et al., 2009b; Mo et al., 2009; Mo et al., 2005; Wen et al., 2008b; Zhang et al., 2010a). The increased intensity of magmatism and southward migration of volcanism at this time is inferred to record roll back of the (flat lying) subducting Neo-Tethys oceanic slab, rollback, and subsequent break-off commencing with the onset of the India-Eurasia continental collision, coincident with peak magmatic activity at ca. 50 Ma (Ji et al., 2009a; Ji et al., 2009b; Wen et al., 2008a).

“Large variation in εHf(t) values” indicates magma mixing between juvenile, mantle-type melts typical of those producing Mesozoic Gangdese granitoids and ancient

continental crust of either the Indian continental crust (Ji et al., 2009b) or the Lhasa terrane basement (Mo et al., 2009). As this signature coincides with the arrival of the Indian continent to close proximity of the Asian continent, and evidence of contributions of Lhasa basement to the melt source is lacking during the previous ~145 Ma of magmatism, this variation in εHf(t) is most likely the result of the incorporation of Indian sediment along the leading edge of the plate into the subduction zone (Chu et al., 2011).

The majority of magmatic zircons from igneous rocks of the Gangdese Batholith are characterized by high, positive εHf(t) values, suggesting melts were generated from a depleted mantle source of Phanerozoic age (Chu et al., 2011; Ji et al., 2012; Ji et al., 2009b; Mo et al., 2005; Mo et al., 2009; Mo et al., 2007). Eocene igneous rocks with adakitic geochemical affinities, together with a marked enrichment in radiogenic hafnium observed in plutons formed at this time, is interpreted as indicating the presence of thickened crust in the southern Lhasa terrane at this time (Ji et al., 2012). The oldest adakite identified has an age of ~51 Ma, suggesting a thickened crust beneath the southern Lhasa terrane was present, at least locally, as early as the Early Eocene (Ji et al., 2012).

2.4. Oligocene-Miocene postcollisional adakites, potassic and ultrapotassic rocks

Post-collisional Oligocene to Middle Miocene porphyritic, adakitic and potassic to ultra-potassic igneous rocks were emplaced in low volumes as dykes, stocks and sills throughout the southern Lhasa terrane and contain zircons dominated by juvenile, mantle-derived Hf isotopic values (εHf(t) values of +2 to +12), similar to those observed in Palaeogene Gangdese magmatic rocks (Chung et al., 2009; Chung et al., 2005; Guo et al., 2011; Guo et al., 2012; Ji et al., 2009a; Ji et al., 2009b; Zhang et al., 2010a; Zhou et al., 2010). In the southern Lhasa terrane, generation of these late stage magmas are attributed to partial melting of a basaltic lower crust, possibly driven by heating from asthenospheric upwelling following the removal of the lithospheric root beneath the southern Lhasa terrane (Chung et al., 2009; Chung et al., 2005; Guan et al., 2012). Felsic magmatism in southeast Tibet is attributed to the diachronous break-off of the subducted Indian continental slab initiating in the eastern Himalayan syntaxis region during the Oligocene (ca. 30–24 Ma), roughly coeval with Late Oligocene to Early

Miocene exhumation-driven, retrograde amphibolite-facies metamorphism and anatectic melt production recorded by zircons of Asian plate metasedimentary and metaigneous rocks north of Namche Barwa (Dong et al., 2010; Guo et al., 2011; Pan et al., 2012; Xu et al., 2013; Xu et al., 2010; Zhang et al., 2008; Zhang et al., 2010a; Zhang et al., 2010c).

2.5. Magmatic belts of the Namche Barwa syntaxis, southeast Tibet, western Yunnan and eastern Burma

In the easternmost part of the Lhasa terrane in southeast Tibet, northwest-southeast trending granitoid plutons of the eastern Transhimalayan batholiths intrude meta-sedimentary rocks and are associated with the Ranwu volcanic strata that outcrop north and east of the Namche Barwa syntaxis, north of the Indus-Yarlung suture zone (~ 95 to 97.5°E and ~30.25 to 28.5°N); they are composed primarily of monzogranites, granodiorites and granites (Figure 2.1, Figure 2.2) (Booth et al., 2004; Chiu et al., 2009; Lee et al., 2009; Liang et al., 2008; Lin et al., 2012; Lin et al., 2009). The batholiths are traditionally sub-divided into three geographical regions: (1) granitoids of the Tungmai-Bomi-Ranwu area that extend from directly north of the Namche Barwa syntaxis and outcrop immediately north of the Jiali shear zone and its north-eastern splay, the Parlung Fault, (2) granitoids of the Basu-Ranwu transect which extend from the Jiali Fault at Ranwu northward towards Basu and the projected continuation of the Bangong-Nujiang suture around the eastern Himalayan syntaxis, and (3) the most south-eastern plutons of the Chayu-Shama region are exposed along the Parlung Fault (Figures 2.1, 2.2). As the plutons are contemporaneous and share similar geochemical characteristics, granites of this region are discussed collectively and termed the ‘eastern Transhimalayan batholiths’ for the duration of this thesis.

In situ U-Pb and Hf isotopic analyses of magmatic zircon from the eastern Transhimalayan batholiths indicate two main stages of emplacement, primarily during the Early Cretaceous (ca. 132–110 Ma) and subordinately during the Palaeocene (ca. 65–56 Ma). One granite of Lower Jurassic (ca. 197 Ma) age, characterized by predominantly negative zircon εHf(t) values, is indicative of melting of older continental crust to produce S-type granitoids (Booth et al., 2004; Chiu et al., 2009; Liang et al., 2008; Zhu et al., 2009c). This is consistent with the presence of minor

inherited zircons yielding early Mesozoic, Palaeozoic and Neoproterozoic U-Pb ages, that likely reflect re-melting of Palaeozoic cover strata and Proterozoic basement of the northern Lhasa terrane, during crustal thickening following Jurassic-Early Cretaceous continental collision between the Lhasa and Qiangtang terranes (Chiu et al., 2009; Chu et al., 2006; Zhu et al., 2011, 2009b). Zircons of Cretaceous granitoids display a general trend towards zircons that are less enriched in radiogenic hafnium through time; ~124 Ma deformed granites or gneiss record the most negative values and ~110 Ma granitoids have less negative εHf(t) values (Chiu et al., 2009; Liang et al., 2008; Zhu et al., 2009c). Isotopic diversion towards less radiogenic hafnium values during peak magmatism (~110 Ma) is also observed in the northern Lhasa magmatic belt, suggesting the eastern Transhimalayan batholiths represent the eastern continuation of this granite belt around the eastern Himalayan syntaxis (Chiu et al., 2009; Chu et al., 2011; Chu et al., 2006; Liang et al., 2008; Zhang et al., 2012c; Zhu et al., 2009b; Zhu et al., 2011). Whole-rock Sr-Nd isotopic analyses on a sub-set of these same plutons are consistent with zircon Hf isotope compositions, where the majority of granitoids were generated by the re-melting of older continental crust with εNd(t) values of -7.1 to -12.7, and initial $^{87}Sr/^{86}Sr$ ratios between 0.7089 and 0.7274. Two plutons from the Chayu-Shama region contain zircons with less radiogenic Hf an also contain less radiogenic Nd, with εNd(t) values of -3.6 and -4.0 and initial Sr ratios of 0.7029 and 0.7115 (Lin et al., 2012).

A north-south trending belt of Early Cretaceous to Tertiary granitoids intrude Proterozoic metamorphic basement and Late Palaeozoic sedimentary and carbonate rocks in the Gaoligong-Tengliang-Yingjiang area, along the border of western Yunnan, China and northeast Burma, and are bounded to the east by the Cenozoic Gaoligong shear zone (Figure 2.1, Figure 2.2) (Liang et al., 2008; Ma et al., 2014; Xu et al., 2012; Xu et al., 2008). Zircon U-Pb dating of these magmatic rocks reveals a younging of magmatism from northeast to the southwest, towards the Neo-Tethyan oceanic realm (Liang et al., 2008; Xu et al., 2012). Early Cretaceous granites of the Gaoligong area (Gongshan-Lushi area) are composed of S-type, peraluminous biotite- and muscovite-bearing monzogranites, granodiorites and local leucogranites (Xu et al., 2012; Xu et al., 2008). *In situ* U-Pb and Hf isotopic analyses of magmatic zircon extracted from four

samples indicate granitoids were emplaced in the Gaoligong area during the Early Cretaceous (ca. 135–109 Ma) and Late Cretaceous (~84–64 Ma) and yield predominately negative zircon εHf(t) values (Liang et al., 2008; Xu et al., 2012).

In the Tengliang area to the southwest, Late Cretaceous granites were emplaced mainly from ~76–66 Ma and subordinately from ~86–80 Ma, intruding Late Palaeozoic sediments and Proterozoic metamorphic basement (Liang et al., 2008; Xu et al., 2012). Hf isotopic analysis of magmatic zircons extracted from these granitoids record exclusively negative εHf(t) values, similar to the isotopic composition observed in the Gaoligong belt, and thus represents the southwest continuation of S-type magmatism, migrating towards the Neo-Tethyan oceanic realm during the Early to Late Cretaceous.

The youngest magmatism observed in this region is represented by Latest Cretaceous to Early Eocene granites exposed in the Yingjiang area, and these intrude mostly Proterozoic metamorphic basement. They also represent the farthest south and west of the granites dated in this area. There is some spatial variation in lithology as the eastern Yingjiang has similar petrography to Gaoligong and Tengliang areas and strong peraluminous affinity, while western Yingjiang is composed of I-type granites, meta- to peraluminous, and a number of gabbroic intrusions (Ma et al., 2014; Xu et al., 2012; Xu et al., 2008).

2.6. Cenozoic conglomerates in the Indus Yarlung suture zone

The deposition of the Palaeogene (~54 Ma; maximum depositional age) Liuqu and Oligo-Miocene Gangrinboche fluvial conglomerates along the Indus Yarlung suture zone suggests a proximal source terrane of significant relief existed along the southern margin of the Lhasa terrane at this time (Figure 2.3) (Aitchison et al., 2002; Aitchison et al., 2011; Davis et al., 2004; Wang et al., 2013). Davis et al. (2002) used detailed stratigraphic studies and clast petrography to conclude sediment of the Palaeogene Liuqu Conglomerate was deposited within an oblique strike-slip basin along the southern margin of an intra-Neotethys ocean island arc, sourced from the northern margin of the Indian continent, as no Gangdese-derived detritus sourced from north of the Indus Yarlung suture zone is observed. Alternatively, Wang et al. (2010) utilized petrographic, U-Pb and Lu-Hf isotopic analyses on detrital zircons of this formation to

postulate both Asian and Indian sources contributed to the Liuqu Formation, and interpreted the formation as synorogenic Palaeogene (Middle Eocene) molasse. Late Cretaceous to Triassic zircons with positive εHf(t) values are interpreted to be derived from sediment recycling of the Xigaze forearc basin, containing detritus sourced entirely from the Gangdese Batholith (Wu et al., 2010), while Cretaceous zircons with negative εHf(t) values are interpreted as being sourced from the Tethyan Himalaya or the northern Lhasa terrane, and Triassic to Proterozoic zircons are thought to have been derived from the Triassic Langjiexue Group of northern Lhasa and the Tethyan Himalaya (Wang et al., 2010).

Based on a mismatch between the zircon U-Pb ages of the potential source terrane with that of detrital zircons from the Liuqu Conglomerate, Aitchison et al. (2011) suggested that sediments of the Xigaze forearc basin were sourced from rocks of the eastern Himalaya and Burma and were translated westward to its present position along an oblique, dextral forearc sliver during the Late Cretaceous to Eocene. Additionally, they suggest conglomeratic units, now south of the Xigaze terrane, were deposited along the margins of an intra-oceanic island arc that collided with India at ca. 55 Ma, prior to collision with Asia at ca. 35 Ma (Aitchison et al., 2011). The Lhasa terrane achieved significant uplift prior to, or during, the deposition of conglomeratic strata on the southern Lhasa terrane, either due to the initiation of Tertiary thrusts and/or uplift generated by slab breakoff of the down going Neotethyan oceanic lithosphere at ca. 50 Ma. Additional support for Palaeocene-Eocene Neotethyan slab roll-back and breakoff at this time comes from the coeval peak in magmatism and volcanism in the southern Lhasa terrane at 50 Ma, with geochemical evidence for crustal thickening within Palaeogene granitoids (He et al., 2007; Ji et al., 2012; Ji et al., 2009a; Ji et al., 2009b; Lee et al., 2009; Mo et al., 2008; Wen et al., 2008b; Zhang et al., 2010a), onset of fast cooling of the Gangdese Batholith at ca. 42 Ma (Dai et al., 2013; He et al., 2007), and emplacement of mafic intraplate dykes within the Gaoligong-Tengliang belt at roughly 42–40 Ma (Ma et al., 2014; Xu et al., 2008). Isostatic uplift following slab breakoff was likely the driver for rapid exhumation of rocks of the southern Lhasa terrane, and subsequent rapid erosion and proximal deposition.

The Upper Oligocene to Lower Miocene Gangrinboche conglomerates outcrop north of the Indus Yarlung suture zone in a narrow, east-west trending belt stretching over 2,000 kilometres, indicating a regional mechanism for creating significant relief along the southern Lhasa terrane at this time (Figure 2.3). These conglomeratic sedimentary units were collectively termed the Gangrinboche conglomerates by Aitchison et al. (2002), and include the locally named Qiuwu and Dazhuka Formations of other works (e.g. Davis et al., 2004; Davis et al., 2002; Wang et al., 2013). Although previous studies suggest a tectonic contact between the Oligocene to Miocene conglomerates and rocks of the Lhasa terrane (south-directed Gangdese Thrust) (Yin and Harrison, 2000; Yin et al., 1994), Aitchison et al. (2003) reports these conglomerates were deposited unconformably onto an erosion surface of igneous rocks of the Gangdese Batholith, and mylonites within the shear zone actually record a strong regional foliation within the Mesozoic strata of the Lhasa terrane. Initial interpretations based on detailed stratigraphic and petrographic studies suggests these sediments represent molasse, with a change from a northern Lhasa terrane source to increasing contributions from the Yarlung Tsangpo suture zone and continental India to the south up-section, invoking an Oligocene-Early Miocene age of collision, consistent with the interpretations of Davis et al. (2002) for the Liuqu Conglomerate (Aitchison et al., 2002). These sediments were laid down by an axial braided river (palaeo- Yarlung Tsangpo), running parallel to the east-west strike of the Himalayan orogen (Aitchison et al., 2002; Aitchison et al., 2011).

Based on conglomerate and sandstone petrology, detrital Cr-spinel geochemistry, detrital zircon geochronology and palaeocurrent data from the Qiuwu and overlying Dazhuka formations sampled ~10–40 kilometres west of Xigaze, Wang et al. (2013) inferred a change in source provenance from a solely northern Gangdese Batholith source during deposition of the Qiuwu Formation to mixed Indian (including Indus Yarlung suture zone) and Asian detritus with west-ward directed palaeoflow, appearing at the base of the Dazhuka Formation. They interpreted this change in provenance and palaeocurrent direction from south-flowing to west-flowing during deposition of the lowermost Miocene member of the Dazhuka Formation to record the initiation of a W-NW-flowing palaeo-Yarlung Tsangpo at ~23 Ma (Wang et al., 2013). However, the palaeocurrent, detrital Cr-spinel geochemistry and detrital zircon geochronology used in

the Wang study may be interpreted differently, and calls into question the conclusions reached in this study, particularly when the syn-depositional (Oligo-Miocene) regional tectonic history of the southern Lhasa terrane in taken into consideration. First, the palaeocurrent data do not provide strong support for determining palaeoflow as they are highly variable (Chirouze et al., 2012b; Wang et al., 2013) and the method used to measure the orientation of cross bedding, as described by DeCelles et al. (1983), requires between 15–30 measurements from each outcrop to determine the palaeoflow direction (error of +/- 25°) and assumes symmetric infilling. The Wang et al. (2013) dataset is small and the conglomeratic nature of the sedimentary infill, combined with the scoured contact with the underlying Gangdese Batholith, is problematic in determining the true palaeo-flow direction of the entire system, and instead may reflect local tectonics. Detrital Cr-spinel geochemistry also does not discriminate between the Indus Yarlung Suture Zone and Xigaze forearc strata derivation, as grains are widely overlapping, and not concentrated within one specific field. Detrital zircon geochronology shows age distributions similar to the Xigaze forearc basin and Gangdese Batholith are prominent in all formations. A significant change in the detrital zircon age distribution is observed in the middle Deri Member of the Dazhuka Formation, where ages younger than 75 Ma are no longer a significant population (loss of source terrane with 60–40 Ma ages and a peak at 50 Ma) and Palaeozoic-Proterozoic ages are more common, likely sourced from the Xigaze forearc basin and Tethyan Himalaya, respectively (Wang et al., 2013).

2.7. Cenozoic Tectonics and Exhumation of the Lhasa terrane

The southernmost part of the Asian Lhasa terrane, outcropping north of the Indus-Yarlung suture zone, is dominated by the Jurassic to Tertiary Gangdese magmatic arc and associated flat-lying Cretaceous to Palaeogene volcanic-volcaniclastic Linzizong Formation. The latter are separated by a regional angular unconformity from the underlying folded Cretaceous Takena fore-arc and older sedimentary and metasedimentary rocks of the Lhasa terrane (Lee et al., 2009; Leier et al., 2007a; Mo et al., 2008). The majority of deformation in the Lhasa terrane pre-dates the Himalayan orogeny, and is related to Meso-Tethys ocean closure and continent-continent collision between the Qiangtang Block to the north and the Lhasa terrane during the late Jurassic

to early Cretaceous (Kapp et al., 2005b) and far-field affects of this collision during the Cretaceous to Palaeocene (Kapp et al., 2007a; Kapp et al., 2007b).

This region underwent episodes of rapid uplift and significant erosion intermittent with extended periods of slow cooling and differential exhumation. Following the latest Jurassic-early Cretaceous collision between the Qiangtang and Lhasa terranes, Late Cretaceous to earliest Tertiary upper crustal shortening of Palaeozoic-Mesozoic strata of the southern Lhasa terrane is recorded by strongly folded bedding, overlain unconformably by the flat-lying Linzizong volcanic succession dated using $^{40}Ar/^{39}Ar$ on mica and zircon U-Pb at 69 to 47 Ma (He et al., 2007; Lee et al., 2009; Zhou et al., 2004). Additionally, significant Late Cretaceous-Palaeogene exhumation and erosion is indicated by the deposition of the Xigaze Group fore-arc sediments and coeval Takena Formation retro-arc, or back-arc, sediments, derived from the Gangdese pluton, at this time (Aitchison et al., 2011; Dürr, 1996; Leier et al., 2007a; Wu et al., 2010). The majority of crustal shortening in the Lhasa terrane occurred prior to the Cenozoic (Yin, 2010).

2.8. Regional geology and plate tectonic evolution of Burma

2.8.1. Introduction and plate boundaries

Burma lies along the eastern margin of the active India-Asia collision zone, where the generally east-west striking structures of the Himalaya and southern Tibet bend around the eastern Himalayan syntaxis and continue through Burma striking north-south. It occupies an area of transition between active continent-continent collision in the Himalayas, extension in the Andaman Sea spreading center to the south, and active subduction of the Indian oceanic crust beneath Southeast Asia in the Andaman-Nicobar-Sumatra trench to the south and west. The geology of Burma is largely controlled by pre-Himalayan terrane amalgamation forming Southeast Asia and the subsequent interaction between the India and Eurasia plates and the Burma micro-plate during the on-going India-Asia collision. The tectonic evolution of Burma occurred in two main stages: Mesozoic to Early Cenozoic subduction related arc magmatism, followed by events directly or indirectly related to the collision of India with the southern margin of Asia in the early Eocene (Mitchell, 1981, 1989).

Structurally, Burma can be subdivided into an Eastern Province lying on the western margin of the Sibumasu continental block and a Western Province lying on the West Burma Block (or micro plate), generally bounded to the east by the dextral strike-slip Sagaing Fault. Burma is traditionally divided into three geological provinces, which from east to west are: the Sibumasu terrane, comprised of the Shan Plateau, Slate Belt and the Mogok Metamorphic Belt, and the Central Burma Basin and the Indo-Burman Ranges to the west located on the west Burma block (Figure 2.1, Figure 2.2). Present day active plate boundaries include the hyper-oblique eastward subduction of Indian oceanic crust along the Andaman-Sumatra subduction zone and the accommodation of northward movement of the coupled India-west Burma block along the dextral strike-slip Sagaing Fault. The western-most boundary is delimitated by the northern continuation of the Andaman-Sumatra trench, where the east-dipping Indian Plate is currently subducting at a hyper-oblique angle beneath Burma. The generally north-south trending Cenozoic sedimentary basins of western Burma formed as a result of oblique north-eastward subduction of the Indian oceanic crust beneath Burma and subsequent multi-plate deformation, resulting in a regional extensional regime (Bertrand and Rangin, 2003; Bertrand et al., 2001; Bertrand et al., 1999; Mitchell, 1993; Pivnik et al., 1998). These Late Cretaceous to Quaternary sedimentary and volcanic successions of western Burma are bounded to the east by the roughly north-striking Mogok Metamorphic Belt and dextral strike-slip Sagaing Fault, which connects with the Andaman Sea spreading center in the south, to the west by the uplifted Palaeogene to Neogene Indo-Burman Ranges and, further east, an oblique subduction zone, and to the north by the east-northeast striking Lohit Thrust (Allen et al., 2008; Bender, 1983 ; Bertrand et al., 2001; Mitchell, 1993; Pivnik et al., 1998). The Central Burma Basin is divided into a narrow back-arc basin, or Eastern Trough, and a fore-arc basin, or Western Trough, separated by a sporadically active magmatic arc of mid-Cretaceous to Recent age (Bertrand and Rangin, 2003; Mitchell et al., 2012; Mitchell, 1993; Pivnik et al., 1998; Stephenson and Marshall, 1984).

The proximity of Burma to the Himalayan orogen has led to indications of a link between sedimentation and the uplift of the Himalayas and Tibet (Hall, 2009). Draining central and western Burma, the roughly 2,010 kilometre long Irrawaddy River and its

main tributary, the Chindwin River, have a catchment area covering 415,700 km^2 and 114,000 km^2, respectively (Bender, 1983 ; Robinson et al., 2007). The approximately 2800 kilometre long Salween River flows through the Sino-Burman Ranges of eastern Burma and has a drainage area of 272,000 km^2. The combined modern Irrawaddy-Salween river system of Burma is considered to supply one-fifth of the total sediment flux from the Himalayan orogen (Robinson et al., 2007). The headwaters of the Irrawaddy River is located near the eastern Himalayan syntaxis, and drains metamorphic and intrusive rocks of the Mogok Metamorphic Belt, Proterozoic to Cretaceous sedimentary succession of the Shan Plateau region, Triassic to Neogene sedimentary rocks of western Burma and Cretaceous and Quaternary arc plutons (Allen et al., 2008; Mitchell et al., 2007). Sources within the Irrawaddy catchment include the mostly Cretaceous-Palaeocene granitoids of the eastern Transhimalayan batholiths, Gaoligong-Tengliang belt in western Yunnan (Chiu et al., 2009; Liang et al., 2008; Xu et al., 2012) and granitoids intruded along the Mogok Metamorphic Belt (Barley et al., 2003; Cobbing et al., 1986; Mitchell et al., 2012; Searle et al., 2007; Searle et al., 2012). High temperature Palaeogene metamorphism affected rocks of the Mogok Metamorphic Belt (Barley et al., 2003; Searle et al., 2007), however, $^{40}Ar/^{39}Ar$ biotite, muscovite and phlogopite cooling ages indicate these rocks were not exhumed until 27 Ma in the south and 16 Ma in the central-north Shan Scarps (Bertrand et al., 2001; Bertrand et al., 1999).

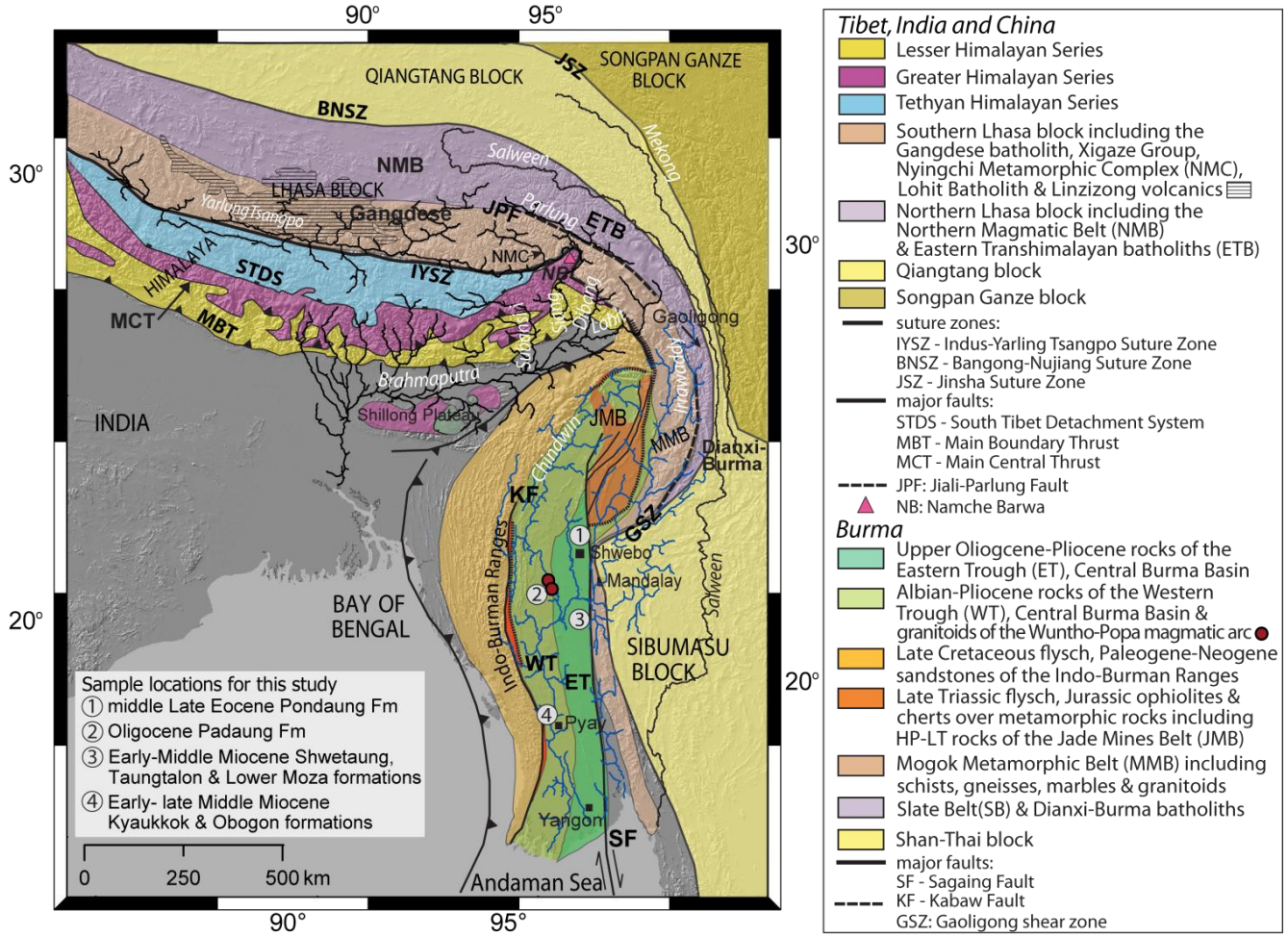

Figure 2.1 Geological map of the eastern Himalayan region and Burma. Modified from Robinson et al. (2014). Detailed geological map of the sampling localities (labelled 1-4) for the Eocene, Oligocene and Miocene sedimentary samples analyzed in this study and stratigraphic relationships are given in Figure 3.1.

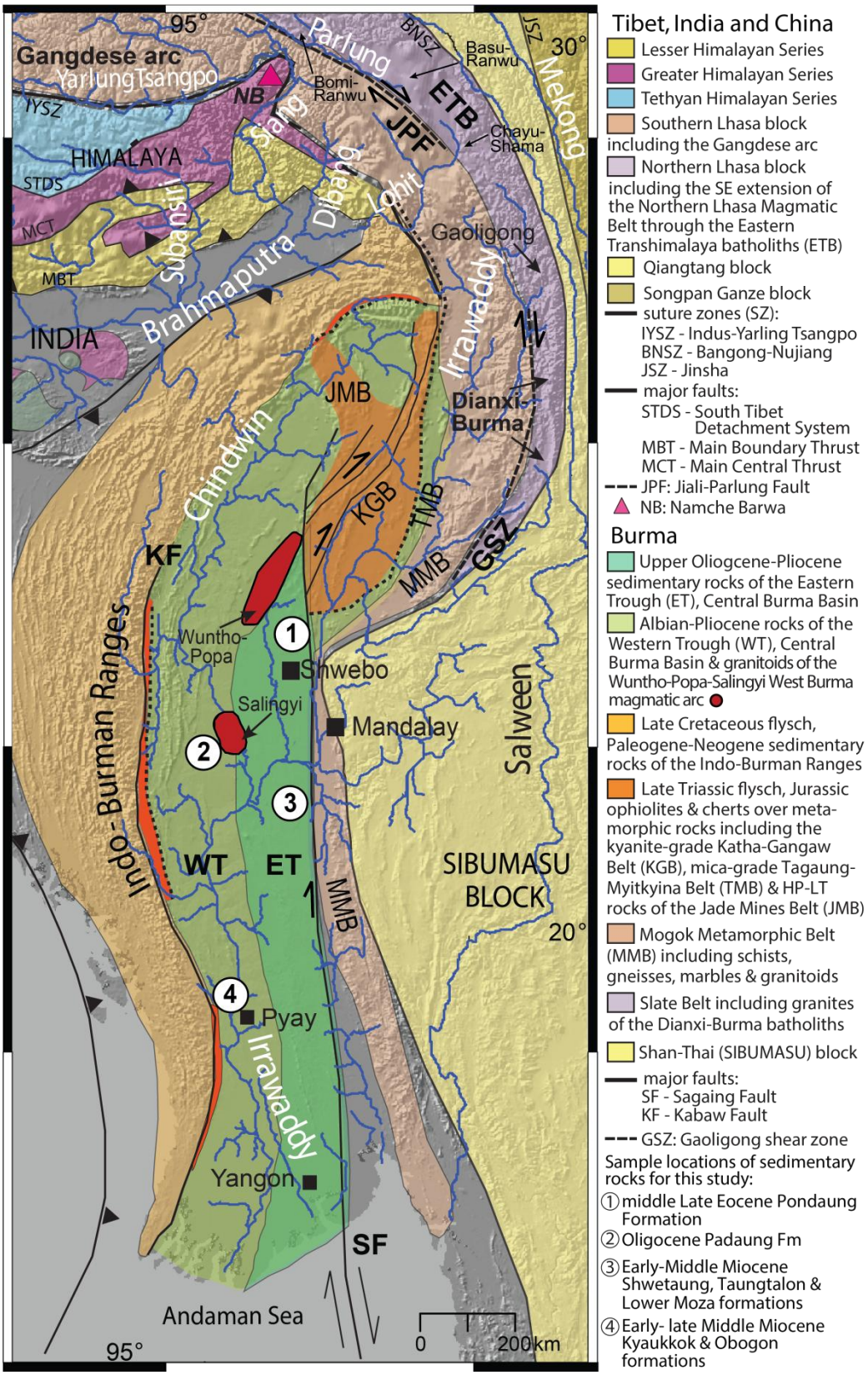

Figure 2.2 Detailed geological map of the eastern Himalayan region and Burma, focused on the study area. Modified from Robinson et al. (2014). Sampling localities (labelled 1-4) for the Eocene, Oligocene and Miocene sedimentary samples analyzed in this study.

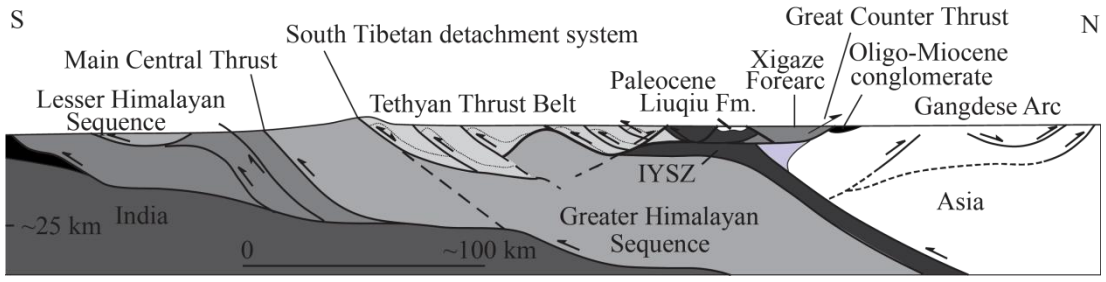

Figure 2.3 Schematic north-south cross-section of the Himalayan front showing major geological units and structural boundaries. IYSZ = Indus Yalung suture zone. After Carrapa et al. (2014) and Yin and Harrison (2000).

2.8.2. Pre-Cenozoic Geology and Tectonics of Eastern Burma (Sibumasu terrane)

The eastern province of Burma is part of the Sibumasu continental block (Barber et al., 2005; Metcalfe, 2002; Metcalfe, 2011) which extends east and south into western Thailand, western Malaysia and eastern Sumatra and is thought to be continuous with the Qiangtang block of central Tibet to the north around the eastern syntaxis (Barber et al., 2005; Metcalfe, 2011). The western margin of the Sibumasu terrane occupies the eastern province of Burma and is comprised of Proterozoic, Palaeozoic and Mesozoic sedimentary units of the Shan Plateau, Slate Belt and the Mogok Metamorphic Belt which experienced a complex thermal history with multiple Mesozoic to Cenozoic metamorphic and magmatic events. The block is derived from the India-Australian margin of north-west Gondwana, characterized by Late Palaeozoic Gondwana biotas and Late Carboniferous to Early Permian glacial-marine diamictites (Metcalfe, 2000; Metcalfe, 2011; Mitchell et al., 2007). Early to Middle Permian rifting associated with the opening of the Meso-Tethys ocean resulted in separation of the block from Gondwana, followed by its northward migration and eventual collision with Indochina in the Early (Metcalfe and Irving, 1990; Mitchell, 1989, 1993) or Late Triassic (Metcalfe, 2011). The eastern margin of the block is bounded by the Changning-Menglian, Chiang Mai/Inthanon and Bentong-Raub suture zones in China, Malaysia and Thailand, respectively, separating continental Sibumasu from closed back-arc basin terranes accreted to Indochina in the Late Permian, which mark the final closure of the Devonian to Middle Triassic Palaeo-Tethys ocean (Metcalfe, 2000, 2002; Metcalfe, 2009, 2011; Sone and Metcalfe, 2008). Microplate convergence and final suturing between Sibumasu and Indochina occurred in the Middle to Late Triassic (250–200 Ma)

resulting in the Indosinian orogeny, responsible for the generation of Permo-Triassic S-type granite belts of Cobbing et al. (1986) throughout Southeast Asia (Searle et al., 2012). U-Pb zircon data from the metamorphic basement of Vietnam shows an episode of ductile deformation and metamorphism caused by the accretion of Sibumasu to Indochina between 258 ± 6 Ma and 243 ± 5 Ma (Carter et al., 2001). The suture zone continues northward as the Lancangjiang suture zone in Tibet marking the northern boundary of the Qiangtang block, however, it is not identified around the eastern syntaxis.

2.8.3. Shan Plateau and Slate Belt

The Shan Plateau is a region of uplift extending from eastern Burma into western Thailand with maximum elevations of 1,500 meters (Figure 2.1, Figure 2.2) (Morley, 2009). Here, a succession of predominantly Cambrian to Devonian carbonate sequences structurally overlie metamorphic rocks of the Chaung Magyi Group (Mitchell, 1993; Mitchell et al., 2007) of possible Triassic age, and are unconformably overlain by Permian to Triassic Plateau Limestones. The Chaung Magyi Group is overlain by undeformed Upper Jurassic-Lower Cretaceous red beds. Apatite fission track data from similar red beds in northern Thailand show metamorphism of the Chang Magyi Group pre-dates the maximum burial age between 70 and 50 Ma (Searle et al., 2007). The Slate Belt includes Carboniferous to Lower Permian sedimentary rocks of the Mergui Group (Mitchell, 1992, 1993) which contain Gondwana glacial-marine diamictites and lies west of the Shan Plateau, extending from Mandalay to the south, continuous with the Mergui Group of offshore Thailand and Sumatra (Barber et al., 2005; Mitchell et al., 2004; Searle et al., 2007). These rocks have been interpreted as a passive margin sequence of the Sibumasu terrane deposited on the southern margin of Asia (Bender, 1983), or alternatively, the result of an eastward emplaced nappe (Mitchell et al., 2004; Mitchell, 1992; Mitchell et al., 2007).

2.8.4. Mogok Metamorphic Belt

The Mergui Group is bordered on the west by gneisses, schists, marbles and granites of the Mogok Metamorphic Belt (MMB), exposed along the western boundary of the Sibumasu terrane, east of the Sagaing Fault. The Mogok Metamorphic Belt forms the western margin of the Sibumasu terrane, outcropping along the northwest margin of the

Shan Plateau and further south between the Sagaing Fault and the Shan Scarp. It is composed of high-grade amphibolite to granulite facies marbles, schists and gneiss pervasively intruded by Mesozoic and Cenozoic granitoids (Barley et al., 2003; Mitchell et al., 2012; Mitchell, 1993; Mitchell et al., 2007; Searle et al., 2007). North of Mandalay, the belt forms an eastward convex arc, thought to extend into the eastern Himalayan syntaxis, north of the Lohit Thrust and form the south-eastern continuation of the Jurassic to Cenozoic subduction-related calc-alkaline magmatic arc of the southern Lhasa terrane (Mitchell, 1993; Mitchell et al., 2007; Searle et al., 2007). Originally considered to be Precambrian in age (Bender, 1983), the protoliths for the high-grade amphibolite to locally granulite facies metamorphic rocks are now known to be the Palaeozoic carbonate and siliciclastic successions of the Shan Plateau that are seen to grade into calc-schists and diopside-bearing marbles to the west (Mitchell et al., 2012; Mitchell et al., 2007; Searle et al., 2007). Ruby-bearing marbles near Mogok with relic Ordovician, Silurian and mid-Permian fossils have been correlated with un-metamorphosed carbonates of the Shan Plateau sequence to the east (Mitchell et al., 2007; Thein, 1988). The Mogok Metamorphic Belt is extensively intruded by Jurassic to Cretaceous and mid-Tertiary magnetite and ilmenite series I-type and S-type granitoids that are continuous with the Western Granite Province of Thailand (Cobbing et al., 1986; Cobbing, 1992) and southwest Thailand-east Burma (Searle et al., 2012). The rocks of the Mogok Metamorphic Belt experienced a complex Jurassic to Miocene thermal history of magmatism and metamorphism.

These thermal events have been variably attributed to tectonic block collision during the amalgamation of present-day Southeast Asia and the long-lasting subduction of the Indian oceanic crust beneath Burma. Early interpretations for magmatism and metamorphism in this region based on field relationships and limited K-Ar dating invoked a west Burma block- Sibumasu collision during the Jurassic and Jurassic to Early Cretaceous collision of the eastern Indo-Burman Ranges with west Burma creating a back-arc fold- and- thrust belt, implying west Burma was not part of southeast Asia until this time (Mitchell, 1981). Mitchell (1993) interpreted the Mogok Metamorphic Belt to be the northern continuation of the magmatic arc of western Burma, prior to dextral offset of as much as 1100 kilometres along the Sagaing Fault,

and suggested extension observed in this region is related to thermally weakened crust following granitoid intrusion and, more controversially, the collision of a mafic arc and eastward emplacement of the Mawgyi nappe over the western margin of the Shan Plateau sequence in the Early Cretaceous. However, evidence of offset along the Sagaing fault in excess of 1000 kilometres is lacking, with most researchers agreeing movement was likely less than 450 kilometres (Bertrand and Rangin, 2003; Curray, 2005). Additionally, evidence for regional high-grade metamorphism in the western Burma arc is absent.

As noted above, the Jurassic to early Cenozoic batholiths intruding the rocks of the Mogok Metamorphic Belt and the Shan Scarps were thought to be the south-eastern continuation of the long-lived Andean-type Gangdese magmatic arc of the Southern Lhasa terrane around the eastern Himalayan syntaxis, with calc-alkaline magmatism resulting from the northward subduction of the Indian oceanic crust beneath the southern margin of Asia, prior to the collision of India (Barley et al., 2003; Mitchell et al., 2012; Mitchell, 1992, 1993; Mitchell et al., 2007; Searle et al., 2007). Rb/Sr whole rock and U-Pb zircon geochronology of deformed calc-alkaline I-type granodiorite and orthogneiss indicate Jurassic to Cretaceous (171−120 Ma) subduction related magmatism occurred along the margin of Burma, supporting the suggestion that prior to the collision of India, Andean-type magmatism extended along the southern margin of Asia, from Pakistan through Burma (Barley et al., 2003; Cobbing et al., 1992; Mitchell et al., 2007; Searle et al., 2007). Additionally, the recognition of the Late Cretaceous Wuntho-Popa arc batholith in western Burma led some authors to suggest this represents the southern continuation of the Mogok arc, translated over 1100 kilometres northwards along the dextral strike-slip Sagaing Fault, but initiated in the Late Cretaceous (Mitchell et al., 2012). High-temperature Late Cretaceous to Palaeogene metamorphic and magmatic events have been suggested to be genetically linked to fold and thrust belt development in Thailand and Malaysia (Morley, 2004) and therefore the Mogok Metamorphic Belt may represent a western extension of major metamorphic core complexes in northwest Thailand (Dunning et al., 1995; Searle et al., 2007). However, the Sagaing Fault clearly post-dates regional fabric forming metamorphism in the Mogok Metamorphic Belt and the two are not genetically related (Bertrand et al.,

1999; Bertrand et al., 2001), therefore if Mitchell et al. (2012) are correct, regional metamorphism of the western margin of the Shan Plateau carbonate sequence occurred before the Late Cretaceous. Although these batholiths are similar in age and rock type, only recent initial $^{87}Sr/^{86}Sr$ ratios and εNd(t) values obtained from granitoids of eastern Burma reveal these share similar enriched isotopic characteristics with S-type granitoid complexes of western Yunnan, eastern Transhimalaya and northern Lhasa magmatic belt, characterized by elevated initial strontium ratios and negative εNd(t) values (Chiu et al., 2009; Chu et al., 2006; Liang et al., 2008; Liu et al., 2009; Mitchell et al., 2012; Xu et al., 2012). In contrast, rocks of the Wuntho-Popa arc batholith in western Burma show middle Cretaceous U-Pb ages, low initial strontium ratios and positive εNd(t) values indicating a juvenile depleted mantle source, analogous with the Lohit batholith in Assam and Gangdese batholith of southern Tibet (Chiu et al., 2009, 2011; Chu et al., 2006; Ji et al., 2012, 2009a, b; Lin et al., 2013; Mitchell et al., 2012; Mo et al., 2009; Wen et al., 2008).

A Palaeocene metamorphic event is indicated by a 58 ± 1 Ma inherited component to an orthogneiss with a metamorphic age of 37.4 ± 1.3 Ma from Kyanigan, ending with the emplacement of biotite granite dikes with a magmatic age of 59.5 ± 0.9 Ma cross-cutting highly deformed metamorphic rocks at the Belin quarry. A second longer lasting Tertiary metamorphic event spanned the late Eocene to Oligocene, resulting in metamorphic overgrowths on Jurassic zircons at 43-47 Ma and formation of late magmatic zircon rims and syn-tectonic syenites and leucogranites dated at 37 to 24 Ma (Barley et al., 2003; Searle et al., 2007). High temperature sillimanite grade metamorphism peaked at 680^{o}C and 4.9 kbar between 45 and 33 Ma resulting in the growth of metamorphic monazite, replacement of andalusite by sillimanite and muscovite, and crustal melting forming syn-tectonic hornblende syenites and leucogranites (Searle et al, 2007). Metamorphism pre-dates 24.5 ± 0.3 Ma, the age of crustal-derived leucogranites cross-cutting all earlier fabrics (Searle et al., 2007), in agreement with the youngest thermal event recorded by Barley et al. (2003) in the MMB: the peraluminous Yesin Dam syenogranite dated at 22.64 ± 0.4 Ma. Farther north of Yesin Dam but within the same syenogranite suite that cross-cuts regional fabrics and older intrusions, the Guwa Chaung batholith gave a Rb/Sr whole rock

isochron age of 22 ± 7 Ma with a very high initial $^{87}Sr/^{86}Sr$ ratio of 0.7157 ± 0.0007, indicating these mid-Tertiary S-type granites have a significant crustal influence, contrasting with pre-dominantly mantle derived Mesozoic plutons preserved to the north (Cobbing et al., 1992).

2.8.5. Pre-Cenozoic Geology and Tectonics of Western Burma (West Burma Block)

The origin, timing and nature of amalgamation of western Burma to Southeast Asia remain controversial. Together with Indochina, East Malaysia and West Sumatra, West Burma is believed to have separated from Gondwanaland by the opening of the Palaeo-Tethys in the Devonian, drifted northwards from the Sibumasu and Qiangtang blocks which were still part of Gondwanaland, and formed Cathaysialand characterized by Early Permian biotas and floral provinces of Cathaysian affinity that do not contain Early Permian glacial-marine diamictites (Barber et al., 2005; Barber and Crow, 2009; Metcalfe, 2011; Morley, 2012).

In western Burma, the thick succession of Palaeozoic and Mesozoic sedimentary and meta-sedimentary sequences of the Shan Plateau are not observed, leading Mitchell (1981, 1993) to propose either this succession is buried beneath the thick Late Cretaceous to Cenozoic sedimentary sequences of the Central Burma Basin, or that the absence of these rocks in western Burma indicates it was not attached to Southeast Asia until the mid-Mesozoic.

2.8.6. Metamorphic Belts of Northern Burma

In northern Burma, three metamorphic belts exposed along splays of the Sagaing Fault from east to west are the Katha-Gangaw belt, the Tagaung-Myitkyina belt and the Jade Mines Belt (Figure 2.1, Figure 2.2). Kyanite grade schists and gneisses of the Katha-Gangaw Range grade eastwards into lower grade mica schists of the Tagaung-Myitkyina belt, thought to be the former western margin of the Mogok Metamorphic Belt carried north by the Sagaing Fault (Mitchell et al, 2007; Searle et al, 2007). Mica schists exposed on the eastern margin of the Indo-Burman Ranges (Mount Victoria) may represent the right-lateral offset equivalent of the Katha-Gangaw belt, translated along the Sagaing Fault (Mitchell, 1993; Mitchell et al, 2007). It has been suggested that Upper Triassic flysch and Early Jurassic ophiolites bordering the Indo-Burman

Ranges and Katha-Gangaw belt to the east may be correlated with the Yarlung-Tsangpo suture zone of southern Tibet (Mitchell et al., 2004; Shi et al., 2009). It has also been suggested the ophiolite complex that hosts jadeite was obducted eastward onto the Burma microplate in the early Jurassic, was later metamorphosed during east dipping subduction, and exhumed prior to shearing along the dextral strike-slip Sagaing Fault (Mitchell et al, 2007; Searle et al, 2007).

The Jade Mines Belt (Tract) located in northern Burma in the Hpakan region of Kachin State, west of the northern-most strands of the dextral strike-slip Sagaing Fault, consists of serpentinized ultramafic rocks associated with blueschists and garnet-bearing amphibolites (Qi et al., 2013). Jadeite occurs as veins within serpentinized peridotite, surrounded by high pressure, low temperature metamorphic blue schist, mica schist and gneiss (Qui et al, 2009; Searle et al, 2007). Combined U-Pb geochronology and εHf(t) isotope geochemistry on zircons of the Burma jadeite show high positive εHf(t) values (13.8 ± 0.3), indicating jadeite formation occurred in the Late Jurassic (158 ± 2 Ma) through fluid-induced metasomatism resulting from dehydration of a subducted oceanic slab (Qui et al, 2009; Shi et al, 2009). Zircon SHRIMP U-Pb dating of Burma jadeite indicate an inherited magmatic protolith age of ca. 163 Ma and hydrothermal (high pressure-low temperature metamorphic) zircon crystallization, coeval with metasomatic jadeite formation, at ~147 Ma (Shi et al., 2008), whose average age of 157 Ma is in agreement with LA-MC-ICPMS zircon U-Pb ages of ~158 Ma (Qiu et al., 2009) from the same locality. Direct dating of jadeite using $^{40}Ar/^{39}Ar$ stepwise heating gave a plateau age of 123.9 ± 3.4 Ma, and associated sodic-calcic amphibole gave a plateau age of 134.8 ± 1.4 Ma (Qi et al., 2013). Because the estimated metamorphic temperature of the jadeite (estimates range from 250° to 500°C, reported in Shi et al., 2012) are lower than the argon isotopic system closure temperature for both jadeite and amphibole (~650°C and 540°C, respectively; Qi et al., 2013), their plateau ages date the timing of formation (Qi et al., 2013). Amphibole from a vein cross-cutting the jadeite gave a $^{40}Ar/^{39}Ar$ plateau age of 92.7 ± 1.2 Ma (Qi et al., 2013). The combined age data indicates jadeite formation in the Jade Mines Belt (Tract) occurred in a high pressure/low temperature subduction zone environment during the Early to Late Cretaceous, involving at least two, potentially three, stages of metasomatism at

approximately 147 Ma, 135 Ma and 93 Ma (Qi et al., 2013; Shi et al., 2008, 2012). This is further evidence of Cretaceous subduction of Neo-Tethys oceanic crust beneath continental Burma, prior to the India-Asia collision.

2.8.7. The Wuntho-Popa magmatic arc and central volcanic line

The Wuntho-Popa magmatic arc of western Burma consists of Late Cretaceous granodiorite to tonalite batholiths, Neogene volcanics and three extinct strato-volcanoes of Quaternary age (Mitchell et al., 2012) and separates the Western and Eastern Troughs of the Central Burma Basin, and continues southwards linking with Quaternary and inactive volcanoes in the Andaman Sea and Sumatra (Curray, 1979; Curray, 2005). Eastward dipping subduction of Neo-Tethyan oceanic crust beneath Burma during at least the middle Cretaceous and Late Miocene to Quaternary is inferred for the generation of granitoids with I-type geochemistry. The absence of substantial arc plutons south of Salingyi is attributed to burial beneath thick Palaeogene to Quaternary sedimentary rocks of the Central Burma Basin (Mitchell, 1993).

2.8.8. Cretaceous arc magmatism

The Wuntho-Popa magmatic arc of western Burma is composed of calc-alkaline I-type diorite and granodiorite plutons intruding basic to intermediate volcanic rocks (Mawgyi Andesites) at Banmauk and amphibolite facies schists at Salingyi, exposed as isolated complexes surrounded by Quaternary alluvial sediments (Cobbing, 1992; Mitchell, 1993). Several locations within the northern composite Wuntho batholith have been sampled for geochemical analysis and age determinations; coarse, biotite-hornblende-bearing granodiorite of the Khanza Chaung and Shangalon biotite-hornblende-bearing granodiorite with mafic enclaves were sampled from the margins of the Wuntho complex to the southwest and southeast, respectively (Cobbing, 1992). Cobbing (1992) conducted whole rock Rb-Sr isotopic analyses on these granitoids, however due to the uniform $^{87}Sr/^{86}Sr$ ratios resulting in shallow slopes of the regression line and subsequently large errors on the middle to Late Cretaceous ages that cannot be regarded as geologically meaningful. Well constrained initial $^{87}Sr/^{86}Sr$ ratios of 0.7052 ± 0.0007 and 0.7055 ± 0.0004 for the Khanza Chaung and Shangalon granitoids, respectively, suggest derivation from a juvenile mantle source, consistent with the metaluminous I-type geochemistry for granitoids of the western Burma Wuntho-Popa

magmatic arc (Cobbing, 1992). K-Ar dating of granodiorites of the Khanza Chaung pluton yields biotite cooling ages of 93.7 ± 3.4 Ma and 97.8 ± 3.6 Ma (Mitchell et al., 2012; Mitchell, 1993), a whole rock Rb/Sr age of 90 ± 78 Ma (Zaw, 1998) and a SHRIMP zircon age of 94.6 ± 1 Ma (Zaw, 1998), suggesting a lower Late Cretaceous age for arc magmatism in this area.

The significantly less voluminous Salingyi plutons of hornblende granodiorites outcrop southwest of Monywa, and include porphyry copper deposits associated with Miocene diorite dyke intrusion and andesitic volcaniclastics east of Monywa (Cobbing, 1992; Mitchell et al., 2012; Zaw, 1998). Diorites in the Salingyi area have hornblende K-Ar ages of 106 ± 7 Ma and 91 ± 8 Ma and a K-Ar biotite age on granite of 103 ± 4 Ma (Mitchell et al., 2012; Mitchell, 1993). Recently, Mitchell et al. (2012) reported a zircon U-Pb age of 105.3 ± 1.7 Ma for a diorite dyke intruding amphibolite facies schist at Salingyi with a low initial $^{87}Sr/^{86}Sr$ ratio of 0.7040 and εNd(t) of +4.5. This is in good agreement with the Middle Cretaceous K-Ar biotite and hornblende ages and is consistent with the interpretation of Mitchell (1993) and Barley et al. (2003) where Cretaceous to Palaeocene I-type magmatism generated by the northward subduction of the Indian oceanic crust beneath the southern margin of the Asian crust extended from the Gangdese batholith of southern Tibet, southwards through Burma, the Andaman Sea and Sumatra.

2.8.9. Neogene to Quaternary volcanism

$^{40}Ar/^{39}Ar$ ages from volcanic rocks from Mount Popa and two volcanoes from the Monywa area indicate two stages of volcanism, recording a distinct change in magma chemistry; Middle Miocene (~16 to 13 Ma) volcanism is characterized by high-K calc-alkaline volcanism with intermediate compositions, whereas the Quaternary (<1 Ma) stage is characterized by high-Al basaltic magmatism and volcanism with εHf(t) values ranging from + 17.4 to +10.7 and εNd(t) values ranging from +3.6 to +2.1 (Lee et al., 2010). Additionally, an andesite porphyry dyke intruding early Miocene sediments from an ore body at the Monywa copper deposit, gave a U-Pb age of 13.6 ± 0.1 Ma, interpreted as the age of mineralization, with an initial Sr ratio of 0.7046 and εNd(t) value of +3.2 (Mitchell et al., 2012).

Three extinct calc-alkaline stratovolcanoes (Mount Popa, Mount Taungthonlon and Mount Loimye) of the central volcanic line are bounded by Late Miocene and Pliocene sediments of the Central Burma Basin, are interbedded with andesitic volcanics and unconformably overlain by Quaternary to Recent basalts. Whole rock Rb-Sr analysis on basalts give low initial strontium ratios (0.70431 to 0.70453) suggesting the presence of eastward subducting oceanic crust of the Indian plate beneath Burma and generation of juvenile mantle-derived melts (Stephenson and Marshall, 1984).

2.8.10. Timing of the subduction of the Neo-Tethyan oceanic crust beneath Burma

Subduction of Neo-Tethyan oceanic crust beneath the Burma margin was occurring from at least the Middle Cretaceous. Jurassic-aged cores of zircons from an I-type pluton in the MMB indicate subduction generated arc magmatism was occurring as early as ~170 Ma (Barley et al., 2003). Mitchell (1993) proposed the collision of a northeast facing island arc (Mawgyi Nappe) with the Burman margin during the Late Cretaceous, slightly later than the collision of an island arc (Woyla Nappe) farther south along the outer margin of Sumatra, and this may have interrupted subduction. In the Andaman Islands, zircon U-Pb dating of the base of an obducted ophiolite sequence gave a Late Cretaceous formation age of 95 ± 2 Ma, indicating in this part of the arc, subduction of Neo-Tethyan oceanic crust was renewed at this time (Pedersen et al., 2010).

2.8.11. Indo-Burman Ranges

Previously, the west-vergent Cenozoic sedimentary sequences of the Indo-Burman Ranges were interpreted to be accretionary prism sediments from the Bengal Fan (Curray, 1979). Subsequent field and detrital provenance studies reveal the Indo-Burman Ranges are composed of an eastern Palaeogene belt, interpreted to be the western extension of the Western Trough fore-arc basin (Mitchell, 1993; Mitchell et al., 2007), separated from a western Neogene belt by the north- striking Kaladan Fault, and it is composed primarily of detritus shed from the Himalayan front by the Bengal Fan which was incorporated into an accretionary prism following subduction of the Indian plate beneath western Burma (Allen et al., 2008). The succession becomes younger to the west, where Neogene flysch-type sediments and minor Late Cretaceous mudstones and pelagic limestones of the western Neogene belt are exposed, lying along the active

subduction zone between the Indian plate and Burma (Allen et al., 2008; Mitchell, 1993; Mitchell et al., 2007). Allen et al. (2008) noted that the Palaeogene sedimentary rocks in the Indo-Burman Ranges contain arc-derived detritus, sourced from the Burmese arc to the east rather than a Transhimalayan arc source of the southern Lhasa terrane because of its proximity to the site of deposition and the lack of significant arc-derived material in Oligocene sedimentary sequences of the Himalayan foreland and Bengal Basin (Najman et al., 2012; Najman et al., 2008). On the eastern margin of the Indo-Burman Ranges, Cretaceous-Palaeogene sedimentary rocks of the eastern belt unconformably overlie Late Triassic turbidites, Triassic-Cretaceous metamorphic rocks and ophiolitic rocks of a suggested Late Cretaceous age, considered to be the southern continuation of the Indus-Yarlung-Tsangpo suture zone around the eastern Himalayan syntaxis or the remnants of an eastward verging nappe carrying older rocks to their current position (Bender, 1983; Mitchell, 1993; Searle et al., 2007). The Kabaw Fault separates the Indo-Burman Ranges from the Western Trough of the Central Burma Basin (Bender, 1983; Mitchell, 1993). Mitchell (1993) suggested uplift of the Indo-Burman Ranges, which led to the compartmentalization of the Central Burma Basin from the Indian Ocean, occurred in the late Eocene or early Oligocene, supported by a ca. 37 Ma youngest detrital zircon fission-track population in the Palaeogene sediments, suggesting deposition and exhumation of these succession occurred after this time (Allen et al., 2008).

2.8.12. Sagaing Fault

During the Miocene, a regional transtensional stress regime associated with the coupling and northward movement of the India and west Burma plate, leading to the development of the major north-striking dextral strike-slip Sagaing Fault, which links to the seafloor spreading centre in the Andaman Sea to the south and developed several splay fault in the north (Figure 2.1, Figure 2.2), where a compressional regime dominates, due to the buttressing of the coupled plates (Bertrand and Rangin, 2003; Pivnik et al., 1998). At the latitude of Mogok, this fault defines the boundary between the Central Burma Basin to the west and the Mogok Metamorphic Belt to the east (Figure 2.1, Figure 2.2). Estimates on the amount of offset that occurred along this fault range from 150 kilometres (Bertrand and Rangin, 2003), 300 to 450 kilometres (Curray,

2005; Maung, 1987) and as much as 1100 kilometres (Mitchell et al., 2012; Mitchell, 1993), most of which occurred post- early Miocene (Curray, 2005; Morley, 2002; Pivnik et al., 1998). This fault is presently active and is thought to accommodate two-thirds of the northward movement of the Indian plate relative to Eurasia in this area (Socquet et al., 2006) and may be part of a larger Miocene regional dextral shear zone connecting northwards with the Gaoligong shear zone of western Yunnan (Lin et al., 2009; Wang et al., 2008; Wang et al., 2006; Xu et al., 2012; Zhang et al., 2012a) and the Jiali-Palung Fault (Lee et al., 2003; Lin et al., 2009), north of the eastern Himalayan syntaxis, which forms the western boundary of lower crustal flow and crustal rotation clockwise around Namche Barwa (Clark and Royden, 2000; Schoenbohm et al., 2006).

2.8.13. Cenozoic tectonic framework

A major regional kinematic reorganization of the eastern Himalayas occurred during the Late Oligocene to Early-Middle Miocene times. During the Palaeogene-Oligocene, hyper oblique collision between the India and Burma plates, enhanced by the SE-ward extrusion of Indochina, led to the development of a back-arc mobile belt in the hot, weakened crust of eastern Burma-western Thailand (Morley, 2009; Morley, 2004). In western Thailand, transpression resulted in the initiation of sinistral shear along the Mae Ping and Three Pagodas Faults at ~50–40 Ma (Upton et al., 1999), lasting until approximately 36–30 Ma (Lacassin et al., 1997), after which time there was a reversal in shear sense. Morley (2009, 2004) interprets this left-lateral transpression as resulting from initiation of west Burma-India coupling, and the change to dextral shear (after ~30 Ma) during the late Oligocene-early Miocene, which records the northward movement of the now coupled block and is contemporaneous with the initiation of strike-slip deformation in the Andaman Sea (Curray, 2005; Morley, 2009; Morley, 2012, 2013).

During the Oligocene to early Miocene, the regional kinematics of western Thailand and Burma indicate a change from a transpressional sinistral strike-slip along Mae Ping and Three Pagodas Faults (Lacassin et al., 1997; Morley, 2009, 2004) and uplift of the Indo-Burman Ranges (Allen et al., 2008; Mitchell, 1993) to a transtensional regime characterized by a reverse in shear sense in the strike-slip faults of western Thailand, initiation of strike-slip extension in the Andaman Sea (Curray, 2005), and the NNW-

SSE orientated extension within the Mogok Metamorphic Belt (Bertrand et al., 1999, 2001) and the Central Burma Basin (Pivnik et al., 1998).

Additional evidence within Burma supports an Oligocene-early Miocene timing for the coupling of the Indian plate with the west Burma block. Fission track dating of detrital zircons from the Palaeogene Indo-Burman Ranges indicates sub-aerial uplift occurred after ca. 37 Ma (Allen et al., 2008) in agreement with the late Eocene to Oligocene age suggested by Mitchell (1993) based on geological field studies and rock relationships. Radiometric dating indicates rocks of the Mogok Metamorphic Belt underwent a Palaeocene (~59 Ma) and protracted Eocene-Oligocene (~37–29 Ma) sillimanite grade high temperature metamorphism, with zircon overgrowths (~47–43 Ma) and localized crustal melting (23 Ma) (Barley et al., 2003; Mitchell et al., 2012; Searle et al., 2007), followed by Oligocene to Early Miocene diachronous south to north NNW-SSE orientated extension and exhumation recorded by $^{40}Ar/^{39}Ar$ mica cooling ages (27–16 Ma) (Bertrand et al., 2001; Bertrand et al., 1999). This diachronous cooling records the northward movement of the now coupled block, characterized by a transtensional regime. Uplift to the east and west resulted in the compartmentalization of the Central Burma Basin, where little deformation and nearly continuous sedimentation from the Cretaceous-Pliocene suggests it is "floored by stronger, cooler oceanic crust" (Morley, 2009).

Strain accommodation over a broad area of eastern Burma-western Thailand was focused along the dextral Sagaing Fault that developed during the Middle Miocene, accommodating two-thirds of the northward motion of the coupled plates. In the Late Miocene to Pliocene (Pivnik et al., 1998), the progressive northward movement of India led to the development of ENE-directed transpression and basin inversion along re-activated Miocene extensional faults within the Central Burma Basin (Pivnik et al., 1998; Trevena and Varga, 1991).

2.8.14. Cenozoic Tectonics in Central Burma Basin

The Central Burma Basin, containing over twelve kilometres of Cenozoic fluvial and deltaic sedimentary rocks deposited by the Irrawaddy River, may represent one of the most complete records of early Himalayan erosion from the eastern Himalaya. Situated

on the west Burma microplate, the Central Burma Basin consists of a fore-arc basin, or Western Trough, and a back-arc basin, or Eastern Trough, consisting of Late Cretaceous to Quaternary shallow marine and non-marine sedimentary and volcanic successions overlying Albian limestones, minor ophiolite and metamorphic basement, separated by a north-south trending volcanic and magmatic arc consisting of granodiorites to andesites of middle Cretaceous and Quaternary in age (Bertrand and Rangin, 2003; Mitchell, 1992, 1993; Pivnik et al., 1998; Stephenson and Marshall, 1984). It is bounded to the west by the Indo-Burman Ranges and to the east by the Mogok Metamorphic Belt and Sagaing Fault (Figure 2.1, Figure 2.2). The Central Burma Basin may be separated into seven, generally north-trending sub-basins (Irrawaddy, Delta, Prome, Salin, Shwebo, Chindwin and Hukawng), separated by tectonically controlled areas of uplift (Figure 2.1, Figure 3.1) (Bender, 1983; Pivnik et al., 1998). Cenozoic strata of the Western Trough have received more attention than the Eastern Trough because of the known hydrocarbon potential of this region (Pivnik et al., 1998; Trevana and Varga, 1991) and the discovery of primate fossil-bearing beds (Beard et al., 2009; Benammi et al., 2002; Ciochon and Gunnell, 2002; Khin et al., 2014; Maung et al., 2005; Soe et al., 2002; Tsubamoto et al., 2002). Cretaceous uplift of the Shan Plateau in the east and later the Indo-Burman ranges in the west created a low-lying region where sedimentation was nearly continuous from the Cretaceous to the Miocene as extensional fault controlled sub-basins were progressively in-filled by fluvial and deltaic sediments of the proto-Irrawaddy River in the north, and marine sedimentation in the south, where an increase in terrestrial input towards the north and in stratigraphically younger units is observed within the sequences as the basin was infilled (Ciochon and Gunnell, 2002).

The Central Burma Basin was formed in an extensional regime, with deposition of Late Cretaceous to Quaternary sedimentary and volcanic successions controlled by trench parallel syn-sedimentary normal faults active during east-northeast directed oblique subduction of the Indian oceanic crust beneath the western Burma continental margin (Bender, 1983; Bertrand et al., 2003; Pivnik et al., 1998). Synthetic east-west cross-sections from seismic reflection profiles taken at the latitude of Mandalay show an over nine kilometre thick succession of Cretaceous to Pliocene-Quaternary sedimentary rocks units in the Western Trough, with continuous sedimentation prevailing prior to an

Upper Miocene basin inversion (Figure 2.4) (Bertrand and Rangin, 2003; Pivnik et al., 1998). In contrast, the Eastern Trough contains an approximately six kilometre thick sedimentary sequence, where the Oligocene units taper out to the east, and in places Miocene and Pliocene-Quaternary units sit unconformably on metamorphic basement (Figure 2.4) (Bertrand and Rangin, 2003). Seismic reflection and well log data from the Salin sub-basin of the Western Trough reveals northeast-southwest-striking syn-sedimentary normal faults that may have controlled pre-middle to late Miocene sedimentation within the Central Burma Basin during a regional transtensional regime (Bertrand and Rangin, 2003; Pivnik et al., 1998; Rangin et al., 1999). Here, the absence of substantial thickness changes or unconformities in the over fifteen kilometre thick succession of Late Cretaceous to Pliocene-Pleistocene sedimentary rocks is observed until the base of the Pliocene-Pleistocene Irrawaddy Formation, indicating continuous sedimentation from the Eocene to late Miocene (Bender, 1983; Bertrand et al., 2003; Pivnik et al., 1998). Conversely, the Eastern Trough contains a roughly eight kilometre thick sedimentary succession with a prominent mid-Oligocene unconformity observed at the base of the Miocene Pegu Group and the base of the Pliocene-Pleistocene Irrawaddy Group (Bender, 1983; Bertrand et al., 2003; Pivnik et al., 1998).

A change in the regional stress regime from transtensional to transpressional is recorded by Middle to Late Miocene basin inversion, where the normal faults of en-echelon pull-apart basins were re-activated as reverse faults, developing N20W–N40W trending folding of the Eocene to Miocene sedimentary units (Bertrand and Rangin, 2003; Pivnik et al., 1998). In the western Salin sub-basin, the Pondaung Formation outcrops in the hanging-wall of the basin bounding reverse faults, suggesting these structures connect with a major detachment rooted in the shale-dominated upper Tabyin formation (Pivnik et al., 1998; Trevena and Varga, 1991). Fault-propagation folding of the Eocene to Miocene sedimentary units occurs along the limbs of the basin, and it is though deformation is late to post-Miocene based on the continuity of the Cenozoic stratigraphic section (Pivnik et al., 1998). Based on stratigraphic and apatite fission track data, Trevena and Varga (1991) suggest a Pliocene-Pleistocene age of uplift, initiating at ca. 10 Ma, and alternatively attribute this to the development of a regional east-west compression, rather than a regional transpression (Pivnik et al., 1998). This

change from regional transtensive to transpressive stresses within Burma is attributed to the coupling of the India and Burma plates following hyper-oblique subduction, and the translation of this amalgamated terrane northwards with respect to Southeast Asia, leading to compartmentalization of the Central Burma Basin (Pivnik et al., 1998).

2.8.15. Stratigraphy and Age Controls

Pre-existing stratigraphic correlations rely predominantly on lithostratigraphic correlation across the two troughs and the nomenclature for the Cenozoic stratigraphy of similar ages varies to some extent between sub-basins. In this work, we will use the nomenclature outlined by Thein (1966) for the Eastern Trough and the nomenclature outlined by Bender (1983) for the Western Trough. These are the Eocene Pondaung Formation and Miocene Shwetaung, Taungtalon and Moza Formations of the Upper Pegu Group (Thein, 1966) and Oligocene Padaung Formation and Miocene Obogon and Kyaukkok Formation (Bender, 1983). The majority of the Cenozoic Central Burma Basin formations are lacking well constrained depositional ages, and are instead sub-divided based on litho- and biostratigraphy determined from index fossils present in primarily marine beds. Radiometric ages for the Cenozoic stratigraphy of the Eastern Trough are absent, and therefore are correlated lithostratigraphically with the Cenozoic formations of the adjoining Western Trough, whose ages have been determined (Figure 2.5) (Bender, 1983).

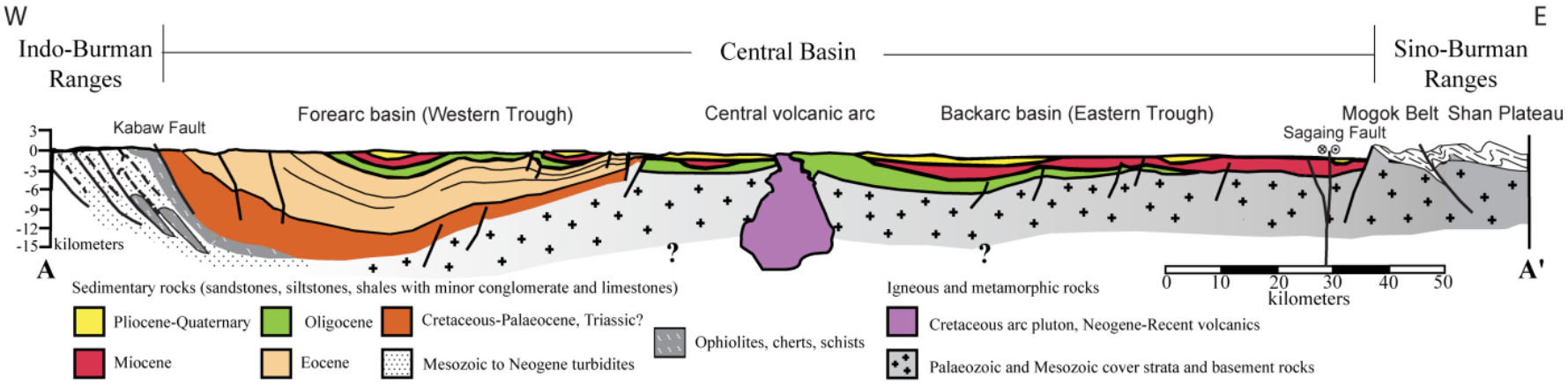

Figure 2.4 Synthetic east-west geological cross-section from seismic reflection profiles of the Central Burma Basin. Modified from Bertrand and Rangin (2003) and Naing et al. (2013).

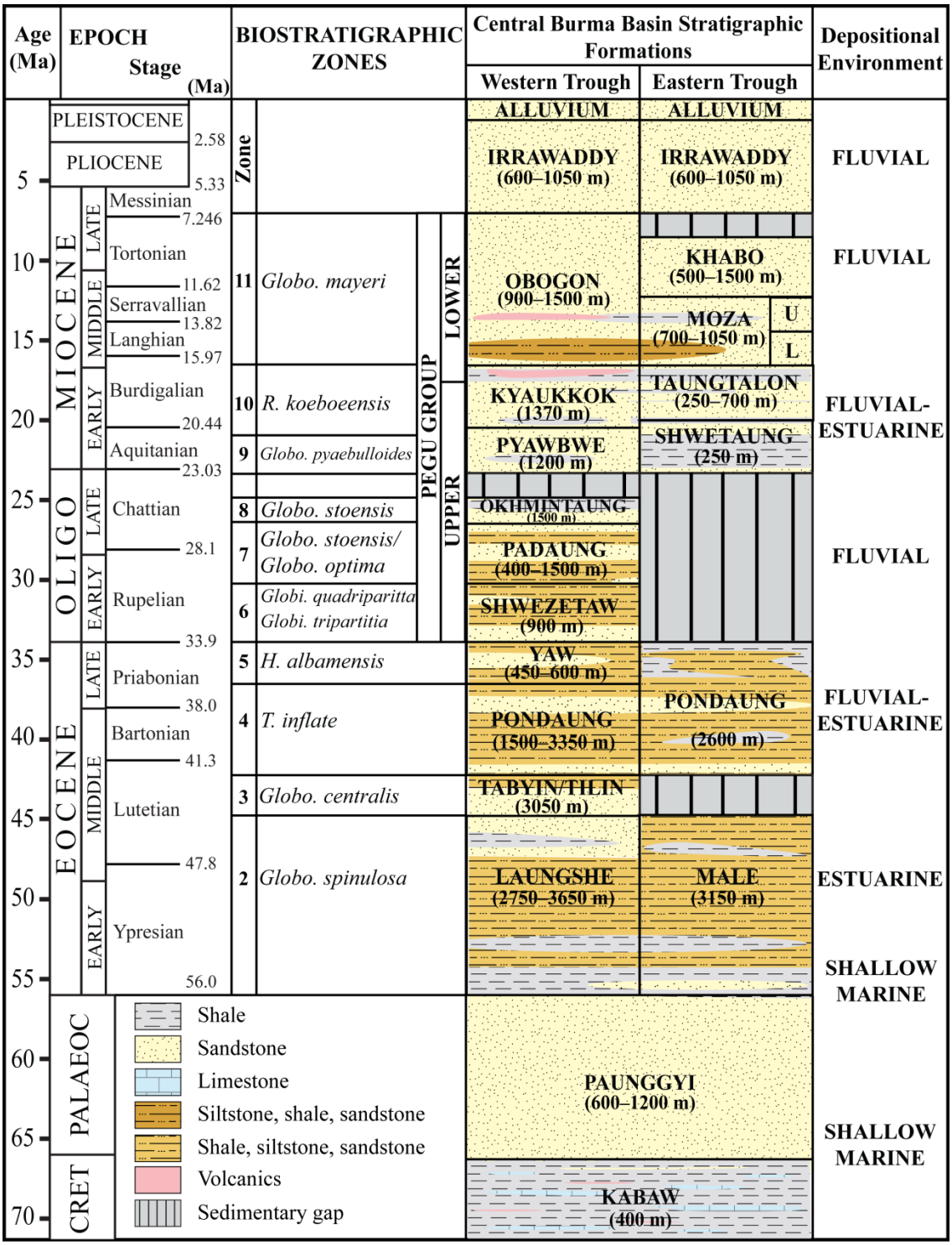

Figure 2.5 Cenozoic stratigraphy of the Central Burma Basin. Stratigraphy and formation thicknesses of the Western Trough from Bender (1983) and stratigraphy of the Eastern Trough from Bender (1983) and Thein (1966). Biostratigraphic zones based on planktonic foraminifera from Maung (1970) and Bender (1983), modified by Chit Saing (2003; pers comm.). Lithology modified from Wandrey (2006). Geological timescale and age boundaries after Gradstein (2012) and Cohen (2012). The depositional environment from Eocene to Miocene time is characterized by a prograding delta system (north to south) with increasing continental influence towards the north and through time.

The Central Burma Basin is comprised primarily of siliciclastic and carbonate Palaeocene to Recent sedimentary rocks (Bender, 1983), showing increasing terrestrial influence towards the north, and through time, as the proto-Irrawaddy fills in the basin. The oldest sedimentary unit recognized in the Central Burma Basin is the Upper Cretaceous to Palaeocene Kabaw Formation, unconformably overlain by limestones, sandstones, shales and conglomerates of the latest Palaeocene to lower Eocene Paunggyi (Conglomerate) Formation, exposed along the boundary between the Western Trough and the Eastern Belt of the Indo-Burman Ranges (Bender, 1983; Mitchell, 1993). The Eocene sedimentary units of the Central Burmese Basin comprise a stratigraphic section over 10,000 meters thick (Ciochon and Gunnell, 2002; Maung et al., 2005). From oldest to youngest, the Eocene stratigraphy of the Central Burma Basin is divided into the Laungshe (Clay), Tilin (Sandstone), Tabyin (Clay), Pondaung (Sandstone) and Yaw (Shale) formations which range from shallow marine to terrestrial siliciclastic and carbonate sedimentary rocks (Figure 2.5) (Bender, 1983).

The Laungshe Formation is composed primarily of shale with occasional layers of sandstone and conglomerates, particularly in the lower part, and rare limestone beds containing calcareous red algae (*Lithothamnia)*; the presence of the planktonic foraminifera type fossil *Nummulites atacicus* provides a maximum depositional age of Lower to Middle Eocene (Bender, 1983). The Tilin Formation is predominantly sandstone, where silicified wood, red beds and gravel in the upper portion indicates deposition in a terrestrial, rather than marine environment; rare fossils include Eocene macroformanifera (Bender, 1983). The Tabyin Formation is composed primarily of shale with minor coal seams and thin sandstone beds, and is conformable with the underlying Tilin Formation and the overlying Pondaung Formation; the amount of fine-grained sandstone beds increases towards the north. Although relatively unfossilferous, the type fossil is *Nummulities acutus* is preserved for which a Lower to Middle Eocene age is assumed, providing an absolute maximum deposition age for the conformably overlying Pondaung Formation (Bender, 1983).

The Pondaung Formation consists of interbedded sequences of sandstone, clay and conglomerate and detailed sequence stratigraphic studies of this succession suggest deposition in a fluvial-deltaic environment (Soe et al., 2002). It is divided into a

shallow marine lower member and a terrestrial upper member deposited by fluvial systems (Maung et al., 2005) In the Lower Member, clays are more prevalent with occasional marine molluscs preserved, and are seen to interfinger with clays of the underlying Tabyin Formation (Bender, 1983; Ciochon and Gunnell, 2002). The Upper Member consists of clays and sandstones, the lower half of which is overwhelmingly terrestrial, noted by the presence of red beds, silicified wood, characterized by diverse mammalian, in particular primate (*Pondaungia* and *Amphipithecus)* fossil-bearing beds (Beard et al., 2009; Benammi et al., 2002; Ciochon and Gunnell, 2002; Khin et al., 2014; Maung et al., 2005; Soe et al., 2002; Tsubamoto et al., 2002). In the Western Trough, fossilferous beds of the Pondaung Formation outcrop in a 22 x 18 kilometre area between 22°N to 21°38'N and 94°30'E to 94°50'E, and are thought to be deposited coevally (Soe et al., 2002).

Early estimates of the depositional age of the Pondaung Formation are Middle to Late Eocene based on stratigraphy and index fossils (Bender, 1983) and Late Middle Eocene (Bartonian) based on the correlation of mammalian fauna with those in Europe and North America (Ciochon and Gunnell, 2002). More recent biostratigraphy assigns the Pondaung Formation to the *Trochammina inflate* biostratigraphic zone and the conformably overlying Yaw Formation to the *Hantkenina albamensis* zone, a planktonic foraminifera that first appears in the Lutetian and goes extinct in the Rupelian, constraining the maximum deposition age of the Pondaung Formation to Lutetian or older (Middle Eocene) (Chit Saing, 2003). Magnetostratigraphic correlations from the Pondaung Formation reported by Benammi et al. (2002) assigned a depositional age between 37.4 to 37.0 Ma, however, this data is challenged by Zaw et al. (2014), as they question the choice of correlation to chron C7n.1n and regard the age as poorly constrained. Recent radiometric dating on zircon extracted from a tuff bed located approximately one meter stratigraphically above the anthropoid fossil bearing beds give a zircon fission-track age of 37.2 ± 1.3 Ma (Tsubamoto et al., 2002) and LA-MC-ICPMS U-Pb zircon dating gave a slightly older age of 40.31 ± 0.65 Ma and 40.22 ± 0.86 Ma (Zaw et al., 2014).

The Pondaung Formation samples were obtained from an outcrop north of Mandalay in the Eastern Trough and correlate litho- and bio-stratigraphically with the Pondaung

Formation of the Western Trough. Two sedimentary units with trough cross-bedding within lenticular sand bodies, interpreted as fluvial and deltaic sediments eroded from a northern source and deposited by the Irrawaddy river, were sampled: a medium-grained lithic arenite (Pondaung 1) and a coarse-grained sub-arkosic arenite (Pondaung 2) (Maung et al., 2005; Soe et al., 2002; Thein, 1966). The underlying upper member of the Male Formation is comprised predominantly of sandstone deposited in a non-marine environment and is considered to be middle to early Eocene in age (Bender, 1983). The overlying Yaw Formation consists largely of shales with interbedded limestones, with an increasing amount of sandstone beds towards the top of the formation, and is interpreted as being deposited in a marine environment (Bender, 1983). The presence of benthic foraminifera (*Nummulites yawensis*, *Discocylina sella*, *Operculina* cf. *canalifera*) and molluscan fossils including *Velates perversus* within beds of this formation indicate an Late Eocene age of deposition in a marine environment (Bender, 1983).

Since much of the Oligocene in the Eastern Trough is represented by a depositional hiatus, samples from the Oligocene Padaung Formation were collected from outcrops in the Western Trough. From base to top, the Oligocene sediments in the Salin sub-basin are divided lithostratigraphically into the Shwezetaw, Padaung, and Okmintaung formations (Figure 2.5). In the Western Trough, the late Eocene to early Oligocene Shwezetaw Formation, is composed of interbedded shallow marine carbonates, siltstones and shales, with Upper Eocene and early Oligocene fauna. The base of the overlying Padaung Formation is composed of 1,500 meter thick shale beds, with thickening of sandstone beds upsection, grading into the overlying siliciclastic and carbonate rocks of late Oligocene Okhmintaung Formation (Bender, 1983). The *Globorotalia opima* zone (P21/N2) of the Upper Oligocene provides a lower age boundary for the Padaung Formation (Bender, 1983), which also contains gastropods *Lyria varicose, Neoathleta theobaldi* and *Turricula (Orthosurcula) birmanica* (Bender, 1983).

The Miocene sequences of the Western Trough are separated from the underlying late Oligocene Okhmintaung Formation by an erosional unconformity (Figure 2.5). The base of the Miocene succession consist of conglomerates, followed by interbedded fine-

to medium grained sandstones, siltstones and shales of the late Oligocene to early Miocene Pyawbwe Formation, overlain by the middle Miocene Kyaukkok Formation the middle Miocene Obogon Formation (Bender, 1983; Wandrey, 2006). Ostracod fossils in the Pyawbwe Formation indicate a Miocene age (Bender, 1983). The Kyaukkok Formation has a higher sandstone concentration from the Pyawbwe Formation and is characterized by gastropod (*Conus (Leptoconus) bonneti*; Aquitanian) and bivalve (*Cardium (Trachycardium) minbuense*; early Miocene) fauna, whereas the Obogon Formation consists of stratified fine-grained sands and clays with trace fossils indicating the fine sand layers represent beach sands; it belongs to the *mayeri* biostratigraphic zone of the Middle Miocene (Bender, 1983). A late Miocene to Pliocene period of non-deposition and erosion is marked by an angular unconformity, separating medium- to coarse-grained cross-bedded fluvial sandstones, siltstones and conglomerates of the Pliocene to Quaternary Irrawaddy Formation from the underlying Obogon Formation (Bender, 1983; Pivnik et al., 1998; Wandrey, 2006).

Thein (1966) divided the Miocene sedimentary sequences in the Eastern Trough of the Central Burma Basin into four major stratigraphic units based on lithological characteristics and palaeontological evidence: the Shwetaung (Clay) Formation, Taungtalon (Sandstone) Formation, Moza Formation and Khabo (Sandstone) Formation in ascending order ranging in age from Early to Late Miocene (Figure 2.5). Deposition of tide-dominated estuary muds, shallow marine clastics, and fluvial deposits occurred in a back-arc basin between the Mogok Metamorphic Belt and Shan Plateau to the east, and Central Volcanic Line to the west (Ciochon & Gunnell 2002; Khin and Myitta 1999). Fluvial sandstones of the Irrawaddy Group (Late Miocene to Pleistocene) unconformably overlie the Miocene deposits of this region, which are in turn overlain by Quaternary to Recent alluvium (San, 1981; Thein, 1966; Win, 1986).

The early Miocene Shwetaung Formation is composed primarily of laminated shales and siltstones and minor sandstones and is observed in the field as an inlier, faulted against the Moza Formation (Thein, 1966). Although the exact stratigraphic position of this formation is unknown, it is believed to represent the oldest and stratigraphically lowest Miocene formation in the Eastern Trough (Thein, 1966). The Early to Middle Miocene Taungtalon Formation, exposed in the cores of northwest plunging anticlines,

shared similar lithological characteristics with the middle Miocene Kyaukkok Formation of the Western Trough and consists of medium- to coarse- grained sandstones and interbedded siltstones and minor shales (Khin and Myitta, 1999; Thein, 1966). The Moza Formation is separated into a Lower Member of interbedded sandstones and minor shales and an Upper Member of laminated siltstones and shales and is assigned a late middle Miocene age based on the presence of the gastropod *Cerithium sp.* (Khin and Myitta, 1999; San, 1981; Thein, 1966; Win, 1986). The overlying Khabo Formation is made up of medium- to coarse-grained, cross-stratified sandstone, constraining the bivalve *Cyrena sp.*, for which it is assigned a Late Miocene age (Khin and Myitta, 1999; San, 1981; Thein, 1966).

Miocene sedimentary rocks of the Eastern Trough are generally arkosic arenites of recycled orogen provenance (Figure 2.6), exposed in north-west plunging anticlines and heavy mineral maturity decreases up-section, with a significant change noted at the unconformable Miocene Pegu Group-Irrawaddy Formation boundary (San, 1981; Thein, 1966; Win, 1986). Several studies on Miocene sediments of the Eastern Trough over an area approximately 45 miles wide and 75 miles long (N20°18' to N22°45', E95°10' to E°95°50') record northeast to southwest and north to south palaeoflow data and petrography and heavy minerals indicate sediments of this area were sourced from granitic bodies, medium to high grade metamorphic rocks and older sedimentary rocks outcropping to the north, possibly in the Wuntho and Mogok areas (San, 1981; Thein, 1966; Win, 1986). This is consistent with deposition of sediment derived from a region to the north and northeast by a river of low sinuosity throughout the Neogene, consistent with a proto-Irrawaddy river infilling the Central Burma Basin from the north. Despite the spatial and temporal diversity of the Neogene successions, the continuity of palaeoflow indicators, sedimentary petrology and heavy minerals recorded within them, indicates that detritus of the Central Burma Basin was derived from a constant source region and similar sediment pathways, at least during the Miocene. Based on stratigraphic relationships, at least two phases of deformation are recognized: a late Miocene event resulting in the uplift and folding of the Miocene Pegu Group and a younger post-Pliocene event that resulted in the faulting and folding of Pegu Group and the overlying Irrawaddy Formation (Bender, 1983; Pivnik et al., 1998; San, 1981).

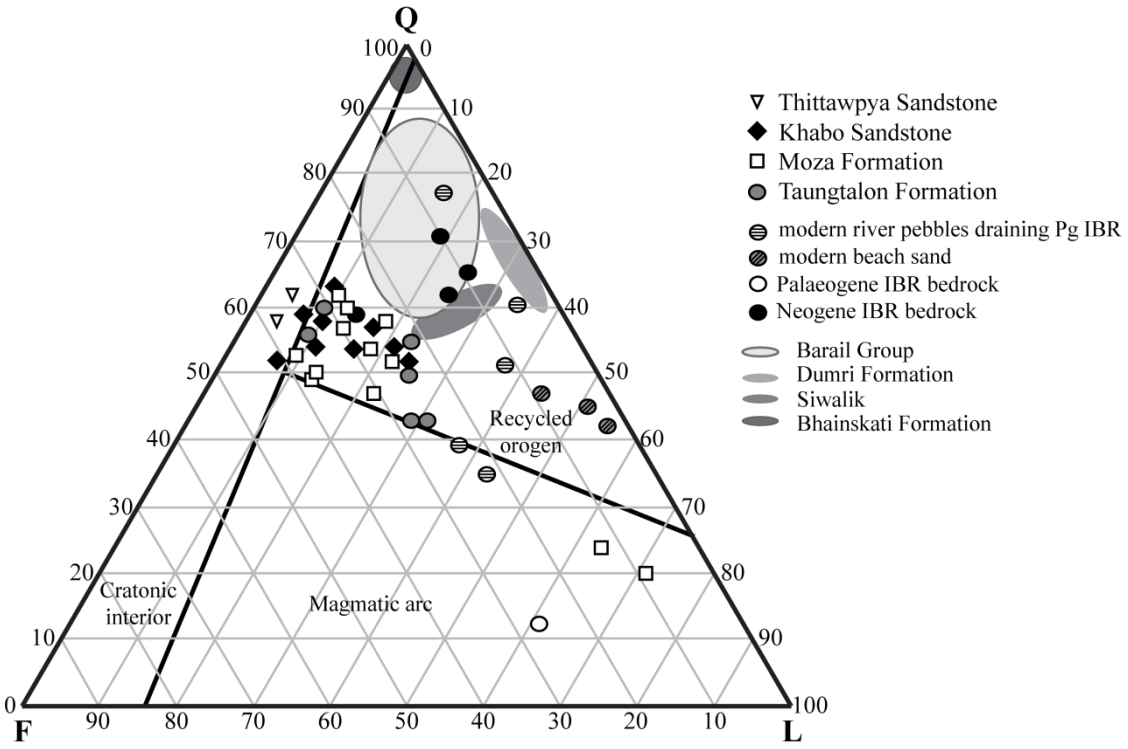

Figure 2.6 Sediment petrography of the Miocene Pegu Group from the Eastern Trough (San, 1981; Thein, 1966; Win, 1986) and coeval sedimentary rocks from the Indo-Burman Ranges, eastern Himalayan foreland basin and Bengal Basin plotted on a QFL diagram (Dickinson, 1985). Q = quartz, F = feldspar, L = lithics. Data from Palaeogene and Neogene sedimentary rocks and modern sands of the Indo-Burman Ranges (IBR) from Allen et al. (2008) and sedimentary rocks of the eastern Himalayan foreland and Bengal Basin including the Eocene Bhainskati, Oligocene Barail, Miocene Dumre formations and Miocene to Recent Siwaliks from Najman et al. (2008, 2005), Szulc et al. (2006), DeCelles et al. (1998), modified from Allen et al. (2008).

2.9. Previous provenance studies

2.9.1. Sedimentary records of river capture of major Southeast Asian river systems

Building on the works of Brookfield (1998) and Clark et al. (2004), numerous studies have been conducted using provenance studies on modern and palaeo-river sediment from onshore and offshore basins of Southeast Asia, in order to test hypotheses involving major drainage capture of the Red River by adjacent system and linking detritus to specific source regions.

The pre-Himalayan evolution of the Asian continent involved the Palaeozoic to Mesozoic amalgamation of Gondwana-derived terranes separated by suture zones

through rift, drift and accretionary tectonics (e.g. Metcalfe, 1996). These terranes experienced different geological histories and, as a result, contain different age and geochemical signatures that can be used to discriminate provenance between eroded sediment deposited by modern and palaeo-rivers draining this region in order to determine the geodynamic evolution of drainage systems in Southeast Asia (Clift et al., 2006; Liang et al., 2008; van Hoang et al., 2009; van Hoang et al., 2010). Bodet and Schärer (2000) utilized combined U-Pb dating and Hf isotope analysis of detrital zircon and baddeleyite from modern river bank sediment of the Red, Mekong, Salween and Irrawaddy rivers as a proxy for the crustal evolution of Southeast Asia and a provenance tracer, where the various amalgamated terranes of Southeast Asia contain distinct U-Pb age populations, with each river system containing sediment unique to the terrane that it is presently draining. Clark et al. (2004) suggested that prior to onset of the Himalayan collision, the Yarlung Tsangpo, Irrawaddy, Salween and Mekong rivers were major tributaries of the Red River and post-collisional shortening and uplift led to the progressive westward capture of their headwaters by the Yarlung Tsangpo, culminating in capture of this system from the Irrawaddy River by headward erosion of the Brahmaputra River. Assuming the drainage evolution and river capture model proposed by Clark et al. (2004) is correct, than sediment derived from accreted terranes west of the present river system must be present within the Cenozoic sedimentary deposits of the palaeo-Red River. Clift et al. (2006) used mass balancing of palaeo-Red River sedimentary deposits in offshore basins and the volume of eroded material in the modern basin and changes in the neodymium isotope bulk sediment composition to show major river capture affected the palaeo-Red River system beginning in the Eocene and continuing to the Late Miocene, interpreting a shift in the neodymium isotopic values to less negative during the Early Miocene to represent disconnection of the Yarlung Tsangpo, or upper Pearl River. Recent work by Hoang et al. (2009, 2010) and Clift et al. (2006) utilizing combined U-Pb, Lu-Hf isotopic analysis of detrital zircon, Nd analysis of bulk sediment, and $^{40}Ar/^{39}Ar$ muscovite dating on modern sands and Middle to Upper Miocene sedimentary rocks of the Red River demonstrates the Yarlung-Tsangpo and the Irrawaddy were never connected to the Red River, and constrained the loss of the Yangtze River from the headwaters of the Red River prior to the Middle Miocene, consistent with the results of Clift et al. (2006).

2.9.2. Sedimentary repositories of Burma

Using combined U-Pb dating and Lu-Hf analysis of detrital zircons from modern sands, Bodet and Schärer (2000) showed the Irrawaddy River contains a number of anomalous zircons with ages ranging from 130 to 4 Ma derived from juvenile mantle magmas, for which a source in the Himalayas could not be identified. Building on this knowledge and the hypothesis of Clark et al. (2004) and Brookfield (1998), Liang et al. (2008) utilized the U-Pb and Lu-Hf isotopic systems of detrital zircons from a single, poorly constrained Late Miocene (ca. 10–5 Ma) sandstone sampled from the Central Burma Basin to show evidence for a Yarlung Tsangpo-Irrawaddy connection at the time of deposition. They established the Lu-Hf isotope system as a useful provenance indicator to discriminate between the Yarlung Tsangpo and Irrawaddy catchments which have similar age properties and rock types, where the Gangdese Batholith in southern Tibet has a unique high positive εHf(t) isotopic signature, contrasting with the negative εHf(t) values of the eastern Transhimalayan batholiths of the eastern syntaxis, Western Yunnan and north east Burma (Liang et al., 2008). In a detailed provenance study of the sedimentary deposits of the Indo-Burma Ranges, thought to be the uplifted western extension of the Central Burma Basin (Mitchell, 1993), it is proposed that Palaeogene deposits are derived from Cretaceous to Eocene arc rocks from an intra-Burma source, and accreted proto-Bengal Fan sediments as previously suggested (Curray, 2005), while the Neogene deposits show a contrasting provenance derived from the Himalayan orogenic front, showing close affinities to the Miocene foreland basin deposits (Allen et al., 2008).

In spite of its potential to shed light on the evolution of eastern syntaxis rivers, timing of uplift and significant erosion of the early eastern Himalayas since collision, published age and geochemical data are particularly sparse for sedimentary rocks in the Central Burma Basin and for source rocks within the Irrawaddy catchment. Existing provenance interpretations are mostly based on petrographic, stratigraphic and heavy mineral studies conducted by Burmese postgraduate students during the 1970s and 1980s. This provenance study seeks to identify, and place time constraints on, areas of significant deformation, exhumation, erosion and sedimentation in the eastern Himalaya that were previously unidentified or undervalued.

2.9.3. Sedimentary repositories of the eastern Himalayan foreland and remnant ocean basins

Evidence of drainage capture by the Brahmaputra River should also be recorded in the onshore and offshore sedimentary repositories of the eastern Himalaya. U-Pb dating of detrital zircons sampled from Upper Miocene and Pliocene sedimentary rocks of the eastern foreland basin, Arunachal Himalaya show substantial Cretaceous and Palaeocene age populations, interpreted to be sourced from the Asian Mesozoic to Tertiary magmatic arc, located north of the Yarlung Tsangpo Suture Zone (Cina et al., 2007). In agreement with these results, Cina et al. (2009) and Chirouze et al. (2012a, b) used combined U-Pb and Lu-Hf analysis of detrital zircon from the same Neogene sequences in Assam to show Gangdese detritus being deposited in this basin from the Late Miocene (ca. 11 Ma) onward, invoking a Yarlung Tsangpo-Brahmaputra river system connecting the Lhasa terrane and foreland basin at this time, providing a minimum age for capture from the Irrawaddy River. This is in contrast with suggestions of a Pliocene-Pleistocene capture event (Brookfield, 1998; Burg et al., 1998; Clark et al., 2004; Stewart et al., 2008), but is in agreement with a Late Miocene disconnection (Booth et al., 2009; Ding et al., 2001; Liang et al., 2008). A prolific Oligocene unconformity occurring after deposition of an oxisol is seen throughout the entire foreland basin along strike (DeCelles et al., 1998) and is interpreted to represent the uplift and passage of a southward migrating forebulge. Compositional studies of Palaeogene sedimentary rocks of the eastern Himalayan foreland basin, Assam, indicate erosion from an uplifting orogenic belt in this region by the Eocene, with an increasing contribution from volcanic rocks and higher grade metamorphic in the middle-late Oligocene and are shown have similar compositions to coeval sedimentary rocks of the foreland basin deposits to the west (Uddin et al., 2007). In contrast, the Palaeogene sequences of the Bengal remnant ocean basin are significantly different, as the early Palaeogene sedimentary rocks do not contain significant Himalayan input and deposition occurred farther from the orogenic front (Uddin and Lundberg, 1998a, b).

The provenance of Palaeogene sedimentary rocks deposited in the Bengal Basin is debated, with Indian craton, Indo-Burman Range, and Himalayan sources suggested (Najman et al., 2008, 2012; Uddin and Lundberg, 1998a, b). These sequences have

poor age controls, are absent in onshore outcrop, or all together, and are thought to have experienced intense chemical weathering during deposition near the equator, that potentially inhibits sedimentary provenance studies (Uddin and Lundberg, 1998a, b).

Sandstone composition and heavy mineral studies advocate a proximal Indian craton origin for Palaeogene sedimentary rocks, characterized by stable heavy mineral assemblages and quartzose nature with no contribution from an orogenic source, although it is recognized this may be the result of chemical weathering during equatorial deposition, and a Himalayan or Indo-Burman Ranges source is not ruled out (Uddin and Lundberg, 1998a, b). Johnson and Nur Alam (1991) suggest the initiation of Himalayan and Indo-Burma Range sedimentation into the basin began in the Oligocene, with increased subsidence and sedimentation beginning in the Miocene. In a detailed provenance study, Najman et al. (2008) showed rapid exhumation and deposition of Himalayan derived sediment, inconsistent with an Indian continent or Burma source, during the Late Eocene to Early Miocene, beginning at ca. 38 Ma, although it is acknowledged older eroded material may have been deposited elsewhere.

The first unambiguous evidence of significant Himalayan derived input into the Bengal Basin occurs during the Miocene, with deposition of abundant blue-green amphibole, suggestive of erosion from arc and ophiolite source rocks (Uddin and Lundberg, 1998a, b) coupled with the arrival of Himalayan aged mica, indicating rapid Middle Miocene unroofing of crystalline rocks of the eastern Himalaya (Rahman and Faupl, 2003; Uddin et al., 2010). Najman et al. (2012) showed the Late Miocene (ca. 8 Ma) sedimentary rocks of the eastern Bengal Basin are overwhelmingly Himalayan derived with subordinate arc and ophiolitic input from the uplifted Palaeogene Indo-Burman Ranges to the east and/or the Transhimalayan arc terrane to the north.

2.9.4. Bengal Fan

The Bengal Fan has only been drilled to depths dated at 18–17 Ma at the base of the core from Ocean Drilling Program Leg 116 (Copeland and Harrison, 1990; Copeland et al., 1990; Corrigan and Crowley, 1990; France-Lanord et al., 1993; France-Lanord et al., 2000; Galy et al., 1996). Analysis of the strontium, neodymium and osmium isotopic composition of sediment deposited in the Bengal Fan indicate a stable source

area over the past 17 Ma, derived predominantly from the Greater Himalayan sequence and subordinate contributions from the Lesser Himalaya, Tethyan Himalayan sequence (Derry and France-Lanord, 1996; France-Lanord et al., 1993; Galy et al., 2010) minor contributions from the Transhimalayan batholiths north of the Indus Yarlung suture zone are detected in the Bengal Fan since 12 Ma, consistent with the establishment of a Yarlung Tsangpo-Brahmaputra river connection by this time (Galy et al., 2010).

2.9.5. Evidence of erosion from the Southern Lhasa terrane in the Palaeogene sedimentary rocks of the foreland and remnant ocean basins, Eastern Himalaya

In the Himalayan foreland basin of Nepal, Early Cretaceous to Early Eocene strata are derived from a northern continental Indian source containing predominantly monocrystalline quartz and U-Pb zircon age populations older than 1500 Ma (DeCelles et al., 2004, 1998). In contrast, Middle to Late Eocene strata show a predominant contribution from the rising Tethyan Himalaya meta-sedimentary rocks to the north, marked by 500 to 1500 Ma detrital zircon ages, and a minor contribution from Asian rocks north of and including the Indus-Yarlung Suture zone is speculated based on the presence of Cr-spinel, less negative whole rock Sr and Nd isotope values and Cretaceous aged zircons, interpreted as foreland basin deposition in a backbulge region (DeCelles et al., 2004, 1998; Najman et al., 2000). The first definitive evidence of Himalayan erosion is in deposition beginning in the Early Miocene with evidence of SW-ward flowing fluvial channels (DeCelles, 1998), interpreted as deposition in the forebulge, abundant low-grade metamorphic lithics and plagioclase sediment. Cretaceous aged detrital zircons, the presence of Cr-spinel and less negative whole rock Nd isotope values in the late Eocene to early Miocene Bengal Basin sedimentary rocks are used to infer provenance from Asian magmatic arc rocks, north of the Indus Yarlung suture zone (Najman et al., 2008). In contrast, the Neogene sediments are interpreted to reflect an increasing contribution from the rising Greater and Lesser Himalayan sequences, supported by a lack of Cretaceous aged zircons and arc-derived lithics, with the uplifting orogen creating a barrier for the Gangdese arc source terrane.

However, it may be argued that there is a paucity of evidence for significant transport of detritus eroded from the Cretaceous-Tertiary magmatic arc of the southern Asian margin to the foreland and remnant ocean basins. Although provenance from the

Tethyan meta-sedimentary sequence with its distinctive age population at 520 to 470 Ma, and possibly Cambrian Pan-African granites intruded into the Greater Himalaya (DeCelles et al., 2004; Gehrels et al., 2011), is undisputable, a second possible source region for Cretaceous aged zircons and volcanic detritus within the Palaeogene foreland and remnant basin deposits remains under explored. The number of Cretaceous zircons present in the Palaeogene foreland basin deposits is 2 out of 297 grains (DeCelles et al., 2004) and 4 out of 83 in the Bengal Basin (Najman et al., 2008), and it is possible these grains are recycled from the Cretaceous Tethyan Himalaya (Garzanti et al., 2004), potentially sourced from granitoids and extensive volcaniclastics formed along the Indian margin associated with Cretaceous extension and rifting from Gondwanaland (Gehrels et al., 2011; Hu et al., 2010; Zhu et al., 2009a; Zhu et al., 2008). Evidence of significant crustal thickening and peak metamorphism by the Late to Middle Eocene in the Tethyan Himalaya fold and thrust belt, is characterized by emplacement of granitoids at ca. 44 Ma (Aikman et al., 2008), growth of metamorphic mica (Dunkl et al., 2011; Ratschbacher et al., 1994), east-west trending south facing folding and top to the south thrusting (Antolín et al., 2011) and this deformation may have occurred considerably south of the Indus Yarlung Suture Zone (Murphy and Yin, 2003). The Late Cretaceous Comei large igneous province is exposed over a wide area in the central-eastern Tethyan Himalayas, and may have also contributed sediment to the Bengal fan during the Palaeogene (Zhu et al., 2009a; Zhu et al., 2008). Additionally, there is evidence that uplift began in central Tibet during the Late Cretaceous and expanded into a proto-Himalayan Plateau by ca. 45 Ma, coeval with significant shortening and crustal thickening (Kapp et al., 2005b; Rohrmann et al., 2012). In comparison with published literature data, the Jurassic and Cretaceous strata of the Tethyan Himalaya remains underrepresented, where ophiolites are over-represented in the Sr and Nd isotope dataset for the Asian Transhimalaya (e.g. Najman et al., 2000). Cr-spinel with low TiO2, identified within the Palaeogene sedimentary deposits are also characteristic of the Wolong volcaniclastic suite deposited along the northern margin of India in the Cretaceous (Hu et al., 2010).

The presence of long lasting antecedent rivers draining the Asian terrane prior to and during latest Palaeocene- earliest Eocene collision and the delay of substantial

sedimentation in the Himalayan foreland basin and Bay of Bengal derived from north of the Indus-Yarlung suture zone prior to the Miocene, deposited by rivers transverse to the rising orogen, cannot be reconciled with evidence of significant pre-Himalayan crustal thickening, uplift and erosion of the Lhasa terrane, recorded in the Cretaceous to Palaeogene sediments deposited in forearc (Durr, 1996; Wu et al., 2010) and back-arc (Leier et al., 2007a) basins in Tibet and extensive crustal melt granites to the north (Chiu et al., 2009).

In this study, it is hypothesized that the Yarlung Tsangpo-Irrawaddy system was the major river system draining the eastern Himalayas prior to capture of the Yarlung Tsangpo by the Brahmaputra River in the Early Miocene. The twelve kilometre thick succession of Cenozoic syn-orogenic sedimentary rocks deposited by this system in the Central Burma Basin, Burma, represent the most complete and accessible sedimentary record of early erosion from the eastern Himalayas and south-eastern Lhasa terrane following the collision of India with Eurasia at ca. 55 Ma. This palaeo-geographic reconstruction may in part explain the obscurity of early orogenic detritus, particularly sediment derived from north of the Indus-Yarlung suture zone, within the eastern foreland basin (Uddin et al., 2007; Cina et al., 2009), the Bengal Basin remnant ocean (Uddin & Lundberg, 1998a, b) and the Bengal Fan (e.g. France-Lanord et al., 2000).

Chapter 3. Methods and Results

3.1. Sampling

Changing patterns in source areas and sediment pathways in the eastern Himalaya lead to changes in the sediment composition transported from the hinterland to adjacent sedimentary repositories. It is proposed that the Cenozoic sedimentary rocks of the Central Burma Basin potentially record the evidence for an antecedent Yarlung Tsangpo-Irrawaddy river and the subsequent capture of the Yarlung Tsangpo by headward erosion of the Brahmaputra River. Therefore, a detailed provenance study of these detrital sediments has the potential to constrain the timing and nature of river capture in this region, providing essential information to better understand the link between crustal and surface processes in active orogenic settings. This study uses geochronology, thermochronology and geochemical analyses on single grain detrital minerals extracted from a suite a sequence of Eocene, Oligocene, Miocene and modern fluvial and deltaic syn-orogenic sediments deposited in the Central Burma Basin by the Irrawaddy River system, thought to be involved in one of the last major river capture events in the eastern Himalaya, in order to determine the Cenozoic evolution of this river system.

Samples were collected from the Central Burma Basin in 2007 by Dr Ruth Robinson of the University of St Andrews, UK, Dr Nay Win Oo of the Department of Geography, University of Pyay, Burma and Professor Myint Thein of the Department of Geology, University of Mandalay, Burma. Because the Cenozoic sequence is not preserved in its entirety within the basin, rocks had to be taken from three separate locations in order to obtain a more complete stratigraphic succession. Sample localities are shown in Figure 3.1 in conjunction with a stratigraphic column showing the Cenozoic formations sampled.

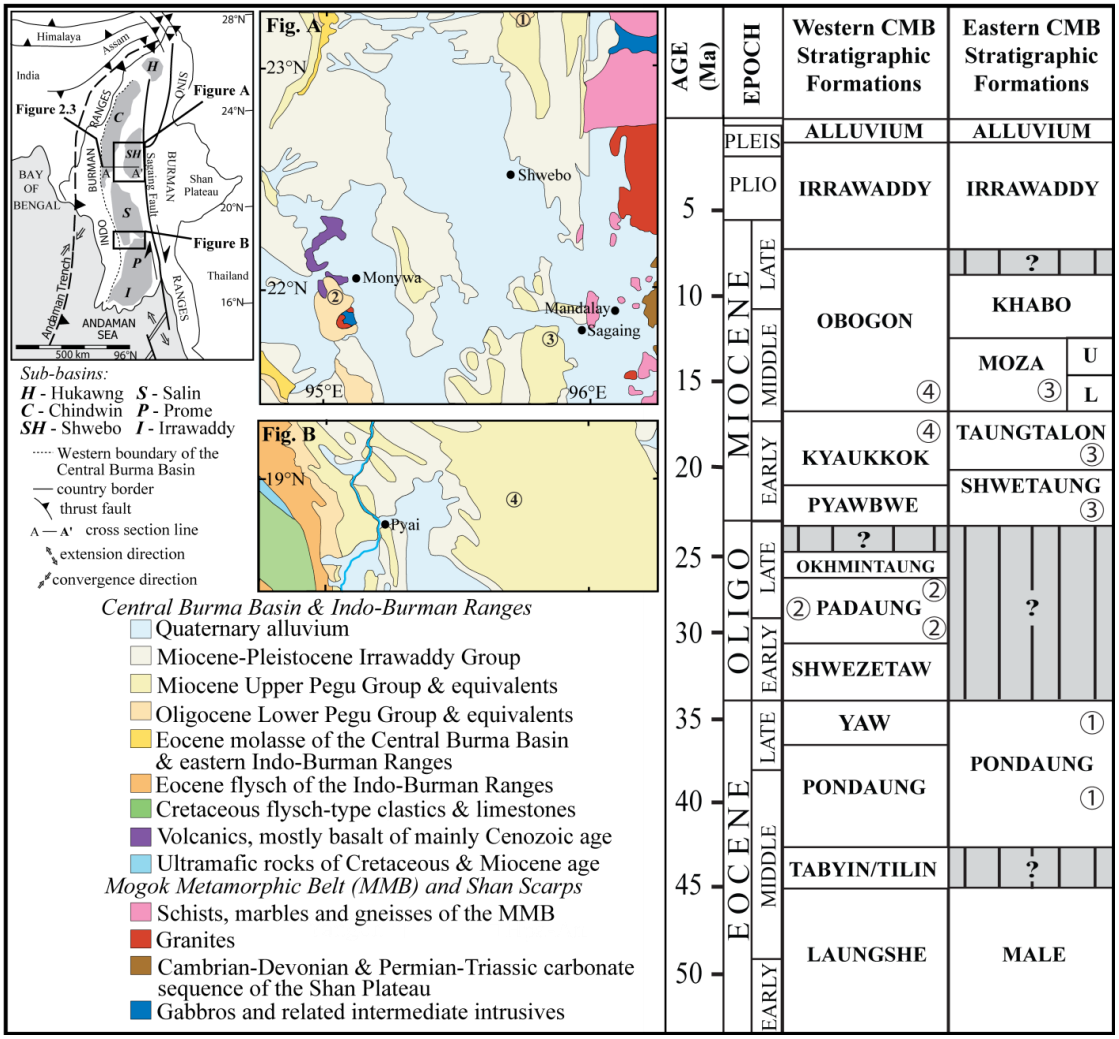

Figure 3.1 Simplified geology map of Burma and corresponding Cenozoic stratigraphy with sample localities. Modified from Bender (1983).

Two sedimentary bedrock samples were taken from the Eocene Pondaung Formation from outcrops located along the eastern edge of the Eastern Trough, approximately 42 kilometres north and 31 kilometres east of Shwebo (elevation ~170 metres) (Figure 3.1). Pondaung 1 (22.9888°N, 95.8812°E) represents the oldest sedimentary sample taken, and Pondaung 2 (22.9905°N, 95.8863°E) collected 0.5 kilometres apart. Lithologically correlated sandstones of the non-marine Pondaung Formation in the Western Trough have been more widely studied because of the presence of *Pondaungia* (*Eosimiidae*) and *Amphipithecus* anthropoid primate fossils (Ciochon and Gunnell, 2002; Khin et al., 2014; Tsubamoto et al., 2002); absolute dating methods applied to an ash bed within the Pondaung Formation at this locality has been assigned a Middle to Late Eocene age

(Benammi et al., 2002; Khin et al., 2014; Tsubamoto et al., 2002). The sedimentary units of the Pondaung Formation are composed of medium-grained lithic arenites (Pondaung 1) and coarse-grained sub-arkosic arenites (Pondaung 2), which exhibit trough cross-bedding and are interpreted as fluvial and deltaic sediments derived from a northern source (Maung et al., 2005; Soe et al., 2002; Thein, 1966). Since much of the Oligocene in the Eastern Trough is represented by a depositional hiatus, three samples from the Oligocene Padaung Formation were collected from outcrops in the Western Trough, approximately sixteen kilometres west of Monywa (elevation ~125 meters) (Figure 3.1).

The sedimentary units from which samples Padaung 1 (22.1028°N, 94.9791°E) and Padaung 3 (22.1073°N, 94.9774°E) were collected represent non-marine fluvial deposits and consist of medium- to- coarse-grained lithic and feldspathic arenites and local basal conglomerate lenses with prominent trough cross-bedding (Figure 3.1). Padaung 2 (22.0991°N, 94.9961°E) was sampled from interbedded coarse-grained feldspathic arenites (10 to 30 cm thick), mudstones and siltstones, representing a point bar deposit. This sample is assumed to be part of the Padaung Formation; however, it potentially may represent the lower Okhmintaung Formation, as there is a gradational contact, marked by thickening of sandstone layers, between the two formations, making the exact position of the basal contact unclear (Bender, 1983). Padaung 3 is the stratigraphically lowest, and therefore oldest, sample from the Padaung Formation and was collected approximately 300 meters stratigraphically below Padaung 1 and the youngest sample (Padaung 2) was collected approximately 1.8 kilometres apart from Padaung 1.

Three sedimentary rock samples were collected from exposures of the Upper Pegu Group in the Eastern Trough of the Central Burma Basin at outcrops located 45 km southwest of Mandalay (Figure 3.1): the Early Miocene Shwetaung Formation, the Middle Miocene Taungtalon Formation and the Middle- to Late- Miocene Lower Moza Formation (Khin & Myitta 1998; San 1981; Thein 1966). These units are composed siltstones and sandstones deposited in fluvial and estuarine environments (Khin & Myitta 1998; San, 1981; Thein, 1966). Additionally, two Middle- to- Late Miocene medium- to fine-grained quartz arenite sedimentary rock samples with prominent trough

cross-bedding were collected from the Obogon and Kyaukkok formations outcropping in the Western Trough, approximately five kilometres north of Pyay (18.8833°N, 95.2167°E) (Figure 3.1). The Middle Miocene Kyaukkok Formation and Middle- to-Late Miocene Obogon Formations are lithologically similar to the respective coeval Taungtalon Formation and Lower Moza Formations deposited in the Eastern Trough (San, 1981; Thein, 1966). The Early Miocene Shwetaung Formation is thought to be the eastern equivalent of the Pyawbye Formation, deposited in the Mimbu (Salin) sub-basin in the Western Trough (San, 1981; Thein, 1966).

3.2. Detrital zircon U-Pb geochronology

U-Pb dating of detrital zircon is widely used in provenance studies, as zircon is resistant to physical and chemical weathering during transport and burial which often modify sediment composition (Morton and Hallsworth, 1999). The closure temperature for the U-Pb isotopic system in zircon is ~750°C (Schaltegger et al., 1999; Spear and Parrish, 1996) recording the timing of crystallization in a magma, or high grade and retrograde metamorphism. In addition to preserving age information, the morphology and internal textures determined by back-scatter and cathodoluminescence imaging can be used to discriminate between a metamorphic or magmatic source (Corfu et al., 2003; Hoskin and Black, 2000). High precision laser ablation zircon dating, with a typical spot size of 25–50 μm, can precisely target a specific homogeneous zone, whether it represents an initial magmatic or metamorphic growth event or later re-crystallization which are recorded in zircon rims (Corfu et al., 2003; Košler and Sylvester, 2003). The uranium concentration in zircon controls the degree of metamictization, and radiation damage due to α-decay within the crystal increases over time (Hallsworth et al., 2000). Numerous studies have demonstrated the application of U-Pb dating of detrital zircons to infer maximum depositional ages of stratigraphic successions (Dickinson and Gehrels, 2009), and as a provenance tool in both modern and ancient sedimentary records (Allen et al., 2008; Bodet and Schärer, 2000; Cawood et al., 2003; DeCelles et al., 2004; DeCelles et al., 2000; DeCelles et al., 1998; Fedo et al., 2003; Morton et al., 2005; Najman, 2006; Najman et al., 2008; Zhang et al., 2012b), where detrital ages are compared with bedrock U-Pb zircon ages in the source terranes. Temporal variations in detrital zircon age populations for a stratigraphic succession in a basin can reflect

changes in source provenance and sediment transport pathways (Aitchison et al., 2011; Alizai et al., 2011; Cina et al., 2009; DeCelles et al., 2004; DeCelles et al., 1998; Haughton et al., 1991; Henderson et al., 2010; van Hoang et al., 2009). This technique is often used to build palaeogeographic reconstructions and orogenic models, by tracing the spatial variation of metamorphism, magmatism, and denudation in the source region. The pre-Himalayan Gondwana-derived terranes forming the Asian continent are shown to have distinct geological histories and age characteristics that can aid linking sediment source to sink in provenance studies (Allen et al., 2008; Bodet and Schärer, 2000; Cina et al., 2009; DeCelles et al., 2004; Gehrels et al., 2011; Leier et al., 2007b; Liang et al., 2008; Najman et al., 2012; Najman et al., 2008; Najman et al., 2000; van Hoang et al., 2009; Wu et al., 2007; Zhang et al., 2012b). However, where multiple source regions contain similar rock types with age-equivalent zircons, as in the Jurassic to Eocene Transhimalayan batholiths outcropping in the modern Yarlung Tsangpo and Irrawaddy River catchments, additional information is required. High precision U-Pb dating and Lu-Hf isotopic analyses that characterise zircons by age and mantle contributions to the original melt were carried out on detrital zircon from Eocene, Oligocene and Miocene sedimentary rocks from the Central Burma Basin in order to determine provenance and link temporal changes in the detrital signature to the drainage evolution of the Irrawaddy River system.

Detrital zircon grains were separated from bulk sedimentary rock samples using standard crushing, sizing, density liquid separation (2.85 g/cm^3) and Frantz magnetic separation techniques. A brief overview of the detrital heavy mineral species present within each formation is given in Appendix A1. Prior to analysis, cathodoluminescence (CL) and back-scattered electron (BSE) images were obtained for each grain using a JEOL JXA-8600 electron microprobe, with an accelerating voltage of 15 kV and a beam current of 15 to 20 nA, in the Department of Earth and Environmental Sciences at the University of St Andrews, Scotland, in order to identify internal structures (i.e. zoning and core/rim) and to select the optimum analytical spot positions for U-Pb and Hf isotope analyses that are devoid of fractures and inclusions (Figure 3.2, Appendix A4). *In situ* zircon U-Pb data were obtained by laser ablation multi-collector inductively coupled plasma mass spectrometry (LA-MC-ICP-MS), using a Nu Plasma MC-ICP-MS

coupled with an UP-193SS laser ablation system operating at a wavelength of 193 nanometres using a 35 µm spot, performed over several sessions at the NERC Isotope Geosciences Laboratory, UK. $^{206}Pb/^{238}U$ ages are used for zircons <1000 Ma and $^{207}Pb/^{206}Pb$ ages are used for zircon >1000 Ma; uncertainties on individual analyses are reported as 2σ and are not common lead corrected (% common Pb is low). Methodology and analytical procedures are described in more detail in Appendix A2 and the full analytical dataset is presented in Appendix Table A1. All age distribution diagrams were made using Isoplot v. 3.00 (Ludwig, 2003) add-in for Microsoft Excel and the Java script Density Plotter program of Vermeesch (2009) and Vermeesch (2012). A probability density plot showing all zircon U-Pb ages for the sampled Cenozoic formations arranged in stratigraphic order is presented in Figure 3.3. As only 10% of the 492 detrital zircons from the Cenozoic samples have Palaeozoic and Proterozoic U-Pb ages, much of the focus is on age data younger than 250 Ma. A probability density plot showing the U-Pb age distributions for each sample, with only ages younger than 250 Ma is presented in Figure 3.4.

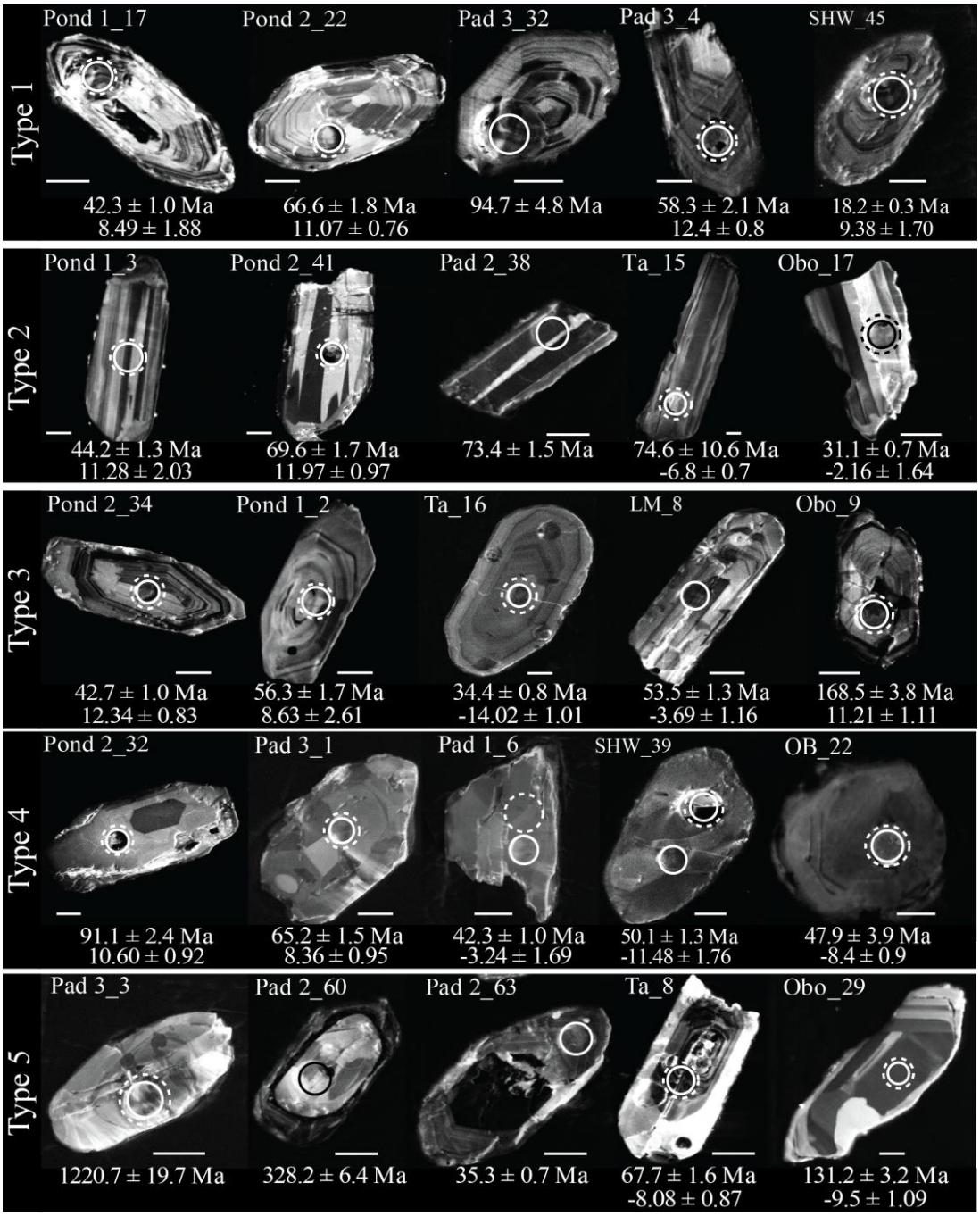

Figure 3.2 Cathodoluminescence (CL) images of representative detrital zircons extracted from Eocene, Oligocene and Miocene sedimentary rocks of the Central Burma Basin. Solid circles indicate the ablation spot locations for LA-MC-ICPMS U-Pb analyses and dashed circles indicate the locations for Lu-Hf analyses. The scale bar is 50 microns. Types 1 and 2 (most common): Oscillatory zoning indicative of igneous zircon. Wider growth zones may indicate slower crystallization within shallow plutons. Type 3: Sector zoning and oscillatory zoned zircons of igneous origin with localized re-crystallization and new growth of zircon rims during a high temperature event secondary to initial zircon formation. Type 4: Homogeneous zircons with limited internal structures showing minor resorption along edges that suggest a magmatic origin. Type 5: Complex internal structures revealing xenocrystic zircon cores surrounded by new zircon growth. The full CL image dataset is presented in Appendix A4. Interpretations after Corfu et al. (2003) and Hoskin and Schaltegger (2003).

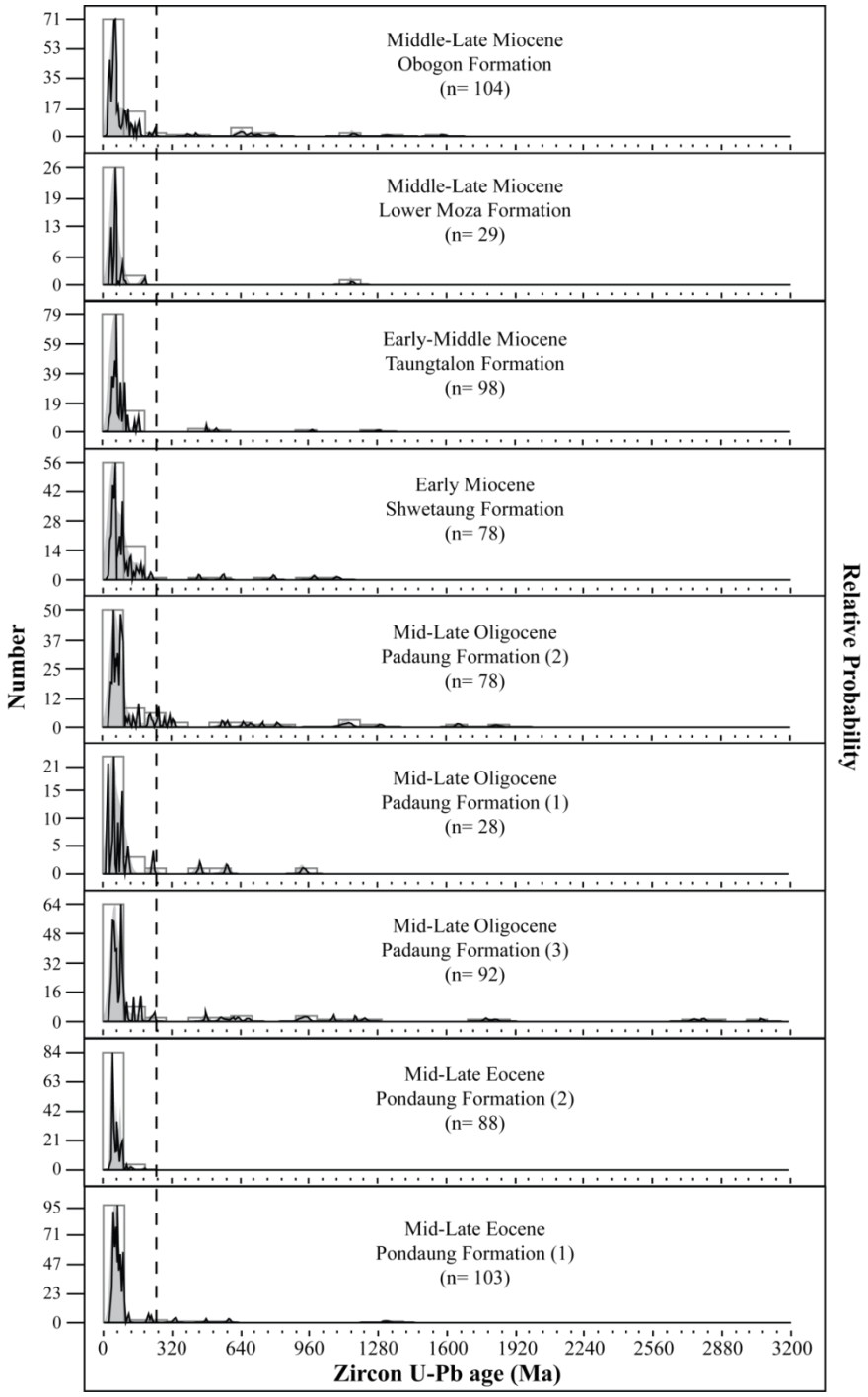

Figure 3.3 Probability density plot showing the zircon U-Pb age distributions for all Cenozoic formations analyzed, arranged in stratigraphic order. As early Mesozoic to Precambrian aged zircons are scarce, the focus is on ages younger than 250 Ma (dotted line) that are plotted in Figure 3.4.

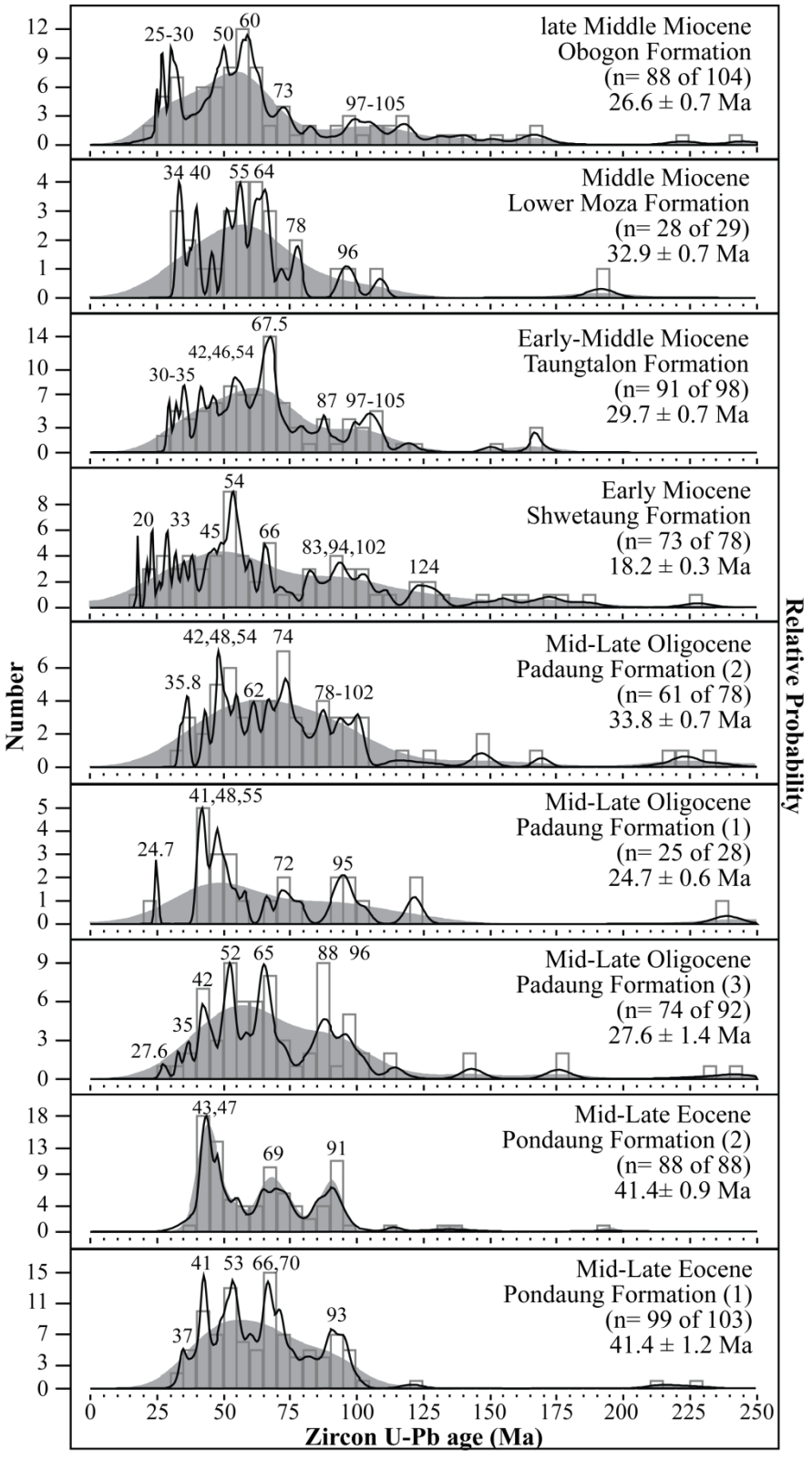

Figure 3.4 Probability density plot showing detrital zircon $^{206}Pb/^{238}U$ age distributions for Eocene, Oligocene and Miocene sedimentary rocks of the Central Burma Basin, arranged in stratigraphic order. Only zircons younger than 250 Ma are displayed. Detrital age peaks and the $^{206}Pb/^{238}U$ age of the youngest concordant (less than 10% discordance) detrital zircon in each formation are shown.

3.2.1. Eocene Pondaung Formation

A total of sixty-one U-Pb analyses on single grain detrital zircons extracted from the stratigraphically lowest, and therefore oldest sedimentary rock sample, Pondaung 1, were accepted. The youngest concordant detrital zircon has a $^{206}Pb/^{238}U$ age of 41.4 ± 1.2 Ma, and two slightly discordant grains of Priabonian age, indicate a Middle to Late Eocene maximum depositional age for this sample (Figure 3.3). This is in agreement with zircon fission track (37.2 ± 1.3 Ma) (Tsubamoto et al., 2002) and LA-ICP-MS U-Pb (40.2 ± 0.5 Ma) (Khin et al., 2014) age determinations on an ash bed within the Upper Pondaung Formation southwest of Monywa (Figure 3.1). Age distributions for zircons from the Pondaung 1 sample show three peaks of Middle to Late Eocene, Late Cretaceous to Early Palaeocene and early Upper Cretaceous, with a mode at ~ 45 Ma (Figure 3.4).

A total of forty-eight U-Pb analyses on single grain detrital zircons extracted from the Pondaung 2 sample were accepted. The youngest concordant detrital zircon has a $^{206}Pb/^{238}U$ age of 41.4 ± 0.9 Ma, consistent the depositional age of Pondaung 1. The age distributions show a similar three peak distribution of Eocene, latest Cretaceous to Early Palaeocene and early Upper Cretaceous, with a mode at ~ 43 Ma (Figure 3.4).

3.2.2. Oligocene Padaung Formation

A total of seventy U-Pb analyses on single grain detrital zircons extracted from the stratigraphically lowest, and therefore oldest sedimentary rock sampled from the Padaung Formation, Padaung 3, were accepted. The youngest detrital zircon has a Late Oligocene $^{206}Pb/^{238}U$ age of 27.6 ± 1.4 Ma and the youngest age peak is ~36.6 Ma, indicating a maximum Oligocene depositional age for the Padaung Formation (Figure 3.4). Twelve grains have Cambrian-Ordovician and Proterozoic U-Pb ages. The age distributions of the other fifty-eight zircons show Eocene to Oligocene, Early Palaeocene and Late Cretaceous peaks, with modes at ~ 42 Ma, 52 Ma, 65 Ma and 92 Ma (Figure 3.4).

A total of twenty-eight U-Pb analyses on single grain detrital zircons extracted from the Padaung 1 sample were accepted. The youngest detrital zircon has a $^{206}Pb/^{238}U$ age of 24.7 ± 0.6 Ma, suggesting a Late Oligocene depositional age for this sample (Figure

3.4). Three grains have early Palaeozoic and Precambrian U-Pb ages (Figure 3.4). The age distributions of the remaining twenty-five zircons show three age peaks at Palaeocene to Middle Eocene, Early and Late Cretaceous, with a main peak at ~ 42 Ma (Figure 3.4).

A total of seventy-eight U-Pb analyses on single grain detrital zircons extracted from Padaung 2 were accepted. The youngest detrital zircon has an earliest Oligocene $^{206}Pb/^{238}U$ age of 33.8 ± 0.7 Ma and the youngest age peak is ~36 Ma (Figure 3.4). Five grains have early Palaeozoic U-Pb ages and twelve zircons have Proterozoic U-Pb ages. The age distributions of the remaining sixty-six zircons show a wide spread of ages from ~100 Ma to 36 Ma, with two main age peaks at ~43 Ma and ~74 Ma (Figure 3.4).

3.2.3. Miocene formations

A total of fifty-two U-Pb analyses on single grain detrital zircons extracted from the Early Miocene Shwetaung Formation were accepted. The youngest detrital zircon has an Early Miocene $^{206}Pb/^{238}U$ age of 18.2 ± 0.3 Ma, providing a maximum depositional age for this sample (Figure 3.4). Four zircons have early Palaeozoic and Proterozoic U-Pb ages. The age distributions of the forty-eight Mesozoic and Cenozoic zircons display a wide range of ages spanning Middle Jurassic to Early Miocene, with a main peak at ~54-53 Ma (Figure 3.4).

A total of forty-four single grain detrital zircons extracted from the Early to Middle Miocene Taungtalon Formation were analyzed using LA-ICP-MS U-Pb dating, four of which had appropriate internal structure to facilitate core and rim measurements. The two youngest detrital zircons have Early Oligocene $^{206}Pb/^{238}U$ ages of 29.7 ± 0.7 Ma (Figure 3.4). One grain has a Proterozoic U-Pb age. Forty-seven analyses yield U-Pb ages spanning from Middle Jurassic to Early Oligocene time, with a main peak at ~67 Ma and lesser peaks in the Early Oligocene to Late Eocene (~35 to 30 Ma) and Middle Eocene (~47 to 41 Ma) (Figure 3.4). Two zircons show a significant difference in the core and rim age, where the cores have ages of ~78.5 Ma and ~41 Ma with corresponding rims dated at 29.7 and ~35 Ma, respectively.

A total of seventy-eight U-Pb analyses on single grain detrital zircons extracted from the Middle to Late Miocene Obogon Formation were accepted. The youngest detrital

zircon has a Late Oligocene $^{206}Pb/^{238}U$ age of 24.8 ± 0.4 Ma, and a youngest peak age of ~27 Ma (Figure 3.4). Four zircons have Silurian to Permian U-Pb ages and seven grains have Late Proterozoic U-Pb ages. The other sixty-seven analyses reveal prominent Oligocene, and Palaeocene to Eocene age peaks, with minor amounts of Jurassic to Cretaceous ages, and a Late Palaeocene mode at ~57 Ma (Figure 3.4).

A total of twenty-nine U-Pb analyses on single grain detrital zircons extracted from the Middle to Late Miocene Lower Moza Formation were accepted. The youngest detrital zircon has an earliest Oligocene $^{206}Pb/^{238}U$ age of 32.9 ± 0.7 Ma, and a youngest peak age of ~33 Ma (Figure 3.4). One zircon records a Proterozoic U-Pb age and the remaining ages range from Early Jurassic to Early Oligocene, with a prominent Palaeocene to Late Eocene clustering of ages (~65 to 50 Ma) (Figure 3.3 and 3.4). One zircon shows a diachronous core and rim relationship; the core has a Late Jurassic $^{206}Pb/^{238}U$ age (191.6 ± 5.2 Ma) and a Middle Eocene rim (40.3 ± 1.1 Ma).

Zircons were scarce in the Middle to Late Miocene Kyaukkok Formation, therefore no LA-MC-ICPMS U-Pb zircon ages were obtained for this sample.

3.2.4. Summary of U-Pb data

Zircons from all samples analyzed contain a significant proportion of detritus shed from rocks affected by the Himalayan orogeny (<56 Ma), therefore Himalayan orogenic molasse was being deposited in the Central Burma Basin at least as far back as the middle Eocene, the age of the oldest formation sampled (Figure 3.4). Additionally, minor Jurassic and Cretaceous age populations are recorded in all samples. The Eocene Pondaung, Oligocene Padaung and Early Miocene Shwetaung formations show a progressive decrease in the age of the youngest zircon with increasing stratigraphic succession, a signature expected to be recorded in a sedimentary basin receiving detritus shed from progressive unroofing of an active source terrane (DeCelles et al., 2004). The youngest zircon analyzed has a $^{206}Pb/^{238}U$ age of 18.2 ± 0.3 Ma, obtained from the Shwetaung Formation and is within error of the known Early Miocene depositional age, indicating that the lag time between the time of crystallisation, exhumation and deposition is short. Conversely, the younger Middle to Late Miocene formations show a progressive increase in the youngest zircon ages, accompanied by a shift in the

youngest age peaks to slightly older ages within stratigraphically younger units, suggesting that lag times have increased and previously deposited stratigraphic units are being recycled (Figure 3.4).

3.3. Detrital zircon Lu-Hf geochemistry

Additional provenance information can be obtained using combined high precision U-Pb dating and Lu-Hf isotope analysis of single grain detrital zircons, as this allows detrital minerals to be linked to source lithologies with corresponding age and geochemical properties (Bodet and Schärer, 2000; Howard et al., 2009; Liang et al., 2008; van Hoang et al., 2009; Wu et al., 2010; Zhang et al., 2012b). Owen (1987) was the first to propose the usefulness of Lu-Hf analysis as a provenance indicator where genetic relationships between source and sink exist. The epsilon hafnium (εHf) values of zircon records the composition of the melt from which it is derived at the time of crystallization (t), where zircons with positive εHf values are derived from juvenile mantle sources and those with negative εHf values are indicative of evolved crustal sources (Belousova et al., 2002; Hoskin and Schaltegger, 2003; Kinny and Maas, 2003).

To enhance provenance detection and discriminate between zircons from bedrock in Tibet, Burma, China and Thailand, a sub-set of single grain U-Pb dated detrital zircons from two Eocene, two Oligocene and four Miocene samples were also analyzed for Lu-Hf geochemistry using laser ablation multi-collector inductively coupled plasma mass spectrometry (Nu Plasma MC-ICP-MS) coupled with an UP-193SS laser ablation system operating at a wavelength of 193 nanometres using a 50 µm spot. The analyses focus on zircons with ages younger than 250 Ma. Analytical spots for Lu-Hf isotopic analyses were positioned over or within the same zone as the U-Pb ablation pits. εHf(t) values were calculated for each zircon using its $^{206}Pb/^{238}U$ age if <1000 Ma and its $^{207}Pb/^{206}Pb$ age if >1000 Ma, assuming values for the chondritic reservoir $^{176}Hf/^{177}Hf$ ratio of 0.282772 and $^{176}Lu/^{177}Hf$ of 0.0332 (Blichert-Toft and Albarède, 1997) and the decay constant for ^{176}Lu of 1.867×10^{-11} $year^{-1}$ (Söderlund et al., 2004). All quoted εHf(t) values are calculated with a 2σ uncertainty. The full analytical results of detrital zircon Lu-Hf isotope analysis is presented in Appendix Table A4 with a detailed description of the methodology and analytical procedures in Appendix A2.

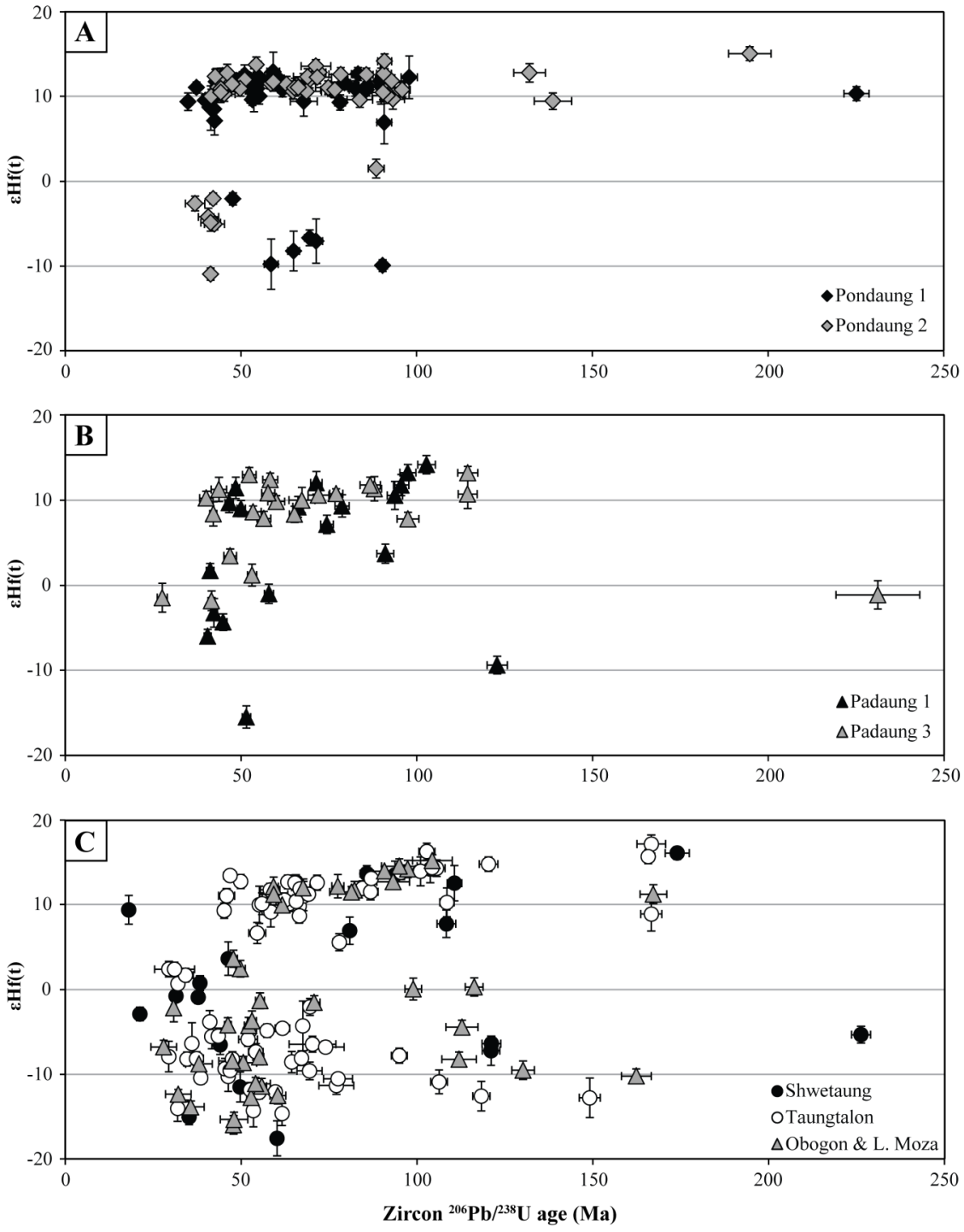

Figure 3.5 $^{206}Pb/^{238}U$ age vs. εHf(t) value for single grain detrital zircons extracted from Eocene (A), Oligocene (B) and Miocene (C) sedimentary bedrock samples of the Central Burma Basin. Only grains with ages less than 250 Ma shown. $^{206}Pb/^{238}U$ age error bars are 1σ uncertainty and εHf(t) value error bars are 2σ uncertainty.

3.3.1. Eocene Pondaung Formation

A total of eighteen detrital zircon grains from the stratigraphically lowest, and therefore oldest, unit sampled, Pondaung 1, were analyzed for their Lu-Hf geochemistry. A bimodal distribution of εHf(t) values is seen where fifteen of the eighteen grains (83%) display high positive values ranging from 6.93 ± 2.51 to 12.9 ± 2.3, and the remainder range between -7.03 ± 2.61 to -9.75 ± 2.96 (Figure 3.5). $^{206}Pb/^{238}U$ ages of zircons characterized by high positive εHf(t) values are Middle Eocene to Late Cretaceous (ca. 41 to 98 Ma), whereas zircons characterized by more negative values have Palaeocene to Latest Cretaceous ages (ca. 59 to 71 Ma) (Figure 3.5).

A total of nineteen detrital zircon grains from sample Pondaung 2 were analyzed for their Lu-Hf geochemistry. As observed in Pondaung 1, a bimodal distribution of εHf(t) values is seen where sixteen of the nineteen grains (84%) display a more restricted range of high positive values from 10.27 ± 0.8 to 14.13 ± 0.99, and the three remaining zircon have values of 1.5 ± 1.11, -2.03 ± 0.66 and -10.92 ± 0.71 (Figure 3.5). Zircons characterized by high positive εHf(t) values from the Pondaung 2 sample have Middle Eocene and Late Cretaceous $^{206}Pb/^{238}U$ ages (ca. 43–54 Ma and 66–96 Ma), while those with negative values are Middle Eocene in age (Figure 3.5). A Middle Late Cretaceous age (88.5 ± 2.3 Ma) is observed for the zircon with a corresponding εHf(t) value of 1.5 ± 1.1.

3.3.2. Oligocene Padaung Formation

Single grain Lu-Hf geochemical analysis was applied to a total of eleven detrital zircons from the Padaung 3 sample. A bimodal distribution of εHf(t) values is seen where roughly half of the zircons analyzed (55%) display high positive values ranging from 8.36 ± 0.95 to 11.36 ± 1.44. The other five zircons have restricted εHf(t) values lying either side of CHUR (εHf(t) = 0) from 2.88 ± 1.51 to -1.82 ± 1.16 (Figure 3.5). Zircons characterized by high positive εHf(t) values are Middle Eocene and Early Palaeocene to Aptian in age (ca. 42–43 Ma and 65–114 Ma), whereas zircons characterized by more negative values have a wider spread of ages including Late Oligocene (Chattian), Early to Middle Eocene, Triassic and Proterozoic (Figure 3.4).

A sub-set of twenty-two detrital zircon grains from sample Padaung 1 were analyzed for their Lu-Hf geochemistry. Similar to the zircons of Padaung 3, more than half (59%) of the zircons analyzed exhibit high positive εHf(t) values ranging from 3.73 ± 1.13 to 14.2 ± 1.07, the majority of which are > 7 (Figure 3.5), and one Proterozoic-aged grain has a value of 22.82 ± 1.47. Zircons characterized by unradiogenic hafnium compositions have Early to Middle Eocene and Late Cretaceous U-Pb crystallization ages. The other nine zircons show diverse εHf(t) values ranging from 1.73 ± 0.83 to -15.5 ± 1.32, with seven of these zircons enriched in radiogenic hafnium, displaying values less than -3 (Figure 3.5). Three of these zircons have older Late Cretaceous, Palaeozoic and Proterozoic U-Pb crystallization ages, whereas the remainder have $^{206}Pb/^{238}U$ ages spanning the Early Palaeocene to Middle Eocene.

3.3.3. Miocene formations

Single grain Lu-Hf geochemical analysis was applied to a total of seventeen detrital zircons from the early Miocene Shwetaung Formation. A significant change in the zircon Lu-Hf geochemistry is observed in the Miocene formations, initiating during the deposition of the early Miocene Shwetaung Formation (Figure 3.5). A more wide spread range of εHf(t) values is observed, with an increasing contribution of zircons enriched in radiogenic hafnium up-section. Roughly half of the grain (47%) display high positive εHf(t) values ranging from 3.6 to 14, with corresponding $^{206}Pb/^{238}U$ middle Eocene and Cretaceous ages (Figure 3.5). The youngest zircon with a strongly unradiogenic hafnium isotopic composition in the Shwetaung Formation has a $^{206}Pb/^{238}U$ age of 18.2 ± 0.3 Ma and an εHf(t) value of 9.38 ± 1.7. The remaining nine zircons have hafnium isotopic compositions near CHUR (chrondritic values) (Late Eocene and Early Miocene in age) or are strongly enriched in radiogenic hafnium, with εHf(t) values from 0.75 to -17.5 (one grain with value of -35) with lower Palaeogene, Lower Cretaceous, Palaeozoic and Proterozoic U-Pb ages (Figure 3.5).

A total of thirty-seven single grain detrital zircons from the Taungtalon Formation were additionally analyzed for their Lu-Hf geochemistry. In contrast to the Eocene and Oligocene formations, only 38% of zircons have unradiogenic hafnium isotope compositions, with εHf(t) values of 5.6 to 17, most of which are > 8, and have earliest Eocene to Albian and Middle Jurassic U-Pb ages (Figure 3.5). The majority of zircons

(62%) have a wide spread of εHf(t) values from 2.4 to -14.6 with predominantly Oligocene to Upper Cretaceous $^{206}Pb/^{238}U$ ages (Figure 3.5); one Proterozoic zircon has an εHf(t) value of -16.91 ± 1.74. One grain has an Upper Cretaceous core (78.5 Ma) with a hafnium composition of 5.55 and a Rupelian (Oligocene) age of 29.7 Ma with a corresponding εHf(t) value of 2.41.

Single grain Lu-Hf geochemical analysis was applied to a total of twenty-four detrital zircons from the middle Miocene Obogon Formation. Only five of the twenty-four grains analyzed (21%) have high positive εHf(t) values of 11.21 ± 1.11 to 14.19 ± 1.01 and have early Palaeogene to Upper Cretaceous and Middle Jurassic U-Pb ages (Figure 3.5). Four of the analyzed zircons are sourced from older crustal material, with Devonian and late Proterozoic U-Pb crystallization ages, with εHf(t) values ranging from 1.27 to -7. The remaining thirteen zircons with hafnium compositions near CHUR or that are enriched in radiogenic hafnium have Oligocene, middle Eocene to Lower Cretaceous and Middle Jurassic $^{206}Pb/^{238}U$ crystallization ages.

Only three Lu-Hf isotopic analyses on single grain detrital zircons from the Lower Moza Formation were accepted. One zircon dated at 78.1 ± 1.7 Ma has a high positive εHf(t) value of 12.15 ± 1.38, whereas two zircons with ages of ca. 53.5 and 56 Ma have negative εHf(t) values of -3.7 to -7.9 (Figure 3.5).

3.3.4. Summary of detrital hafnium data

In the Eocene Pondaung Formation, zircons of depleted mantle origin, characterized by high positive εHf(t) values from 7 to 14 with middle Eocene to late Palaeocene and Upper Cretaceous $^{206}Pb/^{238}U$ ages, are dominant, comprising 84% of analyzed grains (Figure 3.5). The youngest zircon with this juvenile mantle signature has a $^{206}Pb/^{238}U$ of 41.4 ± 1.2 Ma and the youngest peak age with this signature is ~43 Ma (Figure 3.4), roughly coeval with the previously assumed middle Eocene depositional age of the Pondaung Formation from which it was extracted. The presence of detrital zircon with U-Pb crystallization ages coeval with a Middle Eocene depositional age indicates detritus was shed from a juvenile mantle source terrane that experienced rapid exhumation, erosion and deposition in the Central Burma Basin during the early stages of the Himalayan orogeny. Similar to the Pondaung Formation, the Oligocene Padaung

Formation is dominated by zircons with unradiogenic hafnium isotopic compositions (58% have εHf(t) values >3.5), indicating derivation from rocks with a juvenile mantle signature with zircon U-Pb crystallization ages of middle to late Eocene and earliest Palaeocene to upper Lower Cretaceous (Figure 3.4, Figure 3.5). The youngest zircon recording this high positive εHf(t) signature in the Padaung Formation is 42.1 ± 1 Ma and the youngest peak age with this signature is ~42 Ma (Figure 3.4). A significant change in provenance during the Miocene is recorded by a change in the detrital zircon hafnium isotope composition, with an increasing contribution of zircons enriched in radiogenic hafnium observed with decreasing stratigraphic age.

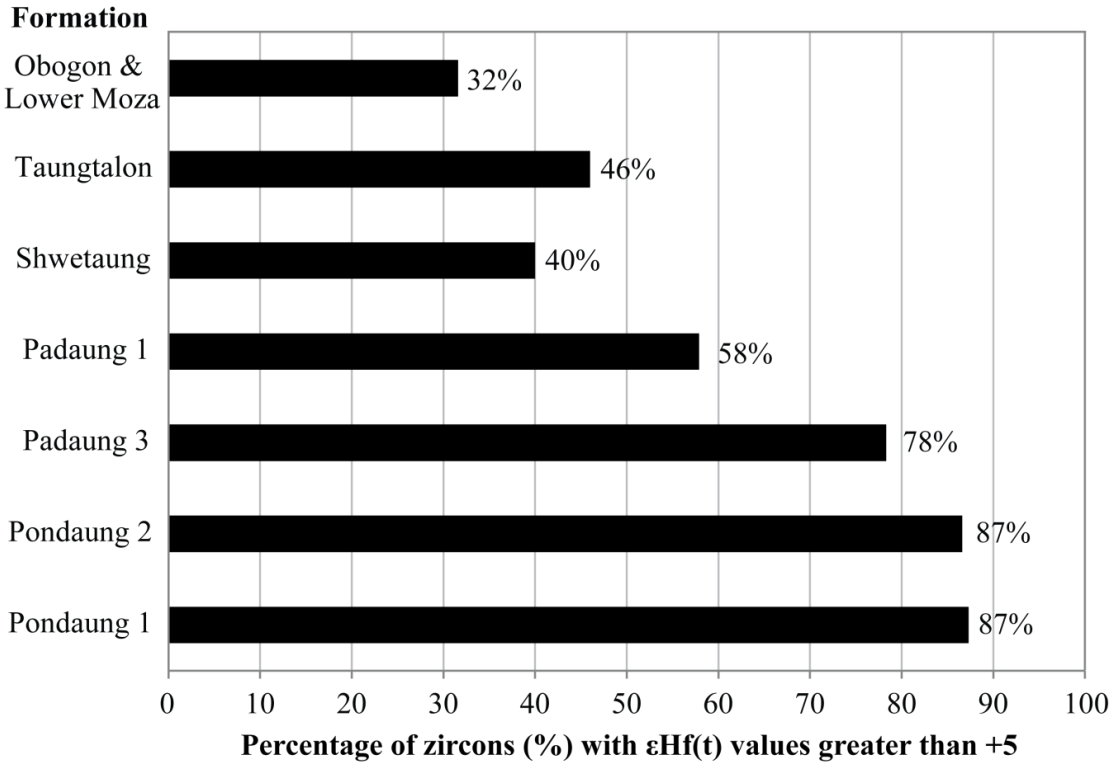

Figure 3.6 Percentage of single grain detrital zircons characterized by unradiogenic hafnium compositions (high positive εHf(t) values) for each sample arrange in stratigraphic order.

In the early Miocene Shwetaung Formation, 47% of zircons are characterized by high positive εHf(t) compositions, decreasing to 38% in the early-middle Miocene Taungtalon Formation, and 30% in the combined middle-upper Miocene Obogon and Lower Moza Formations (Figure 3.5). The youngest zircon recording the anomalous

unradiogenic hafnium isotope signature (εHf(t) = 9.38 ± 1.7) observed in the sampled Central Burma Basin sediments is 18.2 ± 0.3 Ma, occurring in the early Miocene Shwetaung Formation (Figure 3.4), although this is a single grain age and there is no age population present. The absence of zircons with this signature younger than the early Miocene (ca. 18 Ma) in the middle to late Miocene sediments suggests the rocks with a juvenile mantle signature (likely arc terrane) were no longer a source for detritus deposited in the Central Burma Basin after the early Miocene.

3.4. Mid to Low Temperature Thermochronology

The application of mid to low temperature thermochronology in provenance studies records the progressive exhumation of the hinterland through mid- and upper crustal levels, and provides constraints on the timing of exhumation relative to ages of peak and retrograde metamorphism, the timing of faulting and shear zone development, and the maximum depositional age of sedimentary deposits, as long as minerals have not experienced post-depositional heating sufficient enough to re-set cooling ages. Combining $^{40}Ar/^{39}Ar$ dating of white mica and zircon fission track in provenance studies widens the range of source lithologies contributing detritus and better constrains the timing of denudation and erosion by recording cooling from middle to upper crustal levels. Carrapa et al. (2004) and Carter and Bristow (2003) demonstrated the potential of $^{40}Ar/^{39}Ar$ detrital white mica and detrital zircon fission track, respectively, as a provenance tool and used their data to identify exhumation patterns in the hinterland through time to interpret the reorganization and development of the palaeo-drainage systems, and attributed these to an interval of increased tectonic activity.

Where post depositional temperatures in the basin remain insufficient to re-set the grain cooling age, this technique can be used to constrain maximum depositional ages of the sedimentary unit from which they were extracted (Henderson et al., 2010; Najman et al., 2008; Najman et al., 2005; Najman et al., 1997; Tsubamoto et al., 2002). If temperatures within the basin were high enough to cause partial or total re-setting (Garver et al., 2005; Verdel et al., 2012), mid-low temperature thermochronology may be used to reconstruct post-depositional basin dynamics, recording the timing of tectono-thermal events involving the sedimentary sequences. In the Central Burma

Basin, the mid and low temperature thermochronometers are sensitive to post-depositional re-setting, and may be useful in understanding the basin's burial history.

3.4.1. $^{40}Ar/^{39}Ar$ detrital white mica thermochronology

Total fusion $^{40}Ar/^{39}Ar$ dating of detrital white micas records the passage of the mineral through the closure temperature of ~300–400°C (Carter, 1999; Harrison et al., 2009; Hodges, 1991) and the technique is used as a provenance indicator where the thermo-tectonic, metamorphic and denudation history of the source terrane is known (Hodges et al., 2005; Najman, 2006; Uddin et al., 2010; von Eynatten and Dunkl, 2012). Mid to low temperature thermochronology is also used to determine cooling rates through time, and identify changes in exhumation pattern (Brewer et al., 2003; Carrapa et al., 2004; Van Hoang et al., 2010). The presence of multi-modal cooling age populations reflect multiple and/or diverse source regions contributing to the sediment load. The lag time between age populations and the width of the age peaks provides constraints on whether source rock exhumation and cooling is rapid (narrow peak) or slow (broad peak) (Stuart, 2002). Constant exhumation rates from a sustained source region will be represented as broad age distributions for any thermochronometer. Additionally, provenance studies utilizing multiple minerals reduces bias from interpretations based on information derived from a single mineral and application of this technique will enhance provenance interpretations by widening the range of lithologies sampled.

Sedimentary repositories of rivers which are antecedent to the orogen should initially contain older cooling ages recording erosion of the terrane before collision, followed by progressively younger age peaks in younger stratigraphic successions; this represents a record of continual exhumation of crustal rocks through the mineral closure temperature through time (Ruiz et al., 2004). Where the source regions experience rapid, episodic exhumation, a well resolved peak will temporally persist throughout the sedimentary basin sequences, reflecting the timing at which source rocks passed through the closure isotherm at a given time, followed by slower erosion (Carrapa et al., 2004). An up-section change in the detrital cooling populations can also reflect tectonically driven river capture (Carrapa et al., 2004; Van Hoang et al., 2010), where sediment eroded from actively uplifting source terranes is no longer being tapped. In order to determine

if river capture in the eastern Himalayan syntaxis was driven by increased deformation and uplift in the eastern Himalayan syntaxis or due to tectonism, it must be established whether continuous or episodic exhumation occurred in the source region.

The $^{40}Ar/^{39}Ar$ total laser fusion method has been applied to single grain detrital white micas extracted from ten Cenozoic sedimentary rocks sampled from the Central Burma Basin: two Eocene, three Oligocene and five Miocene aged samples. A total of 950 detrital white micas were analyzed; 538 grains from Miocene Shwetaung, Taungtalon, Obogon, Kyaukkok and Lower Moza formations, 318 grains from the Oligocene Padaung formation and 94 grains from the Eocene Pondaung formation. Analyses were conducted using a MAP 215-50 multi-collector noble gas mass spectrometer and automated sample extraction system coupled with a mid-infrared Merchantek 20W CO2 UC2000 Laser system at the Natural Environment Research Council (NERC) Argon Isotope Laboratory at SUERC, East Kilbride, Scotland. Analytical procedures are described in Appendix A3 and all data are presented in Appendix Table A6. $^{40}Ar/^{39}Ar$ white mica age distributions are plotted as combined probability and kernel density plots arranged in stratigraphic order (Figure 3.7), using the Java script Density Plotter program of Vermeesch (2009). Ages younger than 250 Ma are presented in Figure 3.8. Peak ages were calculated using a Finite Mixture Model (Galbraith and Green, 1990; Galbraith and Laslett, 1993). All reported ages have errors of 1σ uncertainty.

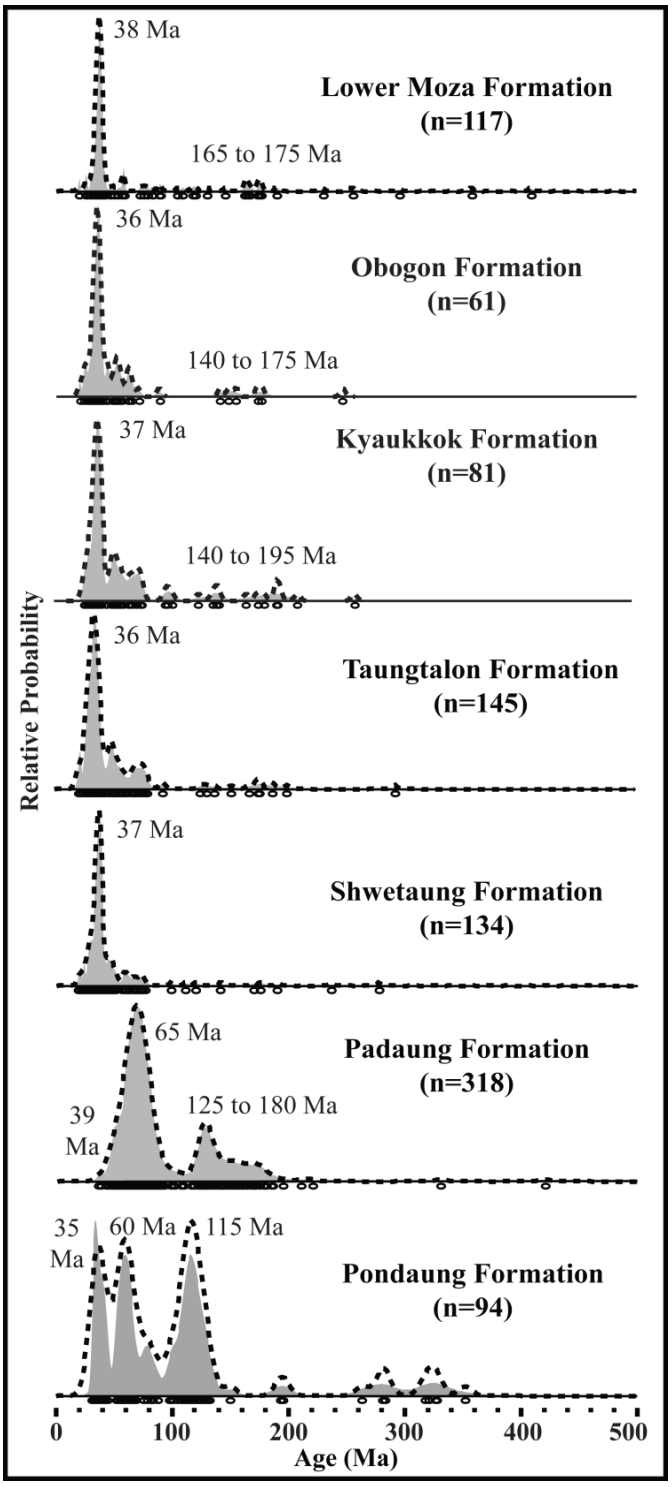

Figure 3.7 Probability density (shaded gray) and kernel estimation (dotted black line) plots for detrital white mica $^{40}Ar/^{39}Ar$ cooling age distributions for all samples, arranged in stratigraphic order.

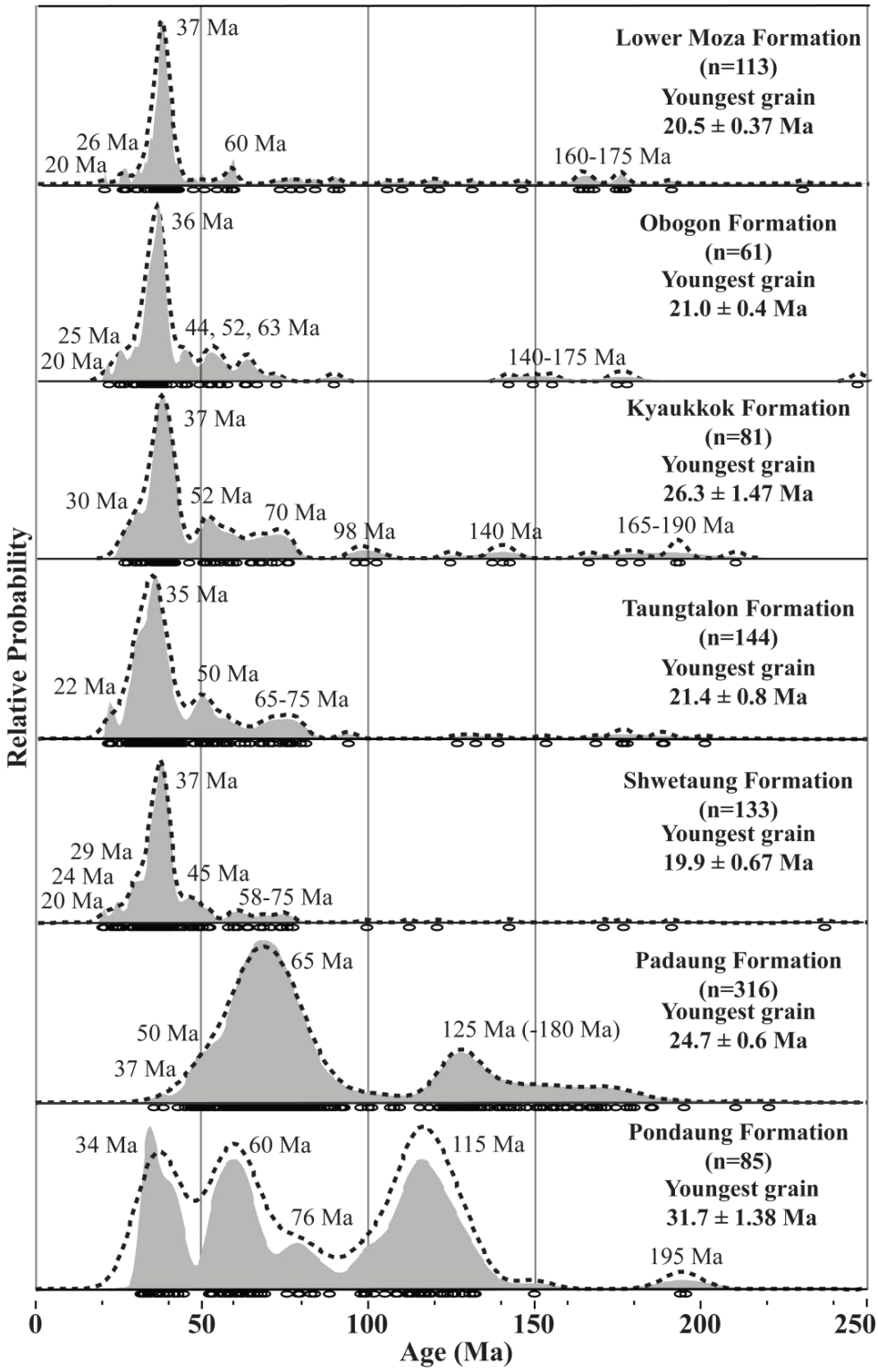

Figure 3.8 Probability density (shaded gray) and kernel estimation (dotted black line) plots for detrital white mica $^{40}Ar/^{39}Ar$ cooling age distributions for ages younger than 250 Ma for all samples, arranged in stratigraphic order.

3.4.2. Eocene Pondaung Formation

The sandstones of the Pondaung Formation are unmicaceous relative to other samples, and 74.5% of the detrital grains have $^{40}Ar/^{39}Ar$ ages > 56 Ma with only a quarter having cooling ages younger than 56 Ma, representing Himalayan orogenic detritus (Figure 3.7, 3.8). Age distributions are characterized by a spread of ages with wide peak bases and multi-modal cooling age populations of 60 Ma, 76 Ma and 115 Ma, suggesting derivation from a variety of source terranes that experienced differential cooling, both temporally and spatially, prior to the India-Asia collision (> 56 Ma). The Pondaung Formation is thought to be Late Middle or Late Eocene, based on stratigraphic correlation with dated units in the Western Trough (Tsubamoto et al., 2002), however a significant number of grains fall in population with a modal age of 34 Ma, younger than the expected depositional age. There are either some reset white micas within the populations in this sample, or the depositional age is Latest Eocene or younger.

The stratigraphically lowest, and oldest, sample from the Eocene Pondaung Formation (Pondaung 1) is unmicaceous, with only eleven ages obtained. The youngest age population has a peak of ~35 Ma (Figure 3.7, 3.8) which is younger than the known depositional age and therefore may indicate the presence of a significant proportion of white micas with re-set ages. The limited dataset for this sample may be the result of the very fine grained nature of this sample and consequently the white mica grains are smaller than the 250 μm range. This limits the ability of one to successfully and accurately date a grain because of the limited amount of argon contained within the sample. It has been shown in laboratory settings that the closure temperature for the argon system in mica is controlled, at least in part, by the grain diameter, therefore smaller mica grains may have lower argon retentiveness and may be more likely to be re-set at lower temperatures (Harrison et al., 2009). It must be noted that the >250μm fraction of white mica grains were preferentially selected, and this sampling bias may miss cooling age populations that are characterized by smaller grain size fractions. The unmicaceous nature of the Pondaung 1 sample may indicate its origin from an arc-dominated source region, as white mica is rarely present in the composition of juvenile magmatic rocks.

Eighty-three detrital white mica grains were analyzed from the Eocene Pondaung 2 sample. Approximately half (53%) have a Mesozoic age, two-thirds of which consist of Lower Cretaceous ages (Figures 3.8, 3.9). Over a third (36%) of the grains are Palaeogene in age, consisting of predominantly Eocene and Palaeocene ages (even distribution of ages for each stage throughout the Eocene and Palaeocene), with only two grains giving an Oligocene age. Pondaung 2 also contains a minor Palaeozoic age population (11%) of Permian and Carboniferous age, the most prominent Palaeozoic population seen for all samples. A quarter of the cooling ages (25.5%) are younger than 56 Ma, representing Himalayan molasse. The majority of the cooling ages represent cooling of the older Asian crust prior to India-Asia collision. The youngest peak gives an age of ca. 37 Ma, in agreement with the expected Late Middle Eocene depositional age.

3.4.3. Oligocene Padaung Formation

The detrital white mica cooling ages from the Oligocene Padaung 1, Padaung 2 and Padaung 3 samples are presented together given the similarity in their age distributions. A total of 101, 76 and 141 detrital white mica grains were analyzed from Padaung 1, Padaung 2 and Padaung 3 samples, respectively, or 318 grains in total for the Padaung Formation. Sandstones of the Padaung Formation are much more micaceous than those of the Pondaung Formation. Most of the cooling ages range from Middle Eocene (~43 Ma) to Early Jurassic (~195 Ma), with rare Late Eocene, Late Triassic and Palaeozoic grains; between 83 and 95% of these mica ages are Palaeocene and older, reflecting thermal histories prior to the Indo-Asian collision. The majority of the grains are Mesozoic in age (72%), with a minor Palaeogene (27%), and almost negligible Palaeozoic population (1%). The Oligocene Padaung Formation is characterized by a spread of ages from ca. 41 to 95 Ma, and ca 115 to 190 Ma (Figure 3.7, 3.8); a dominant peak occurs at ~69 Ma, with less well defined peaks at ca. 130 and 165-174 Ma. The broad age range and numbers of populations are, like the Pondaung Formation above, suggestive of derivation from source terranes that experienced spatially and temporally differential exhumation prior to the India-Asia collision (ca. 56 Ma). A minor Oligocene (37 Ma) age peak is also observed (Figure. 3.8).

Only 9% of the ages in the Oligocene Padaung Formation are younger than 56 Ma. The overwhelming majority are Cretaceous in age (61%), with ~44% of grains having a Late Cretaceous age and 17% have an Early Cretaceous age (Figure 3.9). The remainder of the zircons are clustered into Eocene (9%), Palaeocene (18%) and Jurassic (10%) populations. Two Triassic-, one Carboniferous- and one Silurian-aged grain make up the remaining 2%. The absence of younger (36–38 Ma) ages in Padaung 2 may be due to fewer grains being measured for Padaung 2 (n= 75) relative to Padaung 1 (n = 100) and Padaung 3 (n = 141). These younger ages represent a very small population (one grain in each sample) in Padaung 1 and 3 which is most likely under-represented in Padaung 2 because of the small number of grains analysed. The next youngest grain is part of a larger population within error of the youngest grain dated in Padaung 2. The youngest age from Padaung 1 and Padaung 3 are consistent with the known Oligocene depositional age for these samples, however, Oligocene ages are rare.

3.4.4. Miocene formations

A significant change in provenance is observed in the Miocene, characterized by a narrow range of $^{40}Ar/^{39}Ar$ white mica ages that reflect a change of provenance between deposition of the Eocene-Oligocene and the Miocene units. In contrast to the Palaeogene formations, the Miocene formations are dominated by Himalayan cooling ages that are younger than 56 Ma and fall within a very narrow age range (Figure 3.7, 3.8). The youngest age obtained is 19.9 ± 0.67 Ma from the early Miocene Shwetaung Formation, and the youngest age of subsequent Miocene formations is Early Miocene to Latest Oligocene (ranging from 20 to 26 Ma). In all five Miocene samples, 64–83% of ages are Eocene and younger, with a predominant Priabonian peak (37–35 Ma) persisting throughout all stratigraphic levels. This narrow peak is indicative of a single source region for the Miocene sedimentary rocks which was rapidly uplifted through the 350° C isotherm (mid-upper crustal levels) during the Late Eocene, followed by exhumation to the surface by at least the Early Miocene.

All Miocene deposits are dominated by white micas of Palaeogene age which make up between 72 to 89% of the total ages in each sample. Mesozoic ages make up between 11 to 20% in the Miocene formations of the Eastern Trough and between 13–27% in the Miocene formations of the Western Trough, with a general trend of increasing influence

of Mesozoic ages in younger formations. Minor populations of Miocene-aged grains are present in all samples, except for the Kyaukkok Formation, with the Shwetaung and Taungtalon formations having the most Miocene grains (3 to 5 grains). Minor Palaeozoic age populations are present in all Miocene formations, except the Obogon formation, with the Lower Moza Formation containing the highest number of Palaeozoic grains (4 grains). A significant proportion of the Mesozoic cooling ages are Upper Cretaceous and Lower Jurassic, and Palaeozoic ages are largely absent.

A total of 134 detrital white mica grains from the early Miocene Shwetaung Formation were analyzed, with $^{40}Ar/^{39}Ar$ cooling ages ranging between 19.9 ± 0.67 and 278.0 ± 7.69 Ma, with a prominent peak at ~37.5 Ma (Figure 3.8, 3.9). The majority (63%) give Eocene cooling ages and almost a quarter are Oligocene in age. Both the Taungtalon and Shwetaung Formations contain the largest number of Miocene aged grains (5 and 3 grains, respectively).

A total of 145 detrital white mica grains were dated from the Taungtalon Formation. Eocene and Oligocene aged grains make up 71% of the sample, respectively. Additionally, 17 grains (11.7%) gave an Upper Cretaceous age.

A total of 61 grains were analysed for the Obogon Formation. Approximately 77% of cooling ages are Eocene to Oligocene in age. No Palaeozoic ages are recorded in this formation. The Kyaukkok Formation had 81 white mica grains analyzed; Eocene-Oligocene aged grains make up 64% of sample, with minor Palaeocene (7%), Cretaceous (18.5%) and Jurassic (~7%) populations. The Lower Moza had a total of 117 detrital white mica grains were analyzed. 64 % (74 grains) gave an Eocene age, with the majority giving Priabonian and Bartonian ages. Ages also indicate 2 grains from the Permian and 2 of Devonian age, the only formation to record Devonian white mica cooling ages.

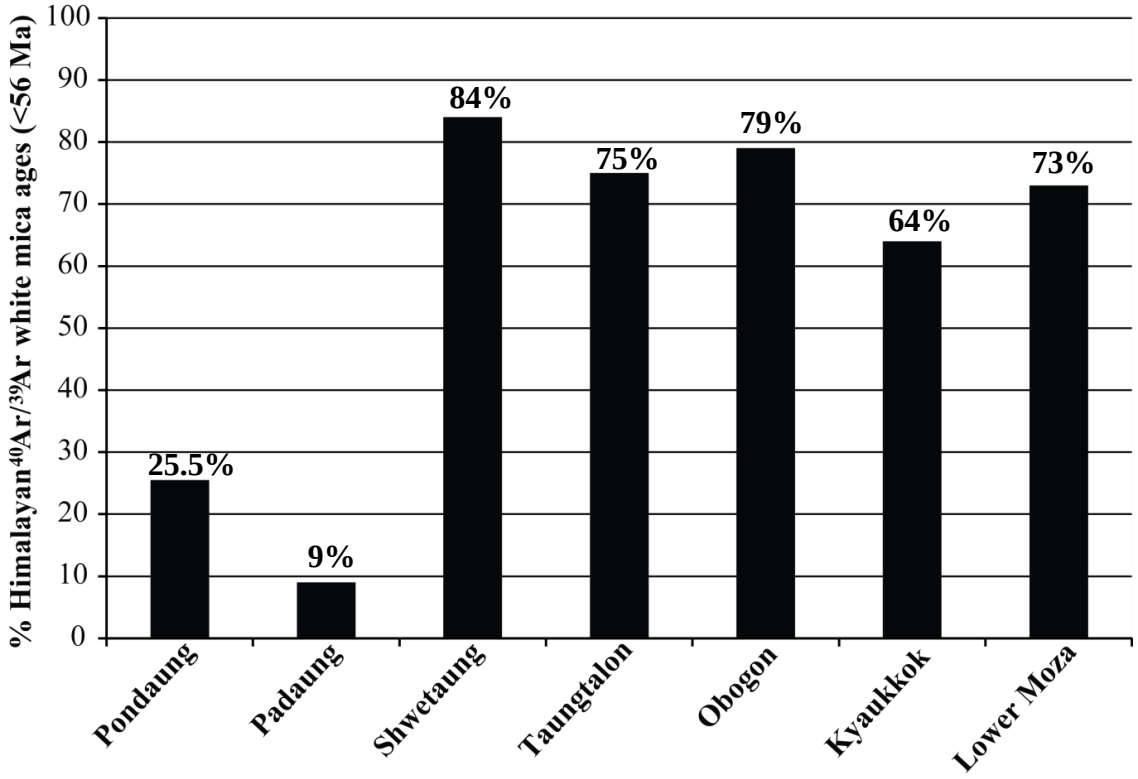

Figure 3.9 Percentage of $^{40}Ar/^{39}Ar$ detrital white mica ages younger than 56 Ma for all samples. Note the significant increase in Himalayan aged detritus appearing in the Miocene formations, initiated during deposition of the Early Miocene Shwetaung Formation.

3.5. Zircon fission track and U-Pb double dating with Lu-Hf geochemistry

Zircon fission track dating in sedimentary provenance studies provides information on provenance, the rate of source exhumation and erosion, and changes in the tectonic-denudation processes through time (Bernet et al., 2004; Carter, 1999). Double dating of detrital zircon grains by U-Pb and fission track methods is an effective provenance tool that combines the primary crystallization age and the timing of cooling and exhumation through the upper crust (Bernet et al., 2006; Bodet and Schärer, 2000; Carter, 1999; Carter and Bristow, 2000; Clift, 2006). The further use of Lu-Hf geochemical analysis provides a more robust approach to source rock characterization, where the crystallization age and isotopic geochemistry link detritus to a specific region, and fission track dating records the timing of exhumation, and subsequent erosion (Curvo et al., 2013). This study presents the first combined U-Pb and fission track dating with Lu-Hf analysis of detrital zircons; the usefulness of combining low temperature

thermochronology with an isotopic provenance tracer has been demonstrated by (Foster and Carter, 2007) using combined detrital apatite fission track dating and Sm-Nd isotopic analysis.

The annealing temperature for zircon fission track is dependent on cooling rate and is often cited as ranging between ~200-380°C (Bernet et al., 2004; Hurford and Carter, 1991; Tagami et al., 1996; Tagami et al., 1998; Yamada et al., 1995). Zircons with significant radiation damage and higher uranium concentration can have lower annealing temperatures (~180° to 200°C), and post-depositional thermal overprinting in some, but not all, grains is possible (Garver et al., 2005; Marsellos and Garver, 2010). To minimize zircon selection bias during processing because of varying magnetic susceptibility, zircons were selected from a range of magnetic fractions (Fedo et al., 2003) as it has been shown that zircons with higher alpha dosages have higher magnetic susceptibility (Murakami et al., 1991).

More than 200 individual zircon grains from two Eocene, one Oligocene and three Miocene sedimentary rock samples were analyzed for fission track (ZFT) and ICP-MS U-Pb dating. Detrital zircon separation and grain selection was carried out at the University of St Andrews. Single grain detrital zircon U-Pb and fission track dating was conducted by Dr. Andy Carter and was carried out using an ICP-MS Agilent 7500 at the Geochronology Laboratory of the School of Earth Sciences, Birkbeck University, London. Fission track ages were obtained using both ICP-MS and conventional methods. The conventional fission track ages are used in this study as uranium zoning is prevalent in zircons from the Central Burma Basin, in particular those >50 Ma, and the ICP-MS approach lacks the ability to take this into account because the ablation depth and spot size may exceed the fission track length (Andrew Carter, pers. comm., 2012). The full methodology and analytical protocols are given in Appendix A2 and analytical results are presented in Appendix Tables A2 (ICPMS U-Pb zircon dating) and A3 (zircon fission track dating). Cathodoluminescence images are presented in Appendix A4. All zircon fission track and U-Pb ages are quoted at 2σ uncertainty.

A sub-set of double dated zircons have been analyzed for Lu-Hf geochemistry, in order to provide another method of linking the detrital zircon cooling age to a specific

provenance. All analyses were conducted by Dr. Bruno Dhuime at the Bristol Isotope Laboratory, University of Bristol, UK using LA-MC-ICPMS. All εHf(t) values are quoted at 2σ uncertainty; full methodology and analytical protocols are given in Appendix A2 and full analytical results are given in Appendix Table A5.

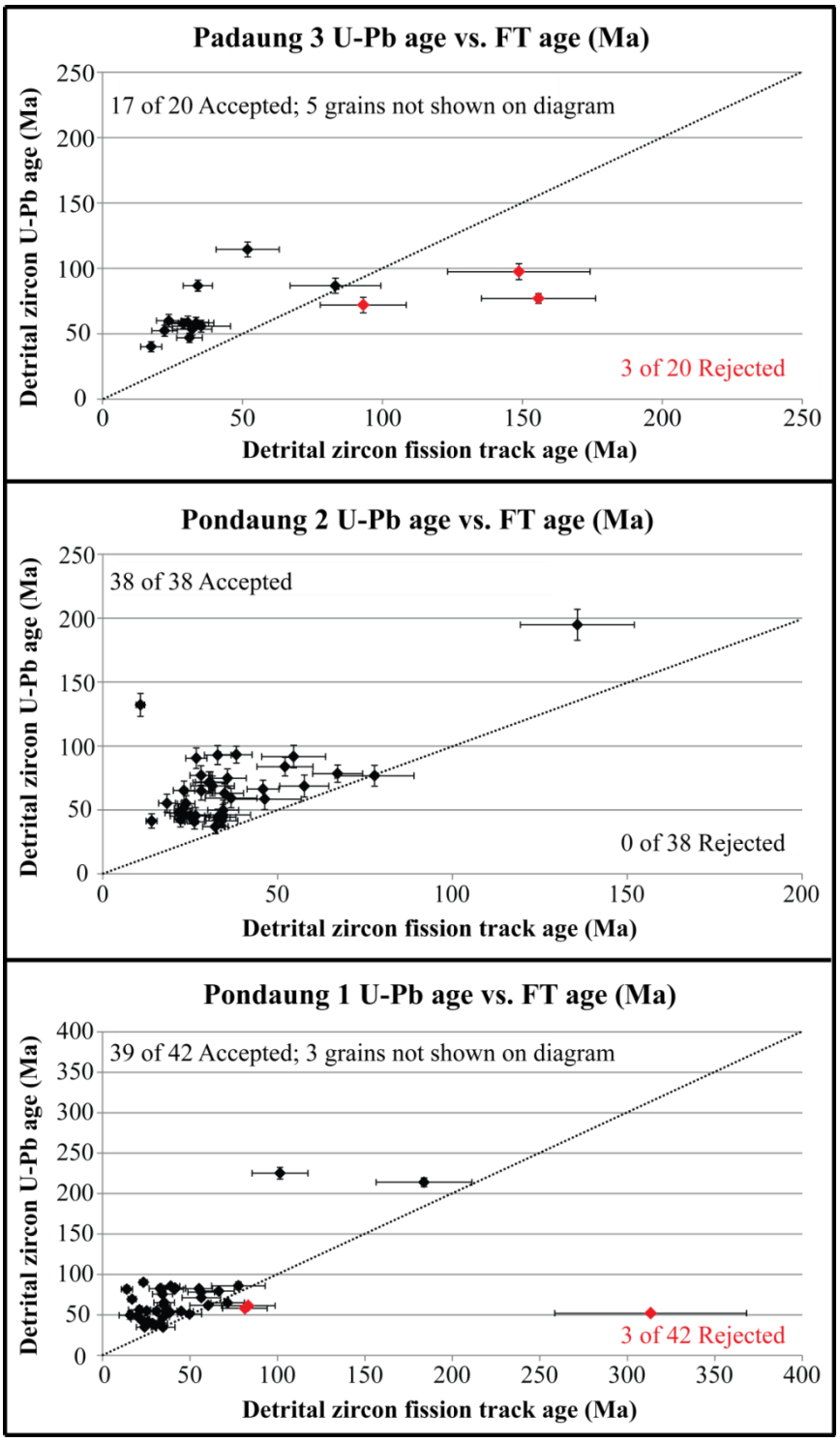

Figure 3.10 Single grain detrital zircon ICP-MS U-Pb and fission track age for the Eocene and Oligocene formations. The black 1:1 line indicates where the U-Pb age is the same as the fission track age. Analyses that fall below this line were not accepted and are not discussed further in this study.

3.5.1. Eocene Pondaung Formation

3.5.1.1. Sample Pondaung 1

A total of 44 zircons from sample Pondaung 1 were dated by ICP-MS U-Pb and fission track methods. Three analyses were rejected as the fission track age was older than the U-Pb age, attributed to both sample preparation and analytical error. Fission track ages obtained from single grain detrital zircons from the oldest sandstone sampled in this study (Pondaung 1) have a diverse range of ages spanning Jurassic to Middle Miocene (13.9 ± 3.2 to 208.7 ± 41.5 Ma). Although the majority of the fission track ages are middle Eocene to Miocene, eleven zircons (28%) have Palaeocene to Upper Cretaceous and Lower Jurassic ages. Roughly half of the detrital zircons have Oligocene-Miocene fission track ages, younger than the Eocene depositional age of the sampled unit, indicating a significant population of thermally re-set ages (Figure 3.10).

Zircon U-Pb crystallization ages from Pondaung 1 range from 34.8 ± 2.3 to 1319.0 ± 31.1 Ma, with dominant Late Cretaceous and Middle Eocene populations (ca. 76 Ma and 43 Ma; 87% of ages) and minor Early Mesozoic and Proterozoic ages present. The dominance of Upper Cretaceous to Middle Eocene zircon U-Pb ages are similar to those observed in the LA-MC-ICPMS zircon U-Pb dataset.

Twenty-eight of the double-dated zircons were further analyzed for Lu-Hf isotope geochemistry; εHf(t) values range from -9.9 ± 0.7 to 12.6 ± 0.8 and twenty-three grains (82%) have positive values > 9. Zircons characterized by high positive εHf(t) values show a wide spread of fission track and U-Pb crystallization ages between Late Cretaceous and Early Miocene and Upper Cretaceous to Eocene, respectively. Those with more negative values have fission track ages that cluster between 35 and 17 Ma, and Late Cretaceous and Early Eocene U-Pb ages.

3.5.1.2. Sample Pondaung 2

A total of 38 single detrital zircon grains were analyzed using combined U-Pb and fission track dating methods (Figure 3.10). Fission track ages range from 10.8 ± 1.2 to 135.7 ± 16.3 Ma; three grains are Cretaceous in age and the remainder are Palaeocene to Miocene in age. Fission track age distributions show Late Eocene (~34 Ma) and Late Oligocene (~23.7 Ma) clusters, with minor Early Palaeocene (~60.7 Ma) and Middle

Miocene (12 Ma) peaks also observed (Figure 3.11). Over half of the zircons analyzed (58%) have Oligocene to Middle Miocene ZFT ages (~33 to 10.8 Ma), indicating a significant proportion of the analyzed zircons have thermally re-set fission track ages, younger than the depositional age of the sedimentary sample from which they were extracted (Late Eocene).

U-Pb ages of zircons from the Pondaung 2 sample range from 37.0 ± 5.5 to 194.8 ± 12.1 Ma, with dominant Upper Cretaceous to Middle Eocene populations (ca. 90 to 40 Ma). The zircon crystallization age distributions are in good agreement with age distributions observed in the LA-MC-ICPMS zircon U-Pb dataset.

A sub-set of thirty-one double-dated zircons were also analyzed to obtain their Lu-Hf geochemistry. Twenty-seven zircons (86%) are characterized by high positive εHf(t) values between 9.6 ± 0.9 and 15.0 ± 0.8, and the remaining four zircons are characterized by negative values from -2.6 ± 0.9 to -5.0 ± 0.7. Zircons with high positive εHf(t) values are also characterized by U-Pb crystallization ages from ca. 200 to 41 Ma and Cretaceous to Early Miocene fission track ages, whereas those with more negative values have Middle Eocene U-Pb crystallization ages (ca. 42 to 37 Ma) and Oligocene to Miocene ZFT ages (ca. 32 to 14 Ma) (Figure 3.10).

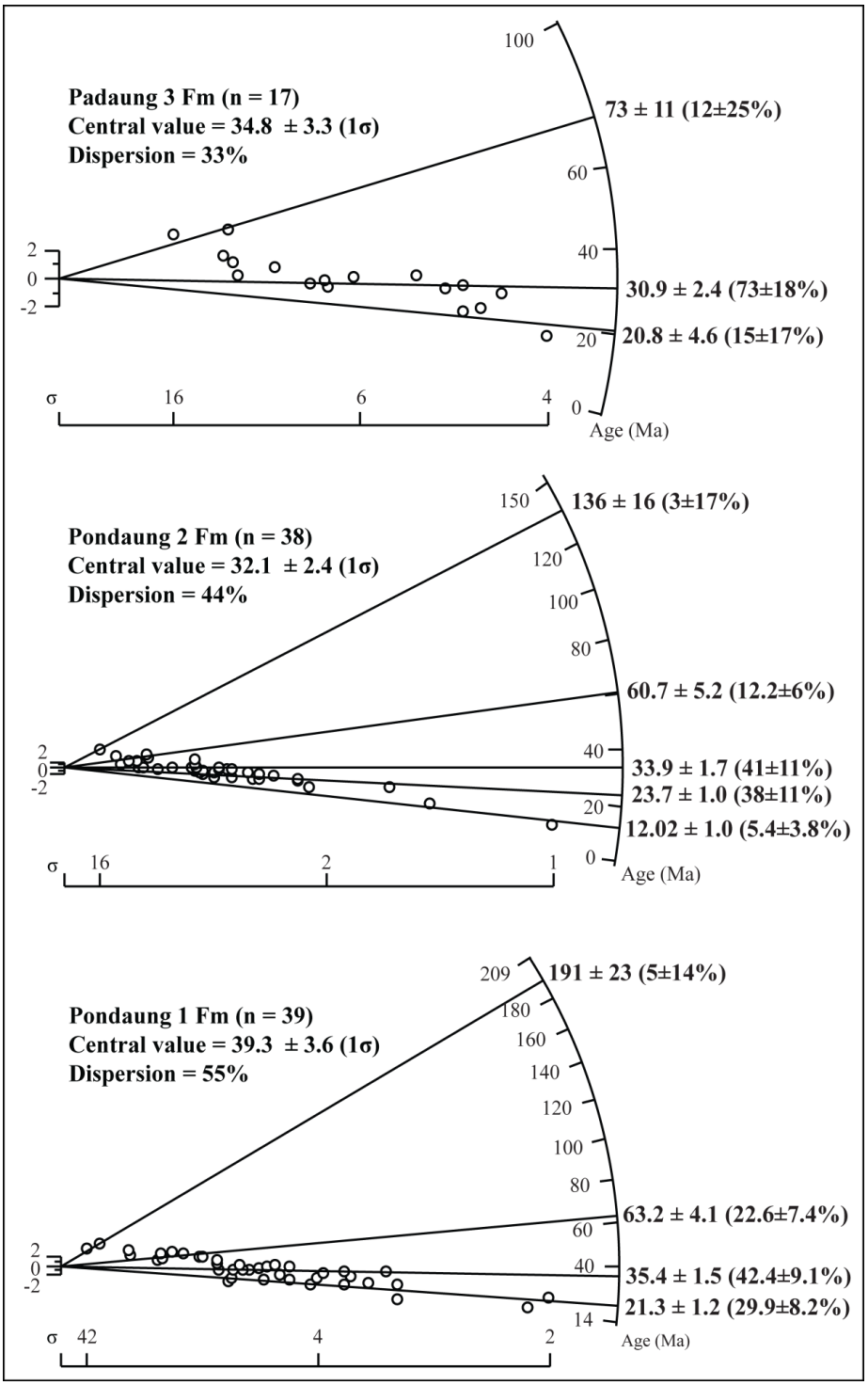

Figure 3.11 Detrital zircon fission track data for the Eocene and Oligocene samples, presented as radial plots. Populations are calculated using Vermeesch (2012).

3.5.2. Oligocene Padaung Formation

3.5.2.1. Sample Padaung 3

A total of twenty zircons were double-dated using the U-Pb and fission track method. Three grains were rejected where the crystallization age is younger than the ZFT age (Figure 3.10). ZFT ages range from 17.4 ± 3.8 to 83.2 ± 16.2 Ma; fifteen of the seventeen zircons have Early Eocene to Late Miocene ZFT ages and the remaining two grains have Late Cretaceous ages (Figure 3.10, 3.11). The presence of zircons with Early Miocene ZFT ages in the Oligocene Padaung Formation indicates a minor population of re-set ages.

U-Pb ages of zircons from Padaung 3 range from 40.1 ± 3.9 Ma to 3072.6 ± 20.2 Ma. Just under half (~48%) have either Middle to Late Cretaceous or Precambrian U-Pb ages, and although the percentage of zircons of this age may be an artefact of the small sample size, it is in general agreement with the observation that the Oligocene Padaung Formation contains a significant Precambrian population, unlike the other formations sampled.

Seventeen zircons, with predominantly Upper Cretaceous to Eocene U-Pb crystallization ages and Oligocene to Miocene ZFT ages underwent additional Lu-Hf isotopic analysis. Eight analyses were rejected based on analytical error. All zircons show positive εHf(t) values ranging from 3.5 ± 0.8 to 13.2 ± 0.8, with one grain having a value.

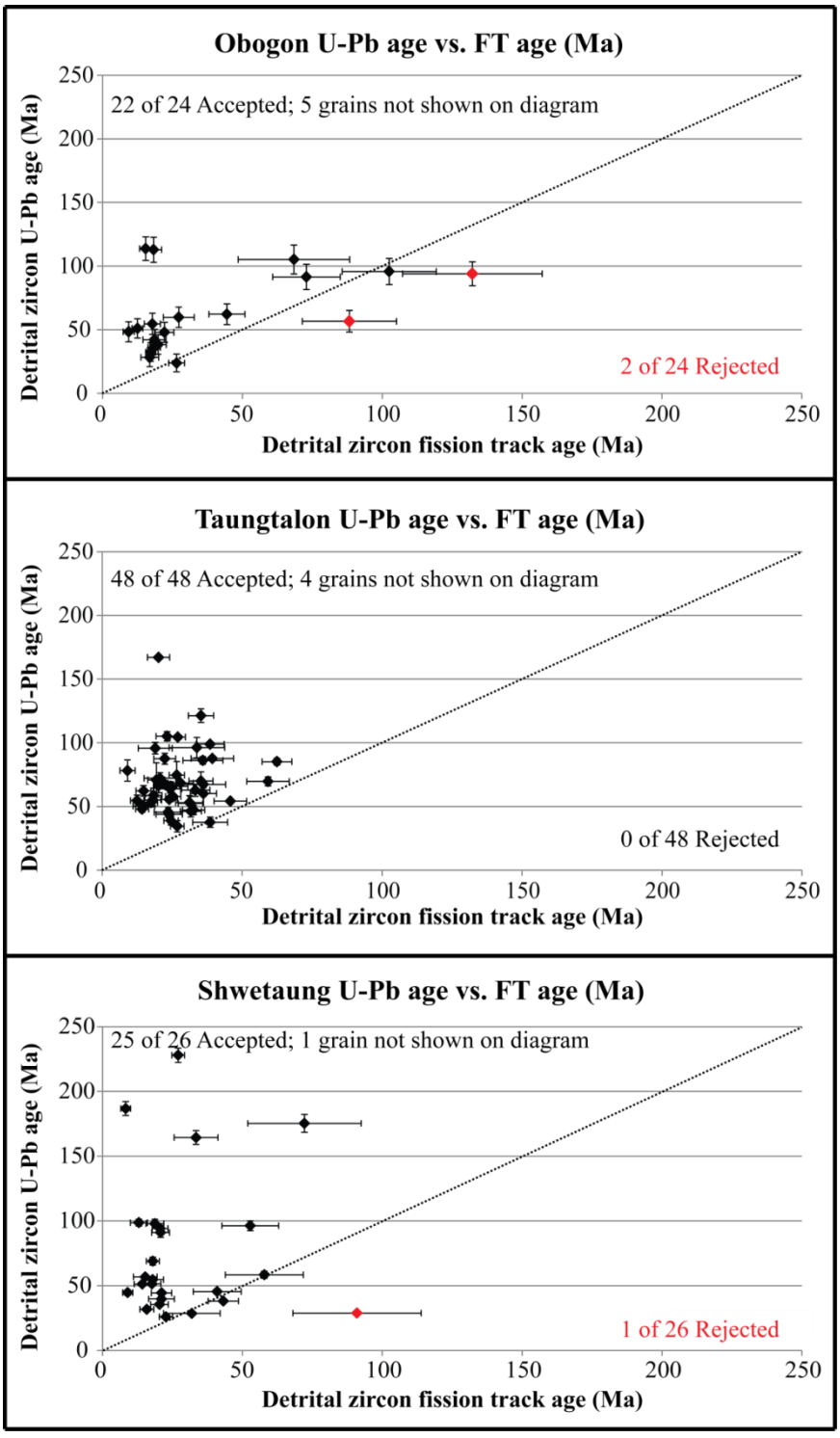

Figure 3.12 Single grain detrital zircon ICP-MS U-Pb and fission track age for the Early to Middle Miocene formations. The black 1:1 line indicates where the U-Pb age is the same as the fission track age.

3.5.3. Early to Middle Miocene formations

3.5.3.1. Shwetaung Formation

A total of twenty-six grains were double-dated by the fission track and U-Pb methods. One analysis was rejected because the U-Pb age is significantly younger than the fission track age (Figure 3.12). ZFT ages range from 8.3 ± 1.7 Ma to 91.0 ± 22.9 Ma, with a main Early Miocene peak at 18.8 ± 1 Ma (>50% of ages), and minor Late Miocene (9 ± 1.3 Ma), Oligocene (26.1 ± 3.1 Ma) and Early Eocene (46.2 ± 4.3 Ma) populations (Figure 3.13). All twenty-five zircon grains record Cenozoic ZFT ages, and the majority are Miocene in age. A significant number of ZFT ages between ca. 18–20 Ma support the depositional age of this formation as determined from the youngest LA-MC-ICPMS U-Pb zircon age and $^{40}Ar/^{39}Ar$ white mica age. Six of the twenty-five zircons have ZFT ages ranging from ca. 8 to 16 Ma which are younger than the depositional age of the Shwetaung Formation, indicating post-depositional thermal re-setting of some, but not all fission track ages in this sample. Double-dated detrital zircons from the Shwetaung Formation have U-Pb ages ranging from 26.0 ± 0.9 Ma to 995.0 ± 21.8 Ma, with peaks at ca. 38, 91 and 175 Ma. Over half of the zircons have Cenozoic U-Pb ages (~58%), with minor Triassic-Jurassic and Late Cretaceous populations. Of the five grains with Jurassic, Triassic and Precambrian U-Pb ages, four have Cenozoic ZFT ages indicating source rocks of this age experienced exhumation and erosion resulting from the Himalayan orogeny, and may also indicate multi-cycle detrital grains. The U-Pb age distributions of the double-dated zircons are generally in agreement with the U-Pb age distributions of detrital zircons dated using LA-MC-ICPMS, with dominant Late Palaeocene to Early Miocene ages.

A sub-set of eight double-dated grains were analyzed for Lu-Hf geochemistry. One analysis was rejected based on analytical error. Detrital zircon εHf(t) values range from -15.0 ± 0.9 to 16.0 ± 0.7. Although there is a limited dataset, it is shown that zircons with Cenozoic ZFT and U-Pb ages have εHf(t) values that are negative (up to -15) or near chondritic (εHf(t) = 0) (Figure 3.14, 3.15). One grain with a Late Jurassic crystallization age and a Late Cretaceous ZFT age has a high positive εHf(t) value of +16, whereas two zircons with Triassic and Proterozoic crystallization ages and Middle to Late Oligocene ZFT ages have more negative εHf(t) values. It is important to note

that the limited number of analyses for this sample limits the weight placed on interpretations of this formation with regards to εHf(t) values, however, as seen in section 3.2, these values are consistent with εHf(t) values from a larger dataset.

3.5.3.2. Taungtalon Formation

U-Pb crystallization and ZFT ages were obtained from a total of forty-eight detrital zircon grains extracted from sedimentary rocks sampled from the Taungtalon Formation (Figure 3.12). All detrital zircons record Cenozoic ZFT ages that range from 9.0 ± 2.7 to 62.4 ± 5.3 Ma, with predominantly Early Miocene, Late Oligocene and Latest Eocene peaks (ca. 19, 26 and 35 Ma) and minor Early Palaeocene and Middle Miocene peaks (ca. 61 and 13 Ma) (Figure 3.13). The latter are interpreted as reset ages, as they are younger than the early Middle Miocene depositional age of the Taungtalon Formation, likely recording post-depositional thermal re-setting of the zircon fission track system in some, but not all, grains.

Detrital zircon U-Pb ages range from 34.5 ± 4.4 to 980.2 ± 3.8 Ma, with a large proportion of ages (60%) between ca. 45 to 75 Ma. The U-Pb age distributions of the double-dated zircons are generally in agreement with the U-Pb age distributions of detrital zircons dated using LA-MC-ICPMS.

A sub-set of forty-one grains were additionally analyzed for Lu-Hf geochemistry and show a bi-modal pattern, characterized by high positive εHf(t) values from roughly +6 to +15 and more negative values from +1.7 to -18.

Combined double U-Pb and ZFT dating and Lu-Hf isotope analysis show zircons with Jurassic to Eocene crystallization ages and Palaeocene to Miocene ZFT ages are characterized by high positive εHf(t) values, whereas zircons with more negative values have Late Cretaceous to Eocene U-Pb crystallization ages and fission track ages < 40 Ma (Figure 3.14, 3.15).

3.5.3.3. Obogon Formation

A total of twenty-four zircons were double dated by fission track and U-Pb methods. Two analyses were rejected because the U-Pb age was younger than the FT age (Figure 3.12). Fission track ages range from 9.3 ± 2.0 Ma to 200.2 ± 54.4 Ma, and have a bi-

modal age distribution that gives two main peaks: an Early Miocene peak at 17.2 ± 0.69 Ma and a Late Palaeocene peak of 58.1 ± 4.5 Ma (Figure 3.13). Over 70% of the cooling ages are Himalayan in age (younger than 56 Ma), of which are mostly Oligo-Miocene in age, and represent detritus derived from source rocks that were exhumed through the upper crust at this time. Two or three of the twenty-two grains have ZFT ages that are younger than the Middle Miocene depositional age of the formation from which it was sampled: 9.3 ± 2.0 Ma, 12.5 ± 1.9 Ma, and potentially 15.4 Ma.

The double-dated detrital zircons from the Obogon Formation have U-Pb ages ranging from 23.8 ± 7.0 Ma to 1586.2 ±22.4 Ma. The majority of ages are Cretaceous to Oligocene in age, with a minor Proterozoic population. Of the five grains with Proterozoic U-Pb ages, three have Cenozoic ZFT ages indicating these may be polycyclic. The U-Pb age distributions of the double-dated zircons are generally in agreement with the U-Pb age distributions of detrital zircons dated using LA-MC-ICPMS. However, the Early Cretaceous to Jurassic population is not observed, although this is attributed to the smaller sampling size of the double dated grains that missed more minor populations. The presence of a much older Proterozoic age population in the double dated grains (ca. 795, 1180 to 1580 Ma) versus that in the LA-MC-ICPMS data (ca. 600-700 Ma) is more difficult to explain.

A subset of twenty zircons double dated by fission track and U-Pb also underwent Lu-Hf isotopic analysis. Two analyses were rejected based on analytical error. Detrital zircon εHf(t) values range from -15.3 ± 0.7 to 15.2 ± 0.7 and are plotted against zircon fission track ages (Figure 3.14, 3.15) and U-Pb ages (Figure 3.15). Significantly, zircons with Miocene fission track ages are all characterized by negative εHf(t) values. Conversely, zircons with older Eocene to Cretaceous fission track ages are characterized by high positive εHf(t) values. This trend is mimicked where εHf(t) values are plotted against zircon U-Pb age, where all Himalayan aged zircons (younger than 56 Ma) have negative εHf(t) values and earliest Palaeocene and Late Cretaceous have positive εHf(t) values.

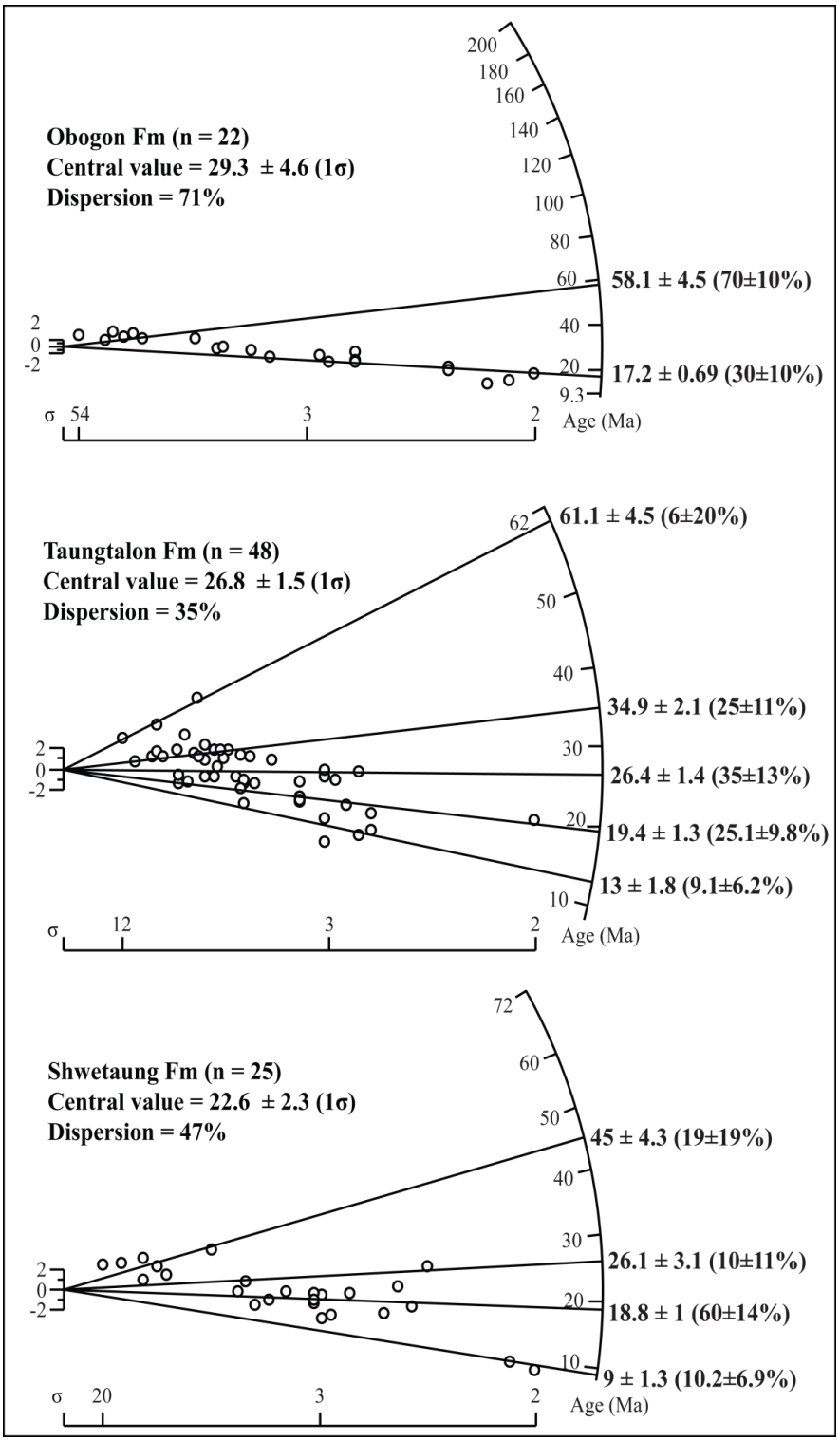

Figure 3.13 Radial plots showing detrital zircon fission track age distributions for Early to Late Miocene samples, arranged in stratigraphic order.

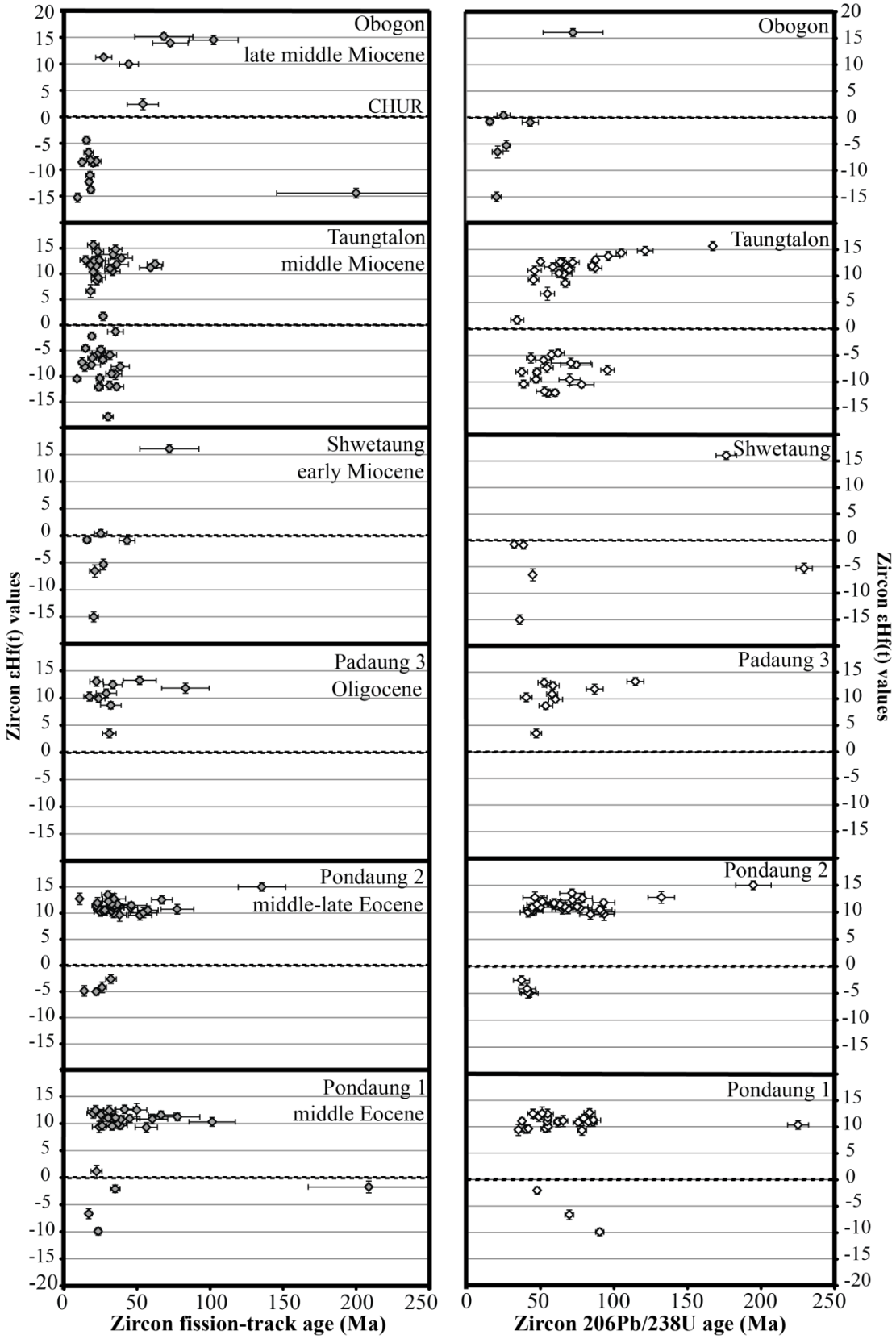

Figure 3.14 Double dated detrital zircon U-Pb (right) and fission track ages (left) vs εHf(t) values for a subset of sedimentary rock samples from the Central Burma Basin, arranged in stratigraphic order.

3.6. Summary of all datasets

Combined U-Pb dating and Lu-Hf geochemistry on detrital zircons from the Eocene Pondaung Formation and the Oligocene Padaung Formation indicate mostly Mesozoic and Cenozoic crystallization ages, the majority of which have high positive εHf(t) values, indicative of derivation from mantle derived, juvenile crust. Additional fission track dating on these grains display a wide spread of ages between Lower Cretaceous to Miocene, indicating exhumation of a Mesozoic-Cenozoic aged juvenile arc terrane through the upper crust at this time, followed by erosion, transport and deposition in the Central Burma Basin during the Eocene to Oligocene. Eocene, Oligocene and early Miocene fission track ages represent the most dominant populations in the Pondaung Formation, highlighting significant re-setting of ages in the oldest formation sampled. The Padaung Formation is dominated by an Oligocene population (ca. 30.9 Ma), although a minor early Miocene population is observed, younger than the Oligocene depositional age of this sample, and therefore representing re-set ages. This early Miocene re-set population is observed in all samples (~23–20 Ma), and a late Miocene (~12 Ma) re-set population is seen in the Pondaung 2 sample.

The most dominant fission track age population in sample Pondaung 1 is 35.4 ± 1.5 Ma, consistent with age of 37.2 ± 1.3 Ma obtained from zircon fission track of an ash bed from the same formation reported in Tsubamoto et al. (2002) from a locality farther to the west and with the known biostratigraphic depositional age (Late Middle Eocene). The dominant age peak of 33.9 ± 1.4 Ma for the Pondaung 2 sample is consistent with its known Late Eocene depositional age and is younger than the Pondaung 1 sample that was sampled from a stratigraphically lower position in the formation, and therefore represents the oldest sample obtained. The main ZFT age peak in the Oligocene Padaung Formation is 30.9 ± 2.4 Ma, similar to the known depositional age (Middle Oligocene).

Detrital ZFT ages from the Eocene Pondaung and Oligocene Padaung formations with Mesozoic and Cenozoic U-Pb crystallization ages display a wide spread between Lower Cretaceous to Miocene (~140 Ma to ~11 Ma), the majority of which have high positive εHf(t) values (89%), characteristics associated with mantle derived, juvenile bedrock of an arc terrane (Figure 3.14, 3.15). Zircons of the Pondaung Formation are

separate into two distinct populations based on εHf(t) values: the dominant population has values between +9 to +15, whereas the second population is more widespread between +3.5 to -6.7, and one zircon has a value of -9.9. Zircons of the Padaung Formation all have positive εHf(t) values lying between +8 to +13, with one grain giving a value of +3.5.

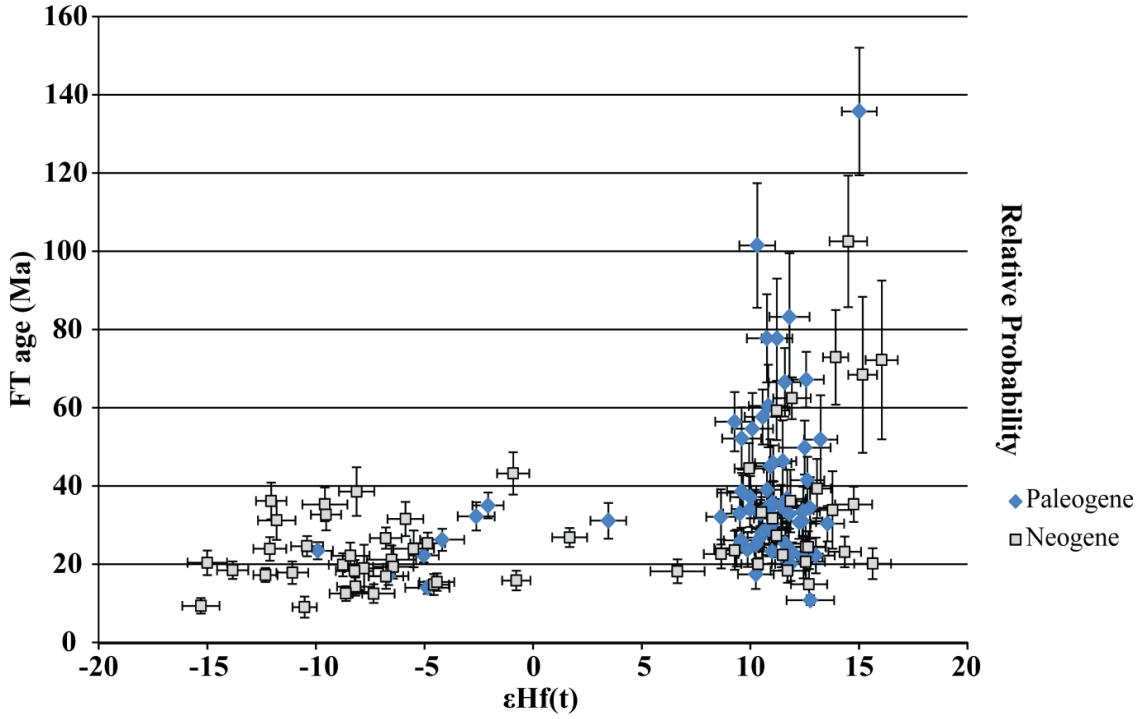

Figure 3.15 Detrital zircon fission-track ages of the combined Eocene and Oligocene samples (Palaeogene) and the Miocene samples (Neogene) vs. their εHf(t) values. Only zircons with Jurassic to Cenozoic U-Pb ages shown and error bars are 2 sigma.

A significant change in the thermochronological and geochemical characteristics of detrital zircon is observed in the Miocene formations. Detrital zircon fission track ages from the early Miocene Shwetaung Formation, Middle Miocene Taungtalon Formation, and late Middle Miocene Obogon Formation display a more narrow range, mostly younger than 40 Ma, and the majority of which are late Oligocene to early Miocene in age. In opposition to the majority of zircons with high positive εHf(t) values from the Eocene and Oligocene formations, zircons from the Miocene formations show bi-modal εHf(t) values, with a general trend towards more negative values increasing up-section

(Figure 3.14, 3.15). Additionally, the U-Pb crystallization age of zircons with more negative εHf(t) values, also decreases up section (Figure 3.14). All Miocene formations also contain a minor population of late Miocene re-set fission track ages, younger than the known depositional age of the sample, from ca. 14–8 Ma, also observed in the Pondaung 2 sample.

The most dominant fission track age population the Shwetaung Formation is 18.8 ± 1 Ma (60%), consistent its known early Miocene depositional age. The Taungtalon and Obogon formations have a similar early Miocene population at 19.4 ± 1.3 Ma and 17.2 ± 0.69 Ma, respectively, representing 25–30 % of grains.

Chapter 4. Synthesis of published and new data

4.1. Introduction

The Central Burma Basin located in the eastern region of the Himalayan orogenic zone contains a sequence of Cenozoic flysch- and molasse-type sedimentary units over twelve kilometres in thickness that potentially contain a well preserved record of tectono-thermal events in the early stages of the Himalayan orogeny. This record may be unique in that early phases of the orogeny are not recorded in the Himalayan foreland basin and remnant ocean basins due to non-deposition, burial or destruction along the convergent plate boundary (Najman et al., 2002, 2004; Clift & VanLaningham, 2010; DeCelles et al., 1998a,b; Yin and Harrison, 2000; Curray and Moore, 1971; Curray, 2005; Najman, 2006). This understudied region also potentially contains evidence of a palaeo-Yarlung Tsangpo-Irrawaddy river system and the capture of the Yarlung Tsangpo by the Brahmaputra River during the late Cenozoic (Brookfield, 1998; Clark et al., 2004; Liang et al., 2008). This capture event is the precursor to the development of the modern drainage systems observed today, where the Irrawaddy River now drains a region south and east of the eastern Himalayan syntaxis, including western Yunnan and Burma (Figure 4.1, 4.2), and the Brahmaputra River, linked with the antecedent Yarlung Tsangpo, drains a large area encompassing southern Tibet, the eastern syntaxis and the eastern Himalayan front. If the Yarlung Tsangpo-Irrawaddy formed a single longitudinal river, this would have been the major river draining the eastern Himalayas at this time, and sediment derived from bedrock that was exposed in the modern Yarlung Tsangpo drainage within southern Tibet would be present within the Central Burma Basin. If the Irrawaddy was not involved in a river capture event, the sediment preserved in the basin should be representative of the bedrock exposed in the modern Irrawaddy catchment. Therefore, changes in sediment provenance of Cenozoic syn-orogenic sedimentary rocks of the Central Burma Basin through time may potentially document the evolution of the large river systems draining the eastern Himalaya during the early stages of orogenesis, which may have major implications for geodynamic models involving the interaction between crustal deformation, exhumation, surface uplift and major drainage capture in the eastern syntaxis region. The recognition of early Himalayan molasse deposits in Burma may have implications for the timing of the

Himalayan orogeny occurring prior to the Oligocene (Aitchison et al., 2007, 2002; Davis et al., 2002).

In order to determine the source provenance for Eocene- to Miocene-aged sedimentary rocks of the Central Burma Basin sampled in this study, the isotopic dataset obtained in this study is compared to published literature data from bedrock of the potential source terranes within the modern Irrawaddy River and Yarlung Tsangpo catchments. An integrated approach, including geochronological, thermochronological and geochemical data (zircon U-Pb and fission track dating combined with Lu-Hf isotopic analysis and white mica $^{40}Ar/^{39}Ar$ dating) is implemented to characterize the tectono-thermal evolution of potential source terranes in south-eastern Tibet, western Yunnan and Burma in order to test the hypothesis that the Yarlung Tsangpo formerly drained into the proto-Irrawaddy River prior to its capture by the Brahmaputra River, and if so, the timing and mechanism of disconnection. The isotopic characteristics of these source regions are described below and are summarized in Table 4.1. The full literature datasets are presented in Appendix A6.

Detrital zircons and white mica of the Eocene to Miocene Central Burma Basin strata sampled in this study are dominated by mainly Cenozoic and subordinate middle to late Mesozoic age populations, reflecting a significant contribution of detritus from rocks involved in the closure of the Meso-and Neo-Tethys oceans (Figure 3.3, 3.7). The abundance of zircons yielding Himalayan U-Pb ages (younger than 55 Ma) suggests the studied strata represent orogenic molasse shed during the early stages of the Himalayan orogeny was accumulating in the Central Burma Basin since at least the Late Eocene, the age of the oldest sample analyzed in this study. Minor Proterozoic to Palaeozoic aged grains are also present, forming less than six percent of the total population in strata of the Eastern Trough, whereas strata of the Western Trough have higher percentages between 11–22% (Figure 3.3). The higher percentage of detrital zircon older than 250 Ma in the Western Trough is likely due to localized input from the adjacent Indo-Burma Ranges that were uplifted during late Eocene to early Oligocene time (Allen et al., 2008; Mitchell, 1993), in which detrital zircons from Palaeogene and Neogene aged sedimentary rocks contain prominent age peaks between 2800-280 Ma (Allen et al., 2008; Naing et al., 2014). As the older Proterozoic to Palaeozoic zircons

and white mica represent only a minor proportion of the detrital grains analyzed in this study, and do not form any age populations that can be interpreted with significance, the following sections and discussion focuses on data for the last 250 Ma.

4.2. Source terrane characterization

4.2.1. Isotopic correlation of northern and southern Transhimalayan magmatic belts

An extensive number of studies have shown that the Gangdese Batholith of southern Tibet is dominated by positive εHf(t) values (Chu et al., 2011; Chu et al., 2006; Chung et al., 2003; Chung et al., 2009; Guan et al., 2012; Hou et al., 2009; Ji et al., 2012; Ji et al., 2009a; Ji et al., 2009b; Ma et al., 2013; Mo et al., 2005; Mo et al., 2009; Mo et al., 2007; Wen et al., 2008a; Wen et al., 2008b; Xiaoming et al., 2007; Zhang et al., 2010a; Zhang et al., 2010b), similar to the Lohit Batholith of northeast India which lies to the north of continuation of the Indus Yarlung suture zone around the eastern syntaxis (Figure 4.1, 4.3, 4.8) (Lin et al., 2013). In contrast, predominantly negative εHf(t) values characterise the northern Lhasa magmatic belt (Chu et al., 2006; Zhu et al., 2009b; Zhu et al., 2011), the eastern Transhimalayan batholiths of the Namche Barwa syntaxis (Chiu et al., 2009; Liang et al., 2008; Zhu et al., 2009c), and their southern counterparts in the Gaoligong-Tengliang-Yingjiang region of western Yunnan, China, termed the Dianxi-Burma batholiths (Figure 4.1, 4.3, 4.8) (Chiu et al., 2009; Liang et al., 2008; Ma et al., 2014; Xu et al., 2008; Xu et al., 2012). More specifically, recent work utilizing zircon U-Pb and Lu-Hf and whole rock Sr-Nd isotope systematics on these three plutonic suites illustrates that although the magmatic rocks are similar in age and composition, the Gangdese Batholith in southern Tibet within the present-day catchment of the modern, longitudinal Yarlung Tsangpo is shown to be significantly more juvenile and distinct from the crustally-derived granitoids within the syntaxis and the modern Irrawaddy catchment (Figure 4.2, 4.3, 4.4) (Chiu et al., 2009; Liang et al., 2008; Mitchell et al., 2012; Xu et al., 2012). Although no Lu-Hf data currently exists for Jurassic- to Miocene-aged Burma granitoids within the current Irrawaddy and Chindwin river catchments, whole rock Sr and Nd isotopic data reveals Late Cretaceous granodiorites of the Wuntho-Popa magmatic arc of western Burma, that divide the Central Burma Basin into fore-arc (Western Trough) and back-arc (Eastern Trough)

regions, have low initial $^{87}Sr/^{86}Sr$ ratios and positive εNd(t) values, similar to juvenile, mantle-derived igneous rocks of the Gangdese Batholith (Figure 4.1, 4.4) (Chung et al., 2005; Chu et al., 2006; Ma et al., 2013; Mitchell et al., 2012; Mo et al., 2005; Wen et al., 2008; Zhang et al., 2007). Cretaceous- to Miocene-aged granitoids emplaced in the Mogok Metamorphic Belt and Shan Scarps yield higher initial $^{87}Sr/^{86}Sr$ ratios and less radiogenic neodymium (negative εNd(t) values), analogous to S-type granites of the northern Lhasa terrane (Chu et al., 2006; Mitchell et al., 2012). In the southern part of the Mogok Metamorphic Belt, a quartz diorite dyke sampled ~110 kilometres east of Yangon yields a zircon U-Pb age of 90.8 ± 0.8 Ma and positive εNd(t) value of + 2.7, that is similar in age and isotopic characteristics to plutons of the western Burma magmatic arc exposed near Wuntho and Salingyi (Mitchell et al., 2012). Further south, I-type and S-type plutons of the Southwest Thailand-East Burma granite province of Cobbing (1992) yield Triassic U-Pb zircon core ages (212 ± 2 Ma and 214 ± 2 Ma) and Late Cretaceous rim ages (81.2 ± 1.2 Ma and 85–75 Ma (Searle et al., 2012). Therefore, based on age and isotopic data, the northern Lhasa magmatic belt, eastern Transhimalayan batholiths, Dianxi-Burma batholiths and their southern continuation into the Mogok Metamorphic Belt and Shan Scarps of eastern Burma are considered to form a continuous belt, generated by crustal thickening following late Jurassic to early Cretaceous Meso-Tethys ocean closure (Chiu et al., 2009; Mitchell et al., 2012; Xu et al., 2012). The southeastern continuation of the Gangdese Batholith is complicated by its disappearance in the eastern Himalayan syntaxis region, however, recent work has linked the Lohit Batholith of northeast India and the Wuntho-Popa-Salingyi plutons of the western Burma magmatic arc, and its assumed continuation beneath the Cenozoic sediments of the Central Burma Basin, to the Gangdese (Li et al., 2013; Lin et al., 2013; Mitchell et al., 2012; Wang et al., 2014).

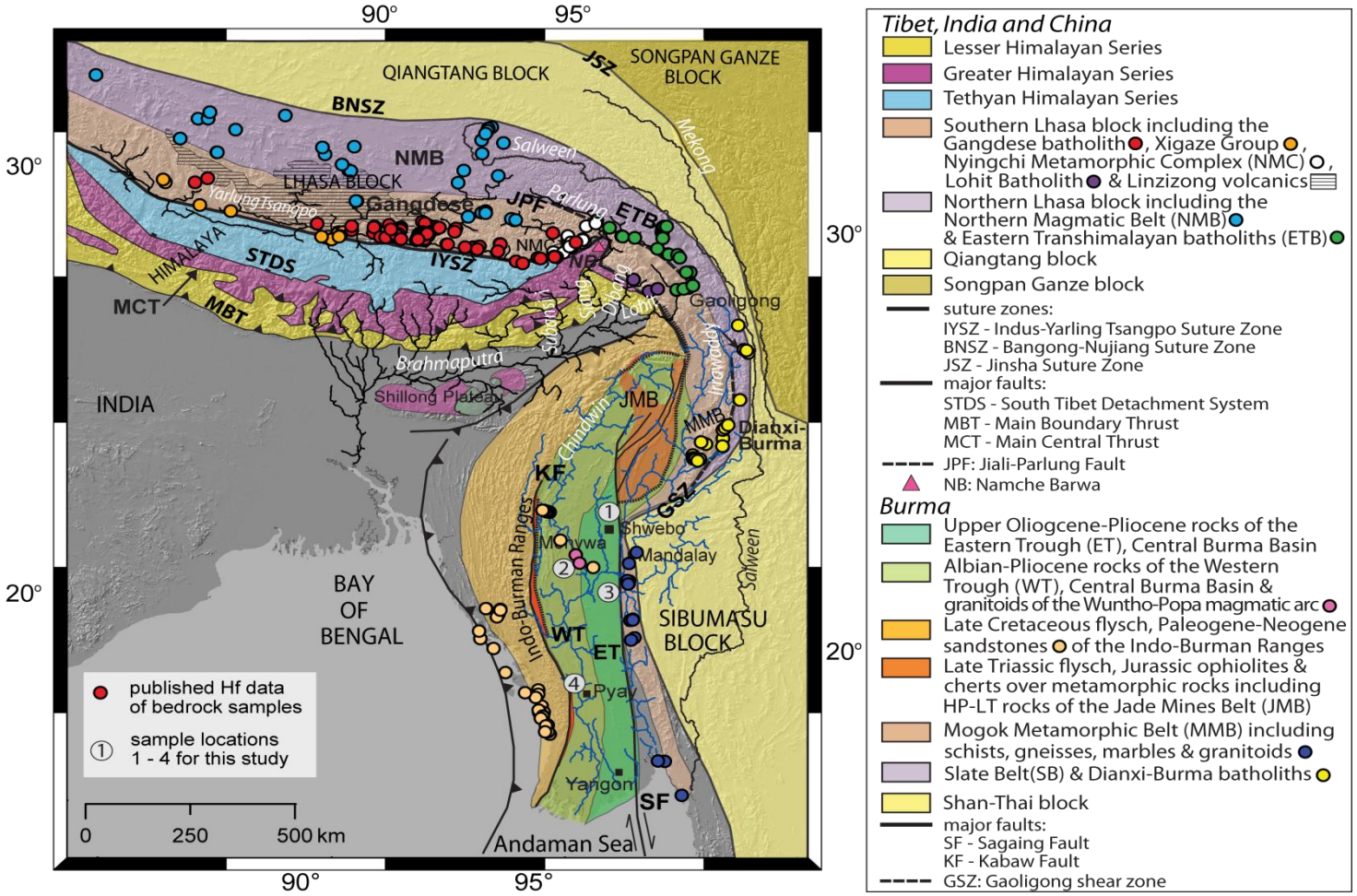

Figure 4.1 Simplified geological map showing major terranes, tectonic boundaries, geological units and major modern rivers in the eastern Himalayan region and Burma. Locations of published U-Pb and Hf data used in this study are also displayed (see text for references). Locations 1–4 represent the sampling localities for the sedimentary rock samples of the Central Burma Basin analyzed in this study. Figure modified from Robinson et al. (2014).

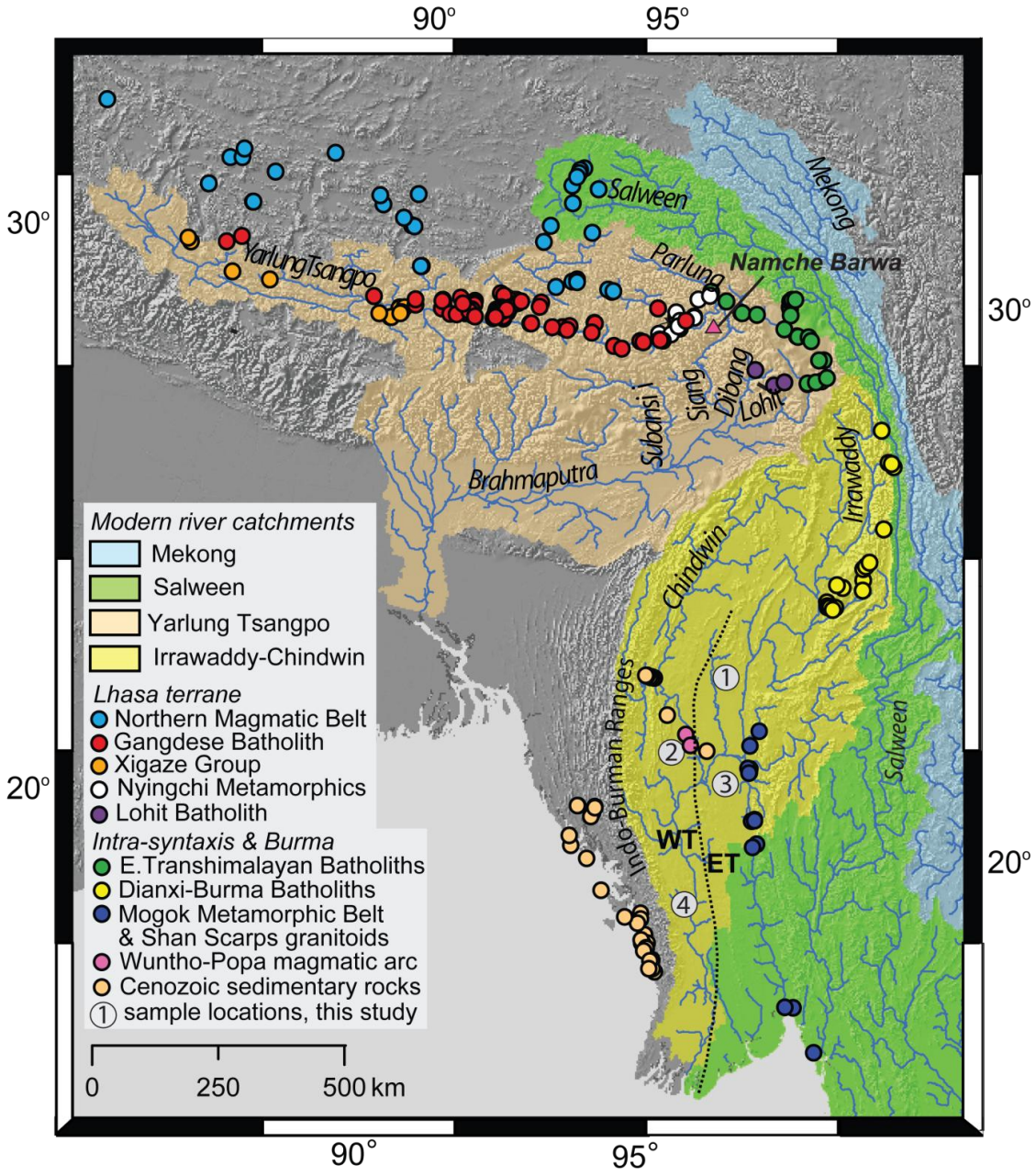

Figure 4.2 Simplified map showing the modern river catchments of the major rivers draining the eastern region of the Himalayan orogenic zone. Locations of published U-Pb and Hf data used in this study are displayed (see text for references). Locations 1–4 represent the sampling localities for the sedimentary rock samples of the Central Burma Basin analyzed in this study.

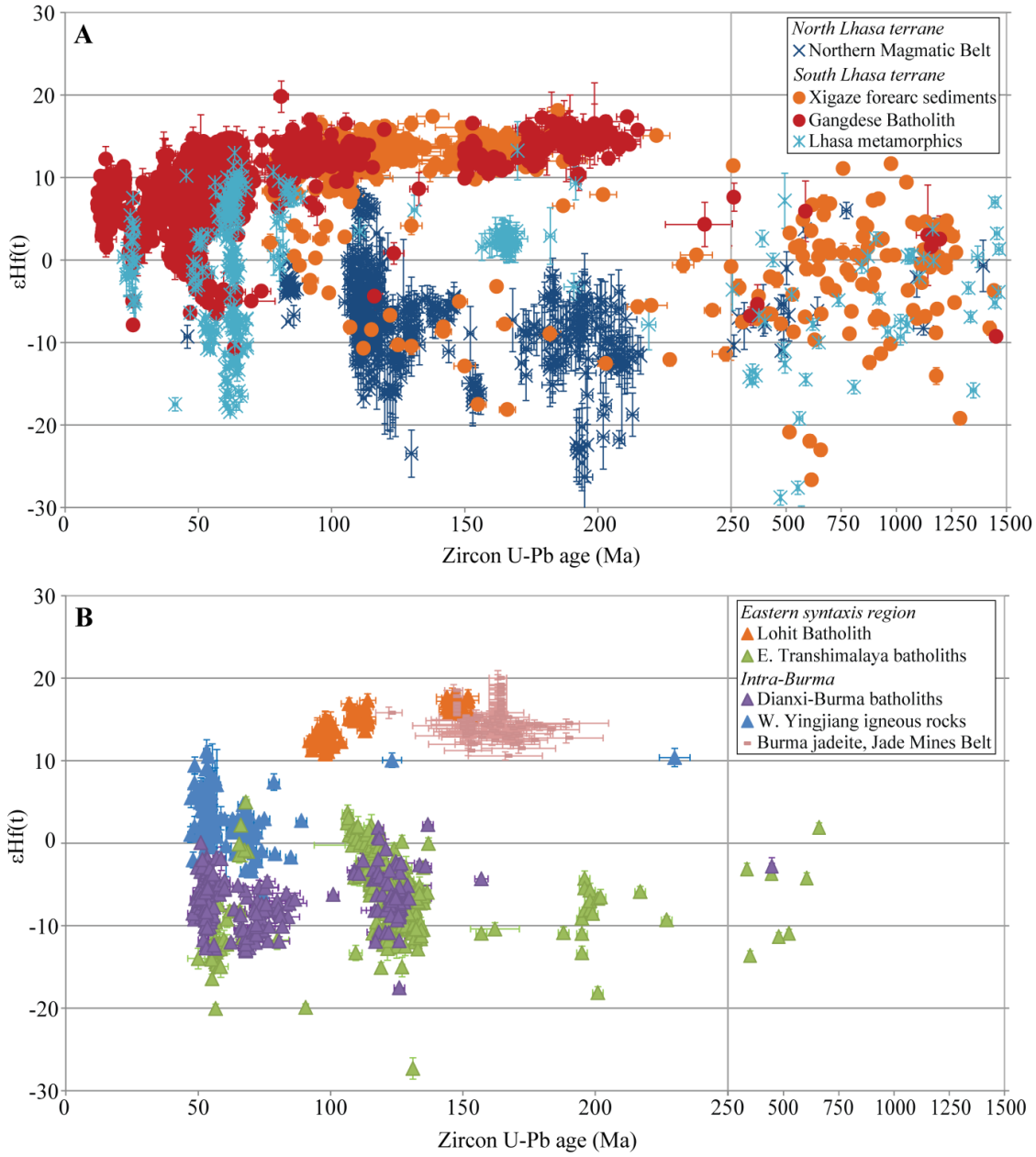

Figure 4.3 Comparison of U-Pb and εHf(t) values for published zircon data of bedrock samples from potential source regions in southeast Tibet, western Yunnan and Burma (see text for references). Error bars are 2 sigma for εHf(t) values and 1 sigma for the U-Pb ages. A. Published data for the Gangdese batholith of Tibet, Northern Magmatic Belt, and Nyingchi metamorphic complex west of Namche Barwa. B. Published data for the eastern Transhimalayan batholiths, Dianxi-Burma batholiths, western Yingjiang and Burma jadeite. Sampling locations are shown in Figure 4.1. Tabulated literature datasets are presented in Supplementary Table A7.

4.2.1. Lhasa terrane zircon U-Pb and Lu-Hf (Yarlung Tsangpo catchment)

4.2.1.1. Gangdese Batholith, southern Lhasa terrane

Two periods of magmatism, Late Triassic to Late Jurassic (ca. 215–150 Ma) and middle Early to middle Late Cretaceous (ca. 120–78 Ma), are characterized by zircons with juvenile mantle-derived Lu-Hf isotopic signatures and εHf(t) values ranging from +9.9 to +17.4 (± 0.5–4.9) and +6.2 to +19.8 (± 0.4–2.5), excluding two outliers with values of +0.8 and -4.4 (± 1.3 and 1.6), respectively (Figure 4.1, 4.3) (Chu et al., 2011, 2006; Ji et al., 2009a, b; Ma et al., 2013; Wen et al., 2008a, b). The younger magmatic episode is coeval with, and slightly younger than, peak magmatism in the northern Lhasa magmatic belt (ca. 135–100 Ma) and has been attributed to both crustal thickening (Chu et al., 2011; Chu et al., 2006) and back-arc extension (Zhu et al., 2009b; Zhu et al., 2011) following the Lhasa-Qiangtang continental collision.

Continuous magmatism in the southern Lhasa terrane occurred during Palaeocene to Eocene time (ca. 65–34 Ma), with increasing neodymium and hafnium enrichment of source melts expressed in the bi-modal distribution of εNd(t) and εHf(t) isotopic values, particularly observed in Early to Middle Eocene-aged granitoids (Chu et al., 2011, 2006; Guan et al., 2012; Ji et al., 2012, 2009a, b; Mo et al., 2005; Wen et al., 2008; Zhang et al., 2010a). Although the majority of zircons display εHf(t) values greater than +6, Palaeocene and Eocene magmatic zircons exhibit more heterogeneous εHf(t) values ranging from +14.7 ± 0.8 to -6.6 ± 0.4, with one outlier of -10.7 ± 2.0, contrasting with the homogeneous, high positive εHf(t) values of the Mesozoic Gangdese Batholith (+6 to +20) (Figure 4.3) (Chu et al., 2011; Guan et al., 2012; Ji et al., 2012; Ji et al., 2009b; Mo et al., 2009; Zhang et al., 2010a).

Post-collisional Oligocene to Middle Miocene porphyritic, adakitic and potassic to ultra-potassic igneous rocks were emplaced in low volumes as dykes, stocks and sills throughout the south-southeast Lhasa terrane and contain zircons dominated by juvenile, mantle-derived Hf isotopic values (εHf(t) values of +2 to +12), similar to those observed in Palaeogene Gangdese magmatic rocks (Chung et al., 2003; Chung et al., 2009; Chung et al., 2005; Chung et al., 1998; Guo et al., 2011; Hou et al., 2009; Ji et al.,

2009a; Ji et al., 2009b; Pan et al., 2012; Xiaoming et al., 2007; Zhang et al., 2010a; Zhou et al., 2010).

4.2.1.2. Xigaze Group, southern Lhasa terrane

Cretaceous to earliest Palaeocene (ca. 116–65 Ma) sedimentary rocks of the Xigaze fore-arc basin are dominated (75% of total population) by detrital zircons ages that are primarily middle Early to Middle Late Cretaceous (130–80 Ma) and subordinately Jurassic (190–150 Ma). The zircons are characterized by high, positive εHf(t) values (Figure 4.1, 4.3). Of the 226 zircons with U-Pb ages younger than 250 Ma, 224 zircons (99%) have positive εHf(t) values, with the majority of values lying between +9 to +17, with a peak of +13 (Figure 4.3). Only 4 zircons have εHf(t) values < +6. The positive εHf(t) values are the same as the Gangdese Batholith and are thus interpreted to be sourced from this magmatic arc to the north. Zircons of Palaeozoic to Proterozoic and Mesozoic age with negative εHf(t) values, thought to be sourced from Palaeozoic cover strata, Cretaceous foreland basin sedimentary rocks and Mesozoic granitoids of the back-arc region, are observed and possibly reflect the development of south-ward flowing river systems that cut across the uplifted Gangdese arc, linking the northern Lhasa terrane to the Xigaze fore-arc basin (Wu et al., 2010).

Early Cretaceous granitoids of the Gangdese Batholith are largely absent in present-day surface exposures, and while this may be the result of incomplete characterization of the magmatic arc due to accessibility issues, Wu et al. (2010) interpret the large population of Early Cretaceous zircons with high positive εHf(t) values in the Xigaze forearc basin to more likely be the result of exhumation and complete erosion of significant amounts of Early Cretaceous and Jurassic-aged Gangdese rocks during deposition of the Xigaze forearc basin sediments. If correct, the forearc basin would be the only record of this stage of Gangdese magmatism.

4.2.1.3. The Northern Magmatic Belt, northern Lhasa terrane

Zircons from predominantly S-type granitoids of the Northern Lhasa Magmatic Belt record Late Triassic to Early Cretaceous U-Pb ages, with a peak at ~110 Ma, characterized by enriched Hf isotopic signatures. Late Triassic to Early Cretaceous-

aged zircons (~216 to ~120 Ma) yield negative εHf(t) values ranging from -26.3 ±4.1 to -1.9 ± 2.1, with the majority recording values less than -5 (Chu et al., 2006; Zhu et al., 2009b; Zhu et al., 2011). Isotopic deviation to less enriched Hf isotope compositions (less negative εHf(t) values) is observed during peak magmatism in the northern Lhasa terrane (120–109 Ma), where a bi-modal distribution of εHf(t) values between -16.8 to +3.4 is recorded by magmatic zircon, although most zircons record values less than zero. The abundance of magmatic zircons with enriched Hf isotope signatures (negative εHf(t) values) and S-type geochemical signature of the majority of granitoids within the northern Lhasa magmatic belt suggests magma generation through re-melting of older (Proterozoic) crustal material, and supports suggestions that the central Lhasa terrane is a micro-continent, bounded to the north and south by magmatic arcs of Mesozoic and Mesozoic-Cenozoic age, respectively. Zircons from a Late Cretaceous (87–83 Ma; 84.5 ± 0.2 Ma) granitoid give εHf(t) values of -0.3 to -4.4 and -7.5 to -7.7. Conversely, one sample in northernmost central Lhasa contains zircons with U-Pb ages ranging from 116–109 Ma (n=20) with high, positive εHf(t) values (+5.3 to +7.8), attributed to the remnants of a magmatic arc overlying juvenile, mantle-like material along the Lhasa-Qiangtang plate boundary (Zhu et al., 2009b; Zhu et al., 2011).

4.2.1.4. The Nyingchi Group metamorphic rocks, Eastern Himalayan syntaxis region

Metamorphic rocks of the Nyingchi Group, exposed directly west of the Namche Barwa syntaxis (Figure 4.1) in the southeastern Lhasa terrane, contain discrete Mesozoic and Palaeogene zircon U-Pb age peaks and display very heterogeneous εHf values ranging from -18 to + 9 (Figure 4.3) (Guo et al., 2011; Xu et al., 2013; Zhang et al., 2010c). The wide range of εHf isotopic compositions is likely the result of mixing between juvenile mantle-derived magmas of the Gangdese batholith and melts formed from the sedimentary units and basement material of the Lhasa terrane, during multi-stage high grade metamorphism and anataxis at mid-crustal levels (Guo et al., 2011; Xu et al., 2013; Zhang et al., 2010c). The exposure of high grade meta-sedimentary and meta-igneous rocks of the southern Lhasa terrane is limited to the syntaxis regions and indicates that these rocks are the product of tectono-thermal and deformation unique to

these regions. The high-grade metamorphism can be inferred to be related to specific processes occurring in the syntaxis region, including burial of the leading edge of Asian plate with the subducting Indian plate, subduction and crustal thickening enhanced around the Indian indentor regions, and increased and focused exhumation linked to the presence of large river systems draining the syntaxis region (Booth et al., 2009; Burg et al., 1998; Finnegan et al., 2008; Xu et al., 2013; Zeitler et al., 2001; Zhang et al., 2012d; Zhang et al., 2010c).

4.2.2. Intra-syntaxis zircon U-Pb and Lu-Hf (Irrawaddy catchment)

In contrast to the Gangdese Batholith of southern Tibet, where magmatism is observed to have persisted from Late Triassic to Miocene times, granites younger than the Early Eocene (~50 Ma) are absent in the Eastern Transhimalayan batholiths and intra-syntaxis Dianxi-Burma batholiths. Most magmatic zircons reflect that two main stages of emplacement occurred during the Early Cretaceous and Late Cretaceous to earliest Eocene.

4.2.2.1. The Eastern Transhimalayan Batholiths, southeast Tibet

The Eastern Transhimalayan batholiths of the eastern syntaxis region outcrop parallel to the strike of the Jiali shear zone, between the Bangong-Nujiang and Indus-Yarlung suture zones (Figure 4.1, 4.2). Magmatic zircons from these plutons range in age from 227 ± 2.0 Ma to 50.0 ± 4.0 Ma, with dominant Early Cretaceous (~132–115 Ma and ~110–107 Ma) and subordinate latest Cretaceous to Early Eocene (~65.5–56 Ma) and Jurassic (~196.5 Ma) U-Pb age peaks (Figure 4.3) (Booth et al., 2004; Chiu et al., 2009; Liang et al., 2008; Zhu et al., 2009c). Corresponding zircon εHf(t) values range from -27.29 ± 0.65 to +4.99 ± 0.32, with a peak at -8 (Figure 4.3) (Chiu et al., 2009; Liang et al., 2008; Zhu et al., 2009c). The majority of zircons with $^{206}Pb/^{238}U$ ages younger than 250 Ma yield negative εHf(t) values (94%) and over 75% are significantly enriched in radiogenic hafnium with εHf(t) values less than -5. Late Cretaceous-aged zircons from one sample (~68–65 Ma) and late Early Cretaceous aged zircons (~115–107 Ma) yield more heterogeneous εHf(t) values that lie between +5 to -1.4 and +4 and -6,

respectively. Minor (2%) inherited Palaeozoic and Proterozoic aged zircons have εHf(t) values of -13.62 ± 0.28 to 1.91 ± 0.28 (Figure 4.3).

4.2.2.2. The Dianxi-Burma Batholiths, western Yunnan-northeast Burma border

Zircon U-Pb dating of the Dianxi-Burma magmatic rocks in the Gaoligong-Tengliang-Yingjiang region of western Yunnan, China and northeast Burma (Figure 4.1, 4.2) reveals a younging of magmatism from northeast to the southwest. Although described separately below, the Gaoligong, Tengliang and eastern Yingjiang granites are plotted together as plutons of the Dianxi-Burma batholith after Liang et al. (2008), for the remainder of the discussion, based on their overlapping zircon ages and Hf isotopic compositions, while the western Yingjiang is plotted separately. It is important to note that the literature data from this region is obtained primarily from rocks that are volumetrically much smaller than the other granite belts.

Granites of the Gaoligong area are composed of S-type, peraluminous biotite- and muscovite-bearing monzogranites, granodiorites and local leucogranites that range in age from 136.8 ± 2.0 Ma to 63.6 ± 4.0 Ma, with one zircon displaying an inherited Late Jurassic age (157 ± 2.5 Ma) (Figure 4.3) (Liang et al., 2008; Xu et al., 2012). Thirteen grains are Late Cretaceous to Early Palaeocene in age (15%), whereas the overwhelming majority of zircons are Early Cretaceous in age (84%). Corresponding Lu-Hf analyses reveal predominantly negative zircon εHf(t) values with a peak at -8 (Figure 4.3) (Liang et al., 2008; Xu et al., 2012). The overwhelming majority of zircons (95%) have negative εHf(t) values less than -2 and the remaining zircons have near chrondritic to slightly positive εHf(t) values of +0.59 to +2.25.

Zircons from S-type granitoids of the Tengliang area have ages ranging from 101 ± 2 Ma to 56.4 ± 2.5 Ma, with the majority having Late Cretaceous to Palaeocene U-Pb ages (86.5 ± 3.2 Ma to 66.0 ± 2.5 Ma) (Figure 4.3) (Liang et al., 2008; Xu et al., 2012). Corresponding εHf(t) values are exclusively negative, ranging from -5 to -13 similar to that observed in the Gaoligong area, with a systematic enrichment in radiogenic Hf with time (Figure 4.3) (Liang et al., 2008; Xu et al., 2012).

In the southernmost region of the Gaoligong shear zone in the Yingjiang area, granitoids display a spatial variation in lithology and zircon Lu-Hf isotopic composition between the S-type, peraluminous granitoids of eastern Yingjiang and the I-type meta-to peraluminous gabbroic to granite intrusions of western Yingjiang (Xu et al., 2012). In eastern Yingjiang, zircon U-Pb ages range from 65 ± 2 Ma to 48 ± 2 Ma, with minor Early Cretaceous inheritance observed in one sample (125.7 ± 5.2 Ma to 120.9 ± 4 Ma) (Figure 4.3) (Liang et al., 2008; Ma et al., 2014; Xu et al., 2012). Inherited Cretaceous and younger zircons yield exclusively negative εHf(t) values ranging from roughly -2 to -13; one outlier of 51 ± 1.2 Ma has an εHf(t) value of +0.05 ± 0.74 (Figure 4.3) (Liang et al., 2008; Ma et al., 2014; Xu et al., 2012). The westernmost Yingjiang region, along the border between western Yunnan, China and northeast Burma is marked by the north-trending Nabang dextral shear zone. This granite belt is thought to extend southwards to the granites of eastern Burma that outcrop within the Mogok Metamorphic Belt and the Shan Scarps (Chiu et al., 2009; Liang et al., 2008; Ma et al., 2014; Mitchell et al., 2012; Xu et al., 2012). Zircons extracted from mafic dykes, gneissic granites and leucogranites of western Yingjiang are predominantly Late Cretaceous to Eocene in age, with a main peak at ~53 Ma and a minor age peak at ~68 Ma (Ma et al., 2014; Xu et al., 2012). Two inherited zircons record Early Cretaceous (123.2 ± 3.6 Ma) and Late Triassic (230 ± 5.8 Ma) ages (Ma et al., 2014; Xu et al., 2012). Of the younger population (ca. 60–47 Ma), 86 of the total 95 grains (91%) have positive εHf(t)values and in the older population (ca. 90–63 Ma), 31 of the total 45 grains (69%) have positive εHf(t) values. The former is generally recorded by zircons extracted from early Eocene mafic dykes of this region that were specifically targeted and although they represent a volumetrically small amount of the surface exposure in this region, are over-represented in the literature data compilation. Latest Palaeocene-to Eocene-aged zircons (ca. 60–47 Ma) display εHf(t) values ranging from +10.5 to -4.5, with most values clustering between 0 to +7 (Figure 4.3) (Ma et al., 2014; Xu et al., 2012). Late Cretaceous- to Palaeocene-aged zircons (ca. 90–63 Ma) have heterogeneous Hf compositions, with corresponding εHf(t) values displaying a bi-modal distribution between -6 to +7, with most values clustered between -4 and +4 (Figure

4.3) (Ma et al., 2014; Xu et al., 2012). The involvement of both ancient continental crust and juvenile crust during magma genesis may explain the heterogeneous εHf values observed from rocks of this area. Ma et al. (2014) and Xu et al. (2008) interpret the generation of melts depleted in radiogenic hafnium to the re-melting of underplated basaltic rocks formed during the northward subduction of the Neo-Tethyan slab beneath the Asian margin following slab roll back at ~55–50 Ma.

In summary, magmatic zircons of the Dianxi-Burma granitoids record primarily Early Cretaceous, secondary Late Cretaceous to Early Eocene and Late Triassic to Jurassic stages of emplacement. Of the total number of zircons measured, 98% have negative εHf(t) values, ranging mostly from -2 to -13, and the remaining grains have positive εHf(t) values ranging from +0.5 ± 0.74 to + 2.25 ± 0.34. Some variation in the heterogeneity of these values is observed in zircons of late Early Cretaceous and latest Cretaceous age. Neoproterozoic to Palaeozoic zircons with U-Pb ages ranging from ~661–335 Ma are present in very minor amounts with negative εHf(t) values as low as -11.

4.2.2.3. Granites of the Mogok Metamorphic Belt, Slate Belt and Shan Scarps, east Burma

The Mogok Metamorphic Belt and Slate Belt of eastern Burma are pervasively penetrated by granitoids of Jurassic and Cretaceous to early Eocene age (Barley et al., 2003; Mitchell et al., 2012; Searle et al., 2007). Originally believed to be generated during Neo-Tethyan subduction, recent whole rock Sr-Nd isotopic studies reveal genetic link with the more S-type granites of Dianxi-Burma, Eastern Transhimalayn batholiths and northern Lhasa magmatic belt (Mitchell et al., 2012). The I-type geochemistry may be attributed to fractionization, as also observed in the Zayu pluton (I-type with negative zircon Hf values) outcropping in the southeast Eastern Transhimalayan batholith (Zhu et al., 2009c). Whole rock Sr-Nd isotopic analysis conducted on magmatic rocks of Cretaceous, early Eocene and Miocene age reveal all but one sample are enriched in radiogenic neodymium (εNd(t) values of -5 to -12) and yield high initial $^{87}Sr/^{86}Sr$ ratios (> 0.708) (Mitchell et al., 2012). These data points plot within an S-type granite field

and are thought to be correlated with contemporaneous S-type granites of the Eastern Transhimalayan batholith and the northern Lhasa magmatic belt and are likely to also enriched in radiogenic hafnium (Figure 4.4) (Chiu et al., 2009; Mitchell et al., 2012). A quartz diorite dyke intruding a biotite granite sampled from the southernmost Mogok Metamorphic Belt (17°25'N, 96°55'E), yielding a zircon U-Pb age of 90.8 ±0.8 Ma and positive εNd(t) value of +2.7, plots within the I-type Gangdese Batholith field (Figure 4.4) (Mitchell et al., 2012).

In a comparative sediment provenance study conducted by Liang et al. (2008) on a Late Miocene sample from the Upper Pegu Group of the Central Burma Basin, a proportion of detrital zircons with U-Pb ages ranging from ca. 40–24 Ma characterized by negative εHf(t) values lay outwith bedrock data of potential source regions. They suggest a Mogok Metamorphic Belt source, which experienced coeval high grade metamorphism and syntectonic granitoid emplacement during the Eocene-Early Miocene (ca. 47–23 Ma) (Barley et al., 2003; Mitchell et al., 2012; Searle et al., 2007). Although no zircon Hf isotopic data is available for these rocks, whole rock Sr-Nd isotopic analysis reveals predominantly S-type magmatism and granites emplaced in this belt are thought to be the southern continuation of the Eastern Transhimalayan batholiths and Dianxi-Burma Batholiths into central and southern Burma, and thus would likely share similar zircon geochemistry, enriched in radiogenic hafnium (Chiu et al., 2009; Liang et al., 2008; Mitchell et al., 2012; Xu et al., 2012).

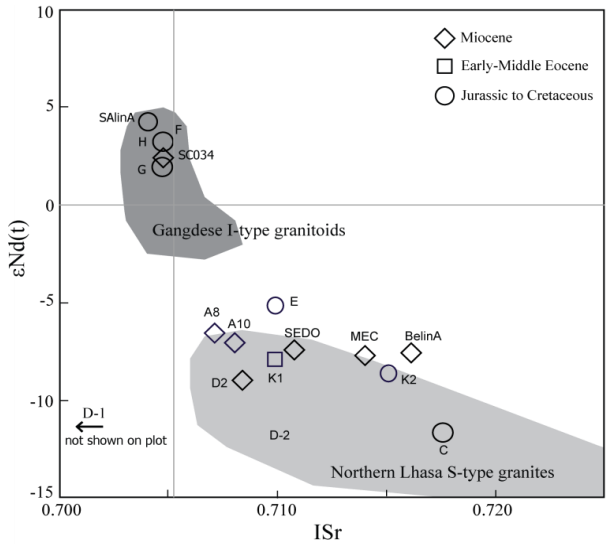

Sample	Rock type	$^{206}Pb/^{238}U$ age	ISr	εNd(t)
Mogok Metamorphic Belt, Shan Scarps:				
D-1	gneiss	491 ± 4 (2σ, n=28)	0.6503	-10.3
D-2	granite dyke	17.0 ± 0.3 (2σ, n=20)	0.7081	-8.4
MEC 1	granite dyke	44.8 ± 2.7 (2σ, n=5)	0.7140	-7.6
Belin A	pegmatitic granite dyke	45.9 ± 0.7 (2σ, n=17)	0.7161	-7.6
E	diorite	128 ± 1 (2σ, n=23)	0.7099	-5.1
K1	dacite dyke	50.0 ± 0.6 (2σ, n=21)	0.7099	-7.8
A8	dacite porphyry dyke	20.7 ± 0.3 (2σ, n=16)	0.7071	-6.5
A10	dacite porphyry dyke	20.7 ± 0.5 (2σ, n=19)	0.7080	-7.0
K2	augen gneiss	122 ± 2 (2σ, n=19)	0.7151	-8.6
C	granite	71.8 ± 0.5 (2σ, n=17)	0.7177	-7.1
SEDO A	granite	48.0 ± 0.9 (2σ, n=13)	0.7107	-7.5
G	quartz diorite	90.8 ± 0.8 (2σ, n=23)	0.7046	2.7
Wuntho-Popa magmatic arc, western Burma:				
Salin A	diorite	105 ± 2 (2σ, n=15)	0.7040	4.5
SCO 34	andesite porphyry dyke	13.6 ± 0.1 (2σ, n=24)	0.7046	3.2

Figure 4.4 Whole rock Sr-Nd and zircon U-Pb isotopic analysis of granitoids of the Mogok Metamorphic Belt, Slate Belt and the Wuntho-Popa magmatic arc of western Burma. From Mitchell et al. (2012).

4.2.2.4. The Lohit Batholith, northeast India

Granitoids of the Lohit Batholith of northeast India are considered to be the southeastern continuation of the Gangdese belt around the eastern Himalayan syntaxis, and to continue southward into the Wuntho-Popa magmatic arc of western Burma (Figure 4.1, 4.2). They are characterized by Mesozoic zircon U-Pb ages and high, positive εHf(t) values, indicative of derivation from juvenile, depleted mantle material (Lin et al., 2013). Zircon U-Pb age distributions reveal three main age peaks of 148 Ma, 110 Ma and 98 Ma, with corresponding εHf(t) values of +16 to +17, +13.6 to +17.3 and +11 to +14.6, respectively (Figure 4.3) (Lin et al., 2013).

4.2.2.5. Jade Mines Belt, central northern Burma

Zircon U-Pb and εHf(t) values extracted from jadeite and associated high pressure, low temperature metamorphic rocks of the Jade Mines Belt in northern Burma (Figure 4.1) reveal predominantly Jurassic $^{206}Pb/^{238}U$ ages ranging from 189 to 146.5 Ma, with one zircon having an Early Cretaceous age (~122 Ma), and all yield corresponding high, positive εHf(t) values ranging from +10.6 to +20, with a peak at +14 (Figure 4.3) (Qiu et al., 2009; Shi et al., 2009; Shi et al., 2008). More recently, Qi et al. (2013) suggested

the jadeite of this region experienced long-lasting and multi-stage metasomatism during Jurassic (~146 Ma), Early Cretaceous (~135 Ma) and Late Cretaceous (~93 Ma) time based on $^{40}Ar/^{39}Ar$ laser stepwise heating of jadeite and associated amphibole sampled from this area, consistent with the zircon U-Pb studies.

4.2.2.6. West Burma magmatic arc batholiths

The present-day surface outcrop of the Wuntho-Popa magmatic arc of western Burma consists of Late Cretaceous diorites, granodiorites and granite plutons exposed in the Salingyi and Wuntho regions (Figure 4.1). This magmatic arc developed during subduction of the Neo-Tethys oceanic lithosphere beneath the southern margin of Eurasia and likely represents the continuation of the Gangdese arc into Burma (Li et al., 2013; Lin et al., 2013; Mitchell et al., 2012). Hornblende K/Ar dating of two diorites and biotite K/Ar dating of a granite from the Salingyi region yielded ages of 91 ± 1 Ma, 106 ± 7 Ma and 103 ± 1 Ma, respectively (Mitchell et al., 2012; Mitchell, 1993). This is consistent with a recently reported zircon U-Pb age of 105.3 ± 1.7 Ma obtained from a diorite sampled from this area, with corresponding whole rock Sr-Nd isotopic analysis recording a low initial $^{87}Sr/^{86}Sr$ ratio of 0.7040 and an εNd(t) value of +4.5 (Figure 4.4) (Mitchell et al., 2012). Radiometric data available for granodiorites of the Wuntho region (Khanza Chaung batholith) include biotite K/Ar ages of 93.7 ± 3.4 Ma and 97.8 ± 3.6 Ma (Barley et al., 2003; Mitchell et al., 2012) and a 94.6 ± 1 Ma zircon U-Pb age (Mitchell et al., 2012). Two stages of juvenile volcanism occurred within the Central Burma Basin at Mt. Popa and near Monywa during the middle Miocene (ca. 16–13 Ma; calc-alkaline) and the Quaternary (<1 Ma), the latter of which yielded εHf values of +10.7 to +17.4 and +3.7 (Lee et al., 2010; Stephenson and Marshall, 1984). An andesite porphyry dyke sampled at Monywa gave a zircon U-Pb age of 13.6 ± 0.1 Ma and a juvenile εNd(t) value of +3.2 (Mitchell et al., 2012). Bodet and Schärer (2000) recorded a minor population of detrital zircon with Middle Miocene (ca. 15–12 Ma) and Pliocene (ca. 5–3 Ma) U-Pb ages characterized by high, positive εHf(t) values (+7 to +12) within the modern Irrawaddy River that was likely locally sourced from the proximal volcanic centres within the basin.

4.2.3. Summary of published literature dataset (zircon U-Pb and Lu-Hf)

In summary, the published εHf literature data demonstrate that the Gangdese batholith is characterized by late Triassic- to Miocene-aged zircons with predominantly high, positive εHf(t) values (generally > +5), and it lies exclusively within the modern Yarlung Tsangpo catchment (Figure 4.1, 4.3, 4.8). Zircons with high, positive εHf(t) values are not exclusively limited to the Gangdese Batholith, however, they are temporally and spatially more constricted. Within the modern Irrawaddy River catchment, rocks with magmatic zircons with juvenile εHf signatures that have been reported in the literature occur in gneisses and mafic dykes of western Yingjiang (southernmost Dianxi-Burma), the Jade Mines Belt of central northern Burma, the Western Burma magmatic arc, and locally as a dyke within the southernmost Mogok Metamorphic Belt (Figure 4.2) (Ma et al., 2014; Mitchell et al., 2012; Qiu et al., 2009; Shi et al., 2009; Shi et al., 2008; Xu et al., 2008). Zircons from the northern Lhasa magmatic belt, eastern Transhimalayan batholiths and Dianxi Burma batholiths have negative εHf values (Fig 4.1, 4.3, 4.8). The U-Pb age and εHf(t) values of zircons from the described potential source areas can be compared to the detrital zircon signatures of the Eocene to Miocene Central Burma Basin sedimentary rocks, in order to determine their provenance and evaluate whether a linked Yarlung Tsangpo-Irrawaddy River system existed during their deposition.

Table 4.1 Source region & Rock description	Zircon U-Pb age (Ma)	Zircon εHf(t) value	$^{40}Ar/^{39}Ar$ mica age (Ma)	Whole rock εNd, $^{87}Sr/^{86}Sr$
Gangdese magmatic arc, S Lhasa Calc-alkaline, I-type granitoid batholiths	Mesozoic (ca. 215–78 Ma), Paleocene to Miocene (ca. 65–13 Ma); peak at ca. 50 Ma	97% positive; Mesozoic > +5 Cenozoic +15 to -7	Oligo-Early Miocene (28-18 Ma); Rare Paleocene-Eocene	0.9 to 5.5 *>0.7044*
Linzizong Fm, S Lhasa Andesite, rhyolite, basalt	ca. 69–43 Ma	n/a, likely similar to coeval Gangdese	ca. 65–44 Ma; ca. 50 Ma peak	-5 to 9, most > 0 *>0.7047*
Xigaze fore-arc basin, S Lhasa Cretaceous-Paleocene (ca. 116–65 Ma) forearc basin sedimentary rocks	Mainly Mesozoic ages (75%); Cretaceous (130–80 Ma) and Jurassic (190–150 Ma) peaks	99% of grains < 250 Ma have positive values (most +9 to +17)	n/a	n/a, likely similar to Gangdese
Lohit Batholith, Northeast India Gabbro, granodiorite	Peaks at 98 Ma, 110 Ma and 148 Ma	100% of grains have positive values ranging from +10 to +18	n/a	n/a
Northern Lhasa magmatic belt S-type granitoids, dacite-rhyolite volcanics	Late Triassic-Early Cretaceous ages; peak at ca. 110 Ma	Over 95% of grains have negative values (mainly -3 to -16)	165–150, 130–110, 45–35 Ma	-3.6 to -13.7
Nyingchi and Lower Bomi Group, EHS High grade metasedimentary and metaigneous rocks; granitic melts	81% of grains < 250 Ma; Peaks at 24, 50, 63, 83, 165 Ma; 19% mainly Proterozoic, minor Paleozoic	Heterogeneous εHf(t) values -18 to + 9, mixed Lhasa cover-India(?)-Gangdese signal	n/a	n/a
Eastern Transhimalayan batholiths, SE Tibet S-type granites intruding Palaeozoic sedimentary and low grade metasedimentary Lhasa terrane cover	Dominant Early Cretaceous (~132–107 Ma) and subordinate latest Cretaceous to Early Eocene (~65.5–56 Ma) and Jurassic (~196.5 Ma)	Range from -27 to +5, with a peak at -8; 94% of grains < 250 Ma yield negative εHf(t) values; over 75% are less than -5	Main stage of shear along the Jiali Fault from 22–11 Ma; change from sinistral to dextral at 18 Ma	-3.61 to -11.4 *0.7056-0.7449* *Most > 0.715*
Dianxi-Burma batholiths, W Yunnan, Northeast Burma S-type granites intruding Paleozoic-Proterozoic sedimentary cover; gneiss; Eocene mafic dykes	Early Cretaceous (126–115 Ma), Late Cretaceous (80–67 Ma) and Eocene (53 Ma) peaks	Gaoligong-Tengliang- E Yingjiang: 98% have negative values up to -19; mostly < -5; W. Yingjiang: 84% have positive values (up to +11), remainder have negative values (as low as -6);	Main stage of dextral shear along the Gaoligong Fault from 18-13 Ma; ca. 41-42 Ma (Eocene mafic dykes)	-0.3 to -3.85 *0.7066 to 0.715* (Mafic dykes) +0.8 to -7 *<0.709* (gneiss)
Mogok Metamorphic Belt, Slate Belt and Shan Scarps, Eastern Burma Schist, gneiss marble; mostly S-type granites; Palaeozoic Shan Plateau sedimentary cover rocks; Proterozoic basement gneiss	Jurassic, Cretaceous and Eocene ages for granite bodies; High temperature metamorphism at ca. 59 Ma and 47–23 Ma	n/a	Oligocene-middle Miocene; Range from ca. 27-25 Ma (S. Shan Scarps) to 22.7-16.6 Ma in the north, associated with NW-SE extension;	-10 to -5 *0.7087–0.7177* +2.7 (quartz diorite dyke, S MMB)
Jade Mines Belt, Northern Burma HT-LP metamorphic rocks, mafic bodies	Main Jurassic (178-162 Ma, 155-145 Ma) & minor Early Cretaceous (122 Ma) peaks	100% have positive values, ranging from + 10.5 to +20	Jurassic (152 Ma) & Cret. (135, 124, 93 Ma) ages	n/a
Cretaceous West Burma magmatic arc Diorites and granodiorites	U-Pb zircon age ca. 94–105 Ma	n/a	Cretaceous biotite, K-feld & hbl K-Ar age ca. 106–91 Ma	+4.5 *<0.7055*

4.3. Provenance interpretations based on isotopic data

By comparing the detrital zircon U-Pb age distribution with the zircon U-Pb ages of bedrock within the potential source regions (modern Yarlung Tsangpo and Irrawaddy catchments) reported in the literature, the detrital sediment of the sedimentary strata may be linked to specific source regions. A potential for bias must be noted, as much of the dataset is focused on igneous rocks within the source region and bedrock of the catchment region have not yet been fully characterized. However, as the majority of detrital ages obtained in this study are of Jurassic and younger ages, it is likely that these rocks sufficiently characterize, and discriminate between, potential source regions. The paucity of Late Palaeozoic to Proterozoic detrital zircon ages within the sedimentary rocks analyzed in this study indicate the sedimentary cover strata and/or metamorphic basement of the Lhasa, Sibumasu and west Burma terranes were not significant contributors to the sediment load. Mesozoic- to Cenozoic-aged magmatic and metamorphic rocks of Tibet, western Yunnan and Burma that formed during closure of the Meso- and Neo-Tethys oceans are considered to form the main potential source regions investigated in this study, therefore the following interpretations are focused on data for the last 250 Ma. Previous provenance studies utilizing detrital zircon U-Pb and εHf(t) data do not suggest a significant proportion of detritus is derived from an uncharacterized source terrane (Liang et al., 2008).

4.3.1. Eocene Pondaung Formation

U-Pb ages of detrital zircon from sandstones of the Eocene Pondaung Formation (Pondaung 1 and Pondaung 2), sampled from the Eastern Trough of the Central Burma Basin range from 34.4 ± 0.9 Ma to 1319.0 ± 31.1 Ma (2σ), with three age peaks ca. 43 Ma, 68.5 Ma and 91 Ma (Figure 4.5). The two younger age peaks encompass minor populations between ~54–43 Ma and ~71–65 Ma. The majority of ages are Cretaceous to Eocene (96%), with a small number of grains being of Late Triassic to Jurassic and Palaeozoic to Proterozoic age. This distribution is similar to that observed in magmatic zircon of the Gangdese Batholith within the modern Yarlung Tsangpo catchment and of the Eastern Transhimalaya, Dianxi-Burma, and western Yingjiang batholiths within the modern Irrawaddy catchment (Figure 4.5, 4.8). The former yields homogeneous, high

positive εHf(t) values generally greater than +6 and the latter yields mostly negative εHf(t) values (Figure 4.8).

A sub-set of these detrital zircons underwent additional Lu-Hf isotopic analysis in order to differentiate between the potential source regions. The majority of the detrital zircons in the stratigraphically lowest, and thus oldest, sample from the Late Eocene Pondaung Formation (Pondaung 1), ranging in age from 97.9 ± 2.3 Ma to 39.9 ± 0.8 Ma with one outlier of 225.2 ± 3.6 Ma, yield εHf(t) values that lie within the Gangdese field (83% of the total zircon population, n = 35 of 42) (Figure 4.5, 4.8). Age distributions of these zircons reveal main Eocene age peaks of ca. 55 and 42 Ma, and subordinate Palaeocene and Late Cretaceous peaks of ca. 68–62 Ma and ca. 91–78 Ma, consistent with typical zircon ages observed in the Gangdese Batholith (Chu et al., 2011, 2006; Guan et al., 2012; Ji et al., 2012, 2009a, b; Mo et al., 2009, 2005; Wen et al., 2008; Zhang et al., 2010). A minor population of Late Cretaceous- to Palaeocene-aged zircons with corresponding εHf(t) values of -7 to -9.8 lie within the fields of the eastern Transhimalayan batholiths and Gaoligong granite belt of western Yunnan, China (Figure 4.5). Although these zircons also overlap with the Nyingchi Group metamorphic rocks of the southeastern Lhasa terrane, this is an unlikely source as these rocks experienced coeval granulite- to amphibolite-facies metamorphism and anatectic melting at lower crustal levels (25–40 kilometres depth) during the early Palaeocene to Late Eocene and were not exhumed until Oligocene to Early Miocene time (Booth et al., 2009; Gao et al., 2012; Guo et al., 2011; Guo et al., 2012; Palin et al., 2014; Zhang et al., 2008; Zhang et al., 2010a; Zhang et al., 2013).

The stratigraphically higher, and thus younger, Pondaung 2 sample from the Late Eocene Pondaung Formation is also dominated with detrital zircons ages and Hf isotopic compositions that overlap with those observed in the Gangdese Batholith (88.5% of the total population, n = 46 of 52) (Figure 4.5, 4.8). These zircons range in age from 194.8 ± 6.0 Ma to 41.6 ± 2.7 Ma, with well defined age peaks at ca. 91 Ma, 69 Ma and 45 Ma. A cluster of zircons with ages of roughly 43–37 Ma and corresponding εHf(t) values of -2 to -5 and one outlier of -11 do not correspond with any available

literature data for the potential source regions (Figure 4.5). These zircons may be sourced from bedrock of the intra-syntaxis region, where far fewer geochronological and geochemical studies exist than within the Lhasa terrane. Detrital zircons with similar age and isotopic characteristics present within a Late Miocene sedimentary sample from the Central Burma Basin were interpreted as sourced from the Mogok Metamorphic Belt (Liang et al., 2008). Although no Lu-Hf data exists for the bedrock of the Mogok Metamorphic Belt and Slate Belt of eastern Burma, Middle Eocene to Early Miocene partial melting and granite emplacement coeval with high temperature sillimanite facies metamorphism occurred at ~47–29 Ma (Barley et al., 2003; Mitchell et al., 2012; Searle et al., 2007).

The abundance of detrital zircon U-Pb age and depleted Hf isotopic compositions, analogous with those of the juvenile, mantle-derived melts that formed the Gangdese batholith along the southern Lhasa margin, suggests detrital zircons of the Late Eocene Pondaung Formation were sourced primarily from the erosion of Gangdese plutons and associated volcanic cover of early Late Cretaceous to middle Eocene age. The youngest detrital zircon in the oldest Pondaung sample with an εHf(t) value has a $^{206}Pb/^{238}U$ age of 39.9 ± 0.8 Ma (1σ) with a corresponding εHf(t) value of +9.5 ± 0.8 (2σ), and the youngest age peak of zircons that plot within the Gangdese field of ca. 42 Ma, suggesting the Gangdese Batholith of the southern Lhasa terrane was contributing sediment to the Central Burma Basin at least as early as the Mid-Late Eocene. A minor contribution of detritus is sourced from Late Cretaceous to Palaeocene S-type granites of the eastern Transhimalayan and Dianxi-Burma batholiths and from an unidentified Middle Eocene source containing zircons enriched in radiogenic hafnium. This source potentially lies within the intra-syntaxis region, possibly the proximal metamorphic belts of east Burma, as zircons with similar age and Hf isotopic signatures are observed in all strata analysed in this study. Alternatively, these zircons may record a stage of magmatism in the Gangdese Batholith for which there is no literature data, as progressively decreasing εHf(t) values are observed in Palaeocene- to Eocene-aged magmatic zircons (Ji et al., 2012).

Detrital zircons with U-Pb ages closely matching the Late Eocene stratigraphic age of the Pondaung Formation indicate a potential volcanic origin for the youngest zircons within this sample, as a magmatic Gangdese Batholith source would require emplacement, uplift, erosion and sediment transportation over 1000 kilometres in a short period of time. The presence of a tuff bed within the stratigraphic succession of the Pondaung Formation suggests active volcanism was occurring in the Central Burma Basin during deposition of this formation and therefore local sources with juvenile, mantle-derived signatures may have attributed to the sediment load. No geochemical bedrock data is available for the Pondaung tuff bed. However, the wide age range of the detrital zircons with high positive εHf(t) values observed in this formation cannot be explained by intra-basin volcanic contributions alone and closely matches with the timing of magmatism within the Gangdese Batholith. No tuff beds or strata of volcanic origin were observed in the sampling localities of this study. Low temperature thermochronology from the Gangdese Batholith of the southern Lhasa terrane do record a period of rapid unroofing from ca. 48–46 Ma, whereby emplacement zircon U-Pb dating and biotite $^{40}Ar/^{39}Ar$ dating of an Eocene granitoid revealed emplacement and subsequent uplift and cooling below ~300°C (Dai et al., 2013), supporting the possibility of rapid tectono-thermal processes operating in the southern Lhasa terrane during Middle-Late Eocene time.

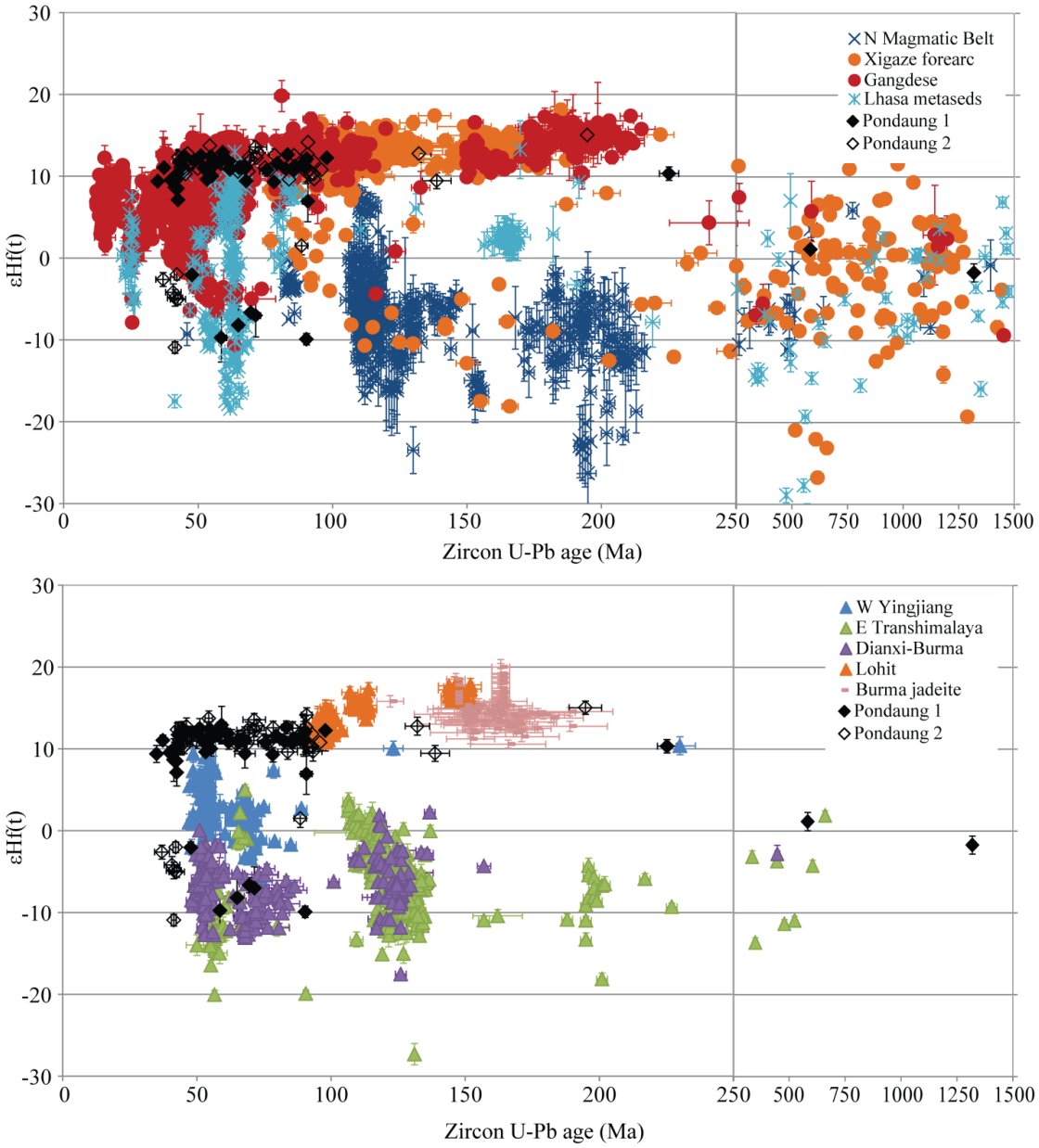

Figure 4.5 Comparison of U-Pb age and εHf(t) values for published zircon bedrock data and for single grain detrital zircons extracted from the Middle to Late Eocene Pondaung Formation of the Central Burma Basin analysed in this study in order to delineate provenance between several potential source regions (see text for references). A. Published data for the Gangdese Batholith and Cretaceous forearc sediments of the Xigaze Group of the southern Lhasa terrane, Northern Lhasa Magmatic Belt, and Nyingchi metamorphic complex west of the Namche Barwa syntaxis. B. Published data for the eastern Transhimalayan batholiths, the Dianxi-Burma batholiths and Western Yingjiang igneous rocks within the northern continuation of the Mogok Metamorphic Belt and the Slate Belt into western Yunnan, and a jadeite sample from the Jade Mines Belt of northeast Burma. Error bars are 1 sigma for U-Pb ages and 2 sigma for εHf(t) values.

4.3.2. Oligocene Padaung Formation

Sandstones of the Oligocene Padaung Formation sampled from the Western Trough in the Central Burma Basin contain detrital zircons ranging in age from 24.7 ± 0.6 Ma to 3072.6 ± 20.2 Ma (2σ), roughly two-thirds of which are Late Cretaceous to Late Eocene in age. The age distributions of detrital zircons younger than 250 Ma are similar to those observed in the Pondaung Formation, with age concentrations between ~52–42 Ma, ~73–65 Ma and ~94–88 Ma and minor Early Cretaceous (ca. 125–113 Ma), Early Jurassic (ca. 145 Ma) and Late-Middle Jurassic (ca. 175 Ma) clusters (Figure 3.4, 4.6). A larger proportion of Triassic- to Archean-aged detrital zircons are observed in the samples from the Western Trough versus the Eastern Trough (Padaung and Obogon formations), and may reflect either sediment mixing with detritus shed from the nascent Himalayan (mixing with Bengal Fan material), sediment recycling from the Indo-Burman Ranges that contain zircons of this age, or derivation from an older source, localized source, within the fore-arc basin (Allen et al., 2008).

A sub-set of detrital zircons underwent additional Lu-Hf isotopic analysis, focusing on those with U-Pb ages younger than 250 Ma, in order to differentiate between the potential source regions. A significant proportion of detrital zircons (74% of the total population, n = 29 of 39) from the Oligocene Padaung Formation (Padaung 1 and Padaung 3) yield U-Pb ages (ca. 114 to 40 Ma) and corresponding εHf(t) values that overlap with the Gangdese Batholith and the mid- to Late Cretaceous Xigaze fore-arc basin fields of the southern Lhasa terrane (Figure 4.6). Although there is overlap with the Western Yingjiang field, the number of zircons with high, positive εHf(t) values that plot outside this field indicate this is not a significant or primary source, and a Gangdese source more closely matches the zircon age and εHf values observed in the detrital sediment. The Gangdese Batholith and associated volcanics of the southern Lhasa terrane are much more significant, volumetrically.

The remaining zircons older than approximately 51 Ma lie within the fields delineated by intra-syntaxis plutons and the northern Lhasa magmatic belt. A minor population of zircons of ca. 45–40 Ma that yield εHf(t) values of -4 to -6 do not overlap

any field of literature dataset. Similar zircons are observed in the Eocene Pondaung Formation and are potentially sourced from a region presently drained by the modern Irrawaddy River, as similar zircons are observed in younger formations, the Mogok Metamorphic Belt being the favoured interpretation for source provenance of this detritus. Five zircons of ~103–94 Ma and ~114 Ma are similar to values of the Lohit Batholith (Lin et al., 2013) and, likely its southern continuation to the west Burma magmatic arc (Mitchell et al., 2012), although no Hf isotopic data exists from these rocks for direct comparison.

During deposition of the Oligocene Padaung Formation, detritus was still primarily derived from the Gangdese magmatic arc as indicated by the significant proportion of detrital zircon age distributions and depleted Hf isotopic compositions typical of magmatic zircons of the Gangdese Batholith (Figure 4.6, 4.8). Like the Eocene Pondaung Formation, these also plot within the magmatic arc provenance field of Dickinson (1985) (Figure 4.9). The youngest Gangdese-type zircon in the Padaung Formation is found in the stratigraphically lowest sample (Padaung 3) and has a U-Pb age of 27.6 ± 1.4 Ma and an εHf(t) value of -1.5 ± 1.7, which matches closely with the known Middle Oligocene depositional age for this formation based on biostratigraphy. The youngest detrital zircon with a U-Pb age of 24.7 ± 0.6 Ma is found in the stratigraphically highest Padaung 1 sample, and gives an indication of a maximum depositional age of Late Oligocene for the upper Padaung Formation. A decrease in the percentage of Gangdese-type detrital zircons is observed moving up-section, from 89% (16 of 18 grains) in Padaung 3 to 62% (13 of 21 grains) in Padaung 1. However, as only 39 combined U-Pb and Hf analyses are available for the Padaung Formation it must be noted that detrital populations may be under-represented, or not represented at all (Vermeesch, 2004).

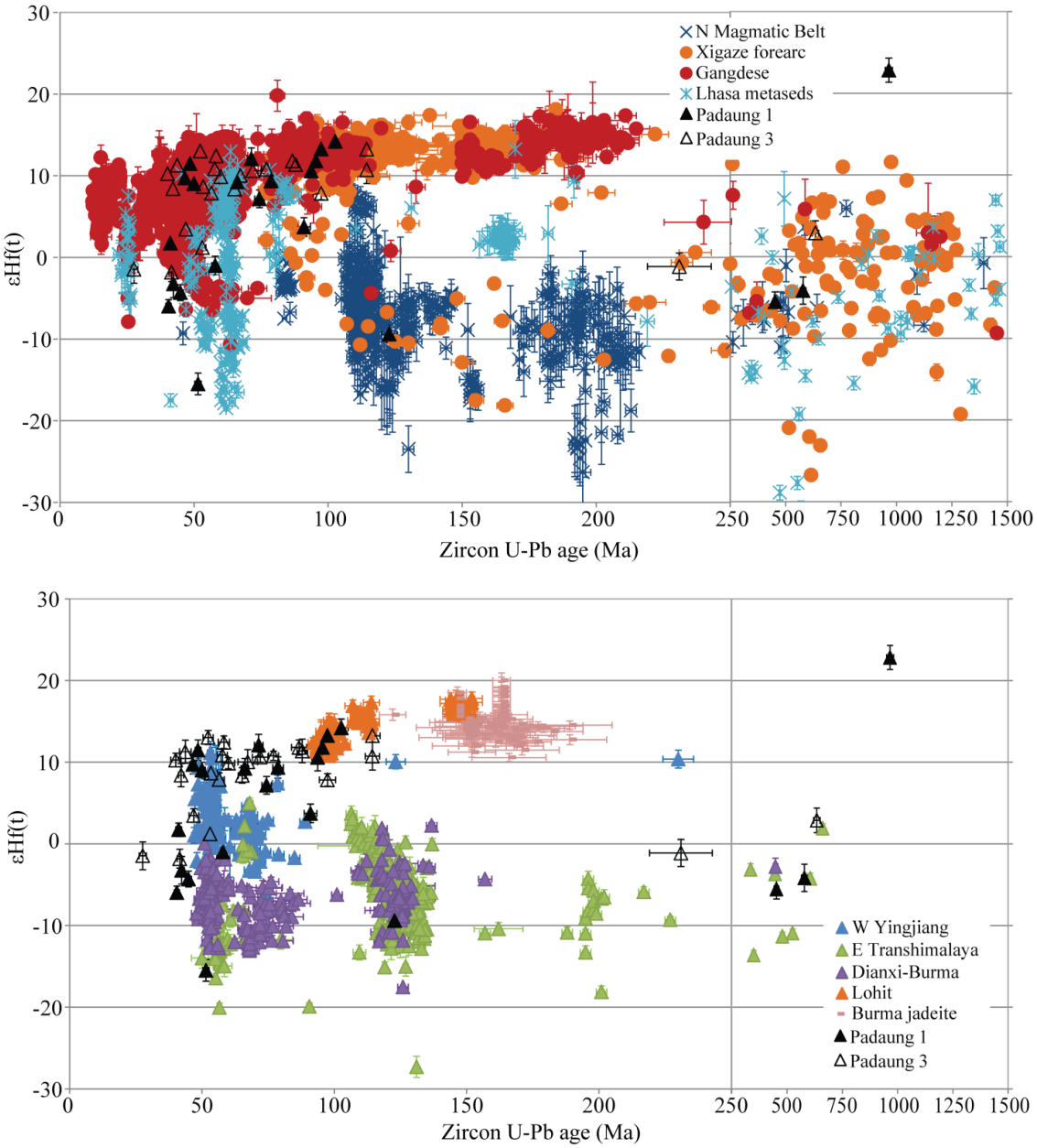

Figure 4.6 Comparison of U-Pb and εHf(t) values for published zircon bedrock data to data obtained from single grain detrital zircons of the Middle Oligocene Padaung Formation of the Central Burma Basin analysed in this study in order to delineate provenance between several potential source regions (see text for references). A. Published data for the Gangdese Batholith and Cretaceous forearc sediments of the Xigaze Group of the southern Lhasa terrane, Northern Lhasa Magmatic Belt, and Nyingchi metamorphic complex west of the Namche Barwa syntaxis. B. Published data for the eastern Transhimalayan batholiths, the Dianxi-Burma batholiths and Western Yingjiang igneous rocks within the northern continuation of the Mogok Metamorphic Belt and the Slate Belt into western Yunnan, and a jadeite sample from the Jade Mines Belt of northeast Burma. Error bars are 1 sigma for U-Pb ages and 2 sigma for εHf(t) values.

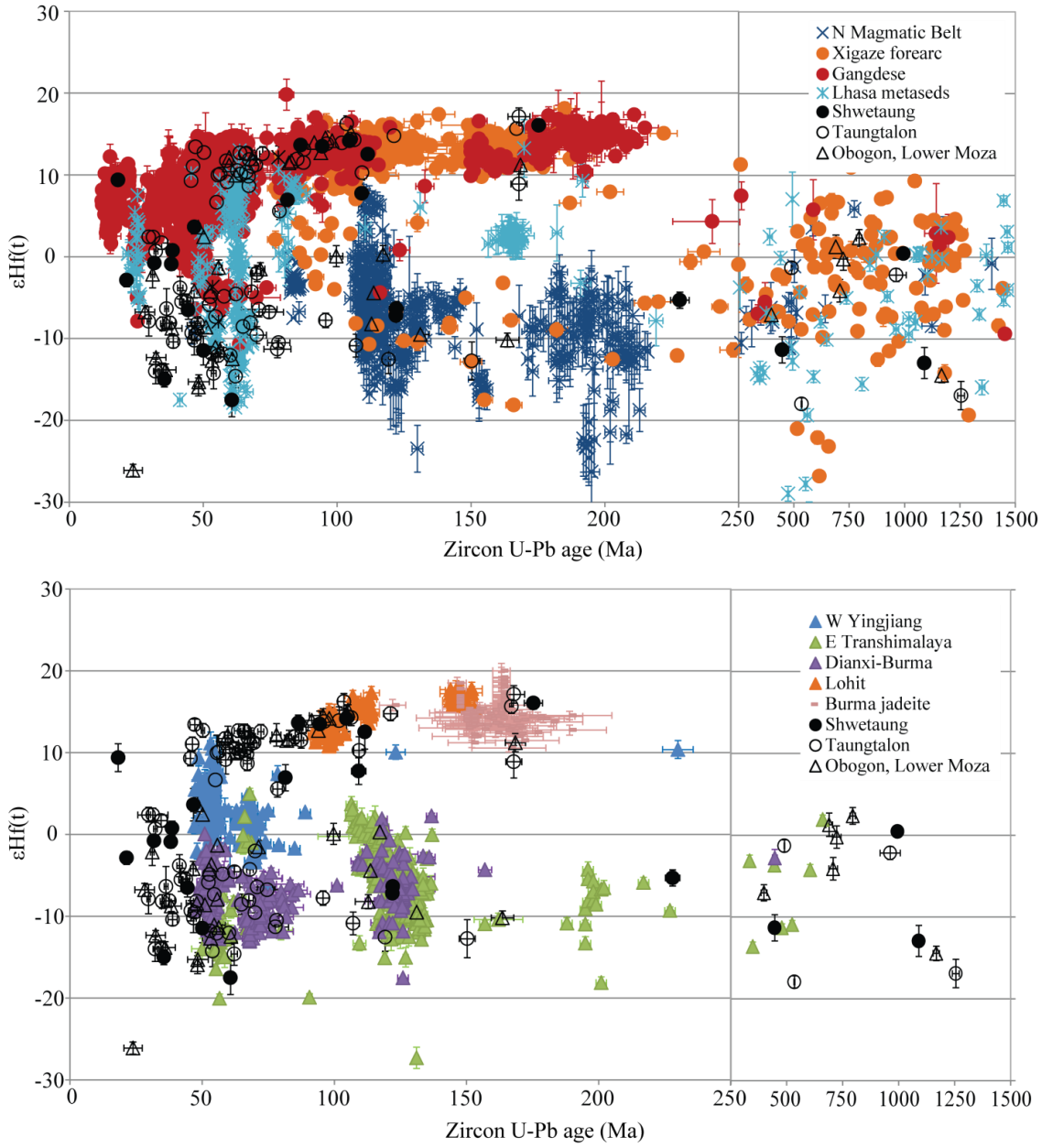

Figure 4.7 Comparison of U-Pb and εHf(t) values for published zircon bedrock data and single grain detrital zircons extracted from Early to Middle Late Miocene sedimentary rocks of the Central Burma Basin analysed in this study in order to delineate provenance between several potential source regions (see text for references). A. Published data for the Gangdese Batholith and Cretaceous forearc sediments of the Xigaze Group of the southern Lhasa terrane, Northern Lhasa Magmatic Belt, and Nyingchi metamorphic complex west of the Namche Barwa syntaxis. B. Published data for the eastern Transhimalayan batholiths, the Dianxi-Burma batholiths and Western Yingjiang igneous rocks within the northern continuation of the Mogok Metamorphic Belt and the Slate Belt into western Yunnan, and a jadeite sample from the Jade Mines Belt of northeast Burma. Error bars are 1 sigma for U-Pb ages and 2 sigma for εHf(t) values.

4.3.3. Miocene Formations

In contrast to the more homogeneous juvenile zircon Hf isotope compositions observed in the Palaeogene sediments, a change towards more heterogeneous zircon Hf values, with an increase in negative εHf(t) values, is observed in the Miocene strata, where less than half of the total zircon population from the Miocene strata lie within the Gangdese field (Figure 4.7, 4.8). Eleven of twenty-four (46%) of detrital zircons from the Early Miocene Shwetaung Formation plot within the Gangdese field and the youngest zircon (18.2 ± 0.3 Ma) has an εHf(t) value of +9.4 ± 1.7 (Figure 4.7). The remaining zircons plot within the eastern Transhimalaya batholith and Dianxi-Burma batholith fields. A minor proportion with ages ranging from ca. 44–21 Ma with negative εHf(t) values ranging from +0.75 to -15 do not overlap with any fields, as there are no zircons younger than the Early Eocene with negative εHf(t) values recorded in the literature data. An intra-syntaxis source or Mogok Metamorphic Belt are potential sources based on the enriched Hf composition and because similar zircons are present within all formations analyzed.

The proportion of Early-Middle Miocene Taungtalon Formation zircons plotting within the Gangdese field is 48% and most of the remaining zircons plot primarily within the Dianxi-Burma field and subordinately within the Eastern Transhimalayan batholiths field (Figure 4.7, 4.8). A minor population (younger than 42 Ma) with negative εHf(t) values plot outside any of the values covered in the available bedrock εHf datasets. The youngest two zircons are the same age (29.7 ± 0.6 Ma and 29.7 ± 0.7 Ma) and have εHf values of -7.9 and +2.4, respectively. Finally, 29.5% of detrital zircons from the Middle-Late Miocene Lower Moza and Obogon formations plot within the Gangdese field; the majority of the remaining zircons plot within the eastern Transhimalaya and Dianxi-Burma fields (Figure 4.7, 4.8). The youngest zircon from the Obogon Formation (23.8 ± 3.5 Ma) from the sub-set that underwent additional Lu-Hf isotopic analysis has an εHf value of -26.

Throughout deposition of the Miocene formations, Jurassic-aged detrital zircons with corresponding εHf(t) values of > +10 are present which overlap with both the Gangdese

Batholith field and the Burma jadeite field. Jadeite boulders and clasts are present within proximal Middle and Lower Miocene conglomerates of the Central Burma Basin, indicating the Jade Mines Belt was exposed to become a localized source at this time (Bender, 1983; Mitchell et al., 2007).

A Burma jadeite source for these grains as opposed to sourcing from the re-working of Gangdese-type zircons from older, underlying sedimentary strata within the basin is supported by the paucity of jadeite-derived detrital zircons within the older Eocene and Oligocene samples.

4.3.4. Summary

The potential source areas for the Central Burma Basin are sufficiently differentiated by the combination of U-Pb and εHf(t) isotopic data and therefore the interpretation of sources area is well justified. Combined U-Pb and εHf(t) isotopic data for detrital zircons extracted from sedimentary rocks of the Middle-Late Eocene Pondaung Formation reveal the Gangdese Batholith of southern Tibet as the dominant provenance, with subordinate input from the eastern Transhimalayan and Dianxi-Burma batholiths (Figure 4.1, 4.5, 4.8). The Gangdese Batholith lies exclusively within the modern Yarlung Tsangpo catchment (Figure 4.1, 4.2), therefore the presence of detrital zircons derived from this region within the Eocene Pondaung Formation of the Central Burma Basin supports the hypothesis of a Yarlung Tsangpo-Irrawaddy River connection that dates back to at least Middle-Late Eocene time (ca. 41 Ma), based on the maximum depositional age of the oldest sample from the Pondaung Formation as determined by the $^{206}Pb/^{238}U$ age of the youngest concordant detrital zircon (41.4 ± 1.2 Ma; 1σ) and the minimum age peak for the Pondaung Formation calculated using a Finite Mixture Model (Galbraith and Green, 1990; Galbraith and Laslett, 1993). Detrital zircons from the Middle-Late Oligocene Padaung Formation are similarly dominated by detrital zircons with Gangdese-type U-Pb and Hf isotopic signatures, with subordinate input from the eastern Transhimalayan and Dianxi-Burma batholiths (Figure 4.1, 4.6, 4.8). This is interpreted as evidence for a continued Yarlung Tsangpo-Irrawaddy connection throughout Oligocene time, consistent with sedimentary petrology that reveals

Palaeogene sedimentary rocks of the Central Burma Basin and Indo-Burman Ranges are dominated by volcanic detritus and plot within the "magmatic arc" provenance field of the Dickinson (1985) QFL diagram (Figure 4.9).

Detrital zircon U-Pb and εHf(t) isotopic data demonstrate a distinct change in provenance between deposition of the Palaeogene (Eocene and Oligocene) and Miocene samples. Initiating during deposition of the Early Miocene Shwetaung Formation and continuing during deposition of the younger Miocene sedimentary rocks analyzed in this study, the proportion of detrital zircons derived from the Gangdese Batholith decreases significantly. This change in provenance is interpreted to signal the disconnection of the Tsangpo-Irrawaddy river system and subsequent capture of the Yarlung Tsangpo by a tributary of the Brahmaputra River. Based on the data obtained in this study, the disconnection of the palaeo-Yarlung Tsangpo-Irrawaddy system is suggested to have occurred during the Early Miocene, the timing of which is constrained by the maximum depositional age of the Shwetaung Formation (ca. 19–18 Ma) and the age of the youngest detrital zircon (18.2 ± 0.2 Ma, 1σ) with a high, positive εHf(t) value (+9.38 ± 1.7, 2σ) that is interpreted to be sourced from the Gangdese arc. This is earlier than the Late Miocene age of disconnection proposed by Liang et al. (2008) based on the presence of Gangdese-type zircons within the Upper Pegu Group sample of ca. 10–5 Ma age and the Pliocene-Pleistocene age for capture suggested by Clark et al. (2004), Burg et al. (1998) and Zeitler et al. (2001). The resulting loss of the southern Lhasa terrane, and specifically the Gangdese magmatic arc, as a source is reflected in both the dramatic decrease in the proportion of Gangdese-type zircons and arc-derived detritus, as determined by sedimentary petrology, deposited in the Central Burma Basin from the Early Miocene onwards (Figure 4.8, 4.9). The Miocene sandstones of the Central Burma Basin plot within the "recycled orogen" field of the Dickinson (1985) QFL diagram, contrasting with the "magmatic arc" provenance of the Eocene and Oligocene sandstones that are dominated by volcanic lithic fragments (Figure 4.9) (Licht et al., 2013; San, 1981; Thein, 1966; Wang et al., 2014; Win, 1986).

Crustal-derived source terranes of the intra-syntaxis region, including granitoids of the Eastern Transhimalayan and Dianxi-Burma batholiths, and metamorphic and intrusive rocks of the Mogok Metamorphic Belt, Slate Belt and Shan Scarps of east Burma, become the primary source provenance for post-Early Miocene sedimentary units. The proportion of detrital zircon sourced from eastern Transhimalayan granitoids, Dianxi-Burma granitoids and the Mogok Metamorphic Belt increases in the Middle-Late Miocene formations with decreasing stratigraphic age. The presence of detrital zircons derived from the Gangdese Batholith zircons within all the Miocene formations analyzed in this study and within the Late Miocene (ca. 10–5 Ma) Upper Pegu Group sandstone sample of Liang et al. (2008) (Figure 5.2) is attributed to the re-working of Eocene and Oligocene sedimentary strata that are dominated by Gangdese-type detrital zircons during the Miocene. The cannibalization of older sediments within the Central Burma Basin following disconnection is not unlikely given that following the loss of the high elevation Yarlung Tsangpo, the headwaters of the Irrawaddy would have lost significant steam power, resulting in the formation of a wide braided and meandering river system across the Central Burma Basin (Liang et al., 2008).

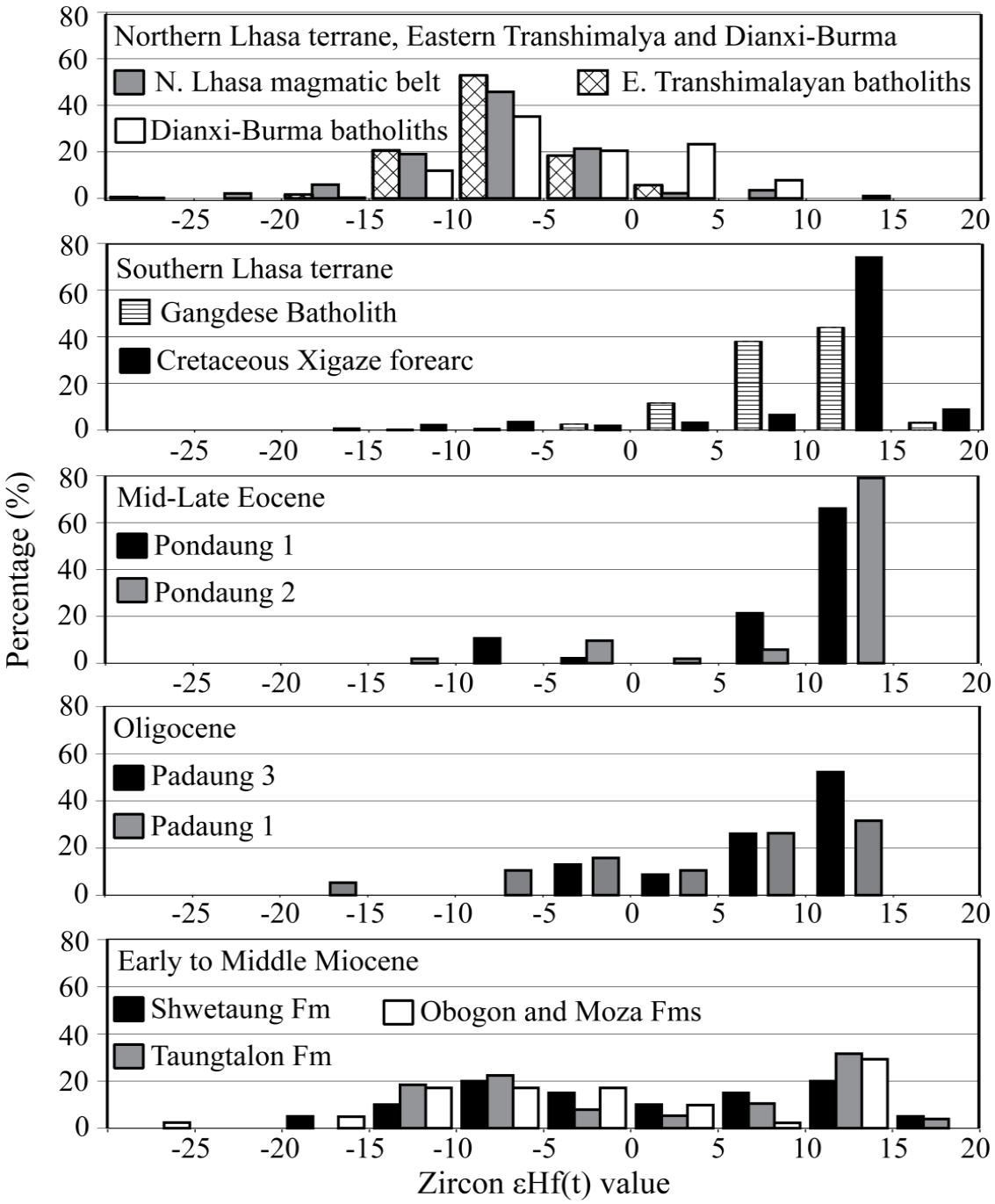

Figure 4.8 Histograms comparing the εHf(t) value distribution of published bedrock data to detrital zircon data from Eocene to Miocene aged Cenozoic Central Burma Basin sedimentary deposits obtained in this study. See text for references.

4.4. Exhumation history of the potential source regions

$^{40}Ar/^{39}Ar$ dating of detrital white mica and zircon fission track analysis were implemented in this study to 1) provide a more robust provenance study by widening the range of lithologies sampled and reduce bias arising from using one mineral for interpretation, 2) identify which source regions were undergoing exhumation during the periods of sedimentation, and 3) provide an inferred exhumation rate throughout the depositional history of the basin for the formations sampled. By combining multiple provenance tools, it is possible to determine how changes in provenance from Late Eocene to early Miocene time are related to exhumation and landscape evolution in the eastern sector of the Himalayan orogen. In active orogenic settings, changes in source region can be identified through changing populations of mineral cooling ages through time, and the thermochronological data can help constrain the timing of river disconnection (Carrapa et al., 2004; Hodges et al., 2005; Najman et al., 2003; Van Hoang et al., 2010; von Eynatten and Dunkl, 2012; Von Eynatten and Wijbrans, 2003; White et al., 2002).

The detrital data from the Central Burma Basin is compared with published low temperature thermochronology datasets for potential source terranes within the modern day Irrawaddy (eastern syntaxis region and Burma) and Yarlung Tsangpo (Lhasa terrane) catchments to further test provenance models established by the detrital zircon U-Pb and Hf dataset, link the detrital cooling ages to specific exhumation events and source terranes, and explore whether increases in rates of exhumation and deformation during the Early Miocene led to the disconnection of the Yarlung Tsangpo-Irrawaddy river system (Figure 4.2). The signal of this accelerated exhumation should be reflected in progressively decreasing lag times between detrital mineral cooling ages and depositional ages, and lag times are expected to increase when exhumation rates reduce (Bernet and Spiegel, 2004; Carrapa et al., 2009; Carrapa et al., 2004; Hodges et al., 2005; Ruiz et al., 2004; Szulc et al., 2006). Additionally, thermochronometers that have experienced post-depositional heating sufficient to re-set the age provides information on basin dynamics and post-depositional tectono-thermal evolution of the sedimentary rocks.

4.4.1. Exhumation history of the Lhasa terrane

Lying exclusively in the Yarlung Tsangpo catchment, the Jurassic to Tertiary Gangdese magmatic arc and associated flat-lying Cretaceous to Palaeogene Linzizong Formation volcanic successions represent a long-lived Andean-type margin formed along the southern margin of Asia in response to northward subduction of the Indian oceanic plate. This region underwent episodes of rapid uplift and significant erosion intermittent with extended periods of slow cooling and differential exhumation. Evidence for significant and differential uplift within the Northern Lhasa terrane prior to, and during, collision is recorded by $^{40}Ar/^{39}Ar$ biotite and muscovite cooling ages with peaks of ca. 165–150 Ma, ca. 130–110 Ma and ca. 45–35 Ma (Wang et al., 2007). The majority of deformation in the Lhasa terrane pre-dates the Himalayan orogeny, and is related to Meso-Tethys ocean closure and continent-continent collision between the Qiangtang Block to the north and the Lhasa terrane during the late Jurassic to early Cretaceous (Kapp et al., 2007b; Zhang et al., 2012c), and to far-field affects of this collision during the Cretaceous to Palaeocene (Kapp et al., 2007a; Kapp et al., 2007b; Kapp et al., 2005b; Leier et al., 2007a; Murphy et al., 1997; Pullen et al., 2008; Volkmer et al., 2007). Following the Lhasa-Qiangtang continental collision, crustal shortening on the scale of 47–60% (Kapp et al., 2007b; Murphy et al., 1997) led to significant thickening of the crust and elevation gain via a southward propagating fold and thrust belt in the northern Lhasa terrane (Kapp et al., 2005a; Kapp et al., 2007b) and a northward propagating fold and thrust belt in the central-southern Lhasa terrane, in the retro-arc region of the Gangdese Batholith (Kapp et al., 2007a; Leier et al., 2007a; Leier et al., 2007b; Pullen et al., 2008). Late Cretaceous to earliest Tertiary upper crustal shortening of Palaeozoic and Mesozoic strata of the southern Lhasa terrane is recorded by strongly folded bedding, separated by a regional angular unconformity from the overlying un-deformed Linzizong volcanic succession that erupted between ca. 69–47 Ma (He et al., 2007; Lee et al., 2009; Mo et al., 2008; Zhou et al., 2004). Additionally, significant Late Cretaceous to Palaeogene exhumation and erosion is indicated by the deposition of the Xigaze conglomeratic fore-arc sediments and coeval Takena retro-arc sediments, derived from the Gangdese pluton, at this time (Aitchison et al., 2011; Dürr,

1996; Leier et al., 2007a; Pullen et al., 2008; Wu et al., 2010). The majority of crustal shortening and elevation gain in the Lhasa terrane occurred during Cretaceous to Eocene time (Yin, 2010), with the establishment of the central Tibetan Plateau in its current form by ca. 45 Ma (Rohrmann et al., 2012).

Late Cretaceous granitoids with adakitic geochemical features recorded in the southeastern Gangdese arc accompanied the waning stages of Mesozoic magmatism and coeval high temperature, medium pressure granulite-facies metamorphism (ca. 90 Ma) has been attributed to the upwelling of asthenosphere following subduction of a mid-ocean ridge segment that created a tear in the subducting slab ('slab window') (Zhang et al., 2010b; Zhang et al., 2010c), or from roll-back of the subducted Neo-Tethyan slab (Ma et al., 2013; Wen et al., 2008a; Wen et al., 2008b). This is followed by a ~10 Ma magmatic quiescence in the Gangdese Batholith, attributed to the flattening of the angle of the subducting Neo-Tethys oceanic slab (Wen et al., 2008b). Flab slab subduction may have driven, or enhanced the crustal shortening observed in the Lhasa terrane during this magmatic gap (ca. 80–70 Ma) (Murphy et al., 1997; Wen et al., 2008b; Yin and Harrison, 2000), as evidenced by the folding of the Cretaceous Takena Formation, with a maximum depositional age of ca. 90–80 Ma (Leier et al., 2007a), uplift and erosion prior to deposition of the widespread, flat-lying Palaeogene Linzizong volcanic succession from ~69 Ma to at least 43 Ma (He et al., 2007; Lee et al., 2009; Mo et al., 2008; Zhou et al., 2004).

The post-collisional cooling history of the Gangdese pluton is characterized by differential and slow exhumation with intermittent periods of localized rapid uplift in the Middle Eocene (~48–46 Ma) and Early Miocene (~22–18 Ma). $^{40}Ar/^{39}Ar$ (biotite, K-feldspar, hornblende), fission track (apatite, zircon) and (U-Th)/He (apatite, zircon) low temperature thermochronology data from the Gangdese Batholith record the beginning of accelerated uplift at ca. 27 Ma, culminating in rapid exhumation to upper crustal levels (< 200°C) at ca. 20 Ma (Chen et al., 1999a; Chen et al., 1999b; Copeland et al., 1995; Copeland et al., 1987; Dai et al., 2013; Harrison et al., 2000; Pan et al., 1993; Richter et al., 1991; Yuan et al., 2009), recording cooling through upper crustal levels

following thrusting of Asian crust southwards over the Tethyan Himalaya along the Gangdese Thrust, active from ca. 30–23 Ma to ca. 18 Ma based on low temperature $^{40}Ar/^{39}Ar$ and fission track thermochronology (Harrison, 2000; Yin, 1994). Alternatively, Dai et al. (2013) suggest the removal of the thickened lithospheric root (Chung et al., 2009; Chung et al., 2005; Guan et al., 2012) and upwelling of asthenosphere beneath southern Tibet, marked by widespread emplacement of adakitic and potassic to ultra-potassic igneous and volcanic rocks throughout the southern Lhasa terrane during Oligocene to Late Miocene time (ca. 30–10 Ma) (Chung et al., 2003; Chung et al., 2009; Chung et al., 2005; Guo et al., 2011; Pan et al., 2012; Zhang et al., 2010a; Zhou et al., 2010), led to regional surface uplift of the Gangdese arc. Felsic magmatism in southeast Tibet is attributed to the diachronous break-off of the subducted Indian continental slab initiating in the eastern Himalayan syntaxis region during the Oligocene (ca. 30–24 Ma), roughly coeval with Late Oligocene to Early Miocene exhumation-driven, retrograde amphibolite-facies metamorphism and anatectic melt production recorded by zircons of Asian plate metasedimentary and metaigneous rocks north of Namche Barwa (Guo et al., 2011; Pan et al., 2012; Xu et al., 2013; Xu et al., 2010; Zhang et al., 2008; Zhang et al., 2010a). In the Gangdese Batholith, Oligocene-Miocene rapid uplift and crustal thickening along the Gangdese Thrust was accompanied by erosion of the arc and deposition of the Gangrinboche conglomerate in the Indus-Tsangpo suture zone during the Late Oligocene to Early Miocene (Aitchison et al., 2002; Aitchison et al., 2011; Davis et al., 2004; Wang et al., 2013).

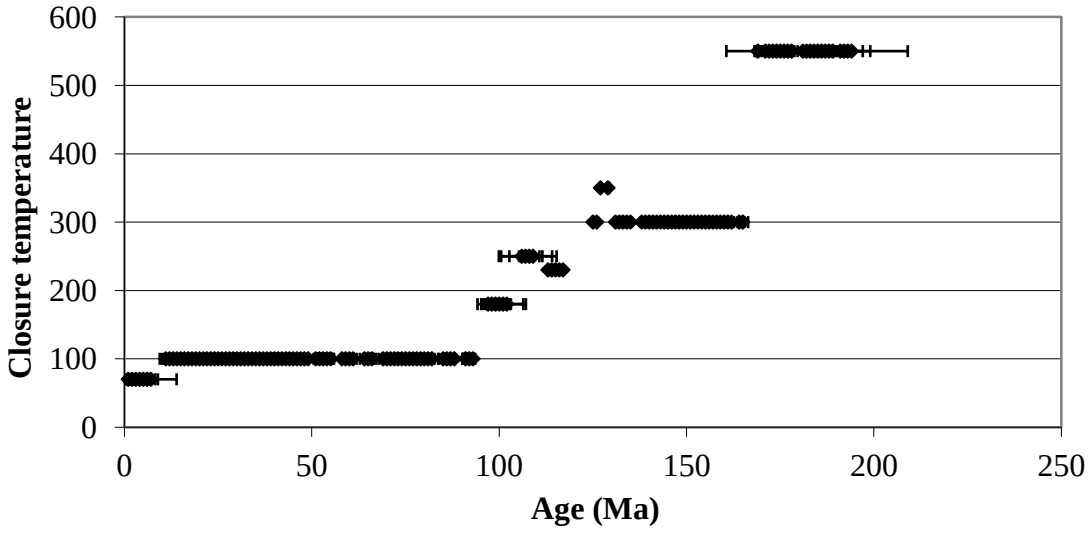

Figure 4.9 Summary of published low temperature thermochronology data from bedrock of the Gangdese Batholith, southern Lhasa terrane. Apatite and zircon (U-Th)/He data from Dai et al. (2013); apatite fission track data compiled from Copeland et al. (1987, 1995), Pan et al. (1993), and Yuan et al. (2000, 2009); biotite $^{40}Ar/^{39}Ar$ data from Copeland et al. (1987); K-feldspar data from Copeland et al. (1995).

4.4.2. Exhumation history of the intra-syntaxis region (Irrawaddy catchment)

Exhumation within the intra-syntaxis region was driven by tectonics, where Oligocene-Early Miocene $^{40}Ar/^{39}Ar$ biotite, muscovite and phlogopite cooling ages (ca. 27–16 Ma) record extension along the Mogok Metamorphic Belt (Bertrand et al., 2001; Bertrand et al., 1999), and Early-Middle Miocene $^{40}Ar/^{39}Ar$ biotite and muscovite cooling ages (ca. 22–13 Ma) are recorded for the Jiali and Gaoligong shear zones in the eastern syntaxis (Lee et al., 2003; Lin et al., 2009). $^{40}Ar/^{39}Ar$ dating of bulk hornblende separates from deformed amphibolite and mylonite of the Nabang shear zone in western Yingjiang yield plateau ages of 32.8 ± 0.2 Ma and 32.1 ± 0.3 Ma (1σ error), respectively (Wang et al., 2006), however, recent investigations utilizing mid-low temperature thermochronology indicate rocks of the Gaoligong shear zone remained at metamorphic conditions above 500°C prior to exhumation coeval with dextral strike-slip motion during the Early to Middle Miocene (Lin et al., 2009; Wang et al., 2008; Zhang et al., 2012a). Magmatic and metamorphic events in potential source areas that could also be

related to uplift and cooling include Cretaceous-Palaeocene granite emplacement (Barley et al., 2003; Liang et al., 2008; Mitchell et al., 2012; Mitchell et al., 2007) and high grade metamorphism at ca. 59 Ma and ca. 47–29 Ma (Searle et al., 2007) in the Mogok Metamorphic Belt, the Jurassic, Cretaceous, and Palaeocene-Eocene Transhimalayan magmatic phases recorded throughout western Yunnan, Burma and the Western granite province of Thailand (Chiu et al., 2009; Gao et al., 2012; Hou et al., 2012; Ji et al., 2009b; Liang et al., 2008; Watkinson et al., 2008). A transtensional regime associated with Southeast Asian extrusion is thought to have developed in the Early Miocene and is related to movement along the Sagaing Fault (Bertrand and Rangin, 2003; Mitchell, 1993; Pivnik et al., 1998). This was replaced by a transpressional regime in the Middle-Upper Miocene (Bertrand and Rangin, 2003) or Pliocene (Pivnik et al., 1998) associated with the coupling of the Indian plate to the West Burma Block.

If the approximately 450 kilometres of northward movement of the West Burma Block along the dextral strike-slip Sagaing Fault, active from the Middle Miocene onwards, is taken into account, the southernmost region of eastern Burma and western Thailand may also be considered a potential proximal source region. During the Eocene to Oligocene, the Shan Plateau and western Thailand experienced regional sinistral transpression characterised by the development of branching fault networks between the NE-striking Mae Ping and Three Pagodas Fault zones. Uplift of rocks from mid-crustal levels during the waning stages of ductile sinistral shear is recorded by $^{40}Ar/^{39}Ar$ biotite cooling ages of ca. 33–30 Ma for the Mae Ping Fault and ca. 36–33 Ma for the Three Pagodas Fault (Lacassin et al., 1997; Morley, 2009, 2007). Farther south, deformation and uplift occurs on the Khlong Marui and Ranong Faults in western Thailand during the Eocene (Watkinson et al., 2011; Watkinson et al., 2008). This is most likely associated with early motion of the West Burma block relative to Sibumasu and the increased coupling of India and Burma during collision (Morley, 2007, 2004). Faults within the Shan Scarp region were later re-activated during ductile extension (Morley, 2009).

4.5. Provenance interpretations based on low temperature thermochronology

White mica $^{40}Ar/^{39}Ar$ age distributions demonstrate a distinct change in provenance between deposition of the Palaeogene (Eocene and Oligocene) and Miocene samples. Both the Eocene Pondaung Formation and the Oligocene Padaung Formation reveal multi-modal white mica $^{40}Ar/^{39}Ar$ cooling populations of Mesozoic and early Cenozoic age with wide peak bases indicating derivation from multiple source regions that experienced differential exhumation through the mid-crustal levels during pre-Himalayan times. The former is dominated by Cretaceous, Palaeocene, and Eocene ages with 71% of the grains older than 55 Ma and the latter is dominated by Cretaceous, Jurassic and Palaeocene ages, where 91% of the ages are older than 55 Ma (Figure 3.9, 3.10, 4.12). The oldest unit sampled, Pondaung 1, is unmicaceous with only 11 grains analyzed. The lack of white mica may be attributed to the fine-grained nature of this sample, or its derivation from lithologies that lack white mica, likely mafic to intermediate juvenile magmatic rocks. Both formations contain a broad range of Cretaceous to Miocene (~80 to 10 Ma) zircon fission track ages, sourced from juvenile mantle material as indicated by εHf(t) values of +9 to +13 (Figure 3.12, 3.15, 4.11).

In contrast, the Miocene formations are dominated by Himalayan ages, younger than 55 Ma, and populations are defined by narrower peaks (Figure 3.9). The Early Miocene Shwetaung Formation shows the first distinct change with 84% of the grains having Himalayan cooling ages, with a peak at ~37 Ma (Figure 3.10). The Middle Miocene Taungtalon, Lower Moza, Kyaukkok, and Obogon formations show similar trends; 79 to 73% of the micas record Himalayan ages (younger than 55 Ma), with a persistent peak at ~37 to 35 Ma (Figure 3.9, 3.10, 4.12). The Miocene samples contain a dominant Early Miocene (19–17 Ma), and minor Cretaceous and Palaeocene, zircon fission track populations, with a much larger range of εHf(t) values from -18 to +16 (Figure 3.14, 3.15, 4.11).

4.5.1. Sediment provenance interpretations, Palaeogene (Eocene and Oligocene)

As the majority of white mica cooling ages obtained from the Palaeogene sediments pre-date the Himalayan orogeny, together with the relative paucity of mica within the

oldest sample, the sediment provenance is interpreted to be derived from the juvenile magmatic arc terrane of southern Lhasa, and the un-reset cooling populations suggest multiple source regions were variably uplifted in the Cretaceous and Palaeogene, followed by slower erosion, consistent with the known exhumation history of the Lhasa terrane.

Geochronology on the magmatic and metamorphic rocks of the Mogok Metamorphic Belt indicates the main fabric forming metamorphism occurred prior to the India-Asia collision, with a mid Early Cretaceous minimum age for regional metamorphism constrained by the U-Pb zircon age of the oldest undeformed granite (ca. 128 Ma), although the timing of this event is suggested to be older, perhaps relating to inferred Late Jurassic-Early Cretaceous collision of West Burma with Sibumasu (Shan-Thai Block) (Mitchell et al., 2012). These ages are consistent with minor populations of older Jurassic ages observed in the Padaung Formation, however this is unlikely to be a source as the rocks of this region were undergoing high temperature metamorphism at this time and ductile exhumation along the Mogok Metamorphic Belt post-dates the depositional age of this formation.

Although the eastern margin of Burma experienced crustal thickening, Palaeocene (~59 Ma) and Eocene-Oligocene (~37–29 Ma) high temperature metamorphism, and granitoid emplacement at this time (Barley et al., 2003; Searle et al., 2007; Mitchell et al., 2012), $^{40}Ar/^{39}Ar$ ages on rocks of the Mogok Metamorphic Belt suggest extension and exhumation did not occur until the latest Oligocene-Early Miocene (~26–16 Ma) (Bertrand et al., 1999, 2001). Additionally, Jurassic- and Cretaceous-aged granitoids intruding the Mogok Metamorphic Belt experienced high temperature, sillimanite-grade metamorphism recorded by the coeval growth of metamorphic monazite and zircon rims dated at ~47–43 Ma (Barley et al., 2003; Searle et al., 2007), indicating these rocks were not experiencing active exhumation during deposition of the Eocene Pondaung Formation and are therefore considered unlikely as a significant source region for sediments of the Central Burma Basin at this time. This is supported by the detrital zircon U-Pb and Hf isotopic data which shows a paucity of Cretaceous to Eocene aged

detrital zircons with low, negative εHf(t) values within the Eocene and Oligocene formations, consistent with their deposition prior to exposure of middle level crustal sections along eastern Burma, western Yunnan and southeast Tibet, that are perversely intruded by S-type granites characterized by negative εHf(t) values, via ductile extension and major dextral strike-slip faults of the eastern syntaxis region during Early-Middle Miocene time (Sagaing, Gaoligong and Jiali shear zones) (Lee et al., 2003; Lin et al., 2009). This crustal material was likely not exposed along eastern margin of the Irrawaddy catchment, or not a major source region until after major Oligo-Miocene extension and dextral shearing that uplifted rocks from mid-crustal depths (Bertrand et al., 2001; Bertrand et al., 1999).

It is possible that the influx of detrital white mica cooling ages that closely resemble the depositional age of this formation is due to volcanic eruptions during the time of deposition, recording an event that is disproportionally represented in the Pondaung Formation (see Section 4.3.1). However, given a significant proportion of the detrital fission track ages within this sample are younger than the known depositional age, a significant degree of post-depositional heating had occurred. The preferred interpretation for this young population is that the Pondaung Formation likely experienced post-depositional heating at temperatures high enough, or lingered within the partial retention zone for a significant period of time enough to enhance the diffusion of $^{40}Ar^*$, resulting in a lowering of the closure isochron, allowing for partial re-setting (Verdel et al., 2012). As this occurs in some, but not all grains, damage to the crystal structure is likely a shared characteristic among the reset grains, as this also enhances argon diffusion (see Section 4.5.3).

Both the Eocene Pondaung Formation and the Oligocene Padaung Formation contain a broad range of Jurassic to Miocene detrital zircon fission track ages, mostly ranging from Cretaceous to Miocene (~93–11 Ma), a sub-set of which additionally underwent Lu-Hf isotopic analysis. The Pondaung Formation contains fission track modes of Late Miocene, Early Miocene, latest Eocene, Palaeocene, and Late Jurassic-Early Cretaceous age (Figure 3.12). The Miocene aged modes record the partial re-setting of some grains

as are significantly younger than the known depositional age and therefore do not provide information on source terrane exhumation, but post-depositional thermal disturbance (discussed further in Sections 4.5.3 and 4.5.4). The use of fission track age peaks cannot be used to determine the maximum depositional age, as the peaks include both re-set and non-reset ages and because of the large errors associated with these ages, it is difficult state with certainty whether zircons forming the Late Eocene cooling age population have been partially re-set or represent the best estimate of the depositional age for this sample. The Padaung Formation contains detrital zircon fission track modes of Early Miocene, Oligocene and Late Cretaceous age, the former representing a population zircons have experienced post depositional heating significant enough to reset the fission track age of some, but not all of the grains (Figure 3.12). Of the U-Pb and fission track double dated detrital zircons that underwent additional Lu-Hf isotopic analysis, >80% of those from the Palaeogene formations display isotopic values analogous with those observed in the Gangdese (Figure 3.15, 4.11). The majority of un-reset detrital zircon fission track ages recorded in the Eocene Pondaung Formation and Oligocene Padaung Formation are Cretaceous to Eocene in age and Cretaceous in age, respectively, suggesting source terranes with rocks that were uplifted to upper crustal levels at this time. Both reset and un-reset ages from the Palaeogene sequences are dominated by high, positive εHf(t) values (Figure 3.15, 4.11) analogous with the Gangdese batholith indicating uplift and erosion of this terrane that cooled through the upper crust during the Cretaceous and eroded, transported and deposited during the Eocene-Oligocene, consistent with suggestions of limited Cenozoic crustal deformation of the Lhasa terrane (Yin, 2010). The broad range in un-reset fission track ages in Gangdese-type zircons confirms interpretations based on the white mica cooling age data from these samples that indicate a source region undergoing differential exhumation, consistent with evidence that rocks of the Gangdese Batholith in the southern Lhasa terrane were undergoing exhumation and erosion at this time (Aitchison et al., 2011; Guo et al., 2012, 2011; Kapp et al., 2005; Leier et al., 2007a; Pullen et al., 2008; Wu et al., 2010).

Double dating of detrital zircon using U-Pb and fission track methods combined with Lu-Hf isotopic analysis reveal dominant populations of Gangdese-type zircons, with U-Pb ages clustering between 95–40 Ma and fission track ages of Late Eocene-Early Miocene (mostly re-set) and Late Cretaceous-Middle Eocene (un-reset). The appearance of significant populations with U-Pb ages ~65–40 Ma, characterized by relatively homogeneous depleted hafnium values interpreted as derived from the Gangdese Batholith, as well as a non-reset fission track mode of ca. 55 Ma for zircons with positive εHf(t) values (> +9), is consistent with coeval syn-sedimentary deposition and peak magmatic activity in the southern Lhasa terrane at this time (Ji et al., 2009; Mo et al., 2009; Wen et al., 2008). Paired apatite and zircon (U-Th)/He data from the Gangdese Batholith indicates a period of rapid cooling, at least locally, during the Early Eocene (ca. 48–46 Ma), consistent with the low temperature data from detritus derived from this source reported here (Dai et al., 2013). Wider inferences on the exhumation history within the Gangdese batholith based on the detrital fission track data is hindered by the significant thermal re-setting of the majority of fission track ages present within the Palaeogene sediments. Therefore, the dominance of un-reset $^{40}Ar/^{39}Ar$ white mica and zircon fission track data displaying pre-Himalayan ages older than 55 Ma, dominated by juvenile Hf isotopic signatures, is consistent with the interpretation that the Gangdese magmatic arc along the southern margin of Asia was contributing to the Irrawaddy River sediment load during deposition of the Eocene Pondaung Formation and Oligocene Padaung Formation.

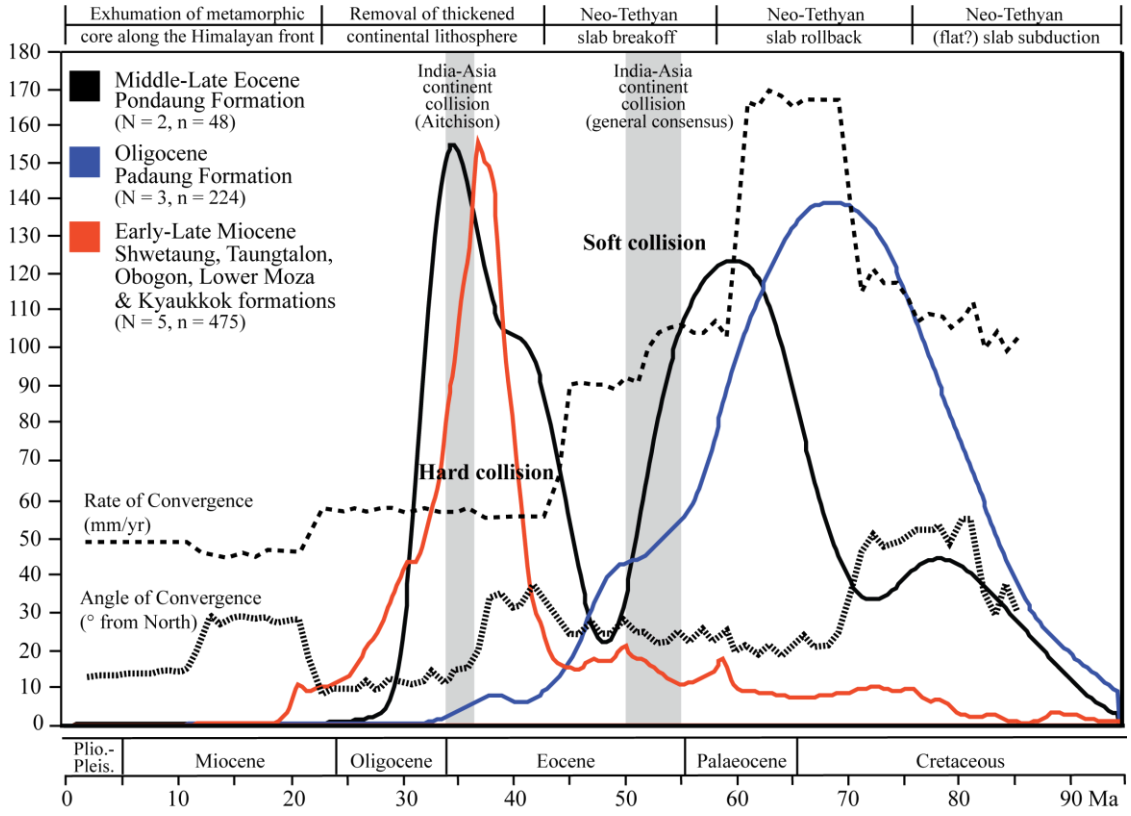

Figure 4.10 Rate and angle of convergence of India since 85 Ma after Lee and Lawver (1995) and Xia et al. (2011) compared with detrital white mica $^{40}Ar/^{39}Ar$ probability density curves of Eocene, Oligocene and Miocene aged sedimentary rocks sampled in this study to show the evolutionary relationship between regional plate tectonic events and source exhumation as recorded by low temperature thermochronology. Only ages younger than 95 Ma are displayed.

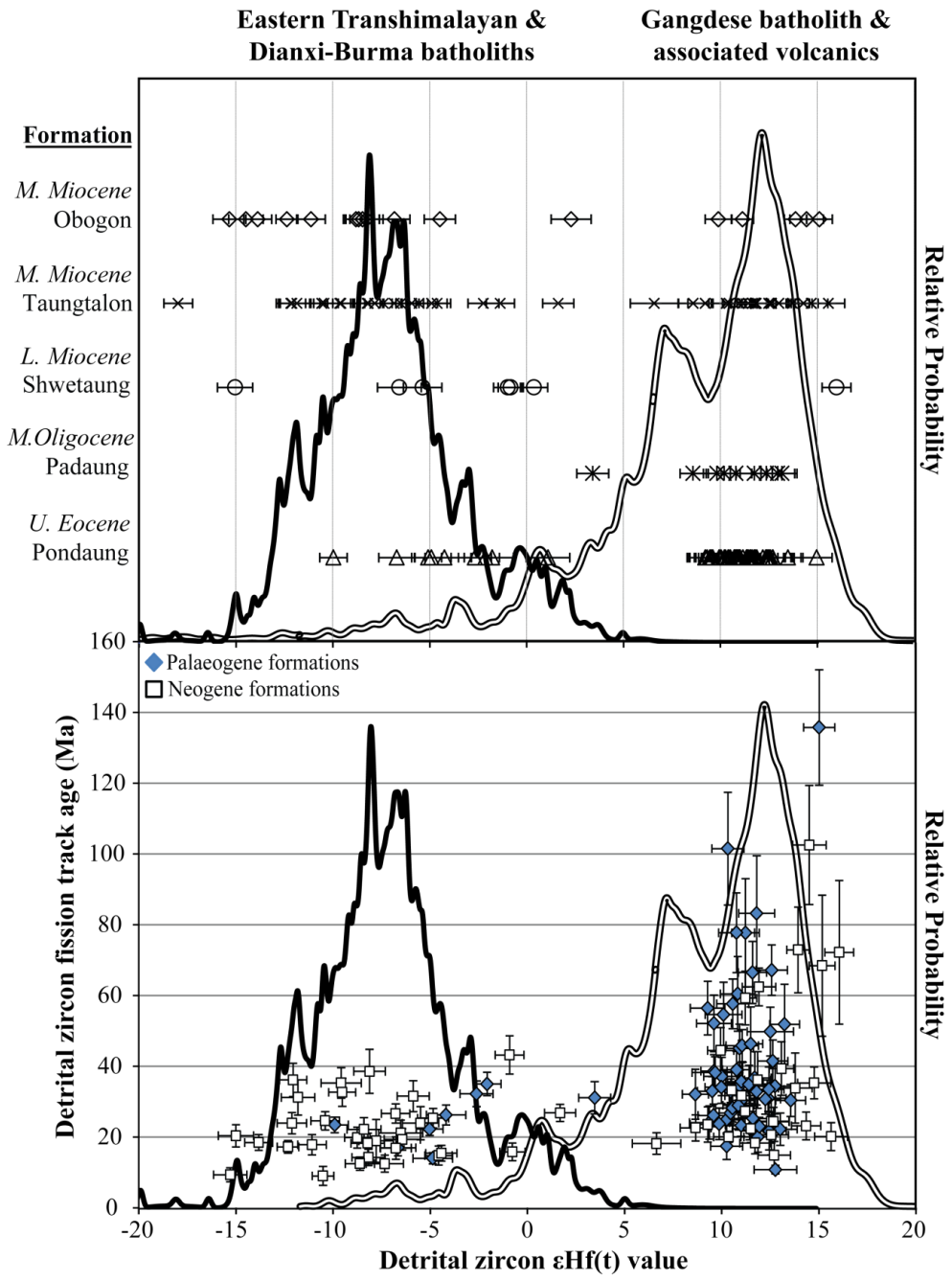

Figure 4.11 The distribution of εHf(t) values for a sub-set of detrital zircons dated using the fission track method from Eocene-Miocene aged sedimentary rocks from the Central Burma Basin compared with εHf(t) values of zircon from bedrock in the potential source regions. The upper diagram shows the distribution of detrital zircon εHf(t) values within each formation that underwent fission track dating, arranged in stratigraphic order (error bars are 2σ). The bottom diagram plots the detrital fission track age (1σ) against the corresponding εHf(t) value. Probability distributions showing the range of εHf(t) values of magmatic zircon extracted from bedrock of the Gangdese Batholith and intra-syntaxis batholiths (Dianxi-Burma and Eastern Transhimalayan) plotted for comparison. See text for literature data sources.

4.5.2. Sediment provenance interpretations for Miocene formations

To enhance the robustness of this provenance study and widen the range of lithologies that can be detected within the potential source region, a second mineral (white mica) is used to confirm provenance change in the Early Miocene, constrain the timing of disconnection using a second geochronometers and test whether increasing deformation and crustal uplift rates resulted in the breakdown of the Yarlung Tsangpo-Irrawaddy system.

The $^{40}Ar/^{39}Ar$ cooling age data presented in this study shows a change in provenance occurred between deposition of the Oligocene Padaung Formation and Early Miocene Shwetaung Formation indicated by both a change in the age populations from pre-dominantly Cretaceous to Palaeocene ages (older than 55 Ma) to ages younger than 55 Ma. The more narrow and consistent age peak for all Miocene deposits suggest a single source area which was rapidly cooled around ~40–30 Ma, with a peak at 37–35 Ma (Figure 4.10), and this became a sustained source area for younger Miocene formations.

Although mica ages of 37–35 Ma have not yet been reported for source rocks within the Irrawaddy catchment and therefore cannot be directly related to a specific source region, we can infer their derivation based on the thermo-tectonic and exhumation history within the potential source areas. Fission track dating of detrital zircons from modern rivers draining the Asian crust of the eastern Himalayan syntaxis reveal peak ages of 18 Ma, 26 Ma, 35 Ma and 55 Ma indicating the cooling of bedrock within these catchments through mid-upper crustal levels during multiple tectonic and thermal events, un-related to the Late Cenozoic development and exhumation of the Namche Barwa metamorphic core (Enkelmann et al., 2011). The presence of the 35 Ma age mode in catchments laying outwith the Jiali shear zone to the west suggests a regional, rather than localized, uplift event to explain the detrital fission track population over a region that includes the upper reaches of the Irrawaddy catchment. In the eastern Himalayan syntaxis, geochronology from felsic melts and the hosting metasedimentary rocks of the Nyingchi Group and Bomi Group presently exposed intruding these metasediments, combined with metamorphic petrology, suggests contemporaneous

high-grade metamorphism and anatexis occurred within the Lhasa terrane at mid-crustal levels at ~37–32 Ma (Xu et al., 2008; Zhang et al., 2010). Therefore, the generation of felsic melts, high grade metamorphism and anatexis related to continental slab subduction and slab interactions may have driven localized surface uplift in southeast Tibet.

A significant change in the angle of convergence of India with respect to Eurasia from 35° from north to 10° from north occurred at approximately 35 Ma (Figure 4.10) (Lee and Lawver, 1995). The counter-clockwise rotation of the Indian continent would have focused deformation within the eastern syntaxis region, however additional bedrock thermochronology on the Asian terrane of this region is needed to further explore the possibility of a late Eocene-early Oligocene timing for regional uplift in this area. The correlation of this timing of this plate rotation and the detrital cooling age peak within the Miocene suggests the Central Burma Basin potentially records a regional uplift event within the eastern Himalaya that has not yet been explored in bedrock studies.

Alternatively, the source rocks contributing detrital white mica with 37–35 Ma cooling ages may lie within the modern Irrawaddy catchment proper. The tectono-thermal history of the metamorphic belts exposed in northeast Burma that are composed primarily of mica schist, bounding the Upper Irrawaddy Basin to the west, is poorly understood. These rocks may have originally formed part of the Mogok Metamorphic Belt or Slate Belt offset by the Sagaing Fault (Mitchell, 1993), or represent the southward continuation of garnet-sillimanite gneiss and marbles exposed in the Lohit River valley (Gururajan and Choudhuri, 2003). The rocks of the Mogok Metamorphic Belt experienced high temperature metamorphism accompanied by sillimanite, metamorphic monazite and zircon rim growth occurred between ca. 47–33 and ca. 29 Ma accompanied by syn-tectonic melt generation, and culminating with the emplacement of cross-cutting leucogranites at 24.5 ± 0.3 Ma (Searle et al., 2007; Barley et al., 2003; Mitchell et al., 2012). Subsequent extension and exhumation is recorded by mica cooling ages along the Shan Scarp than young from south (ca. 27–25 Ma) to north

(ca. 23–17 Ma) (Bertrand et al., 1999, 2001) and apatite fission track ages of 18.7–14.6 Ma (Torres et al., 1997). The exhumation of this material through upper crustal levels is coincident with the known depositional ages of the Miocene formations sampled, and suggest the metamorphic rocks of east Burma are the source of the enigmatic 37–35 Ma peak. The 37–35 Ma peak may represent cooling ages from rocks along the Mogok Metamorphic Belt-Shan Scarps region affected by this same event that lay at shallower structural levels than that observed in present day outcrops that have been removed by erosion and deposited in the adjacent Central Burma Basin, whereby the diachronous nature of the present-day outcrop could be the result of increased erosion in the northern region. However, the static peak in mica cooling ages observed throughout the Miocene formations sampled is at odds with the expected detrital signature for this scenario whereby a gradual decrease in cooling age with decreasing stratigraphic age is expected as erosion tapped deeper parts of the metamorphic belt. Additionally, peak metamorphic temperatures reached ~680–600°C (Searle et al., 2007), therefore $^{40}Ar/^{39}Ar$ mica ages sourced from this belt would record post-metamorphic cooling ages younger than 37–35 Ma.

If the several hundred kilometres of post-Middle Miocene offset of the West Burma Block along the dextral strike-slip Sagaing Fault, is taken into account, the southernmost region of eastern Burma and western Thailand may also be considered a potential proximal source region. Sinistral shearing along a network of faults within the eastern Shan Plateau and western Thailand occurred during Eocene to Oligocene time. $^{40}Ar/^{39}Ar$ dating of biotite and K-feldspar records the final stages of ductile shear along the Mae Ping and Three Pagodas Faults at 40–30 Ma and apatite fission track dating records cooling through the upper crust during Late Oligocene to earliest Miocene time (ca. 33–21 Ma) (Lacassin et al., 1997; Morley et al., 2012; Upton, 1999; Barr et al., 2002). This deformation is thought to be related to the coupling of the India and Burma plates (Morley, 2004, 2007). A definitive source for this population cannot be determined at this time based on the available bedrock data.

The Miocene samples contain mainly Early Miocene and minor Cretaceous and Palaeocene detrital zircon fission track populations (Figure 3.14, 4.11). Like the Palaeogene samples, all of the Miocene sedimentary strata sampled contain a minor proportion of fission track ages younger than the known depositional age of the sample based on biostratigraphy, and are therefore interpreted as reset ages (ca. 14 to 8 Ma). The presence of this population in Miocene formations of both the Eastern and Western Troughs suggest a post-depositional, basin-wide event led to the resetting of some, but not all grains (discussed further in sections 4.5.3 and 4.5.4). The dominant Early Miocene (ca. 19–17 Ma) fission track population suggested the source region experienced a significant stage of uplift through upper crustal levels at this time and remained a sustained sediment source throughout the Miocene, consistent with the $^{40}Ar/^{39}Ar$ detrital white mica age data.

A subset of U-Pb and fission track double dated detrital zircons underwent additional Lu-Hf isotopic analysis in order to determined sediment provenance. In contrast with the Palaeogene sedimentary samples, detrital zircons of the Miocene formations show a wider diversity in εHf(t) values (-18 to +16; 53% are enriched in radiogenic hafnium relative to the chrondritic value), with a general trend towards more negative values increasing up-section. The presence of zircons with strongly positive εHf(t) values strongly mimics the trend of the Eocene and Oligocene formations, suggesting that cannibalization of this older units may have attributed to the sediment load of the Irrawaddy during the Miocene. Grains with positive εHf(t) values have a broader range of fission track ages than the negative εHf(t) values (Figure 4.11).

Early Miocene $^{40}Ar/^{39}Ar$ mica cooling ages are found along the central and northern portions of the Mogok Metamorphic Belt (Mandalay to Mogok), recording the timing of ductile extension and cooling though mid-crustal temperatures (Bertrand et al., 1999; Bertrand & Rangin, 2003) in close proximity to the depositional area. Recent whole rock Sr-Nd isotopic analysis of magmatic rocks in this region indicate the granitoids were generated primarily by the melting of older continental crust, enriched in radiogenic neodymium and record high initial $^{87}Sr/^{86}Sr$ ratios (Figure 4.4) (Mitchell et

al., 2012). The increasing heterogeneity of zircon εHf(t) values with time reflects increasing contribution to the sediment load from the Mogok Metamorphic Belt, or their northern continuation (Dianxi-Burma and Eastern Transhimalayan batholiths). Contrasting with the Palaeogene formations, only 41% of the U-Pb and fission track double dated detrital zircons that underwent additional Lu-Hf isotopic analysis overlap with the Gangdese field in Miocene formations, and the percentage of those that Gangdese-type isotopic values decrease with increasing stratigraphic age from 44% to 33% in the Shwetaung-Taungtalon and Obogon formations, respectively (Figure 4.12). Detrital zircons within the Miocene formations are characterized by more heterogeneous εHf(t) values and fission track ages clustered between ca. 25–15 Ma with corresponding U-Pb ages ranging between ca. 97–82 Ma. These observations are consistent with the larger detrital zircon U-Pb and Hf isotopic dataset from this study and indicate increasing contributions from intra-syntaxis sources including the Dianxi-Burma batholiths and Mogok Metamorphic Belt within younger formations. The absence of fission track populations younger than the Early Miocene in zircons with a Gangdese U-Pb and Hf isotopic signature is consistent with the loss of the southern Lhasa terrane as a sediment source for the Middle-Late Miocene sediments. The greater proportion of Mesozoic fission track ages within the Obogon Formation sampled from the Western Trough versus the predominantly Neogene fission track ages within the Shwetaung and Taungtalon formations sampled from the Eastern Trough is likely due to localized input from erosion of the uplifted Indo-Burman Ranges that contain significant Cretaceous fission track modes (Allen et al., 2008).

Interpretations of provenance and source exhumation for the Shwetaung Formation are severely constrained by the limited number of fission track dated grains that were also analyzed for Hf isotopic composition. Three zircons with Early Miocene fission track ages (~21–20 Ma) with corresponding U-Pb ages of ~44–35 Ma and negative εHf(t) values possibly record cooling following ductile extension of the Mogok Metamorphic Belt in the Shan Scarps region and signals the initiation of contribution from this source to the Central Burma Basin. However, no great geological significance can be placed on these interpretations due to the limited dataset.

Within the larger dataset available for the Taungtalon Formation, five grains with a Gangdese signature have un-reset Early Miocene fission track ages ranging from ca. 20–18 Ma, the youngest of which gives a fission track age of 18.1 ± 3.0 Ma. This provides further support for a Yarlung Tsangpo-Irrawaddy connection linking the southern Lhasa terrane to the Central Burma Basin until disconnection in the Early Miocene, hypothesized here to be tectonically driven by increased exhumation and deformation within the eastern Himalayan syntaxis region. One younger grain, also recording a Gangdese signature, gives a fission track age of 14.8 ± 3.9 Ma, interpreted as a re-set age, it is younger than the known depositional age of this formation and four similarly aged zircons with negative εHf(t) values are also present. Fission track ages of ca. 14–9 Ma are observed in all formations and are interpreted as partially re-set zircons due to post-depositional thermal disturbance within the basin (see section 4.5.4 for further discussion).

In the Obogon Formation, detrital zircons with Early-Middle Miocene fission track ages (ca. 18–15 Ma) are characterized by negative εHf(t) values, whereas the youngest zircon with a Gangdese signature is ~27 Ma. The zircon recording a fission track age of 15 Ma, together with its enrichment in radiogenic hafnium and Cretaceous U-Pb age may be linked to a Dianxi-Burma or Eastern Transhimalayan source. These observations are consistent with the loss of an actively eroding southern Lhasa terrane source and increasing contributions from bedrock outcropping within the modern Irrawaddy catchment following Yarlung Tsangpo-Irrawaddy disconnection.

The change in provenance from a predominant southern Lhasa terrane source, best characterized by the significant proportion of detrital zircon with U-Pb and Hf isotopic values indistinguishable from those observed in the Gangdese Batholith, within the Eocene and Oligocene sediments to a predominant source provenance from the intra-syntaxis Dianxi-Burma batholiths and Mogok Metamorphic Belt within the Miocene sediments is interpreted to be the result of Early Miocene river disconnection. The change in provenance in the Early Miocene, coupled with the highest inferred exhumation rate, indicates the inability of the system to keep pace with deformation and

its rapid breakdown in a geological time scale suggests disconnection is likely related to tectonic forcing. It is hypothesized that increased exhumation and focused deformation in the eastern syntaxis contributed to disconnection of the Yarlung Tsangpo-Irrawaddy River and gave rise to the Yarlung Tsangpo-Brahmaputra system.

Fission track dating of detrital zircon extracted from sands of the Modern Irrawaddy River reveal middle and early Miocene (14.1 ± 0.7 Ma, 22.9 ± 0.8 Ma), earliest Oligocene (31.0 ± 1.7 Ma), early Eocene (49.2 ± 2.6 Ma) and middle Late Cretaceous (82.0 ± 4.9 Ma) age modes (Allen et al., 2008). The age modes are similar to those observed in the Central Burma Basin sedimentary rocks analysed in this study, including a ca. 14–11 Ma peak that is observed in all samples of this study and is interpreted to represent grains that have been partially or fully re-set during basin-wide post-depositional deformation and inversion active during Middle to Late Miocene time (Bertrand and Rangin., 2003; Pivnik et al., 1998) (see section 4.5.4). Alternatively, this peak may reflect contributions from Middle Miocene volcanism that occurred within the basin, dated at ca. 16–13 Ma (Lee, 2010), however substantial input of detritus from these proximal sources, recorded by detrital zircons with Middle Miocene U-Pb ages within contemporaneous sedimentary formations sampled in this study is lacking suggesting either the samples analyzed were deposited prior to the initiation of this stage of volcanism or, in the more likely case, volcaniclastic deposition and lava flows at this time were limited to localized areas of the basin, proximal to the volcanic center.

This resemblance in the detrital zircon fission track age distributions suggests the modern Irrawaddy River sands contain grains that are being recycled from older Cenozoic sedimentary sequences stored within the Central Burma Basin, consistent with similar observations based on detrital zircon U-Pb and Hf isotopic analysis conducted in this study. Based on the large degree of thermal re-setting of the fission track systems within the Eocene and Oligocene samples and a more minor component of young re-set ages within the younger Miocene samples in this study, a degree of caution is required in interpreting low temperature data of modern river systems within Burma and the implications of this data for exhumation and erosion of bedrock and/or the timing of

active volcanism within the catchment. Additional analysis (e.g. illite crystallinity, clay mineralogy or vitrinite reflectance) is required to determine the degree of post-depositional heating affecting Cenozoic Central Burma Basin strata.

4.5.3. Minimum ages and implications of age overprinting

$^{40}Ar/^{39}Ar$ and fission track ages can be entirely or partially reset if the sedimentary rocks have undergone sufficient burial after deposition such that rocks pass through the mineral closure temperature or sit in the partial retention/annealing zone (Verdel et al., 2012). In zircon fission track dating, higher uranium concentration and alpha recoil damage can cause selective thermal overprinting in some, but not all, grains (Marsellos and Garver, 2010). $^{40}Ar/^{39}Ar$ white mica dating of the Eocene Pondaung Formation reveals a young population of re-set ages between 37–31 Ma that are younger than the expected middle Late Eocene depositional age. The older Eocene sample (Pondaung 1) is unmicaceous, and only 11 grains were measured; the youngest mica age is 33.2 ± 0.7 Ma. There are 83 measurements for the younger Eocene sample (Pondaung 2) and the youngest age is 31.7 ± 0.3 Ma. The presence of re-set $^{40}Ar/^{39}Ar$ white mica and zircon fission track ages in the Pondaung Formation hinders the use of mid- to low-temperature thermochronology in constraining the depositional age of this formation. The partial re-setting of some, but not all grains, during post-depositional re-heating within the basin setting and as the entire population is not affected, temperatures most likely did not exceed ~350°C. Grains that are smaller or those with damaged crystal structures may lower the temperature at which argon is retained (enhanced diffusion of $^{40}Ar^*$ within a damaged lattice), resulting in a lowering of the closure isochron which allows for partial re-setting (Harrison et al., 2009; Hodges et al., 2005; Verdel et al., 2012). Additionally, if damaged grains experienced prolonged heating at lower temperatures, this may have affected the argon retentiveness of some, but not all, white mica grains.

A significant number of fission track ages in the Eocene Pondaung Formation and minor populations in the Oligocene Padaung and Miocene Shwetaung, Taungtalon and Obogon formations are younger than the depositional age, as previously determined by

biostratigraphy and lithostratigraphic correlation of radiometrically dated units, and therefore reset (Figure 3.12, 3.14). As a limited number of grains are affected, re-setting of fission track ages within the Oligocene and Miocene formations is attributed to higher uranium concentrations and alpha-recoil damage in these zircons which is known to reduce the closure temperature and can cause selective resetting of some, but not all, detrital zircons in a sample, (Bernet and Garver, 2005; Bernet et al., 2006; Marsellos and Garver, 2010). The partial resetting of a proportion fission track ages in all the samples analyzed provides information on the depth of burial and timing of exhumation of the sedimentary sequences within the Central Burma Basin. The significance of the re-set populations will be discussed in the following section. Illite crystallinity and clay mineralogy would provide some insight into the degree of post-depositional heating that affected these sediments. Based on the degree of re-set zircon fission track ages and white mica ages within the Pondaung Formation, this formation likely experienced post-depositional heating to temperatures above 250°C and/or lingered within the partial annealing zone for an extended period of time (~10 Ma). The presence of re-set zircon fission track ages in all formations analyzed in this study hinders the use of this method in constraining the depositional age of the sampled Eocene, Oligocene and Miocene sedimentary strata.

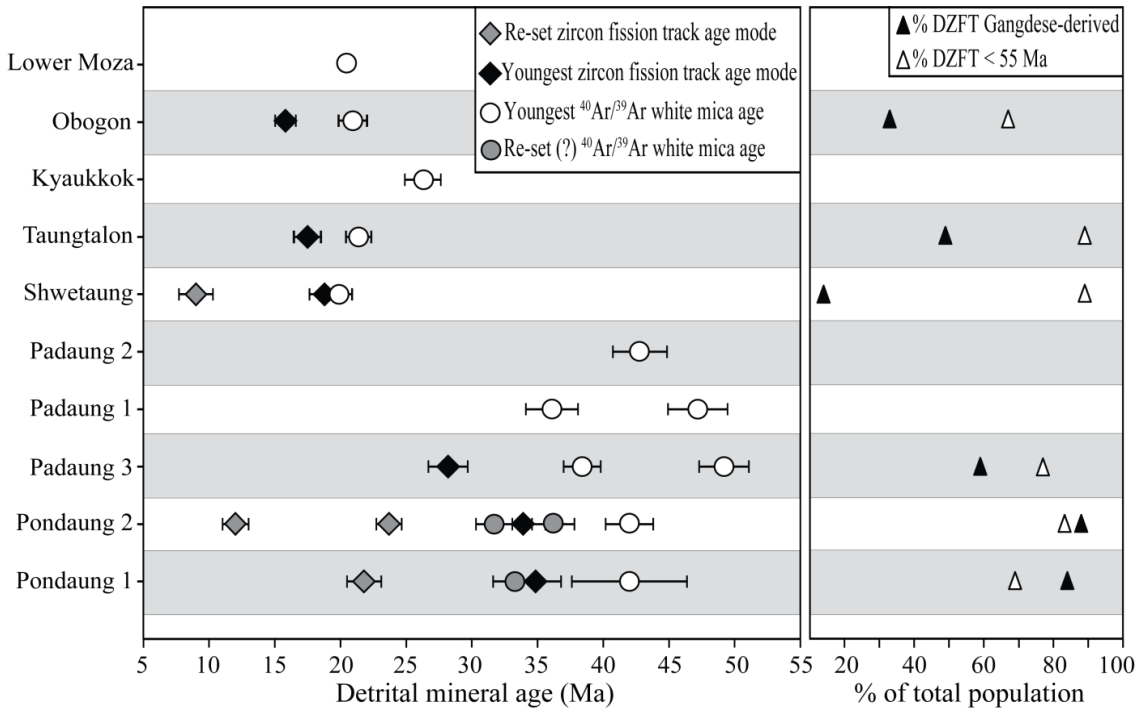

Figure 4.12 Minimum ages of Cenozoic Central Burma Basin sedimentary rocks analyzed in this study based on low temperature thermochronology, with samples arranged in stratigraphic order. Only ages younger than 55 Ma are shown. Error bars are 2σ and are not shown where the symbol is larger than its assigned error. The total percentage of the detrital zircon fission track dataset with Gangdese-type εHf(t) values and U-Pb ages is also shown. It must be noted the Shwetaung Formation dataset is limited and therefore not much emphasis can be placed on interpretations.

4.5.4. Insights into post-depositional basin mechanics based on re-set low temperature data

In addition to semi-quantifying exhumation rates within the source area, the low temperature thermochronology dataset obtained in this study provides a record of post-depositional basin mechanics and deformation. This dataset, specifically re-set detrital fission track ages, can be used to test hypotheses of structural reorganization within Burma marked by a shift in the regional stress regime from transtensional to transpressive during Middle to Late Miocene time in response to the coupling of the India and Burma plates, whereby their continued northward migration led to thrusting, basin inversion and folding of strata along re-activated Miocene extensional faults within the Central Burma Basin (Bertrand and Rangin, 2003; Pivnik et al., 1998; Vigny et al., 2003). $^{40}Ar/^{39}Ar$ and $^{40}K/^{40}Ar$ mica and K-feldspar cooling ages, together with

structural synthesis from field studies and thin sections, record Oligocene to Early Miocene NNW-SSE directed ductile extension along the length of the Mogok Metamorphic Belt in the Shan Scarps region, followed by east-northeast-striking brittle normal faulting (Bertrand and Rangin, 2003; Bertrand et al., 2001; Bertrand et al., 1999). This coincides with active extension within the Central Burma Basin along northeast-striking syn-sedimentary normal faults during the Miocene, as determined from seismic reflection data, which accommodated sedimentary infill leading to thickened Miocene strata (Bertrand and Rangin, 2003; Pivnik et al., 1998).

The combined use of $^{40}Ar/^{39}Ar$ white mica thermochronology recording cooling through mid-crustal temperatures and detrital zircon fission track dating recording cooling through the upper crust on the sedimentary rocks sampled in this study allows for examination of hypotheses involving post-depositional basin mechanics within the Central Burma Basin. The presence of a small population of re-set $^{40}Ar/^{39}Ar$ white mica ages in the oldest strata sampled (Pondaung Formation) and re-set zircon fission track ages in all samples indicate a degree of post-depositional thermal alteration affected some, but not all grains. A young static zircon fission track mode of middle to late Miocene age (ca. 14–9 Ma) is observed in all formations sampled, indicating a basin-wide event occurred at this time. This is consistent with Middle to Late Miocene timing for basin inversion within the Central Burma Basin suggested by (Pivnik et al., 1998) and (Bertrand and Rangin, 2003) based on seismic reflection and well log data. The presence of an erosion unconformity between the underlying Upper Miocene Obogon Formation and the overlying Pliocene-Pleistocene Irrawaddy Group suggest uplift occurred following deposition of the latter (Pivnik et al., 1998). A shift in the angle of convergence of India counter clockwise (from ~30° to 15° from north) during the Late Miocene (ca. 12–10 Ma), accompanied by a slight increase in the convergence rate (ca. 55 mm/yr), would have increased the obliquity of subduction beneath Burma, enhancing coupling of the India plate and Burmese fore-arc sliver, accommodated by dextral strike-slip motion along the north-trending Sagaing Fault to the east (Lee and Lawver, 1995). Additionally, the 14–9 Ma timing of basin inversion is contemporaneous with the uplift of the Shillong Plateau from 14–8 Ma, which is attributed to a regional

kinematic change in the stress regime of the eastern Himalayan orogen, and suggests deformation along the India-Burma plate boundary may play a significant role in dictating Miocene tectonics in this region (Clark and Bilham, 2008). Due to the large errors on the fission track ages and limited dataset, the timing of inferred post-depositional deformation within the basin based on the fission track data is tentatively suggested and further work is required. Low temperature thermochronology utilizing minerals with lower closure temperatures than the zircon fission track system (i.e. apatite fission track dating, zircon or apatite (U-Th)/He dating may be used to better understand the timing of post depositional deformation and degree of heating of the Central Burma Basin sedimentary rocks.

4.5.5. Rates of exhumation inferred from detrital lag times

Changes in this detrital signature through time may be used to document the evolution of the Irrawaddy River system during Eocene to Miocene time, which may have major implications for geodynamic models of the early Himalayan orogeny and the interaction between crustal deformation, exhumation, surface uplift and major drainage capture. In order to robustly quantify source exhumation rates from detrital low temperature data, the depositional age of the sample must be well constrained. It is acknowledged that the refinement of the stratigraphic ages of the sequences analyzed in this study is necessary to understand the timing of uplift and exhumation and thermal evolution of the source terranes, however the following section tentatively addresses changes in the inferred exhumation rates of source regions contributing sediment to the Central Burma Basin through time and implications for drainage evolution during the Cenozoic in the context of a working dataset that requires further study. In cases where the maximum depositional age of a formation has not been determined through absolute age dating (Middle to Upper Miocene formations), the depositional ages are based on biostratigraphy. Detrital white mica cooling ages are used instead of zircon fission track data because all samples contain a small population of fission track ages that have been partially or fully reset. It must be noted that the minimum $^{40}Ar/^{39}Ar$ white mica cooling age for the Pondaung Formation is likely re-set. The detrital lag time is determined by the difference between the age of the low temperature chronometer and the depositional

age of the sample, recording the time that passes between uplift of the grain through its closure temperature in the source terrane (~350°C for white mica), erosion, transport and deposition within the sedimentary basin (Bernet et al., 2004; Bernet and Garver, 2005; Garver et al., 1999). An increase in lag times through time reflects decreasing exhumation rates, whereas the convergence of detrital lag times reflects an increase in the exhumation rate in the source terrane (Bernet and Spiegel, 2004; Carrapa et al., 2009; Carrapa et al., 2004; Hodges et al., 2005; Ruiz et al., 2004; Szulc et al., 2006).

The stratigraphic trends in cooling ages shows that the lag time between the minimum $^{40}Ar/^{39}Ar$ white mica cooling age (as a proxy for depositional age), and the minimum U-Pb zircon crystallisation ages, converge in the Early Miocene (Figure 4.11). This is interpreted to reflect that the inferred exhumation rate of source terrains is highest during deposition of the Early Miocene Shwetaung Formation and sustained source with reduced exhumation rate for younger Miocene strata, consistent with the loss of a source experiencing active uplift. The percentage of Tertiary mica cooling ages increase up-section (Figure 3.10), indicating progressive exhumation in the hinterland, with the exhumation rate reaching a maximum in the Early Miocene as evidenced by the short lag time between the youngest mica cooling age and the youngest U-Pb age. This Early Miocene age (ca. 19–18 Ma) coincides with the reversal of shear sense from sinistral to dextral along the Jiali shear zone, that was most active from ca. 22–13 Ma (Booth et al., 2004; Lee et al., 2003; Lin et al., 2009).

The Parlung River flows along the trace of the Jiali shear zone. It is suggested to have connected the Yarlung Tsangpo to the Irrawaddy River prior to disconnection. This focused and increased deformation within the eastern Himalayan syntaxis may have played a role in the breakdown of the Yarlung Tsangpo-Irrawaddy River system, which could not keep pace. This is supported by wind gaps located between the Parlung and headwaters of the Irrawaddy (Clark et al., 2004). The absence of $^{40}Ar/^{39}Ar$ detrital mica ages recording movement along this fault in the Miocene deposits of the Central Burma Basin suggests the rivers were disconnected by this time (Figure 5.5, Figure 5.6). Therefore, the change in provenance observed in the detrital zircon U-Pb and fission track ages, Hf isotopic composition and $^{40}Ar/^{39}Ar$ white mica data are shown to support

an Early Miocene disconnection between the Yarlung Tsangpo and Irrawaddy River systems and this is likely tectonically driven and occurred relatively rapidly. Following disconnection, the Yarlung Tsangpo carrying Gangdese-derived detritus was re-routed into the proto-Brahmaputra that captured the Yarlung Tsangpo through headward erosion.

Chapter 5. Discussion

5.1. Cenozoic evolution of the Yarlung Tsangpo and Irrawaddy River systems

By combining multiple analytical techniques on single detrital minerals, it is possible to determine how changes in provenance throughout the Cenozoic are related to exhumation and landscape evolution in the eastern sector of the Himalayan orogen. This study adopted a multi-technique approach to determine the sediment provenance of a suite of Eocene, Oligocene and Miocene sedimentary rocks from the Central Burma Basin in order to test the hypothesis that the Yarlung Tsangpo of southern Tibet formerly drained into the proto-Irrawaddy River prior to its capture by the Brahmaputra River via headward erosion. To discriminate between source terranes, detrital zircon U-Pb and εHf(t) and low temperature thermochronology data obtained in this study is compared with published bedrock data of potential source regions in southern Tibet, western Yunnan and Burma. It has been demonstrated there is evidence that a Yarlung Tsangpo-Irrawaddy connection existed as early as the Late Eocene and have constrained the timing of disconnection to the Early Miocene (ca. 19–18 Ma), earlier than the post-Late Miocene age (ca. 10–5 Ma) age of disconnection proposed by Brookfield (1998) and Liang et al. (2008) based on the presence of Gangdese-derived zircons within a Miocene sedimentary sample from the Central Burma Basin. This study is at odds with the river capture model of Clark et al. (2004) that suggested a palaeo-Yarlung Tsangpo-Red river that drained into the South China Sea prior to capture by the Irrawaddy River in the Late Cenozoic. It supports the findings of Hoang et al. (2009) and Clift et al. (2006) that used sediment provenance studies on onshore and offshore sedimentary repositories of the Red River to show such a connection never existed. Rather, an antecedent palaeo-Yarlung Tsangpo-Irrawaddy system is postulated to have been the major orogen parallel river draining the eastern Himalayas during the early stages of the orogeny. Although this system may have developed similarly to the other major river systems draining the southeast Tibetan Plateau, focused deformation in the eastern syntaxis region coupled with the onset of the Asian monsoon in the eastern syntaxis region led to the breakdown of the Yarlung Tsangpo-Irrawaddy River.

The change in sediment provenance, as evidenced by single grain detrital mineral analysis conducted in this study, between deposition of Eocene-Oligocene and Miocene sedimentary rocks of the Central Burma Basin is interpreted as the result of the breakdown of a singular Yarlung Tsangpo-Irrawaddy river system and subsequent capture of the Yarlung Tsangpo by the Brahmaputra River, leading to the loss of the southern Lhasa terrane, and specifically the Gangdese Batholith, as a source terrane from the Early Miocene onwards. Based on the comparison of detrital zircon U-Pb and εHf(t) data obtained in this study with published bedrock data of potential source terranes and identification of a dominantly Gangdese source for detrital zircons within the Pondaung Formation, a Yarlung Tsangpo-Irrawaddy connection is shown to have existed as early as the Late Eocene. This detrital signature, with significant contributions of Gangdese-derived detrital zircons, is similarly observed within the Oligocene sedimentary rocks of the Padaung Formation analysed in this study. Double dating of detrital zircon by U-Pb and fission track methods combined with Lu-Hf isotopic analysis confirms the predominance of zircon with Gangdese-like high, positive εHf(t) values and U-Pb ages in the Eocene and Oligocene samples, yielding corresponding Cretaceous to Late Eocene un-reset fission track ages. However, zircons recording negative values, likely derived from intra-syntaxis granitic sources, have relatively higher uranium contents and record re-set fission track ages (Early-Middle Miocene). Detrital white mica $^{40}Ar/^{39}Ar$ age distributions within the Eocene and Oligocene samples reflect a broad range of cooling events that are Jurassic to Oligocene in age and indicate primary derivation from multiple source terranes that experienced differential exhumation through mid-crustal temperatures prior to the India-Asia collision (majority of ages older than 55 Ma), consistent with a source within the Lhasa terrane. This region experienced significant deformation, exhumation and erosion during Cretaceous to earliest Eocene time (Aitchison et al., 2011; Dürr, 1996; Hetzel et al., 2011; Kapp et al., 2007a; Kapp et al., 2007b; Kapp et al., 2005b; Leier et al., 2007a; Leier et al., 2007b; Murphy et al., 1997; Pullen et al., 2008; Rohrmann et al., 2012; Volkmer et al., 2007; Wang et al., 2007; Wu et al., 2010; Xu et al., 2013; Yin, 2010), widespread volcanism during latest Cretaceous to Eocene time (Coulon et al., 1986; He

et al., 2007; Lee et al., 2009; Zhou et al., 2004), and episodic cooling following intrusion of the Gangdese Batholith from the Jurassic to Tertiary time (Copeland et al., 1995; Copeland et al., 1987; Dai et al., 2013; Harrison et al., 2000; Pan et al., 1993; Richter et al., 1991).

In contrast, during deposition of the Early Miocene Shwetaung Formation and continuing through deposition of younger Miocene formations, the contribution of arc-derived detritus as indicated by detrital zircons with Gangdese-like isotopic signatures decreases and input from intra-syntaxis orogenic source terranes increase through time. This change in provenance is also observed in the detrital white mica $^{40}Ar/^{39}Ar$ age distributions, which record dominant derivation from a singular source terrane that experienced exhumation and cooling through mid-crustal levels at ca. 37–35 Ma, likely resulting from the Himalayan orogeny, unlike the older, pre-Himalayan multi-modal cooling populations observed in the older Eocene and Oligocene sedimentary samples. The abrupt change in $^{40}Ar/^{39}Ar$ age spectra observed in the oldest Miocene deposits and all the younger Miocene deposits sampled reflects a change in provenance from a single source area which is interpreted to most likely be in eastern Burma. Based on the data obtained in this study an Early Miocene timing of disconnection is suggested, however this is inhibited in part by the poorly constrained depositional ages of the units sampled. The youngest detrital zircon in the Early Miocene Shwetaung Formation, yielding a $^{206}Pb/^{238}U$ age of 18.2 ± 0.3 Ma (1σ) and εHf(t) value of 9.4 ± 1.7 (2σ), is tentatively assigned a Gangdese arc province, providing a maximum age for disconnection of the Yarlung Tsangpo-Irrawaddy River systems. During deposition of this formation, a change in provenance is observed both in the detrital zircon U-Pb and Hf and white mica $^{40}Ar/^{39}Ar$ age distributions, interpreted to be the result of the loss of the southern Lhasa terrane as a sediment source. A general trend towards increasingly older ages of the youngest detrital zircon with decreasing stratigraphic age is observed in the Miocene formations, suggesting the loss of an actively exhuming source terrane providing detritus to the Central Burma Basin following deposition of the Early Miocene Shwetaung Formation. An increasing contribution of detritus sourced from intra-syntaxis regions through time, including the Eastern Transhimalayan and Dianxi-Burma

batholiths, supports the hypothesis that following the Early Miocene disconnection the Irrawaddy River lost significant stream power and formed a meandering, braided river system. This is evidenced by the increase in detrital lag times (stagnant lag times) and the recycling of older sediment (cannibalization of pre-Miocene strata) that deposited Gangdese-type zircons within younger sediments although the Irrawaddy was no longer connected to this source. Because of the poor constraint on the depositional age of the formations, the timing of disconnection is assigned an Early Miocene age, and based on the available age constraints obtained in this study, occurred between ca. 24 Ma (the maximum depositional age of the Oligocene Padaung Formation) and 18 Ma (the maximum depositional age of the Shwetaung Formation, where the change in provenance is observed).

5.2. Contrasting models for the Cenozoic evolution of the Irrawaddy River system

The Cenozoic Central Burma Basin sedimentary units contain evidence of an orogen-parallel palaeo-Yarlung Tsangpo-Irrawaddy river system that existed as far back as the Middle-Late Eocene and the capture of the Yarlung Tsangpo by the proto-Brahmaputra River during the Early Miocene is coincident with deformation along the strike slip Jiali and Gaoligong faults in the eastern syntaxis (Lin et al., 2009), and the Sagaing Fault in Myanmar (Mitchell et al., 2007). This capture event is the precursor to the development of the modern drainage systems observed today, where the Irrawaddy River now drains a region south and east of the eastern Himalayan syntaxis, including western Yunnan and Burma (Figures 4.1, 4.2, 5.1 C), and the Brahmaputra River, linked with the antecedent Yarlung Tsangpo, drains a large area encompassing southern Tibet, the eastern syntaxis and the eastern Himalayan front. The results of this study provide temporal constraints on the development of the modern Yarlung Tsangpo–Brahmaptura river system that drains Namche Barwa massif in the eastern syntaxis.

Two contrasting models exist to explain the anomalous bend in the Yarlung Tsangpo-Siang-Brahmaputra River within the Namche Barwa massif: large scale river capture of the Yarlung Tsangpo from the proto-Irrawaddy by a tributary of the

Brahmaputra in the late Cenozoic (Brookfield, 1998; Clark et al., 2004; Liang et al., 2008; Seeber and Gornitz, 1983) versus progressive deformation of an antecedent Yarlung Tsangpo-Siang-Brahmaputra system during the crustal-scale folding and northward propagation of the Namche Barwa syntaxis (Lang and Huntington, 2014; Seward and Burg, 2008) (Figure 5.1). If the Yarlung Tsangpo-Irrawaddy formed a single longitudinal river, sediment derived from bedrock that was exposed in the modern Yarlung Tsangpo drainage within southern Tibet would be present within the Central Burma Basin. If the Irrawaddy was not involved in a river capture event (Yarlung Tsangpo-Siang-Brahmaputra antecedence prior to the Early Miocene), the sediment preserved in the basin should be representative of the bedrock exposed in the modern Irrawaddy catchment. Therefore, the identification of detritus derived from the Gangdese magmatic arc, exposed in the modern Yarlung Tsangpo catchment in southern Tibet, within Cenozoic syn-orogenic sedimentary rocks of the Central Burma Basin provides evidence of a Yarlung Tsangpo-Irrawaddy connection. A change in sediment provenance between deposition of the Palaeogene and Miocene formations is attributed to the capture of the Yarlung Tsangpo from the Irrawaddy River by the Brahmaputra and loss of the Gangdese arc as a actively contributing source region after ca. 18–19 Ma. Thus, changes in sediment provenance of Cenozoic formations within the Central Burma Basin through time has the potential to document the evolution of the large river systems draining the eastern Himalaya during the early stages of orogenesis, which may have major implications for geodynamic models involving the interaction between crustal deformation, exhumation, surface uplift and major drainage capture in the eastern syntaxis region.

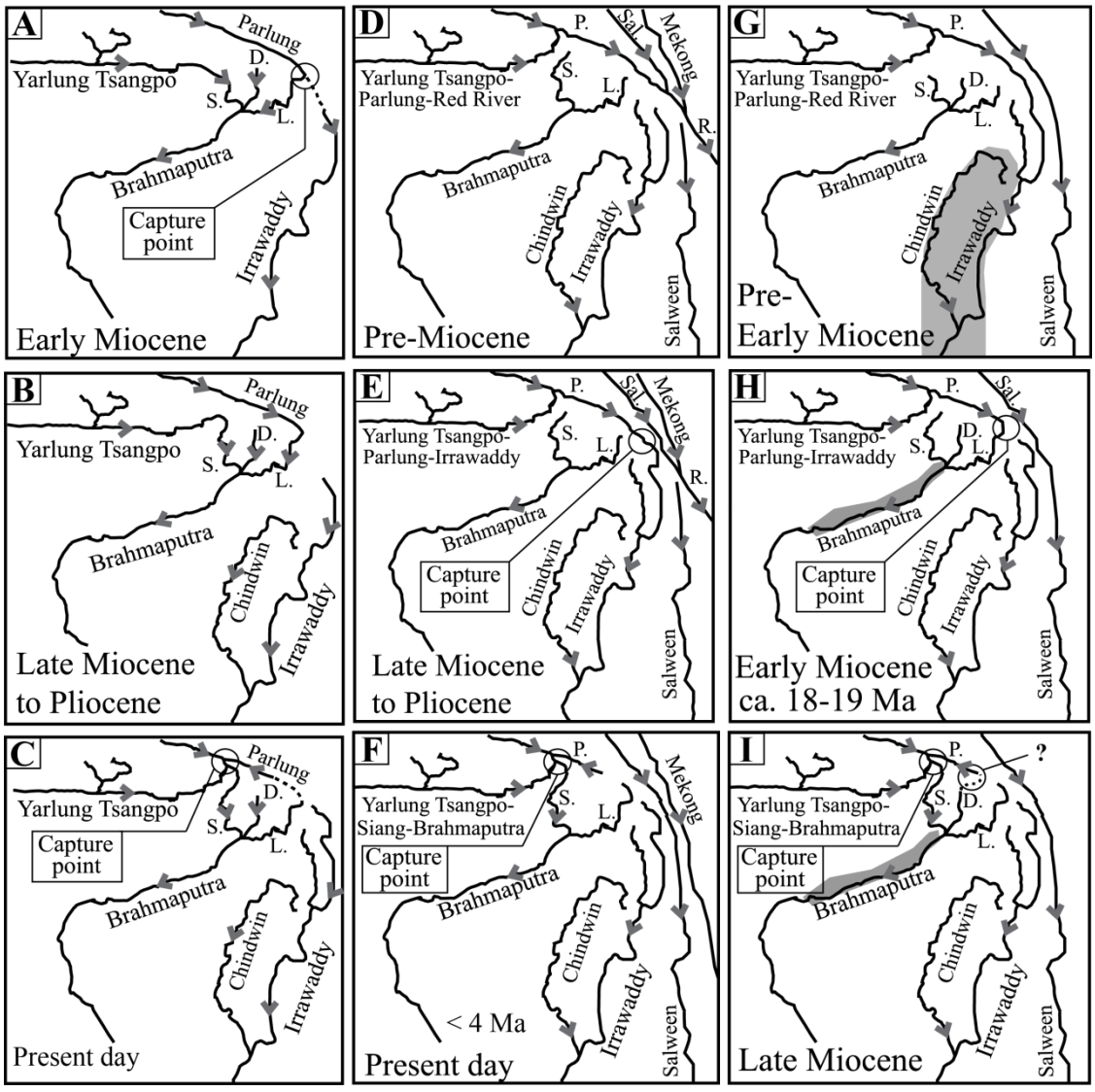

Figure 5.1 Cenozoic drainage evolution of the major rivers draining the eastern Himalaya from pre-Miocene to present day in response to the Himalayan orogeny R. = Red River; P. = Parlung River; D. = Dibang River; L. = Lohit River. A, B, C) River evolution after Seward and Burg (1998) and Lang and Huntington (2014) whereby an antecedent Yarlung Tsangpo-Brahmaputra system was distorted due to northward migration and exhumation of the Namche Barwa massif. A) Dual antecedent systems consisting of the Yarlung Tsangpo-Brahmaputra and the Parlung-Irrawaddy with a hypothesized Early-Middle Miocene capture of the Parlung River from the Irrawaddy River by the Lohit River, a tributary to the Brahmaputra. D, E, F) River evolution after Clark et al. (2004), Liang et al. (2008) and Brookfield (1998) which attributes the anomalous drainage patterns of SE Asian river systems to river capture and reversal in response to regional surface uplift, with one of the last river capture events involving the loss of the Yarlung Tsangpo from the Irrawaddy River via headward erosion and capture by a tributary to the Brahmaputra during the Late Cenozoic (ca. 10 Ma or 4 Ma) (Brookfield, 1998; Clark et al,. 2004; Liang et al., 2008). D) Pre-Miocene proposed river connections for the Yarlung Tsangpo in Tibet and the upper reaches of the Salween and Mekong as tributaries to the Red River, which formed a single, southeast flowing system empting into the South China Sea (Clark et al., 2004). E, F) Late Miocene to present day palaeo-river reconstruction of Yarlung Tsangpo-Parlung-Irrawaddy river, and its disconnection

and subsequent capture by the Lhuit and the Brahmaputra (after Clark et al., 2004; Brookfield, 1988; Liang et al., 2008). G, H, I) River evolution model proposed in this study whereby a Yarlung Tsangpo-Parlung-Irrawaddy connection existed as far back as the Late Eocene and capture of the Yarlung Tsangpo from the Irrawaddy by a tributary of the Brahmaputra (Lohit River) occurred during the Early Miocene (ca. 18 Ma), coinciding with initiation of dextral shear along the Jiali Fault zone along which the Parlung River flows (Lin et al., 2009). The shaded regions represent the depo-centers for detritus sourced from the Gangdese magmatic arc, used to infer a palaeo-Yarlung Tsangpo connection. Prior to capture, the Central Burma Basin received the majority of detritus shed from the Gangdese magmatic arc. Following capture by the Brahmaputra through headward erosion of its tributaries, Gangdese derived zircons appear within the eastern Himalayan foreland basin (from the Middle Miocene onwards; Cina et al., 2009, Lang and Huntington, 2014). H, I) Initial capture of the Yarlung Tsangpo is suggested to have been by the Lohit River, and then occurred in a clockwise pattern around the eastern Himalayan syntaxis by the Dibang River (?) and finally the Siang River, prior to rapid exhumation of the Namche Barwa syntaxis at ca. 10 Ma (Booth et al., 2004, 2009). C, F, I) Present day orientation of the major river systems of the eastern Himalayan syntaxis region, where Burma is internally drained by the Irrawaddy River. The Early Miocene timing of capture proposed in this study (ca. 18 Ma) places a maximum age constraint on the development of the modern Yarlung Tsangpo-Brahmaputra river system. Modified from Clark et al. (2004), Lang and Huntington (2014), Liang et al. (2008) and Seward and Burg (2008).

The results of this work support previous hypotheses of a palaeo-Yarlung Tsangpo-Irrawaddy connection in the late Cenozoic and places new constraints on the timing of initiation and subsequent re-organization of this system through river capture resulting from the headward erosion of the palaeo-Brahmaputra River (Figure 5.1, D-F) (Brookfield, 1998; Clark et al., 2004; Liang et al., 2008; Seeber and Gornitz, 1983). The dominance of detritus sourced from the Gangdese magmatic arc of southern Tibet that lies exclusively within the Yarlung Tsangpo catchment is observed within Eocene and Oligocene sedimentary samples from the Central Burma Basin deposited by the proto-Irrawaddy River is best explained by a Yarlung Tsangpo-Irrawaddy connection at the time of deposition which existed at least as far back as the Middle-Late Eocene (Figures 4.5, 4.5, 5.1). This work does not support models that invoke the existence of an antecedent Yarlung Tsangpo-Brahmaputra system in which the Yarlung Tsangpo was never connected to the proto-Irrawaddy (Figure 5.1, A-C) (Lang and Huntington, 2014; Seward and Burg, 2008). Lang and Huntington (2014) attribute the dominant Gangdese-derived detrital signature within the Late Eocene Pondaung and Oligocene Padaung sedimentary formations of the Central Burma Basin (Robinson et al., 2014) to an antecedent Parlung-Irrawaddy River system, however the bedrock within the Parlung-Irrawaddy catchment alone cannot fully characterize the range of detrital zircon

U-Pb and εHf(t) signatures that are observed. In the latter scenario, the Palaeogene sedimentary rocks of the Central Burma Basin would contain dominant Cretaceous to Early Eocene detrital zircon age populations with corresponding negative εHf(t) values that characterize the rocks of the modern Irrawaddy catchment, however, the dataset presented in this study reveals that the Eocene and Oligocene samples are dominated by detritus with a juvenile magmatic arc provenance that is most consistent with a Gangdese magmatic arc source, rather than an Eastern Transhimalayan batholith source (Figures 4.2, 4.5, 4.6). A Yarlung Tsangpo-Irrawaddy River connection during Eocene-Oligocene deposition in the Central Burma Basin, rather than a Parlung-Irrawaddy River connection (Lang and Huntington, 2014), best fits the dataset presented in this study. Additionally, the resulting loss of the southern Lhasa terrane, and specifically the Gangdese magmatic arc, as a source is reflected in both the dramatic decrease in the proportion of Gangdese-type zircons and arc-derived detritus deposited in the Central Burma Basin from the Early Miocene onwards (Figures 4.8, 4.9) and is most consistent with the loss of the Gangdese magmatic arc as a source region via disconnection of the Yarlung Tsangpo-Irrawaddy river system via river capture. Therefore, models of catchment deformation within the eastern syntaxis region that do not require the capture of the Yarlung Tsangpo from the Irrawaddy River by the Brahmaputra River (Lang and Huntington, 2014; Seward and Burg, 1998) are insufficient to explain the presence of detritus derived from the Gangdese magmatic arc within the Central Burma Basin sedimentary rocks.

A modified version of the Clark et al. (2004) model is favoured whereby the Yarlung Tsangpo of southern Tibet formerly drained into the proto-Irrawaddy River prior to its capture first by the proto-Brahmaputra River via headward erosion during the Early Miocene (ca. 18 Ma) (Figure 5.1, G-I). This is earlier than the Late Miocene age of disconnection proposed by Liang et al. (2008) based on the presence of Gangdese-type zircons within the Upper Pegu Group sample of ca. 10–5 Ma age and the Pliocene-Pleistocene age for capture suggested by Clark et al. (2004), Burg et al. (1998) and Zeitler et al. (2001). The interpretation that the Yarlung Tsangpo-Irrawaddy flowed into the palaeo-Red River (Figure 5.1, D) (Clark et al., 2004) is unsupported by the data

presented in this study which shows the former system was transporting detritus from the southern Lhasa terrane to the Central Burma Basin as early as the Middle-Late Eocene, possibly earlier. The Early Miocene timing of river capture of the Yarlung Tsangpo by the proto-Brahmaputra River is coincident with deformation along the strike slip Jiali and Gaoligong faults in the eastern syntaxis (Lin et al., 2009) and the Sagaing Fault in Myanmar (Mitchell et al., 2007).

This study favors the hypothesis that aggressive headward erosion of the proto-Brahmaputra River was an additional driver for river capture (Brookfield, 1998; Clark et al., 2004; Liang et al., 2008) given the synchronicity of disconnection with the exhumation of the Greater Himalayan Sequence and onset of the southeast Asian monsoon during the Early to Middle Miocene that would have enhanced headward erosion of the short, transverse rivers of the Himalayan front (Clift et al., 2008; Hodges, 2006) (Figures 5.1, 5.4). Additionally, the arrival of Gangdese-derived detritus within the Middle Miocene (ca. 15 Ma) and younger sedimentary rocks of the eastern Himalayan foreland basin support a Yarlung Tsangpo-Brahmaputra connection at this time (Cina et al., 2009; Lang and Huntington, 2014).

The Early Miocene timing of Yarlung Tsangpo-Irrawaddy River disconnection provides temporal constraint on the establishment of the Yarlung–Siang–Brahmaputra River (post-18 Ma) and the coupling of rapid uplift of the Namche Barwa massif and fluvial incision (Late Miocene or Pliocene) provides a lower age constraint of the development of the system as it was likely antecedent to rapid exhumation of the eastern Himalayan syntaxis (Clark et al., 2004). Therefore, the drainage evolution and river capture involving the major systems of the eastern Himalayan syntaxis region partially reflect the uplift and tectonic evolution of the region, and that the timing of river capture events in the Himalayas and southeast Asia can be used to better understand the landscape response to uplift and focused deformation in active orogenic settings.

5.3. New Interpretations in the context of pre-existing provenance studies of the Cenozoic Central Burma Basin and Indo-Burman Ranges

This study adopted a multi-technique approach to determine the sediment provenance of a suite of Eocene, Oligocene and Miocene sedimentary rocks from the Central Burma Basin in order to test the hypothesis that the Yarlung Tsangpo of southern Tibet formerly drained into the proto-Irrawaddy River prior to its capture by the Brahmaputra River via headward erosion. In the following section, the results of this study are discussed in the context of data obtained in previous provenance studies conducted on Cenozoic sedimentary rocks of the Central Burma Basin cited in the literature.

Although the interpretation of the data varies from study to study, the data itself is not inconsistent with the hypothesis presented in this work, whereby a palaeo-Yarlung Tsangpo-Irrawaddy River system carried arc-detritus from the southern Lhasa terrane to the Central Burma Basin from at least late Eocene time, prior to the breakdown of the system in the Early Miocene due to focused deformation in the eastern syntaxis region and capture of the Yarlung Tsangpo by a tributary of the Brahmaputra River through headward erosion. Prior to disconnection, the Eocene and Oligocene sedimentary rocks were dominated by a juvenile, calc-alkaline magmatic arc provenance with minor crustal input, as determined by the significant proportion of detrital zircons with U-Pb and εHf(t) isotopic characteristics analogous to those observed in the Gangdese Batholith and associated volcanic rocks of southern Tibet, un-reset $^{40}Ar/^{39}Ar$ detrital white mica multi-modal cooling populations and detrital zircon fission track dates of predominantly Jurassic to Eocene age. The maximum depositional age, as determined by the youngest detrital zircon $^{206}Pb/^{238}U$ age in each sample, decreases with time indicating erosion from source terranes undergoing active exhumation during deposition of the Eocene Pondaung Formation, Oligocene Padaung Formation and Early Miocene Shwetaung Formation (Figure 3.4). A significant change in provenance is observed in the Early Miocene Shwetaung and younger Miocene formations, interpreted to be the result of the breakup of the palaeo- Yarlung Tsangpo-Irrawaddy system, after which the southern Lhasa terrane was cut off as a sediment source to the Central Burma Basin and

the proportion of intra-syntaxis derived detritus contributing to the sediment load increases through time.

Previous detrital provenance studies on Cenozoic sedimentary rocks of the Central Burma Basin and Indo-Burman Ranges utilizing sedimentary petrology, heavy mineral analysis and single grain detrital zircon (U-Pb and fission track dating, Lu-Hf isotopic analysis), white mica ($^{40}Ar/^{39}Ar$ dating) and whole rock Sr and Nd isotopic analysis document a predominantly arc terrane source for Palaeogene aged sedimentary rocks and a change to a predominantly recycled orogen source for Miocene and younger sediments (Figure 5.2, 5.3). Burmese, Himalayan and southern Lhasa source terranes have been proposed. A significant change in source provenance, from arc-dominated to recycled orogen-dominated, during the deposition of Miocene and younger sedimentary formations is recorded in all previous provenance studies conducted on Cenozoic rocks of the Central Burma Basin and Indo-Burman Ranges. However different mechanisms are interpreted to explain the temporal shift in detrital sediment patterns (Allen et al., 2008; Liang et al., 2008; Licht et al., 2013; Naing et al., 2013; San, 1981; Thein, 1966; Wang et al., 2012, 2014; Win, 1986). The presence of arc-derived detritus present in the Palaeogene sediments of both the back-arc (Eastern Trough) and fore-arc (Western Trough) regions of the Central Burma Basin as well as the Palaeogene Indo-Burman Ranges eastern belt suggests a common source terrane was providing sediment to this region at this time. The overwhelming proportion of detrital zircons with positive εHf(t) values and arc-derived heavy minerals and lithic fragments present in these sedimentary rocks lead to two possible models for sedimentary deposition at this time, and by proxy, the palaeo-geography of the Irrawaddy River system throughout the Palaeogene. One possibility is that the arc-derived sediment was sourced locally from the Burmese portion of the Gangdese magmatic arc (southern extension) or was derived from the Gangdese arc itself. The latter lies exclusively in the Yarlung Tsangpo catchment area and thus determining a southern Lhasa terrane source for the sedimentary rocks deposited in the Central Burma Basin has major implications for the evolution of the Yarlung Tsangpo-Irrawaddy River system during the Cenozoic. Therefore, it is essential to discriminate between a Burmese or southern Transhimalayan

source when assigning arc-derived detritus from Central Burma Basin sedimentary rocks to a specific source region.

5.3.1. Discriminating between a Burmese or southern Lhasa terrane arc source in the Central Burma Basin

In Figure 5.3, U-Pb age versus εHf(t) isotopic values for detrital zircons younger than 250 Ma from Upper Cretaceous to Miocene sedimentary rocks of the Central Burma Basin and modern Irrawaddy River from pre-existing provenance studies are compared with similar data obtained in this study. Simplified literature data fields for the Gangdese Batholith, Dianxi-Burma batholiths, Eastern Transhimalayan batholiths, Mogok Metamorphic Belt, Slate Belt and West Burma arc are also plotted. Although no zircon Hf data is available for source regions within Burma, whole rock Sr-Nd data is used to infer isotopically enriched (εHf(t) < 0) or depleted sources (εHf(t) > 0).

In a recent provenance study, Wang et al. (2014) utilized combined detrital zircon U-Pb and Lu-Hf isotopic analysis and sedimentary petrology on a succession of Upper Cretaceous to Lower Miocene sedimentary rocks sampled from the westernmost margin of the Chindwin Basin (Western Trough) and a Upper Cretaceous sample from the Hukawng Basin from Shi et al. (2012) (Figure 5.2, 5.3). They argue the significant detrital zircon populations of late Early Cretaceous to Eocene age yielding positive εHf(t) values, coupled with petrographic data reveal primary sediment sourcing from juvenile granitoids of the West Burma magmatic arc and infer the sedimentary rocks of the Central Burma fore-arc basin record a main stage of magmatism between 110–80 Ma and a subordinate stage between 70–40 Ma, that is not observed in the present-day bedrock exposures of the Wuntho-Popa-Salingyi magmatic arc (Wang et al., 2014). Zircons with Palaeozoic and Proterozoic ages are attributed to secondary sediment sourcing from the recycling of older sedimentary rocks of the Burmese margin.

Several lines of evidence are discussed below that support this study's interpretation of a significant contribution from a Gangdese arc source within the southern Lhasa terrane, rather than a Burmese source, for the majority of arc-derived detritus present within Palaeogene sedimentary rocks of the Central Burma Basin. A significant

proportion of Palaeogene samples from the Central Burma Basin and Indo-Burman Ranges plot within the magmatic arc provenance field of Dickinson (1985), and significantly are observed to overlap with data obtained from Oligo-Miocene Gangrinboche conglomerates deposited in the southern Lhasa terrane (Figure 5.2) (Wang et al., 2013). These sedimentary units are interpreted to be derived mainly from the local Gangdese Batholith and provide an indication for the sediment composition sourced from this region. Rocks of the West Burma magmatic arc have a limited age range from ca. 105–90 Ma, whereas magmatism in the Gangdese Batholith extended from Jurassic to Neogene time, with peak magmatism occurring at ca. 65–37 Ma. Wang et al. (2014) cited presence of detrital zircons with Early Cretaceous to Eocene U-Pb age populations yielding positive εHf(t) values within Middle to Upper Eocene and Lower Miocene sedimentary rocks of the westernmost Central Burma Basin as evidence for Late Cretaceous to Eocene juvenile arc magmatism in the West Burma arc, contemporaneous with magmatism in its northern continuation (Gangdese arc), that is not recorded within surface outcrops. Geochronological studies reveal arc magmatism in the eastern continuation of the Gangdese arc around the eastern Himalayan syntaxis (Lohit Batholith, Wuntho-Popa arc) has a restricted age range and bedrock evidence for significant arc magmatism younger than the Late Cretaceous (ca. 90 Ma) and older than Middle Miocene and Quaternary volcanism is absent (Li et al., 2013; Mitchell et al., 2012; Mitchell, 1993; Stephenson and Marshall, 1984). Detrital zircons with Cretaceous ages (primarily 108–87 Ma) present within the Upper Cretaceous and Palaeocene samples have a more diverse range of εHf(t) values (ranging mainly between -0.5 to +6) than observed in magmatic zircons of the same age from bedrock of the Gangdese Batholith (values > +6) and Lohit Batholith (> +10) indicating a juvenile magmatic arc source other than the Gangdese batholith, with more crustal contamination of source melt, was contributing detritus to the Central Burma Basin at this time (Figure 5.3). Although the Cretaceous West Burma magmatic arc may have been a localized, primary source for the Cretaceous Kabaw Formation (ca. 70 Ma) and Palaeocene Paungyyi Formation (ca. 64 Ma) deposited in a forearc basin setting within the westernmost Central Burma Basin, additional source terranes appear during

deposition of the Middle Eocene Tilin Formation (ca. 47 Ma) and Upper Eocene Pondaung Formation (ca. 47–42 Ma). This is characterized by a change in the detrital zircon age and Hf isotopic distributions from a narrow range of Cretaceous aged zircons (102-94 Ma) yielding εHf(t) values clustering between 0 to +8 in the former to a wider range of ages and εHf(t) values mainly > +6, with divergence towards more enriched values at ca. 50 Ma (Figure 5.3) (Wang et al., 2014).

The detrital signature is similar to the Pondaung Formation samples observed in this study. It is therefore proposed the non-Cretaceous aged zircons with high, positive εHf(t) values are sourced from the Gangdese Batholith of southern Tibet, as source provenance within Burma is not sufficient to explain the detrital zircon age and Lu-Hf isotopic distribution observed in the detrital populations. This leads to the posing of an additional hypothesis that the development of the antecedent Yarlung Tsangpo as a major longitudinal river was established by at least the Middle Eocene (ca. 48–47 Ma, depositional age of the Tilin Formation based on zircon U-Pb). This is similar to the Early Eocene timing proposed for initiation of the Indus River (Clift et al., 2002; Clift et al., 2001), and a Yarlung Tsangpo-Irrawaddy River system delivering detritus sourced from the Lhasa terrane north of the Indus Yarlung suture zone to the Central Burma Basin, which is in fact slightly earlier than the timing inferred from the data of this study. This Middle Eocene age for initiation of the Yarlung Tsangpo-Irrawaddy system is in agreement with an Eocene (ca. 47 Ma) origin for the *Badidae* family of freshwater fish found in the modern Yarlung Tsangpo-Brahmaputra, Ganges and Upper Irrawaddy rivers based on molecular phylogenetic modeling (Rüber et al., 2004). A singular Yarlung Tsangpo-Irrawaddy clade is shown to have diverged into separate Yarlung Tsangpo-Brahmaputra and Irrawaddy clades that evolved independently after an Early Miocene vicariant event, attributed to the capture of the Yarlung Tsangpo from the Irrawaddy River by a tributary of the Brahmaputra River (Rüber et al., 2004). Coeval Eocene and Oligo-Early Miocene sedimentary units sourced from the Gangdese Batholith and deposited along the southern margin of the Lhasa terrane in a forearc basin setting (Gangrinboche conglomerate and Bomi Group) contain significant populations of Palaeocene to Eocene and Oligocene aged detrital zircons with high

positive εHf(t) values, suggesting active erosion was occurring in this region (Aitchison et al., 2011; Wang et al., 2013; Xu et al., 2013). These populations are similarly observed in contemporaneous strata deposited in the Central Burma Basin, both of which contain zircon U-Pb age populations (ca. 70–40 Ma) and high, positive εHf(t) values, suggesting the Gangdese Batholith was likely a common source for both locations.

Licht et al (2013) conducted a provenance study on sedimentary rocks of the Late Eocene Pondaung Formation and overlying Yaw Formation sampled from the Western Trough utilizing palaeocurrent data, whole rock Sr-Nd isotopic analysis and sedimentary petrology to argue against a Yarlung Tsangpo-Irrawaddy connection at the time of deposition, and instead attributed the dominant arc-derived and secondary orogenic-derived detritus to a Burmese source to the east. The main lines of evidence used to support this hypothesis of a proximal source are palaeocurrent data supporting west-ward directed sediment transport, the presence of low grade metamorphic lithic fragments and heterogeneity of Sr and Nd isotopic values, thus reflecting both juvenile and enriched source terranes. Their interpretation that the Central Burma Basin was filled by westward propagating fluvial and deltaic systems during the Late Eocene is contrary to all previous interpretations that the basin was infilled from north to south (Bender, 1983; Ciochon and Gunnell, 2002). When 20–30° of post-Eocene clockwise rotation of Burma is taken into account, the "west-ward directed" palaeocurrent data (Licht et al., 2014) reflects a south-southwest-directed palaeo-flow, consistent with the infilling of the westernmost Central Burma Basin by a river whose headwaters lie to the north. Additionally, balanced cross-sections of the sub-surface strata from seismic and well log data do not reveal a thickening of Eocene continental strata to the east that would be expected in a west-ward prograding deltaic system (Bertrand and Rangin, 2003; Pivnik et al., 1998). Low grade metamorphic lithic fragments, interpreted as being derived from the Burmese metamorphic basement (Licht et al., 2014), are not exclusive to eastern Burma, and significantly outcrop widely in southeast Tibet. Low grade metamorphic rocks outcrop particularly within the in the Asian crust of the eastern Himalayan syntaxis region and Parlung River catchment, and therefore are not a

reliable indicator for discriminating between a Burmese or Transhimalayan source provenance (Booth et al., 2004; Yin and Harrison, 2000). The averaged whole rock εNd values (-5.3 and -4.3) are similar to those observed in the Palaeogene Indo-Burman Ranges (-4 to -7.4) and together with a broad range of $^{87}Sr/^{86}Sr$ isotopic values, reflect incorporation of detritus mainly from juvenile source rocks, with subordinate input from enriched sources (Allen et al., 2008; Licht et al., 2014). The depleted Nd isotopic signature is consistent with the Gangdese arc contributing detritus to the Central Burma Basin during the Palaeogene. Whole rock Sr and Nd isotopic analysis does not sufficiently discriminate between Burmese or Transhimalayan arc source rocks, and detrital zircon proves a more powerful tool for sediment provenance discrimination for sedimentary rocks of the Central Burma Basin, particularly when combined with Lu-Hf isotopic analysis.

A second change in provenance is observed during initiation of deposition in the Lower Miocene Pegu Group samples analyzed by Wang et al. (2004). This change is characterized by an influx of sedimentary and metamorphic detritus (Figure 5.2) and Cretaceous to Cenozoic aged detrital zircons yielding negative εHf(t) values. They attribute this signal to the addition of an orogenic source from the eastern Himalayan syntaxis region or eastern Burma (Mogok Metamorphic Belt) (Figure 5.3). Two sedimentary samples, with maximum depositional ages of 16.8 ± 0.6 Ma (1σ) and 28.5 ± 0.8 Ma (1σ) based on the youngest detrital zircon within the sample, reveal very similar U-Pb age and εHf(t) values to coeval sedimentary rocks analyzed in this study. Similarly, a sandstone sample from the Upper Miocene Pegu Group (depositional age of 10–5 Ma) shows a similar detrital zircon U-Pb age and Hf isotopic distribution as the Middle-Late Miocene sedimentary rocks analyzed in this study. Roughly three-quarters of the total zircon population consist of Cretaceous and Palaeogene aged grains, just over half of which have positive εHf(t) values. These are analogous to those observed in the Gangdese bedrock, the youngest of which has a Middle Eocene age, supporting the idea that the Gangdese-type detrital zircons present within the Miocene formations of the central Burma Basin represent grains recycled from erosion of underlying strata. Increased input from intra-Burmese sources is observed both in the detrital zircon U-Pb

and Lu-Hf isotopic data and evolution in sediment composition through time, whereby an increase in quartz content reflects input from orogenic source terranes and older sedimentary cover rocks (Figure 5.2). This is consistent with heavy mineral provenance studies conducted by Thein (1966), where sediment is proposed to be sourced from metamorphic and granitic rocks to the north-northeast, likely the Mogok Metamorphic Belt. Palaeocurrent data from Miocene strata sampled over a wide area in the central basin reveals consistent palaeo-flow directions towards the south-southeast (Thein, 1966; San, 1981; Win, 1986) indicating a system closely resembling the modern Irrawaddy River was established during the Middle-Late Miocene, following disconnection. This is supported by the similarity in isotopic data from the Modern Irrawaddy River and Middle-Late Miocene sedimentary rocks (Allen et al., 2008; Bodet and Scharer, 2000), indicating that following disconnection in the Early Miocene, sediment provenance remains relatively unchanged from the Middle Miocene to present day. The detrital zircon U-Pb and Lu-Hf isotopic data obtained for the modern Irrawaddy reveals a larger contribution of Early Cretaceous ages with negative εHf(t) values (sourced from the Dianxi-Burma batholiths, Mogok Metamorphic Belt and Slate Belt that were exposed along the developing Sagaing-Gaoligong-Jiali dextral shear zone most active during the Middle Miocene) and an additional Late Miocene population with high, positive εHf(t) values (Bodet and Scharer, 2000), likely sourced from late Cenozoic volcanic activity in localized regions in the central basin.

5.3.2. Discriminating between a Burmese or southern Lhasa terrane arc source in the Indo-Burman Ranges

Allen et al. (2008) identified a Cretaceous arc-derived contribution to Palaeogene sedimentary rocks of the eastern Indo-Burman Ranges and interpreted this material to be sourced from Burma to the east rather than the Tibetan Transhimalaya (carried by the Brahmaputra River) given the scarcity of arc-derived material within coeval sedimentary rocks of the Bengal Basin. The lack of significant detritus sourced from north of the Indus Yarlung suture zone (juvenile, Late Mesozoic to Cenozoic Tibetan Transhimalayan batholiths) within the Bengal Basin during the Palaeogene is not inconsistent with the existence of a Yarlung Tsangpo-Irrawaddy River system

during the Palaeogene that transported sediment from the Gangdese magmatic arc in the southern Lhasa terrane to the Central Burma Basin and proto-Indo-Burman Ranges. Combined U-Pb and Lu-Hf isotopic analysis on detrital zircon extracted from the Palaeogene sedimentary rocks of this region would aid in testing this hypothesis. The Neogene sedimentary rocks of the western Indo-Burman Ranges also record a change in source provenance to largely being derived from Himalayan sources of Indian affinity and display similar isotopic characteristics to the Himalayan foreland basin deposits (Allen et al., 2008). A potential mechanism driving changes in sedimentary provenance, both within the Indo-Burman Ranges and Central Burma Basin, between Palaeogene and Neogene time is the uplift in the Indo-Burman Ranges followed by extension and normal faulting in the basin in the early Miocene (Bertrand and Rangin, 2003; Pivnik et al., 1998) that led to compartmentalization of the Central Burma Basin from the Indo-Burman Ranges and Bengal Fan (Robinson et al., 2014). Prior to this uplift, the palaeo-Yarlung Tsangpo-Irrawaddy River transported sediment to both these regions, in agreement with the hypothesis that the Palaeogene Indo-Burman Ranges represent the western extension of the Western Trough forearc basin (Mitchell, 1993).

The higher proportion of Archean to Palaeozoic aged detrital zircons within the westernmost region of the Central Burma Basin and Indo-Burman Ranges is attributed to either localized sources that have not yet been identified within Burma, or mixing with detritus shed from the nascent Himalayas. A basement source to the east is unlikely given the paucity of these older ages within the Eastern Trough, suggesting a specific source was contributing to one area but not the other. Prior to uplift of the Indo-Burman Ranges that compartmentalized the Central Burma Basin, the westernmost strata may have mixed with proximal proto-Bengal Fan detritus shed from the Indian Himalaya due to its proximity, or alternatively is sourced locally from a region that is not yet identified.

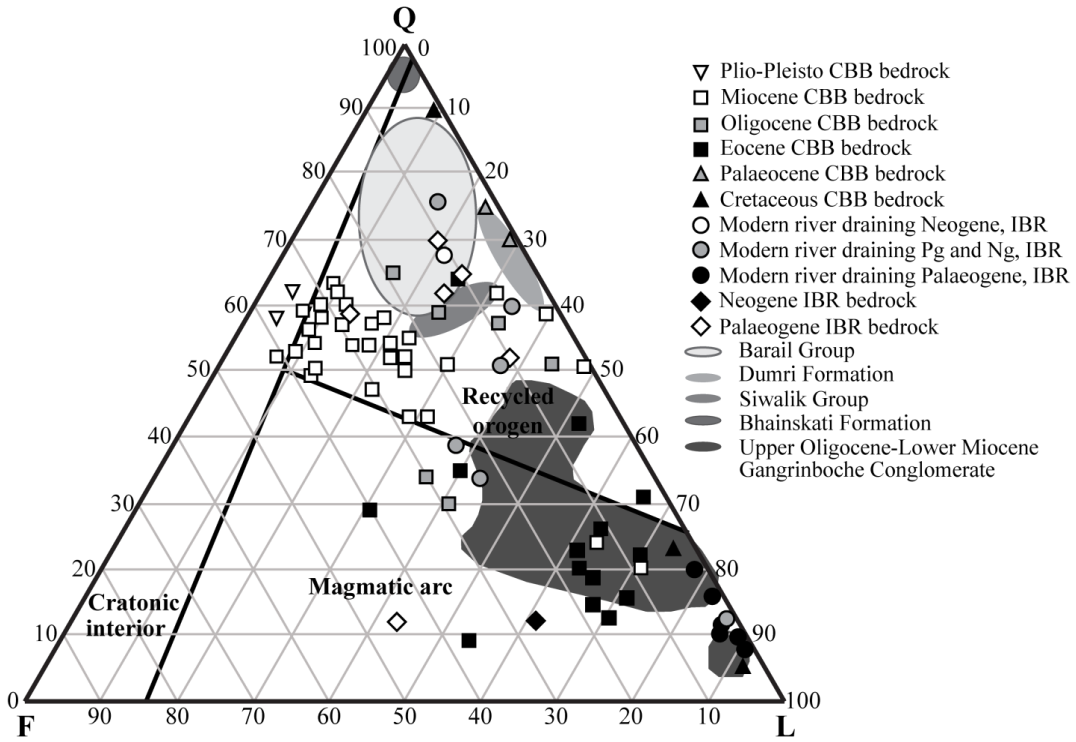

Figure 5.2 Sandstone composition plotted on a QFL diagram for Lower Cretaceous and Cenozoic sedimentary rocks of the Central Burma Basin and Indo-Burman Ranges, compared with data from coeval sedimentary rocks of the eastern Himalayan foreland basin, Bengal Basin and southern Lhasa terrane. Q = quartz, F = feldspar, L = lithics. Provenance fields based after Dickinson (1985). Central Burma Basin (CBB) data from Wang et al. (2013), Licht et al. (2014), Win (1986), Thein (1966) and San (1981). Data for the Indo-Burman Ranges (IBR) from Allen et al. (2008) and Naing et al. (2013). Data for modern rivers draining the Indo-Burman Ranges from Allen et al. (2008). Gangrinboche Conglomerate (southern Lhasa terrane) data from Wang et al. (2014). Data for the eastern Himalayan foreland and Bengal Basin including the Eocene Bhainskati, Oligocene Barail, Miocene Dumre formations and Miocene to Recent Siwaliks from Najman et al. (2008, 2005), Szulc et al. (2006), and DeCelles et al. (1998).

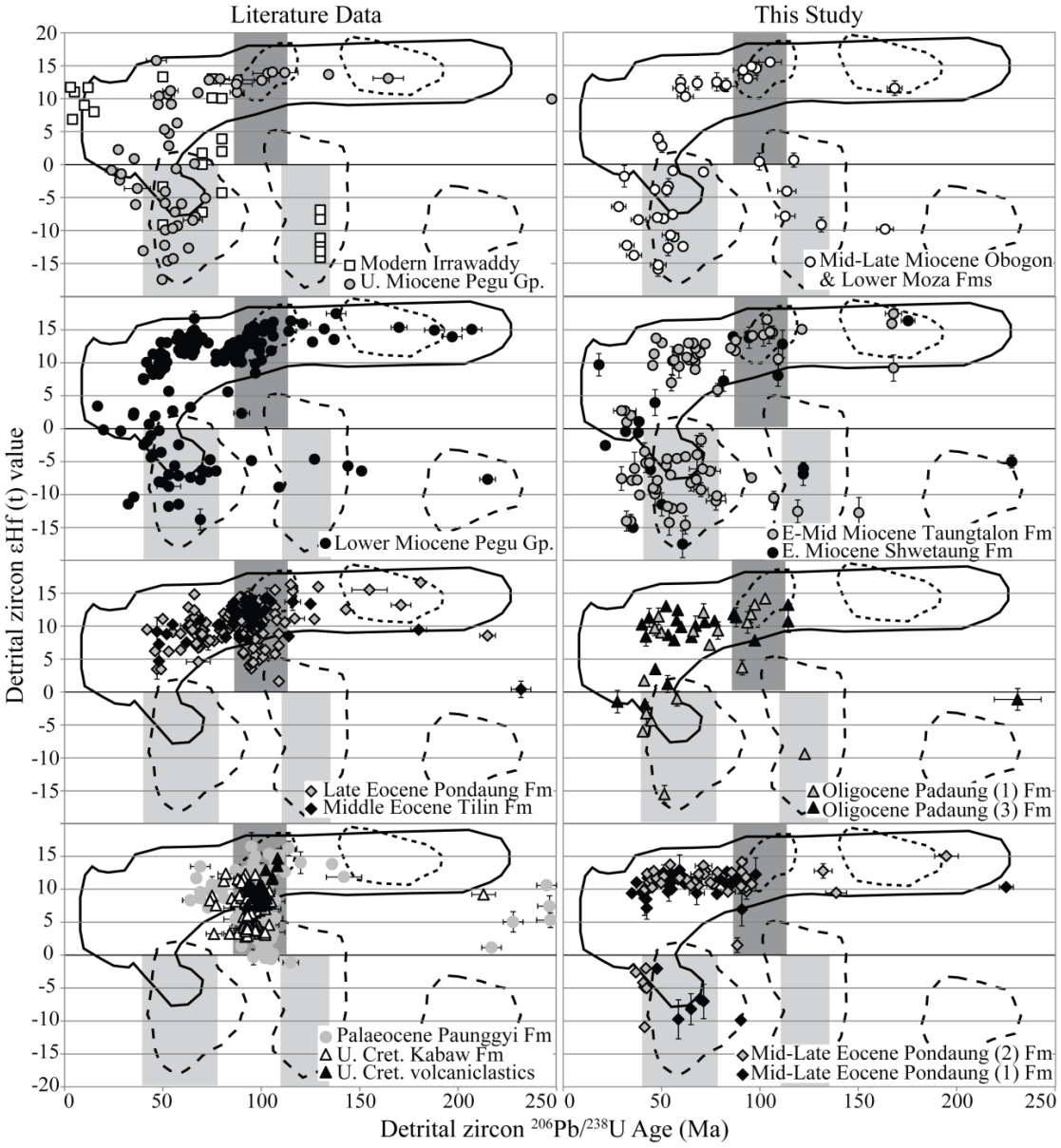

Figure 5.3 Detrital zircon U-Pb age vs εHf(t) values for sedimentary rocks of the Central Burma Basin from this study and existing studies depicting the evolving provenance record through time. Literature data from sedimentary rocks of the Central Burma Basin for Upper Cretaceous-Lower Miocene (Wang et al., 2014), Upper Miocene (Liang et al., 2008) and modern Irrawaddy River (Bodet and Scharer, 2000) samples. Error bars are 2σ for the Hf values and 1σ for the U-Pb age; error bars are only shown when they are larger than the symbol. The literature data fields are for the Gangdese Batholith (solid black line), Dianxi-Burma and Eastern Transhimalayan batholiths (dashed line), Burmese jadeite (Jurassic-Early Cretaceous) and Lohit Batholith (ca. 105–90 Ma) (dotted line). The square fields represent available age data for rocks of the Mogok Metamorphic Belt, Slate Belt and West Burma magmatic arc. Although no zircon Hf data is available for the latter, whole rock Sr-Nd data is used to infer isotopically enriched (εHf(t) < 0; light gray boxes, MMB and Slate Belt) or depleted sources (εHf(t) > 0; dark gray box, West Burma arc). See text for references.

5.4. Timing and Mechanism of Disconnection

This study proposes that focused exhumation and deformation within the eastern Himalayan syntaxis region, together with increased coupling of the India and Burma plates drove the breakdown of the Yarlung Tsangpo-Irrawaddy river system. Tectonic forcing and the inability of the linked river system to keep pace is the preferred mechanism driving river disconnection as major regional kinematic reorganization of the eastern Himalayas occurred during the Late Oligocene to Early Miocene times, contemporaneous with major drainage re-organization in the Namche Barwa syntaxis region (Figure 5.4). The onset of the Asian monsoon during the early Miocene (Clift et al., 2008) that likely enhanced headward erosion of the palaeo-Brahmaputra River suggests a dynamic link between tectonics, climate, exhumation and erosion largely controlled the re-organization of major river systems within the eastern Himalayan syntaxis during the Late Cenozoic. It is hypothesized that the river could not keep pace with increasing deformation and tectonic forcing. The stratigraphic changes observed in the detrital zircon U-Pb and Lu-Hf isotopic distributions and cooling age populations are attributed to a change in the regional plate tectonic regime and attribute this to the coupling and northward movement of the India-Burma plate along an increasingly hyper-oblique plate boundary, leading to compartmentalization of the Central Burma Basin and the onset of large scale dextral shear along the Sagaing-Gaoligong-Jiali shear zones. Focused deformation within the eastern syntaxis inevitably led to the disconnection of the Yarlung Tsangpo-Irrawaddy river system during the Early Miocene, as recorded by the change in provenance during deposition of the Shwetaung Formation.

During the Palaeogene-early Miocene, regional kinematics of western Thailand and Burma indicate a change from a transpressional sinistral strike-slip along Mae Ping and Three Pagodas Faults (Lacassin et al., 1997; Morley, 2009, 2004) and uplift of the Indo-Burman Ranges (Allen et al., 2008; Mitchell, 1993) to a transtensional regime characterized by a reverse in shear sense in the strike-slip faults of western Thailand,

initiation of strike-slip extension in the Andaman Sea (Curray, 2005), and the NNW-SSE-directed extension within the Mogok Metamorphic Belt (Bertrand et al., 2001, 1999) and the Central Burma Basin (Pivnik et al., 1998) (Figure 5.4). Hyper-oblique collision between the India and Burma plates, enhanced by the southeast-ward extrusion of Indochina, led to the development of a back-arc mobile belt in the hot, weakened crust of eastern Burma-western Thailand (western Sibumasu) (Morley, 2009, 2004). In western Thailand, transpression resulted in the initiation of sinistral shear along the Mae Ping and Three Pagodas Faults at ca. 50–40 Ma (Upton et al., 1999), lasting until ca. 36–30 Ma (Lacassin, 1997), after which time there was a reversal in shear sense. Morley (2009, 2004) interprets this left-lateral transpression as resulting from initiation of west Burma-India coupling, and the change to dextral shear (after ~30 Ma) during the late Oligocene-early Miocene recording the northward movement of the now coupled block, contemporaneous with the initiation of strike-slip deformation in the Andaman Sea (e.g. Curray, 2005; Morley, 2012). Additional evidence within Burma supports an Oligocene-early Miocene timing for the coupling of the Indian plate with the west Burma block. Fission track dating of detrital zircons from the Palaeogene Indo-Burman Ranges indicates sub-aerial uplift occurred after ca. 37 Ma (Allen et al., 2008; Mitchell, 1993) (Figure 5.4). Radiometric data from the metamorphic rocks of the Mogok Metamorphic Belt record a Palaeocene (~59 Ma) and protracted Eocene-Oligocene (~37–29 Ma) sillimanite grade high temperature-low pressure metamorphism, with zircon overgrowths (~47–43 Ma) and localized crustal melting (23 Ma) (Barley et al., 2003; Searle et al., 2007; Mitchell et al., 2012), followed by Oligocene to Early Miocene diachronous NNW-SSE orientated extension and exhumation recorded by $^{40}Ar/^{39}Ar$ mica cooling ages that decrease in age from south to north (27–16 Ma) (Bertrand et al., 2001; Bertrand et al., 1999) (Figure 5.4). This diachronous cooling records the northward movement of the now coupled India-Burma Block, characterized by a transtensional regime. Uplift to the east and west resulted in the compartmentalization of the Central Burma Basin, where little deformation and nearly continuous sedimentation from the Cretaceous-Pliocene suggests it is "floored by stronger, cooler oceanic crust" (Morley, 2009).

Contemporaneous with the northward indentation of the coupled India-Burma plate focused at the eastern syntaxis, the previously sinistral motion of the Jiali fault initiating at 22 Ma that accommodated the southeast-directed extrusion of Indochina, reversed to dextral at 18 Ma, linking with the Gaoligong shear zone to the south, forming the southwest boundary of clockwise rotation and extrusion of Tibet around the eastern Himalayan syntaxis (Lee et al., 2003; Lin et al., 2009) (Figure 5.4). Additional evidence for transpression and crustal thickening focused in the eastern syntaxis at this time is seen in the Asian fore-arc Bomi Group, outcropping directly north of the Indus Yarlung suture zone. These sediments were thought to have been part of the overriding Asian plate that were entrained along the Indian plate boundary and subducted to lower-mid crustal depths, followed by rapid exhumation and anatexis at ca. 37 Ma (Xu et al., 2008). The Parlung River flows along the trace of the Jiali shear zone, and is suggested to have connected the Yarlung Tsangpo to the Irrawaddy River prior to disconnection (Clark et al., 2004). A component of vertical offset along the Jiali Fault is also present, although the total amount of offset, both vertically and laterally is unknown. Mica $^{40}Ar/^{39}Ar$ cooling ages from bedrock within the Jiali shear zone indicate cooling through the middle crust between 18–11 Ma, during the main stage of dextral shear (Malloy, 2004; Lin et al., 2009; Lee et al., 2003). The absence of $^{40}Ar/^{39}Ar$ detrital mica ages of this age within the Miocene deposits of the Central Burma Basin suggests this source region in Yarlung Tsangpo-Parlung river catchment was no longer being tapped consistent with the breakdown of Yarlung Tsangpo-Irrawaddy connection during or shortly after deposition of Early Miocene Shwetaung Formation and younger formations (Figure 5.4, 5.5).

Figure 5.4 Time diagram showing the co-evolution of geological events in the eastern Himalaya and Burma and major river systems draining this region, correlated with provenance changes observed in Eocene to Miocene aged syn-orogenic sedimentary rocks of the Central Burma Basin. See text for references.

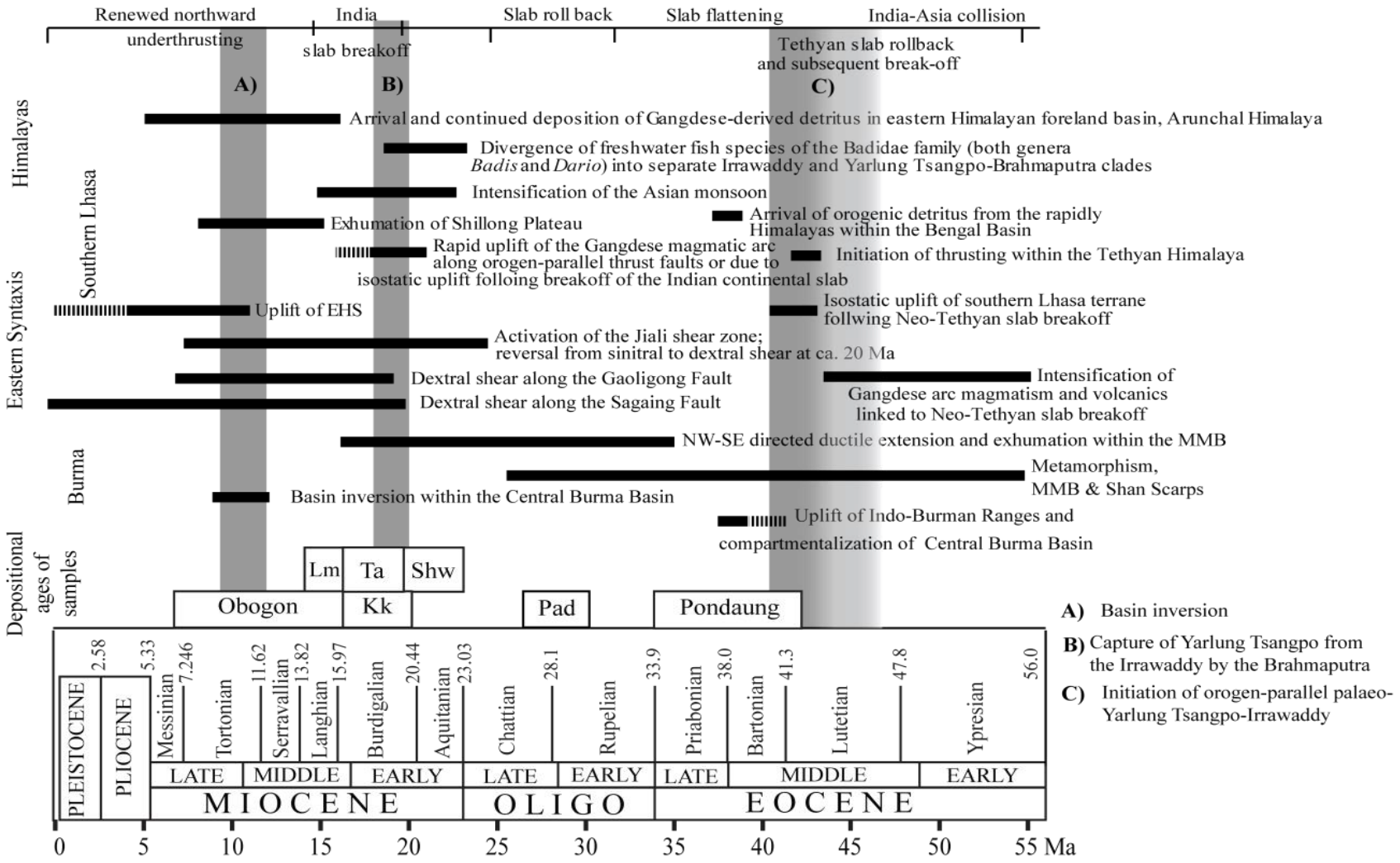
Renewed northward underthrusting
India slab breakoff
Slab roll back
Slab flattening
India-Asia collision
Tethyan slab rollback and subsequent break-off
A)
B)
C)
Himalayas
Southern Lhasa
Eastern Syntaxis
Burma
Arrival and continued deposition of Gangdese-derived detritus in eastern Himalayan foreland basin, Arunchal Himalaya
Divergence of freshwater fish species of the Badidae family (both genera Badis and Dario) into separate Irrawaddy and Yarlung Tsangpo-Brahmaputra clades
Intensification of the Asian monsoon
Exhumation of Shillong Plateau
Arrival of orogenic detritus from the rapidly Himalayas within the Bengal Basin
Rapid uplift of the Gangdese magmatic arc along orogen-parallel thrust faults or due to isostatic uplift folloing breakoff of the Indian continental slab
Initiation of thrusting within the Tethyan Himalaya
Uplift of EHS
Isostatic uplift of southern Lhasa terrane follwing Neo-Tethyan slab breakoff
Activation of the Jiali shear zone; reversal from sinitral to dextral shear at ca. 20 Ma
Dextral shear along the Gaoligong Fault
Intensification of Gangdese arc magmatism and volcanics linked to Neo-Tethyan slab breakoff
Dextral shear along the Sagaing Fault
NW-SE directed ductile extension and exhumation within the MMB
Metamorphism, MMB & Shan Scarps
Basin inversion within the Central Burma Basin
Uplift of Indo-Burman Ranges and compartmentalization of Central Burma Basin
Depositional ages of samples
Lm
Ta
Shw
Obogon
Kk
Pad
Pondaung
2.58
5.33
7.246
11.62
13.82
15.97
20.44
23.03
28.1
33.9
38.0
41.3
47.8
56.0
PLEISTOCENE
PLIOCENE
Messinian
Tortonian
Serravallian
Langhian
Burdigalian
Aquitanian
Chattian
Rupelian
Priabonian
Bartonian
Lutetian
Ypresian
LATE
MIDDLE
EARLY
LATE
EARLY
LATE
MIDDLE
EARLY
MIOCENE
OLIGO
EOCENE
0
5
10
15
20
25
30
35
40
45
50
55 Ma
A) Basin inversion
B) Capture of Yarlung Tsangpo from the Irrawaddy by the Brahmaputra
C) Initiation of orogen-parallel palaeo-Yarlung Tsangpo-Irrawaddy

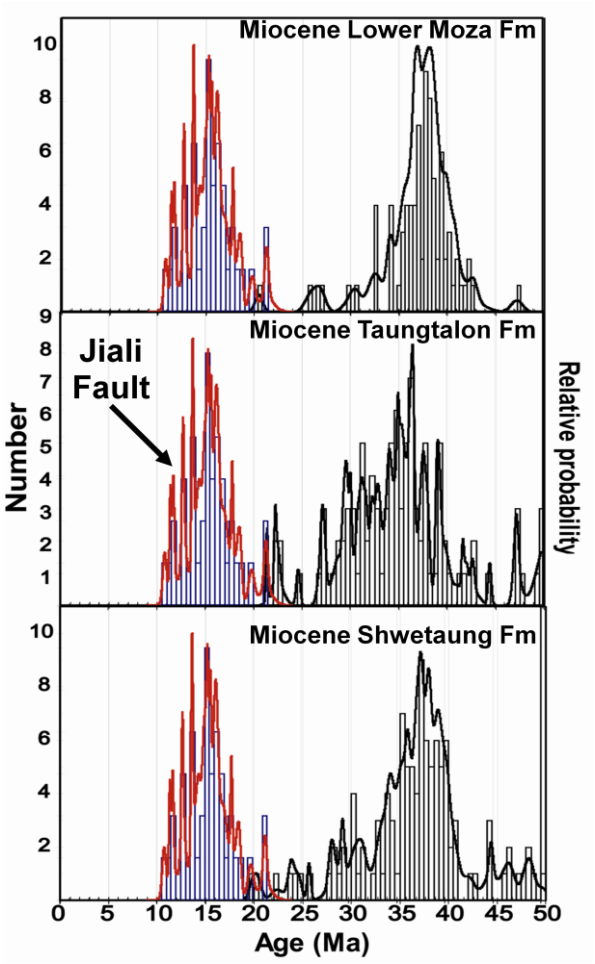

Figure 5.5 Probability density plot of $^{40}Ar/^{39}Ar$ detrital white mica cooling ages from the Miocene Central Burma Basin, arranged in stratigraphic order, compared with literature data for the Jiali Fault. Only ages less than 50 Ma are shown. For simplicity, only the stratigraphic succession from the Eastern Trough is shown. A minor overlap is observed in the Early Miocene Shwetaung Formation, however, for the most part, the cooling age populations from the Jiali shear zone are not recorded in sedimentary rocks of the Central Burma Basin that were deposited coevally with the main stage of shear. See text for references.

Two detrital sand samples taken from the Parlung River, northeast of the Namche Barwa syntaxis are dominated by detrital zircon fission track ages with older peak, not associated with the uplift of the Namche Barwa antiform that is thought to have initiated during the Late Miocene (~11 Ma), that include significant cooling populations of 18 ± 2 Ma, 24 ± 2 Ma, 35 ± 5 Ma, and 55 ± 10 Ma (Enkelmann et al., 2011; Stewart et al., 2008). The 18 Ma age mode represents a dominant population in the Parlung River,

indicating bedrock within the catchment experienced cooling through the zircon fission track closure temperature (~240° C) coincident with the timing of Jiali shear.

Strain accommodation over a broad area of Eastern Burma-Western Thailand was focused along the dextral Sagaing Fault that developed during the middle Miocene, accommodating two-thirds of the northward motion of the coupled plates (Bertrand et al., 2001; Pivnik et al., 1998). During the late Miocene and Pliocene, the progressive northward movement of the coupled India-west Burma plate led to the development of ENE-directed transpression and basin inversion along re-activated Miocene extensional faults within the Central Burma Basin (Pivnik et al., 1998) (Figure 5.4). This basin inversion is recorded in minor re-set zircon fission track ages, however additional low temperature thermochronology using a system with a lower closure temperature is required to better constrain the post-depositional deformation and possible burial re-heating within the Central Burma Basin.

5.4.1. Independent support for an Early Miocene timing for river capture

Independent evidence supporting and Early Miocene capture of the Yarlung Tsangpo from the Irrawaddy by the proto-Brahmaputra is found in studies conducting molecular phloygenetic analysis of two separate freshwater fish species of the Yarlung Tsangpo, Irrawaddy and Brahmaputra Rivers based on mitochondrial and nuclear genes. An Early Miocene (ca. 23–19 Ma; Ruber et al., 2004) timing for molecular divergence from a Yarlung Tsangpo-Irrawaddy clade into separate Yarlung Tsangpo-Brahmaputra and Irrawaddy clades that evolved independently since this time (Ratmuangkhwang et al., 2014; Rüber et al., 2004). The independent evolution of these fish species beginning in the Early Miocene supports the disconnection of the palaeo-Yarlung Tsangpo-Irrawaddy system via headward capture of the Yarlung Tsangpo by the Brahmaputra at a time consistent with the timing proposed in this study (Figure 5.4). Additionally, the intensification of the Asian monsoon during the Early Miocene (initiating at approximately 23 Ma) is contemporaneous with the rapid headward erosion of the proto-Brahmaputra River that resulted in the capture of the antecedent Yarlung Tsangpo from the Irrawaddy River, accelerated by enhanced erosion of the Greater Himalayan

metamorphic core and movement along the Main Central Thrust as a positive feedback system between climate, tectonics, exhumation and erosion developed in the eastern Himalayan orogen at this time (Clift et al., 2008; Clift et al., 2004; Zeitler, 2001) (Figure 5.4). Therefore the coupling of climatic, tectonic and surface processes plays a major role in the evolution of major river systems in the eastern Himalayan orogen.

Evidence of drainage capture by a tributary of the Brahmaputra River should also be recorded in the onshore and offshore sedimentary repositories of the eastern Himalaya. An Early Miocene timing of disconnection and capture of the Yarlung Tsangpo by a tributary of the proto-Brahmaputra system is consistent with the appearance of Gangdese-derived detritus in the eastern Himalayan foreland basin Siwalik Group sedimentary rocks (Cina et al., 2009; Chirouze et al., 2013; Lang and Huntington, 2014) (Figure 5.4). U-Pb dating of detrital zircons sampled from Upper Miocene and Pliocene sedimentary rocks of the eastern foreland basin, Arunachal Himalaya show substantial Cretaceous and Palaeocene age populations, interpreted to be sourced from the Asian Mesozoic to Tertiary magmatic arc, located north of the Yarlung Tsangpo Suture Zone (Cina et al., 2007). Cina et al. (2009) conducted U-Pb and Hf isotopic analysis on detrital zircon from the Middle and Upper Miocene Dafla and Subansiri Formations and the Pliocene Kimin Formation of the eastern Himalayan foreland basin (92-94°E) and showed the presence of Gangdese-derived detritus (15–30% of total zircon population) within sedimentary rocks from the Itanagar area (sampled near confluence of Subansiri and Brahmaputra Rivers) and the Bhalukpong area (sampled near confluence of Kameng and Brahmaputra river). In contrast, Gangdese detritus is absent from Lower Miocene to Pliocene foreland basin strata located farther west in the Sikkim Himalaya (88-89°E) (Cina et al., 2009). In their preferred model, the Yarlung Tsangpo was linked to the Brahmaputra River through the Subansiri River from ca. 10–3 Ma, prior to capture of the Yarlung Tsangpo by the Siang River at ca. 3 Ma, depositing detritus sourced from north of the Indus Yarlung suture zone in the eastern Himalayan foreland basin by 10 Ma via a west-ward flowing Brahmaputra River. Chirouze et al. (2013) demonstrated Miocene-Pliocene Siwalik Group sedimentary rocks sampled from the Bhalukpong area record the establishment of the modern Yarlung Tsangpo-

Brahmaputra system, connecting the Lhasa terrane and foreland basin by 7 Ma. The arrival of Gangdese detritus in the eastern foreland basin provides a minimum age for capture from the Irrawaddy River. The 10 Ma and 7 Ma timing contrasts with suggestions of a Pliocene-Pleistocene capture event (Brookfield, 1998; Burg et al., 1998; Clark et al., 2004; Stewart et al., 2008), but is in agreement with a Late Miocene disconnection (Booth et al., 2009; Ding et al., 2001; Liang et al., 2008).

Most recently, Lang & Huntington (2014) utilized detrital zircon U-Pb geochronology on Lower Miocene to Pliocene sedimentary rocks of the eastern Himalayan foreland basin sampled east of the Subansiri-Brahmaputra confluence to show the presence of Gangdese-derived detritus in the Lower, Middle and Upper Siwalik Group, consistent with an Early Miocene timing for the disconnection of the Yarlung Tsangpo-Irrawaddy system and the re-routing of Gangdese-derived sediment into the proto-Brahmaputra. A connection through the Subansiri is no longer viable, as these sediments were deposited east of the confluence of the Subansiri River and the west-ward flowing Brahmaputra River.

Their preferred model invokes an antecedent Yarlung-Siang-Brahmaputra River existing as far back as the early Miocene, earlier than the 10 Ma age proposed by Burg et al. (1998) and does not require a palaeo-Yarlung Tsangpo-Irrawaddy connection. Instead, they suggest a Parlung-Irrawaddy system transported Gangdese-derived detritus to the Central Burma Basin until capture of the Parlung River by the transverse Lohit River during the Early Miocene (Robinson et al., 2014). We reject this palaeo-connection as the upper reaches of the Parlung River lie within the northern Lhasa terrane, and suggest the arrival of Gangdese-derived detritus in the Lower Miocene Siwalik Group of the Himalayan foreland basin is consistent with the geologically rapid capture event, tentatively inferred from the short lag time (~ 1 Ma) inferred for the Shwetaung Formation, that suggests high exhumation rates within the source region.

The initial capture of the Yarlung Tsangpo from the Irrawaddy River during the Early Miocene (ca. 18 Ma) may have occurred by the transverse Lohit or Siang rivers, both tributaries to the Brahmaputra. Clark et al. (2004) suggest a palaeo Yarlung

Tsangpo-Irrawaddy system was initially captured by the Lohit River, followed by capture by the transverse Siang River that flows through the eastern Himalayan syntaxis. It is proposed here that the Yarlung Tsangpo was initially captured from the Irrawaddy River by the Lohit River during the Early Miocene (ca. 18 Ma) and the northward of the migration and uplift of the eastern Himalayan syntaxis during the Middle to Late Miocene led to successive capture of the Yarlung Tsangpo by the transverse Siang River, although a prior connection through the Dibang cannot be ruled out. The Jiali shear zone changed shear sense from sinistral to dextral at approximately 18 Ma and continued until 13 Ma (Lin et al., 2009). It is proposed here the Yarlung Tsangpo suffered a series of river capture events in a clockwise pattern, whereby several in flow of the Parlung River re-directed flow of the Yarlung Tsangpo into the Siang River prior to 10 Ma, after which, crustal processes and erosion became coupled, driving the rapid exhumation of the eastern Himalayan syntaxis that dominates the sediment load of the modern Brahmaputra River today. More detailed provenance analysis of the Cenozoic sedimentary rocks of the eastern Himalayan foreland basin is required to better delineate the post-Early Miocene evolution of the tributaries to the Brahmaputra River. Specifically, combined detrital zircon U-Pb and Lu-Hf isotopic analysis would trace detritus to specific source terranes, the isotopic signatures of which are well characterized by previous works. Additionally, late Cenozoic river terraces, if found to exist, within the upper reaches the Lohit, Dibang, Siang and Parlung Rivers would prove significant in better understanding the evolution of these river systems and the link between surface and crustal processes in tectonically active orogenic zones.

The Bengal Fan has only been drilled to depths dated at 18–17 Ma at the base of the core from Ocean Drilling Program Leg 116 (Copeland & Harrison, 1990; Corrigan & Crowley, 1990; Galy et al., 1996; France-Lanord et al., 2000). Analysis of the strontium, neodymium and osmium isotopic composition of sediment deposited in the Bengal Fan indicate a stable source area over the past 17 Ma, derived predominantly from the Greater Himalayan sequence and subordinate contributions from the Lesser Himalaya, Tethyan Himalayan sequence (France-Lanord et al., 1993; Derry and France-Lanord, 1996; Galy et al., 2010) minor contributions from the Transhimalayan

batholiths north of the Indus Yarlung suture zone are detected in the Bengal Fan since 12 Ma, consistent with the establishment of a Tsangpo-Brahmaputra river connection by this time (Galy et al., 2010). The presence of long lasting antecedent rivers draining the Asian terrane prior to and during latest Palaeocene-earliest Eocene collision and the delay of substantial sedimentation in the Himalayan foreland basin and Bay of Bengal derived from north of the Indus-Yarlung suture zone prior to the Miocene, deposited by rivers transverse to the rising orogen, cannot be reconciled with evidence of significant pre-Himalayan crustal thickening, uplift and erosion of the Lhasa terrane, recorded in the Cretaceous to Palaeogene sediments deposited in forearc (Durr, 1996; Wu et al., 2010) and back-arc (Leier et al., 2007a) basins in Tibet and extensive S-type granites derived from crustal melting to the north (Chiu et al., 2009; Zhu et al., 2011, 2009b).

This study has demonstrated an antecedent Yarlung Tsangpo-Irrawaddy system was established as the major river system draining the eastern Himalayas from as early as the Late Eocene, prior to capture of the Yarlung Tsangpo by the Brahmaputra River in the Early Miocene. The twelve kilometre thick succession of Cenozoic synorogenic sedimentary rocks deposited by this system in the Central Burma Basin may represent the most complete and accessible sedimentary record of early erosion from the eastern Himalayas and southern Lhasa terrane following the collision of India with Eurasia at ca. 55 Ma, and developed contemporaneously with the Indus Fan recording early erosion from Tibetan Transhimalayan sources of the western Himalaya (Clift et al., 2002; Clift, 2006). This palaeo-geographic reconstruction may in part explain the obscurity of early orogenic detritus, particularly sediment derived from north of the Indus-Yarlung suture zone, within the eastern foreland basin (Uddin et al., 2007; Cina et al., 2009) and the Bengal and Assam Basins (Uddin & Lundberg, 1998a; Uddin and Lundberg 1998b).

5.5. New Palaeogeographic Reconstruction

The following section illustrates the preferred model for sediment routing in the eastern Himalaya, sedimentation within the Central Burma Basin and specifically the evolution of the Irrawaddy River system through the Cenozoic. Adopting modified

palaeogeographic reconstructions of Hall (2002) and Morley (2011) from the Eocene onwards, the terrane evolution is shown to not contradict the palaeo-river system evolution suggested in this study, based on detrital provenance analysis of Cenozoic sedimentary rocks from the Central Burma Basin. This study adopts a moderate estimate of 300–450 kilometres for post- early Miocene offset along the dextral Sagaing Fault (Curray, 2005; Maung, 1987; Morley, 2002; Pivnik et al., 1998), as more extreme estimations (> 1100 kilometres) were based on the assumption that the West Burma magmatic arc was continuous with the Mogok Metamorphic Belt prior to shear (Mitchell, 1993). This is considered unlikely as granitoids within these two regions are shown to be isotopically, and largely temporally, distinct (Barley et al., 2003; Li et al., 2013; Mitchell et al., 2012; Mitchell, 1993; Searle et al., 2007). Additionally, detrital evidence for this amount of offset is lacking, as detrital zircon extracted from the Cenozoic Central Burma Basin sedimentary deposits do not record significant Permo-Triassic populations (This study; Liang et al., 2008; Wang et al., 2014) sourced from granitoids of this age that were widely emplaced throughout central and southern Thailand and Sumatra (Cobbing et al., 1992, 1986; Searle et al., 2012), that would have lain in close proximity to the West Burma Block prior to dextral shear. The major river systems, including the palaeo-Yarlung Tsangpo-Irrawaddy river system, flow parallel to major remnant Tethyan ocean suture zones, formed parallel to the developing orogen. The northern Lhasa magmatic belt is shown to be continuous with the Eastern Transhimalayan batholiths, Dianxi-Burma batholiths and the Eastern Burma-Western Thailand granite belt that intrudes the Mogok Metamorphic Belt and Slate Belt of Burma. The Tibetan Transhimalayan arc includes the Gangdese batholith, and extends around the eastern Himalayan syntaxis forming the Lohit Batholith of northeast India and the West Burma magmatic arc. The Central Burma Basin is offset from its northern extension into the Upper Irrawaddy Basin by the dextral Sagaing Fault.

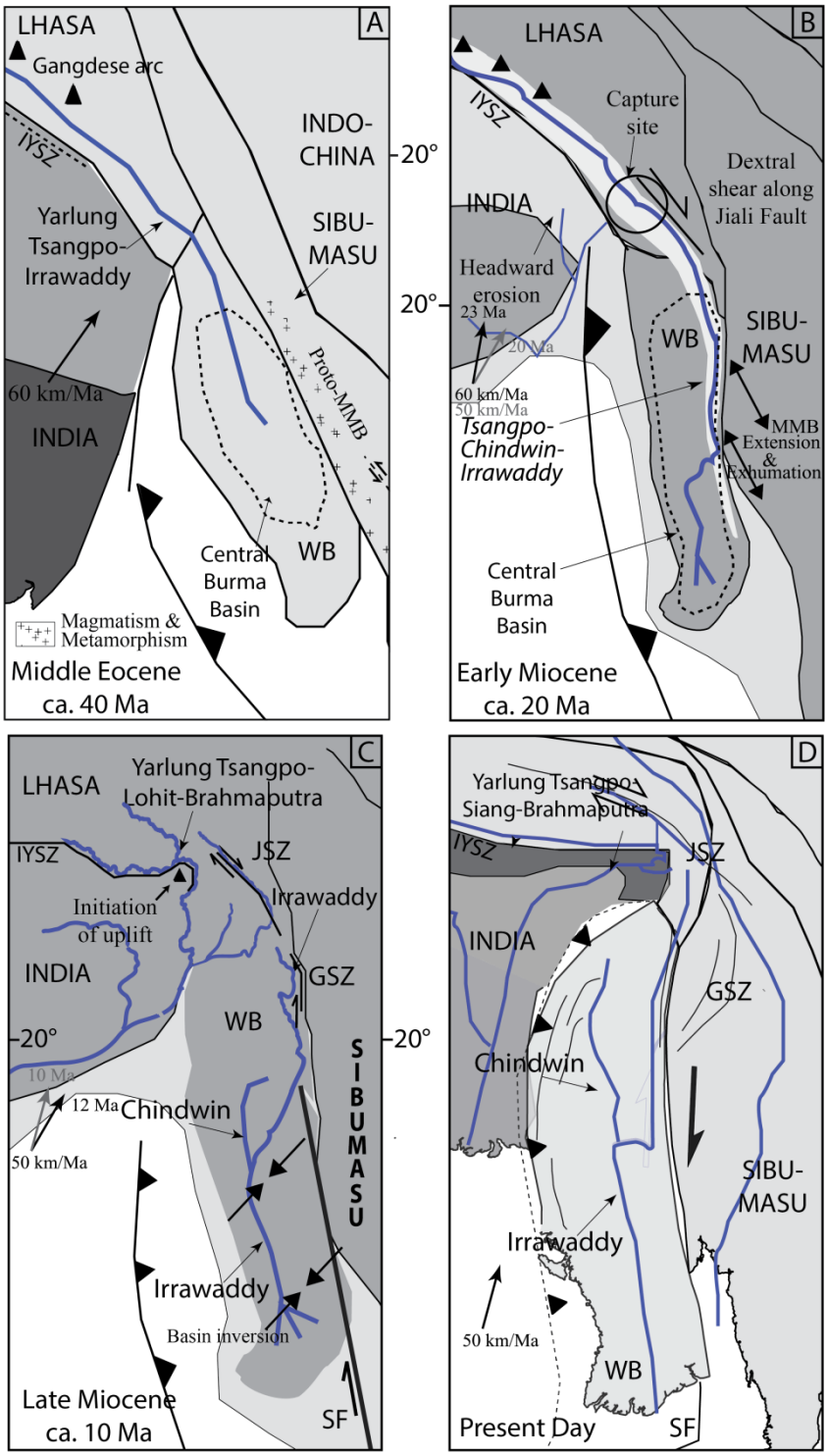

Figure 5.6 Schematic palaeogeographic reconstruction of the eastern Himalayan orogen from Late Eocene to Latest Miocene time. A) During the Late Eocene, and continuing through the Oligocene an antecedent Yarlung Tsangpo-Irrawaddy system was established transporting detritus sourced from the Gangdese magmatic arc of southern Tibet to the Central Burma Basin (modified from

Robinson et al., 2014 and Hall and Morley, 2004). B) During the Early Miocene, increased deformation is focused in the eastern syntaxis region through increased oroclinal bending and initiation of dextral shear along the Jiali shear zone. Hyper-oblique collision has coupled the West Burma Block and the Indian Plate (from Robinson et al., 2014). C) By the Middle Miocene, the Yarlung Tsangpo has been captured by the proto-Brahmaputra River as the singular system could not keep pace with deformation (From Robinson et al., 2014). D) During the Late Cenozoic, the West Burma Block continues to move northward along the Sagaing Fault. The Irrawaddy River and Yarlung Tsangpo-Siang-Brahmaputra Rivers have established catchment regions similar to that observed today (Modified from Hall and Morley, 2004). Rate and angle of convergence of India from Lee and Lawver (1995). IYSZ = Indus Yarlung suture zone; WB = West Burma Block; JSZ = Jiali shear zone; GSZ = Gaoligong shear zone; SF = Sagaing Fault

5.5.1. Middle-Late Eocene (ca. 42–34 Ma) and Oligocene (ca. 34–23 Ma)

During the early stages of the Himalayan orogeny, an antecedent, longitudinal Yarlung Tsangpo-Irrawaddy river system developed parallel to the orogen and data from this study reveals this connected existed as far back at the Late Eocene (ca. 42 Ma), and possibly as early as the Middle Eocene (ca. 46 Ma) based on independent biological and geological evidence (Rüber et al., 2004; Wang et al., 2014). This system likely linked through the Parlung River (Clark et al., 2004; Seeber and Gornitz, 1983), transporting arc-derived detritus of the Gangdese Batholith and associated volcanics of the southern Lhasa terrane, which represents the predominant sediment provenance, to the Central Burma Basin, infilling the basin from north to south through a prograding fluvial-deltaic system (Figure 5.5, A). The Eocene palaeo-shoreline lay at the approximate latitude of present day Mandalay (Khin, 1968). This region was experiencing differential exhumation and erosion following Neo-Tethyan slab breakoff beneath the southern Lhasa terrane and peak magmatic activity coinciding with the arrival of the Indian continent at ca. 50 Ma.

The early record of erosion from sedimentary depocenters in the eastern Himalayan foreland basin and remnant ocean basins shows a lack of orogenic material and specifically detritus sourced from Tibetan Transhimalayan regions, that is best explained by the transport of detritus to sedimentary basins that developed along the margins of the collision zone at this time, rather than through the Brahmaputra River. A minor arc-derived component was reported for Palaeogene sedimentary rocks of the Bengal Basin analyzed by Najman et al. (2008) that was linked to a Tibetan

Transhimalayan source, however it is possible this detritus was sourced from Tibetan Transhimalayan detritus carried to the Central Burma Basin by the Yarlung Tsangpo-Irrawaddy River. The Oligocene Padaung Formation contains a minor component of Palaeozoic to Proterozoic aged detrital zircons that are possibly derived from sediment mixing with detritus shed from the Indian continent in the westernmost region of the basin. At this time, the Indo-Burman Ranges were just beginning to experience uplift and exhumation initiating during the Late Eocene and continuing to the Oligocene (Allen et al., 2008; Mitchell, 1993) and may not yet have formed a barrier to depocenters to the west. Additionally, erosion of the uplifted Indo-Burman Ranges, containing material of mixed Tibet-Burma-India provenance, would have contributed sediment to both the east and west, as evidenced by the higher proportion of Palaeozoic and Proterozoic aged detrital zircons within Miocene formations of the Western Trough relative to those in the Eastern Trough.

Throughout the Oligocene, the Yarlung Tsangpo-Irrawaddy continued to carry detritus sourced from the Gangdese magmatic arc to the Central Burma Basin, which provided the predominant source for sediment at this time. During this time, the clockwise rotation of Southeast Asia increased coupling of the India and Burma plates as the subduction margin became progressively hyper-oblique. The unconformity in the Eastern Trough of the Central Burma Basin is speculatively related to crustal thickening and isostatic uplift due to ongoing high temperature metamorphism and granite emplacement along the eastern margin of Burma (Mogok Metamorphic Belt and Slate Belt). Initiation of northwest-southeast directed extension began during the middle Oligocene in the southern Shan Scarps and migrated northwards throughout the Early to Middle Miocene, when it contributed a greater proportion of detritus to the Central Burma Basin (Bertrand et al., 2001, 1999). In the eastern Himalayan syntaxis region, progressive northward movement of the continental Indian plate led to bending of suture zone and increased deformation at the northeast indenter region marked by metamorphism and magmatism as recorded by the Lhasa metasediments (Bomi and Nyingchi Group) (Zhang et al., 2008; Xu et al., 2013; Guo et al., 2012, 2011; Guan et al., 2011). Regional surface uplift may have accompanied the breakoff of the Indian

continental slab during the Oligocene that led to the generation of S-type magmatism in the eastern syntaxis region (Zhang et al., 2010), possibly recorded by detrital fission track populations within the modern Parlung River that record Palaeogene modes of ca. 35 Ma and 26 Ma (Enkelmann et al., 2011). This is supported by rapid retrograde metamorphism within the Lhasa terrane metasedimentary rocks that is thought to accompany rapid exhumation and anatexis (Dong et al., 2010; Guo et al., 2011; Pan et al., 2012; Xu et al., 2013; Xu et al., 2010; Zhang et al., 2008; Zhang et al., 2010a; Zhang et al., 2010c).

The Palaeogene sedimentary record within the Yarlung Tsangpo component of the river system is largely absent and poorly documented. Studied formations consist of the Palaeogene (~54 Ma; maximum depositional age) Liuqu and Oligo-Miocene Gangrinboche fluvial conglomerates that are exposed within the Indus Yarlung suture zone (Figure 2.3) (Aitchison et al., 2002; Aitchison et al., 2011; Davis et al., 2004; Wang et al., 2013). Davis et al. (2002) used detailed stratigraphic studies and clast petrography to conclude sediment of the Palaeogene Liuqu Conglomerate was deposited within an oblique strike-slip basin along the southern margin of an intra-Neotethys ocean island arc, sourced from the northern margin of the Indian continent, as no Gangdese-derived detritus sourced from north of the Indus Yarlung suture zone is observed. Alternatively, Wang et al. (2010) utilized petrographic, U-Pb and Lu-Hf isotopic analyses on detrital zircons of this formation to postulate both Asian and Indian sources contributed to the Liuqu Formation, and interpreted the formation as synorogenic Palaeogene (Middle Eocene) molasse. The Gangdese component of the detrital record is interpreted to be primarily derived from sediment recycling of the Xigaze forearc basin itself due to lack of ages < 80 Ma despite contemporaneous magmatism and volcanism in the Gangdese arc (Wang et al., 2010). Wang et al. (2010) suggest the deposition of the Liuqu Formation is linked to isostatic uplift of the southern margin of the Lhasa terrane in the Middle-Late Eocene following Neotethyan slab breakoff (Dai et al., 2013; He et al., 2007; Lee et al., 2009) and the uplifted region lay to the north, creating a barrier for sediment transport to the fore-arc region. This is

contemporaneous with the proposed timing of initiation of the Yarlung Tsangpo-Irrawaddy River, the development of which may be linked to this uplift.

Deformation and thrusting within the Indus Yarlung suture zone region following the collision of India with Asia may have led to tectonic burial of the Yarlung Tsangpo Palaeogene sedimentary record or removed through uplift and erosion following thrusting of Asian crust southwards over the Tethyan Himalaya along the Gangdese Thrust (Figure 2.3), active from ca. 30–23 Ma to ca. 18 Ma based on low temperature $^{40}Ar/^{39}Ar$ mica and fission track thermochronology (Harrison, 2000; Yin, 1994).

In the eastern Himalayan syntaxis, rocks of the lower Bomi Group, which experienced amphibolite-facies metamorphism and anatexis at ca. 37 Ma, are exposed directly north of the Indus Yarlung suture zone and contain zircons with inherited magmatic cores ranging in age from ca. 74–41.5 Ma (Xu et al., 2008). These rocks are interpreted as relic forearc basin sediments sourced primarily from the Gangdese magmatic arc that were entrained and subducted with Indian continental crust to mid-crustal levels (Xu et al., 2008). These rocks were later exposed due to the high rates of exhumation within the Namche Barwa massif, and indicate Palaeogene sedimentary rocks of the Gangdese forearc basin along strike may also have been, and remain buried beneath the southern Lhasa terrane.

The Upper Oligocene to Lower Miocene Gangrinboche conglomerates outcrop north of the Indus Yarlung suture zone in a narrow, east-west trending belt stretching over 2,000 kilometres, indicating a regional mechanism for creating significant relief along the southern Lhasa terrane at this time (Figure 2.3) (Aitchison et al., 2002; Davis et al., 2004; Davis et al., 2002; Wang et al., 2013). Although previous studies suggest a tectonic contact between the Oligocene to Miocene conglomerates and rocks of the Lhasa terrane (south-directed Gangdese Thrust) (Yin and Harrison, 2000; Yin et al., 1994), Aitchison et al. (2003) reports these conglomerates were deposited unconformably onto an erosion surface of igneous rocks of the Gangdese Batholith, and mylonites within the shear zone actually record a strong regional foliation within the Mesozoic strata of the Lhasa terrane. These sediments were laid down by an axial

braided river (palaeo-Yarlung Tsangpo), running parallel to the east-west strike of the Himalayan orogen (Aitchison et al., 2002; Aitchison et al., 2011).

5.5.2. Early Miocene (ca. 23-18 Ma)

A significant change in sediment provenance is observed in the Early Miocene sedimentary units of the Central Burma Basin interpreted to reflect the breakdown of the Yarlung Tsangpo-Irrawaddy river system and re-routing of Tibetan Transhimalayan detritus to the eastern Himalayan foreland basin via a tributary to the Brahmaputra (Figure 5.6 B, C). This accompanied increased coupling and northward migration of the India-Burma plates throughout Oligo-Miocene times leading to a change in the regional stress regime within Burma, where northwest-southeast directed extension in Burma migrated to the northern Shan Scarps and renewed extension occurred within the Central Burma Basin (Bertrand and Rangin, 2003; Morley, 2009; Pivnik et al., 1998).

The initiation of sinistral motion along the Jiali shear zone from ca. 22–18 Ma and change to dextral shear from 18 Ma onwards, accommodated the clockwise rotation of crustal blocks around the eastern Himalayan syntaxis and southeast-directed lower crustal flow of the Tibetan Plateau (Clark and Royden, 2000; Lee et al., 2003; Lin et al., 2009). This shift in strain accommodation from farther afield along the Red River shear zone to major dextral strike-slip shear zones (Jiali-Gaoligong-Sagaing) also coincides with the initiation of the Asian monsoon leading to focused precipitation along the Himalayan front and is dynamically linked to the onset exhumation of the Greater Himalayan Sequence metamorphic core (Clift et al., 2008). This likely accelerated the headward erosion of the proto-Brahmaputra River, whereas the Yarlung Tsangpo-Irrawaddy River, could not keep pace with increasing and focused deformation in the eastern syntaxis region. A recent study by Lang and Huntington (2014) shows promise in independently verifying the Early Miocene age of disconnection between the Yarlung Tsangpo-Irrawaddy system and subsequent capture by a tributary of the Brahmaputra. The arrival of detritus sourced from the Gangdese magmatic arc in the Lower Miocene sedimentary rocks of the Eastern Himalayan foreland basin, upstream of the Subansiri-Brahmaputra confluence strongly suggests the latter was not involved in the initial re-

routing of sediment sourced from north of the Indus Yarlung suture zone to the foreland basin as suggested by Cina et al. (2009) (Figure 1.1, inset, 5.1). It is proposed that the Yarlung Tsangpo was initially captured by the Lohit River, followed by a later capture by the Siang River, possibly as dextral shear along the Jiali Fault intensified and the Parlung River reversed its flow, however further work is needed to explore these ideas.

5.5.3. Middle to Late Miocene (ca. 16-10 Ma)

By the Middle Miocene, the Yarlung Tsangpo and Irrawaddy River systems were disconnected (Figure 5.6 C, D). The loss of stream power in the headwaters of the Irrawaddy system led to the development of a meandering river system over a broad flood plain. During the Middle to Late Miocene, the West Burma Block, coupled with the Indian Plate, was carried northward along the dextral Sagaing Fault, accompanying extension in the Andaman Sea (Curray, 2005; Morley et al., 2013). Strain accommodation within Burma shifted from a transpressional regime in the western Sibumasu Block to a transtensional regime, where northwest-southeast direction extension dominated the regional geology during the Middle Miocene (Bertrand et al., 2001, 1999; Bertrand and Rangin, 2003; Morley, 2009), followed by compressional deformation that re-activated faults within the basin (Pivnik et al., 1998). This uplift may have driven headward erosion of the Chindwin River (tributary to the Irrawaddy River) towards the northwest.

Chapter 6. Future Work and Conclusions

6.1. Future Work

The co-evolution of surface, crustal, climatic processes with major river systems in orogenic settings, particularly the understudied eastern Himalayan region, is an exciting topic for future research With the dataset obtained in this study, it has been established that sediment provenance studies on Cenozoic sedimentary rocks of the Central Burma Basin utilizing isotopic analysis of single grain detrital minerals have demonstrated the establishment of an antecedent Yarlung Tsangpo-Irrawaddy river system as early as the Late Eocene, possibly the Middle Eocene (ca. 46 Ma) (Rüber et al., 2004; Wang et al., 2014). This highlights the need for further investigation into the sediment source provenance of Central Burma Basin strata older than that sampled in this study (Late Eocene) as this data may have important implications for the co-evolution of longitudinal, orogen-parallel river systems, surface and crustal processes and erosion during the early stages of the Himalayan orogeny.

Prior to disconnection, the Gangdese magmatic arc of the southern Lhasa terrane was the dominant source provenance, with intra-syntaxis sources becoming more important following capture. This knowledge can be used to test the viability of other detrital heavy mineral suites for future provenance research, such as garnet and chrome spinel geochemistry, which are less expensive techniques and more readily available. The potential for these mineral suites to complement geochronology data would prove particularly useful in sediment provenance, where bedrock studies within the catchment allowing for direct comparison are absent. This may prove highly successful in identifying local source lithologies outcropping within Burma, where bedrock studies are limited and largely inhibited by lack of accessibility and provide an important record of the geological evolution of Burma. It is hypothesized that a change in detrital garnet geochemistry would be observed between the Palaeogene and Neogene samples, reflecting the loss of the prominent arc source and increasing contribution from metamorphic and magmatic rocks generated from crustal melting within the Dianxi-Burma and Mogok Metamorphic Belt during progressive exhumation throughout the

Miocene. Additionally, it would interesting to address the applicability of garnet geochemistry provenance fields in ternary diagrams available in the literature that are largely based on garnet analysis from regions within Scotland and the North Sea (Morton et al., 2004; Morton et al., 2005). Chrome spinel geochemistry is expected to record a supra-subduction zone geochemistry and the proportion is hypothesized to decrease through time.

The present work is limited by the sampling of incomplete stratigraphic successions, necessitated by the presence of an Oligocene aged unconformity within the Eastern Trough of the Central Burma Basin. Additionally, geochronology and thermochronology conducted in this study were largely unable to better resolve the depositional age of the sedimentary formations sampled. Future sedimentary provenance studies in the Central Burma Basin would benefit from detailed geological mapping of a more complete sedimentary section, or ideally drilling core, with emphasis on specific marker beds. This would allow cross-basin correlation of stratigraphic units and possible variations in the sedimentation history between the Eastern and Western Troughs, which could aid in hydrocarbon exploration studies.

Interpretations of stratigraphic age, re-set low temperature data and inferred rate of source exhumation (detrital lag times) and would be greatly enhanced by clay mineralogy and illite crystallinity data determined by X-ray diffraction (Kübler and Jaboyedoff, 2000), which can be used to provide a semi-quantitative estimate of post-depositional burial temperatures achieved in the basin to determine whether there is the potential for thermal resetting of grains.

This work has highlighted the usefulness of combined detrital zircon U-Pb and Lu-Hf isotopic analysis in determining sediment provenance of rocks deposited in the eastern Himalayan sedimentary repositories, as the source regions contain isotopically distinct bedrock signatures. A recent study by Lang and Huntington (2014) shows promise in independently verifying the Early Miocene age of disconnection between the Yarlung Tsangpo-Irrawaddy system and subsequent capture by a tributary of the Brahmaputra, whereby detrital zircon U-Pb age distributions were used to identify the

arrival of detritus source from the Gangdese magmatic arc in the Lower Miocene sedimentary rocks of the Eastern Himalayan foreland basin. The use of Lu-Hf isotopic analysis would greatly enhance the robustness of this interpretation and is an avenue that is worth exploring. This sedimentary record also has to potential to record the initiation of the Yarlung Tsangpo-Siang-Brahmaputra system that is believed to be established prior to rapid uplift and river incision and the role of this system as a driver in the rapid exhumation of the eastern Himalayan syntaxis, which may not longer be recorded in bedrock due to erosion. An Early Miocene maximum age for the development of the modern Yarlung Tsangpo-Brahmaputra system is provided by this study. Additionally, detailed sedimentary provenance studies in this region can be used to test hypotheses of post-Early Miocene drainage re-organization (i.e. clockwise capture of the Yarlung Tsangpo by the Lohit-Dibang prior to Siang River).

6.2 Conclusions

This research set out to investigate the evolution of major river systems draining the eastern Himalayan syntaxis and the role of major river capture events in the development of the eastern Himalayan orogen. This study adopted a multi-technique approach to determine the sediment provenance of a suite of Eocene, Oligocene and Miocene sedimentary rocks from the Central Burma Basin deposited by the Irrawaddy River in order to test the hypothesis that the Yarlung Tsangpo of southern Tibet formerly drained into the proto-Irrawaddy River prior to its capture by the Brahmaputra River via headward erosion. The timing and mechanism for this river capture event was largely unknown with Late Miocene (< 10 Ma) (Booth et al., 2009; Booth et al., 2004; Brookfield, 1998; Ding et al., 2001; Liang et al., 2008) and Pliocene (ca. 4 Ma) (Burg et al., 1998; Clark et al., 2004; Stewart et al., 2008) ages suggested. Specifically, detrital mineral geochronology (zircon U-Pb), thermochronology (zircon fission track and white mica $^{40}Ar/^{39}Ar$) and geochemistry (zircon Lu-Hf) datasets were compared to published literature datasets from bedrock of isotopically distinct potential source regions in the modern Yarlung Tsangpo and Irrawaddy River catchments.

Data from the Late Eocene Pondaung Formation records a primary sediment source provenance from the Gangdese magmatic arc that lies exclusively within the modern Yarlung Tsangpo catchment, as evidenced by detrital zircons with Cretaceous to Eocene U-Pb and fission track ages characterized by predominantly high, positive εHf(t) values and mostly pre-Himalayan $^{40}Ar/^{39}Ar$ white mica cooling ages, consistent with the cooling history of the Lhasa terrane. It is concluded that an antecedent Yarlung Tsangpo-Irrawaddy river system was established as early as the Late Eocene (ca. 42 Ma), transporting detritus derived from north of the Indus Yarlung suture zone to the Central Burma Basin and formed the major river system draining the eastern Himalayan orogen at this time. Therefore, the Yarlung Tsangpo-Irrawaddy river system evolved independently from the other major river systems of Southeast Asia (Red, Mekong, Salween rivers) draining the southeast Tibetan Plateau during the Cenozoic, in agreement with the works of van Hoang et al. (2010, 2009) and (Clift et al., 2006a; Clift et al., 2006b) and contrary to the work of Clark et al. (2004). The Oligocene Padaung Formation also records a dominant juvenile, magmatic arc source provenance, interpreted as the Gangdese magmatic arc, suggesting the singular Yarlung Tsangpo-Irrawaddy system persisted throughout Oligocene time.

A significant change in provenance is observed during the deposition of the Early Miocene Shwetaung Formation and younger Miocene formations. The contribution of arc-derived detritus as indicated by detrital zircons with Gangdese-like isotopic signatures decreases and input from intra-syntaxis orogenic source terranes increase through time. The abrupt change in $^{40}Ar/^{39}Ar$ age spectra observed in the oldest Miocene deposits and all the younger Miocene deposits sampled reflects a change in provenance from a single, sustained source area which is interpreted to most likely be in the modern Irrawaddy catchment, potentially from the metamorphic rocks of east Burma.

The change in sediment provenance, as evidenced by single grain detrital mineral analysis conducted in this study, between deposition of Eocene-Oligocene and Miocene sedimentary rocks of the Central Burma Basin is interpreted to be the result of the

breakdown of a singular Yarlung Tsangpo-Irrawaddy river system and subsequent capture of the Yarlung Tsangpo by the Brahmaputra River, leading to the loss of the southern Lhasa terrane, and specifically the Gangdese Batholith, as a source terrane from the Early Miocene onwards. This disconnection is attributed to increased deformation in the eastern Himalayan syntaxis region in response to the continued northward migration of the Indian continent and the palaeo-river could not keep pace. Following disconnection, the Irrawaddy River established a course similar to that observed in the present day. It is suggested that the Yarlung Tsangpo was initially captured by the Lohit River, and later by the Siang River, as the eastern Himalayan syntaxis migrated northward, forming a crustal-scale antiform, antecedent to rapid exhumation driven in part by erosion.

This study enhances the understanding of the evolution of major river systems in active orogenic settings and the potential of the synorogenic sedimentary rocks to record major river capture events. This in turn can provide insight into tectono-thermal events that may not be recorded in the hinterland bedrock and the dynamic relationship between surface and crustal processes. This work describes one such relationship where Cenozoic drainage evolution and river capture events involving the major river systems draining the eastern Himalayan syntaxis region (Yarlung Tsangpo, Irrawaddy and Brahmaputra river systems) are shown to be driven by the coupling of tectonics, climate, exhumation and erosion. Understanding the rate of landscape response and mechanisms driving drainage re-organization is essential for future studies exploring the link between focused deformation in the eastern Himalayan syntaxis region and riverine driven erosion.

References

Aikman, A. B., Harrison, T. M., and Lin, D., 2008, Evidence for Early (<44 Ma) Himalayan Crustal Thickening, Tethyan Himalaya, southeastern Tibet: Earth and Planetary Science Letters, v. 274, no. 1–2, p. 14-23.

Aitchison, J. C., Davis, A. M., Badengzhu, and Luo, H., 2003, The Gangdese thrust: a phantom structure that did not raise Tibet: Terra Nova, v. 15, no. 3, p. 155-162.

Aitchison, J. C., Davis, A. M., and Luo, H., 2002, New constraints on the India–Asia collision: the lower Miocene Gangrinboche conglomerates, Yarlung Tsangpo suture zone, SE Tibet: Journal of Asian Earth Sciences, v. 21, no. 3, p. 251-263.

Aitchison, J. C., Xia, X., Baxter, A. T., and Ali, J. R., 2011, Detrital zircon U–Pb ages along the Yarlung-Tsangpo suture zone, Tibet: Implications for oblique convergence and collision between India and Asia: Gondwana Research, v. 20, no. 4, p. 691-709.

Ali, J. R., and Aitchison, J. C., 2008, Gondwana to Asia: Plate tectonics, paleogeography and the biological connectivity of the Indian sub-continent from the Middle Jurassic through latest Eocene (166–35 Ma): Earth-Science Reviews, v. 88, no. 3–4, p. 145-166.

Alizai, A., Carter, A., Clift, P. D., VanLaningham, S., Williams, J. C., and Kumar, R., 2011, Sediment provenance, reworking and transport processes in the Indus River by U–Pb dating of detrital zircon grains: Global and Planetary Change, v. 76, no. 1, p. 33-55.

Allen, R., Najman, Y., Carter, A., Barfod, D., Bickle, M., Chapman, H., Garzanti, E., Vezzoli, G., Ando, S., and Parrish, R. R., 2008, Provenance of the Tertiary sedimentary rocks of the Indo-Burman Ranges, Burma (Myanmar): Burman arc or Himalayan-derived?: Journal of the Geological Society, v. 165, no. 6, p. 1045-1057.

Antolín, B., Appel, E., Montomoli, C., Dunkl, I., Ding, L., Gloaguen, R., and El Bay, R., 2011, Kinematic evolution of the eastern Tethyan Himalaya: constraints from magnetic fabric and structural properties of the Triassic flysch in SE Tibet: Geological Society, London, Special Publications, v. 349, no. 1, p. 99-121.

Barber, A. J., Crow, M. J., and De Smet, M. E. M., 2005, Chapter 14 Tectonic Evolution: Geological Society, London, Memoirs, v. 31, no. 1, p. 234-259.

Barley, M. E., Pickard, A. L., Zaw, K., Rak, P., and Doyle, M. G., 2003, Jurassic to Miocene magmatism and metamorphism in the Mogok metamorphic belt and the India-Eurasia collision in Myanmar: Tectonics, v. 22, no. 3, p. 1019.

Beard, K. C., Marivaux, L., Chaimanee, Y., Jaeger, J.-J., Marandat, B., Tafforeau, P., Soe, A. N., Tun, S. T., and Kyaw, A. A., 2009, A new primate from the Eocene Pondaung Formation of Myanmar and the monophyly of Burmese amphipithecids: Proceedings of the Royal Society B: Biological Sciences.

Beaumont, C., Jamieson, R., Nguyen, M., and Lee, B., 2001, Himalayan tectonics explained by extrusion of a low-viscosity crustal channel coupled to focused surface denudation: Nature, v. 414, no. 6865, p. 738-742.

Belousova, E., Griffin, W., O'Reilly, S., and Fisher, N., 2002, Igneous zircon: trace element composition as an indicator of source rock type: Contributions to Mineralogy and Petrology, v. 143, no. 5, p. 602-622.

Benammi, M., Soe, A. N., Tun, T., Bo, B., Chaimanee, Y., Ducrocq, S., Thein, T., Wai, S., and Jaeger, J. J., 2002, First magnetostratigraphic study of the Pondaung Formation: implications for the age of the Middle Eocene anthropoids of Myanmar: The journal of geology, v. 110, no. 6, p. 748-756.

Bender, F., 1983 Geology of Burma, Berlin, Borntraeger, 260 p.:

Bernet, M., Brandon, M. T., Garver, J. I., and Molitor, B. R., 2004, Fundamentals of detrital zircon fission-track analysis for provenance and exhumation studies with examples from the European Alps.

Bernet, M., and Garver, J. I., 2005, Fission-track analysis of detrital zircon: Reviews in mineralogy and geochemistry, v. 58, no. 1, p. 205-237.

Bernet, M., and Spiegel, C., 2004, Introduction: detrital thermochronology: Geological Society of America Special Papers, v. 378, p. 1-6.

Bernet, M., van der Beek, P., Pik, R., Huyghe, P., Mugnier, J. L., Labrin, E., and Szulc, A., 2006, Miocene to Recent exhumation of the central Himalaya determined from combined detrital zircon fission-track and U/Pb analysis of Siwalik sediments, western Nepal: Basin Research, v. 18, no. 4, p. 393-412.

Bertrand, G., and Rangin, C., 2003, Tectonics of the western margin of the Shan plateau (central Myanmar): implication for the India–Indochina oblique convergence since the Oligocene: Journal of Asian Earth Sciences, v. 21, no. 10, p. 1139-1157.

Bertrand, G., Rangin, C., Maluski, H., and Bellon, H., 2001, Diachronous cooling along the Mogok Metamorphic Belt (Shan scarp, Myanmar): the trace of the northward migration of the Indian syntaxis: Journal of Asian Earth Sciences, v. 19, no. 5, p. 649-659.

Bertrand, G., Rangin, C., Maluski, H., Han, T. A., Thein, M., Myint, O., Maw, W., and Lwin, S., 1999, Cenozoic metamorphism along the Shan scarp (Myanmar): evidences for ductile shear along the Sagaing fault or the northward migration of the eastern Himalayan syntaxis?: Geophysical Research Letters, v. 26, no. 7, p. 915-918.

Blichert-Toft, J., and Albarède, F., 1997, The Lu-Hf isotope geochemistry of chondrites and the evolution of the mantle-crust system: Earth and Planetary Science Letters, v. 148, no. 1–2, p. 243-258.

Bodet, F., and Schärer, U., 2000, Evolution of the SE-Asian continent from U-Pb and Hf isotopes in single grains of zircon and baddeleyite from large rivers: Geochimica et Cosmochimica Acta, v. 64, no. 12, p. 2067-2091.

Booth, A. L., Chamberlain, C. P., Kidd, W. S. F., and Zeitler, P. K., 2009, Constraints on the metamorphic evolution of the eastern Himalayan syntaxis from geochronologic and petrologic studies of Namche Barwa: Geological Society of America Bulletin, v. 121, no. 3-4, p. 385-407.

Booth, A. L., Zeitler, P. K., Kidd, W. S. F., Wooden, J., Liu, Y., Idleman, B., Hren, M., and Chamberlain, C. P., 2004, U-Pb zircon constraints on the tectonic evolution of southeastern Tibet, Namche Barwa area: American Journal of Science, v. 304, no. 10, p. 889-929.

Bouvier, A., Vervoort, J. D., and Patchett, P. J., 2008, The Lu–Hf and Sm–Nd isotopic composition of CHUR: Constraints from unequilibrated chondrites and

implications for the bulk composition of terrestrial planets: Earth and Planetary Science Letters, v. 273, no. 1–2, p. 48-57.

Brewer, I., Burbank, D., and Hodges, K., 2003, Modelling detrital cooling-age populations: Insights from two Himalayan catchments: Basin Research, v. 15, no. 3, p. 305-320.

Brookfield, M. E., 1998, The evolution of the great river systems of southern Asia during the Cenozoic India-Asia collision: rivers draining southwards: Geomorphology, v. 22, no. 3–4, p. 285-312.

Burg, J. P., Nievergelt, P., Oberli, F., Seward, D., Davy, P., Maurin, J. C., Diao, Z., and Meier, M., 1998, The Namche Barwa syntaxis: evidence for exhumation related to compressional crustal folding: Journal of Asian Earth Sciences, v. 16, no. 2, p. 239-252.

Carrapa, B., DeCelles, P. G., Reiners, P. W., Gehrels, G. E., and Sudo, M., 2009, Apatite triple dating and white mica $^{40}Ar/^{39}Ar$ thermochronology of syntectonic detritus in the Central Andes: A multiphase tectonothermal history: Geology, v. 37, no. 5, p. 407-410.

Carrapa, B., Orme, D., DeCelles, P., Kapp, P., Cosca, M., and Waldrip, R., 2014, Miocene burial and exhumation of the India-Asia collision zone in southern Tibet: Response to slab dynamics and erosion: Geology, p. G35350. 35351.

Carrapa, B., Wijbrans, J., and Bertotti, G., 2004, Detecting provenance variations and cooling patterns within the western Alpine orogen through 40Ar/39Ar geochronology on detrital sediments: The Tertiary Piedmont Basin, northwest Italy: Geological Society of America Special Papers, v. 378, p. 67-103.

Carter, A., 1999, Present status and future avenues of source region discrimination and characterization using fission track analysis: Sedimentary Geology, v. 124, no. 1–4, p. 31-45.

Carter, A., and Bristow, C., 2003, Linking hinterland evolution and continental basin sedimentation by using detrital zircon thermochronology: a study of the Khorat Plateau Basin, eastern Thailand: Basin Research, v. 15, no. 2, p. 271-285.

Carter, A., and Bristow, C. S., 2000, Detrital zircon geochronology: enhancing the quality of sedimentary source information through improved methodology and combined U–Pb and fission-track techniques: Basin Research, v. 12, no. 1, p. 47-57.

Cawood, P. A., Nemchin, A. A., Freeman, M., and Sircombe, K., 2003, Linking source and sedimentary basin: Detrital zircon record of sediment flux along a modern river system and implications for provenance studies: Earth and Planetary Science Letters, v. 210, no. 1–2, p. 259-268.

Chen, W., Li, Q., Hao, J., Zhou, X., and Sun, M., 1999a, New evidence II for MDD model of thermal evolution history of Gangdese batholith: Chinese Science Bulletin, v. 44, no. 8, p. 736-739.

Chen, W., Li, Q., Hao, J., Zhou, X., Wan, J., and Sun, M., 1999b, Postcrystallization thermal evolution history of Gangdese batholithic zone and its tectonic implication: Science in China Series D: Earth Sciences, v. 42, no. 1, p. 37-44.

Chen, Z., Liu, Y., Tang, W., Zhao, J., Zhang, X., Burchfiel, B., King, R., Royden, L., and Wang, E., 2000, Global Positioning System measurements from eastern

Tibet and their implications for India/Eurasia intercontinental deformation: Journal of Geophysical Research, v. 105, no. B7, p. 16,215-216,227.

Chirouze, F., Bernet, M., Huyghe, P., Erens, V., Dupont-Nivet, G., and Senebier, F., 2012a, Detrital thermochronology and sediment petrology of the middle Siwaliks along the Muksar Khola section in eastern Nepal: Journal of Asian Earth Sciences, v. 44, no. 0, p. 94-106.

Chirouze, F., Huyghe, P., van der Beek, P., Chauvel, C., Chakraborty, T., Dupont-Nivet, G., and Bernet, M., 2012b, Tectonics, exhumation, and drainage evolution of the eastern Himalaya since 13 Ma from detrital geochemistry and thermochronology, Kameng River Section, Arunachal Pradesh: Geological Society of America Bulletin.

Chiu, H. Y., Chung, S. L., Wu, F. Y., Liu, D., Liang, Y. H., Lin, I., Iizuka, Y., Xie, L. W., Wang, Y., and Chu, M. F., 2009, Zircon U–Pb and Hf isotopic constraints from eastern Transhimalayan batholiths on the precollisional magmatic and tectonic evolution in southern Tibet: Tectonophysics, v. 477, no. 1, p. 3-19.

Chu, M.-F., Chung, S.-L., O'Reilly, S. Y., Pearson, N. J., Wu, F.-Y., Li, X.-H., Liu, D., Ji, J., Chu, C.-H., and Lee, H.-Y., 2011, India's hidden inputs to Tibetan orogeny revealed by Hf isotopes of Transhimalayan zircons and host rocks: Earth and Planetary Science Letters, v. 307, no. 3–4, p. 479-486.

Chu, M.-F., Chung, S.-L., Song, B., Liu, D., O'Reilly, S. Y., Pearson, N. J., Ji, J., and Wen, D.-J., 2006, Zircon U-Pb and Hf isotope constraints on the Mesozoic tectonics and crustal evolution of southern Tibet: Geology, v. 34, no. 9, p. 745-748.

Chung, S.-L., Liu, D., Ji, J., Chu, M.-F., Lee, H.-Y., Wen, D.-J., Lo, C.-H., Lee, T.-Y., Qian, Q., and Zhang, Q., 2003, Adakites from continental collision zones: Melting of thickened lower crust beneath southern Tibet: Geology, v. 31, no. 11, p. 1021-1024.

Chung, S. L., Chu, M. F., Ji, J., O'Reilly, S. Y., Pearson, N. J., Liu, D., Lee, T. Y., and Lo, C. H., 2009, The nature and timing of crustal thickening in Southern Tibet: geochemical and zircon Hf isotopic constraints from postcollisional adakites: Tectonophysics, v. 477, no. 1, p. 36-48.

Chung, S. L., Chu, M. F., Zhang, Y., Xie, Y., Lo, C. H., Lee, T. Y., Lan, C. Y., Li, X., Zhang, Q., and Wang, Y., 2005, Tibetan tectonic evolution inferred from spatial and temporal variations in post-collisional magmatism: Earth-Science Reviews, v. 68, no. 3, p. 173-196.

Chung, S. L., Lo, C. H., Lee, T. Y., Zhang, Y., Xie, Y., Li, X., Wang, K. L., and Wang, P. L., 1998, Diachronous uplift of the Tibetan plateau starting 40 Myr ago: Nature, v. 394, no. 6695, p. 769-773.

Cina, S. E., Yin, A., Grove, M., Dubey, C. S., Shukla, D. P., Lovera, O. M., Kelty, T. K., Gehrels, G. E., and Foster, D. A., 2009, Gangdese arc detritus within the eastern Himalayan Neogene foreland basin: Implications for the Neogene evolution of the Yalu–Brahmaputra River system: Earth and Planetary Science Letters, v. 285, no. 1, p. 150-162.

Ciochon, R. L., and Gunnell, G. F., 2002, Chronology of primate discoveries in Myanmar: Influences on the anthropoid origins debate: American Journal of Physical Anthropology, v. 119, no. S35, p. 2-35.

Clark, M., Schoenbohm, L., Royden, L., Whipple, K., Burchfiel, B., Zhang, X., Tang, W., Wang, E., and Chen, L., 2004, Surface uplift, tectonics, and erosion of eastern Tibet from large-scale drainage patterns: Tectonics, v. 23, no. 1, p. TC1006.

Clark, M. K., and Bilham, R., 2008, Miocene rise of the Shillong Plateau and the beginning of the end for the Eastern Himalaya: Earth and Planetary Science Letters, v. 269, no. 3–4, p. 337-351.

Clark, M. K., and Royden, L. H., 2000, Topographic ooze: Building the eastern margin of Tibet by lower crustal flow: Geology, v. 28, no. 8, p. 703-706.

Clift, P. D., 2006, Controls on the erosion of Cenozoic Asia and the flux of clastic sediment to the ocean: Earth and Planetary Science Letters, v. 241, no. 3–4, p. 571-580.

Clift, P. D., and Blusztajn, J., 2005, Reorganization of the western Himalayan river system after five million years ago: Nature, v. 438, no. 7070, p. 1001-1003.

Clift, P. D., Blusztajn, J., and Nguyen, A. D., 2006a, Large-scale drainage capture and surface uplift in eastern Tibet–SW China before 24 Ma inferred from sediments of the Hanoi Basin, Vietnam: Geophysical Research Letters, v. 33, no. 19, p. L19403.

Clift, P. D., Carter, A., Campbell, I. H., Pringle, M. S., Van Lap, N., Allen, C. M., Hodges, K. V., and Tan, M. T., 2006b, Thermochronology of mineral grains in the Red and Mekong Rivers, Vietnam: Provenance and exhumation implications for Southeast Asia: Geochemistry, Geophysics, Geosystems, v. 7, no. 10, p. n/a-n/a.

Clift, P. D., Hodges, K. V., Heslop, D., Hannigan, R., Van Long, H., and Calves, G., 2008, Correlation of Himalayan exhumation rates and Asian monsoon intensity: Nature Geoscience, v. 1, no. 12, p. 875-880.

Clift, P. D., Lee, J. I., Hildebrand, P., Shimizu, N., Layne, G. D., Blusztajn, J., Blum, J. D., Garzanti, E., and Khan, A. A., 2002, Nd and Pb isotope variability in the Indus River System: implications for sediment provenance and crustal heterogeneity in the Western Himalaya: Earth and Planetary Science Letters, v. 200, no. 1, p. 91-106.

Clift, P. D., Shimizu, N., Layne, G. D., and Blusztajn, J., 2001, Tracing patterns of erosion and drainage in the Paleogene Himalaya through ion probe Pb isotope analysis of detrital K-feldspars in the Indus Molasse, India: Earth and Planetary Science Letters, v. 188, no. 3, p. 475-491.

Cobbing, E. J., Mallick, D. I. J., Pitfield, P. E. J., and Teoh, L. H., 1986, The granites of the Southeast Asian Tin Belt: Journal of the Geological Society, v. 143, no. 3, p. 537-550.

Cobbing, E. J., Pitfield, P.E.J, Darbyshire, D.P.F., and Mallick D.I.J., 1992, The granites of the South-East Asian tin belt. : Overseas Memoir of the British Geological Survey, v. No. 10.

Cohen, K. M., Finney S., and Gibbard, P. L. , International Chronostratigraphic Chart: International Commission on Stratigraphy, *in* Proceedings 34th International Geological Congress, Brisbane, Australia, 2012.

Copeland, P., and Harrison, T. M., 1990, Episodic rapid uplift in the Himalaya revealed by $^{40}Ar/^{39}Ar$ analysis of detrital K-feldspar and muscovite, Bengal fan: Geology, v. 18, no. 4, p. 354-357.

Copeland, P., Harrison, T. M., and Heizler, M. T., 1990, $^{40}Ar/^{39}Ar$ Single-crystal dating of detrital muscovite and K-feldspar from Leg 116, southern Bengal Fan: implications for the uplift and erosion of the Himalayas.

Copeland, P., Harrison, T. M., Pan, Y., Kidd, W. S. F., Roden, M., and Zhang, Y., 1995, Thermal evolution of the Gangdese batholith, southern Tibet: A history of episodic unroofing: Tectonics, v. 14, no. 2, p. 223-236.

Copeland, P., Mark Harrison, T., Kidd, W. S. F., Xu, R., and Zhang, Y., 1987, Rapid early Miocene acceleration of uplift in the Gangdese Belt, Xizang (southern Tibet), and its bearing on accommodation mechanisms of the India-Asia collision: Earth and Planetary Science Letters, v. 86, no. 2–4, p. 240-252.

Corfu, F., Hanchar, J. M., Hoskin, P. W. O., and Kinny, P., 2003, Atlas of Zircon Textures: Reviews in mineralogy and geochemistry, v. 53, no. 1, p. 469-500.

Corrigan, J. D., and Crowley, K. D., Fission-track analysis of detrital apatites from sites 717 and 718, Leg 116, Central Indian Ocean, *in* Proceedings Proc. Ocean Drill. Program Sci. Results1990, Volume 116, p. 75-92.

Cottle, J. M., Horstwood, M. S. A., and Parrish, R. R., 2009, A new approach to single shot laser ablation analysis and its application to in situ Pb/U geochronology: Journal of Analytical Atomic Spectrometry, v. 24, no. 10, p. 1355-1363.

Coulon, C., Maluski, H., Bollinger, C., and Wang, S., 1986, Mesozoic and cenozoic volcanic rocks from central and southern Tibet:39Ar-40Ar dating, petrological characteristics and geodynamical significance: Earth and Planetary Science Letters, v. 79, no. 3–4, p. 281-302.

Curray, J., 1979, Tectonics of the Andaman sea and Burma: Amer. Assoc. Petroleum Geol. Mem., v. 29, p. 189-198.

Curray, J. R., 2005, Tectonics and history of the Andaman Sea region: Journal of Asian Earth Sciences, v. 25, no. 1, p. 187-232.

Curvo, E. A. C., Tello S, C. A., Carter, A., Dias, A. N. C., Soares, C. J., Nakasuga, W. M., Resende, R. S., Gomes, M. R., Alencar, I., and Hadler, J. C., 2013, Zircon fission track and U–Pb dating methods applied to São Paulo and Taubaté Basins located in the southeast Brazil: Radiation Measurements, v. 50, no. 0, p. 172-180.

Dai, J., Wang, C., Hourigan, J., Li, Z., and Zhuang, G., 2013, Exhumation History of the Gangdese Batholith, Southern Tibetan Plateau: Evidence from Apatite and Zircon (U-Th)/He Thermochronology: The journal of geology, v. 121, no. 2, p. 155-172.

Davis, A. M., Aitchison, J. C., Badengzhu, and Hui, L., 2004, Conglomerates record the tectonic evolution of the Yarlung-Tsangpo suture zone in southern Tibet: Geological Society, London, Special Publications, v. 226, no. 1, p. 235-246.

Davis, A. M., Aitchison, J. C., Luo, H., and Zyabrev, S., 2002, Paleogene island arc collision-related conglomerates, Yarlung–Tsangpo suture zone, Tibet: Sedimentary Geology, v. 150, no. 3–4, p. 247-273.

Debon, F., Fort, P., Sheppard, S. M. F., and Sonet, J., 1986, The Four Plutonic Belts of the Transhimalaya-Himalaya: a Chemical, Mineralogical, Isotopic, and Chronological Synthesis along a Tibet-Nepal Section: Journal of Petrology, v. 27, no. 1, p. 219-250.

DeCelles, P., Gehrels, G., Najman, Y., Martin, A., Carter, A., and Garzanti, E., 2004, Detrital geochronology and geochemistry of Cretaceous–Early Miocene strata of Nepal: implications for timing and diachroneity of initial Himalayan orogenesis: Earth and Planetary Science Letters, v. 227, no. 3, p. 313-330.

DeCelles, P. G., Gehrels, G. E., Quade, J., LaReau, B., and Spurlin, M., 2000, Tectonic Implications of U-Pb Zircon Ages of the Himalayan Orogenic Belt in Nepal: Science, v. 288, no. 5465, p. 497-499.

DeCelles, P. G., Gehrels, G. E., Quade, J., and Ojha, T. P., 1998, Eocene-early Miocene foreland basin development and the history of Himalayan thrusting, western and central Nepal: Tectonics, v. 17, no. 5, p. 741-765.

DeCelles, P. G., Langford, R. P., and Schwartz, R. K., 1983, Two new methods of paleocurrent determination from trough cross-stratification: Journal of sedimentary Research, v. 53, no. 2, p. 629-642.

Derry, L. A., and France-Lanord, C., 1996, Neogene Himalayan weathering history and river 87Sr/86Sr: impact on the marine Sr record: Earth and Planetary Science Letters, v. 142, no. 1–2, p. 59-74.

Dhuime, B., Hawkesworth, C. J., Storey, C. D., and Cawood, P. A., 2011, From sediments to their source rocks: Hf and Nd isotopes in recent river sediments: Geology, v. 39, no. 4, p. 407-410.

Dickinson, W., 1985, Interpreting Provenance Relations from Detrital Modes of Sandstones, *in* Zuffa, G. G., ed., Provenance of Arenites, Volume 148, Springer Netherlands, p. 333-361.

Dickinson, W. R., and Gehrels, G. E., 2009, Use of U–Pb ages of detrital zircons to infer maximum depositional ages of strata: A test against a Colorado Plateau Mesozoic database: Earth and Planetary Science Letters, v. 288, no. 1–2, p. 115-125.

Ding, L., Zhong, D., Yin, A., Kapp, P., and Harrison, T. M., 2001, Cenozoic structural and metamorphic evolution of the eastern Himalayan syntaxis (Namche Barwa): Earth and Planetary Science Letters, v. 192, no. 3, p. 423-438.

Dong, X., Zhang, Z., and Santosh, M., 2010, Zircon U-Pb Chronology of the Nyingtri Group, Southern Lhasa Terrane, Tibetan Plateau: Implications for Grenvillian and Pan-African Provenance and Mesozoic-Cenozoic Metamorphism: The journal of geology, v. 118, no. 6, p. 677-690.

Dunkl, I., AntolÍn, B., Wemmer, K., Rantitsch, G., Kienast, M., Montomoli, C., Ding, L., Carosi, R., Appel, E., El Bay, R., Xu, Q., and Von Eynatten, H., 2011, Metamorphic evolution of the Tethyan Himalayan flysch in SE Tibet: Geological Society, London, Special Publications, v. 353, no. 1, p. 45-69.

Dunning, G. R., Macdonald, A. S., and Barr, S. M., 1995, Zircon and monazite U・Pb dating of the Doi Inthanon core complex, northern Thailand: implications for extension within the Indosinian Orogen: Tectonophysics, v. 251, no. 1–4, p. 197-213.

Dürr, S. B., 1996, Provenance of Xigaze fore-arc basin clastic rocks (Cretaceous, south Tibet): Geological Society of America Bulletin, v. 108, no. 6, p. 669-684.

Enkelmann, E., Ehlers, T. A., Zeitler, P. K., and Hallet, B., 2011, Denudation of the Namche Barwa antiform, eastern Himalaya: Earth and Planetary Science Letters, v. 307, no. 3–4, p. 323-333.

Fedo, C. M., Sircombe, K. N., and Rainbird, R. H., 2003, Detrital Zircon Analysis of the Sedimentary Record: Reviews in mineralogy and geochemistry, v. 53, no. 1, p. 277-303.

Finnegan, N. J., Hallet, B., Montgomery, D. R., Zeitler, P. K., Stone, J. O., Anders, A. M., and Yuping, L., 2008, Coupling of rock uplift and river incision in the Namche Barwa–Gyala Peri massif, Tibet: Geological Society of America Bulletin, v. 120, no. 1-2, p. 142-155.

Foster, G. L., and Carter, A., 2007, Insights into the patterns and locations of erosion in the Himalaya — A combined fission-track and in situ Sm–Nd isotopic study of detrital apatite: Earth and Planetary Science Letters, v. 257, no. 3–4, p. 407-418.

France-Lanord, C., Derry, L., and Michard, A., 1993, Evolution of the Himalaya since Miocene time: isotopic and sedimentological evidence from the Bengal Fan: Geological Society, London, Special Publications, v. 74, no. 1, p. 603-621.

France-Lanord, C., Spiess, V., Mohar, P., and Curray, J., 2000, Summary on the Bengal fan–an introduction to a drilling proposal, March 2000.

Galbraith, R. F., and Green, P. F., 1990, Estimating the component ages in a finite mixture: International Journal of Radiation Applications and Instrumentation. Part D. Nuclear Tracks and Radiation Measurements, v. 17, no. 3, p. 197-206.

Galbraith, R. F., and Laslett, G. M., 1993, Statistical models for mixed fission track ages: Nuclear Tracks and Radiation Measurements, v. 21, no. 4, p. 459-470.

Galy, A., France-Lanord, C., and Derry, L. A., 1996, The Late Oligocene-Early Miocene Himalayan belt constraints deduced from isotopic compositions of Early Miocene turbidites in the Bengal Fan: Tectonophysics, v. 260, no. 1, p. 109-118.

Galy, V., France-Lanord, C., Peucker-Ehrenbrink, B., and Huyghe, P., 2010, Sr–Nd–Os evidence for a stable erosion regime in the Himalaya during the past 12 Myr: Earth and Planetary Science Letters, v. 290, no. 3–4, p. 474-480.

Gao, E. L., Zeng, L., and Xie, K., 2012, Eocene high grade metamorphism and crustal anatexis in the North Himalaya Gneiss Domes, Southern Tibet: Chinese Science Bulletin, v. 57, no. 6, p. 639-650.

Garver, J. I., Brandon, M. T., Roden-Tice, M., and Kamp, P. J. J., 1999, Exhumation history of orogenic highlands determined by detrital fission-track thermochronology: Geological Society, London, Special Publications, v. 154, no. 1, p. 283-304.

Garver, J. I., Reiners, P. W., Walker, L. J., Ramage, J. M., and Perry, S. E., 2005, Implications for Timing of Andean Uplift from Thermal Resetting of

Radiation-Damaged Zircon in the Cordillera Huayhuash, Northern Peru: The journal of geology, v. 113, no. 2, p. 117-138.
Garzanti, E., Doglioni, C., Vezzoli, G., and Andò, S., 2007, Orogenic Belts and Orogenic Sediment Provenance: The journal of geology, v. 115, no. 3, p. 315-334.
Garzanti, E., Vezzoli, G., Andò, S., France-Lanord, C., Singh, S. K., and Foster, G., 2004, Sand petrology and focused erosion in collision orogens: the Brahmaputra case: Earth and Planetary Science Letters, v. 220, no. 1, p. 157-174.
Gehrels, G., Kapp, P., DeCelles, P., Pullen, A., Blakey, R., Weislogel, A., Ding, L., Guynn, J., Martin, A., McQuarrie, N., and Yin, A., 2011, Detrital zircon geochronology of pre-Tertiary strata in the Tibetan-Himalayan orogen: Tectonics, v. 30, no. 5, p. TC5016.
Gradstein, F. M., Ogg, J.G., Schmitz, M.D., et al., 2012, The Geologic Time Scale: Boston, USA, Elsevier.
Griffin, W. L., Pearson, N. J., Belousova, E., Jackson, S. E., van Achterbergh, E., O'Reilly, S. Y., and Shee, S. R., 2000, The Hf isotope composition of cratonic mantle: LAM-MC-ICPMS analysis of zircon megacrysts in kimberlites: Geochimica et Cosmochimica Acta, v. 64, no. 1, p. 133-147.
Guan, Q., Zhu, D.-C., Zhao, Z.-D., Dong, G.-C., Zhang, L.-L., Li, X.-W., Liu, M., Mo, X.-X., Liu, Y.-S., and Yuan, H.-L., 2012, Crustal thickening prior to 38 Ma in southern Tibet: Evidence from lower crust-derived adakitic magmatism in the Gangdese Batholith: Gondwana Research, v. 21, no. 1, p. 88-99.
Guo, L., Zhang, H.-F., Harris, N., Pan, F.-B., and Xu, W.-C., 2011, Origin and evolution of multi-stage felsic melts in eastern Gangdese belt: Constraints from U–Pb zircon dating and Hf isotopic composition: Lithos, v. 127, no. 1–2, p. 54-67.
Guo, L., Zhang, H.-F., Harris, N., Parrish, R., Xu, W.-C., and Shi, Z.-L., 2012, Paleogene crustal anatexis and metamorphism in Lhasa terrane, eastern Himalayan syntaxis: Evidence from U–Pb zircon ages and Hf isotopic compositions of the Nyingchi Complex: Gondwana Research, v. 21, no. 1, p. 100-111.
Gururajan, N. S., and Choudhuri, B. K., 2003, Geology and tectonic history of the Lohit Valley, Eastern Arunachal Pradesh, India: Journal of Asian Earth Sciences, v. 21, no. 7, p. 731-741.
Hallet, B., and Molnar, P., 2001, Distorted drainage basins as markers of crustal strain east of the Himalaya: Journal of Geophysical Research: Solid Earth, v. 106, no. B7, p. 13697-13709.
Hallsworth, C. R., Morton, A. C., Claoué-Long, J., and Fanning, C. M., 2000, Carboniferous sand provenance in the Pennine Basin, UK: constraints from heavy mineral and detrital zircon age data: Sedimentary Geology, v. 137, no. 3–4, p. 147-185.
Harrison, T. M., Célérier, J., Aikman, A. B., Hermann, J., and Heizler, M. T., 2009, Diffusion of 40Ar in muscovite: Geochimica et Cosmochimica Acta, v. 73, no. 4, p. 1039-1051.

Harrison, T. M., Yin, A., Grove, M., Lovera, O. M., Ryerson, F. J., and Zhou, X., 2000, The Zedong Window: A record of superposed Tertiary convergence in southeastern Tibet: Journal of Geophysical Research: Solid Earth, v. 105, no. B8, p. 19211-19230.

Haughton, P. D. W., Todd, S. P., and Morton, A. C., 1991, Sedimentary provenance studies: Geological Society, London, Special Publications, v. 57, no. 1, p. 1-11.

He, S., Kapp, P., DeCelles, P. G., Gehrels, G. E., and Heizler, M., 2007, Cretaceous–Tertiary geology of the Gangdese Arc in the Linzhou area, southern Tibet: Tectonophysics, v. 433, no. 1, p. 15-37.

Henderson, A. L., Najman, Y., Parrish, R., BouDagher-Fadel, M., Barford, D., Garzanti, E., and Andò, S., 2010, Geology of the Cenozoic Indus Basin sedimentary rocks: Paleoenvironmental interpretation of sedimentation from the western Himalaya during the early phases of India-Eurasia collision: Tectonics, v. 29, no. 6, p. TC6015.

Hetzel, R., Dunkl, I., Haider, V., Strobl, M., von Eynatten, H., Ding, L., and Frei, D., 2011, Peneplain formation in southern Tibet predates the India-Asia collision and plateau uplift: Geology, v. 39, no. 10, p. 983-986.

Hodges, K., Ruhl, K., Wobus, C., and Pringle, M., 2005, 40Ar/39Ar thermochronology of detrital minerals: Reviews in mineralogy and geochemistry, v. 58, no. 1, p. 239-257.

Hodges, K. V., 1991, Pressure-Temperature-time paths: Annual Review of Earth and Planetary Sciences, v. 19, p. 207-236.

-, 2000, Tectonics of the Himalaya and southern Tibet from two perspectives: Geological Society of America Bulletin, v. 112, no. 3, p. 324-350.

-, 2006, A synthesis of the Channel Flow-Extrusion hypothesis as developed for the Himalayan-Tibetan orogenic system: Geological Society, London, Special Publications, v. 268, no. 1, p. 71-90.

Hoskin, P. W. O., and Black, L. P., 2000, Metamorphic zircon formation by solid-state recrystallization of protolith igneous zircon: Journal of Metamorphic Geology, v. 18, no. 4, p. 423-439.

Hoskin, P. W. O., and Schaltegger, U., 2003, The Composition of Zircon and Igneous and Metamorphic Petrogenesis: Reviews in mineralogy and geochemistry, v. 53, no. 1, p. 27-62.

Hou, Z.-Q., Zheng, Y.-C., Zeng, L.-S., Gao, L.-E., Huang, K.-X., Li, W., Li, Q.-Y., Fu, Q., Liang, W., and Sun, Q.-Z., 2012, Eocene-Oligocene granitoids in southern Tibet: Constraints on crustal anatexis and tectonic evolution of the Himalayan orogen: Earth and Planetary Science Letters, v. 349, p. 38-52.

Hou, Z., Yang, Z., Qu, X., Meng, X., Li, Z., Beaudoin, G., Rui, Z., Gao, Y., and Zaw, K., 2009, The Miocene Gangdese porphyry copper belt generated during post-collisional extension in the Tibetan Orogen: Ore Geology Reviews, v. 36, no. 1–3, p. 25-51.

Howard, K. E., Hand, M., Barovich, K. M., Reid, A., Wade, B. P., and Belousova, E. A., 2009, Detrital zircon ages: Improving interpretation via Nd and Hf isotopic data: Chemical Geology, v. 262, no. 3–4, p. 277-292.

Hu, X., Jansa, L., Chen, L., Griffin, W. L., O'Reilly, S. Y., and Wang, J., 2010, Provenance of Lower Cretaceous Wölong Volcaniclastics in the Tibetan Tethyan Himalaya: Implications for the final breakup of Eastern Gondwana: Sedimentary Geology, v. 223, no. 3–4, p. 193-205.

Hurford, A. J., and Carter, A., 1991, The role of fission track dating in discrimination of provenance: Geological Society, London, Special Publications, v. 57, no. 1, p. 67-78.

Hurford, A. J., and Green, P. F., 1983, The zeta age calibration of fission-track dating: Chemical Geology, v. 41, no. 0, p. 285-317.

Ji, W.-Q., Wu, F.-Y., Liu, C.-Z., and Chung, S.-L., 2012, Early Eocene crustal thickening in southern Tibet: New age and geochemical constraints from the Gangdese batholith: Journal of Asian Earth Sciences, v. 53, no. 0, p. 82-95.

Ji, W., Wu, F., Liu, C., and Chung, S., 2009a, Geochronology and petrogenesis of granitic rocks in Gangdese batholith, southern Tibet: Science in China Series D: Earth Sciences, v. 52, no. 9, p. 1240-1261.

Ji, W. Q., Wu, F. Y., Chung, S. L., Li, J. X., and Liu, C. Z., 2009b, Zircon U–Pb geochronology and Hf isotopic constraints on petrogenesis of the Gangdese batholith, southern Tibet: Chemical Geology, v. 262, no. 3, p. 229-245.

Johnson, S. Y., and Nur Alam, A. M., 1991, Sedimentation and tectonics of the Sylhet trough, Bangladesh: Geological Society of America Bulletin, v. 103, no. 11, p. 1513-1527.

Kapp, J. L. D. A., Harrison, T. M., Kapp, P., Grove, M., Lovera, O. M., and Lin, D., 2005a, Nyainqentanglha Shan: A window into the tectonic, thermal, and geochemical evolution of the Lhasa block, southern Tibet: Journal of Geophysical Research: Solid Earth, v. 110, no. B8, p. n/a-n/a.

Kapp, P., DeCelles, P., Leier, A., Fabijanic, J., He, S., Pullen, A., Gehrels, G., and Ding, L., 2007a, The Gangdese retroarc thrust belt revealed: GSA Today, v. 17, no. 7, p. 4.

Kapp, P., DeCelles, P. G., Gehrels, G. E., Heizler, M., and Ding, L., 2007b, Geological records of the Lhasa-Qiangtang and Indo-Asian collisions in the Nima area of central Tibet: Geological Society of America Bulletin, v. 119, no. 7-8, p. 917-933.

Kapp, P., Yin, A., Harrison, T. M., and Ding, L., 2005b, Cretaceous-Tertiary shortening, basin development, and volcanism in central Tibet: Geological Society of America Bulletin, v. 117, no. 7-8, p. 865-878.

Khin, A. a. W., Kyaw, 1968, Preliminary studies of the paleogeography of Burma during the Cenozoic: Union of Burma Science and Technology Journal, v. 1, p. 241–251.

Khin, K., and Myitta, 1999, Marine transgression and regression in Miocene sequences of northern Pegu (Bago) Yoma, Central Myanmar: Journal of Asian Earth Sciences, v. 17, no. 3, p. 369-393.

Khin, Z., Meffre, S., Takai, M., Suzuki, H., Burrett, C., Thaung, H., Zin Maung Maung, T., Tsubamoto, T., Egi, N., and Maung, M., 2014, The oldest anthropoid primates in SE Asia: Evidence from LA-ICP-MS U–Pb zircon age in the Late

Middle Eocene Pondaung Formation, Myanmar: Gondwana Research, v. 26, no. 1, p. 122-131.
Kinny, P. D., and Maas, R., 2003, Lu–Hf and Sm–Nd isotope systems in zircon: Reviews in mineralogy and geochemistry, v. 53, no. 1, p. 327-341.
Koons, P. O., Zeitler, P. K., Chamberlain, C. P., Craw, D., and Meltzer, A. S., 2002, Mechanical links between erosion and metamorphism in Nanga Parbat, Pakistan Himalaya: American Journal of Science, v. 302, no. 9, p. 749-773.
Košler, J., and Sylvester, P. J., 2003, Present Trends and the Future of Zircon in Geochronology: Laser Ablation ICPMS: Reviews in mineralogy and geochemistry, v. 53, no. 1, p. 243-275.
Kübler, B., and Jaboyedoff, M., 2000, Illite crystallinity: Comptes Rendus de l'Académie des Sciences - Series IIA - Earth and Planetary Science, v. 331, no. 2, p. 75-89.
Kuiper, K. F., Deino, A., Hilgen, F. J., Krijgsman, W., Renne, P. R., and Wijbrans, J. R., 2008, Synchronizing Rock Clocks of Earth History: Science, v. 320, no. 5875, p. 500-504.
Lacassin, R., Maluski, H., Leloup, P. H., Tapponnier, P., Hinthong, C., Siribhakdi, K., Chuaviroj, S., and Charoenravat, A., 1997, Tertiary diachronic extrusion and deformation of western Indochina: Structural and 40Ar/39Ar evidence from NW Thailand: Journal of Geophysical Research: Solid Earth, v. 102, no. B5, p. 10013-10037.
Lang, K. A., and Huntington, K. W., 2014, Antecedence of the Yarlung–Siang–Brahmaputra River, eastern Himalaya: Earth and Planetary Science Letters, v. 397, no. 0, p. 145-158.
Lee, H.-Y., Chung, S.-L., Lo, C.-H., Ji, J., Lee, T.-Y., Qian, Q., and Zhang, Q., 2009, Eocene Neotethyan slab breakoff in southern Tibet inferred from the Linzizong volcanic record: Tectonophysics, v. 477, no. 1–2, p. 20-35.
Lee, H.-Y., Chung, S.-L., Yang, H.-M., Chu, C.-H., Lo, C.-H., and Mitchell, A.H.G, Age and geochemical constraints on the Petrogenesis of Late Cenozoic volcanism in Myanmar, *in* Proceedings Tectonic Crossroads: Evolving Orogens of Eurasia-Africa-Arabia, Ankara, Turkey, 5 October, 2010 2010, Volume Session No. 25. Magmatism in evolving orogens: Collision to extension. Part 2, The Geological Society of America.
Lee, H. Y., Chung, S. L., Wang, J. R., Wen, D. J., Lo, C. H., Yang, T. F., Zhang, Y., Xie, Y., Lee, T. Y., and Wu, G., 2003, Miocene Jiali faulting and its implications for Tibetan tectonic evolution: Earth and Planetary Science Letters, v. 205, no. 3, p. 185-194.
Lee, T.-Y., and Lawver, L. A., 1995, Cenozoic plate reconstruction of Southeast Asia: Tectonophysics, v. 251, no. 1–4, p. 85-138.
Leier, A. L., DeCelles, P. G., Kapp, P., and Ding, L., 2007a, The Takena Formation of the Lhasa terrane, southern Tibet: The record of a Late Cretaceous retroarc foreland basin: Geological Society of America Bulletin, v. 119, no. 1-2, p. 31-48.

Leier, A. L., Kapp, P., Gehrels, G. E., and DeCelles, P. G., 2007b, Detrital zircon geochronology of Carboniferous–Cretaceous strata in the Lhasa terrane, Southern Tibet: Basin Research, v. 19, no. 3, p. 361-378.

Li, R., Mei, L., Zhu, G., Zhao, R., Xu, X., Zhao, H., Zhang, P., Yin, Y., and Ma, Y., 2013, Late Mesozoic to Cenozoic tectonic events in volcanic arc, West Burma Block: Evidences from U-Pb zircon dating and apatite fission track data of granitoids: Journal of Earth Science, v. 24, no. 4, p. 553-568.

Liang, Y. H., Chung, S. L., Liu, D., Xu, Y., Wu, F. Y., Yang, J. H., Wang, Y., and Lo, C. H., 2008, Detrital zircon evidence from Burma for reorganization of the eastern Himalayan river system: American Journal of Science, v. 308, no. 4, p. 618-638.

Licht, A., France-Lanord, C., Reisberg, L., Fontaine, C., Soe, A. N., and Jaeger, J.-J., 2013, A palaeo Tibet–Myanmar connection? Reconstructing the Late Eocene drainage system of central Myanmar using a multi-proxy approach: Journal of the Geological Society, v. 170, no. 6, p. 929-939.

Lin, I. J., Chung, S.-L., Chu, C.-H., Lee, H.-Y., Gallet, S., Wu, G., Ji, J., and Zhang, Y., 2012, Geochemical and Sr–Nd isotopic characteristics of Cretaceous to Paleocene granitoids and volcanic rocks, SE Tibet: Petrogenesis and tectonic implications: Journal of Asian Earth Sciences, v. 53, no. 0, p. 131-150.

Lin, T.-H., Chung, S.-L., Kumar, A., Wu, F.-Y., Chiu, H.-Y., and Lin, I. J., 2013, Linking a prolonged Neo-Tethyan magmatic arc in South Asia: Zircon U-Pb and Hf isotopic constraints from the Lohit Batholith, NE India: Terra Nova, v. 25, no. 6, p. 453-458.

Lin, T. H., Lo, C. H., Chung, S. L., Hsu, F. J., Yeh, M. W., Lee, T. Y., Ji, J. Q., Wang, Y. Z., and Liu, D., 2009, 40Ar/39Ar dating of the Jiali and Gaoligong shear zones: Implications for crustal deformation around the Eastern Himalayan Syntaxis: Journal of Asian Earth Sciences, v. 34, no. 5, p. 674-685.

Liu, S., Hu, R., Gao, S., Feng, C., Huang, Z., Lai, S., Yuan, H., Liu, X., Coulson, I. M., Feng, G., Wang, T., and Qi, Y., 2009, U–Pb zircon, geochemical and Sr–Nd–Hf isotopic constraints on the age and origin of Early Palaeozoic I-type granite from the Tengchong–Baoshan Block, Western Yunnan Province, SW China: Journal of Asian Earth Sciences, v. 36, no. 2–3, p. 168-182.

Ludwig, K. R., 2003, User's Manual for Isoplot 3.00: A Geochronological Toolkit for Microsoft Excel.: Berkeley Geochronological Centre, Berkeley, California.

Ma, L., Wang, Q., Li, Z.-X., Wyman, D. A., Jiang, Z.-Q., Yang, J.-H., Gou, G.-N., and Guo, H.-F., 2013, Early Late Cretaceous (ca. 93 Ma) norites and hornblendites in the Milin area, eastern Gangdese: Lithosphere–asthenosphere interaction during slab roll-back and an insight into early Late Cretaceous (ca. 100–80 Ma) magmatic “flare-up” in southern Lhasa (Tibet): Lithos, v. 172–173, no. 0, p. 17-30.

Ma, L., Wang, Y., Fan, W., Geng, H., Cai, Y., Zhong, H., Liu, H., and Xing, X., 2014, Petrogenesis of the early Eocene I-type granites in west Yingjiang (SW Yunnan) and its implication for the eastern extension of the Gangdese batholiths: Gondwana Research, v. 25, no. 1, p. 401-419.

Mange, M. A., and Morton, A. C., 2007, Chapter 13 Geochemistry of Heavy Minerals, *in* Maria, A. M., and David, T. W., eds., Developments in Sedimentology, Volume Volume 58, Elsevier, p. 345-391.

Mark, D. F., Barfod, D., Stuart, F. M., and Imlach, J., 2009, The ARGUS multicollector noble gas mass spectrometer: Performance for 40Ar/39Ar geochronology: Geochemistry, Geophysics, Geosystems, v. 10, no. 10, p. Q0AA02.

Marsellos, A. E., and Garver, J. I., 2010, Radiation damage and uranium concentration in zircon as assessed by Raman spectroscopy and neutron irradiation: American Mineralogist, v. 95, no. 8-9, p. 1192-1201.

Maung, H., 1987, Transcurrent movements in the Burma–Andaman Sea region: Geology, v. 15, no. 10, p. 911-912.

Maung, K., 1970, Biostratigraphy of the Central Burma Basin with species reference to the Depositional Conditions during Oligocene and Early Miocene: Union of Burma. Journal of Science & Technology, v. 3, p. 75 – 90.

Maung, M., Htike, T., Tsubamoto, T., Suzuki, H., Sein, C., Egi, N., Win, Z. A. W., Thein, Z. M. M., and Aung, A. K., 2005, Stratigraphy of the primate-bearing beds of the Eocene Pondaung Formation at Paukkaung area, Myanmar: Anthropological Science, v. 113, no. 1, p. 11-15.

Metcalfe, I., 1996, Pre-Cretaceous evolution of SE Asian terranes: Geological Society, London, Special Publications, v. 106, no. 1, p. 97-122.

-, 2000, The Bentong–Raub Suture Zone: Journal of Asian Earth Sciences, v. 18, no. 6, p. 691-712.

-, 2002, Permian tectonic framework and palaeogeography of SE Asia: Journal of Asian Earth Sciences, v. 20, no. 6, p. 551-566.

Metcalfe, I., 2009, Late Palaeozoic and Mesozoic tectonic and palaeogeographical evolution of SE Asia: Geological Society, London, Special Publications, v. 315, no. 1, p. 7-23.

-, 2011, Tectonic framework and Phanerozoic evolution of Sundaland: Gondwana Research, v. 19, no. 1, p. 3-21.

Metcalfe, I., and Irving, E., 1990, Allochthonous Terrane Processes in Southeast Asia [and Discussion]: Philosophical Transactions of the Royal Society of London. Series A, Mathematical and Physical Sciences, v. 331, no. 1620, p. 625-640.

Mitchell, A., Ausa, C., Deiparine, L., Hlaing, T., Htay, N., and Khine, A., 2004, The Modi Taung–Nankwe gold district, Slate belt, central Myanmar: mesothermal veins in a Mesozoic orogen: Journal of Asian Earth Sciences, v. 23, no. 3, p. 321-341.

Mitchell, A., Chung, S. L., Oo, T., Lin, T. H., and Hung, C. H., 2012, Zircon U-Pb ages in Myanmar: Magmatic-metamorphic events and the closure of a neo-Tethys ocean?: Journal of Asian Earth Sciences.

Mitchell, A. H. G., 1981, Phanerozoic plate boundaries in mainland SE Asia, the Himalayas and Tibet: Journal of the Geological Society, v. 138, no. 2, p. 109-122.

-, 1989, The Shan Plateau And Western Burma: Mesozoic-Cenozoic Plate Boundaries and Correlations with Tibet, *in* Şengör, A. M. C., ed., Tectonic Evolution of the Tethyan Region, Volume 259, Springer Netherlands, p. 567-583.

-, 1992, Late Permian-Mesozoic events and the Mergui group Nappe in Myanmar and Thailand: Journal of Southeast Asian Earth Sciences, v. 7, no. 2–3, p. 165-178.
-, 1993, Cretaceous–Cenozoic tectonic events in the western Myanmar (Burma)–Assam region: Journal of the Geological Society, v. 150, no. 6, p. 1089-1102.
Mitchell, A. H. G., Htay, M. T., Htun, K. M., Win, M. N., Oo, T., and Hlaing, T., 2007, Rock relationships in the Mogok metamorphic belt, Tatkon to Mandalay, central Myanmar: Journal of Asian Earth Sciences, v. 29, no. 5–6, p. 891-910.
Mo, X., Dong, G., Zhao, Z., Tieying, G. U. O., Liangliang, W., and Tao, C., 2005, Timing of Magma Mixing in the Gangdisê Magmatic Belt during the India-Asia Collision: Zircon SHRIMP U-Pb Dating: Acta Geologica Sinica - English Edition, v. 79, no. 1, p. 66-76.
Mo, X., Dong, G., Zhao, Z., Zhu, D., Zhou, S., and Niu, Y., 2009, Mantle input to the crust in Southern Gangdese, Tibet, during the Cenozoic: Zircon Hf isotopic evidence: Journal of Earth Science, v. 20, no. 2, p. 241-249.
Mo, X., Hou, Z., Niu, Y., Dong, G., Qu, X., Zhao, Z., and Yang, Z., 2007, Mantle contributions to crustal thickening during continental collision: Evidence from Cenozoic igneous rocks in southern Tibet: Lithos, v. 96, no. 1–2, p. 225-242.
Mo, X., Niu, Y., Dong, G., Zhao, Z., Hou, Z., Zhou, S., and Ke, S., 2008, Contribution of syncollisional felsic magmatism to continental crust growth: A case study of the Paleogene Linzizong volcanic Succession in southern Tibet: Chemical Geology, v. 250, no. 1–4, p. 49-67.
Morley, C., 2009, Evolution from an oblique subduction back-arc mobile belt to a highly oblique collisional margin: the Cenozoic tectonic development of Thailand and eastern Myanmar: Geological Society, London, Special Publications, v. 318, no. 1, p. 373-403.
Morley, C. K., 2002, A tectonic model for the Tertiary evolution of strike–slip faults and rift basins in SE Asia: Tectonophysics, v. 347, no. 4, p. 189-215.
Morley, C. K., 2004, Nested strike-slip duplexes, and other evidence for Late Cretaceous–Palaeogene transpressional tectonics before and during India–Eurasia collision, in Thailand, Myanmar and Malaysia: Journal of the Geological Society, v. 161, no. 5, p. 799-812.
Morley, C. K., 2012, Late Cretaceous–Early Palaeogene tectonic development of SE Asia: Earth-Science Reviews, v. 115, no. 1–2, p. 37-75.
-, 2013, Discussion of tectonic models for Cenozoic strike-slip fault-affected continental margins of mainland SE Asia: Journal of Asian Earth Sciences, v. 76, no. 0, p. 137-151.
Morton, A., Hallsworth, C., and Chalton, B., 2004, Garnet compositions in Scottish and Norwegian basement terrains: a framework for interpretation of North Sea sandstone provenance: Marine and Petroleum Geology, v. 21, no. 3, p. 393-410.
Morton, A. C., and Hallsworth, C. R., 1999, Processes controlling the composition of heavy mineral assemblages in sandstones: Sedimentary Geology, v. 124, no. 1–4, p. 3-29.
Morton, A. C., Whitham, A. G., and Fanning, C. M., 2005, Provenance of Late Cretaceous to Paleocene submarine fan sandstones in the Norwegian Sea:

Integration of heavy mineral, mineral chemical and zircon age data: Sedimentary Geology, v. 182, no. 1–4, p. 3-28.

Murakami, T., Chakoumakos, B. C., Ewing, R. C., Lumpkin, G. R., and Weber, W. J., 1991, Alpha-decay event damage in zircon: American Mineralogist, v. 76, no. 9-10, p. 1510-1532.

Murphy, M. A., and Yin, A., 2003, Structural evolution and sequence of thrusting in the Tethyan fold-thrust belt and Indus-Yalu suture zone, southwest Tibet: Geological Society of America Bulletin, v. 115, no. 1, p. 21-34.

Murphy, M. A., Yin, A., Harrison, T. M., Dürr, S. B., Z, C., Ryerson, F. J., Kidd, W. S. F., X, W., and X, Z., 1997, Did the Indo-Asian collision alone create the Tibetan plateau?: Geology, v. 25, no. 8, p. 719-722.

Naing, T. T., Bussien, D. A., Winkler, W. H., Nold, M., and Von Quadt, A., 2014, Provenance study on Eocene–Miocene sandstones of the Rakhine Coastal Belt, Indo-Burman Ranges of Myanmar: geodynamic implications: Geological Society, London, Special Publications, v. 386, no. 1, p. 195-216.

Najman, Y., 2006, The detrital record of orogenesis: A review of approaches and techniques used in the Himalayan sedimentary basins: Earth-Science Reviews, v. 74, no. 1, p. 1-72.

Najman, Y., Allen, R., Willett, E. A. F., Carter, A., Barfod, D., Garzanti, E., Wijbrans, J., Bickle, M. J., Vezzoli, G., Ando, S., Oliver, G., and Uddin, M. J., 2012, The record of Himalayan erosion preserved in the sedimentary rocks of the Hatia Trough of the Bengal Basin and the Chittagong Hill Tracts, Bangladesh: Basin Research, v. 24, no. 5, p. 499-519.

Najman, Y., Appel, E., Boudagher-Fadel, M., Bown, P., Carter, A., Garzanti, E., Godin, L., Han, J., Liebke, U., Oliver, G., Parrish, R., and Vezzoli, G., 2010, Timing of India-Asia collision: Geological, biostratigraphic, and palaeomagnetic constraints: Journal of Geophysical Research: Solid Earth, v. 115, no. B12, p. n/a-n/a.

Najman, Y., Bickle, M., Boudagher-Fadel, M., Carter, A., Garzanti, E., Paul, M., Wijbrans, J., Willett, E., Oliver, G., and Parrish, R., 2008, The Paleogene record of Himalayan erosion: Bengal Basin, Bangladesh: Earth and Planetary Science Letters, v. 273, no. 1, p. 1-14.

Najman, Y., Bickle, M., and Chapman, H., 2000, Early Himalayan exhumation: Isotopic constraints from the Indian foreland basin: Terra Nova, v. 12, p. 28-34.

Najman, Y., Bickle, M., Garzanti, E., Pringle, M., Barfod, D., Brozovic, N., Burbank, D., and Ando, S., 2009, Reconstructing the exhumation history of the Lesser Himalaya, NW India, from a multitechnique provenance study of the foreland basin Siwalik Group: Tectonics, v. 28, no. 5, p. TC5018.

Najman, Y., Carter, A., Oliver, G., and Garzanti, E., 2005, Provenance of Eocene foreland basin sediments, Nepal: Constraints to the timing and diachroneity of early Himalayan orogenesis: Geology, v. 33, no. 4, p. 309-312.

Najman, Y., and Garzanti, E., 2000, Reconstructing early Himalayan tectonic evolution and paleogeography from Tertiary foreland basin sedimentary rocks, northern India: Geological Society of America Bulletin, v. 112, no. 3, p. 435-449.

Najman, Y., Garzanti, E., Pringle, M., Bickle, M., Stix, J., and Khan, I., 2003, Early-Middle Miocene paleodrainage and tectonics in the Pakistan Himalaya: Geological Society of America Bulletin, v. 115, no. 10, p. 1265-1277.

Najman, Y., Johnson, K., White, N., and Oliver, G., 2004, Evolution of the Himalayan foreland basin, NW India: Basin Research, v. 16, no. 1, p. 1-24.

Najman, Y., Pringle, M., Godin, L., and Oliver, G., 2001, Dating of the oldest continental sediments from the Himalayan foreland basin: Nature, v. 410, no. 6825, p. 194-197.

Najman, Y., Pringle, M., Godin, L., and Oliver, G., 2002, A reinterpretation of the Balakot Formation: Implications for the tectonics of the NW Himalaya, Pakistan: Tectonics, v. 21, no. 5, p. 9-1-9-18.

Najman, Y., Pringle, M., Johnson, M., Robertson, A., and Wijbrans, J., 1997, Laser 40Ar/39Ar dating of single detrital muscovite grains from early foreland-basin sedimentary deposits in India: Implications for early Himalayan evolution: Geology, v. 25, no. 6, p. 535-538.

Owen, M. R., 1987, Hafnium content of detrital zircons, a new tool for provenance study: Journal of sedimentary Research, v. 57, no. 5, p. 824-830.

Palin, R. M., Searle, M. P., St-Onge, M. R., Waters, D. J., Roberts, N. M. W., Horstwood, M. S. A., Parrish, R. R., Weller, O. M., Chen, S., and Yang, J., 2014, Monazite geochronology and petrology of kyanite- and sillimanite-grade migmatites from the northwestern flank of the eastern Himalayan syntaxis: Gondwana Research, v. 26, no. 1, p. 323-347.

Pan, F.-B., Zhang, H.-F., Harris, N., Xu, W.-C., and Guo, L., 2012, Oligocene magmatism in the eastern margin of the east Himalayan syntaxis and its implication for the India–Asia post-collisional process: Lithos, v. 154, no. 0, p. 181-192.

Pan, Y., Copeland, P., Roden, M. K., Kidd, W. S. F., and Mark Harrison, T., 1993, Thermal and unroofing history of the Lhasa area, Southern Tibet—evidence from apatite fission track thermochronology: Nuclear Tracks and Radiation Measurements, v. 21, no. 4, p. 543-554.

Pearce, N. J. G., Perkins, W. T., Westgate, J. A., Gorton, M. P., Jackson, S. E., Neal, C. R., and Chenery, S. P., 1997, A Compilation of New and Published Major and Trace Element Data for NIST SRM 610 and NIST SRM 612 Glass Reference Materials: Geostandards Newsletter, v. 21, no. 1, p. 115-144.

Pedersen, R. B., Searle, M. P., Carter, A., and Bandopadhyay, P. C., 2010, U–Pb zircon age of the Andaman ophiolite: implications for the beginning of subduction beneath the Andaman‐Sumatra arc: Journal of the Geological Society, v. 167, no. 6, p. 1105-1112.

Pivnik, D. A., Nahm, J., Tucker, R. S., Smith, G. O., Nyein, K., Nyunt, M., and Maung, P. H., 1998, Polyphase deformation in a fore-arc/back-arc basin, Salin subbasin, Myanmar (Burma): Aapg Bulletin, v. 82, no. 10, p. 1837-1856.

Pullen, A., Kapp, P., Gehrels, G. E., DeCelles, P. G., Brown, E. H., Fabijanic, J. M., and Ding, L., 2008, Gangdese retroarc thrust belt and foreland basin deposits in the Damxung area, southern Tibet: Journal of Asian Earth Sciences, v. 33, no. 5–6, p. 323-336.

Qi, M., Xiang, H., Zhong, Z.-Q., Qiu, H.-N., Wang, H., Sun, X.-L., and Xu, B., 2013, 40Ar/39Ar geochronology constraints on the formation age of Myanmar jadeitite: Lithos, v. 162–163, no. 0, p. 107-114.

Qiu, Z., Wu, F., Yang, S., Zhu, M., Sun, J., and Yang, P., 2009, Age and genesis of the Myanmar jadeite: Constraints from U-Pb ages and Hf isotopes of zircon inclusions: Chinese Science Bulletin, v. 54, no. 4, p. 658-668.

Rahman, M. J. J., and Faupl, P., 2003, 40Ar/39Ar multigrain dating of detrital white mica of sandstones of the Surma Group in the Sylhet Trough, Bengal Basin, Bangladesh: Sedimentary Geology, v. 155, no. 3–4, p. 383-392.

Ratmuangkhwang, S., Musikasinthorn, P., and Kumazawa, Y., 2014, Molecular phylogeny and biogeography of air sac catfishes of the Heteropneustes fossilis species complex (Siluriformes: Heteropneustidae): Molecular Phylogenetics and Evolution, v. 79, no. 0, p. 82-91.

Ratschbacher, L., Frisch, W., Liu, G., and Chen, C., 1994, Distributed deformation in southern and western Tibet during and after the India-Asia collision: Journal of Geophysical Research: Solid Earth, v. 99, no. B10, p. 19917-19945.

Richter, F. M., Lovera, O. M., Mark Harrison, T., and Copeland, P., 1991, Tibetan tectonics from 40Ar/39Ar analysis of a single K-feldspar sample: Earth and Planetary Science Letters, v. 105, no. 1–3, p. 266-278.

Robinson, R. A. J., Bird, M. I., Oo, N. W., Hoey, T. B., Aye, M. M., Higgitt, D. L., X, L. X., Swe, A., Tun, T., and Win, S. L., 2007, The Irrawaddy River Sediment Flux to the Indian Ocean: The Original Nineteenth-Century Data Revisited: The journal of geology, v. 115, no. 6, p. 629-640.

Robinson, R. A. J., Brezina, C. A., Parrish, R. R., Horstwood, M. S. A., Nay Win, O., Bird, M. I., Myint, T., Walters, A. S., Oliver, G. J. H., and Khin, Z., 2014, Large rivers and orogens: The evolution of the Yarlung Tsangpo–Irrawaddy system and the eastern Himalayan syntaxis: Gondwana Research, v. 26, no. 1, p. 112-121.

Rohrmann, A., Kapp, P., Carrapa, B., Reiners, P. W., Guynn, J., Ding, L., and Heizler, M., 2012, Thermochronologic evidence for plateau formation in central Tibet by 45 Ma: Geology, v. 40, no. 2, p. 187-190.

Rowley, D. B., 1996, Age of initiation of collision between India and Asia: A review of stratigraphic data: Earth and Planetary Science Letters, v. 145, no. 1–4, p. 1-13.

Rüber, L., Britz, R., Kullander, S. O., and Zardoya, R., 2004, Evolutionary and biogeographic patterns of the Badidae (Teleostei: Perciformes) inferred from mitochondrial and nuclear DNA sequence data: Molecular Phylogenetics and Evolution, v. 32, no. 3, p. 1010-1022.

Ruiz, G., Seward, D., and Winkler, W., 2004, Detrital thermochronology–a new perspective on hinterland tectonics, an example from the Andean Amazon Basin, Ecuador: Basin Research, v. 16, no. 3, p. 413-430.

San, M. B., 1981, Stratigraphy and sedimentation of the Natogyi-Taungtha area [MSc: Arts and Science University, Mandalay, 85 p.

Schaltegger, U., Fanning, C. M., Günther, D., Maurin, J. C., Schulmann, K., and Gebauer, D., 1999, Growth, annealing and recrystallization of zircon and preservation of monazite in high-grade metamorphism: conventional and in-situ

U-Pb isotope, cathodoluminescence and microchemical evidence: Contributions to Mineralogy and Petrology, v. 134, no. 2-3, p. 186-201.

Schoenbohm, L. M., Burchfiel, B. C., and Liangzhong, C., 2006, Propagation of surface uplift, lower crustal flow, and Cenozoic tectonics of the southeast margin of the Tibetan Plateau: Geology, v. 34, no. 10, p. 813-816.

Searle, M. P., Noble, S. R., Cottle, J. M., Waters, D. J., Mitchell, A. H. G., Hlaing, T., and Horstwood, M. S. A., 2007, Tectonic evolution of the Mogok metamorphic belt, Burma (Myanmar) constrained by U-Th-Pb dating of metamorphic and magmatic rocks: Tectonics, v. 26, no. 3, p. TC3014.

Searle, M. P., Whitehouse, M. J., Robb, L. J., Ghani, A. A., Hutchison, C. S., Sone, M., Ng, S. W.-P., Roselee, M. H., Chung, S.-L., and Oliver, G. J. H., 2012, Tectonic evolution of the Sibumasu–Indochina terrane collision zone in Thailand and Malaysia: constraints from new U–Pb zircon chronology of SE Asian tin granitoids: Journal of the Geological Society, v. 169, no. 4, p. 489-500.

Seeber, L., and Gornitz, V., 1983, River profiles along the Himalayan arc as indicators of active tectonics: Tectonophysics, v. 92, no. 4, p. 335-367.

Seward, D., and Burg, J.-P., 2008, Growth of the Namche Barwa Syntaxis and associated evolution of the Tsangpo Gorge: Constraints from structural and thermochronological data: Tectonophysics, v. 451, no. 1–4, p. 282-289.

Shi, G.-H., Jiang, N., Liu, Y., Wang, X., Zhang, Z.-Y., and Xu, Y.-J., 2009, Zircon Hf isotope signature of the depleted mantle in the Myanmar jadeitite: Implications for Mesozoic intra-oceanic subduction between the Eastern Indian Plate and the Burmese Platelet: Lithos, v. 112, no. 3–4, p. 342-350.

Shi, G., Cui, W., Cao, S., Jiang, N., Jian, P., Liu, D., Miao, L., and Chu, B., 2008, Ion microprobe zircon U–Pb age and geochemistry of the Myanmar jadeitite: Journal of the Geological Society, v. 165, no. 1, p. 221-234.

Sláma, J., Košler, J., Condon, D. J., Crowley, J. L., Gerdes, A., Hanchar, J. M., Horstwood, M. S. A., Morris, G. A., Nasdala, L., Norberg, N., Schaltegger, U., Schoene, B., Tubrett, M. N., and Whitehouse, M. J., 2008, Plešovice zircon — A new natural reference material for U–Pb and Hf isotopic microanalysis: Chemical Geology, v. 249, no. 1–2, p. 1-35.

Socquet, A., Vigny, C., Chamot-Rooke, N., Simons, W., Rangin, C., and Ambrosius, B., 2006, India and Sunda plates motion and deformation along their boundary in Myanmar determined by GPS: Journal of Geophysical Research: Solid Earth, v. 111, no. B5, p. B05406.

Söderlund, U., Patchett, P. J., Vervoort, J. D., and Isachsen, C. E., 2004, The 176Lu decay constant determined by Lu–Hf and U–Pb isotope systematics of Precambrian mafic intrusions: Earth and Planetary Science Letters, v. 219, no. 3–4, p. 311-324.

Soe, A. N., Myitta, Tun, S. T., Aung, A. K., Thein, T., Marandat, B., Ducrocq, S., and Jaeger, J.-J., 2002, Sedimentary facies of the late Middle Eocene Pondaung Formation (central Myanmar) and the palaeoenvironments of its Anthropoid Primates: Comptes Rendus Palevol, v. 1, no. 3, p. 153-160.

Sone, M., and Metcalfe, I., 2008, Parallel Tethyan sutures in mainland Southeast Asia: New insights for Palaeo-Tethys closure and implications for the Indosinian orogeny: Comptes Rendus Geoscience, v. 340, no. 2–3, p. 166-179.

Spear, F. S., and Parrish, R. R., 1996, Petrology and Cooling Rates of the Valhalla Complex, British Columbia, Canada: Journal of Petrology, v. 37, no. 4, p. 733-765.

Stephenson, D., and Marshall, T. R., 1984, The petrology and mineralogy of Mt. Popa Volcano and the nature of the late-Cenozoic Burma Volcanic Arc: Journal of the Geological Society, v. 141, no. 4, p. 747-762.

Stewart, R. J., Hallet, B., Zeitler, P. K., Malloy, M. A., Allen, C. M., and Trippett, D., 2008, Brahmaputra sediment flux dominated by highly localized rapid erosion from the easternmost Himalaya: Geology, v. 36, no. 9, p. 711-714.

Stuart, F. M., 2002, The exhumation history of orogenic belts from $^{40}Ar/^{39}Ar$ ages of detrital micas: Mineralogical Magazine, v. 66, no. 1, p. 121-135.

Szulc, A., Najman, Y., Sinclair, H., Pringle, M., Bickle, M., Chapman, H., Garzanti, E., Ando, S., Huyghe, P., and Mugnier, J. L., 2006, Tectonic evolution of the Himalaya constrained by detrital $^{40}Ar/^{39}Ar$, Sm–Nd and petrographic data from the Siwalik foreland basin succession, SW Nepal: Basin Research, v. 18, no. 4, p. 375-391.

Tagami, T., Carter, A., and Hurford, A. J., 1996, Natural long-term annealing of the zircon fission-track system in Vienna Basin deep borehole samples: constraints upon the partial annealing zone and closure temperature: Chemical Geology, v. 130, no. 1–2, p. 147-157.

Tagami, T., Galbraith, R. F., Yamada, R., and Laslett, G. M., 1998, Revised Annealing Kinetics of Fission Tracks in Zircon and Geological Implications, *in* Haute, P., and Corte, F., eds., Advances in Fission-Track Geochronology, Volume 10, Springer Netherlands, p. 99-112.

Thein, M. M., 1966, Stratigraphy and structure of the Taungtalon area [MSc: Arts and Science University, 141 p.

Tsubamoto, T., Takai, M., Shigehara, N., Egi, N., Tun, S. T., Aung, A. K., Maung, M., Danhara, T., and Suzuki, H., 2002, Fission-track zircon age of the Eocene Pondaung Formation, Myanmar: Journal of Human Evolution, v. 42, no. 4, p. 361-369.

Uddin, A., Hames, W. E., and Zahid, K. M., 2010, Laser 40Ar/39Ar age constraints on Miocene sequences from the Bengal basin: Implications for middle Miocene denudation of the eastern Himalayas: Journal of Geophysical Research: Solid Earth, v. 115, no. B7, p. n/a-n/a.

Uddin, A., Kumar, P., and Sarma, J. N., 2007, Early Orogenic History of the Eastern Himalayas: Compositional Studies of Paleogene Sandstones from Assam, Northeast India: International Geology Review, v. 49, no. 9, p. 798-810.

Uddin, A., and Lundberg, N., 1998a, Cenozoic history of the Himalayan-Bengal system: Sand composition in the Bengal basin, Bangladesh: Geological Society of America Bulletin, v. 110, no. 4, p. 497-511.

-, 1998b, Unroofing history of the eastern Himalaya and the Indo-Burman Ranges: Heavy-mineral study of Cenozoic sediments from the Bengal basin, Bangladesh: Journal of sedimentary Research, v. 68, no. 3.

van der Beek, P., Robert, X., Mugnier, J. L., Bernet, M., Huyghe, P., and Labrin, E., 2006, Late Miocene–Recent exhumation of the central Himalaya and recycling in the foreland basin assessed by apatite fission-track thermochronology of Siwalik sediments, Nepal: Basin Research, v. 18, no. 4, p. 413-434.

Van Hoang, L., Clift, P. D., Mark, D., Zheng, H., and Tan, M. T., 2010, Ar–Ar muscovite dating as a constraint on sediment provenance and erosion processes in the Red and Yangtze River systems, SE Asia: Earth and Planetary Science Letters, v. 295, no. 3, p. 379-389.

van Hoang, L., Wu, F. Y., Clift, P. D., Wysocka, A., and Swierczewska, A., 2009, Evaluating the evolution of the Red River system based on in situ U-Pb dating and Hf isotope analysis of zircons: Geochem. Geophys. Geosyst, v. 10, p. Q11008.

Verdel, C., Pluijm, B., and Niemi, N., 2012, Variation of illite/muscovite 40Ar/39Ar age spectra during progressive low-grade metamorphism: an example from the US Cordillera: Contributions to Mineralogy and Petrology, v. 164, no. 3, p. 521-536.

Vermeesch, P., 2004, How many grains are needed for a provenance study?: Earth and Planetary Science Letters, v. 224, no. 3–4, p. 441-451.

-, 2009, RadialPlotter: A Java application for fission track, luminescence and other radial plots: Radiation Measurements, v. 44, no. 4, p. 409-410.

-, 2012, On the visualisation of detrital age distributions: Chemical Geology, v. 312–313, no. 0, p. 190-194.

Vigny, C., Socquet, A., Rangin, C., Chamot-Rooke, N., Pubellier, M., Bouin, M. N., Bertrand, G., and Becker, M., 2003, Present-day crustal deformation around Sagaing fault, Myanmar: J. geophys. Res, v. 108, no. B11, p. 2533.

Volkmer, J. E., Kapp, P., Guynn, J. H., and Lai, Q., 2007, Cretaceous-Tertiary structural evolution of the north central Lhasa terrane, Tibet: Tectonics, v. 26, no. 6, p. TC6007.

von Eynatten, H., and Dunkl, I., 2012, Assessing the sediment factory: The role of single grain analysis: Earth-Science Reviews, v. 115, no. 1–2, p. 97-120.

Von Eynatten, H., and Wijbrans, J. R., 2003, Precise tracing of exhumation and provenance using 40Ar/39Ar geochronology of detrital white mica: the example of the Central Alps: Geological Society, London, Special Publications, v. 208, no. 1, p. 289-305.

Wandrey, C., 2006, Eocene to Miocene composite total petroleum system, Irrawaddy-Andaman and north Burma geologic provinces, Myanmar: US Geological Survey Bulletin, v. 1.

Wang, E., and Burchfiel, B. C., 1997, Interpretation of Cenozoic Tectonics in the Right-Lateral Accommodation Zone Between the Ailao Shan Shear Zone and the Eastern Himalayan Syntaxis: International Geology Review, v. 39, no. 3, p. 191-219.

Wang, G., Wan, J., Wang, E., Zheng, D., and Li, F., 2008, Late Cenozoic to recent transtensional deformation across the Southern part of the Gaoligong shear zone between the Indian plate and SE margin of the Tibetan plateau and its tectonic origin: Tectonophysics, v. 460, no. 1–4, p. 1-20.

Wang, J.-G., Hu, X.-M., Garzanti, E., and Wu, F.-Y., 2013, Upper Oligocene‐Lower Miocene Gangrinboche Conglomerate in the Xigaze Area, Southern Tibet: Implications for Himalayan Uplift and Paleo-Yarlung-Zangbo Initiation: The journal of geology, v. 121, no. 4, p. 425-444.

Wang, J.-G., Hu, X.-M., Wu, F.-Y., and Jansa, L., 2010, Provenance of the Liuqu Conglomerate in southern Tibet: A Paleogene erosional record of the Himalayan–Tibetan orogen: Sedimentary Geology, v. 231, no. 3–4, p. 74-84.

Wang, J.-G., Wu, F.-Y., Tan, X.-C., and Liu, C.-Z., 2014, Magmatic evolution of the Western Myanmar Arc documented by U–Pb and Hf isotopes in detrital zircon: Tectonophysics, v. 612–613, no. 0, p. 97-105.

Wang, Y., Fan, W., Zhang, Y., Peng, T., Chen, X., and Xu, Y., 2006, Kinematics and $^{40}Ar/^{39}Ar$ geochronology of the Gaoligong and Chongshan shear systems, western Yunnan, China: Implications for early Oligocene tectonic extrusion of SE Asia: Tectonophysics, v. 418, no. 3, p. 235-254.

Wang, Y., Zhang, X., Sun, L., and Wan, J., 2007, Cooling history and tectonic exhumation stages of the south-central Tibetan Plateau (China): Constrained by 40Ar/39Ar and apatite fission track thermochronology: Journal of Asian Earth Sciences, v. 29, no. 2–3, p. 266-282.

Watkinson, I., Elders, C., Batt, G., Jourdan, F., Hall, R., and McNaughton, N. J., 2011, The timing of strike-slip shear along the Ranong and Khlong Marui faults, Thailand: Journal of Geophysical Research-Solid Earth, v. 116.

Watkinson, I., Elders, C., and Hall, R., 2008, The kinematic history of the Khlong Marui and Ranong Faults, southern Thailand: Journal of Structural Geology, v. 30, no. 12, p. 1554-1571.

Wen, D.-R., Chung, S.-L., Song, B., Iizuka, Y., Yang, H.-J., Ji, J., Liu, D., and Gallet, S., 2008a, Late Cretaceous Gangdese intrusions of adakitic geochemical characteristics, SE Tibet: Petrogenesis and tectonic implications: Lithos, v. 105, no. 1–2, p. 1-11.

Wen, D.-R., Liu, D., Chung, S.-L., Chu, M.-F., Ji, J., Zhang, Q., Song, B., Lee, T.-Y., Yeh, M.-W., and Lo, C.-H., 2008b, Zircon SHRIMP U–Pb ages of the Gangdese Batholith and implications for Neotethyan subduction in southern Tibet: Chemical Geology, v. 252, no. 3–4, p. 191-201.

White, N. M., Parrish, R., Bickle, M., Najman, Y., Burbank, D., and Maithani, A., 2001, Metamorphism and exhumation of the NW Himalaya constrained by U–Th–Pb analyses of detrital monazite grains from early foreland basin sediments: Journal of the Geological Society, v. 158, no. 4, p. 625-635.

White, N. M., Pringle, M., Garzanti, E., Bickle, M., Najman, Y., Chapman, H., and Friend, P., 2002, Constraints on the exhumation and erosion of the High Himalayan Slab, NW India, from foreland basin deposits: Earth and Planetary Science Letters, v. 195, no. 1, p. 29-44.

Win, A., 1986, Geology of the Okpo-Kyaunggon area, Budali and Monywa townships [MSc: University of Mandalay, 151 p.
Woodhead, J. D., and Hergt, J. M., 2005, A Preliminary Appraisal of Seven Natural Zircon Reference Materials for In Situ Hf Isotope Determination: Geostandards and Geoanalytical Research, v. 29, no. 2, p. 183-195.
Wu, F.-Y., Clift, P. D., and Yang, J.-H., 2007, Zircon Hf isotopic constraints on the sources of the Indus Molasse, Ladakh Himalaya, India: Tectonics, v. 26, no. 2, p. n/a-n/a.
Wu, F. Y., Ji, W. Q., Liu, C. Z., and Chung, S. L., 2010, Detrital zircon U–Pb and Hf isotopic data from the Xigaze fore-arc basin: constraints on Transhimalayan magmatic evolution in southern Tibet: Chemical Geology, v. 271, no. 1, p. 13-25.
Xiaoming, Q., Hou, Z., Zaw, K., and Youguo, L., 2007, Characteristics and genesis of Gangdese porphyry copper deposits in the southern Tibetan Plateau: Preliminary geochemical and geochronological results: Ore Geology Reviews, v. 31, no. 1–4, p. 205-223.
Xu, R.-H., Schärer, U., and Allègre, C. J., 1985, Magmatism and Metamorphism in the Lhasa Block (Tibet): A Geochronological Study: The journal of geology, v. 93, no. 1, p. 41-57.
Xu, W.-C., Zhang, H.-F., Harris, N., Guo, L., and Pan, F.-B., 2013, Rapid Eocene erosion, sedimentation and burial in the eastern Himalayan syntaxis and its geodynamic significance: Gondwana Research, v. 23, no. 2, p. 715-725.
Xu, W.-C., Zhang, H.-F., Parrish, R., Harris, N., Guo, L., and Yuan, H.-L., 2010, Timing of granulite-facies metamorphism in the eastern Himalayan syntaxis and its tectonic implications: Tectonophysics, v. 485, no. 1–4, p. 231-244.
Xu, Y.-G., Lan, J.-B., Yang, Q.-J., Huang, X.-L., and Qiu, H.-N., 2008, Eocene break-off of the Neo-Tethyan slab as inferred from intraplate-type mafic dykes in the Gaoligong orogenic belt, eastern Tibet: Chemical Geology, v. 255, no. 3–4, p. 439-453.
Xu, Y.-G., Yang, Q.-J., Lan, J.-B., Luo, Z.-Y., Huang, X.-L., Shi, Y.-R., and Xie, L.-W., 2012, Temporal–spatial distribution and tectonic implications of the batholiths in the Gaoligong–Tengliang–Yingjiang area, western Yunnan: Constraints from zircon U–Pb ages and Hf isotopes: Journal of Asian Earth Sciences, v. 53, no. 0, p. 151-175.
Yamada, R., Tagami, T., Nishimura, S., and Ito, H., 1995, Annealing kinetics of fission tracks in zircon: an experimental study: Chemical Geology, v. 122, no. 1, p. 249-258.
Yin, A., 2010, Cenozoic tectonic evolution of Asia: A preliminary synthesis: Tectonophysics, v. 488, no. 1–4, p. 293-325.
Yin, A., and Harrison, T. M., 2000, Geologic evolution of the Himalayan-Tibetan orogen: Annual Review of Earth and Planetary Sciences, v. 28, no. 1, p. 211-280.
Yin, A., Harrison, T. M., Ryerson, F. J., Wenji, C., Kidd, W. S. F., and Copeland, P., 1994, Tertiary structural evolution of the Gangdese Thrust System, southeastern

Tibet: Journal of Geophysical Research: Solid Earth, v. 99, no. B9, p. 18175-18201.

Yuan, W., Deng, J., Zheng, Q., Dong, J., Bao, Z., Eizenhoefer, P. R., Xu, X., and Huang, Z., 2009, Apatite fission track constraints on the Neogene tectono-thermal history of Nimu area, southern Gangdese terrane, Tibet Plateau: Island Arc, v. 18, no. 3, p. 488-495.

Zaw, K., 1998, Geological Evolution of Selected Granitic Pegmatites in Myanmar (Burma): Constraints from Regional Setting, Lithology, and Fluid-Inclusion Studies: International Geology Review, v. 40, no. 7, p. 647-662.

Zeitler, P. K., Meltzer, A. S., Koons, P. O., Craw, D., Hallet, B., Chamberlain, C. P., Kidd, W. S., Park, S. K., Seeber, L., and Bishop, M., 2001, Erosion, Himalayan Geodynamics, and the Geomorphology of Metamorphism: GSA Today, p. 5.

Zhang, B., Zhang, J., Zhong, D., Yang, L., Yue, Y., and Yan, S., 2012a, Polystage deformation of the Gaoligong metamorphic zone: Structures, 40Ar/39Ar mica ages, and tectonic implications: Journal of Structural Geology, v. 37, no. 0, p. 1-18.

Zhang, H.-F., Xu, W.-C., Zong, K.-Q., Yuan, H.-L., and Harris, N., 2008, Tectonic Evolution of Metasediments from the Gangdise Terrane, Asian Plate, Eastern Himalayan Syntaxis, Tibet: International Geology Review, v. 50, no. 10, p. 914-930.

Zhang, H., Harris, N., Guo, L., and Xu, W., 2010a, The significance of Cenozoic magmatism from the western margin of the eastern syntaxis, southeast Tibet: Contributions to Mineralogy and Petrology, v. 160, no. 1, p. 83-98.

Zhang, J. Y., Yin, A., Liu, W. C., Wu, F. Y., Lin, D., and Grove, M., 2012b, Coupled U-Pb dating and Hf isotopic analysis of detrital zircon of modern river sand from the Yalu River (Yarlung Tsangpo) drainage system in southern Tibet: Constraints on the transport processes and evolution of Himalayan rivers: Geological Society of America Bulletin, v. 124, no. 9-10, p. 1449-1473.

Zhang, K.-J., Zhang, Y.-X., Tang, X.-C., and Xia, B., 2012c, Late Mesozoic tectonic evolution and growth of the Tibetan plateau prior to the Indo-Asian collision: Earth-Science Reviews, v. 114, no. 3–4, p. 236-249.

Zhang, Z., Dong, X., Santosh, M., Liu, F., Wang, W., Yiu, F., He, Z., and Shen, K., 2012d, Petrology and geochronology of the Namche Barwa Complex in the eastern Himalayan syntaxis, Tibet: Constraints on the origin and evolution of the north-eastern margin of the Indian Craton: Gondwana Research, v. 21, no. 1, p. 123-137.

Zhang, Z., Dong, X., Xiang, H., Liou, J. G., and Santosh, M., 2013, Building of the Deep Gangdese Arc, South Tibet: Paleocene Plutonism and Granulite-Facies Metamorphism: Journal of Petrology, v. 54, no. 12, p. 2547-2580.

Zhang, Z., Zhao, G., Santosh, M., Wang, J., Dong, X., and Shen, K., 2010b, Late Cretaceous charnockite with adakitic affinities from the Gangdese batholith, southeastern Tibet: Evidence for Neo-Tethyan mid-ocean ridge subduction?: Gondwana Research, v. 17, no. 4, p. 615-631.

Zhang, Z. M., Zhao, G. C., Santosh, M., Wang, J. L., Dong, X., and Liou, J. G., 2010c, Two stages of granulite facies metamorphism in the eastern Himalayan syntaxis,

south Tibet: petrology, zircon geochronology and implications for the subduction of Neo-Tethys and the Indian continent beneath Asia: Journal of Metamorphic Geology, v. 28, no. 7, p. 719-733.

Zhou, S., Mo, X., Dong, G., Zhao, Z., Qiu, R., Guo, T., and Wang, L., 2004, 40Ar-39Ar geochronology of Cenozoic Linzizong volcanic rocks from Linzhou Basin, Tibet, China, and their geological implications: Chinese Science Bulletin, v. 49, no. 18, p. 1970-1979.

Zhou, S., Mo, X., Zhao, Z., Qiu, R., Niu, Y., Guo, T., and Zhang, S., 2010, 40Ar/39Ar geochronology of post-collisional volcanism in the middle Gangdese Belt, southern Tibet: Journal of Asian Earth Sciences, v. 37, no. 3, p. 246-258.

Zhu, B., Kidd, William S. F., Rowley, David B., Currie, B. S., and Shafique, N., 2005, Age of Initiation of the India-Asia Collision in the East-Central Himalaya: The journal of geology, v. 113, no. 3, p. 265-285.

Zhu, D.-C., Chung, S.-L., Mo, X.-X., Zhao, Z.-D., Niu, Y., Song, B., and Yang, Y.-H., 2009a, The 132 Ma Comei-Bunbury large igneous province: Remnants identified in present-day southeastern Tibet and southwestern Australia: Geology, v. 37, no. 7, p. 583-586.

Zhu, D.-C., Mo, X.-X., Niu, Y., Zhao, Z.-D., Wang, L.-Q., Liu, Y.-S., and Wu, F.-Y., 2009b, Geochemical investigation of Early Cretaceous igneous rocks along an east–west traverse throughout the central Lhasa Terrane, Tibet: Chemical Geology, v. 268, no. 3–4, p. 298-312.

Zhu, D.-C., Mo, X.-X., Zhao, Z.-D., Niu, Y., and Chung, S.-L., 2008, Whole-rock elemental and zircon Hf isotopic geochemistry of mafic and ultramafic rocks from the Early Cretaceous Comei large igneous province in SE Tibet: constraints on mantle source characteristics and petrogenesis.

Zhu, D.-C., Zhao, Z.-D., Niu, Y., Mo, X.-X., Chung, S.-L., Hou, Z.-Q., Wang, L.-Q., and Wu, F.-Y., 2011, The Lhasa Terrane: Record of a microcontinent and its histories of drift and growth: Earth and Planetary Science Letters, v. 301, no. 1–2, p. 241-255.

Zhu, D., Mo, X., Wang, L., Zhao, Z., Niu, Y., Zhou, C., and Yang, Y., 2009c, Petrogenesis of highly fractionated I-type granites in the Zayu area of eastern Gangdese, Tibet: Constraints from zircon U-Pb geochronology, geochemistry and Sr-Nd-Hf isotopes: Science in China Series D: Earth Sciences, v. 52, no. 9, p. 1223-1239.

Appendix A-1: Heavy Mineral Assemblages

Heavy minerals are present in concentrations of less than 1% of the bulk sediment. Identifying these minerals and forming mineral assemblages for particular sedimentary units can be very useful in determining provenance, as well as, magmatic and metamorphic events that occurred within the source area. In this study, the identification of heavy mineral species is hindered by the limited amount of bulk sediment, and thus heavy mineral populations, available for analysis. Recent studies utilizing mineralogy and petrography of heavy mineral populations to quantify sandstone provenance using a point counting method requires over 300 grains for each sample (Garzanti et al., 2004). Therefore heavy mineral assemblages in this study were determined using electron microprobe analysis on a representative population of heavy minerals present in each sample.

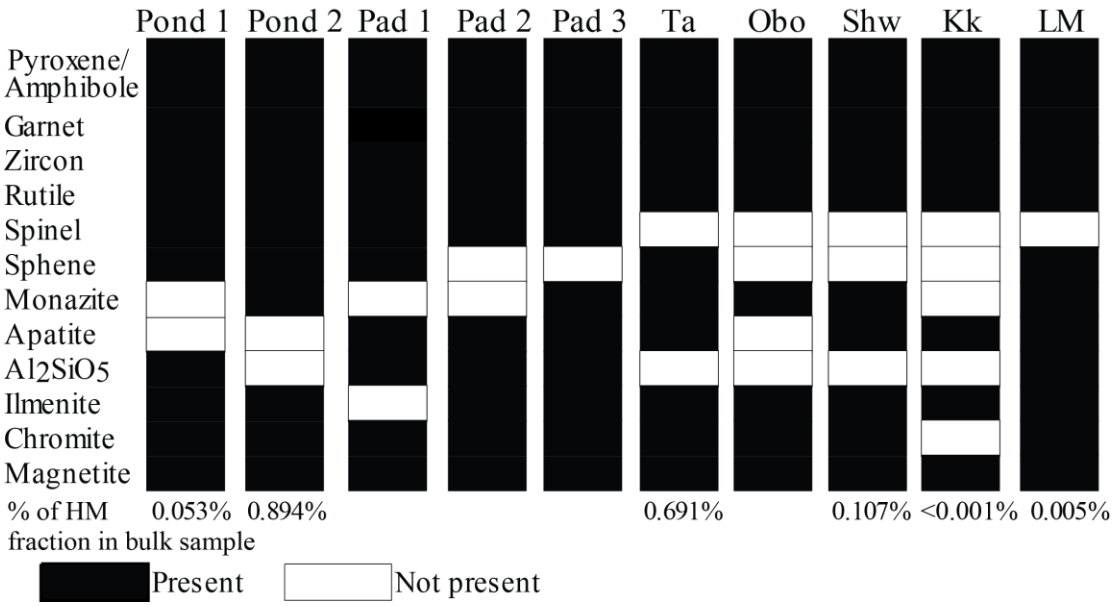

Figure A.1 Main heavy mineral types within each Central Burma Basin sedimentary rock sample.

A general decrease in weight percent of the heavy mineral fraction in the bulk sample is noted moving up-section, with the Lower Moza sample containing less than a hundredth of a gram. The Kyaukkok sample shows a similar pattern and the absence of

heavy minerals (< 15 grains) may be an important provenance indicator. This may be contributed to a change in the source area or decrease in the sediment supply; however, similar heavy mineral associations are noted throughout the entire sequence, indicating erosion of a dominant lithology or multiple lithologies. It is important to note that the relatively large increase in percentage of heavy minerals between the Pondaung 1 – Pondaung 2 and Shwetaung – Taungtalon samples may be contributed to the change to a prograding depositional environment, with an increased input of fluvial sands into the previously deltaic environment. The relatively low heavy mineral concentration and low mica content within the Pondaung 1 sample may reflect increased chemical weathering during deposition. Stratigraphic variations in the relative abundance of heavy minerals may also reflect geodynamic changes within the source area, such as metamorphism and magmatism, changes in the rates of uplift and erosion, and in the methods of transport and depositional environments.

The main minerals present, which occurred in nearly every sample, were pyroxenes, amphibole, garnet, chromite, zircon, monazite, apatite, rutile, magnetite, spinel, ilmenite and Al_2SiO_5 polymorphs (Figure A.1). Distinction between the varieties of amphibole and pyroxene is limited as electron microprobe analysis reveals only the elements present within a mineral. Ultrastable (zircon and rutile) and stable (garnet, apatite and monazite) minerals are present in all samples. The heavy mineral assemblage reveals sediment provenance from both magmatic (granitic and mafic-ultra mafic) and metamorphic source terranes. The presence of epidote, cordierite, and AlSiO polymorphs suggest indicate a high-grade metamorphic source area is contributing to the sediment load. The increasing grade of detritus moving up-section from cordierite in the Early Miocene aged sample (Shwetaung Formation) to kyanite in the Middle Miocene aged samples (Taungtalon, Obogon and Lower Moza formations) suggests the unroofing of a metamorphic terrane. The increase in percentage of heavy minerals during deposition of the Taungtalon formation may indicate a time of increased erosion due to a rapidly uplifting terrane with the first appearance of cordierite.

Detrital garnet geochemistry analysed using electron microprobe techniques reveals a change in garnet composition occurred between deposition of the Oligocene Padaung Formation and the Early Miocene Shwetaung and younger Miocene formations (Figure A.2). The garnet chemistry data shows the loss of a granitic (almandine) source from the Eocene-Oligocene into the Miocene (Shwetaung). There is an increased contribution of low and high grade metamorphic rocks for post-Early Miocene deposits (Taungtalon, Lower Moza and Obogon formations). This is consistent temporally with the change in provenance observed in the detrital zircon and white mica datasets. Additional information regarding specific provenance of detrital garnet would be enhanced by comparison with detrital garnet from the modern Yarlung Tsangpo and Irrawaddy River systems, as garnet datasets from bedrock within these catchments is currently unavailable in the literature.

Heavy minerals may be derived from numerous rock types of varying geological conditions, limiting its usefulness as a provenance indicator considering the extremely complex geological nature of the eastern syntaxis. To be useful as a provenance indicator, mineral assemblages were combined with high precision detrital zircon U-Pb and fission track geochronology, detrital zircon Lu-Hf isotopic analysis and $^{40}Ar/^{39}Ar$ white mica thermochronology.

Figure A.2 Detrital garnet compositions for Eocene, Oligocene and Miocene Central Burma Basin samples illustrated by Almandine ($Fe_3Al_2Si_3O_{12}$) + Spessartine ($Mn_3Al_2Si_3O_{12}$) – Grossular ($Ca_3Al_2Si_3O_{12}$) – Pyrope ($Mg_3Al_2Si_3O_{12}$) and Fe + Mn–Ca–Mg ternary diagrams. Garnet composition fields from Mange and Morton (2007). Type A: High-grade granulite-facies metasedimentary rocks and intermediate-acidic igneous rocks with a deep crustal source; Type B: Amphibolite-facies metasedimentary rocks; Type Bi: Ca <10%, Intermediate-acidic igneous rocks; Type Bii: Ca >10%, Amphibolite facies metasedimentary rocks and acid igneous rocks; Type C: High-grade meta-basic rocks; Type Ci: Mg <40%, metamorphosed mafic rocks; Type Cii: Mg >40%, Metamorphosed ultramafic rocks including pyroxenites and peridotites; Type D: Metasomatic rocks including skarns, low-grade meta-basic rocks and metamorphosed calc-silicate granulites.

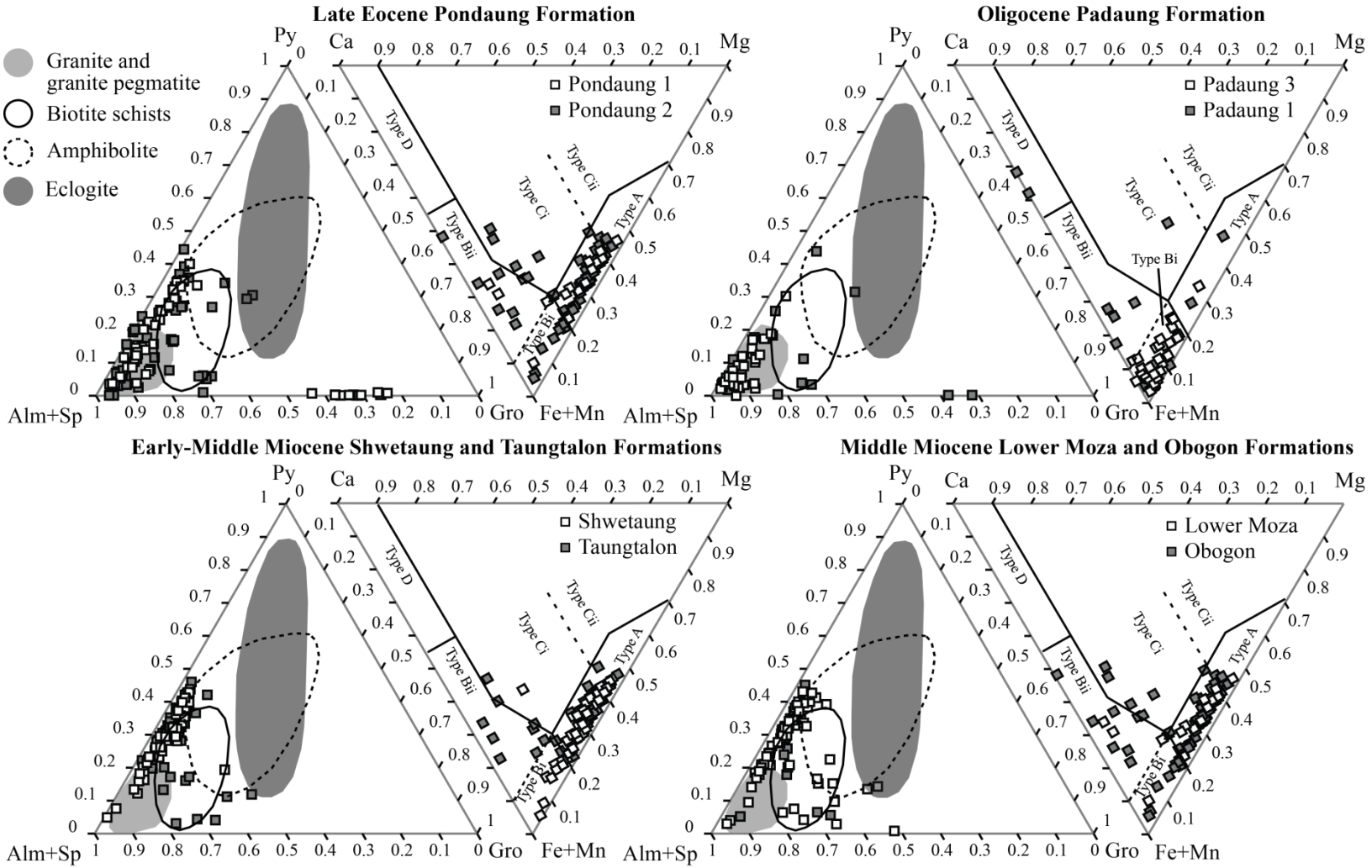
Late Eocene Pondaung Formation
Oligocene Padaung Formation
Early-Middle Miocene Shwetaung and Taungtalon Formations
Middle Miocene Lower Moza and Obogon Formations
Granite and granite pegmatite
Biotite schists
Amphibolite
Eclogite
Pondaung 1
Pondaung 2
Padaung 3
Padaung 1
Shwetaung
Taungtalon
Lower Moza
Obogon
Py
Ca
Mg
Alm+Sp
Gro
Fe+Mn
Type D
Type Bii
Type Ci
Type Cii
Type A
Type Bi

Appendix A-2: Zircon U-Pb Geochronology, Lu-Hf Geochemistry and fission track thermochronology

Ten sedimentary rock samples were prepared for detrital heavy mineral analysis. Standard crushing, sizing, density and magnetic separation techniques were employed at University of St Andrews to extract detrital zircons from ten sedimentary rock samples. Individual crystals were handpicked, mounted in 25mm epoxy resin discs and polished to reveal a bisection of the minerals. Cathodoluminescence (CL) and back-scattered electron (BSE) images were obtained using a JEOL JXA-8600 electron microprobe operating at 15kV in the School of Geography & Geosciences, University of St Andrews, in order to identify the internal zoning and core-rim relationships of each zircon, to determine their quality, and to select positions for U-Pb and Hf isotope analyses.

U-Pb data were acquired over five analytical sessions (June 20-22, 2007; Dec. 4-7, 2007; April 9-10, 2008; December 15, 2008; 30 Sept - Oct 1, 2009). *In situ* zircon U-Pb data were obtained using laser ablation multi-collector inductively coupled plasma mass spectrometry (LA-MC-ICP-MS) performed at the NERC Isotope Geosciences Laboratory, UK, following the procedure described by Cottle et al. (2009). Single spot U-Pb analyses involved a Nu Plasma MC-ICP-MS and a UP-193SS laser ablation system operating at a wavelength of 193 nanometres using a 35 μm spot. Laser fluence was maintained at 2-3 Jcm^{-2}. Each analysis consisted of a 20 second integration with the laser off to allow the previous signal to decay to background and a thirty second integration with the laser ablating the grain with a 5 Hz repetition rate.

Plesovice was used as the primary reference zircon; Mudtank and 91500 were used as secondary reference materials (Figure A.3). Three reference zircons were analyzed for every 10 unknowns in order to correct for fractionation of uranium and lead. Criteria for in-house rejection of data points is based on samples with ^{204}Pb in excess of 300 counts per second (indicating significant common-Pb) and ^{207}Pb mV signals < 0.01 (indicating radiogenic Pb below detection). $^{206}Pb/^{238}U$ ages are used for

zircons <1000 Ma and uncertainties on individual analyses are reported as 2σ. The complete LA-MC-ICPMS zircon U-Pb dataset analysed at NIGL is given in Table A.1.

A sub-set of zircons from each of the Cenozoic samples were selected for Hf isotope analysis using LA-MC-ICPMS at the NERC Isotope Geosciences Laboratory, UK in order to provide further provenance discrimination. In order to differentiate the Tibet and Myanmar sources, only zircons with a U-Pb age less than 250 Ma were selected. *In situ* Lu-Hf measurements were acquired over three analytical sessions (May 5-6, 2009; June 15-19, 2009; Sept. 28, 29 and Oct. 2, 2009). Zircon Hf isotope analyses were measured on top of or within the same zone as the U-Pb ablation pits using a UP-193SS laser ablation system operating at a wavelength of 193 nm using a 50 micron spot. Laser fluence ranged from ~7 to 10.5 Jcm^{-2}. Each analysis consisted of a twenty second integration with the laser off to allow the previous signal to decay to background and a 50 second ablation with a 10 Hz repetition rate.

Mudtank was used as the primary reference zircon with secondary references 91500, Plesovice and GJ-1 used on October 2, 2009. Three measurements of each reference zircon were conducted for every 10 sample analyses. Helium was used as the carrier gas of ablated material. The $^{176}Hf/^{177}Hf$ and Lu-Hf ratios are normalised to 91500 assuming the values of Woodhead and Hergt (2005). εHf(t) values were calculated for each zircon using the $^{206}Pb/^{238}U$ age data and assuming values for the chondritic reservoir $^{176}Hf/^{177}Hf$ ratio of 0.282772 and $^{176}Lu/^{177}Hf$ of 0.0332 (Blichert-Toft and Albarède, 1997) and the decay constant for ^{176}Lu of 1.867×10^{-11} $year^{-1}$ (Söderlund et al., 2004). Uncertainties are quoted as 2σ. The complete zircon Lu-Hf isotopic dataset using LA-MS-ICPMS methods at NIGL is given in Table A.2.

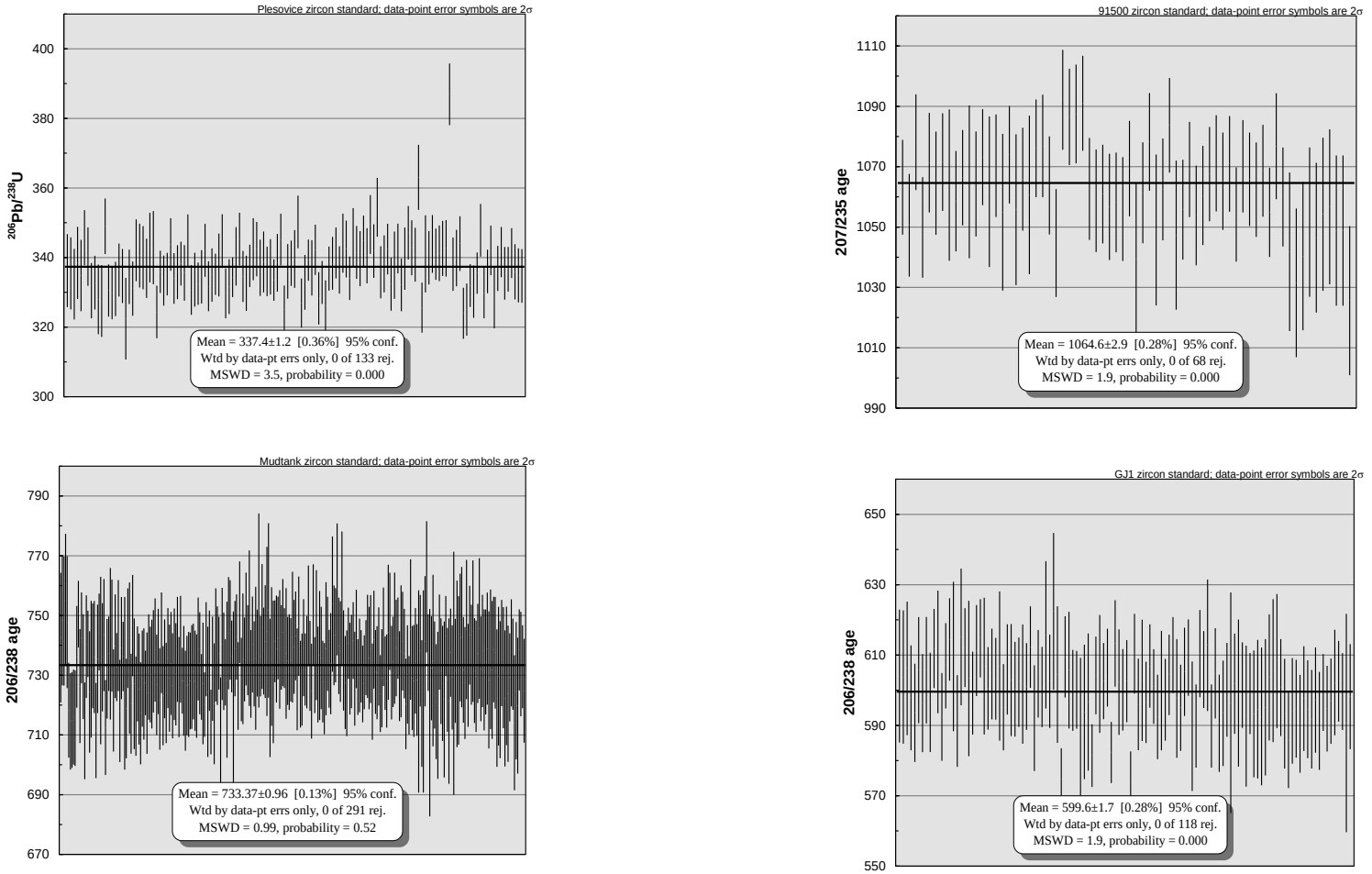

Figure A.3 Zircon standards, U-Pb and Lu-Hf isotopic analysis.

Combined detrital zircon U-Pb and fission track analysis on detrital zircon was carried out by Dr. Andy Carter at the London Geochronology Centre, University College London (UCL). For U-Pb dating, samples were analysed by LA-ICPMS (New Wave NWR 193nm laser ablation system and Agilent 7700x ICP-MS). Real time data were processed using GLITTER 4.4 data reduction software. Repeated measurements of external zircon standard Plesovice (TIMS reference age 337.13±0.37 Ma) (Sláma et al., 2008) and NIST 612 silicate glass (Pearce et al., 1997) were used to correct for instrumental mass bias and depth-dependent inter-element fractionation of Pb, Th and U. Ages were calculated using the $^{206}Pb/^{238}U$ series used for samples dated as <1 Ga, and the $^{207}Pb/^{206}Pb$ series used for grains >1 Ga. Ages were rejected if discordance exceeded 15%. Fission track ages were determined using the external detector method using a zeta calibration factor and conducted using Zeiss Axioplan microscopes with automated Kinetek XY stages. Data is presented in Table A.3.

Lu-Hf isotopic analysis on a sub-set of detrital zircons that were double dated by U-Pb (ICP-MS) and fission track methods was carried out by Dr. Bruno Dhuime at the Bristol Isotope Group, Bristol University, UK. Analysis was conducted using a Thermo-Finnigan, multi-collector inductively coupled plasma mass-spectrometer coupled to a UP193HE Deep-UV (193 nm) Excimer laser with a spot size of 40µm. The $^{176}Hf/^{177}Hf$ measured ratios are normalised to the JMC 45 hafnium standard assuming the values of Woodhead and Hergt (2005). εHf(t) values were calculated for each zircon using the $^{206}Pb/^{238}U$ age data and assuming values for the chondritic reservoir $^{176}Hf/^{177}Hf$ ratio of 0.282785 and $^{176}Lu/^{177}Hf$ of 0.0336 (Bouvier et al., 2008) and the decay constant for ^{176}Lu of 1.867×10^{-11} $year^{-1}$ (Söderlund et al., 2004). Uncertainties are quoted as 2σ. See Dhuime et al. (2011) for analytical details. The zircon Lu-Hf dataset is presented in Table A4.

Appendix A-3: $^{40}Ar/^{39}Ar$ white mica thermochronology

Ten sandstone samples from outcrop exposures of Cenozoic sedimentary rocks of the Central Myanmar Basin were analyzed: two from the Eocene Pondaung Formation (Pondaung 1 and Pondaung 2), three from the Oligocene Padaung Formation (Padaung 1, Padaung 2 and Padaung 3), and one from each of the Miocene Shwetaung Formation, Taungtalon Formation, Lower Moza Formation, Obogon Formation and Kyaukkok Formation. In total, 691 mica grains have been analysed in order to link the thermal history of individual grains to a specific source region. All mineral preparation and grain selection was conducted at the University of St Andrews, Scotland, UK. Sandstone samples were crushed and sieved to isolate the 250 to 500 μm fraction, from which muscovite grains were hand-picked under a binocular microscope. In $^{40}Ar/^{39}Ar$ dating, "data quality is highly dependent on crystal size, and limitations exist for dating mica grains less than 150 μm in diameter, as there is less radiogenic ^{40}Ar to measure, yielding larger uncertainties" (van Hoang et al., 2010). Because of this selection bias based on grain diameter, it must be recognized that age population(s) characterized by muscovite grains < 250μm in diameter are under represented, however, as the majority of the detrital mica are above this analytical cutoff, based on examination of the sediment under a binocular microscope, we are confident the age populations obtained are truly representative (excepting those of the Pondaung Formation).

$^{40}Ar/^{39}Ar$ laser fusion dating of single grain detrital white micas were conducted the Natural Environment Research Council (NERC) Argon Isotope Laboratory, East Kilbride, Scotland. Each sample was sieved to separate the >250 μm fraction and approximately 100 grains were handpicked. Mica grains were then wrapped in aluminium foil packets, stacked into irradiation tubes interspersed with packets containing a mineral standard. Samples were irradiated for 1.92 hours in the Oregon State University CLICIT (cadmium lined) facility. The International $^{40}Ar/^{39}Ar$ Age Standard, Fish Canyon Tuff sanidine (FCs) with a reference age of 28.201 Ma (Kuiper et al., 2008) was used as a neutron fluence monitor and was loaded between each set of 3 unknowns at the top and bottom positions.

After irradiation, the samples and standards were loaded into individual 2 mm diameter pots of a Cu-sample tray and placed in an ultra-high vacuum laser cell with a zinc-selenide window for transmission of IR laser light. Prior to analysis, samples were baked at 150°C to remove excess Ar trapped in clays. Samples and standards were fused using a 25W CO2 laser with a wavelength of 10.6 μm operating at 15% power and data were collected using an ARGUS multi-collector mass spectrometer using a faraday collector array. System blanks were measured every 2 grains and mass discrimination was monitored by analysis of aliquots of air every 6 grains. An in-house Excel program was used for off-line data reduction and age calculation. Procedures followed for analysis and age calculations are the same as those reported by (Mark et al., 2009). Analytical results are presented in Table A.6.

Appendix A-4: Cathodoluminescence (CL) images of detrital zircons

Solid circles indicate the ablation spot locations for LA-MC-ICPMS U-Pb analyses and dashed circles indicate the locations for Lu-Hf analyses. The scale bar is 50 microns.

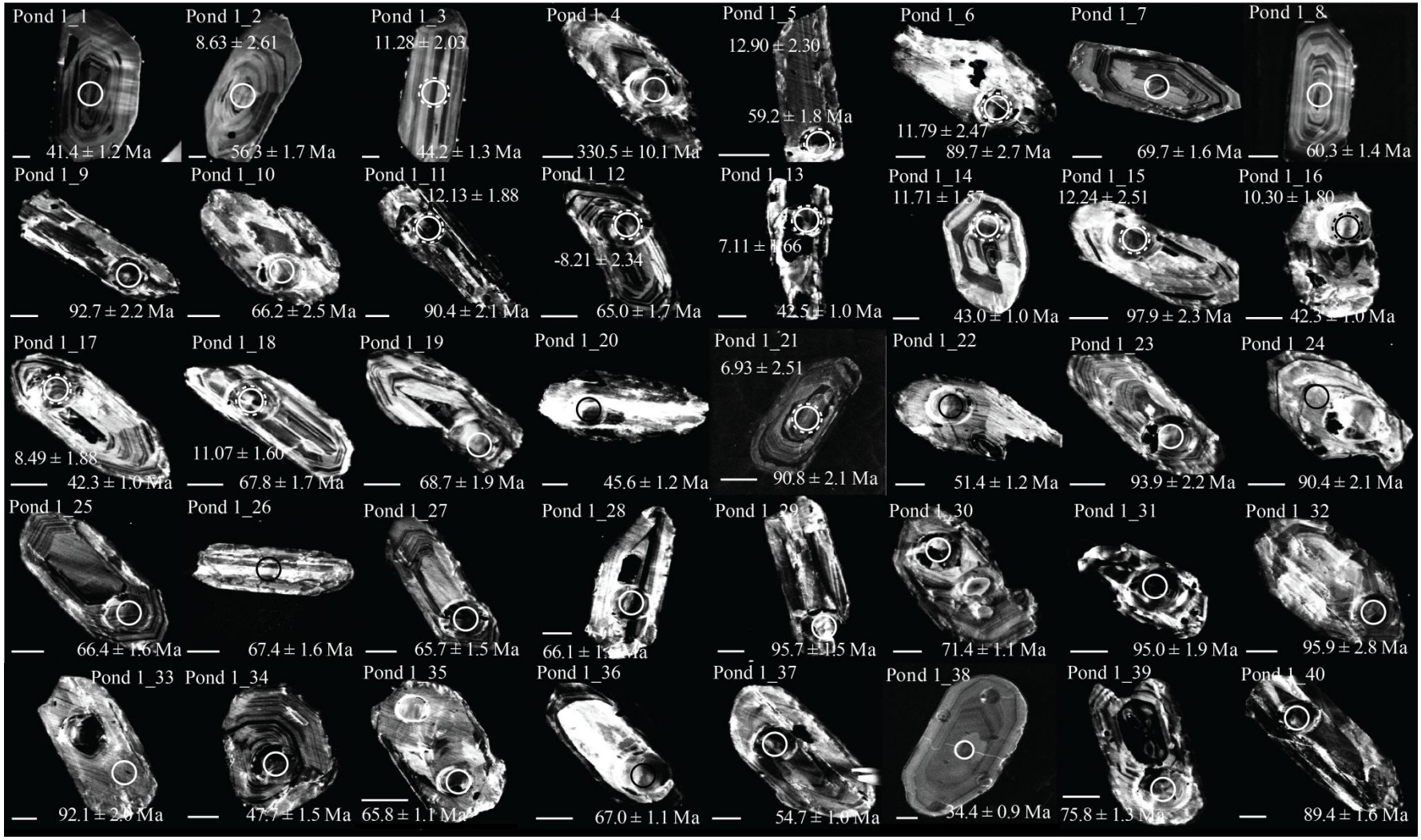
Pond 1_1
41.4 ± 1.2 Ma
Pond 1_2
8.63 ± 2.61
56.3 ± 1.7 Ma
Pond 1_3
11.28 ± 2.03
44.2 ± 1.3 Ma
Pond 1_4
330.5 ± 10.1 Ma
Pond 1_5
12.90 ± 2.30
59.2 ± 1.8 Ma
Pond 1_6
11.79 ± 2.47
89.7 ± 2.7 Ma
Pond 1_7
69.7 ± 1.6 Ma
Pond 1_8
60.3 ± 1.4 Ma
Pond 1_9
92.7 ± 2.2 Ma
Pond 1_10
66.2 ± 2.5 Ma
Pond 1_11
12.13 ± 1.88
90.4 ± 2.1 Ma
Pond 1_12
-8.21 ± 2.34
65.0 ± 1.7 Ma
Pond 1_13
7.11 ± 1.66
42.5 ± 1.0 Ma
Pond 1_14
11.71 ± 1.57
43.0 ± 1.0 Ma
Pond 1_15
12.24 ± 2.51
97.9 ± 2.3 Ma
Pond 1_16
10.30 ± 1.80
42.3 ± 1.0 Ma
Pond 1_17
8.49 ± 1.88
42.3 ± 1.0 Ma
Pond 1_18
11.07 ± 1.60
67.8 ± 1.7 Ma
Pond 1_19
68.7 ± 1.9 Ma
Pond 1_20
45.6 ± 1.2 Ma
Pond 1_21
6.93 ± 2.51
90.8 ± 2.1 Ma
Pond 1_22
51.4 ± 1.2 Ma
Pond 1_23
93.9 ± 2.2 Ma
Pond 1_24
90.4 ± 2.1 Ma
Pond 1_25
66.4 ± 1.6 Ma
Pond 1_26
67.4 ± 1.6 Ma
Pond 1_27
65.7 ± 1.5 Ma
Pond 1_28
Pond 1_29
95.7 ± 1.5 Ma
Pond 1_30
71.4 ± 1.1 Ma
Pond 1_31
95.0 ± 1.9 Ma
Pond 1_32
95.9 ± 2.8 Ma
Pond 1_33
92.1 ± 2.0 Ma
Pond 1_34
47.7 ± 1.5 Ma
Pond 1_35
65.8 ± 1.1 Ma
Pond 1_36
67.0 ± 1.1 Ma
Pond 1_37
54.7 ± 1.0 Ma
Pond 1_38
34.4 ± 0.9 Ma
Pond 1_39
75.8 ± 1.3 Ma
Pond 1_40
89.4 ± 1.6 Ma

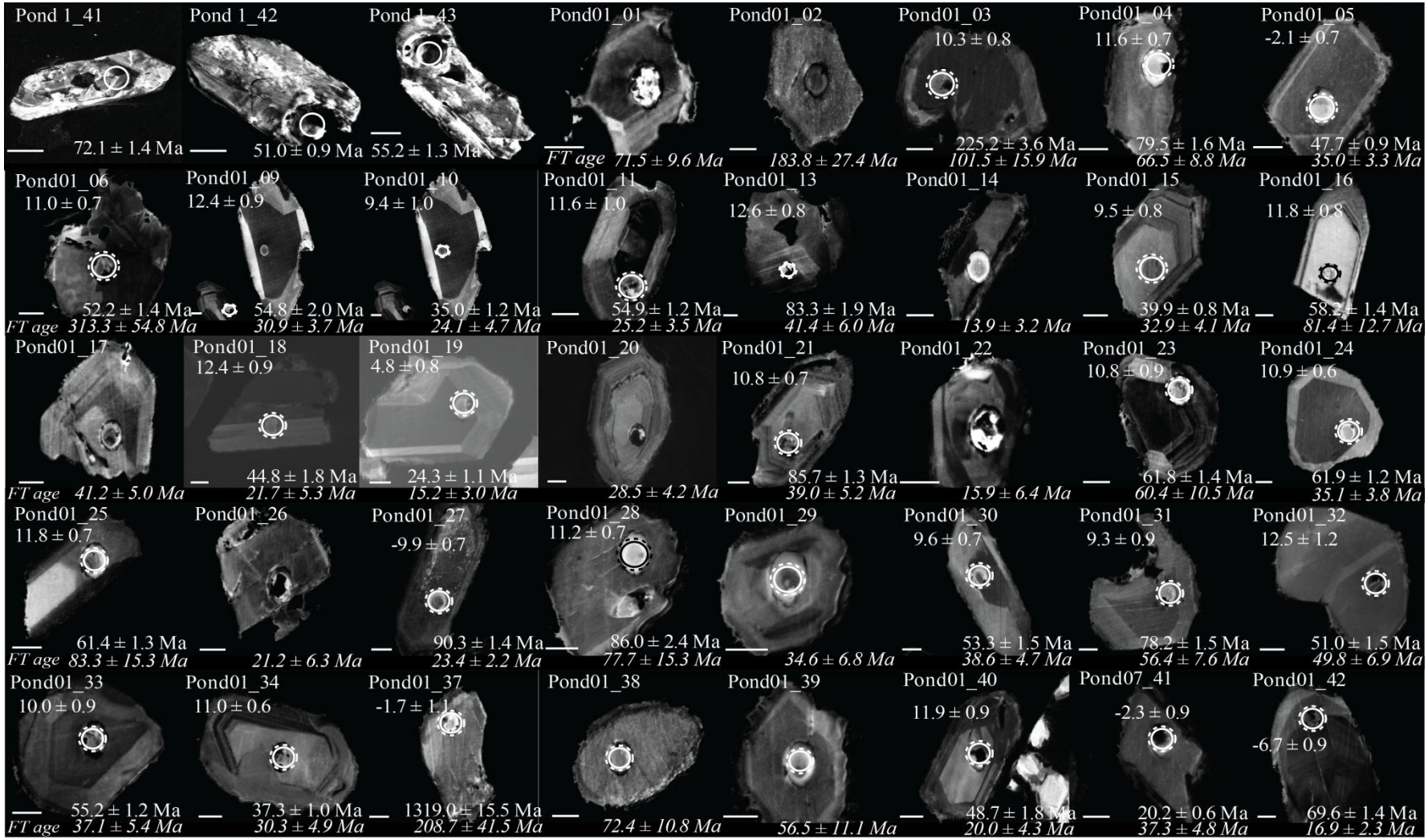
Pond 1_41
72.1 ± 1.4 Ma
Pond 1_42
51.0 ± 0.9 Ma
Pond 1_43
55.2 ± 1.3 Ma
Pond01_01
FT age 71.5 ± 9.6 Ma
Pond01_02
183.8 ± 27.4 Ma
Pond01_03
10.3 ± 0.8
225.2 ± 3.6 Ma
101.5 ± 15.9 Ma
Pond01_04
11.6 ± 0.7
79.5 ± 1.6 Ma
66.5 ± 8.8 Ma
Pond01_05
-2.1 ± 0.7
47.7 ± 0.9 Ma
35.0 ± 3.3 Ma
Pond01_06
11.0 ± 0.7
52.2 ± 1.4 Ma
FT age 313.3 ± 54.8 Ma
Pond01_09
12.4 ± 0.9
54.8 ± 2.0 Ma
30.9 ± 3.7 Ma
Pond01_10
9.4 ± 1.0
35.0 ± 1.2 Ma
24.1 ± 4.7 Ma
Pond01_11
11.6 ± 1.0
54.9 ± 1.2 Ma
25.2 ± 3.5 Ma
Pond01_13
12.6 ± 0.8
83.3 ± 1.9 Ma
41.4 ± 6.0 Ma
Pond01_14
13.9 ± 3.2 Ma
Pond01_15
9.5 ± 0.8
39.9 ± 0.8 Ma
32.9 ± 4.1 Ma
Pond01_16
11.8 ± 0.8
58.2 ± 1.4 Ma
81.4 ± 12.7 Ma
Pond01_17
FT age 41.2 ± 5.0 Ma
Pond01_18
12.4 ± 0.9
44.8 ± 1.8 Ma
21.7 ± 5.3 Ma
Pond01_19
4.8 ± 0.8
24.3 ± 1.1 Ma
15.2 ± 3.0 Ma
Pond01_20
28.5 ± 4.2 Ma
Pond01_21
10.8 ± 0.7
85.7 ± 1.3 Ma
39.0 ± 5.2 Ma
Pond01_22
15.9 ± 6.4 Ma
Pond01_23
10.8 ± 0.9
61.8 ± 1.4 Ma
60.4 ± 10.5 Ma
Pond01_24
10.9 ± 0.6
61.9 ± 1.2 Ma
35.1 ± 3.8 Ma
Pond01_25
11.8 ± 0.7
61.4 ± 1.3 Ma
FT age 83.3 ± 15.3 Ma
Pond01_26
21.2 ± 6.3 Ma
Pond01_27
-9.9 ± 0.7
90.3 ± 1.4 Ma
23.4 ± 2.2 Ma
Pond01_28
11.2 ± 0.7
86.0 ± 2.4 Ma
77.7 ± 15.3 Ma
Pond01_29
34.6 ± 6.8 Ma
Pond01_30
9.6 ± 0.7
53.3 ± 1.5 Ma
38.6 ± 4.7 Ma
Pond01_31
9.3 ± 0.9
78.2 ± 1.5 Ma
56.4 ± 7.6 Ma
Pond01_32
12.5 ± 1.2
51.0 ± 1.5 Ma
49.8 ± 6.9 Ma
Pond01_33
10.0 ± 0.9
55.2 ± 1.2 Ma
FT age 37.1 ± 5.4 Ma
Pond01_34
11.0 ± 0.6
37.3 ± 1.0 Ma
30.3 ± 4.9 Ma
Pond01_37
-1.7 ± 1.1
1319.0 ± 15.5 Ma
208.7 ± 41.5 Ma
Pond01_38
72.4 ± 10.8 Ma
Pond01_39
56.5 ± 11.1 Ma
Pond01_40
11.9 ± 0.9
48.7 ± 1.8 Ma
20.0 ± 4.3 Ma
Pond07_41
-2.3 ± 0.9
20.2 ± 0.6 Ma
37.3 ± 4.8 Ma
Pond01_42
-6.7 ± 0.9
69.6 ± 1.4 Ma
16.9 ± 2.3 Ma

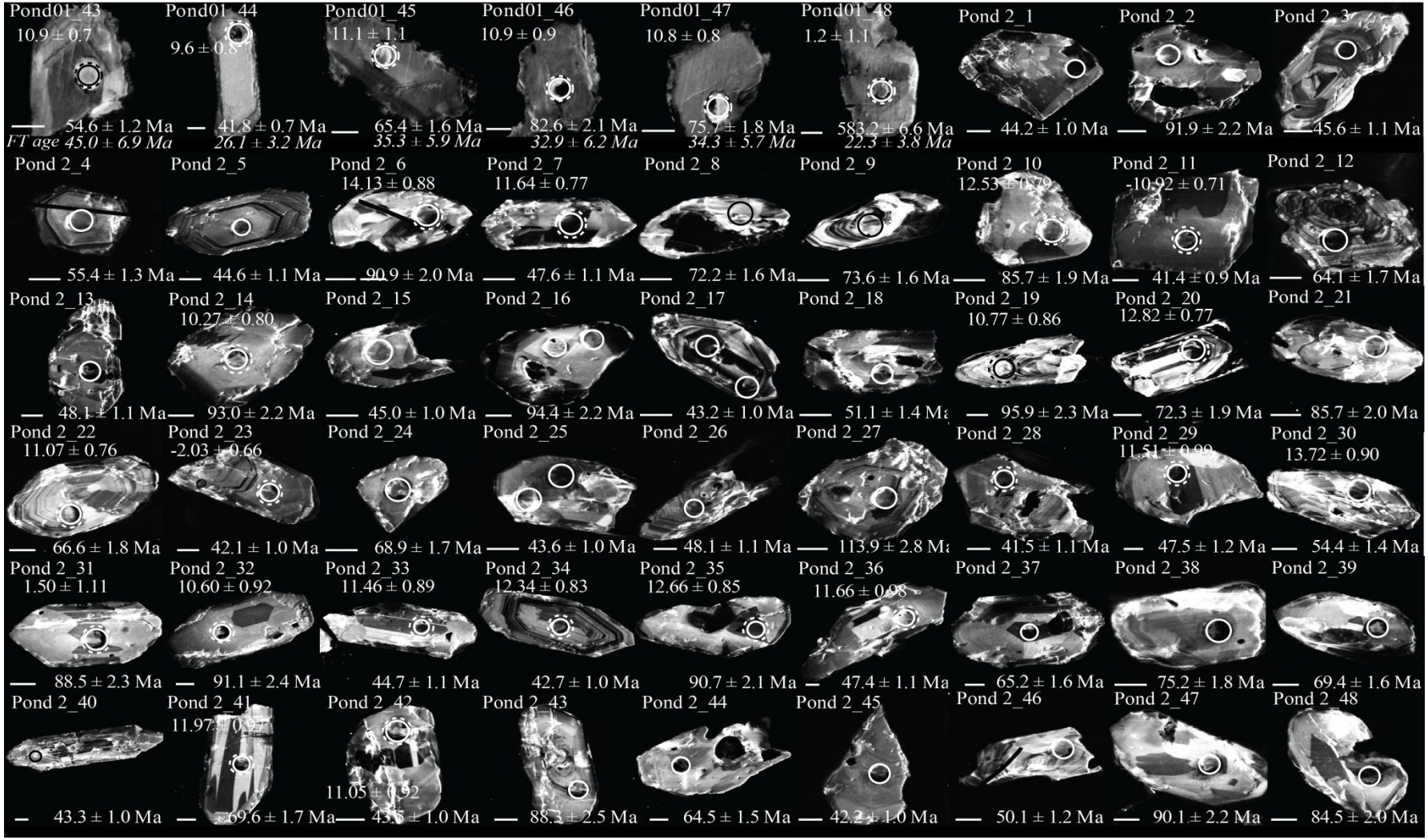
Pond01_43
10.9 ± 0.7
54.6 ± 1.2 Ma
FT age 45.0 ± 6.9 Ma
Pond01_44
9.6 ± 0.8
41.8 ± 0.7 Ma
26.1 ± 3.2 Ma
Pond01_45
11.1 ± 1.1
65.4 ± 1.6 Ma
35.3 ± 5.9 Ma
Pond01_46
10.9 ± 0.9
82.6 ± 2.1 Ma
32.9 ± 6.2 Ma
Pond01_47
10.8 ± 0.8
75.7 ± 1.8 Ma
34.3 ± 5.7 Ma
Pond01_48
1.2 ± 1.1
583.2 ± 6.6 Ma
22.3 ± 3.8 Ma
Pond 2_1
44.2 ± 1.0 Ma
Pond 2_2
91.9 ± 2.2 Ma
Pond 2_3
45.6 ± 1.1 Ma
Pond 2_4
55.4 ± 1.3 Ma
Pond 2_5
44.6 ± 1.1 Ma
Pond 2_6
14.13 ± 0.88
90.9 ± 2.0 Ma
Pond 2_7
11.64 ± 0.77
47.6 ± 1.1 Ma
Pond 2_8
72.2 ± 1.6 Ma
Pond 2_9
73.6 ± 1.6 Ma
Pond 2_10
12.53 ± 0.79
85.7 ± 1.9 Ma
Pond 2_11
-10.92 ± 0.71
41.4 ± 0.9 Ma
Pond 2_12
64.1 ± 1.7 Ma
Pond 2_13
48.1 ± 1.1 Ma
Pond 2_14
10.27 ± 0.80
93.0 ± 2.2 Ma
Pond 2_15
45.0 ± 1.0 Ma
Pond 2_16
94.4 ± 2.2 Ma
Pond 2_17
43.2 ± 1.0 Ma
Pond 2_18
51.1 ± 1.4 Ma
Pond 2_19
10.77 ± 0.86
95.9 ± 2.3 Ma
Pond 2_20
12.82 ± 0.77
72.3 ± 1.9 Ma
Pond 2_21
85.7 ± 2.0 Ma
Pond 2_22
11.07 ± 0.76
66.6 ± 1.8 Ma
Pond 2_23
-2.03 ± 0.66
42.1 ± 1.0 Ma
Pond 2_24
68.9 ± 1.7 Ma
Pond 2_25
43.6 ± 1.0 Ma
Pond 2_26
48.1 ± 1.1 Ma
Pond 2_27
113.9 ± 2.8 Ma
Pond 2_28
41.5 ± 1.1 Ma
Pond 2_29
11.51 ± 0.99
47.5 ± 1.2 Ma
Pond 2_30
13.72 ± 0.90
54.4 ± 1.4 Ma
Pond 2_31
1.50 ± 1.11
88.5 ± 2.3 Ma
Pond 2_32
10.60 ± 0.92
91.1 ± 2.4 Ma
Pond 2_33
11.46 ± 0.89
44.7 ± 1.1 Ma
Pond 2_34
12.34 ± 0.83
42.7 ± 1.0 Ma
Pond 2_35
12.66 ± 0.85
90.7 ± 2.1 Ma
Pond 2_36
11.66 ± 0.98
47.4 ± 1.1 Ma
Pond 2_37
65.2 ± 1.6 Ma
Pond 2_38
75.2 ± 1.8 Ma
Pond 2_39
69.4 ± 1.6 Ma
Pond 2_40
43.3 ± 1.0 Ma
Pond 2_41
11.97 ± 0.97
69.6 ± 1.7 Ma
Pond 2_42
11.05 ± 0.92
43.6 ± 1.0 Ma
Pond 2_43
88.3 ± 2.5 Ma
Pond 2_44
64.5 ± 1.5 Ma
Pond 2_45
42.2 ± 1.0 Ma
Pond 2_46
50.1 ± 1.2 Ma
Pond 2_47
90.1 ± 2.2 Ma
Pond 2_48
84.5 ± 2.0 Ma

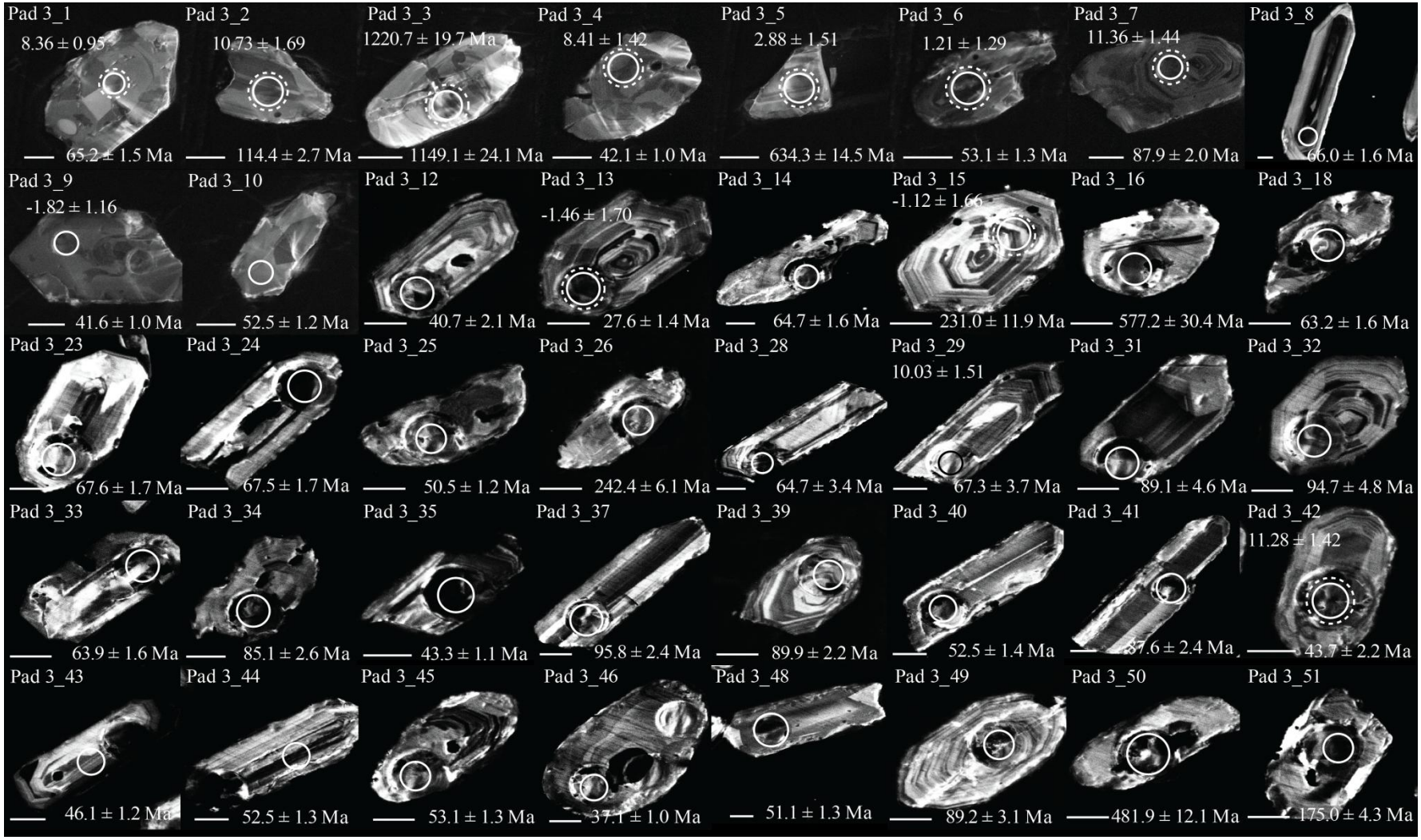
Pad 3_1
8.36 ± 0.95
65.2 ± 1.5 Ma
Pad 3_2
10.73 ± 1.69
114.4 ± 2.7 Ma
Pad 3_3
1220.7 ± 19.7 Ma
1149.1 ± 24.1 Ma
Pad 3_4
8.41 ± 1.42
42.1 ± 1.0 Ma
Pad 3_5
2.88 ± 1.51
634.3 ± 14.5 Ma
Pad 3_6
1.21 ± 1.29
53.1 ± 1.3 Ma
Pad 3_7
11.36 ± 1.44
87.9 ± 2.0 Ma
Pad 3_8
66.0 ± 1.6 Ma
Pad 3_9
-1.82 ± 1.16
41.6 ± 1.0 Ma
Pad 3_10
52.5 ± 1.2 Ma
Pad 3_12
40.7 ± 2.1 Ma
Pad 3_13
-1.46 ± 1.70
27.6 ± 1.4 Ma
Pad 3_14
64.7 ± 1.6 Ma
Pad 3_15
-1.12 ± 1.66
231.0 ± 11.9 Ma
Pad 3_16
577.2 ± 30.4 Ma
Pad 3_18
63.2 ± 1.6 Ma
Pad 3_23
67.6 ± 1.7 Ma
Pad 3_24
67.5 ± 1.7 Ma
Pad 3_25
50.5 ± 1.2 Ma
Pad 3_26
242.4 ± 6.1 Ma
Pad 3_28
64.7 ± 3.4 Ma
Pad 3_29
10.03 ± 1.51
67.3 ± 3.7 Ma
Pad 3_31
89.1 ± 4.6 Ma
Pad 3_32
94.7 ± 4.8 Ma
Pad 3_33
63.9 ± 1.6 Ma
Pad 3_34
85.1 ± 2.6 Ma
Pad 3_35
43.3 ± 1.1 Ma
Pad 3_37
95.8 ± 2.4 Ma
Pad 3_39
89.9 ± 2.2 Ma
Pad 3_40
52.5 ± 1.4 Ma
Pad 3_41
87.6 ± 2.4 Ma
Pad 3_42
11.28 ± 1.42
43.7 ± 2.2 Ma
Pad 3_43
46.1 ± 1.2 Ma
Pad 3_44
52.5 ± 1.3 Ma
Pad 3_45
53.1 ± 1.3 Ma
Pad 3_46
37.1 ± 1.0 Ma
Pad 3_48
51.1 ± 1.3 Ma
Pad 3_49
89.2 ± 3.1 Ma
Pad 3_50
481.9 ± 12.1 Ma
Pad 3_51
175.0 ± 4.3 Ma

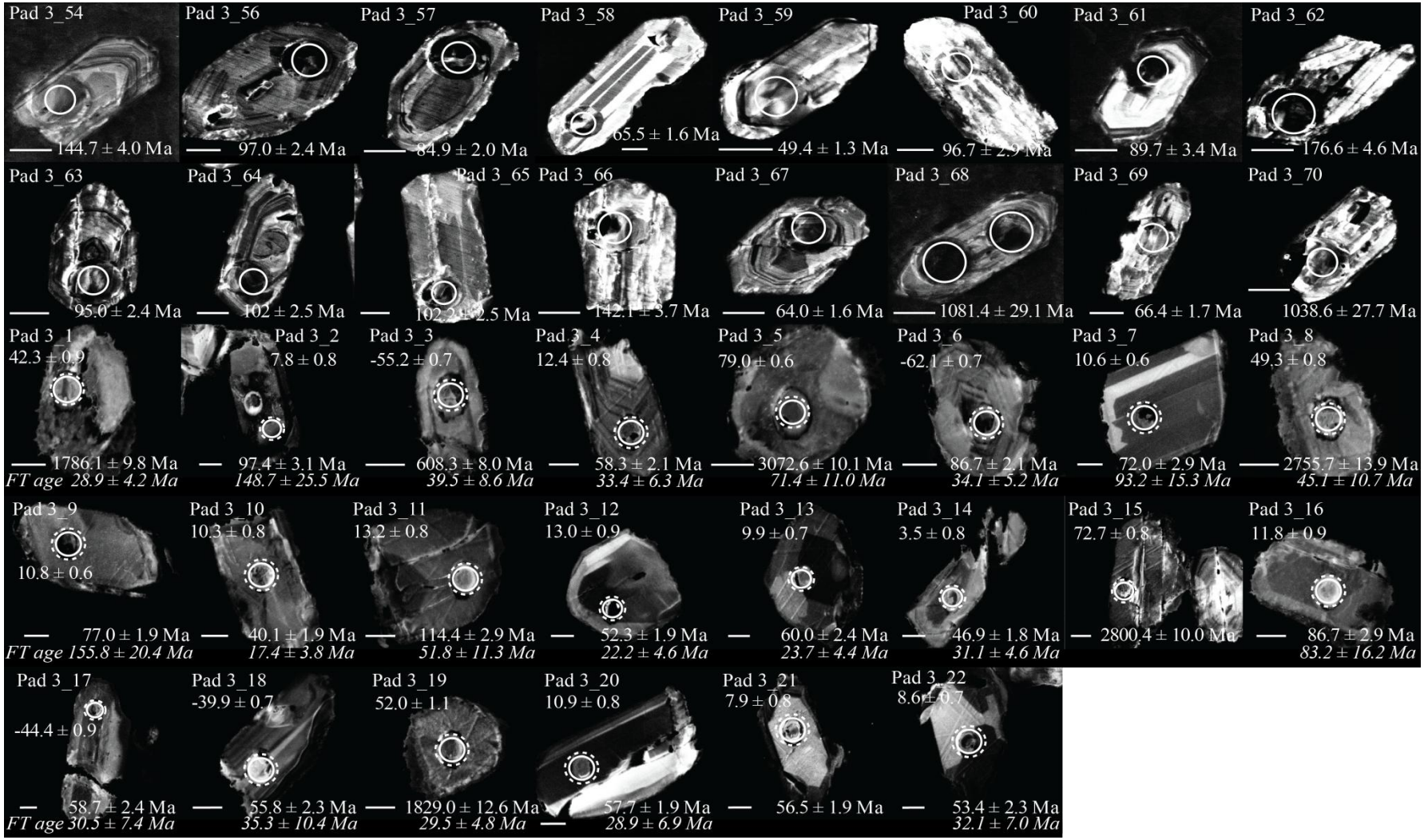
Pad 3_54
144.7 ± 4.0 Ma
Pad 3_56
97.0 ± 2.4 Ma
Pad 3_57
84.9 ± 2.0 Ma
Pad 3_58
65.5 ± 1.6 Ma
Pad 3_59
49.4 ± 1.3 Ma
Pad 3_60
96.7 ± 2.9 Ma
Pad 3_61
89.7 ± 3.4 Ma
Pad 3_62
176.6 ± 4.6 Ma
Pad 3_63
95.0 ± 2.4 Ma
Pad 3_64
102 ± 2.5 Ma
Pad 3_65
102.2 ± 2.5 Ma
Pad 3_66
142.1 ± 3.7 Ma
Pad 3_67
64.0 ± 1.6 Ma
Pad 3_68
1081.4 ± 29.1 Ma
Pad 3_69
66.4 ± 1.7 Ma
Pad 3_70
1038.6 ± 27.7 Ma
Pad 3_1
42.3 ± 0.9
1786.1 ± 9.8 Ma
FT age 28.9 ± 4.2 Ma
Pad 3_2
7.8 ± 0.8
97.4 ± 3.1 Ma
148.7 ± 25.5 Ma
Pad 3_3
-55.2 ± 0.7
608.3 ± 8.0 Ma
39.5 ± 8.6 Ma
Pad 3_4
12.4 ± 0.8
58.3 ± 2.1 Ma
33.4 ± 6.3 Ma
Pad 3_5
79.0 ± 0.6
3072.6 ± 10.1 Ma
71.4 ± 11.0 Ma
Pad 3_6
-62.1 ± 0.7
86.7 ± 2.1 Ma
34.1 ± 5.2 Ma
Pad 3_7
10.6 ± 0.6
72.0 ± 2.9 Ma
93.2 ± 15.3 Ma
Pad 3_8
49.3 ± 0.8
2755.7 ± 13.9 Ma
45.1 ± 10.7 Ma
Pad 3_9
10.8 ± 0.6
77.0 ± 1.9 Ma
FT age 155.8 ± 20.4 Ma
Pad 3_10
10.3 ± 0.8
40.1 ± 1.9 Ma
17.4 ± 3.8 Ma
Pad 3_11
13.2 ± 0.8
114.4 ± 2.9 Ma
51.8 ± 11.3 Ma
Pad 3_12
13.0 ± 0.9
52.3 ± 1.9 Ma
22.2 ± 4.6 Ma
Pad 3_13
9.9 ± 0.7
60.0 ± 2.4 Ma
23.7 ± 4.4 Ma
Pad 3_14
3.5 ± 0.8
46.9 ± 1.8 Ma
31.1 ± 4.6 Ma
Pad 3_15
72.7 ± 0.8
2800.4 ± 10.0 Ma
Pad 3_16
11.8 ± 0.9
86.7 ± 2.9 Ma
83.2 ± 16.2 Ma
Pad 3_17
-44.4 ± 0.9
58.7 ± 2.4 Ma
FT age 30.5 ± 7.4 Ma
Pad 3_18
-39.9 ± 0.7
55.8 ± 2.3 Ma
35.3 ± 10.4 Ma
Pad 3_19
52.0 ± 1.1
1829.0 ± 12.6 Ma
29.5 ± 4.8 Ma
Pad 3_20
10.9 ± 0.8
57.7 ± 1.9 Ma
28.9 ± 6.9 Ma
Pad 3_21
7.9 ± 0.8
56.5 ± 1.9 Ma
Pad 3_22
8.6 ± 0.7
53.4 ± 2.3 Ma
32.1 ± 7.0 Ma

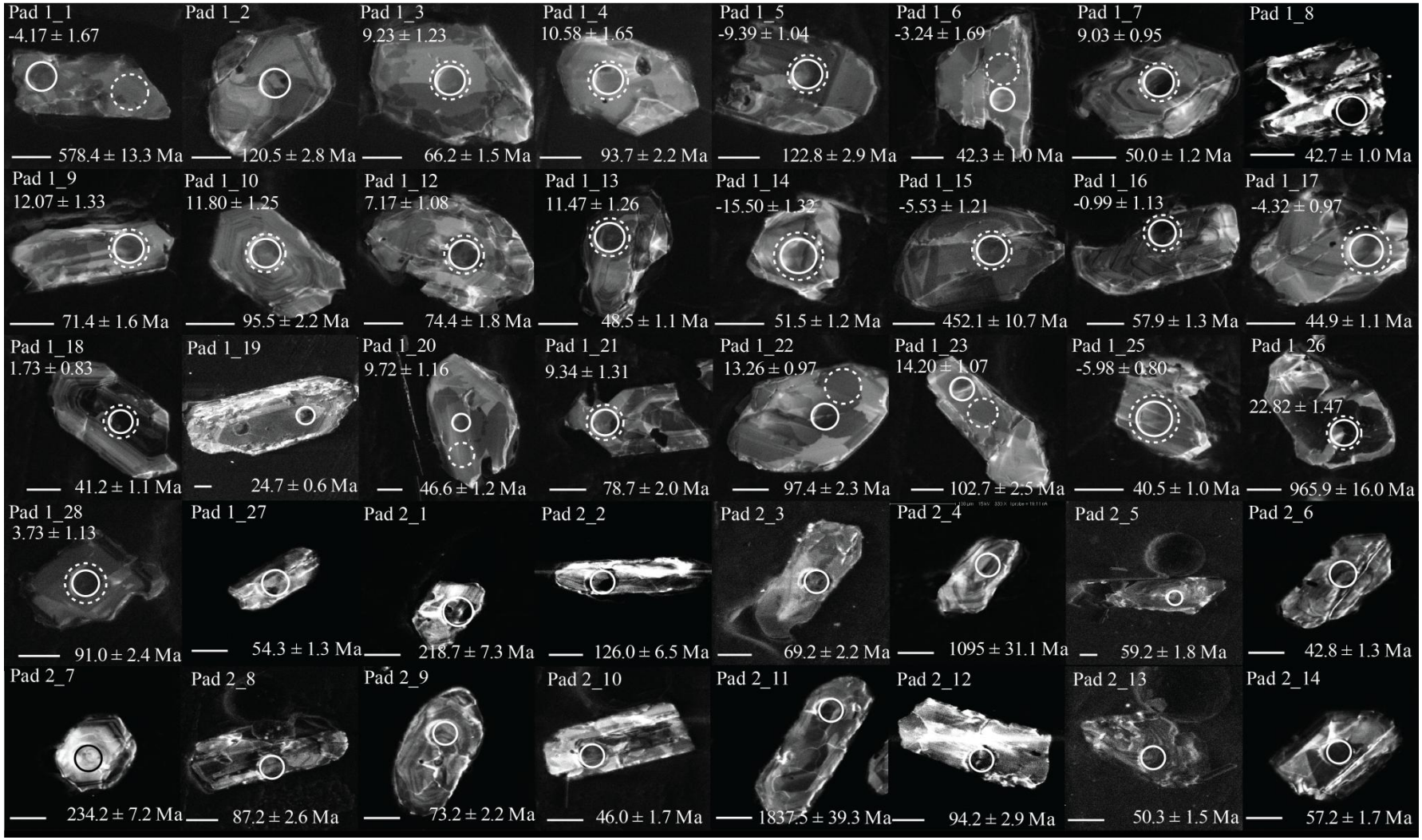
Pad 1_1
-4.17 ± 1.67
578.4 ± 13.3 Ma
Pad 1_2
120.5 ± 2.8 Ma
Pad 1_3
9.23 ± 1.23
66.2 ± 1.5 Ma
Pad 1_4
10.58 ± 1.65
93.7 ± 2.2 Ma
Pad 1_5
-9.39 ± 1.04
122.8 ± 2.9 Ma
Pad 1_6
-3.24 ± 1.69
42.3 ± 1.0 Ma
Pad 1_7
9.03 ± 0.95
50.0 ± 1.2 Ma
Pad 1_8
42.7 ± 1.0 Ma
Pad 1_9
12.07 ± 1.33
71.4 ± 1.6 Ma
Pad 1_10
11.80 ± 1.25
95.5 ± 2.2 Ma
Pad 1_12
7.17 ± 1.08
74.4 ± 1.8 Ma
Pad 1_13
11.47 ± 1.26
48.5 ± 1.1 Ma
Pad 1_14
-15.50 ± 1.32
51.5 ± 1.2 Ma
Pad 1_15
-5.53 ± 1.21
452.1 ± 10.7 Ma
Pad 1_16
-0.99 ± 1.13
57.9 ± 1.3 Ma
Pad 1_17
-4.32 ± 0.97
44.9 ± 1.1 Ma
Pad 1_18
1.73 ± 0.83
41.2 ± 1.1 Ma
Pad 1_19
24.7 ± 0.6 Ma
Pad 1_20
9.72 ± 1.16
46.6 ± 1.2 Ma
Pad 1_21
9.34 ± 1.31
78.7 ± 2.0 Ma
Pad 1_22
13.26 ± 0.97
97.4 ± 2.3 Ma
Pad 1_23
14.20 ± 1.07
102.7 ± 2.5 Ma
Pad 1_25
-5.98 ± 0.80
40.5 ± 1.0 Ma
Pad 1_26
22.82 ± 1.47
965.9 ± 16.0 Ma
Pad 1_28
3.73 ± 1.13
91.0 ± 2.4 Ma
Pad 1_27
54.3 ± 1.3 Ma
Pad 2_1
218.7 ± 7.3 Ma
Pad 2_2
126.0 ± 6.5 Ma
Pad 2_3
69.2 ± 2.2 Ma
Pad 2_4
1095 ± 31.1 Ma
Pad 2_5
59.2 ± 1.8 Ma
Pad 2_6
42.8 ± 1.3 Ma
Pad 2_7
234.2 ± 7.2 Ma
Pad 2_8
87.2 ± 2.6 Ma
Pad 2_9
73.2 ± 2.2 Ma
Pad 2_10
46.0 ± 1.7 Ma
Pad 2_11
1837.5 ± 39.3 Ma
Pad 2_12
94.2 ± 2.9 Ma
Pad 2_13
50.3 ± 1.5 Ma
Pad 2_14
57.2 ± 1.7 Ma

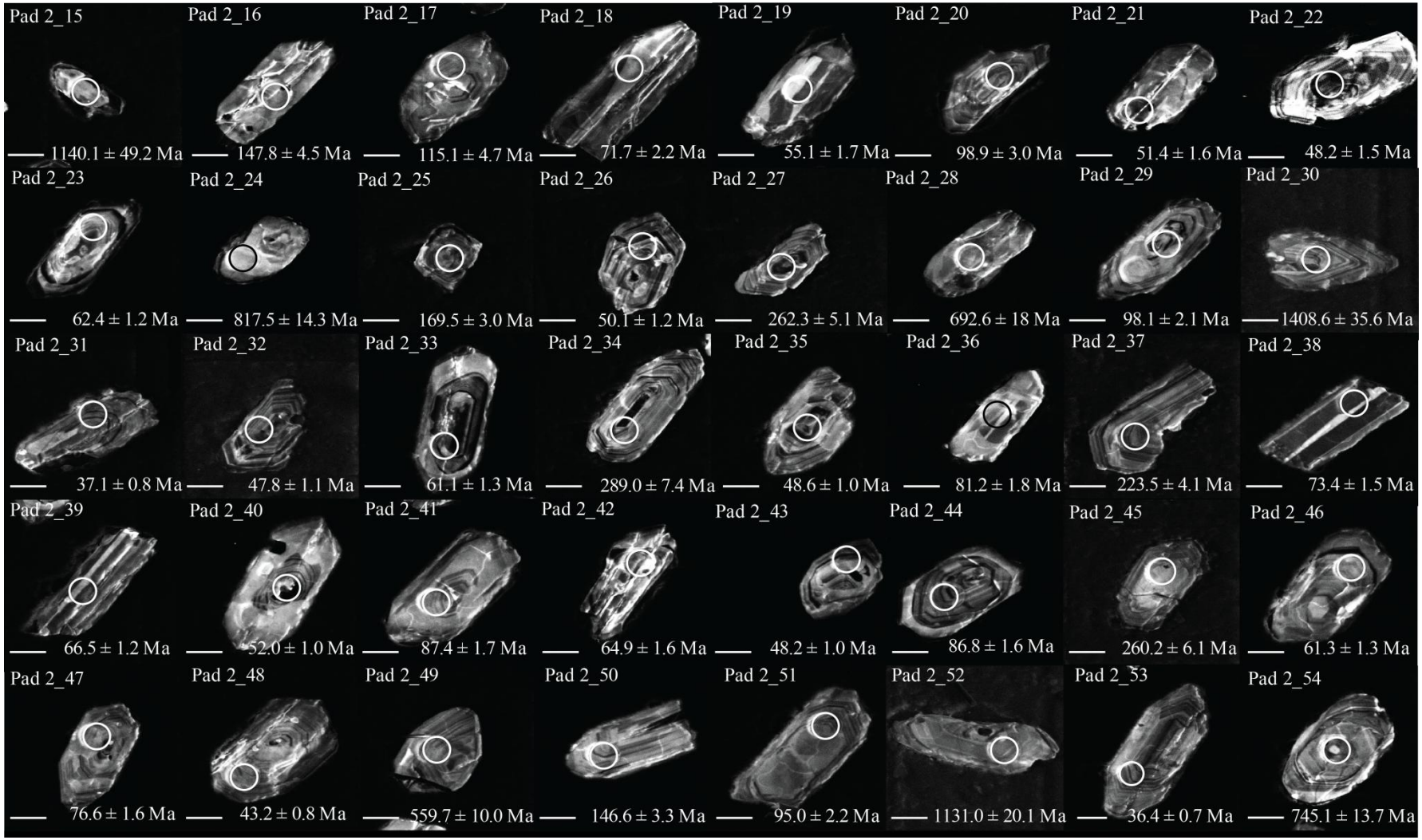
Pad 2_15
1140.1 ± 49.2 Ma
Pad 2_16
147.8 ± 4.5 Ma
Pad 2_17
115.1 ± 4.7 Ma
Pad 2_18
71.7 ± 2.2 Ma
Pad 2_19
55.1 ± 1.7 Ma
Pad 2_20
98.9 ± 3.0 Ma
Pad 2_21
51.4 ± 1.6 Ma
Pad 2_22
48.2 ± 1.5 Ma
Pad 2_23
62.4 ± 1.2 Ma
Pad 2_24
817.5 ± 14.3 Ma
Pad 2_25
169.5 ± 3.0 Ma
Pad 2_26
50.1 ± 1.2 Ma
Pad 2_27
262.3 ± 5.1 Ma
Pad 2_28
692.6 ± 18 Ma
Pad 2_29
98.1 ± 2.1 Ma
Pad 2_30
1408.6 ± 35.6 Ma
Pad 2_31
37.1 ± 0.8 Ma
Pad 2_32
47.8 ± 1.1 Ma
Pad 2_33
61.1 ± 1.3 Ma
Pad 2_34
289.0 ± 7.4 Ma
Pad 2_35
48.6 ± 1.0 Ma
Pad 2_36
81.2 ± 1.8 Ma
Pad 2_37
223.5 ± 4.1 Ma
Pad 2_38
73.4 ± 1.5 Ma
Pad 2_39
66.5 ± 1.2 Ma
Pad 2_40
52.0 ± 1.0 Ma
Pad 2_41
87.4 ± 1.7 Ma
Pad 2_42
64.9 ± 1.6 Ma
Pad 2_43
48.2 ± 1.0 Ma
Pad 2_44
86.8 ± 1.6 Ma
Pad 2_45
260.2 ± 6.1 Ma
Pad 2_46
61.3 ± 1.3 Ma
Pad 2_47
76.6 ± 1.6 Ma
Pad 2_48
43.2 ± 0.8 Ma
Pad 2_49
559.7 ± 10.0 Ma
Pad 2_50
146.6 ± 3.3 Ma
Pad 2_51
95.0 ± 2.2 Ma
Pad 2_52
1131.0 ± 20.1 Ma
Pad 2_53
36.4 ± 0.7 Ma
Pad 2_54
745.1 ± 13.7 Ma

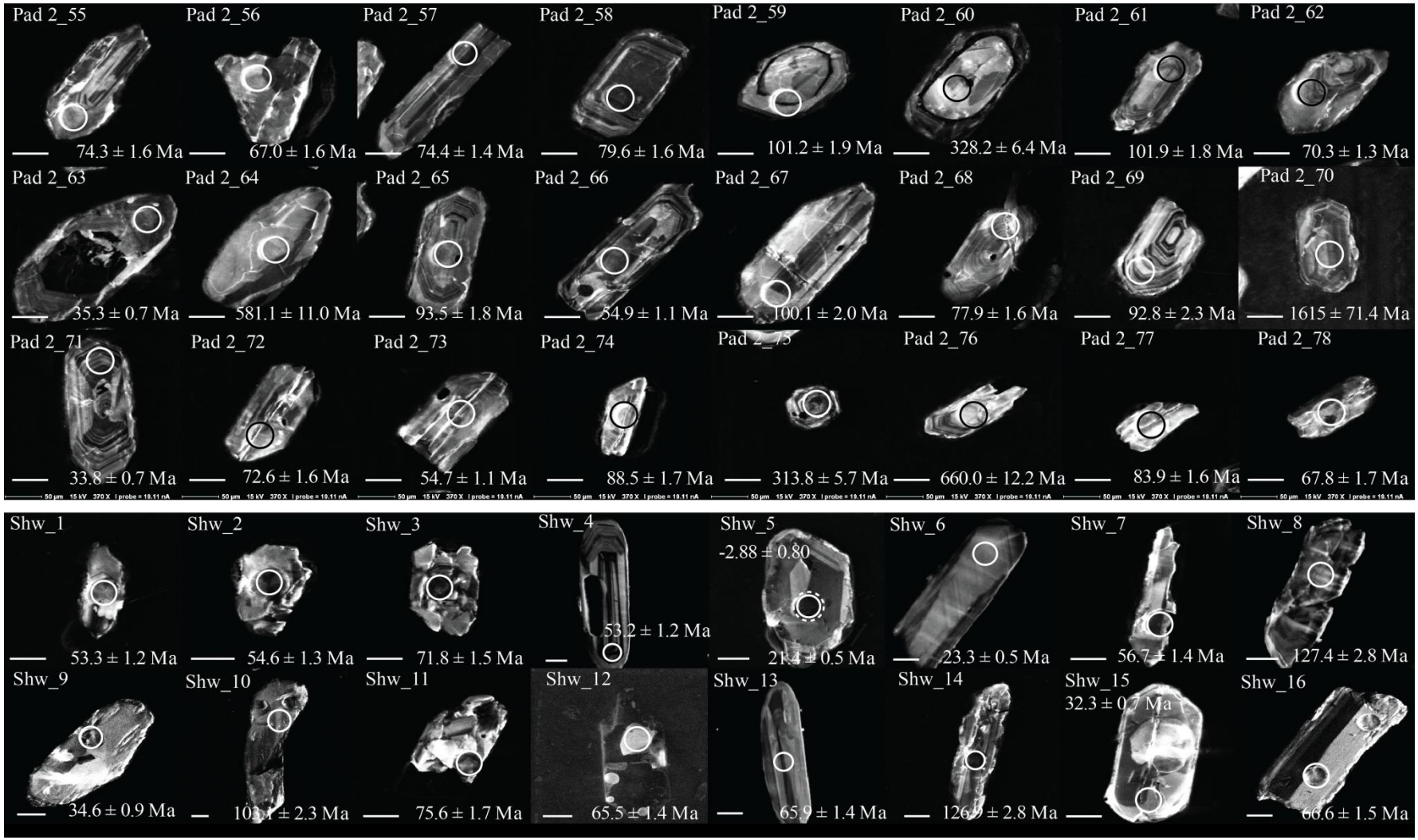
Pad 2_55
74.3 ± 1.6 Ma
Pad 2_56
67.0 ± 1.6 Ma
Pad 2_57
74.4 ± 1.4 Ma
Pad 2_58
79.6 ± 1.6 Ma
Pad 2_59
101.2 ± 1.9 Ma
Pad 2_60
328.2 ± 6.4 Ma
Pad 2_61
101.9 ± 1.8 Ma
Pad 2_62
70.3 ± 1.3 Ma
Pad 2_63
35.3 ± 0.7 Ma
Pad 2_64
581.1 ± 11.0 Ma
Pad 2_65
93.5 ± 1.8 Ma
Pad 2_66
54.9 ± 1.1 Ma
Pad 2_67
100.1 ± 2.0 Ma
Pad 2_68
77.9 ± 1.6 Ma
Pad 2_69
92.8 ± 2.3 Ma
Pad 2_70
1615 ± 71.4 Ma
Pad 2_71
33.8 ± 0.7 Ma
Pad 2_72
72.6 ± 1.6 Ma
Pad 2_73
54.7 ± 1.1 Ma
Pad 2_74
88.5 ± 1.7 Ma
313.8 ± 5.7 Ma
Pad 2_76
660.0 ± 12.2 Ma
Pad 2_77
83.9 ± 1.6 Ma
Pad 2_78
67.8 ± 1.7 Ma
Shw_1
53.3 ± 1.2 Ma
Shw_2
54.6 ± 1.3 Ma
Shw_3
71.8 ± 1.5 Ma
Shw_4
53.2 ± 1.2 Ma
Shw_5
-2.88 ± 0.80
Shw_6
23.3 ± 0.5 Ma
Shw_7
56.7 ± 1.4 Ma
Shw_8
127.4 ± 2.8 Ma
Shw_9
34.6 ± 0.9 Ma
Shw_10
Shw_11
75.6 ± 1.7 Ma
Shw_12
65.5 ± 1.4 Ma
Shw_13
65.9 ± 1.4 Ma
Shw_14
Shw_15
32.3 ± 0.7 Ma
Shw_16
66.6 ± 1.5 Ma

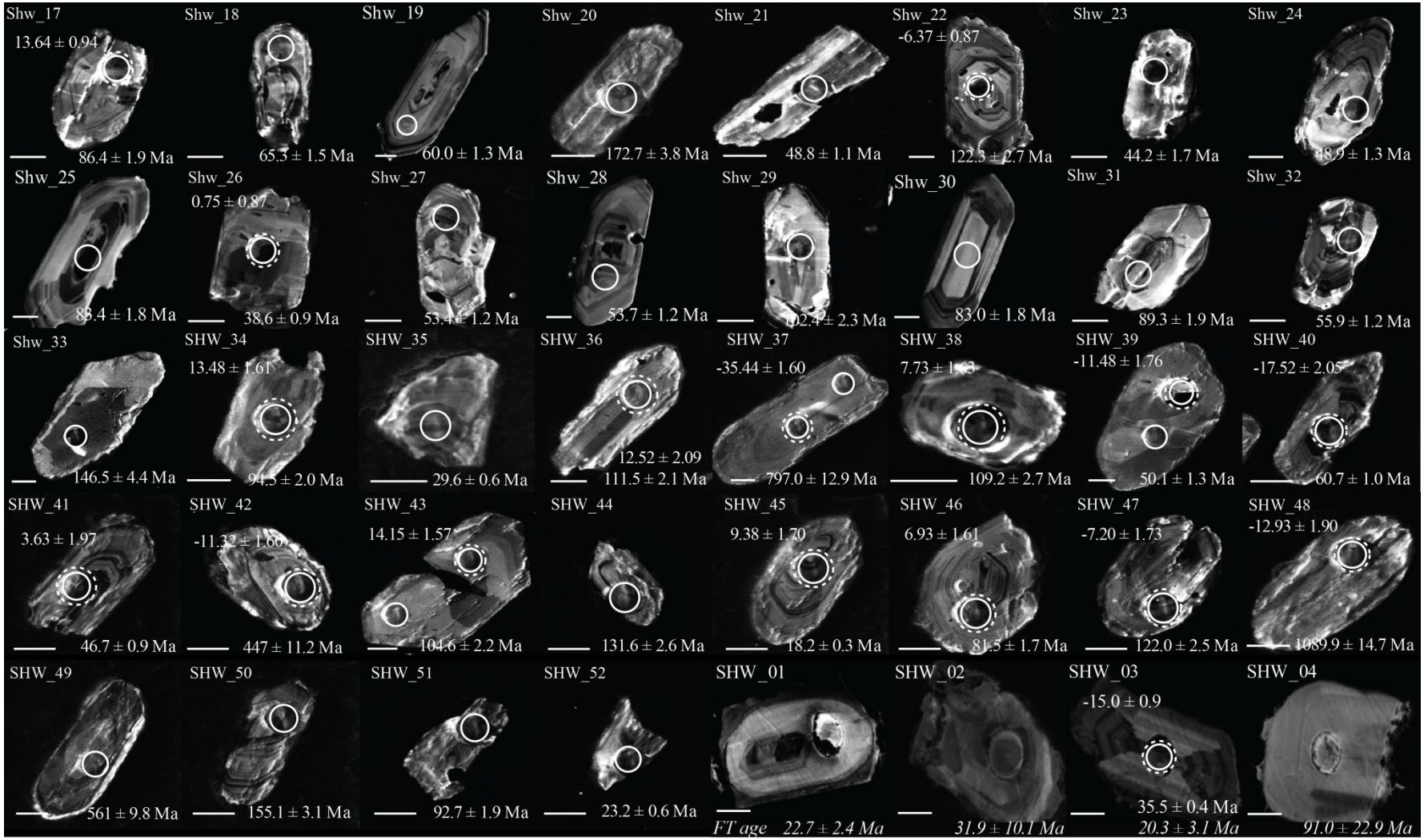
Shw_17
13.64 ± 0.94
86.4 ± 1.9 Ma
Shw_18
65.3 ± 1.5 Ma
Shw_19
60.0 ± 1.3 Ma
Shw_20
172.7 ± 3.8 Ma
Shw_21
48.8 ± 1.1 Ma
Shw_22
-6.37 ± 0.87
122.3 ± 2.7 Ma
Shw_23
44.2 ± 1.7 Ma
Shw_24
48.9 ± 1.3 Ma
Shw_25
83.4 ± 1.8 Ma
Shw_26
0.75 ± 0.87
38.6 ± 0.9 Ma
Shw_27
53.4 ± 1.2 Ma
Shw_28
53.7 ± 1.2 Ma
Shw_29
102.4 ± 2.3 Ma
Shw_30
83.0 ± 1.8 Ma
Shw_31
89.3 ± 1.9 Ma
Shw_32
55.9 ± 1.2 Ma
Shw_33
146.5 ± 4.4 Ma
SHW_34
13.48 ± 1.61
94.5 ± 2.0 Ma
SHW_35
29.6 ± 0.6 Ma
SHW_36
12.52 ± 2.09
111.5 ± 2.1 Ma
SHW_37
-35.44 ± 1.60
797.0 ± 12.9 Ma
SHW_38
7.73 ± 1.63
109.2 ± 2.7 Ma
SHW_39
-11.48 ± 1.76
50.1 ± 1.3 Ma
SHW_40
-17.52 ± 2.05
60.7 ± 1.0 Ma
SHW_41
3.63 ± 1.97
46.7 ± 0.9 Ma
SHW_42
-11.32 ± 1.66
447 ± 11.2 Ma
SHW_43
14.15 ± 1.57
104.6 ± 2.2 Ma
SHW_44
131.6 ± 2.6 Ma
SHW_45
9.38 ± 1.70
18.2 ± 0.3 Ma
SHW_46
6.93 ± 1.61
81.5 ± 1.7 Ma
SHW_47
-7.20 ± 1.73
122.0 ± 2.5 Ma
SHW_48
-12.93 ± 1.90
1089.9 ± 14.7 Ma
SHW_49
561 ± 9.8 Ma
SHW_50
155.1 ± 3.1 Ma
SHW_51
92.7 ± 1.9 Ma
SHW_52
23.2 ± 0.6 Ma
SHW_01
FT age 22.7 ± 2.4 Ma
SHW_02
31.9 ± 10.1 Ma
SHW_03
-15.0 ± 0.9
35.5 ± 0.4 Ma
20.3 ± 3.1 Ma
SHW_04
91.0 ± 22.9 Ma

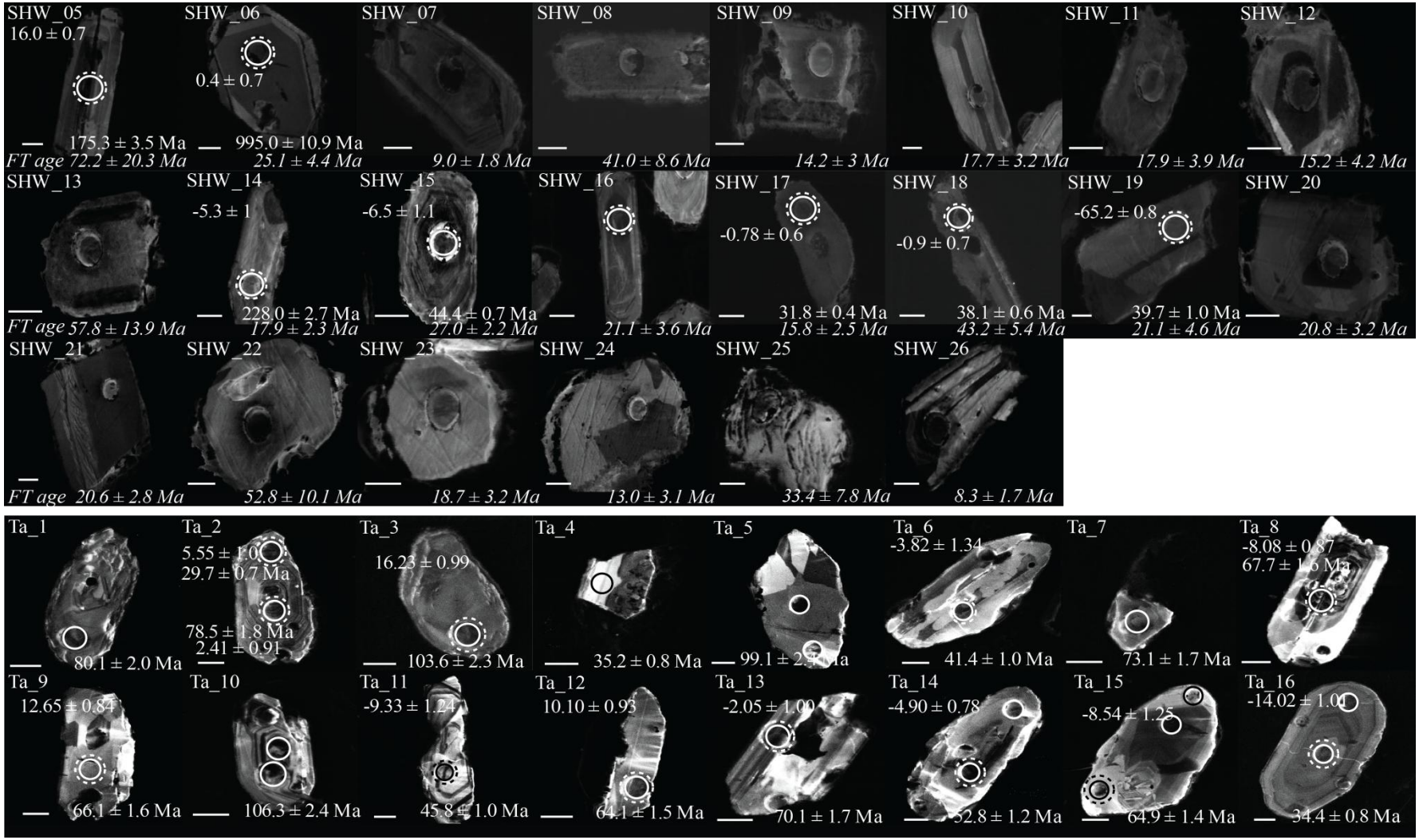
SHW_05
16.0 ± 0.7
175.3 ± 3.5 Ma
FT age 72.2 ± 20.3 Ma
SHW_06
0.4 ± 0.7
995.0 ± 10.9 Ma
25.1 ± 4.4 Ma
SHW_07
9.0 ± 1.8 Ma
SHW_08
41.0 ± 8.6 Ma
SHW_09
14.2 ± 3 Ma
SHW_10
17.7 ± 3.2 Ma
SHW_11
17.9 ± 3.9 Ma
SHW_12
15.2 ± 4.2 Ma
SHW_13
FT age 57.8 ± 13.9 Ma
SHW_14
-5.3 ± 1
228.0 ± 2.7 Ma
17.9 ± 2.3 Ma
SHW_15
-6.5 ± 1.1
44.4 ± 0.7 Ma
27.0 ± 2.2 Ma
SHW_16
21.1 ± 3.6 Ma
SHW_17
-0.78 ± 0.6
31.8 ± 0.4 Ma
15.8 ± 2.5 Ma
SHW_18
-0.9 ± 0.7
38.1 ± 0.6 Ma
43.2 ± 5.4 Ma
SHW_19
-65.2 ± 0.8
39.7 ± 1.0 Ma
21.1 ± 4.6 Ma
SHW_20
20.8 ± 3.2 Ma
SHW_21
FT age 20.6 ± 2.8 Ma
SHW_22
52.8 ± 10.1 Ma
SHW_23
18.7 ± 3.2 Ma
SHW_24
13.0 ± 3.1 Ma
SHW_25
33.4 ± 7.8 Ma
SHW_26
8.3 ± 1.7 Ma
Ta_1
80.1 ± 2.0 Ma
Ta_2
5.55 ± 1.0
29.7 ± 0.7 Ma
78.5 ± 1.8 Ma
2.41 ± 0.91
Ta_3
16.23 ± 0.99
103.6 ± 2.3 Ma
Ta_4
35.2 ± 0.8 Ma
Ta_5
Ta_6
-3.82 ± 1.34
41.4 ± 1.0 Ma
Ta_7
73.1 ± 1.7 Ma
Ta_8
-8.08 ± 0.87
67.7 ± 1.6 Ma
Ta_9
12.65 ± 0.84
66.1 ± 1.6 Ma
Ta_10
106.3 ± 2.4 Ma
Ta_11
-9.33 ± 1.24
45.8 ± 1.0 Ma
Ta_12
10.10 ± 0.93
64.1 ± 1.5 Ma
Ta_13
-2.05 ± 1.00
70.1 ± 1.7 Ma
Ta_14
-4.90 ± 0.78
52.8 ± 1.2 Ma
Ta_15
-8.54 ± 1.25
64.9 ± 1.4 Ma
Ta_16
-14.02 ± 1.01
34.4 ± 0.8 Ma

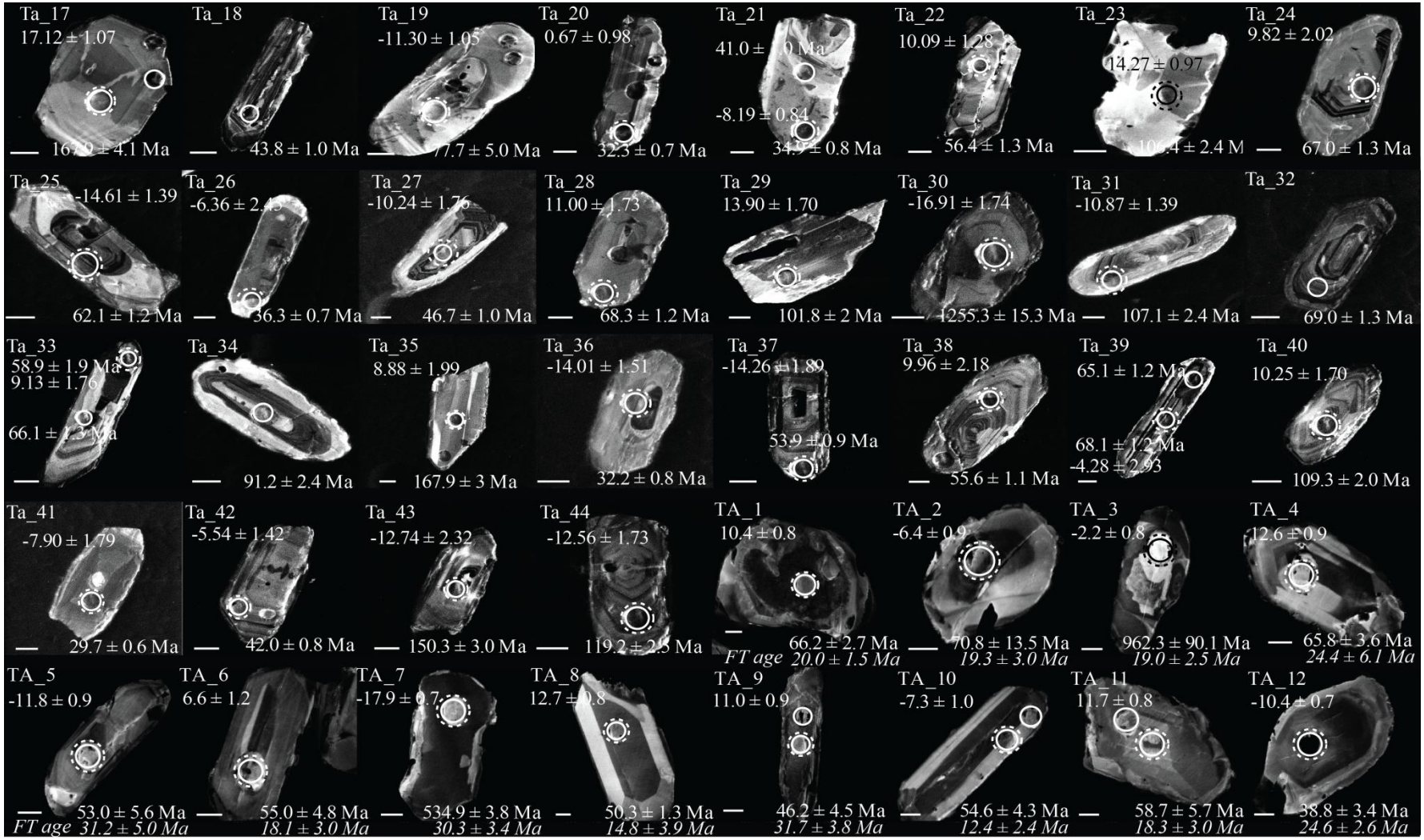
Ta_17
17.12 ± 1.07
16.9 ± 4.1 Ma
Ta_18
43.8 ± 1.0 Ma
Ta_19
-11.30 ± 1.05
77.7 ± 5.0 Ma
Ta_20
0.67 ± 0.98
32.3 ± 0.7 Ma
Ta_21
41.0 ± 0 Ma
-8.19 ± 0.84
34.9 ± 0.8 Ma
Ta_22
10.09 ± 1.28
56.4 ± 1.3 Ma
Ta_23
14.27 ± 0.97
106.4 ± 2.4 M
Ta_24
9.82 ± 2.02
67.0 ± 1.3 Ma
Ta_25
-14.61 ± 1.39
62.1 ± 1.2 Ma
Ta_26
-6.36 ± 2.45
36.3 ± 0.7 Ma
Ta_27
-10.24 ± 1.76
46.7 ± 1.0 Ma
Ta_28
11.00 ± 1.73
68.3 ± 1.2 Ma
Ta_29
13.90 ± 1.70
101.8 ± 2 Ma
Ta_30
-16.91 ± 1.74
1255.3 ± 15.3 Ma
Ta_31
-10.87 ± 1.39
107.1 ± 2.4 Ma
Ta_32
69.0 ± 1.3 Ma
Ta_33
58.9 ± 1.9 Ma
9.13 ± 1.76
66.1 ± 1.3 Ma
Ta_34
91.2 ± 2.4 Ma
Ta_35
8.88 ± 1.99
167.9 ± 3 Ma
Ta_36
-14.01 ± 1.51
32.2 ± 0.8 Ma
Ta_37
-14.26 ± 1.89
53.9 ± 0.9 Ma
Ta_38
9.96 ± 2.18
55.6 ± 1.1 Ma
Ta_39
65.1 ± 1.2 Ma
68.1 ± 1.2 Ma
-4.28 ± 2.93
Ta_40
10.25 ± 1.70
109.3 ± 2.0 Ma
Ta_41
-7.90 ± 1.79
29.7 ± 0.6 Ma
Ta_42
-5.54 ± 1.42
42.0 ± 0.8 Ma
Ta_43
-12.74 ± 2.32
150.3 ± 3.0 Ma
Ta_44
-12.56 ± 1.73
119.2 ± 2.5 Ma
TA_1
10.4 ± 0.8
66.2 ± 2.7 Ma
FT age 20.0 ± 1.5 Ma
TA_2
-6.4 ± 0.9
70.8 ± 13.5 Ma
19.3 ± 3.0 Ma
TA_3
-2.2 ± 0.8
962.3 ± 90.1 Ma
19.0 ± 2.5 Ma
TA_4
12.6 ± 0.9
65.8 ± 3.6 Ma
24.4 ± 6.1 Ma
TA_5
-11.8 ± 0.9
53.0 ± 5.6 Ma
FT age 31.2 ± 5.0 Ma
TA_6
6.6 ± 1.2
55.0 ± 4.8 Ma
18.1 ± 3.0 Ma
TA_7
-17.9 ± 0.7
534.9 ± 3.8 Ma
30.3 ± 3.4 Ma
TA_8
12.7 ± 0.8
50.3 ± 1.3 Ma
14.8 ± 3.9 Ma
TA_9
11.0 ± 0.9
46.2 ± 4.5 Ma
31.7 ± 3.8 Ma
TA_10
-7.3 ± 1.0
54.6 ± 4.3 Ma
12.4 ± 2.4 Ma
TA_11
11.7 ± 0.8
58.7 ± 5.7 Ma
18.3 ± 3.0 Ma
TA_12
-10.4 ± 0.7
38.8 ± 3.4 Ma
24.6 ± 2.6 Ma

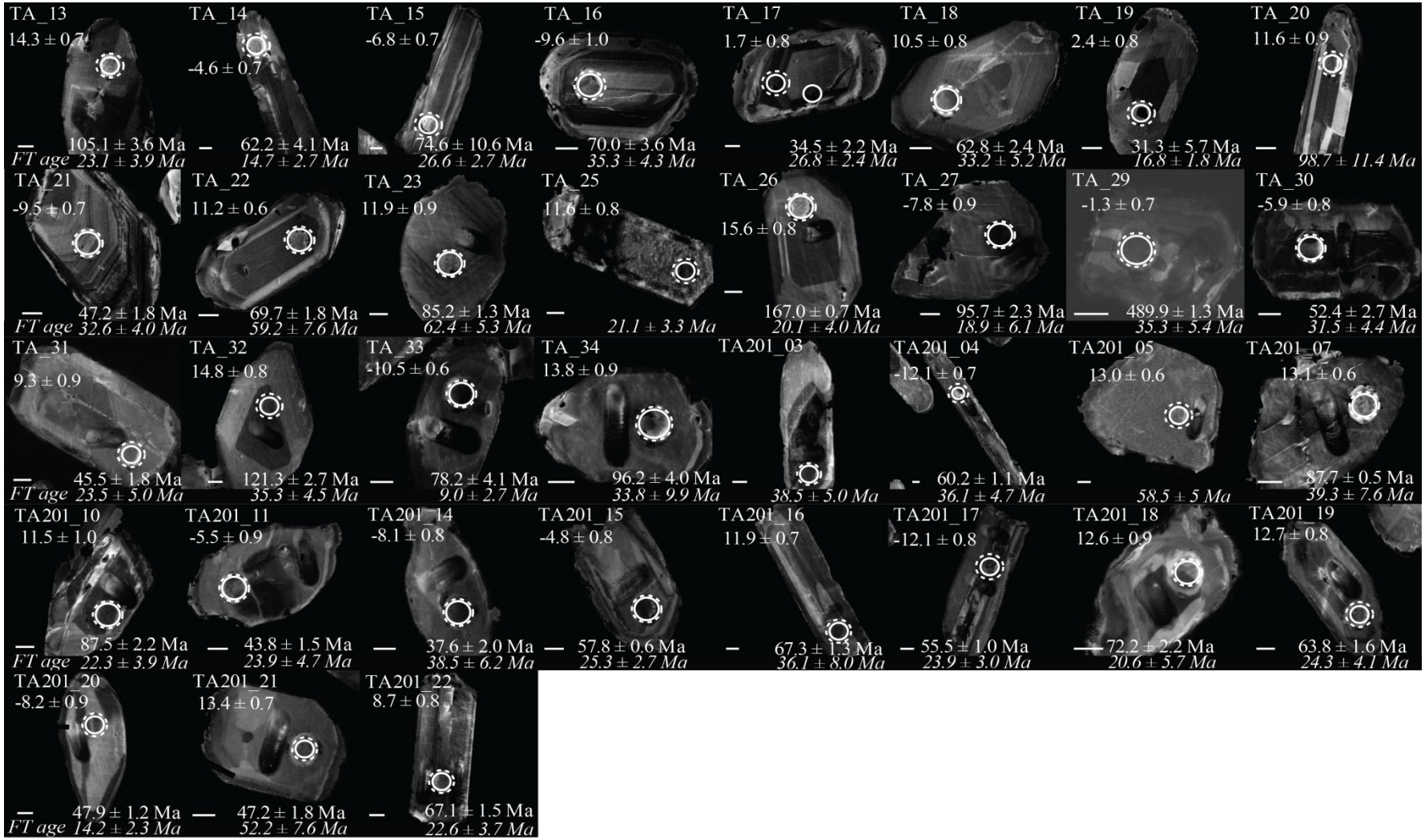
TA_13
14.3 ± 0.7
105.1 ± 3.6 Ma
FT age 23.1 ± 3.9 Ma
TA_14
-4.6 ± 0.7
62.2 ± 4.1 Ma
14.7 ± 2.7 Ma
TA_15
-6.8 ± 0.7
74.6 ± 10.6 Ma
26.6 ± 2.7 Ma
TA_16
-9.6 ± 1.0
70.0 ± 3.6 Ma
35.3 ± 4.3 Ma
TA_17
1.7 ± 0.8
34.5 ± 2.2 Ma
26.8 ± 2.4 Ma
TA_18
10.5 ± 0.8
62.8 ± 2.4 Ma
33.2 ± 5.2 Ma
TA_19
2.4 ± 0.8
31.3 ± 5.7 Ma
16.8 ± 1.8 Ma
TA_20
11.6 ± 0.9
98.7 ± 11.4 Ma
TA_21
-9.5 ± 0.7
47.2 ± 1.8 Ma
FT age 32.6 ± 4.0 Ma
TA_22
11.2 ± 0.6
69.7 ± 1.8 Ma
59.2 ± 7.6 Ma
TA_23
11.9 ± 0.9
85.2 ± 1.3 Ma
62.4 ± 5.3 Ma
TA_25
11.6 ± 0.8
21.1 ± 3.3 Ma
TA_26
15.6 ± 0.8
167.0 ± 0.7 Ma
20.1 ± 4.0 Ma
TA_27
-7.8 ± 0.9
95.7 ± 2.3 Ma
18.9 ± 6.1 Ma
TA_29
-1.3 ± 0.7
489.9 ± 1.3 Ma
35.3 ± 5.4 Ma
TA_30
-5.9 ± 0.8
52.4 ± 2.7 Ma
31.5 ± 4.4 Ma
TA_31
9.3 ± 0.9
45.5 ± 1.8 Ma
FT age 23.5 ± 5.0 Ma
TA_32
14.8 ± 0.8
121.3 ± 2.7 Ma
35.3 ± 4.5 Ma
TA_33
-10.5 ± 0.6
78.2 ± 4.1 Ma
9.0 ± 2.7 Ma
TA_34
13.8 ± 0.9
96.2 ± 4.0 Ma
33.8 ± 9.9 Ma
TA201_03
38.5 ± 5.0 Ma
TA201_04
-12.1 ± 0.7
60.2 ± 1.1 Ma
36.1 ± 4.7 Ma
TA201_05
13.0 ± 0.6
58.5 ± 5 Ma
TA201_07
13.1 ± 0.6
87.7 ± 0.5 Ma
39.3 ± 7.6 Ma
TA201_10
11.5 ± 1.0
87.5 ± 2.2 Ma
FT age 22.3 ± 3.9 Ma
TA201_11
-5.5 ± 0.9
43.8 ± 1.5 Ma
23.9 ± 4.7 Ma
TA201_14
-8.1 ± 0.8
37.6 ± 2.0 Ma
38.5 ± 6.2 Ma
TA201_15
-4.8 ± 0.8
57.8 ± 0.6 Ma
25.3 ± 2.7 Ma
TA201_16
11.9 ± 0.7
67.3 ± 1.3 Ma
36.1 ± 8.0 Ma
TA201_17
-12.1 ± 0.8
55.5 ± 1.0 Ma
23.9 ± 3.0 Ma
TA201_18
12.6 ± 0.9
72.2 ± 2.2 Ma
20.6 ± 5.7 Ma
TA201_19
12.7 ± 0.8
63.8 ± 1.6 Ma
24.3 ± 4.1 Ma
TA201_20
-8.2 ± 0.9
47.9 ± 1.2 Ma
FT age 14.2 ± 2.3 Ma
TA201_21
13.4 ± 0.7
47.2 ± 1.8 Ma
52.2 ± 7.6 Ma
TA201_22
8.7 ± 0.8
67.1 ± 1.5 Ma
22.6 ± 3.7 Ma

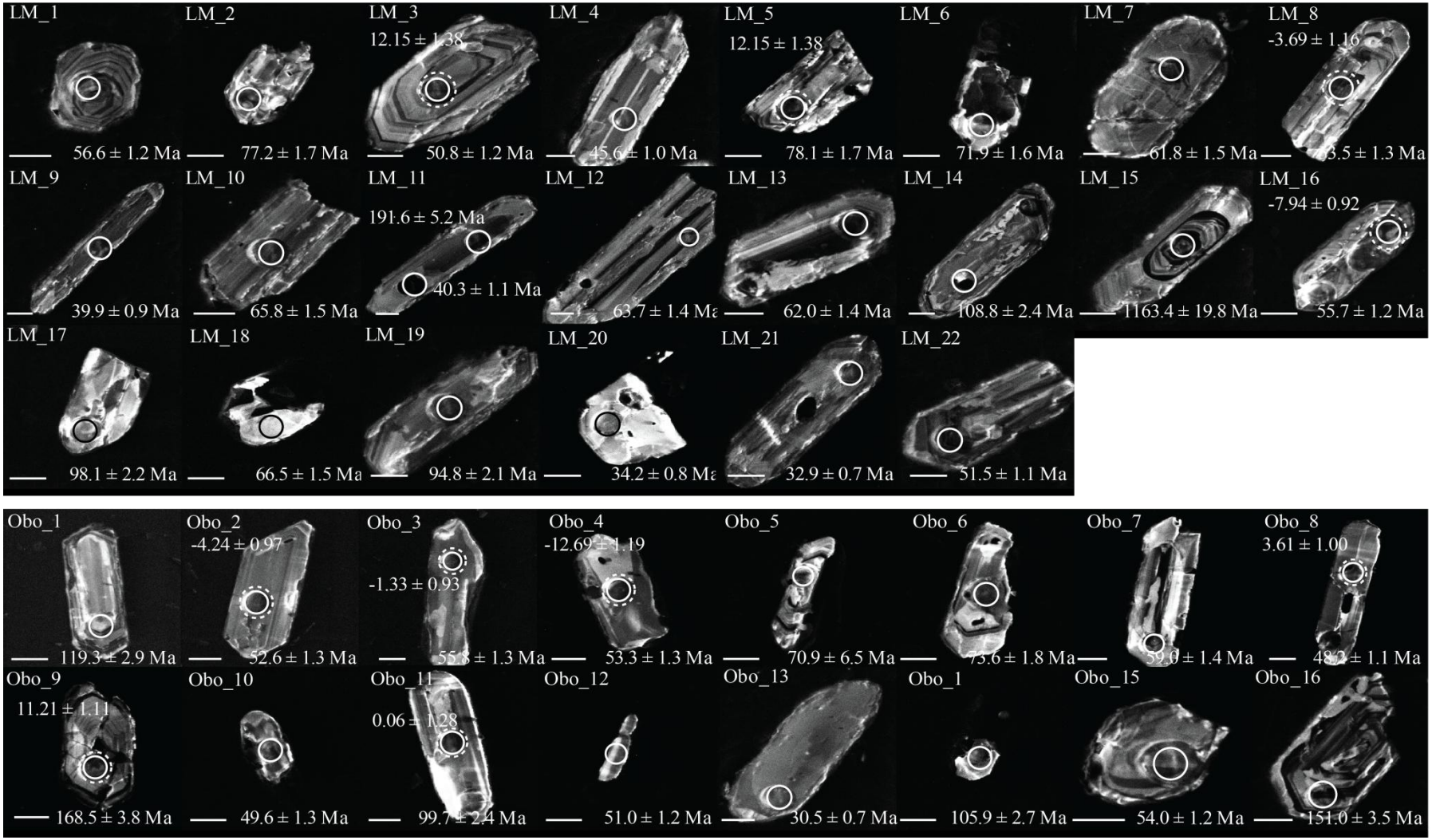
LM_1
56.6 ± 1.2 Ma
LM_2
77.2 ± 1.7 Ma
LM_3
12.15 ± 1.38
50.8 ± 1.2 Ma
LM_4
45.6 ± 1.0 Ma
LM_5
12.15 ± 1.38
78.1 ± 1.7 Ma
LM_6
71.9 ± 1.6 Ma
LM_7
61.8 ± 1.5 Ma
LM_8
-3.69 ± 1.16
3.5 ± 1.3 Ma
LM_9
39.9 ± 0.9 Ma
LM_10
65.8 ± 1.5 Ma
LM_11
191.6 ± 5.2 Ma
40.3 ± 1.1 Ma
LM_12
63.7 ± 1.4 Ma
LM_13
62.0 ± 1.4 Ma
LM_14
108.8 ± 2.4 Ma
LM_15
1163.4 ± 19.8 Ma
LM_16
-7.94 ± 0.92
55.7 ± 1.2 Ma
LM_17
98.1 ± 2.2 Ma
LM_18
66.5 ± 1.5 Ma
LM_19
94.8 ± 2.1 Ma
LM_20
34.2 ± 0.8 Ma
LM_21
32.9 ± 0.7 Ma
LM_22
51.5 ± 1.1 Ma
Obo_1
119.3 ± 2.9 Ma
Obo_2
-4.24 ± 0.97
52.6 ± 1.3 Ma
Obo_3
-1.33 ± 0.93
55.8 ± 1.3 Ma
Obo_4
-12.69 ± 1.19
53.3 ± 1.3 Ma
Obo_5
70.9 ± 6.5 Ma
Obo_6
75.6 ± 1.8 Ma
Obo_7
59.0 ± 1.4 Ma
Obo_8
3.61 ± 1.00
48.2 ± 1.1 Ma
Obo_9
11.21 ± 1.11
168.5 ± 3.8 Ma
Obo_10
49.6 ± 1.3 Ma
Obo_11
0.06 ± 1.28
99.7 ± 2.4 Ma
Obo_12
51.0 ± 1.2 Ma
Obo_13
30.5 ± 0.7 Ma
Obo_1
105.9 ± 2.7 Ma
Obo_15
54.0 ± 1.2 Ma
Obo_16
151.0 ± 3.5 Ma

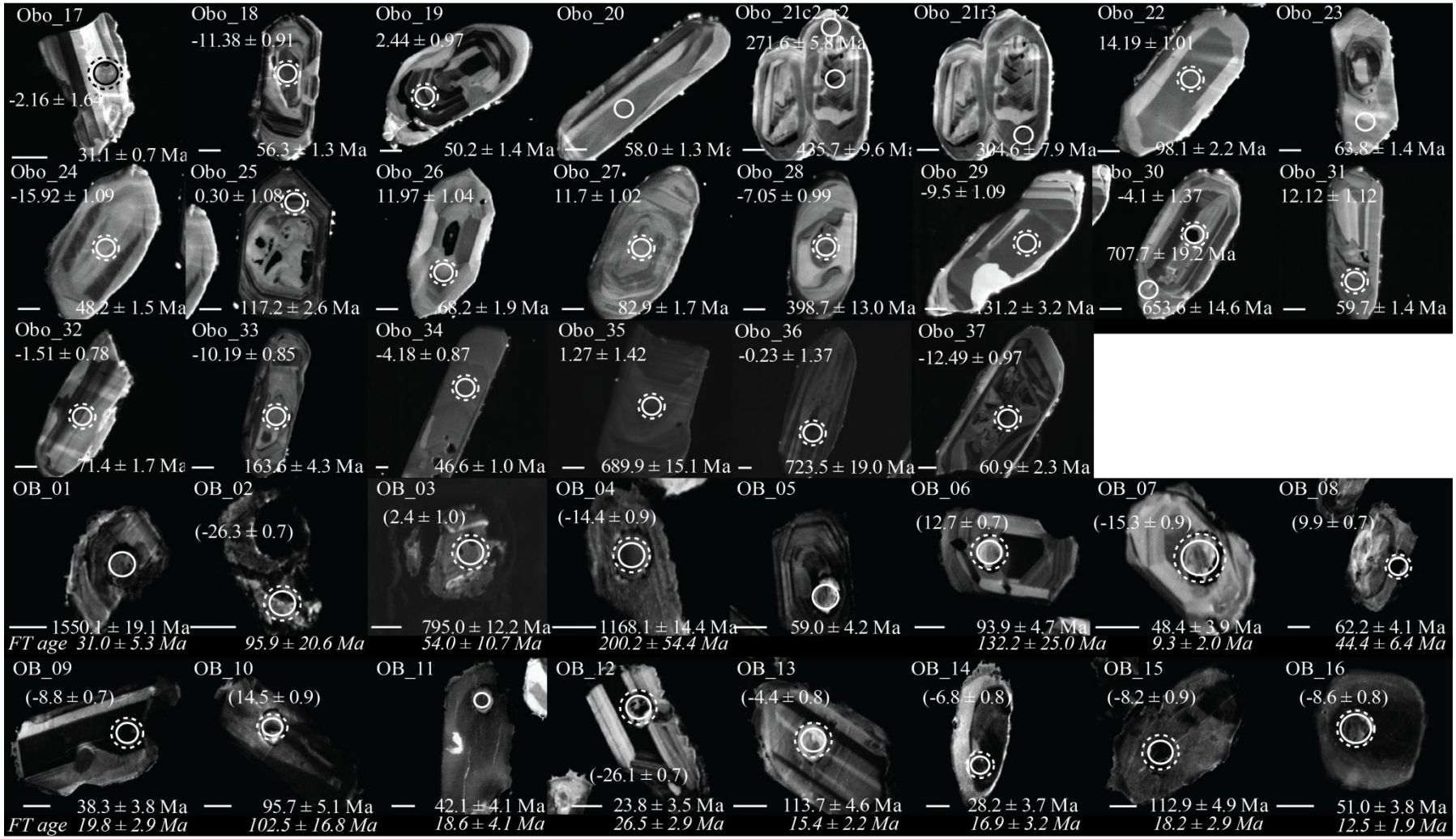
Obo_17
-2.16 ± 1.64
31.1 ± 0.7 Ma
Obo_18
-11.38 ± 0.91
56.3 ± 1.3 Ma
Obo_19
2.44 ± 0.97
50.2 ± 1.4 Ma
Obo_20
58.0 ± 1.3 Ma
Obo_21c2_r2
271.6 ± 5.8 Ma
435.7 ± 9.6 Ma
Obo_21r3
304.6 ± 7.9 Ma
Obo_22
14.19 ± 1.01
98.1 ± 2.2 Ma
Obo_23
63.8 ± 1.4 Ma
Obo_24
-15.92 ± 1.09
48.2 ± 1.5 Ma
Obo_25
0.30 ± 1.08
117.2 ± 2.6 Ma
Obo_26
11.97 ± 1.04
68.2 ± 1.9 Ma
Obo_27
11.7 ± 1.02
82.9 ± 1.7 Ma
Obo_28
-7.05 ± 0.99
398.7 ± 13.0 Ma
Obo_29
-9.5 ± 1.09
131.2 ± 3.2 Ma
Obo_30
-4.1 ± 1.37
707.7 ± 19.2 Ma
653.6 ± 14.6 Ma
Obo_31
12.12 ± 1.12
59.7 ± 1.4 Ma
Obo_32
-1.51 ± 0.78
71.4 ± 1.7 Ma
Obo_33
-10.19 ± 0.85
163.6 ± 4.3 Ma
Obo_34
-4.18 ± 0.87
46.6 ± 1.0 Ma
Obo_35
1.27 ± 1.42
689.9 ± 15.1 Ma
Obo_36
-0.23 ± 1.37
723.5 ± 19.0 Ma
Obo_37
-12.49 ± 0.97
60.9 ± 2.3 Ma
OB_01
1550.1 ± 19.1 Ma
FT age 31.0 ± 5.3 Ma
OB_02
(-26.3 ± 0.7)
95.9 ± 20.6 Ma
OB_03
(2.4 ± 1.0)
795.0 ± 12.2 Ma
54.0 ± 10.7 Ma
OB_04
(-14.4 ± 0.9)
1168.1 ± 14.4 Ma
200.2 ± 54.4 Ma
OB_05
59.0 ± 4.2 Ma
OB_06
(12.7 ± 0.7)
93.9 ± 4.7 Ma
132.2 ± 25.0 Ma
OB_07
(-15.3 ± 0.9)
48.4 ± 3.9 Ma
9.3 ± 2.0 Ma
OB_08
(9.9 ± 0.7)
62.2 ± 4.1 Ma
44.4 ± 6.4 Ma
OB_09
(-8.8 ± 0.7)
38.3 ± 3.8 Ma
FT age 19.8 ± 2.9 Ma
OB_10
(14.5 ± 0.9)
95.7 ± 5.1 Ma
102.5 ± 16.8 Ma
OB_11
42.1 ± 4.1 Ma
18.6 ± 4.1 Ma
OB_12
(-26.1 ± 0.7)
23.8 ± 3.5 Ma
26.5 ± 2.9 Ma
OB_13
(-4.4 ± 0.8)
113.7 ± 4.6 Ma
15.4 ± 2.2 Ma
OB_14
(-6.8 ± 0.8)
28.2 ± 3.7 Ma
16.9 ± 3.2 Ma
OB_15
(-8.2 ± 0.9)
112.9 ± 4.9 Ma
18.2 ± 2.9 Ma
OB_16
(-8.6 ± 0.8)
51.0 ± 3.8 Ma
12.5 ± 1.9 Ma

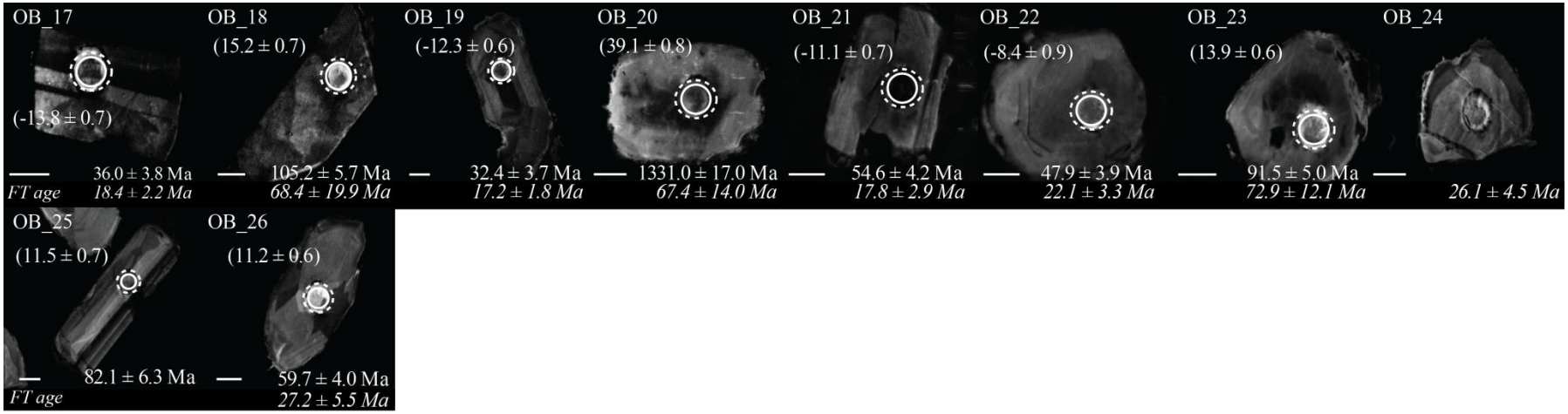
OB_17
(-13.8 ± 0.7)
36.0 ± 3.8 Ma
FT age 18.4 ± 2.2 Ma
OB_18
(15.2 ± 0.7)
105.2 ± 5.7 Ma
68.4 ± 19.9 Ma
OB_19
(-12.3 ± 0.6)
32.4 ± 3.7 Ma
17.2 ± 1.8 Ma
OB_20
(39.1 ± 0.8)
1331.0 ± 17.0 Ma
67.4 ± 14.0 Ma
OB_21
(-11.1 ± 0.7)
54.6 ± 4.2 Ma
17.8 ± 2.9 Ma
OB_22
(-8.4 ± 0.9)
47.9 ± 3.9 Ma
22.1 ± 3.3 Ma
OB_23
(13.9 ± 0.6)
91.5 ± 5.0 Ma
72.9 ± 12.1 Ma
OB_24
26.1 ± 4.5 Ma
OB_25
(11.5 ± 0.7)
82.1 ± 6.3 Ma
FT age
OB_26
(11.2 ± 0.6)
59.7 ± 4.0 Ma
27.2 ± 5.5 Ma

Appendix A-5: Data Tables

Table A1. LA-MC-ICPMS U-Pb dating of single grain detrital zircon (NIGL)

Sample		Isotopic Ratios						Isotopic Ages					
Zircon ID	U (ppm)	$^{207}Pb/^{206}Pb$	1s %	$^{207}Pb/^{235}U$	1s %	$^{206}Pb/^{238}U$	1s %	$^{207}Pb/^{206}Pb$	2σ	$^{206}Pb/^{238}U$	2σ	$^{207}Pb/^{235}U$	2σ
Pondaung 1													
Pond 1_38	1376	0.0523	1.08	0.039	1.66	5.35E-03	1.26	300.0	49.2	34.4	0.9	38.5	1.3
Pond 1_59	627	0.0541	3.31	0.042	4.22	5.58E-03	2.62	373.2	148.9	35.9	1.9	41.4	3.4
Pond 1_1	837	0.047	1.46	0.042	2.09	6.44E-03	1.5	51.6	69.8	41.4	1.2	41.6	1.8
Pond 1_16	544	0.047	1.99	0.043	2.3	6.58E-03	1.15	50.6	95.2	42.3	1.0	42.4	2.0
Pond 1_17	458	0.0468	2.3	0.043	2.58	6.59E-03	1.18	39.5	110.0	42.3	1.0	42.3	2.2
Pond 1_13	445	0.0481	2.39	0.044	2.66	6.61E-03	1.16	102.8	113.2	42.5	1.0	43.6	2.4
Pond 1_55	572	0.065	6.97	0.06	7.07	6.66E-03	1.17	775.4	293.1	42.8	1.0	58.9	8.1
Pond 1_14	392	0.0473	2.63	0.044	2.87	6.69E-03	1.14	65.4	125.2	43.0	1.0	43.4	2.5
Pond 1_46	310	0.0531	1.75	0.05	2.09	6.85E-03	1.14	333.4	79.6	44.0	1.0	49.7	2.0
Pond 1_3	427	0.0449	2.5	0.043	2.92	6.88E-03	1.51	-61.7	122.1	44.2	1.3	42.3	2.5
Pond 1_20	602	0.0471	1.68	0.046	2.1	7.10E-03	1.27	54.8	80.1	45.6	1.2	45.8	2.0
Pond 1_34	271	0.0522	1.79	0.053	2.36	7.43E-03	1.54	292.2	81.7	47.7	1.5	52.9	2.4
Pond 1_45	521	0.0475	1.11	0.05	1.64	7.60E-03	1.21	75.9	52.9	48.8	1.2	49.3	1.6
Pond 1_58	384	0.0467	1.28	0.049	1.57	7.67E-03	0.91	31.5	61.4	49.3	0.9	48.9	1.5
Pond 1_42	666	0.0489	2.17	0.054	2.34	7.94E-03	0.9	143.2	101.6	51.0	0.9	52.9	2.4
Pond 1_22	290	0.0256	5.07	0.028	5.21	8.01E-03	1.2	-1676.9	351.7	51.4	1.2	28.3	3.0
Pond 1_60	258	0.0444	1.82	0.049	2.01	8.03E-03	0.85	-88.4	89.1	51.6	0.9	48.7	1.9
Pond 1_53	82	0.0705	3.63	0.081	3.73	8.29E-03	0.85	943.5	148.8	53.2	0.9	78.7	5.6

Pond 1_57	652	0.0519	0.83	0.06	1.18	8.32E-03	0.84	279.5	37.8	53.4	0.9	58.7	1.3
Pond 1_61	456	0.0528	1.06	0.061	1.47	8.35E-03	1.01	320.4	48.4	53.6	1.1	59.9	1.7
Pond 1_37	356	0.0482	1.3	0.057	1.57	8.52E-03	0.87	110.8	61.5	54.7	1.0	56.0	1.7
Pond 1_43	1580	0.0478	0.62	0.057	1.36	8.60E-03	1.21	91.8	29.2	55.2	1.3	56.1	1.5
Pond 1_2	199	0.0499	3.7	0.06	3.99	8.76E-03	1.49	190.7	172.2	56.3	1.7	59.5	4.9
Pond 1_5	474	0.0497	1.63	0.063	2.22	9.22E-03	1.5	183.1	75.9	59.2	1.8	62.3	2.8
Pond 1_8	101	0.0646	5.32	0.084	5.44	9.40E-03	1.14	#NUM!	224.3	60.3	1.4	81.6	9.2
Pond 1_44	182	0.0471	1.9	0.062	2.45	9.53E-03	1.56	55.9	90.4	61.1	1.9	61.0	2.9
Pond 1_12	187	0.0504	3.38	0.071	3.62	1.01E-02	1.3	215.2	156.3	65.0	1.7	69.2	5.2
Pond 1_27	968	0.0493	0.83	0.07	1.42	1.02E-02	1.15	162.4	39.0	65.7	1.5	68.3	2.0
Pond 1_35	131	0.0548	3.54	0.078	3.63	1.03E-02	0.82	402.1	158.4	65.8	1.1	75.8	5.3
Pond 1_28	204	0.0487	3.04	0.069	3.25	1.03E-02	1.15	133.8	143.1	66.1	1.5	68.0	4.6
Pond 1_10	402	0.0515	1.67	0.073	2.54	1.03E-02	1.91	262.5	76.8	66.2	2.5	71.8	3.8
Pond 1_25	789	0.0483	0.99	0.069	1.58	1.04E-02	1.22	112.6	46.8	66.4	1.6	67.6	2.2
Pond 1_36	36	0.0581	6.61	0.084	6.66	1.04E-02	0.85	533.3	289.3	67.0	1.1	81.5	10.4
Pond 1_26	186	0.0609	2.78	0.088	3.03	1.05E-02	1.19	634.9	119.8	67.4	1.6	85.9	5.4
Pond 1_18	242	0.0481	2.68	0.07	2.96	1.06E-02	1.24	102.1	126.9	67.8	1.7	68.7	4.2
Pond 1_19	360	0.0475	1.82	0.07	2.27	1.07E-02	1.37	73.9	86.3	68.7	1.9	68.8	3.2
Pond 1_50	164	0.0506	1.95	0.075	2.29	1.08E-02	1.19	221.7	90.2	69.0	1.6	73.5	3.2
Pond 1_7	120	0.0553	4.22	0.083	4.37	1.09E-02	1.14	#NUM!	188.2	69.7	1.6	80.9	7.3
Pond 1_51	279	0.0454	1.3	0.069	1.62	1.11E-02	0.96	-34.9	63.0	70.9	1.4	68.0	2.1
Pond 1_30	308	0.048	1.11	0.074	1.37	1.11E-02	0.81	101.5	52.4	71.4	1.1	72.3	1.9
Pond 1_54	92	0.0483	3.47	0.075	3.68	1.12E-02	1.23	113.4	163.8	72.0	1.8	73.2	5.2
Pond 1_41	199	0.0518	1.87	0.08	2.1	1.12E-02	0.95	274.7	85.7	72.1	1.4	78.4	3.2
Pond 1_48	91	0.0479	3.23	0.075	3.53	1.14E-02	1.44	95.1	152.9	73.0	2.1	73.7	5.0
Pond 1_47	216	0.0528	1.43	0.084	1.97	1.15E-02	1.36	320.5	65.1	73.7	2.0	81.6	3.1
Pond 1_39	92	0.0511	2.79	0.083	2.92	1.18E-02	0.87	245.6	128.5	75.8	1.3	81.2	4.6
Pond 1_40	91	0.0474	3.44	0.091	3.55	1.40E-02	0.9	70.2	163.6	89.4	1.6	88.7	6.0
Pond 1_6	168	0.0455	3.11	0.088	3.45	1.40E-02	1.5	-27.8	150.8	89.7	2.7	85.5	6.1
Pond 1_11	129	0.0506	3.41	0.098	3.6	1.41E-02	1.16	221.0	158.0	90.4	2.1	95.4	7.2

Pond 1_24	270	0.0574	1.91	0.112	2.22	1.41E-02	1.13	505.4	84.0	90.4	2.1	107.5	5.0
Pond 1_21	492	0.041	1.26	0.08	1.72	1.42E-02	1.17	-289.7	64.3	90.8	2.1	78.3	2.8
Pond 1_33	155	0.0482	1.52	0.096	1.86	1.44E-02	1.07	110.8	71.7	92.1	2.0	92.8	3.3
Pond 1_9	59	0.0633	5.52	0.126	5.64	1.45E-02	1.16	#NUM!	234.2	92.7	2.2	120.9	14.4
Pond 1_23	429	0.0418	1.39	0.085	1.8	1.47E-02	1.15	-236.7	70.4	93.9	2.2	82.5	3.1
Pond 1_31	80	0.0553	2.4	0.113	2.6	1.48E-02	0.99	425.4	107.2	95.0	1.9	109.0	5.4
Pond 1_52	60	0.0417	3.83	0.086	3.93	1.49E-02	0.89	-242.6	193.5	95.4	1.7	83.6	6.3
Pond 1_29	166	0.0475	1.47	0.098	1.66	1.50E-02	0.78	73.8	69.9	95.7	1.5	94.9	3.0
Pond 1_32	66	0.0498	3.06	0.103	3.4	1.50E-02	1.47	187.1	142.6	95.9	2.8	99.5	6.4
Pond 1_15	138	0.0615	2.76	0.13	2.99	1.53E-02	1.16	657.2	118.2	97.9	2.3	123.9	7.8
Pond 1_49	119	0.0458	1.85	0.099	2.24	1.57E-02	1.26	-10.3	89.3	100.6	2.5	96.2	4.1
Pond 1_56	47	0.0568	3.13	0.148	3.56	1.89E-02	1.71	482.3	138.2	120.7	4.1	140.1	9.3
Pond 1_4	386	0.0526	0.43	0.381	1.55	5.26E-02	1.5	310.0	19.4	330.5	10.1	328.0	12.0
Pondaung 2													
Pond 2_11	232	0.047	5.06	0.042	5.19	6.44E-03	1.15	47.7	241.5	41.4	0.9	41.5	4.2
Pond 2_28	255	0.0469	5.09	0.042	5.26	6.46E-03	1.3	45.7	243.5	41.5	1.1	41.6	4.3
Pond 2_23	287	0.0478	4.23	0.043	4.38	6.55E-03	1.15	90.0	200.4	42.1	1.0	42.9	3.7
Pond 2_45	238	0.0394	5.8	0.036	5.93	6.57E-03	1.22	-390.6	302.0	42.2	1.0	35.6	4.1
Pond 2_34	323	0.0454	3.74	0.042	3.92	6.65E-03	1.19	-34.9	181.3	42.7	1.0	41.4	3.2
Pond 2_17	732	0.0518	1.68	0.048	2.04	6.72E-03	1.15	274.4	77.1	43.2	1.0	47.6	1.9
Pond 2_40	511	0.0482	2.46	0.045	2.72	6.75E-03	1.15	108.6	116.4	43.3	1.0	44.5	2.4
Pond 2_42	1381	0.0468	1.04	0.044	1.58	6.78E-03	1.2	36.9	49.6	43.5	1.0	43.4	1.3
Pond 2_25	180	0.0472	6.08	0.044	6.2	6.79E-03	1.2	61.5	289.9	43.6	1.0	43.9	5.3
Pond 2_1	1416	0.0473	0.98	0.045	1.49	6.87E-03	1.13	64.4	46.6	44.2	1.0	44.5	1.3
Pond 2_5	202	0.0577	4.48	0.055	4.64	6.95E-03	1.2	517.1	196.9	44.6	1.1	54.6	4.9
Pond 2_33	109	0.0436	9.58	0.042	9.66	6.96E-03	1.26	-134.3	473.7	44.7	1.1	41.6	7.8
Pond 2_15	297	0.0478	3.76	0.046	3.93	7.01E-03	1.14	88.0	178.3	45.0	1.0	45.8	3.5
Pond 2_3	662	0.0496	1.73	0.049	2.11	7.10E-03	1.21	177.0	80.5	45.6	1.1	48.1	2.0
Pond 2_36	110	0.041	9.65	0.042	9.72	7.38E-03	1.17	-287.3	492.0	47.4	1.1	41.5	7.9

Pond 2_29	135	0.0457	7.38	0.047	7.49	7.39E-03	1.31	-16.7	356.8	47.5	1.2	46.3	6.8
Pond 2_7	218	0.0474	4.78	0.048	4.92	7.42E-03	1.14	70.0	227.6	47.6	1.1	48.1	4.6
Pond 2_13	168	0.0499	5.68	0.051	5.8	7.48E-03	1.18	190.4	264.1	48.1	1.1	51.0	5.7
Pond 2_26	734	0.0469	1.6	0.048	1.98	7.49E-03	1.16	45.3	76.5	48.1	1.1	48.1	1.9
Pond 2_46	176	0.0384	6.56	0.041	6.66	7.80E-03	1.17	-459.2	346.3	50.1	1.2	41.1	5.3
Pond 2_18	82	0.0747	10.91	0.082	10.99	7.96E-03	1.33	1060.9	439.0	51.1	1.4	80.0	16.8
Pond 2_30	100	0.0449	8.6	0.052	8.7	8.47E-03	1.29	-63.0	419.5	54.4	1.4	51.8	8.8
Pond 2_4	377	0.0531	2.3	0.063	2.57	8.64E-03	1.13	333.0	104.4	55.4	1.3	62.3	3.1
Pond 2_12	117	0.0465	6.32	0.064	6.46	1.00E-02	1.34	22.7	303.4	64.1	1.7	63.1	7.9
Pond 2_44	123	0.0383	7.12	0.053	7.21	1.01E-02	1.18	-464.9	376.2	64.5	1.5	52.5	7.4
Pond 2_37	143	0.0621	5.77	0.087	5.91	1.02E-02	1.25	676.6	246.8	65.2	1.6	84.7	9.6
Pond 2_22	180	0.0499	3.88	0.071	4.1	1.04E-02	1.33	189.2	180.6	66.6	1.8	70.1	5.5
Pond 2_24	106	0.0428	6.84	0.063	6.95	1.07E-02	1.22	-181.4	341.7	68.9	1.7	62.3	8.4
Pond 2_39	70	0.0435	10.01	0.065	10.08	1.08E-02	1.19	-141.2	495.9	69.4	1.6	63.8	12.4
Pond 2_41	105	0.0439	6.88	0.066	6.99	1.09E-02	1.26	-117.1	339.1	69.6	1.7	64.6	8.7
Pond 2_8	2248	0.0487	0.5	0.076	1.22	1.13E-02	1.11	135.4	23.5	72.2	1.6	74.1	1.7
Pond 2_20	193	0.0496	3.38	0.077	3.62	1.13E-02	1.29	175.4	157.7	72.3	1.9	75.4	5.2
Pond 2_9	341	0.0472	2.18	0.075	2.44	1.15E-02	1.1	61.7	103.7	73.6	1.6	73.3	3.4
Pond 2_38	381	0.0461	1.95	0.075	2.3	1.17E-02	1.22	2.6	94.1	75.2	1.8	73.1	3.2
Pond 2_48	660	0.0467	1.15	0.085	1.65	1.32E-02	1.18	32.2	55.3	84.5	2.0	82.8	2.6
Pond 2_10	81	0.0485	6.54	0.089	6.64	1.34E-02	1.14	121.4	308.4	85.7	1.9	87.0	11.0
Pond 2_21	141	0.0519	3.71	0.096	3.88	1.34E-02	1.15	280.4	169.8	85.7	2.0	92.9	6.9
Pond 2_43	177	0.0467	4.3	0.089	4.54	1.38E-02	1.44	32.0	206.2	88.3	2.5	86.3	7.5
Pond 2_31	154	0.0483	3.54	0.092	3.77	1.38E-02	1.28	115.7	167.2	88.5	2.3	89.4	6.4
Pond 2_47	136	0.0426	4.46	0.083	4.63	1.41E-02	1.24	-188.5	223.2	90.1	2.2	80.7	7.2
Pond 2_35	1367	0.0478	0.53	0.093	1.29	1.42E-02	1.18	87.5	25.1	90.7	2.1	90.6	2.2
Pond 2_6	221	0.0487	2.59	0.095	2.82	1.42E-02	1.11	133.7	121.8	90.9	2.0	92.5	5.0
Pond 2_32	90	0.048	5.58	0.094	5.73	1.42E-02	1.3	101.3	264.0	91.1	2.4	91.5	10.0
Pond 2_2	98	0.0565	4.59	0.112	4.74	1.44E-02	1.19	470.4	203.3	91.9	2.2	107.6	9.6
Pond 2_14	154	0.0487	3.42	0.098	3.62	1.45E-02	1.19	132.1	160.7	93.0	2.2	94.5	6.5

Pond 2_16	88	0.0523	5.13	0.106	5.26	1.48E-02	1.16	299.3	234.1	94.4	2.2	102.7	10.2
Pond 2_19	274	0.0494	1.95	0.102	2.3	1.50E-02	1.23	169.0	91.0	95.9	2.3	98.8	4.3
Pond 2_27	157	0.0474	2.89	0.116	3.15	1.78E-02	1.26	69.6	137.6	113.9	2.8	111.9	6.7
Padaung 1													
Pad 1_19	9108	0.0478	0.5	0.025	1.41	3.85E-03	1.32	89.9	23.7	24.7	0.6	25.4	0.7
Pad 1_25	1129	0.0897	7.17	0.078	7.28	6.31E-03	1.27	1419.0	274.2	40.5	1.0	76.3	10.6
Pad 1_18	2355	0.0469	0.73	0.041	1.5	6.41E-03	1.31	44.7	34.9	41.2	1.1	41.2	1.2
Pad 1_6	171	0.0429	7.35	0.039	7.44	6.59E-03	1.17	-173.4	366.2	42.3	1.0	38.8	5.7
Pad 1_8	5571	0.0483	0.5	0.044	1.29	6.65E-03	1.19	112.6	23.6	42.7	1.0	44.0	1.1
Pad 1_17	330	0.0461	3.7	0.044	3.91	7.00E-03	1.27	1.8	178.1	44.9	1.1	44.2	3.4
Pad 1_20	114	0.0434	9.58	0.043	9.66	7.25E-03	1.25	-145.1	475.1	46.6	1.2	43.1	8.1
Pad 1_11	91	0.0533	9.32	0.054	9.39	7.38E-03	1.18	342.3	421.9	47.4	1.1	53.6	9.8
Pad 1_13	419	0.0476	2.71	0.05	2.96	7.55E-03	1.17	80.4	128.9	48.5	1.1	49.1	2.8
Pad 1_7	594	0.0474	2	0.051	2.31	7.78E-03	1.17	67.8	95.2	50.0	1.2	50.4	2.3
Pad 1_14	482	0.0469	2.32	0.052	2.59	8.02E-03	1.14	44.2	111.0	51.5	1.2	51.4	2.6
Pad 1_27	270	0.0509	3.46	0.059	3.65	8.45E-03	1.19	235.3	159.5	54.3	1.3	58.5	4.1
Pad 1_16	571	0.0486	2.37	0.061	2.64	9.03E-03	1.16	129.5	111.7	57.9	1.3	59.7	3.1
Pad 1_3	68	0.0478	10.1	0.068	10.17	1.03E-02	1.16	91.6	478.7	66.2	1.5	66.9	13.1
Pad 1_9	102	0.0512	6.15	0.079	6.25	1.11E-02	1.13	247.9	283.0	71.4	1.6	76.8	9.2
Pad 1_12	106	0.0526	5.66	0.084	5.79	1.16E-02	1.2	313.1	257.6	74.4	1.8	82.1	9.1
Pad 1_21	251	0.0533	5	0.09	5.16	1.23E-02	1.27	340.6	226.6	78.7	2.0	87.7	8.6
Pad 1_28	117	0.048	4.77	0.094	4.94	1.42E-02	1.3	98.6	225.5	91.0	2.4	91.3	8.6
Pad 1_4	146	0.0477	3.91	0.096	4.08	1.46E-02	1.16	82.7	185.8	93.7	2.2	93.3	7.3
Pad 1_10	157	0.0495	3.32	0.102	3.52	1.49E-02	1.17	173.6	154.8	95.5	2.2	98.6	6.6
Pad 1_22	191	0.0473	2.93	0.099	3.16	1.52E-02	1.18	66.7	139.7	97.4	2.3	96.2	5.8
Pad 1_23	145	0.0494	3.43	0.109	3.64	1.61E-02	1.22	166.3	160.1	102.7	2.5	105.4	7.3
Pad 1_2	1861	0.0489	0.5	0.127	1.26	1.89E-02	1.16	141.9	23.5	120.5	2.8	121.5	2.9
Pad 1_5	833	0.0487	0.64	0.129	1.33	1.92E-02	1.17	135.8	29.9	122.8	2.9	123.5	3.1

Pad 1_24	128	0.0528	1.76	0.275	2.09	3.78E-02	1.13	320.1	79.8	238.9	5.3	246.6	9.1
Pad 1_15	94	0.0556	1.2	0.557	1.72	7.26E-02	1.23	437.5	53.2	452.1	10.7	449.7	12.4
Pad 1_1	155	0.0583	0.6	0.755	1.35	9.39E-02	1.2	542.5	26.4	578.4	13.3	571.2	11.7
Pad 1_26	180	0.0736	0.5	1.589	1.29	1.57E-01	1.19	1030.6	20.2	937.7	20.8	965.9	16.0
Padaung 2													
Pad 2_71	1134	0.05	2.09	0.036	2.31	5.26E-03	1	194.5	97.0	33.8	0.7	36.2	1.6
Pad 2_63	370	0.0527	5.15	0.04	5.24	5.49E-03	0.96	318.1	234.0	35.3	0.7	39.7	4.1
Pad 2_53	374	0.0693	4.46	0.054	4.58	5.65E-03	1.02	909.1	183.9	36.4	0.7	53.5	4.8
Pad 2_31	831	0.0521	3	0.041	3.21	5.77E-03	1.14	287.7	137.0	37.1	0.8	41.2	2.6
Pad 2_6	2795	0.048	1.17	0.044	1.92	6.66E-03	1.52	98.2	55.6	42.8	1.3	43.8	1.6
Pad 2_48	662	0.05	4.64	0.046	4.74	6.72E-03	0.97	197.3	215.8	43.2	0.8	46.0	4.3
Pad 2_10	463	0.0561	2.85	0.055	3.38	7.16E-03	1.81	454.4	126.4	46.0	1.7	54.7	3.6
Pad 2_32	3100	0.0613	3.01	0.063	3.22	7.45E-03	1.13	650.2	129.3	47.8	1.1	62.0	3.9
Pad 2_22	603	0.0462	1.97	0.048	2.5	7.50E-03	1.53	6.0	95.0	48.2	1.5	47.3	2.3
Pad 2_43	990	0.0473	1.67	0.049	1.95	7.51E-03	1	66.5	79.5	48.2	1.0	48.6	1.8
Pad 2_35	787	0.0482	2.59	0.05	2.78	7.56E-03	1	109.3	122.5	48.6	1.0	49.8	2.7
Pad 2_26	1401	0.0564	1.38	0.061	1.81	7.81E-03	1.17	466.9	61.2	50.1	1.2	59.8	2.1
Pad 2_13	896	0.0465	1.57	0.05	2.18	7.84E-03	1.52	24.9	75.3	50.3	1.5	49.8	2.1
Pad 2_21	219	0.0421	4.44	0.046	4.7	8.00E-03	1.54	-219.8	223.2	51.4	1.6	46.1	4.2
Pad 2_40	265	0.0559	5.16	0.062	5.26	8.09E-03	1.01	449.6	229.1	52.0	1.0	61.5	6.3
Pad 2_73	351	0.0663	5.13	0.078	5.23	8.52E-03	0.98	814.5	214.7	54.7	1.1	76.1	7.6
Pad 2_66	249	0.0495	4.73	0.058	4.84	8.55E-03	1.02	171.6	220.8	54.9	1.1	57.6	5.4
Pad 2_19	207	0.0442	4.06	0.052	4.35	8.58E-03	1.55	-101.7	199.6	55.1	1.7	51.7	4.4
Pad 2_14	164	0.0438	4.85	0.054	5.08	8.92E-03	1.53	-124.6	239.4	57.2	1.7	53.2	5.3
Pad 2_5	527	0.0484	2.14	0.062	2.64	9.23E-03	1.56	120.5	100.7	59.2	1.8	60.7	3.1
Pad 2_33	545	0.0504	3.75	0.066	3.9	9.52E-03	1.1	215.1	173.5	61.1	1.3	65.1	4.9
Pad 2_46	186	0.0454	6.02	0.06	6.12	9.55E-03	1.1	-34.7	292.3	61.3	1.3	58.9	7.0
Pad 2_23	426	0.0401	3.51	0.054	3.65	9.72E-03	0.98	-346.4	181.3	62.4	1.2	53.1	3.8
Pad 2_42	186	0.0503	5.79	0.07	5.92	1.01E-02	1.2	208.2	268.6	64.9	1.6	68.8	7.8

Pad 2_39	170	0.0615	4.72	0.088	4.81	1.04E-02	0.92	655.9	202.6	66.5	1.2	85.6	7.9
Pad 2_56	141	0.0541	6.26	0.078	6.38	1.04E-02	1.2	376.5	281.9	67.0	1.6	76.2	9.3
Pad 2_78	218	0.0652	4.55	0.095	4.71	1.06E-02	1.23	780.4	191.3	67.8	1.7	92.2	8.3
Pad 2_3	107	0.0375	6.77	0.056	6.95	1.08E-02	1.59	-523.1	362.0	69.2	2.2	55.1	7.4
Pad 2_62	253	0.0476	3.87	0.072	3.98	1.10E-02	0.92	78.6	183.8	70.3	1.3	70.5	5.4
Pad 2_18	350	0.0514	2.15	0.079	2.65	1.12E-02	1.54	256.7	99.0	71.7	2.2	77.4	3.9
Pad 2_72	222	0.063	4.47	0.098	4.61	1.13E-02	1.13	709.4	190.0	72.6	1.6	95.3	8.4
Pad 2_9	207	0.0544	4.23	0.086	4.5	1.14E-02	1.52	386.0	190.1	73.2	2.2	83.4	7.2
Pad 2_38	201	0.0409	5.31	0.065	5.4	1.14E-02	1	-292.2	270.8	73.4	1.5	63.6	6.6
Pad 2_55	194	0.0591	4.3	0.094	4.45	1.16E-02	1.12	570.7	187.3	74.3	1.6	91.6	7.8
Pad 2_57	276	0.0534	4.75	0.085	4.85	1.16E-02	0.97	347.4	214.9	74.4	1.4	83.3	7.7
Pad 2_47	394	0.0523	3.61	0.086	3.77	1.20E-02	1.06	299.6	164.8	76.6	1.6	84.0	6.1
Pad 2_68	296	0.0486	3.03	0.081	3.21	1.22E-02	1.06	129.1	142.7	77.9	1.6	79.5	4.9
Pad 2_58	439	0.0617	3.4	0.106	3.54	1.24E-02	0.99	665.1	145.5	79.6	1.6	102.1	6.8
Pad 2_36	100	0.0604	10.07	0.106	10.13	1.27E-02	1.11	618.2	434.8	81.2	1.8	101.9	19.5
Pad 2_77	501	0.054	2.01	0.097	2.23	1.31E-02	0.98	369.0	90.6	83.9	1.6	94.4	4.0
Pad 2_44	311	0.047	2.69	0.088	2.85	1.36E-02	0.95	47.8	128.4	86.8	1.6	85.5	4.7
Pad 2_8	117	0.0505	4.06	0.095	4.34	1.36E-02	1.52	217.9	188.1	87.2	2.6	92.0	7.6
Pad 2_41	122	0.045	6.34	0.085	6.42	1.37E-02	1	-56.7	309.0	87.4	1.7	82.5	10.1
Pad 2_74	103	0.0565	6.24	0.108	6.31	1.38E-02	0.95	470.7	276.3	88.5	1.7	103.8	12.4
Pad 2_69	1060	0.0493	1.03	0.099	1.62	1.45E-02	1.25	164.2	48.2	92.8	2.3	95.6	3.0
Pad 2_65	395	0.0491	2.1	0.099	2.32	1.46E-02	0.99	152.8	98.3	93.5	1.8	95.7	4.2
Pad 2_12	400	0.0485	1.73	0.098	2.32	1.47E-02	1.54	122.1	81.7	94.2	2.9	95.3	4.2
Pad 2_51	503	0.0485	1.72	0.099	2.06	1.48E-02	1.15	123.8	80.8	95.0	2.2	96.1	3.8
Pad 2_29	614	0.0487	1.37	0.103	1.75	1.53E-02	1.09	133.4	64.2	98.1	2.1	99.5	3.3
Pad 2_20	88	0.0495	4.86	0.106	5.1	1.55E-02	1.52	173.2	227.0	98.9	3.0	101.9	9.8
Pad 2_67	161	0.0566	7.37	0.122	7.44	1.57E-02	1.03	474.9	326.0	100.1	2.0	117.0	16.3
Pad 2_59	171	0.05	4.43	0.109	4.53	1.58E-02	0.95	195.1	206.1	101.2	1.9	105.1	9.0
Pad 2_61	202	0.0545	3.63	0.12	3.74	1.59E-02	0.9	390.9	162.8	101.9	1.8	114.8	8.1
Pad 2_17	505	0.0488	1.4	0.121	2.51	1.80E-02	2.08	140.1	65.9	115.1	4.7	116.3	5.5

Pad 2_2	160	0.0561	2.51	0.153	3.62	1.97E-02	2.6	456.7	111.5	126.0	6.5	144.3	9.7
Pad 2_50	229	0.0518	2.56	0.164	2.8	2.30E-02	1.15	277.8	117.1	146.6	3.3	154.6	8.0
Pad 2_16	1988	0.0505	1.11	0.162	1.88	2.32E-02	1.52	219.1	51.3	147.8	4.5	152.1	5.3
Pad 2_25	631	0.0521	1.08	0.191	1.41	2.66E-02	0.91	289.4	49.4	169.5	3.0	177.8	4.6
Pad 2_1	132	0.0498	1.91	0.237	2.56	3.45E-02	1.71	185.7	89.1	218.7	7.3	216.0	9.9
Pad 2_37	959	0.0505	0.74	0.246	1.2	3.53E-02	0.94	218.4	34.5	223.5	4.1	223.1	4.8
Pad 2_7	117	0.0577	3.12	0.294	3.5	3.70E-02	1.57	519.4	137.2	234.2	7.2	262.1	16.0
Pad 2_45	420	0.0572	1.57	0.325	1.97	4.12E-02	1.19	501.2	69.0	260.2	6.1	285.8	9.7
Pad 2_27	893	0.0544	0.69	0.311	1.21	4.15E-02	0.99	386.7	31.0	262.3	5.1	275.2	5.8
Pad 2_34	902	0.0561	1.12	0.354	1.73	4.58E-02	1.32	454.5	49.8	289.0	7.4	308.0	9.1
Pad 2_75	1095	0.0537	0.58	0.369	1.09	4.99E-02	0.93	359.3	26.2	313.8	5.7	319.2	6.0
Pad 2_60	220	0.0576	1.22	0.415	1.58	5.22E-02	1	516.4	53.5	328.2	6.4	352.6	9.3
Pad 2_49	223	0.0584	0.77	0.731	1.21	9.07E-02	0.93	545.2	33.6	559.7	10.0	556.9	10.3
Pad 2_64	144	0.0594	0.96	0.773	1.38	9.43E-02	0.99	583.0	41.6	581.1	11.0	581.5	12.2
Pad 2_76	156	0.0627	0.82	0.931	1.27	1.08E-01	0.98	696.5	35.0	660.0	12.2	668.3	12.4
Pad 2_28	224	0.0638	0.78	0.998	1.58	1.13E-01	1.37	734.7	33.0	692.6	18.0	702.6	15.9
Pad 2_54	298	0.0675	0.61	1.141	1.15	1.23E-01	0.98	854.2	25.2	745.1	13.7	773.0	12.4
Pad 2_24	67	0.0733	1.17	1.366	1.49	1.35E-01	0.93	1021.6	47.3	817.5	14.3	874.5	17.4
Pad 2_4	132	0.077	1.1	1.966	1.9	1.85E-01	1.55	1121.7	43.7	1095.0	31.1	1104.0	25.2
Pad 2_52	276	0.0783	0.66	2.072	1.17	1.92E-01	0.97	1155.6	26.2	1131.0	20.1	1139.5	15.9
Pad 2_15	41	0.0777	1.24	2.158	1.97	2.01E-01	1.53	1140.1	49.2	1182.5	33.1	1167.6	27.0
Pad 2_30	106	0.0842	0.6	2.837	1.54	2.44E-01	1.41	1298.2	23.5	1408.6	35.6	1365.3	22.8
Pad 2_70	149	0.1018	0.54	3.998	2.57	2.85E-01	2.51	1658.0	19.9	1615.0	71.4	1633.8	40.9
Pad 2_11	194	0.1123	1.08	4.889	1.88	3.16E-01	1.54	1837.5	39.3	1768.5	47.5	1800.4	31.3
Padaung 3													
Pad 3_13	2725	0.0477	0.73	0.028	2.69	4.30E-03	2.58	86.4	34.5	27.6	1.4	28.3	1.5
Pad 3_36	1578	0.0494	0.93	0.035	1.55	5.12E-03	1.24	166.5	43.2	32.9	0.8	34.8	1.1
Pad 3_53	313	0.0503	3.42	0.039	3.74	5.56E-03	1.51	208.4	158.8	35.7	1.1	38.4	2.9
Pad 3_46	430	0.0498	2.79	0.04	3.1	5.77E-03	1.34	187.5	129.9	37.1	1.0	39.5	2.5

Pad 3_12	1359	0.0467	0.92	0.041	2.69	6.33E-03	2.53	36.3	43.9	40.7	2.1	40.6	2.2
Pad 3_9	178	0.0427	7.34	0.038	7.44	6.48E-03	1.21	-184.4	366.9	41.6	1.0	38.0	5.5
Pad 3_4	151	0.0464	7.77	0.042	7.86	6.55E-03	1.19	16.0	373.3	42.1	1.0	41.6	6.4
Pad 3_35	409	0.0599	3.42	0.056	3.63	6.74E-03	1.23	600.9	148.0	43.3	1.1	55.0	4.1
Pad 3_42	794	0.0471	1.37	0.044	2.89	6.81E-03	2.55	55.8	65.3	43.7	2.2	44.0	2.6
Pad 3_30	665	0.0489	1.53	0.047	2.02	6.91E-03	1.32	142.4	71.8	44.4	1.2	46.2	1.9
Pad 3_43	1544	0.0512	0.68	0.051	1.43	7.18E-03	1.26	251.5	31.5	46.1	1.2	50.2	1.5
Pad 3_59	579	0.0474	1.65	0.05	2.13	7.69E-03	1.35	67.1	78.6	49.4	1.3	49.7	2.2
Pad 3_25	333	0.054	2.72	0.059	2.97	7.87E-03	1.21	370.4	122.3	50.5	1.2	57.8	3.5
Pad 3_48	428	0.0466	2.04	0.051	2.39	7.96E-03	1.24	26.7	97.9	51.1	1.3	50.6	2.5
Pad 3_10	255	0.0457	4.09	0.052	4.25	8.18E-03	1.14	-17.4	197.8	52.5	1.2	51.0	4.2
Pad 3_40	175	0.05	4.39	0.056	4.59	8.17E-03	1.34	197.1	203.9	52.5	1.4	55.7	5.2
Pad 3_44	165	0.0566	4.42	0.064	4.59	8.18E-03	1.26	477.8	195.2	52.5	1.3	62.9	5.9
Pad 3_6	391	0.0741	6.97	0.085	7.07	8.27E-03	1.2	1044.5	281.1	53.1	1.3	82.4	11.1
Pad 3_45	138	0.0515	5.12	0.059	5.27	8.27E-03	1.24	262.6	235.2	53.1	1.3	57.9	6.3
Pad 3_55	292	0.0476	2.46	0.06	2.77	9.17E-03	1.27	77.1	117.1	58.8	1.5	59.3	3.4
Pad 3_18	196	0.05	3.57	0.068	3.78	9.84E-03	1.23	193.2	166.0	63.2	1.6	66.6	5.2
Pad 3_33	336	0.0533	2.74	0.073	3.03	9.96E-03	1.28	342.2	124.2	63.9	1.6	71.8	4.5
Pad 3_67	477	0.0483	1.49	0.066	1.96	9.98E-03	1.26	114.5	70.4	64.0	1.6	65.3	2.6
Pad 3_14	267	0.0546	2.3	0.076	2.6	1.01E-02	1.22	394.6	103.3	64.7	1.6	74.3	4.0
Pad 3_28	674	0.0488	1.09	0.068	2.84	1.01E-02	2.62	137.7	51.4	64.7	3.4	66.7	3.9
Pad 3_1	70	0.0472	10.22	0.066	10.29	1.02E-02	1.15	59.8	487.2	65.2	1.5	65.1	12.9
Pad 3_58	149	0.0466	4.09	0.066	4.27	1.02E-02	1.24	29.0	196.1	65.5	1.6	64.6	5.7
Pad 3_8	161	0.0521	4.54	0.074	4.69	1.03E-02	1.18	288.3	207.6	66.0	1.6	72.4	6.5
Pad 3_69	199	0.0624	4.68	0.089	4.85	1.04E-02	1.29	689.1	199.6	66.4	1.7	86.7	8.8
Pad 3_29	247	0.0503	2.87	0.073	3.98	1.05E-02	2.76	208.2	133.2	67.3	3.7	71.4	5.9
Pad 3_24	258	0.0517	2.42	0.075	2.73	1.05E-02	1.25	272.0	111.1	67.5	1.7	73.5	4.1
Pad 3_23	105	0.0486	5.28	0.071	5.41	1.05E-02	1.22	127.7	248.3	67.6	1.7	69.3	7.7
Pad 3_11	130	0.0644	4.18	0.097	4.35	1.09E-02	1.21	755.0	176.4	69.8	1.7	93.7	8.5
Pad 3_47	195	0.0728	2.79	0.113	3.11	1.13E-02	1.38	1008.0	113.2	72.3	2.0	108.9	7.1

Pad 3_22	123	0.0483	4.46	0.076	4.63	1.14E-02	1.23	114.2	210.5	73.0	1.8	74.2	7.1
Pad 3_38	329	0.0481	1.7	0.084	2.14	1.26E-02	1.3	104.4	80.4	80.8	2.1	81.6	3.6
Pad 3_57	280	0.0493	1.81	0.09	2.17	1.33E-02	1.19	160.0	84.6	84.9	2.0	87.5	4.0
Pad 3_34	255	0.0524	2.13	0.096	2.63	1.33E-02	1.54	304.2	97.0	85.1	2.6	93.1	5.1
Pad 3_41	233	0.0688	9.3	0.13	9.4	1.37E-02	1.39	892.7	383.9	87.6	2.4	123.8	24.5
Pad 3_7	375	0.0473	1.81	0.09	2.15	1.37E-02	1.16	66.0	86.4	87.9	2.0	87.1	3.6
Pad 3_31	361	0.0482	1.47	0.093	2.96	1.39E-02	2.57	108.3	69.5	89.1	4.6	89.8	5.6
Pad 3_49	336	0.0489	1.68	0.094	2.39	1.39E-02	1.7	145.4	78.8	89.2	3.1	91.3	4.6
Pad 3_61	243	0.0481	2	0.093	2.73	1.40E-02	1.86	103.0	94.6	89.7	3.4	90.2	5.1
Pad 3_39	314	0.0488	1.58	0.095	2.01	1.40E-02	1.24	140.0	74.1	89.9	2.2	91.7	3.8
Pad 3_32	403	0.0481	1.24	0.098	2.82	1.48E-02	2.53	104.1	58.6	94.7	4.8	95.1	5.6
Pad 3_63	222	0.0493	2	0.101	2.36	1.48E-02	1.25	160.4	93.8	95.0	2.4	97.6	4.8
Pad 3_37	145	0.0488	2.88	0.101	3.14	1.50E-02	1.25	139.4	135.5	95.8	2.4	97.5	6.4
Pad 3_60	112	0.0532	3.93	0.111	4.21	1.51E-02	1.5	336.3	178.1	96.7	2.9	106.7	9.4
Pad 3_56	246	0.0481	1.82	0.101	2.19	1.52E-02	1.21	105.6	86.0	97.0	2.4	97.4	4.5
Pad 3_64	432	0.0483	1.09	0.106	1.62	1.59E-02	1.21	115.1	51.2	102.0	2.5	102.5	3.5
Pad 3_65	101	0.0478	3.82	0.105	4.01	1.60E-02	1.24	91.1	181.0	102.2	2.5	101.7	8.6
Pad 3_2	74	0.047	5.89	0.116	6.01	1.79E-02	1.18	50.3	281.3	114.4	2.7	111.5	12.6
Pad 3_66	97	0.0486	2.96	0.149	3.23	2.23E-02	1.28	130.5	139.5	142.1	3.7	141.4	9.8
Pad 3_54	1133	0.0529	0.73	0.165	1.56	2.27E-02	1.38	323.8	33.0	144.7	4.0	155.5	5.2
Pad 3_51	29	0.051	6.64	0.193	6.75	2.75E-02	1.23	238.6	306.3	175.0	4.3	179.4	26.2
Pad 3_62	78	0.0509	2.92	0.195	3.2	2.78E-02	1.29	234.9	135.0	176.6	4.6	180.7	12.6
Pad 3_15	694	0.051	0.36	0.256	2.55	3.65E-02	2.53	240.1	16.6	231.0	11.9	231.8	13.2
Pad 3_26	400	0.0527	0.51	0.279	1.33	3.83E-02	1.23	317.3	23.2	242.4	6.1	249.5	7.5
Pad 3_20	664	0.0574	0.2	0.614	1.23	7.76E-02	1.22	507.0	8.7	481.6	12.1	486.1	15.2
Pad 3_50	319	0.058	0.33	0.621	1.26	7.76E-02	1.21	528.9	14.5	481.9	12.1	490.2	15.7
Pad 3_21	106	0.0646	0.72	0.794	1.53	8.92E-02	1.35	761.4	30.5	550.5	15.5	593.5	24.3
Pad 3_16	77	0.0587	0.86	0.758	2.67	9.37E-02	2.53	554.9	37.5	577.2	30.4	572.7	40.3
Pad 3_5	150	0.0609	0.56	0.868	1.33	1.03E-01	1.2	636.3	24.1	634.3	14.5	634.7	12.5
Pad 3_27	126	0.0655	0.5	0.999	1.33	1.11E-01	1.23	789.8	21.1	676.6	17.5	703.4	26.5

Pad 3_17	721	0.0708	0.32	1.497	1.3	1.53E-01	1.26	950.9	13.0	920.0	24.9	929.2	38.8
Pad 3_52	250	0.073	0.2	1.59	1.29	1.58E-01	1.28	1013.5	7.9	945.5	25.9	966.2	40.9
Pad 3_19	620	0.0707	0.16	1.548	1.21	1.59E-01	1.2	947.8	6.4	950.3	24.5	949.6	37.3
Pad 3_70	169	0.0753	0.24	1.815	1.26	1.75E-01	1.23	1076.2	9.8	1038.6	27.7	1050.8	45.3
Pad 3_68	414	0.0793	0.11	1.998	1.24	1.83E-01	1.24	1180.2	4.2	1081.4	29.1	1114.7	49.2
Pad 3_3	431	0.081	0.5	2.178	1.25	1.95E-01	1.15	1220.7	19.7	1149.1	24.1	1174.2	17.3
Shwetaung Formation													
Shw_45	906	0.0497	3.14	0.019	3.28	2.83E-03	0.95	182.2	146.5	18.2	0.3	19.5	1.3
Shw_5	696	0.0445	3.61	0.02	3.79	3.33E-03	1.16	-85.6	177.1	21.4	0.5	20.5	1.5
Shw_52	65	0.0796	15.48	0.04	15.52	3.60E-03	1.19	1187.9	611.3	23.2	0.6	39.4	11.9
Shw_6	180	0.0439	11.74	0.022	11.8	3.62E-03	1.14	-115.6	578.9	23.3	0.5	22.0	5.1
Shw_35	4484	0.0474	0.56	0.03	1.12	4.60E-03	0.97	71.0	26.8	29.6	0.6	30.1	0.7
Shw_15	3233	0.053	1.32	0.037	1.73	5.03E-03	1.11	329.4	59.9	32.3	0.7	36.7	1.2
Shw_9	714	0.0497	2.22	0.037	2.55	5.39E-03	1.25	182.1	103.5	34.6	0.9	36.8	1.8
Shw_26	477	0.0536	2.84	0.044	3.05	6.01E-03	1.13	354.6	128.1	38.6	0.9	44.1	2.6
Shw_23	396	0.0507	2.8	0.048	3.4	6.87E-03	1.92	226.9	129.6	44.2	1.7	47.7	3.2
Shw_41	1324	0.0477	1.09	0.048	1.45	7.27E-03	0.95	85.2	51.9	46.7	0.9	47.5	1.3
Shw_21	1558	0.0483	0.84	0.051	1.4	7.59E-03	1.12	112.4	39.8	48.8	1.1	50.1	1.4
Shw_24	282	0.0748	13.61	0.079	13.68	7.61E-03	1.36	1062.9	547.7	48.9	1.3	76.8	20.0
Shw_39	98	0.0452	9.88	0.049	9.96	7.80E-03	1.26	-45.7	480.5	50.1	1.3	48.2	9.3
Shw_4	190	0.046	5.04	0.052	5.17	8.28E-03	1.12	-2.9	243.3	53.2	1.2	52.0	5.2
Shw_1	576	0.0476	1.8	0.054	2.12	8.30E-03	1.11	79.8	85.7	53.3	1.2	53.9	2.2
Shw_27	368	0.051	2.46	0.059	2.71	8.32E-03	1.12	241.8	113.5	53.4	1.2	57.7	3.0
Shw_28	108	0.0585	6.32	0.067	6.42	8.36E-03	1.16	548.0	276.0	53.7	1.2	66.2	8.2
Shw_2	91	0.0505	8.45	0.059	8.53	8.51E-03	1.2	218.8	391.0	54.6	1.3	58.4	9.6
Shw_32	420	0.0504	2.25	0.061	2.51	8.71E-03	1.11	214.8	104.0	55.9	1.2	59.7	2.9
Shw_7	353	0.0529	2.69	0.065	2.98	8.84E-03	1.27	325.9	122.3	56.7	1.4	63.5	3.7
Shw_19	176	0.0484	4.57	0.062	4.7	9.35E-03	1.1	116.8	215.4	60.0	1.3	61.4	5.6
Shw_40	1552	0.0477	0.71	0.062	1.11	9.46E-03	0.85	84.7	33.8	60.7	1.0	61.3	1.3

Shw_18	230	0.0481	3.36	0.068	3.55	1.02E-02	1.14	106.2	158.7	65.3	1.5	66.4	4.5
Shw_12	463	0.0478	1.82	0.067	2.13	1.02E-02	1.1	88.1	86.5	65.5	1.4	66.1	2.7
Shw_13	1411	0.0491	0.73	0.069	1.31	1.03E-02	1.09	151.1	34.1	65.9	1.4	68.2	1.7
Shw_16	179	0.0467	4.3	0.067	4.44	1.04E-02	1.12	32.7	205.9	66.6	1.5	65.7	5.6
Shw_3	317	0.0523	2.65	0.081	2.87	1.12E-02	1.08	298.3	121.1	71.8	1.5	78.9	4.3
Shw_11	262	0.0473	2.61	0.077	2.84	1.18E-02	1.13	64.7	124.2	75.6	1.7	75.2	4.1
Shw_46	324	0.0487	2.05	0.085	2.32	1.27E-02	1.08	132.2	96.6	81.5	1.7	83.2	3.7
Shw_30	1994	0.0495	0.5	0.088	1.19	1.30E-02	1.08	170.2	23.3	83.0	1.8	86.0	2.0
Shw_25	675	0.0486	0.99	0.087	1.48	1.30E-02	1.1	126.3	46.5	83.4	1.8	84.9	2.4
Shw_17	82	0.0487	6.74	0.091	6.84	1.35E-02	1.12	134.2	317.0	86.4	1.9	88.1	11.5
Shw_31	356	0.0503	1.64	0.097	1.97	1.40E-02	1.09	210.4	75.9	89.3	1.9	93.8	3.5
Shw_51	269	0.0529	2.77	0.106	2.96	1.45E-02	1.05	323.1	125.7	92.7	1.9	101.9	5.7
Shw_34	156	0.0485	3.55	0.099	3.7	1.48E-02	1.04	123.9	167.4	94.5	2.0	95.6	6.7
Shw_29	83	0.0556	4.67	0.123	4.8	1.60E-02	1.13	437.6	207.8	102.4	2.3	117.6	10.6
Shw_10	56	0.0457	8.14	0.102	8.22	1.61E-02	1.14	-16.3	393.8	103.1	2.3	98.3	15.3
Shw_43	81	0.0451	6.02	0.102	6.11	1.64E-02	1.04	-48.5	292.8	104.6	2.2	98.4	11.4
Shw_38	355	0.0489	1.47	0.115	1.91	1.71E-02	1.22	144.8	68.9	109.2	2.7	110.8	4.0
Shw_36	65	0.0486	6.41	0.117	6.48	1.75E-02	0.93	127.9	301.9	111.5	2.1	112.3	13.7
Shw_47	322	0.0523	1.66	0.138	1.96	1.91E-02	1.04	300.4	75.8	122.0	2.5	131.1	4.8
Shw_22	200	0.0508	2.05	0.134	2.33	1.92E-02	1.12	231.4	94.6	122.3	2.7	127.8	5.6
Shw_14	406	0.0494	1.1	0.136	1.56	1.99E-02	1.12	168.8	51.2	126.9	2.8	129.0	3.8
Shw_8	315	0.0494	1.38	0.136	1.77	2.00E-02	1.11	166.6	64.4	127.4	2.8	129.4	4.3
Shw_44	736	0.053	1.38	0.151	1.71	2.06E-02	1.01	329.1	62.5	131.6	2.6	142.5	4.5
Shw_33	180	0.0526	2.03	0.167	2.53	2.30E-02	1.51	309.8	92.5	146.5	4.4	156.4	7.3
Shw_50	1112	0.0539	0.8	0.181	1.28	2.44E-02	1	367.8	36.0	155.1	3.1	169.0	4.0
Shw_20	168	0.0553	3.15	0.207	3.34	2.72E-02	1.11	423.7	140.5	172.7	3.8	191.1	11.6
Shw_42	305	0.0573	0.5	0.568	1.39	7.18E-02	1.3	504.8	22.0	447.0	11.2	456.5	10.2
Shw_49	256	0.0587	0.62	0.736	1.1	9.09E-02	0.91	556.6	27.1	561.0	9.8	560.1	9.4
Shw_37	303	0.0715	0.5	1.298	0.99	1.32E-01	0.86	972.4	20.4	797.0	12.9	844.7	11.3
Shw_48	96	0.0759	0.5	1.925	1.11	1.84E-01	0.99	1092.8	20.0	1088.4	19.8	1089.9	14.7

Taungtalon Formation													
Ta_2r	1116	0.046	1.71	0.029	2.06	4.62E-03	1.15	-0.7	82.4	29.7	0.7	29.4	1.2
Ta_41	1408	0.0461	1.48	0.029	1.81	4.61E-03	1.05	0.8	71.3	29.7	0.6	29.3	1.0
Ta_36	2024	0.046	1.05	0.032	1.62	5.01E-03	1.23	-0.1	50.8	32.2	0.8	31.8	1.0
Ta_20	265	0.0438	6	0.03	6.1	5.02E-03	1.11	-121.2	295.9	32.3	0.7	30.4	3.6
Ta_16	1239	0.0475	1.36	0.035	1.81	5.36E-03	1.19	74.7	64.8	34.4	0.8	35.0	1.2
Ta_21r	512	0.0454	3.01	0.034	3.22	5.42E-03	1.14	-33.7	145.9	34.9	0.8	33.9	2.1
Ta_4	657	0.0469	2.49	0.035	2.76	5.47E-03	1.21	41.7	119.0	35.2	0.8	35.2	1.9
Ta_26	362	0.0486	5.53	0.038	5.63	5.65E-03	1.01	126.9	260.6	36.3	0.7	37.7	4.2
Ta_21c	296	0.0458	4.33	0.04	4.49	6.38E-03	1.18	-10.9	209.4	41.0	1.0	40.1	3.5
Ta_6	1242	0.0468	1.21	0.042	1.72	6.45E-03	1.22	39.8	58.1	41.4	1.0	41.4	1.4
Ta_42	451	0.0453	3.04	0.041	3.19	6.53E-03	0.96	-41.7	147.6	42.0	0.8	40.6	2.5
Ta_18	459	0.0474	2.68	0.045	2.94	6.82E-03	1.19	68.8	127.7	43.8	1.0	44.3	2.5
Ta_11	649	0.0471	2.21	0.046	2.48	7.12E-03	1.12	52.4	105.7	45.8	1.0	45.9	2.2
Ta_27	1196	0.0465	1.19	0.047	1.63	7.27E-03	1.11	22.9	57.0	46.7	1.0	46.3	1.5
Ta_14	569	0.0466	1.86	0.053	2.18	8.23E-03	1.14	28.2	89.0	52.8	1.2	52.3	2.2
Ta_37	141	0.0443	6.79	0.051	6.84	8.40E-03	0.85	-94.8	333.2	53.9	0.9	50.8	6.8
Ta_38	158	0.046	5.95	0.055	6.02	8.66E-03	0.96	0.0	286.6	55.6	1.1	54.3	6.4
Ta_22	783	0.0476	1.48	0.058	1.86	8.79E-03	1.13	77.1	70.3	56.4	1.3	56.9	2.1
Ta_33r	222	0.0439	4.55	0.056	4.83	9.19E-03	1.62	-118.9	224.7	58.9	1.9	54.9	5.2
Ta_25	1173	0.05	1.39	0.067	1.7	9.68E-03	0.97	196.3	64.5	62.1	1.2	65.6	2.2
Ta_12	183	0.0452	4.41	0.062	4.56	9.99E-03	1.15	-43.4	214.4	64.1	1.5	61.4	5.4
Ta_15	2628	0.0479	0.5	0.067	1.23	1.01E-02	1.12	94.1	23.7	64.9	1.4	65.7	1.6
Ta_39r	324	0.0463	2.69	0.065	2.86	1.01E-02	0.96	11.9	129.4	65.1	1.2	63.7	3.5
Ta_9	121	0.0445	7.36	0.063	7.46	1.03E-02	1.18	-85.3	360.8	66.1	1.6	62.2	9.0
Ta_33c	220	0.0441	4.02	0.063	4.13	1.03E-02	0.96	-107.5	197.7	66.1	1.3	61.7	4.9
Ta_24	224	0.0434	3.97	0.063	4.09	1.05E-02	0.95	-143.7	197.0	67.0	1.3	61.6	4.9
Ta_8	683	0.0473	1.25	0.069	1.75	1.06E-02	1.22	64.2	59.4	67.7	1.6	67.6	2.3
Ta_39c	275	0.0461	3.05	0.067	3.19	1.06E-02	0.91	1.8	147.1	68.1	1.2	66.3	4.1

Ta_28	175	0.0454	4.58	0.067	4.67	1.07E-02	0.89	-36.2	222.3	68.3	1.2	65.5	5.9
Ta_32	83	0.0413	9.28	0.061	9.33	1.08E-02	0.96	-267.4	471.5	69.0	1.3	60.4	10.9
Ta_13	253	0.0468	2.98	0.071	3.21	1.09E-02	1.2	37.7	142.7	70.1	1.7	69.2	4.3
Ta_7	2081	0.0478	0.5	0.075	1.3	1.14E-02	1.2	88.1	23.7	73.1	1.7	73.6	1.8
Ta_19	93	0.048	6.43	0.08	7.19	1.21E-02	3.23	98.2	304.3	77.7	5.0	78.4	10.8
Ta_2c	1049	0.048	0.79	0.081	1.42	1.22E-02	1.18	96.9	37.3	78.5	1.8	79.1	2.2
Ta_1	959	0.0476	0.79	0.082	1.46	1.25E-02	1.23	81.7	37.7	80.1	2.0	80.1	2.3
Ta_34	554	0.0469	1.3	0.092	1.85	1.43E-02	1.32	44.7	61.9	91.2	2.4	89.6	3.2
Ta_5	60	0.0394	8.81	0.084	8.89	1.55E-02	1.21	-389.6	458.4	99.1	2.4	82.1	13.9
Ta_29	87	0.0451	6.09	0.099	6.16	1.59E-02	0.97	-52.4	296.5	101.8	2.0	95.7	11.2
Ta_3	351	0.0472	1.55	0.105	1.92	1.62E-02	1.13	58.5	74.0	103.6	2.3	101.7	3.7
Ta_10	1783	0.0487	0.5	0.112	1.26	1.66E-02	1.15	134.4	23.5	106.3	2.4	107.5	2.6
Ta_23	70	0.0467	6.83	0.107	6.92	1.66E-02	1.14	33.5	327.2	106.4	2.4	103.4	13.5
Ta_31	762	0.0486	0.84	0.112	1.42	1.68E-02	1.15	129.0	39.5	107.1	2.4	108.0	2.9
Ta_40	245	0.0476	2.2	0.112	2.39	1.71E-02	0.95	79.2	104.4	109.3	2.0	108.0	4.9
Ta_44	467	0.05	1.35	0.129	1.71	1.87E-02	1.05	194.1	62.7	119.2	2.5	122.9	4.0
Ta_43	468	0.0502	0.95	0.163	1.39	2.36E-02	1.01	205.1	44.1	150.3	3.0	153.6	4.0
Ta_17	93	0.0487	3.21	0.177	3.44	2.64E-02	1.24	134.6	150.9	167.9	4.1	165.7	10.5
Ta_35	82	0.0461	4.05	0.168	4.15	2.64E-02	0.89	5.3	195.2	167.9	3.0	157.6	12.0
Ta_30	78	0.0837	0.5	2.443	1.07	2.12E-01	0.94	1286.4	19.5	1237.3	21.2	1255.3	15.3
Lower Moza Formation													
LM_21	8204	0.0478	0.5	0.034	1.24	5.12E-03	1.13	89.3	23.7	32.9	0.7	33.7	0.8
LM_28	548	0.0493	1.94	0.036	2.81	5.26E-03	2.03	161.0	90.8	33.8	1.4	35.7	2.0
LM_20	812	0.0452	2.09	0.033	2.39	5.33E-03	1.16	-43.2	101.5	34.2	0.8	33.2	1.6
LM_23	711	0.0529	2.14	0.042	2.52	5.82E-03	1.34	324.1	97.1	37.4	1.0	42.2	2.1
LM_9	4753	0.0479	0.5	0.041	1.24	6.21E-03	1.13	96.4	23.7	39.9	0.9	40.8	1.0
LM_11r	185	0.0514	5.93	0.044	6.07	6.26E-03	1.31	258.6	272.4	40.3	1.1	44.1	5.2
LM_4	341	0.046	3.22	0.045	3.41	7.11E-03	1.14	-3.8	155.2	45.6	1.0	44.7	3.0
LM_3	147	0.0608	4.77	0.066	4.91	7.90E-03	1.18	630.6	205.5	50.8	1.2	65.1	6.2

LM_22	540	0.0502	2.11	0.056	2.38	8.03E-03	1.11	203.9	97.9	51.5	1.1	54.9	2.5
LM_8	403	0.0467	2.38	0.054	2.67	8.33E-03	1.2	32.3	114.2	53.5	1.3	53.0	2.8
LM_16	265	0.0475	3.3	0.057	3.48	8.69E-03	1.11	73.3	157.0	55.7	1.2	56.1	3.8
LM_1	712	0.0477	1.32	0.058	1.7	8.82E-03	1.08	83.3	62.7	56.6	1.2	57.2	1.9
LM_27	363	0.063	5.19	0.077	5.9	8.83E-03	2.81	708.3	220.8	56.7	3.2	75.1	8.5
LM_24	430	0.0492	1.52	0.061	2.3	8.91E-03	1.72	159.3	70.9	57.2	2.0	59.7	2.7
LM_26	525	0.0542	1.92	0.07	3.88	9.41E-03	3.37	381.3	86.5	60.4	4.0	69.1	5.2
LM_7	108	0.0468	6.57	0.062	6.68	9.63E-03	1.19	40.4	314.5	61.8	1.5	61.3	7.9
LM_13	1200	0.0478	0.81	0.064	1.36	9.66E-03	1.1	86.9	38.4	62.0	1.4	62.6	1.7
LM_12	234	0.0469	3.31	0.064	3.5	9.93E-03	1.14	42.5	158.5	63.7	1.4	63.1	4.3
LM_10	176	0.0478	3.99	0.068	4.15	1.03E-02	1.12	88.1	189.3	65.8	1.5	66.4	5.3
LM_25	954	0.0516	1.1	0.073	1.55	1.03E-02	1.09	266.8	50.4	65.8	1.4	71.5	2.1
LM_18	96	0.0401	8.26	0.057	8.34	1.04E-02	1.13	-346.6	426.3	66.5	1.5	56.5	9.1
LM_6	1656	0.0483	0.53	0.075	1.23	1.12E-02	1.12	113.8	24.9	71.9	1.6	73.1	1.7
LM_2	676	0.0483	1.06	0.08	1.51	1.20E-02	1.08	115.8	50.2	77.2	1.7	78.4	2.3
LM_5	68	0.0399	9.51	0.067	9.57	1.22E-02	1.11	-354.4	491.2	78.1	1.7	66.0	12.1
LM_19	147	0.0448	3.7	0.091	3.87	1.48E-02	1.14	-68.0	180.5	94.8	2.1	88.9	6.6
LM_17	87	0.0423	5.95	0.089	6.06	1.53E-02	1.15	-208.0	298.6	98.1	2.2	87.0	10.1
LM_14	76	0.049	5.27	0.115	5.39	1.70E-02	1.1	148.4	247.3	108.8	2.4	110.5	11.2
LM_11c	709	0.0545	0.5	0.227	1.47	3.02E-02	1.38	392.8	22.4	191.6	5.2	207.6	5.5
LM_15	74	0.0787	0.5	2.114	1.26	1.95E-01	1.16	1163.4	19.8	1147.9	24.3	1153.3	17.3
Obogon Formation													
Obo_55	436	0.0631	3.58	0.034	3.68	3.86E-03	0.85	710.9	152.3	24.8	0.4	33.5	2.4
Obo_71	1569	0.0478	0.82	0.027	1.54	4.14E-03	1.3	87.0	39.1	26.6	0.7	27.3	0.8
Obo_73	490	0.0478	2.16	0.028	2.61	4.23E-03	1.46	89.7	102.5	27.2	0.8	27.9	1.4
Obo_66	832	0.0505	2.28	0.03	2.6	4.26E-03	1.25	218.1	105.5	27.4	0.7	29.7	1.5
Obo_40	141	0.058	5.84	0.035	6.16	4.36E-03	1.97	528.2	255.8	28.0	1.1	34.7	4.2
Obo_68	850	0.0511	1.33	0.033	1.57	4.69E-03	0.83	246.1	61.4	30.2	0.5	33.0	1.0
Obo_13	762	0.0502	2.12	0.033	2.44	4.74E-03	1.21	204.3	98.6	30.5	0.7	32.8	1.6

Obo_17	91	0.0693	10.71	0.046	10.78	4.84E-03	1.19	907.8	441.3	31.1	0.7	45.9	9.6
Obo_70	344	0.0543	2.47	0.037	2.68	4.97E-03	1.03	381.6	111.3	32.0	0.7	37.1	1.9
Obo_56	342	0.0559	5.47	0.039	5.75	5.12E-03	1.77	447.7	243.1	32.9	1.2	39.3	4.4
Obo_38	661	0.0556	2.13	0.039	2.46	5.14E-03	1.24	434.8	94.9	33.0	0.8	39.2	1.9
Obo_62	113	0.0696	6.5	0.056	7.47	5.80E-03	3.69	917.8	267.3	37.3	2.7	55.0	8.0
Obo_41	491	0.0493	1.82	0.044	9.66	6.45E-03	9.49	164.5	85.3	41.4	7.8	43.6	8.2
Obo_59	586	0.0514	1.61	0.046	4.94	6.49E-03	4.68	256.9	74.0	41.7	3.9	45.6	4.4
Obo_51	1084	0.0518	2.03	0.048	6.72	6.75E-03	6.41	278.1	92.8	43.4	5.5	47.8	6.3
Obo_72	236	0.0494	2.97	0.047	3.45	6.83E-03	1.76	164.8	138.9	43.9	1.5	46.2	3.1
Obo_67	435	0.0477	1.55	0.046	3.71	6.99E-03	3.37	85.5	73.5	44.9	3.0	45.7	3.3
Obo_34	466	0.0472	0.75	0.047	1.29	7.26E-03	1.05	57.6	35.8	46.6	1.0	46.8	1.2
Obo_8	58	0.0722	9.9	0.075	9.97	7.51E-03	1.17	992.4	402.5	48.2	1.1	73.2	14.0
Obo_24	212	0.0475	0.79	0.049	1.71	7.51E-03	1.52	75.1	37.6	48.2	1.5	48.8	1.7
Obo_10	149	0.0679	4.82	0.072	4.99	7.73E-03	1.28	865.3	199.9	49.6	1.3	70.9	6.8
Obo_19	1008	0.0473	0.7	0.051	1.52	7.82E-03	1.34	62.3	33.4	50.2	1.4	50.4	1.6
Obo_61	2097	0.0487	0.75	0.053	1.1	7.87E-03	0.81	135.5	35.4	50.5	0.8	52.3	1.1
Obo_12	504	0.0549	2.92	0.06	3.17	7.94E-03	1.23	409.7	130.7	51.0	1.2	59.3	3.6
Obo_2	761	0.0493	1.34	0.056	1.83	8.20E-03	1.24	160.9	62.9	52.6	1.3	55.0	2.0
Obo_4	340	0.0519	2.6	0.059	2.86	8.29E-03	1.18	279.7	119.0	53.3	1.3	58.5	3.2
Obo_15	316	0.051	2.74	0.059	2.96	8.42E-03	1.12	240.2	126.3	54.0	1.2	58.4	3.4
Obo_3	633	0.0494	1.5	0.059	1.9	8.69E-03	1.16	166.4	69.9	55.8	1.3	58.4	2.2
Obo_18	1566	0.054	1.72	0.065	2.09	8.78E-03	1.19	371.8	77.4	56.3	1.3	64.3	2.8
Obo_74	1112	0.0525	0.79	0.064	1.56	8.78E-03	1.34	306.4	35.8	56.3	1.5	62.5	1.9
Obo_54	150	0.0481	3.18	0.059	3.3	8.90E-03	0.88	103.8	150.5	57.1	1.0	58.2	3.7
Obo_20	780	0.0476	0.69	0.059	1.33	9.05E-03	1.14	78.1	32.8	58.0	1.3	58.5	1.6
Obo_47	3021	0.0497	0.51	0.062	1.41	9.04E-03	1.31	181.9	23.5	58.0	1.5	61.1	1.7
Obo_7	287	0.0528	2.77	0.067	3.02	9.20E-03	1.21	321.8	125.6	59.0	1.4	65.8	3.8
Obo_69	595	0.0502	1.57	0.064	1.74	9.28E-03	0.77	204.4	72.7	59.5	0.9	63.2	2.1
Obo_31	189	0.0484	0.88	0.062	1.43	9.30E-03	1.13	119.8	41.3	59.7	1.4	61.2	1.8
Obo_37	7726	0.0473	0.63	0.062	1.98	9.49E-03	1.87	63.7	30.2	60.9	2.3	61.0	2.5

Obo_52	687	0.0553	1.3	0.072	1.58	9.49E-03	0.9	424.5	57.9	60.9	1.1	70.9	2.2
Obo_43	2383	0.0483	0.5	0.064	1.36	9.55E-03	1.27	115.1	23.6	61.3	1.5	62.6	1.7
Obo_42	1273	0.0553	1.22	0.073	1.96	9.60E-03	1.53	425.1	54.6	61.6	1.9	71.8	2.7
Obo_60	1563	0.0542	1.35	0.073	14.52	9.70E-03	14.45	380.9	60.7	62.2	17.9	71.1	19.7
Obo_39	273	0.05	2.12	0.068	2.29	9.85E-03	0.87	197.1	98.3	63.2	1.1	66.8	3.0
Obo_23	320	0.0473	0.74	0.065	1.31	9.95E-03	1.08	66.6	35.1	63.8	1.4	63.9	1.7
Obo_65	1439	0.0493	0.59	0.069	1.42	1.02E-02	1.29	163.8	27.5	65.3	1.7	68.0	1.9
Obo_26	924	0.0479	0.69	0.07	1.54	1.06E-02	1.37	94.7	32.7	68.2	1.9	68.9	2.2
Obo_5	577	0.0526	1.5	0.08	4.88	1.11E-02	4.64	313.3	68.1	70.9	6.5	78.4	7.3
Obo_32	833	0.0476	0.7	0.073	1.36	1.11E-02	1.16	78.0	33.3	71.4	1.7	71.5	2.0
Obo_6	145	0.0572	4.66	0.091	4.82	1.15E-02	1.23	499.5	205.4	73.6	1.8	88.1	8.1
Obo_45	150	0.0637	5.68	0.102	5.91	1.16E-02	1.63	732.9	240.6	74.1	2.4	98.3	11.0
Obo_53	340	0.0487	1.28	0.079	3.25	1.17E-02	2.98	135.5	60.1	75.2	4.5	77.1	4.8
Obo_27	303	0.0503	0.89	0.09	1.35	1.29E-02	1.02	210.0	41.3	82.9	1.7	87.3	2.5
Obo_22	109	0.0484	1.11	0.102	1.58	1.53E-02	1.13	117.7	52.3	98.1	2.2	98.9	3.3
Obo_11c	606	0.0497	0.94	0.107	1.54	1.56E-02	1.21	182.5	43.8	99.7	2.4	103.1	3.0
Obo_11r	389	0.0509	1.39	0.115	1.89	1.63E-02	1.29	237.8	64.1	104.3	2.7	110.1	3.9
Obo_14	312	0.0499	1.54	0.114	2	1.66E-02	1.28	192.1	71.6	105.9	2.7	109.7	4.2
Obo_44	24	0.0643	7.29	0.161	7.75	1.82E-02	2.63	750.8	308.0	116.2	6.0	151.8	21.6
Obo_25	1693	0.0491	0.65	0.124	1.26	1.83E-02	1.08	153.8	30.7	117.2	2.6	118.9	3.2
Obo_1	1245	0.0497	0.5	0.128	1.33	1.87E-02	1.23	180.5	23.3	119.3	2.9	122.2	3.1
Obo_29	351	0.0503	1.62	0.143	2.03	2.06E-02	1.22	210.9	75.3	131.2	3.2	135.4	5.9
Obo_57	604	0.0496	0.88	0.147	2.06	2.16E-02	1.86	175.1	41.2	137.5	5.1	139.6	5.3
Obo_58	1670	0.0488	0.5	0.148	1.22	2.20E-02	1.12	138.5	23.5	140.5	3.1	140.4	3.2
Obo_16	289	0.051	1.22	0.167	1.69	2.37E-02	1.17	240.2	56.3	151.0	3.5	156.4	4.9
Obo_33	635	0.0496	0.65	0.176	1.44	2.57E-02	1.29	175.0	30.3	163.6	4.3	164.3	5.1
Obo_9	232	0.0533	1.3	0.195	1.72	2.65E-02	1.13	342.3	58.7	168.5	3.8	180.6	5.7
Obo_49	554	0.0489	0.5	0.18	2.77	2.66E-02	2.72	143.6	23.5	169.5	9.1	167.8	8.5
Obo_50	894	0.0507	0.5	0.245	1.48	3.51E-02	1.39	226.0	23.1	222.6	6.1	222.9	5.9
Obo_64	568	0.0514	0.5	0.274	1.27	3.87E-02	1.17	258.0	23.0	244.9	5.6	246.2	5.5

Obo_21r2	1500	0.0557	0.63	0.33	1.22	4.30E-02	1.04	439.2	28.2	271.6	5.8	289.8	8.1
Obo_21r3	950	0.0549	0.65	0.366	1.43	4.84E-02	1.27	408.2	29.0	304.6	7.9	316.9	10.5
Obo_28	855	0.0666	0.67	0.586	1.72	6.38E-02	1.59	825.4	27.9	398.7	13.0	468.2	20.3
Obo_21c2	1473	0.0585	0.64	0.564	1.24	6.99E-02	1.06	549.1	27.9	435.7	9.6	454.2	14.1
Obo_63	210	0.0599	0.5	0.841	2.15	1.02E-01	2.09	600.6	21.6	624.8	24.8	619.6	19.7
Obo_46	320	0.0607	0.5	0.877	1.51	1.05E-01	1.43	628.0	21.5	642.2	17.5	639.1	14.3
Obo_30r	806	0.0633	0.8	0.931	1.33	1.07E-01	1.06	717.8	34.1	653.6	14.6	668.3	24.9
Obo_48	303	0.0617	0.5	0.921	3.26	1.08E-01	3.22	663.9	21.4	662.5	40.4	662.8	31.2
Obo_35	245	0.0623	0.64	0.971	1.22	1.13E-01	1.04	685.0	27.3	689.9	15.1	688.7	23.7
Obo_30c	868	0.0652	0.68	1.042	1.46	1.16E-01	1.29	779.4	28.5	707.7	19.2	725.1	30.4
Obo_36	730	0.0641	0.72	1.049	1.44	1.19E-01	1.24	743.8	30.4	723.5	19.0	728.5	30.1

Table A2. ICP-MS U-Pb dating of single grain detrital zircon (UCL)

Sample/ Grain	U (ppm)	Atomic ratios						ICPMS U-Pb Ages (Ma)					
		$^{206}Pb/^{238}U$	± 1σ	$^{207}Pb/^{235}U$	± 1σ	$^{207}Pb/^{206}Pb$	± 1σ	$^{206}Pb/^{238}U$	±2σ	$^{207}Pb/^{235}U$	±2σ	$^{207}Pb/^{206}Pb$	± 2σ
Eocene													
Pondaung Formation (1)													
Pond01_01	250.2	0.0102	0.0002	0.0818	0.0065	0.0529	0.0038	65.1	2.5	79.8	10.5	324.5	39.9
Pond01_02	289.9	0.0338	0.0004	0.2807	0.0126	0.0530	0.0014	214.0	5.4	251.2	12.0	326.7	15.1
Pond01_03	181.4	0.0356	0.0006	0.2958	0.0173	0.0533	0.0025	225.2	7.2	263.1	20.7	342.9	27.1
Pond01_04	280.6	0.0124	0.0002	0.1068	0.0086	0.0573	0.0042	79.5	3.3	103.1	14.0	503.1	58.4
Pond01_05	687.6	0.0074	0.0001	0.0547	0.0036	0.0476	0.0027	47.7	1.7	54.1	5.7	81.4	8.9
Pond01_06	88.3	0.0081	0.0002	0.0857	0.0105	0.0693	0.0083	52.2	2.9	83.5	18.0	908.0	143.1
Pond01_08	270.5	0.0129	0.0003	0.1026	0.0093	0.0526	0.0045	82.5	3.5	99.2	15.3	312.4	45.7
Pond01_09	127.4	0.0085	0.0003	0.1368	0.0151	0.1015	0.0110	54.8	3.9	130.2	24.8	1652.5	176.7
Pond01_10	173.3	0.0054	0.0002	0.0897	0.0083	0.1066	0.0096	35.0	2.4	87.3	14.5	1741.2	149.8
Pond01_11	248.8	0.0086	0.0002	0.0670	0.0058	0.0503	0.0041	54.9	2.4	65.8	9.6	206.6	30.3
Pond01_13	91.8	0.0130	0.0003	0.2845	0.0176	0.1411	0.0074	83.3	3.8	254.2	23.6	2240.5	95.5
Pond01_14	90.2	0.0128	0.0003	0.1092	0.0145	0.0560	0.0072	81.9	4.4	105.2	24.3	450.8	94.4
Pond01_15	357.3	0.0062	0.0001	0.0455	0.0035	0.0485	0.0034	39.9	1.6	45.2	6.1	124.2	16.6
Pond01_16	97.3	0.0091	0.0002	0.0748	0.0070	0.0527	0.0046	58.2	2.8	73.2	11.6	317.6	48.2
Pond01_17	227.6	0.0127	0.0002	0.0950	0.0061	0.0476	0.0026	81.6	2.8	92.2	9.0	79.9	8.5
Pond01_18	63.1	0.0070	0.0003	0.0951	0.0165	0.0900	0.0156	44.8	3.7	92.3	29.0	1425.1	266.1
Pond01_20	404.4	0.0061	0.0001	0.0476	0.0035	0.0504	0.0033	39.4	1.6	47.2	5.8	214.9	25.5
Pond01_21	405.4	0.0134	0.0002	0.1187	0.0061	0.0577	0.0022	85.7	2.6	113.9	8.0	519.9	30.7
Pond01_22	37.9	0.0077	0.0004	0.0504	0.0224	0.0426	0.0190	49.6	4.8	49.9	39.6	-189.2	-184.8
Pond01_23	221.2	0.0096	0.0002	0.0709	0.0070	0.0470	0.0044	61.8	2.8	69.6	11.6	51.3	9.5
Pond01_24	253.3	0.0097	0.0002	0.0734	0.0059	0.0473	0.0035	61.9	2.4	71.9	9.3	62.9	9.2

Pond01_25	177.7	0.0096	0.0002	0.0885	0.0070	0.0593	0.0043	61.4	2.5	86.1	11.2	579.2	63.7
Pond01_26	67.6	0.0088	0.0004	0.3942	0.0276	0.2980	0.0207	56.4	4.7	337.4	43.4	3459.7	136.7
Pond01_27	640.6	0.0141	0.0002	0.1145	0.0059	0.0518	0.0019	90.3	2.8	110.1	7.7	277.0	18.4
Pond01_28	105.2	0.0134	0.0004	0.1133	0.0159	0.0539	0.0074	86.0	4.8	109.0	26.0	366.0	84.6
Pond01_29	167.1	0.0054	0.0002	0.0398	0.0071	0.0467	0.0082	34.8	2.3	39.7	12.4	32.9	11.6
Pond01_30	113.2	0.0083	0.0002	0.0598	0.0093	0.0476	0.0073	53.3	3.0	59.0	16.6	80.4	23.9
Pond01_31	205.6	0.0122	0.0002	0.0910	0.0075	0.0474	0.0036	78.2	3.0	88.4	11.9	70.4	10.5
Pond01_32	163.8	0.0080	0.0002	0.0702	0.0085	0.0558	0.0066	51.0	3.0	68.9	14.4	442.4	85.1
Pond01_33	202.4	0.0086	0.0002	0.0728	0.0059	0.0553	0.0041	55.2	2.4	71.4	9.8	424.8	51.4
Pond01_34	236.4	0.0058	0.0001	0.0560	0.0056	0.0622	0.0059	37.3	2.0	55.4	9.6	679.6	93.8
Pond01_37	47.7	0.2077	0.0026	2.6940	0.1178	0.0852	0.0018	1216.3	28.3	1326.8	35.4	1319.0	31.1
Pond01_38	201.8	0.0772	0.0009	0.7120	0.0305	0.0594	0.0013	479.6	11.5	545.9	20.3	580.3	20.0
Pond01_39	165.3	0.0111	0.0003	0.0805	0.0091	0.0484	0.0053	71.4	3.5	78.6	15.9	117.9	24.5
Pond01_40	79.6	0.0076	0.0003	0.1502	0.0159	0.1314	0.0137	48.7	3.7	142.1	27.2	2116.4	185.5
Pond01_42	564.2	0.0109	0.0002	0.0800	0.0061	0.0497	0.0034	69.6	2.9	78.2	10.2	181.0	23.0
Pond01_43	228.9	0.0085	0.0002	0.0689	0.0060	0.0526	0.0043	54.6	2.4	67.6	10.1	313.3	43.9
Pond01_44	405.0	0.0065	0.0001	0.0443	0.0023	0.0473	0.0018	41.8	1.4	44.0	3.5	66.4	5.0
Pond01_45	131.6	0.0102	0.0002	0.0758	0.0078	0.0488	0.0048	65.4	3.1	74.2	13.2	135.8	25.0
Pond01_46	128.6	0.0129	0.0003	0.0953	0.0111	0.0482	0.0054	82.6	4.2	92.5	18.5	110.1	23.5
Pond01_47	189.7	0.0118	0.0003	0.0933	0.0091	0.0523	0.0048	75.7	3.5	90.6	15.3	296.8	47.7
Pond01_48	230.9	0.0947	0.0011	0.8915	0.0367	0.0610	0.0012	583.2	13.3	647.2	20.3	640.6	18.3
Pondaung Formation (2)													
Pond02_01	215.8	0.0071	0.0002	0.0951	0.0093	0.0901	0.0084	45.5	6.3	92.2	19.8	1427.2	146.7
Pond02_02	513.2	0.0070	0.0001	0.0485	0.0045	0.0477	0.0041	45.2	5.7	48.1	11.9	83.4	17.8
Pond02_03	74.7	0.0108	0.0003	0.1281	0.0188	0.0830	0.0119	69.0	8.2	122.4	36.7	1268.0	212.4
Pond02_04	218.8	0.0131	0.0003	0.0975	0.0087	0.0510	0.0042	83.8	7.3	94.5	18.3	239.9	38.8
Pond02_05	163.6	0.0120	0.0003	0.0830	0.0112	0.0486	0.0064	77.0	7.7	81.0	24.2	127.6	35.5
Pond02_06	172.7	0.0086	0.0002	0.0610	0.0106	0.0490	0.0084	55.3	7.0	60.1	23.3	147.8	51.0
Pond02_07	117.9	0.0107	0.0003	0.0726	0.0136	0.0475	0.0088	68.8	7.7	71.2	28.8	73.4	30.1

Pond02_08	88.5	0.0111	0.0004	0.0647	0.0182	0.0399	0.0111	71.4	8.4	63.7	36.8	-359.4	-236.8
Pond02_09	92.0	0.0098	0.0003	0.0703	0.0131	0.0482	0.0089	63.0	7.5	69.0	27.1	108.6	41.9
Pond02_10	170.2	0.0101	0.0003	0.1235	0.0126	0.0821	0.0080	64.8	7.1	118.3	24.8	1248.4	143.2
Pond02_11	637.5	0.0080	0.0001	0.0582	0.0030	0.0563	0.0020	51.1	5.4	57.4	8.5	462.2	30.5
Pond02_12	367.2	0.0065	0.0001	0.0563	0.0044	0.0596	0.0042	41.6	5.5	55.6	11.4	589.1	66.4
Pond02_13	157.3	0.0071	0.0002	0.0778	0.0082	0.0751	0.0075	45.3	6.1	76.1	18.2	1071.7	136.5
Pond02_14	152.0	0.0102	0.0003	0.0698	0.0120	0.0483	0.0081	65.2	7.4	68.5	25.9	111.5	39.6
Pond02_15	248.6	0.0063	0.0001	0.0429	0.0056	0.0474	0.0060	40.7	5.8	42.7	14.3	68.9	20.7
Pond02_16	56.7	0.0072	0.0003	0.1119	0.0205	0.1110	0.0204	46.1	8.2	107.7	42.1	1815.5	315.4
Pond02_17	308.8	0.0069	0.0002	0.0515	0.0058	0.0535	0.0057	44.3	5.9	51.0	14.7	348.8	67.2
Pond02_18	88.4	0.0146	0.0002	0.1093	0.0058	0.0523	0.0020	93.2	6.6	105.3	11.9	300.3	23.9
Pond02_19	313.4	0.0107	0.0004	0.0745	0.0187	0.0490	0.0123	68.7	8.5	73.0	38.5	147.4	72.6
Pond02_20	183.2	0.0086	0.0002	0.1587	0.0098	0.1269	0.0065	54.9	6.3	149.5	18.6	2055.9	94.5
Pond02_21	181.7	0.0145	0.0003	0.1533	0.0110	0.0705	0.0044	92.9	7.5	144.8	20.4	941.8	80.6
Pond02_22	81.9	0.0078	0.0003	0.1877	0.0201	0.1618	0.0172	49.8	7.9	174.7	38.0	2475.0	201.2
Pond02_23	191.9	0.0103	0.0002	0.0757	0.0087	0.0520	0.0058	66.3	7.0	74.1	19.8	286.7	59.3
Pond02_24	106.4	0.0117	0.0003	0.1290	0.0107	0.0786	0.0060	74.9	7.3	123.2	22.0	1160.8	108.7
Pond02_25	179.8	0.0307	0.0007	2.2794	0.1014	0.5133	0.0139	194.8	12.1	1205.9	51.7	4280.0	58.0
Pond02_26	74.4	0.0120	0.0003	0.1724	0.0189	0.1012	0.0107	76.8	8.2	161.5	35.7	1645.5	176.3
Pond02_27	109.4	0.0143	0.0004	0.0994	0.0167	0.0484	0.0080	91.7	8.8	96.2	33.7	120.8	41.6
Pond02_28	289.4	0.0058	0.0001	0.0641	0.0054	0.0754	0.0058	37.0	5.5	63.1	13.1	1078.7	106.2
Pond02_29	89.8	0.0112	0.0003	0.2351	0.0203	0.1418	0.0116	71.7	8.2	214.4	35.6	2249.8	151.4
Pond02_30	92.9	0.0074	0.0003	0.0711	0.0128	0.0654	0.0117	47.7	7.2	69.7	27.1	787.2	199.6
Pond02_31	380.6	0.0066	0.0001	0.0639	0.0051	0.0663	0.0048	42.5	5.7	62.9	12.7	815.2	85.6
Pond02_32	58.7	0.0091	0.0003	0.2265	0.0226	0.1693	0.0165	58.5	8.2	207.3	41.1	2551.0	186.2
Pond02_33	82.2	0.0092	0.0003	0.2788	0.0194	0.2019	0.0129	59.2	7.5	249.7	33.3	2841.2	125.6
Pond02_34	170.0	0.0069	0.0002	0.0525	0.0085	0.0538	0.0085	44.3	6.3	51.9	19.8	361.8	100.3
Pond02_35	213.2	0.0122	0.0002	0.1547	0.0086	0.0890	0.0038	78.4	6.8	146.0	16.3	1404.8	69.1
Pond02_36	378.2	0.0064	0.0001	0.0580	0.0058	0.0631	0.0060	41.4	5.6	57.3	14.4	712.6	101.0
Pond02_37	74.3	0.0207	0.0004	1.5137	0.0674	0.4855	0.0128	132.1	9.0	935.9	42.5	4197.8	56.5

Pond02_38	45.2	0.0218	0.0005	0.2578	0.0259	0.0805	0.0076	138.8	10.6	232.9	42.5	1209.0	137.6
Pond02_39	120.3	0.0141	0.0003	0.1618	0.0143	0.0766	0.0063	90.5	8.0	152.3	26.3	1109.8	114.3
Pond02_40	96.0	0.0074	0.0002	0.0480	0.0124	0.0469	0.0121	47.5	6.9	47.6	28.0	42.1	25.2
Oligocene													
Padaung Formation (3)													
Pad03_1	688.5	0.3252	0.0037	4.7195	0.1835	0.1092	0.0012	1814.9	37.6	1770.7	27.9	1786.1	19.5
Pad03_2	148.7	0.0152	0.0004	0.1858	0.0140	0.0813	0.0055	97.4	6.1	173.1	22.9	1228.0	98.3
Pad03_3	247.7	0.0990	0.0012	0.8433	0.0349	0.0609	0.0011	608.3	16.0	620.9	21.2	636.1	18.0
Pad03_4	147.4	0.0091	0.0002	0.0609	0.0068	0.0470	0.0050	58.3	4.2	60.0	14.0	48.2	11.8
Pad03_5	244.2	0.4959	0.0057	16.4184	0.6390	0.2330	0.0022	2596.2	50.9	2901.5	30.3	3072.6	20.2
Pad03_6	234.1	0.0135	0.0002	0.1030	0.0051	0.0540	0.0018	86.7	4.2	99.6	8.6	371.0	22.8
Pad03_7	107.9	0.0112	0.0003	0.0892	0.0122	0.0552	0.0074	72.0	5.9	86.8	23.5	418.7	93.1
Pad03_8	97.5	0.5611	0.0070	15.6664	0.6595	0.1916	0.0026	2871.0	59.3	2856.7	36.9	2755.7	27.7
Pad03_9	282.7	0.0120	0.0002	0.0909	0.0045	0.0515	0.0017	77.0	3.7	88.3	7.5	262.8	17.3
Pad03_10	191.0	0.0062	0.0002	0.0471	0.0060	0.0525	0.0065	40.1	3.9	46.8	12.8	306.8	67.0
Pad03_11	139.9	0.0179	0.0003	0.1921	0.0119	0.0737	0.0037	114.4	5.7	178.4	18.5	1031.9	67.5
Pad03_12	115.6	0.0082	0.0002	0.0786	0.0084	0.0643	0.0065	52.3	4.2	76.8	16.0	751.8	109.6
Pad03_13	128.3	0.0094	0.0002	0.0668	0.0087	0.0498	0.0063	60.0	4.8	65.6	17.6	186.6	44.9
Pad03_14	287.3	0.0073	0.0002	0.0650	0.0048	0.0625	0.0041	46.9	3.6	64.0	9.9	690.9	67.1
Pad03_16	191.4	0.0135	0.0003	0.0925	0.0102	0.0479	0.0051	86.7	5.8	89.9	19.8	96.3	21.1
Pad03_17	94.7	0.0091	0.0002	0.0636	0.0084	0.0476	0.0061	58.7	4.8	62.6	16.8	77.4	20.9
Pad03_18	128.5	0.0087	0.0002	0.0793	0.0081	0.0621	0.0060	55.8	4.5	77.5	15.8	677.9	97.9
Pad03_19	224.8	0.3008	0.0035	4.7923	0.1925	0.1118	0.0016	1695.2	36.5	1783.6	32.0	1829.0	25.2
Pad03_20	221.3	0.0090	0.0002	0.0878	0.0058	0.0657	0.0037	57.7	3.7	85.4	10.6	796.8	63.0
Pad03_22	101.1	0.0083	0.0002	0.1110	0.0105	0.0907	0.0082	53.4	4.6	106.9	19.8	1439.9	140.7
Pad03_15	249.3	0.4899	0.0057	13.6171	0.5325	0.1969	0.0019	2570.2	51.1	2723.5	30.3	2800.4	20.0
Pad03_21	197.2	0.0088	0.0002	0.0573	0.0053	0.0447	0.0038	56.5	3.9	56.6	10.8	-74.7	-11.5
Miocene													

Shwetaung Formation

SHW_01	–	–	–	–	–	–	–	26.0	0.9	26.2	3.5	36.0	5.1
SHW_02	–	–	–	–	–	–	–	28.6	0.8	36.4	2.3	474.4	23.9
SHW_03	–	–	–	–	–	–	–	35.5	0.9	44.3	2.4	463.0	19.9
SHW_04	–	–	–	–	–	–	–	28.8	0.8	31.7	2.1	173.5	10.9
SHW_05	–	–	–	–	–	–	–	175.3	6.9	212.5	35.9	672.0	89.5
SHW_06	–	–	–	–	–	–	–	995.0	21.8	998.2	20.3	983.1	14.1
SHW_07	–	–	–	–	–	–	–	44.6	1.9	94.0	10.5	1644.4	89.0
SHW_08	–	–	–	–	–	–	–	45.4	1.9	42.7	11.4	-90.1	-24.9
SHW_09	–	–	–	–	–	–	–	51.2	1.5	61.3	6.0	522.9	38.8
SHW_10	–	–	–	–	–	–	–	51.4	1.4	57.3	3.5	261.5	13.7
SHW_11	–	–	–	–	–	–	–	54.7	1.7	56.7	5.4	119.4	11.0
SHW_12	–	–	–	–	–	–	–	56.8	1.9	48.1	8.8	-393.4	-89.4
SHW_13	–	–	–	–	–	–	–	58.4	2.7	73.9	16.9	568.2	103.3
SHW_14	–	–	–	–	–	–	–	68.9	3.1	107.6	22.1	1064.7	141.4
SHW_15	–	–	–	–	–	–	–	228.0	5.5	250.8	8.3	396.3	10.2
SHW_16	–	–	–	–	–	–	–	44.4	1.4	51.7	4.8	395.9	30.1
SHW_17	–	–	–	–	–	–	–	31.8	0.9	35.7	2.5	259.7	15.6
SHW_18	–	–	–	–	–	–	–	38.1	1.2	42.0	4.0	227.2	19.4
SHW_19	–	–	–	–	–	–	–	39.7	2.1	209.6	21.6	3322.3	98.4
SHW_20	–	–	–	–	–	–	–	91.0	3.7	88.6	21.5	19.0	5.1
SHW_21	–	–	–	–	–	–	–	94.1	2.4	100.3	5.5	255.2	12.1
SHW_22	–	–	–	–	–	–	–	96.3	3.8	126.2	21.7	812.1	96.9
SHW_23	–	–	–	–	–	–	–	97.9	3.3	112.0	13.8	446.0	45.2
SHW_24	–	–	–	–	–	–	–	98.6	2.7	101.3	6.6	165.0	10.1
SHW_25	–	–	–	–	–	–	–	164.4	5.4	179.5	17.1	436.0	34.5
SHW_26	–	–	–	–	–	–	–	186.8	5.4	217.7	15.0	498.1	29.1

Taungtalon Formation

TA_01	2432.6	0.0103	0.0002	0.0681	0.0079	0.0482	0.0063	66.2	5.4	66.9	19.7	108.1	29.3
TA_02	772.9	0.0111	0.0009	0.0719	0.0249	0.0474	0.0017	70.8	13.5	70.5	14.2	70.4	7.4
TA_03	783.5	0.1642	0.0001	1.6101	0.0042	0.0712	0.0050	980.2	3.8	974.1	90.8	962.3	90.1
TA_04	141.8	0.0103	0.0001	0.0570	0.0033	0.0384	0.0054	65.8	3.6	56.3	17.0	-458.2	159.6
TA_05	610.9	0.0083	0.0003	0.0533	0.0087	0.0466	0.0059	53.0	5.6	52.7	15.6	27.7	9.3
TA_06	223.0	0.0086	0.0002	0.0566	0.0038	0.0486	0.0010	55.0	4.8	55.9	5.7	127.6	7.4
TA_07	435.2	0.0865	0.0001	0.6759	0.0034	0.0571	0.0029	534.9	3.8	524.3	44.6	493.9	42.5
TA_08	134.1	0.0078	0.0001	0.0493	0.0034	0.0472	0.0059	50.3	1.3	48.8	12.4	58.3	14.2
TA_09	615.1	0.0072	0.0002	0.0481	0.0062	0.0468	0.0054	46.2	4.5	47.7	12.9	41.1	11.6
TA_10	396.3	0.0085	0.0002	0.0697	0.0043	0.0603	0.0028	54.6	4.3	68.4	9.0	615.8	45.2
TA_11	281.3	0.0092	0.0003	0.0619	0.0080	0.0493	0.0056	58.7	5.7	60.9	16.3	160.7	36.1
TA_12	590.7	0.0060	0.0001	0.0390	0.0026	0.0468	0.0045	38.8	3.4	38.8	9.7	37.0	9.3
TA_13	94.9	0.0164	0.0001	0.1088	0.0031	0.0490	0.0030	105.1	3.6	104.9	14.6	148.8	19.0
TA_14	163.7	0.0097	0.0001	0.0991	0.0039	0.0752	0.0027	62.2	4.1	96.0	9.5	1073.3	50.0
TA_15	414.0	0.0116	0.0007	0.0880	0.0242	0.0546	0.0108	74.6	10.6	85.6	36.0	394.2	131.6
TA_16	780.5	0.0109	0.0004	0.0716	0.0159	0.0477	0.0113	70.0	7.2	70.2	34.8	85.9	41.2
TA_17	1128.6	0.0054	0.0002	0.0368	0.0058	0.0496	0.0086	34.5	4.4	36.7	15.0	177.2	58.5
TA_18	158.3	0.0098	0.0002	0.0875	0.0062	0.0619	0.0038	62.8	4.8	85.1	12.4	670.3	62.5
TA_21	802.5	0.0074	0.0001	0.0478	0.0030	0.0470	0.0040	47.2	3.6	47.4	10.3	49.2	10.5
TA_22	255.4	0.0109	0.0001	0.0700	0.0024	0.0474	0.0023	69.7	3.5	68.7	9.1	68.4	8.9
TA_23	553.2	0.0133	0.0002	0.0856	0.0072	0.0473	0.0069	85.2	2.7	83.4	23.7	61.9	17.4
TA_24	891.1	0.0083	0.0003	0.0532	0.0148	0.0475	0.0105	53.0	3.3	52.7	23.4	71.9	30.8
TA_26	51.9	0.0263	0.0001	0.1740	0.0029	0.0494	0.0025	167.0	1.4	162.8	15.8	165.9	15.6
TA_27	48.5	0.0150	0.0004	0.0980	0.0104	0.0479	0.0028	95.7	4.6	94.9	11.7	91.9	10.4
TA_29	645.7	0.0790	0.0002	0.6150	0.0076	0.0570	0.0057	489.9	2.6	486.7	77.2	489.6	77.1
TA_30	532.3	0.0082	0.0004	0.0520	0.0139	0.0472	0.0055	52.4	5.4	51.4	13.0	56.8	12.8
TA_31	195.6	0.0071	0.0003	0.0454	0.0098	0.0468	0.0060	45.5	3.6	45.1	11.9	40.6	10.2
TA_32	118.6	0.0190	0.0004	0.1215	0.0156	0.0486	0.0079	121.3	5.3	116.4	37.7	129.5	39.6
TA_33	62.2	0.0122	0.0007	0.0790	0.0146	0.0484	0.0011	78.2	8.3	77.2	8.9	119.8	5.3
TA_34	37.4	0.0150	0.0006	0.0937	0.0140	0.0479	0.0011	96.2	8.0	90.9	8.7	93.3	4.0

TA201_01	270.7	0.0155	0.0001	0.1028	0.0021	0.0491	0.0018	98.9	1.2	99.3	7.0	150.2	10.1
TA201_03	1911.0	0.0084	0.0001	0.0546	0.0028	0.0471	0.0022	54.2	1.4	54.0	5.2	52.3	4.9
TA201_04	1557.4	0.0094	0.0002	0.0606	0.0058	0.0474	0.0059	60.2	2.2	59.7	14.9	66.9	16.3
TA201_06	692.6	0.0805	0.0002	0.6113	0.0034	0.0572	0.0016	498.8	1.8	484.4	22.0	499.6	22.0
TA201_07	71.5	0.0137	0.0001	0.0879	0.0021	0.0479	0.0035	87.7	0.9	85.6	12.3	91.9	12.8
TA201_09	241.8	0.0163	0.0002	0.1554	0.0061	0.0708	0.0068	104.5	1.9	146.7	27.0	951.9	118.8
TA201_10	167.1	0.0137	0.0003	0.0898	0.0114	0.0478	0.0061	87.5	4.3	87.3	21.8	90.9	22.2
TA201_11	181.1	0.0068	0.0002	0.0723	0.0081	0.0804	0.0058	43.8	3.0	70.9	11.3	1206.6	101.4
TA201_12	91.6	0.0135	0.0002	0.0896	0.0067	0.0482	0.0031	86.1	2.9	87.1	11.1	107.1	13.1
TA201_13	144.2	0.0107	0.0002	0.0660	0.0052	0.0475	0.0064	68.4	1.9	64.9	18.1	71.9	18.9
TA201_14	232.3	0.0059	0.0003	0.0378	0.0119	0.0470	0.0075	37.6	4.0	37.6	12.5	51.3	16.0
TA201_15	754.2	0.0090	0.0001	0.0575	0.0024	0.0472	0.0020	57.8	1.2	56.8	4.8	57.3	4.6
TA201_16	89.8	0.0105	0.0002	0.0659	0.0061	0.0476	0.0046	67.3	2.6	64.8	12.8	78.9	14.6
TA201_17	1182.5	0.0087	0.0002	0.0559	0.0047	0.0473	0.0047	55.5	1.9	55.2	10.9	62.4	12.0
TA201_18	127.3	0.0113	0.0003	0.0745	0.0139	0.0475	0.0100	72.2	4.4	73.0	29.7	72.9	29.7
TA201_19	144.2	0.0099	0.0003	0.0633	0.0073	0.0474	0.0036	63.8	3.2	62.3	9.8	70.4	10.2
TA201_20	287.6	0.0075	0.0002	0.0478	0.0054	0.0473	0.0026	47.9	2.4	47.4	5.7	61.9	6.5
TA201_22	105.1	0.0105	0.0002	0.2150	0.0082	0.1548	0.0044	67.1	3.1	197.7	13.5	2399.3	52.2
Obogon Formation													
OB_01	299.2	0.2718	0.0032	3.9249	0.1578	0.0980	0.0011	1550.1	38.1	1618.8	32.1	1586.2	24.4
OB_03	253.2	0.1313	0.0016	1.2872	0.0534	0.0667	0.0010	795.0	24.3	840.1	27.7	829.7	23.3
OB_04	126.6	0.2017	0.0025	2.3479	0.0995	0.0788	0.0013	1184.6	33.3	1226.9	34.8	1168.1	28.7
OB_05	293.8	0.0092	0.0002	0.0772	0.0056	0.0577	0.0036	59.0	8.4	75.5	15.2	519.9	57.1
OB_06	245.9	0.0147	0.0003	0.1054	0.0074	0.0486	0.0029	93.9	9.4	101.7	17.4	130.5	20.7
OB_07	292.8	0.0075	0.0001	0.0521	0.0034	0.0469	0.0026	48.4	7.9	51.5	11.6	46.2	11.2
OB_08	282.8	0.0097	0.0002	0.0677	0.0042	0.0477	0.0024	62.2	8.1	66.5	12.5	81.9	14.0
OB_09	492.1	0.0060	0.0001	0.0408	0.0032	0.0468	0.0033	38.3	7.6	40.6	11.7	41.1	11.9
OB_10	159.2	0.0150	0.0003	0.1082	0.0109	0.0486	0.0046	95.7	10.3	104.3	24.0	126.6	28.6
OB_11	217.2	0.0066	0.0002	0.0463	0.0046	0.0481	0.0045	42.1	8.1	46.0	14.3	103.7	24.6

OB_12	780.2	0.0037	0.0001	0.0238	0.0016	0.0464	0.0027	23.8	7.0	23.9	9.0	20.5	8.5
OB_13	600.0	0.0178	0.0002	0.1267	0.0062	0.0485	0.0015	113.7	9.2	121.1	13.6	121.8	13.4
OB_14	369.8	0.0044	0.0001	0.0305	0.0029	0.0472	0.0041	28.2	7.3	30.5	11.3	56.8	15.9
OB_15	383.5	0.0177	0.0003	0.1224	0.0076	0.0470	0.0024	112.9	9.9	117.2	17.2	47.7	10.9
OB_16	339.8	0.0080	0.0001	0.0515	0.0027	0.0472	0.0017	51.0	7.6	51.0	10.0	57.3	10.1
OB_17	830.2	0.0056	0.0001	0.0447	0.0032	0.0565	0.0035	36.0	7.6	44.4	11.7	472.9	53.3
OB_18	103.3	0.0165	0.0004	0.1511	0.0163	0.0618	0.0064	105.2	11.4	142.9	32.6	668.2	106.9
OB_19	1156.0	0.0050	0.0001	0.0392	0.0024	0.0581	0.0028	32.4	7.3	39.0	10.2	533.9	45.9
OB_20	105.9	0.2006	0.0026	2.5555	0.1117	0.0857	0.0016	1178.7	33.9	1288.0	38.7	1331.0	34.1
OB_21	404.1	0.0085	0.0002	0.0701	0.0052	0.0564	0.0037	54.6	8.4	68.8	14.7	469.3	54.9
OB_22	616.0	0.0075	0.0001	0.0522	0.0035	0.0473	0.0027	47.9	7.9	51.7	11.8	65.4	13.4
OB_23	90.6	0.0143	0.0003	0.1023	0.0108	0.0479	0.0048	91.5	10.0	98.9	23.9	95.3	24.2
OB_24	129.9	0.2033	0.0026	2.3568	0.1026	0.0790	0.0015	1193.1	34.0	1229.6	37.6	1171.9	31.9
OB_25	373.8	0.0088	0.0002	0.4169	0.0194	0.3303	0.0101	56.6	8.5	353.9	27.6	3618.5	66.8
OB_26	538.0	0.0093	0.0001	0.0913	0.0048	0.0656	0.0025	59.7	8.0	88.7	12.6	792.7	47.8
OB_27	52.0	0.0128	0.0005	0.1090	0.0255	0.0572	0.0133	82.1	12.6	105.0	50.2	499.3	190.0

Table A3. Conventional fission track dating of single grain detrital zircon

Sample/	CONVENTIONAL ZFT METHOD							FT age		ICPMS U-Pb Age	
Grain	Ng*	Ns†	ρs§	Ni[#]	ρi**	Ns/Ni	U (ppm)	(Ma)	error	(Ma)	±1σ
Pondaung 1											
Pond01_14	10	26	1.876E+06	66	4.762E+06	0.39	307.9	13.9	3.2		
Pond01_22	16	9	4.058E+05	20	9.019E+05	0.45	58.3	15.9	6.4		
Pond01_42	30	84	2.020E+06	175	4.209E+06	0.48	272.1	16.9	2.3	69.6	1.4
Pond01_40	24	34	1.022E+06	60	1.804E+06	0.57	116.6	20.0	4.3	48.7	1.8
Pond01_26	20	18	6.494E+05	30	1.082E+06	0.60	70.0	21.2	6.3		
Pond01_18	20	27	9.740E+05	44	1.587E+06	0.61	102.6	21.7	5.3	44.8	1.8
Pond01_48	15	58	2.790E+06	92	4.425E+06	0.63	286.1	22.3	3.8	583.2	6.6
Pond01_27	20	203	7.323E+06	306	1.104E+07	0.66	713.7	23.4	2.2	90.3	1.4
Pond01_10	15	45	2.165E+06	66	3.175E+06	0.68	205.3	24.1	4.7	35.0	1.2
Pond01_11	25	93	2.684E+06	130	3.752E+06	0.72	242.6	25.2	3.5	54.9	1.2
Pond01_44	20	119	4.293E+06	161	5.808E+06	0.74	375.5	26.1	3.2	41.8	0.7
Pond01_7	12	140	8.418E+06	180	1.082E+07	0.78	699.7	27.4	3.2		
Pond01_20	15	84	4.040E+06	104	5.002E+06	0.81	323.4	28.5	4.2		
Pond01_34	15	73	3.511E+06	85	4.089E+06	0.86	264.3	30.3	4.9	37.3	1.0
Pond01_09	40	136	2.453E+06	155	2.796E+06	0.88	180.8	30.9	3.7	54.8	2.0
Pond01_13	40	70	1.263E+06	79	1.425E+06	0.89	92.1	31.3	5.2		
Pond01_46	20	56	2.020E+06	60	2.165E+06	0.93	139.9	32.9	6.2	82.6	2.1
Pond01_15	15	127	6.109E+06	136	6.542E+06	0.93	422.9	32.9	4.1	39.9	0.8
Pond01_47	15	73	3.511E+06	75	3.608E+06	0.97	233.2	34.3	5.7	75.7	1.8
Pond01_29	12	52	3.127E+06	53	3.187E+06	0.98	206.0	34.6	6.8		
Pond01_05	18	240	9.620E+06	242	9.700E+06	0.99	627.2	35.0	3.3	47.7	0.9
Pond01_24	30	182	4.377E+06	183	4.401E+06	0.99	284.6	35.1	3.8	61.9	1.2

Pond01_45	20	73	2.633E+06	73	2.633E+06	1.00	170.3	35.3	5.9	65.4	1.6
Pond01_33	15	100	4.810E+06	95	4.570E+06	1.05	295.4	37.1	5.4	55.2	1.2
Pond01_30	30	150	3.608E+06	137	3.295E+06	1.09	213.0	38.6	4.7	53.3	1.5
Pond01_35	20	42	1.515E+06	38	1.371E+06	1.11	88.6	39.0	8.8		
Pond01_21	15	125	6.013E+06	113	5.435E+06	1.11	351.4	39.0	5.2	85.7	1.3
Pond01_17	20	152	5.483E+06	130	4.690E+06	1.17	303.2	41.2	5.0		
Pond01_13	20	107	3.860E+06	91	3.283E+06	1.18	212.3	41.4	6.0	83.3	1.9
Pond01_43	15	101	4.858E+06	79	3.800E+06	1.28	245.7	45.0	6.9	54.6	1.2
Pond01_32	28	130	3.350E+06	92	2.371E+06	1.41	153.3	49.8	6.9	51.0	1.5
Pond01_08	12	138	8.297E+06	88	5.291E+06	1.57	342.1	55.2	7.7		
Pond01_31	20	149	5.375E+06	93	3.355E+06	1.60	216.9	56.4	7.6	78.2	1.5
Pond01_39	15	69	3.319E+06	43	2.068E+06	1.60	133.7	56.5	11.1		
Pond01_36	18	79	3.167E+06	48	1.924E+06	1.65	124.4	57.9	10.7		
Pond01_23	12	91	5.471E+06	53	3.187E+06	1.72	206.0	60.4	10.5	61.8	1.4
Pond01_04	16	172	7.756E+06	91	4.104E+06	1.89	265.3	66.5	8.8	79.5	1.6
Pond01_01	16	175	7.891E+06	86	3.878E+06	2.03	250.7	71.5	9.6		
Pond01_38	15	140	6.734E+06	68	3.271E+06	2.06	211.5	72.4	10.8		
Pond01_28	15	84	4.040E+06	38	1.828E+06	2.21	118.2	77.7	15.3	86.0	2.4
Pond01_03	14	162	8.349E+06	56	2.886E+06	2.89	186.6	101.5	15.9	225.2	3.6
Pond01_02	10	290	2.092E+07	55	3.968E+06	5.27	256.6	183.8	27.4		
Pond01_37	18	180	7.215E+06	30	1.203E+06	6.00	77.7	208.7	41.5	1319.0	15.5
Pond01_06	*16*	*336*	*1.515E+07*	*37*	*1.668E+06*	*9.08*	*107.9*	*313.3*	*54.8*	*52.2*	*1.4*
Pond01_16	*24*	*139*	*4.179E+06*	*60*	*1.804E+06*	*2.32*	*116.6*	*81.4*	*12.7*	*58.2*	*1.4*
Pond01_25	*12*	*102*	*6.133E+06*	*43*	*2.585E+06*	*2.37*	*167.2*	*83.3*	*15.3*	*61.4*	*1.3*
Pond01_41	*12*	*128*	*7.696E+06*	*121*	*7.275E+06*	*1.06*	*470.4*	*37.3*	*4.8*	*20.2*	*0.6*
Pond01_19	*30*	*37*	*8.899E+05*	*86*	*2.068E+06*	*0.43*	*133.7*	*15.2*	*3.0*	*24.3*	*1.1*
Pondaung 2											
Pond02_37	60	106	1.275E+06	348	4.185E+06	0.30	270.6	10.8	1.2	132.1	4.5
Pond02_36	20	113	4.076E+06	286	1.032E+07	0.40	667.1	14.0	1.6	41.4	2.8

Pond02_06	50	93	1.342E+06	179	2.583E+06	0.52	167.0	18.3	2.4		
Pond02_30	30	51	1.227E+06	83	1.996E+06	0.61	129.1	21.7	3.9		
Pond02_31	40	277	4.996E+06	440	7.937E+06	0.63	513.1	22.2	1.8	42.5	2.9
Pond02_40	40	86	1.551E+06	136	2.453E+06	0.63	158.6	22.3	3.1	47.5	3.5
Pond02_02	16	71	3.202E+06	110	4.960E+06	0.65	320.7	22.8	3.5		
Pond02_11	20	142	5.123E+06	218	7.864E+06	0.65	508.5	23.0	2.5	51.1	2.7
Pond02_14	40	100	1.804E+06	152	2.742E+06	0.66	177.3	23.2	3.0	65.2	3.7
Pond02_20	50	162	2.338E+06	240	3.463E+06	0.68	223.9	23.8	2.5		
Pond02_13	25	60	1.732E+06	85	2.453E+06	0.71	158.6	24.9	4.2	45.3	3.1
Pond02_15	40	162	2.922E+06	218	3.932E+06	0.74	254.2	26.2	2.8	40.7	2.9
Pond02_01	20	70	2.525E+06	93	3.355E+06	0.75	216.9	26.6	4.3		
Pond02_39	60	144	1.732E+06	190	2.285E+06	0.76	147.7	26.7	3.0	90.5	4.0
Pond02_05	50	145	2.092E+06	182	2.626E+06	0.80	169.8	28.1	3.2		
Pond02_10	50	95	1.371E+06	119	1.717E+06	0.80	111.0	28.2	3.9	64.8	3.6
Pond02_08	60	86	1.034E+06	100	1.203E+06	0.86	77.7	30.3	4.5	71.4	4.2
Pond02_29	60	101	1.215E+06	116	1.395E+06	0.87	90.2	30.7	4.2	71.7	4.1
Pond02_07	20	48	1.732E+06	54	1.948E+06	0.89	126.0	31.4	6.3		
Pond02_28	24	157	4.720E+06	172	5.171E+06	0.91	334.3	32.2	3.6	37.0	2.7
Pond02_21	50	149	2.150E+06	160	2.309E+06	0.93	149.3	32.8	3.8	92.9	3.8
Pond02_34	50	179	2.583E+06	192	2.771E+06	0.93	179.1	32.9	3.5	44.3	3.1
Pond02_12	20	113	4.076E+06	117	4.221E+06	0.97	272.9	34.1	4.6	41.6	2.7
Pond02_17	25	164	4.733E+06	169	4.877E+06	0.97	315.3	34.2	3.8	44.3	2.9
Pond02_16	30	38	9.139E+05	39	9.380E+05	0.97	60.6	34.4	7.9	46.1	4.1
Pond02_22	60	125	1.503E+06	128	1.539E+06	0.98	99.5	34.4	4.4	49.8	4.0
Pond02_09	50	86	1.241E+06	87	1.255E+06	0.99	81.2	34.9	5.4	63.0	3.8
Pond02_24	30	91	2.189E+06	90	2.165E+06	1.01	139.9	35.7	5.4	74.9	3.6
Pond02_33	40	51	9.199E+05	49	8.838E+05	1.04	57.1	36.7	7.4	59.2	3.8
Pond02_18	40	156	2.814E+06	144	2.597E+06	1.08	167.9	38.2	4.5	93.2	3.3
Pond02_23	40	251	4.527E+06	193	3.481E+06	1.30	225.1	45.8	4.5	66.3	3.5
Pond02_32	32	46	1.037E+06	35	7.891E+05	1.31	51.0	46.3	10.4	58.5	4.1

Pond02_04	18	108	4.329E+06	73	2.926E+06	1.48	189.2	52.1	8.0	83.8	3.6
Pond02_27	20	93	3.355E+06	60	2.165E+06	1.55	139.9	54.6	9.1	91.7	4.4
Pond02_19	18	185	7.415E+06	113	4.529E+06	1.64	292.9	57.6	7.0	68.7	4.3
Pond02_35	50	273	3.939E+06	143	2.063E+06	1.91	133.4	67.1	7.1	78.4	3.4
Pond02_26	40	157	2.832E+06	71	1.281E+06	2.21	82.8	77.7	11.3	76.8	4.1
Pond02_25	198	353	1.286E+06	91	3.316E+05	3.88	21.4	135.7	16.3	194.8	6.0
Padaung 3											
Pad03_10	14	32	1.649E+06	65	3.350E+06	0.49	216.6	17.4	3.8	40.1	1.9
Pad03_12	20	39	1.407E+06	62	2.237E+06	0.63	144.6	22.2	4.6	52.3	1.9
Pad03_13	24	49	1.473E+06	73	2.195E+06	0.67	141.9	23.7	4.4	60.0	2.4
Pad03_1	8	90	8.117E+06	110	9.921E+06	0.82	641.4	28.9	4.2	1786.1	9.8
Pad03_20	10	32	2.309E+06	39	2.814E+06	0.82	181.9	28.9	6.9	57.7	1.9
Pad03_19	16	71	3.202E+06	85	3.833E+06	0.84	247.8	29.5	4.8	1829.0	12.6
Pad03_17	15	32	1.539E+06	37	1.780E+06	0.86	115.1	30.5	7.4	58.7	2.4
Pad03_14	12	89	5.351E+06	101	6.073E+06	0.88	392.6	31.1	4.6	46.9	1.8
Pad03_22	24	40	1.203E+06	44	1.323E+06	0.91	85.5	32.1	7.0	53.4	2.3
Pad03_4	15	55	2.646E+06	58	2.790E+06	0.95	180.4	33.4	6.3	58.3	2.1
Pad03_6	12	86	5.171E+06	89	5.351E+06	0.97	346.0	34.1	5.2	86.7	2.1
Pad03_18	9	23	1.844E+06	23	1.844E+06	1.00	119.2	35.3	10.4	55.8	2.3
Pad03_3	8	46	4.149E+06	41	3.698E+06	1.12	239.1	39.5	8.6	608.3	8.0
Pad03_8	12	41	2.465E+06	32	1.924E+06	1.28	124.4	45.1	10.7	2755.7	13.9
Pad03_11	16	53	2.390E+06	36	1.623E+06	1.47	105.0	51.8	11.3	114.4	2.9
Pad03_5	12	132	7.937E+06	65	3.908E+06	2.03	252.7	71.4	11.0	3072.6	10.1
Pad03_16	10	90	6.494E+06	38	2.742E+06	2.37	177.3	83.2	16.2	86.7	2.9
Pad03_2	*6*	*183*	*2.201E+07*	*43*	*5.171E+06*	*4.26*	*334.3*	*148.7*	*25.5*	*97.4*	*3.1*
Pad03_7	*21*	*138*	*4.741E+06*	*52*	*1.787E+06*	*2.65*	*115.5*	*93.2*	*15.3*	*72.0*	*2.9*
Pad03_9	*14*	*330*	*1.701E+07*	*74*	*3.814E+06*	*4.46*	*246.6*	*155.8*	*20.4*	*77.0*	*1.9*

Shwetaung

SHW_26	20	29	1.046E+06	124	4.473E+06	0.23	289.2	8.3	1.7		
SHW_07	16	32	1.443E+06	126	5.682E+06	0.25	367.4	9.0	1.8		
SHW_24	15	25	1.203E+06	68	3.271E+06	0.37	211.5	13.0	3.1		
SHW_09	21	33	1.134E+06	82	2.817E+06	0.40	182.2	14.2	3.0		
SHW_12	12	19	1.142E+06	44	2.646E+06	0.43	171.0	15.2	4.2		
SHW_17	9	59	4.730E+06	132	1.058E+07	0.45	684.2	15.8	2.5	31.8	0.4
SHW_10	28	47	1.211E+06	94	2.422E+06	0.50	156.6	17.7	3.2		
SHW_11	35	33	6.803E+05	65	1.340E+06	0.51	86.6	17.9	3.9		
SHW_14	10	94	6.782E+06	185	1.335E+07	0.51	863.0	17.9	2.3		
SHW_23	10	54	3.896E+06	102	7.359E+06	0.53	475.8	18.7	3.2		
SHW_03	12	68	4.089E+06	118	7.095E+06	0.58	458.7	20.3	3.1	35.5	0.4
SHW_21	20	88	3.175E+06	151	5.447E+06	0.58	352.2	20.6	2.8		
SHW_20	12	70	4.209E+06	119	7.155E+06	0.59	462.6	20.8	3.2		
SHW_19	15	34	1.635E+06	57	2.742E+06	0.60	177.3	21.1	4.6	39.7	1.0
SHW_16	10	55	3.968E+06	92	6.638E+06	0.60	429.2	21.1	3.6	44.4	0.7
SHW_01	12	156	9.380E+06	243	1.461E+07	0.64	944.6	22.7	2.4		
SHW_06	9	57	4.570E+06	80	6.413E+06	0.71	414.7	25.1	4.4	995.0	10.9
SHW_15	14	282	1.453E+07	368	1.897E+07	0.77	1226.2	27.0	2.2	228.0	2.7
SHW_02	15	19	9.139E+05	21	1.010E+06	0.90	65.3	31.9	10.1		
SHW_25	6	36	4.329E+06	38	4.570E+06	0.95	295.4	33.4	7.8		
SHW_08	20	50	1.804E+06	43	1.551E+06	1.16	100.3	41.0	8.6		
SHW_18	10	147	1.061E+07	120	8.658E+06	1.23	559.8	43.2	5.4	38.1	0.6
SHW_22	15	69	3.319E+06	46	2.213E+06	1.50	143.1	52.8	10.1		
SHW_13	20	46	1.659E+06	28	1.010E+06	1.64	65.3	57.8	13.9		
SHW_05	14	39	2.010E+06	19	9.792E+05	2.05	63.3	72.2	20.3	175.3	3.5
SHW_04	*20*	*57*	*2.056E+06*	*22*	*7.937E+05*	*2.59*	*51.3*	*91.0*	*22.9*		

Taungtalon

TA_33	30	14	3.367E+05	55	1.323E+06	0.25	85.5	9.0	2.7	78.2	4.1
TA_10	15	37	1.780E+06	105	5.051E+06	0.35	326.5	12.4	2.4	54.6	2.1
TA201_20	30	54	1.299E+06	134	3.223E+06	0.40	208.4	14.2	2.3	47.9	1.2
TA_14	30	43	1.034E+06	103	2.477E+06	0.42	160.2	14.7	2.7	62.2	2.1
TA_08	20	21	7.576E+05	50	1.804E+06	0.42	116.6	14.8	3.9	50.3	0.6
TA_19	40	141	2.543E+06	296	5.339E+06	0.48	345.2	16.8	1.8	31.3	5.7
TA_24	25	90	2.597E+06	182	5.253E+06	0.49	339.6	17.5	2.3		
TA_06	20	55	1.984E+06	107	3.860E+06	0.51	249.6	18.1	3.0	55.0	2.4
TA_11	25	57	1.645E+06	110	3.175E+06	0.52	205.3	18.3	3.0	58.7	2.8
TA_27	42	15	2.577E+05	28	4.810E+05	0.54	31.1	18.9	6.1	95.7	2.3
TA_03	16	96	4.329E+06	178	8.027E+06	0.54	519.0	19.0	2.5	962.3	45.0
TA_02	14	64	3.298E+06	117	6.030E+06	0.55	389.9	19.3	3.0	70.8	6.7
TA_01	10	292	2.107E+07	515	3.716E+07	0.57	2402.4	20.0	1.5	66.2	2.7
TA_26	50	41	5.916E+05	72	1.039E+06	0.57	67.2	20.1	4.0	167.0	0.7
TA201_18	20	21	7.576E+05	36	1.299E+06	0.58	84.0	20.6	5.7	72.2	1.1
TA_25	49	67	9.865E+05	112	1.649E+06	0.60	106.6	21.1	3.3		
TA201_10	20	55	1.984E+06	87	3.139E+06	0.63	202.9	22.3	3.9	87.5	2.2
TA201_22	36	62	1.243E+06	97	1.944E+06	0.64	125.7	22.6	3.7	67.1	1.5
TA_13	25	59	1.703E+06	90	2.597E+06	0.66	167.9	23.1	3.9	105.1	1.8
TA_31	15	38	1.828E+06	57	2.742E+06	0.67	177.3	23.5	5.0	45.5	1.8
TA201_11	20	44	1.587E+06	65	2.345E+06	0.68	151.6	23.9	4.7	43.8	1.5
TA201_17	16	109	4.915E+06	161	7.260E+06	0.68	469.4	23.9	3.0	55.5	1.0
TA201_19	30	62	1.491E+06	90	2.165E+06	0.69	139.9	24.3	4.1	63.8	1.6
TA_04	20	27	9.740E+05	39	1.407E+06	0.69	91.0	24.4	6.1	65.8	1.8
TA_12	30	165	3.968E+06	237	5.700E+06	0.70	368.5	24.6	2.6	38.8	1.7
TA201_15	16	155	6.990E+06	216	9.740E+06	0.72	629.8	25.3	2.7	57.8	0.6
TA_15	30	178	4.281E+06	236	5.676E+06	0.75	367.0	26.6	2.7	74.6	5.3
TA_17	20	234	8.442E+06	308	1.111E+07	0.76	718.4	26.8	2.4	34.5	2.2
TA201_09	25	185	5.339E+06	242	6.984E+06	0.76	451.6	27.0	2.7		
TA201_13	36	69	1.383E+06	87	1.744E+06	0.79	112.7	28.0	4.6		

TA_07	40	158	2.850E+06	184	3.319E+06	0.86	214.6	30.3	3.4	534.9	1.9
TA_05	12	76	4.570E+06	86	5.171E+06	0.88	334.3	31.2	5.0	53.0	2.8
TA_30	15	101	4.858E+06	113	5.435E+06	0.89	351.4	31.5	4.4	52.4	2.7
TA_09	20	140	5.051E+06	156	5.628E+06	0.90	363.9	31.7	3.8	46.2	2.3
TA_28	40	81	1.461E+06	88	1.587E+06	0.92	102.6	32.5	5.1		
TA_21	18	136	5.451E+06	147	5.892E+06	0.93	381.0	32.6	4.0	47.2	1.8
TA_18	25	81	2.338E+06	86	2.482E+06	0.94	160.5	33.2	5.2	62.8	2.4
TA_34	25	23	6.638E+05	24	6.926E+05	0.96	44.8	33.8	9.9	96.2	4.0
TA_16	25	140	4.040E+06	140	4.040E+06	1.00	261.2	35.3	4.3	70.0	3.6
TA_32	35	127	2.618E+06	127	2.618E+06	1.00	169.3	35.3	4.5	121.3	2.7
TA_29	15	89	4.281E+06	89	4.281E+06	1.00	276.8	35.3	5.4	489.9	1.3
TA201_12	25	52	1.501E+06	51	1.472E+06	1.02	95.2	35.9	7.1		
TA201_16	40	42	7.576E+05	41	7.395E+05	1.02	47.8	36.1	8.0	67.3	1.3
TA201_04	8	125	1.127E+07	122	1.100E+07	1.02	711.4	36.1	4.7	60.2	1.1
TA201_01	12	129	7.756E+06	118	7.095E+06	1.09	458.7	38.5	5.0		
TA201_14	24	82	2.465E+06	75	2.255E+06	1.09	145.8	38.5	6.2	37.6	2.0
TA201_07	25	58	1.674E+06	52	1.501E+06	1.12	97.0	39.3	7.6	87.7	0.5
TA201_03	6	148	1.780E+07	114	1.371E+07	1.30	886.3	45.7	5.8		
TA201_21	25	120	3.463E+06	81	2.338E+06	1.48	151.1	52.2	7.6	47.2	1.8
TA201_05	40	392	7.071E+06	236	4.257E+06	1.66	275.2	58.5	5.0		
TA_22	25	170	4.906E+06	101	2.915E+06	1.68	188.5	59.2	7.6	69.7	1.8
TA201_06	6	78	9.380E+06	44	5.291E+06	1.77	342.1	62.4	11.9		
TA_23	35	415	8.555E+06	234	4.824E+06	1.77	311.9	62.4	5.3	85.2	1.3
TA201_8	50	353	5.094E+06	180	2.597E+06	1.96	167.9	69.0	6.5		
TA_20	30	301	7.239E+06	107	2.573E+06	2.81	166.4	98.7	11.4		
Obogon											
OB_07	16	29	1.308E+06	110	4.960E+06	0.26	320.7	9.3	2.0	48.4	3.9
OB_16	18	60	2.405E+06	170	6.814E+06	0.35	440.6	12.5	1.9	51.0	3.8
OB_13	12	72	4.329E+06	165	9.921E+06	0.44	641.4	15.4	2.2	113.7	4.6

OB_14	15	42	2.020E+06	88	4.233E+06	0.48	273.7	16.9	3.2	28.2	3.7
OB_19	16	147	6.629E+06	302	1.362E+07	0.49	880.5	17.2	1.8	32.4	3.7
OB_21	15	60	2.886E+06	119	5.724E+06	0.50	370.1	17.8	2.9	54.6	4.2
OB_15	18	63	2.525E+06	122	4.890E+06	0.52	316.2	18.2	2.9	112.9	4.9
OB_17	12	108	6.494E+06	207	1.245E+07	0.52	804.7	18.4	2.2	36.0	3.8
OB_11	14	31	1.598E+06	59	3.041E+06	0.53	196.6	18.6	4.1		
OB_09	12	73	4.389E+06	130	7.816E+06	0.56	505.4	19.8	2.9	38.3	3.8
OB_22	12	74	4.449E+06	118	7.095E+06	0.63	458.7	22.1	3.3	47.9	3.9
OB_24	12	60	3.608E+06	81	4.870E+06	0.74	314.9	26.1	4.5		
OB_12	16	159	7.170E+06	212	9.560E+06	0.75	618.1	26.5	2.9	23.8	3.5
OB_26	10	44	3.175E+06	57	4.113E+06	0.77	265.9	27.2	5.5	59.7	4.0
OB_01	12	65	3.908E+06	74	4.449E+06	0.88	287.7	31.0	5.3		
OB_08	12	111	6.674E+06	88	5.291E+06	1.26	342.1	44.4	6.4	62.2	4.1
OB_03	8	66	5.952E+06	43	3.878E+06	1.53	250.7	54.0	10.7	795.0	12.2
OB_20	16	69	3.111E+06	36	1.623E+06	1.92	105.0	67.4	14.0	1331.0	17.0
OB_18	12	35	2.104E+06	18	1.082E+06	1.94	70.0	68.4	19.9	105.2	5.7
OB_23	20	114	4.113E+06	55	1.984E+06	2.07	128.3	72.9	12.1	91.5	5.0
OB_25	12	98	5.892E+06	39	2.345E+06	2.51	151.6	88.2	16.8		
OB_02	9	82	6.574E+06	30	2.405E+06	2.73	155.5	95.9	20.6		
OB_10	20	149	5.375E+06	51	1.840E+06	2.92	119.0	102.5	16.8	95.7	5.1
OB_04	6	92	1.106E+07	16	1.924E+06	5.75	124.4	200.2	54.4	1168.1	14.4
OB_06	*12*	*136*	*8.177E+06*	*36*	*2.165E+06*	*3.78*	*139.9*	*132.2*	*25.0*	*93.9*	*4.7*

Notes:

Ng* is the number of graticule square where 1 square = 1.386E-06 cm^2; Ns† is the number of counted spontaneous tracks;

ρs§ is the spontaneous track density ($x10^5$ tr/cm^2); Ni# is the number of counted induced tracks; ρi** is the induced track density ($x10^5$ tr/cm^2)

Ages were calculated using the zeta calibration method (Hurford and Green, 1983) and a zeta value of 255±8 yr/cm^2 (Fish Canyon Tuff zircon standard). Analyses in italics represent zircons in which the fission track age is older than the U-Pb crystallization age.

Table A4. LA-MC-ICPMS Lu-Hf analysis of single grain detrital zircon (NIGL)

Sample	^{176}Yb		^{176}Lu		$^{176}Hf/$		$^{206}Pb/^{238}U$ age				TDM	
Zircon ID	^{177}Hf	1σ%	^{177}Hf	1σ%	^{177}Hf	1σ%	(Ma)	1σ	εHf(t)	2σ	(Ma)	2σ
Pondaung 1												
Pond 1_70	0.0256	4.7	0.00055	3.2	0.282465	0.0289	58.6	2.0	-9.75	2.96	1059	109
Pond 1_12	0.0437	5.2	0.00089	3.6	0.282509	0.0227	65.0	1.7	-8.21	2.34	1009	87
Pond 1_69	0.0319	8.3	0.00064	6.0	0.282542	0.0255	71.4	1.8	-7.03	2.61	958	97
Pond 1_21	0.0409	6.9	0.00098	5.5	0.282937	0.0244	90.8	2.1	6.93	2.51	430	95
Pond 1_13	0.0365	4.8	0.00085	3.4	0.282942	0.0160	42.5	1.0	7.11	1.66	422	62
Pond 1_17	0.0397	4.8	0.00094	3.7	0.282987	0.0186	42.3	1.0	8.49	1.88	376	75
Pond 1_1	0.0203	9.1	0.00047	7.1	0.282991	0.0258	41.4	1.2	8.63	2.61	365	103
Pond 1_68	0.0745	4.8	0.00158	3.2	0.282998	0.0166	67.9	3.8	9.40	1.74	366	69
Pond 1_16	0.0681	4.7	0.00157	3.2	0.283033	0.0173	42.3	1.0	10.30	1.80	303	68
Pond 1_62	0.0357	5.0	0.00080	3.4	0.283044	0.0247	53.7	1.6	10.72	2.54	282	96
Pond 1_18	0.0412	8.9	0.00097	7.0	0.283054	0.0153	67.8	1.6	11.07	1.60	270	60
Pond 1_63	0.0385	5.3	0.00096	4.5	0.283035	0.0206	89.9	2.7	11.20	2.13	308	84
Pond 1_3	0.0410	4.7	0.00102	3.4	0.283060	0.0196	44.2	1.3	11.28	2.03	262	76
Pond 1_14	0.0299	4.7	0.00073	3.4	0.283072	0.0150	43.0	1.0	11.71	1.57	244	58
Pond 1_6	0.0264	5.1	0.00055	3.5	0.283074	0.0240	89.7	2.7	11.79	2.47	240	92
Pond 1_11	0.0149	4.8	0.00034	3.4	0.283060	0.0183	90.4	2.1	12.13	1.88	268	73
Pond 1_15	0.0291	4.8	0.00067	3.6	0.283087	0.0244	97.9	2.3	12.24	2.51	223	94
Pond 1_5	0.0405	4.8	0.00110	6.8	0.283106	0.0223	59.2	1.8	12.90	2.30	199	88
Pondaung 2												
Pond 2_11	0.0092	7.1	0.00032	8.9	0.282437	0.0069	41.4	0.9	-10.92	0.71	1089	27

Pond 2_23	0.0107	7.0	0.00041	8.9	0.282688	0.0064	42.1	1.0	-2.03	0.66	757	25
Pond 2_31	0.0212	7.2	0.00079	9.0	0.282759	0.0105	88.5	2.3	1.50	1.11	669	42
Pond 2_14	0.0193	7.4	0.00076	9.4	0.283004	0.0075	93.0	2.2	10.27	0.80	336	29
Pond 2_32	0.0099	7.1	0.00038	8.9	0.283014	0.0086	91.1	2.4	10.60	0.92	319	33
Pond 2_19	0.0138	7.2	0.00062	9.1	0.283016	0.0080	95.9	2.3	10.77	0.86	319	31
Pond 2_42	0.0140	7.2	0.00054	9.0	0.283057	0.0089	43.5	1.0	11.05	0.92	262	35
Pond 2_22	0.0329	7.0	0.00135	8.9	0.283044	0.0072	66.6	1.8	11.07	0.76	286	29
Pond 2_33	0.0483	7.1	0.00175	9.0	0.283069	0.0086	44.7	1.1	11.46	0.89	254	35
Pond 2_29	0.0331	7.0	0.00118	8.9	0.283068	0.0096	47.5	1.2	11.51	0.99	252	38
Pond 2_7	0.0389	7.0	0.00145	8.9	0.283072	0.0075	47.6	1.1	11.64	0.77	248	30
Pond 2_36	0.0256	7.0	0.00083	9.0	0.283072	0.0096	47.4	1.1	11.66	0.98	244	37
Pond 2_41	0.0418	7.7	0.00159	9.5	0.283068	0.0092	69.6	1.7	11.97	0.97	255	38
Pond 2_34	0.0395	9.7	0.00158	10.9	0.283095	0.0080	42.7	1.0	12.34	0.83	217	33
Pond 2_10	0.0250	7.0	0.00100	8.9	0.283073	0.0075	85.7	1.9	12.53	0.79	244	30
Pond 2_35	0.0058	7.1	0.00025	8.9	0.283072	0.0080	90.7	2.1	12.66	0.85	240	31
Pond 2_20	0.0538	8.1	0.00218	9.6	0.283091	0.0072	72.3	1.9	12.82	0.77	226	30
Pond 2_30	0.0187	9.3	0.00083	10.3	0.283126	0.0086	54.4	1.4	13.72	0.90	170	34
Pond 2_6	0.0148	8.3	0.00057	9.4	0.283114	0.0083	90.9	2.0	14.13	0.88	185	32
Padaung 3												
Pad 3_9	0.0254	6.1	0.00050	0.8	0.282694	0.0114	41.6	1.0	-1.82	1.16	750	43
Pad 3_13	0.0466	5.0	0.00102	3.6	0.282700	0.0163	27.6	1.4	-1.46	1.70	753	63
Pad 3_15	0.0779	5.1	0.00157	3.4	0.282710	0.0160	231.0	11.9	-1.12	1.66	751	63
Pad 3_6	0.0621	6.2	0.00124	2.0	0.282773	0.0126	53.1	1.3	1.21	1.29	657	49
Pad 3_5	0.0409	6.9	0.00073	3.2	0.282451	0.0117	634.3	14.5	2.88	1.51	1082	45
Pad 3_1	0.0390	6.4	0.00077	1.6	0.282967	0.0092	65.2	1.5	8.36	0.95	386	35
Pad 3_4	0.0403	6.5	0.00091	2.1	0.282983	0.0140	42.1	1.0	8.41	1.42	365	54
Pad 3_29	0.0680	5.4	0.00146	3.8	0.283016	0.0143	67.3	3.7	10.03	1.51	339	59
Pad 3_2	0.0361	6.3	0.00074	2.1	0.283003	0.0163	114.4	2.7	10.73	1.69	337	63
Pad 3_42	0.0341	4.9	0.00082	3.3	0.283065	0.0137	43.7	2.2	11.28	1.42	264	55

Pad 3_7	0.0214	6.8	0.00051	2.8	0.283037	0.0140	87.9	2.0	11.36	1.44	289	54
Padaung 1												
Pad 1_14	0.0305	6.1	0.00061	0.8	0.282301	0.0130	51.5	1.2	-15.50	1.32	1278	49
Pad 1_5	0.0412	6.1	0.00075	0.7	0.282429	0.0098	122.8	2.9	-9.39	1.04	1112	37
Pad 1_25	0.0931	7.8	0.00167	4.6	0.282578	0.0077	40.5	1.0	-5.98	0.80	934	32
Pad 1_15	0.0336	6.1	0.00066	1.4	0.282340	0.0098	452.1	10.7	-5.53	1.21	1277	39
Pad 1_17	0.0246	6.3	0.00049	1.8	0.282621	0.0095	44.9	1.1	-4.32	0.97	848	36
Pad 1_1	0.0270	6.2	0.00051	1.2	0.282285	0.0137	578.4	13.3	-4.17	1.67	1296	51
Pad 1_6	0.0145	6.1	0.00028	0.8	0.282653	0.0166	42.3	1.0	-3.24	1.69	801	63
Pad 1_16	0.0708	6.3	0.00142	2.2	0.282708	0.0110	57.9	1.3	-0.99	1.13	750	43
Pad 1_18	0.1021	6.3	0.00246	1.5	0.282796	0.0080	41.2	1.1	1.73	0.83	647	33
Pad 1_28	0.0434	6.8	0.00078	2.6	0.282820	0.0107	91.0	2.4	3.73	1.13	585	41
Pad 1_12	0.0543	6.1	0.00109	0.9	0.282928	0.0104	74.4	1.8	7.17	1.08	443	40
Pad 1_7	0.0663	6.6	0.00133	2.5	0.282996	0.0092	50.0	1.2	9.03	0.95	352	36
Pad 1_3	0.0361	6.2	0.00067	1.9	0.282991	0.0120	66.2	1.5	9.23	1.23	352	46
Pad 1_21	0.0671	6.1	0.00132	1.0	0.282987	0.0126	78.7	2.0	9.34	1.31	364	49
Pad 1_20	0.0314	6.8	0.00061	3.1	0.283017	0.0113	46.6	1.2	9.72	1.16	316	44
Pad 1_4	0.0209	6.1	0.00039	0.9	0.283011	0.0160	93.7	2.2	10.58	1.65	323	61
Pad 1_13	0.0620	6.2	0.00139	1.3	0.283066	0.0123	48.5	1.1	11.47	1.26	255	48
Pad 1_10	0.0264	7.6	0.00062	3.2	0.283045	0.0120	95.5	2.2	11.80	1.25	279	46
Pad 1_9	0.0643	6.8	0.00153	3.0	0.283069	0.0130	71.4	1.6	12.07	1.33	252	51
Pad 1_22	0.0551	6.3	0.00111	1.3	0.283086	0.0092	97.4	2.3	13.26	0.97	226	36
Pad 1_23	0.0306	6.5	0.00060	1.9	0.283108	0.0101	102.7	2.5	14.20	1.07	193	39
Pad 1_26*	0.0593	15.5	0.00131	13.7	0.282836	0.0101	965.9	16.0	22.82	1.47	595	44
Shwetaung												
Shw_37	0.0287	5.1	0.00060	4.7	0.281738	0.0154	797.0	12.9	-35.44	1.60	2022	58
Shw_40	0.0376	5.9	0.00087	4.2	0.282245	0.0199	60.7	1.0	-17.52	2.05	1362	76
Shw_48*	0.0219	5.0	0.00044	4.0	0.281735	0.0157	1089.9	14.7	-12.93	1.90	2099	61

Shw_39	0.0052	5.5	0.00012	4.5	0.282415	0.0170	50.1	1.3	-11.48	1.76	1112	63
Shw_42	0.0717	7.0	0.00198	4.0	0.282422	0.0153	447.0	11.2	-11.32	1.60	1159	62
Shw_47	0.0581	7.2	0.00119	5.9	0.282537	0.0166	122.0	2.5	-7.20	1.73	978	66
Shw_22	0.0283	8.0	0.00107	5.3	0.282516	0.0080	122.1	2.7	-6.37	0.87	1004	32
Shw_5	0.0799	9.0	0.00267	6.3	0.282678	0.0078	21.4	0.5	-2.88	0.80	819	35
Shw_26	0.0141	8.4	0.00071	7.3	0.282769	0.0085	38.6	0.9	0.75	0.87	654	33
Shw_41	0.0316	7.7	0.00082	4.9	0.282846	0.0195	46.7	0.9	3.63	1.97	573	79
Shw_46	0.0305	5.5	0.00072	4.4	0.282936	0.0154	81.5	1.7	6.93	1.61	427	59
Shw_38	0.0415	5.1	0.00121	4.3	0.282960	0.0156	109.2	2.7	7.73	1.63	401	61
Shw_45	0.0599	5.0	0.00143	4.5	0.283006	0.0163	18.2	0.3	9.38	1.70	339	65
Shw_36	0.0295	5.6	0.00067	4.4	0.283094	0.0202	111.5	2.1	12.52	2.09	212	78
Shw_34	0.0192	5.6	0.00048	4.1	0.283121	0.0154	94.5	2.0	13.48	1.61	175	59
Shw_17	0.0305	8.2	0.00121	5.5	0.283104	0.0089	86.4	1.9	13.64	0.94	202	35
Shw_43	0.0326	4.9	0.00075	4.0	0.283141	0.0150	104.6	2.2	14.15	1.57	150	58
Taungtalon												
Ta_30*	0.0190	5.0	0.00036	3.9	0.281517	0.0139	1255.3	15.3	-16.91	1.74	2389	54
Ta_25	0.0825	6.1	0.00165	4.9	0.282328	0.0133	62.1	1.2	-14.61	1.39	1277	54
Ta_37	0.0902	5.3	0.00170	4.7	0.282338	0.0182	53.9	0.9	-14.26	1.89	1265	73
Ta_16	0.0265	8.0	0.00079	5.4	0.282355	0.0099	34.4	0.8	-14.02	1.01	1261	41
Ta_36	0.0401	4.9	0.00080	3.9	0.282344	0.0145	32.2	0.8	-14.01	1.51	1227	56
Ta_43	0.0442	4.9	0.00080	4.2	0.282380	0.0225	150.3	3.0	-12.74	2.32	1179	86
Ta_44	0.0297	4.8	0.00058	4.0	0.282385	0.0166	119.2	2.5	-12.56	1.73	1165	63
Ta_19	0.0094	8.2	0.00032	5.5	0.282403	0.0094	77.7	5.0	-11.30	1.05	1134	36
Ta_31	0.0400	10.3	0.00100	8.2	0.282433	0.0133	107.1	2.4	-10.87	1.39	1113	53
Ta_27	0.0520	4.8	0.00106	4.0	0.282451	0.0170	46.7	1.0	-10.24	1.76	1091	66
Ta_11	0.0391	7.3	0.00128	9.0	0.282480	0.0122	45.8	1.0	-9.33	1.24	1059	50
Ta_15	0.0488	8.0	0.00165	5.4	0.282491	0.0122	64.9	1.4	-8.54	1.25	1054	50
Ta_21	0.0384	8.0	0.00133	5.3	0.282519	0.0082	34.9	0.8	-8.19	0.84	1007	34
Ta_8	0.0151	7.0	0.00059	8.9	0.282501	0.0083	67.7	1.6	-8.08	0.87	1012	33

Ta_41	0.0505	5.0	0.00087	4.4	0.282517	0.0173	29.7	0.6	-7.90	1.79	997	67
Ta_26	0.0199	4.8	0.00039	4.0	0.282560	0.0238	36.3	0.7	-6.36	2.45	927	90
Ta_42	0.0149	5.1	0.00030	4.0	0.282583	0.0136	42.0	0.8	-5.54	1.42	894	51
Ta_14	0.0306	7.2	0.00113	9.1	0.282601	0.0075	52.8	1.2	-4.90	0.78	890	31
Ta_39	0.0331	5.8	0.00073	4.8	0.282619	0.0286	68.1	1.2	-4.28	2.93	856	109
Ta_6	0.0141	8.0	0.00051	9.4	0.282638	0.0131	41.4	1.0	-3.82	1.34	826	51
Ta_13	0.0729	7.2	0.00292	9.2	0.282673	0.0096	70.1	1.7	-2.05	1.00	832	45
Ta_20	0.0235	10.4	0.00086	7.5	0.282771	0.0097	32.3	0.7	0.67	0.98	654	38
Ta_2r	0.0257	7.1	0.00112	8.9	0.282822	0.0089	29.7	0.7	2.41	0.91	589	36
Ta_2c	0.0415	7.4	0.00166	9.1	0.282881	0.0096	78.5	1.8	5.55	1.00	515	40
Ta_35	0.1096	6.3	0.00250	6.3	0.282993	0.0192	167.9	3.0	8.88	1.99	367	79
Ta_33	0.0710	4.8	0.00159	4.1	0.282999	0.0169	58.9	1.9	9.13	1.76	350	67
Ta_24	0.0445	4.8	0.00105	3.9	0.283018	0.0195	67.0	1.3	9.82	2.02	319	76
Ta_38	0.0485	5.9	0.00106	4.8	0.283022	0.0211	55.6	1.1	9.96	2.18	313	83
Ta_22	0.0556	8.0	0.00270	5.4	0.283024	0.0125	56.4	1.3	10.09	1.28	326	52
Ta_12	0.0348	7.4	0.00132	9.0	0.283018	0.0089	64.1	1.5	10.10	0.93	322	36
Ta_40	0.0354	5.2	0.00086	4.3	0.283030	0.0163	109.3	2.0	10.25	1.70	301	63
Ta_28	0.0261	4.9	0.00056	4.2	0.283051	0.0166	68.3	1.2	11.00	1.73	270	64
Ta_9	0.0342	7.0	0.00130	9.0	0.283089	0.0080	66.1	1.6	12.65	0.84	224	32
Ta_29	0.0329	7.3	0.00065	6.0	0.283133	0.0163	101.8	2.0	13.90	1.70	159	63
Ta_23	0.0160	8.1	0.00065	5.3	0.283111	0.0092	106.4	2.4	14.27	0.97	197	37
Ta_3	0.0160	8.0	0.00059	5.3	0.283168	0.0094	103.6	2.3	16.23	0.99	116	38
Ta_17	0.0260	8.1	0.00102	5.3	0.283151	0.0097	167.9	4.1	17.12	1.07	137	38
Lower Moza												
LM_16	0.0338	8.3	0.00107	5.6	0.282513	0.0089	55.7	1.2	-7.94	0.92	1008	36
LM_8	0.0442	8.7	0.00142	6.2	0.282635	0.0113	53.5	1.3	-3.69	1.16	851	46
LM_5	0.0488	9.2	0.00170	6.0	0.283068	0.0134	78.1	1.7	12.15	1.38	255	54
Obogon												

Obo_24	0.0159	16.1	0.00061	7.0	0.282292	0.0107	48.2	1.5	-15.92	1.09	1291	42
Obo_4	0.0310	8.0	0.00103	5.3	0.282380	0.0116	53.3	1.3	-12.69	1.19	1186	46
Obo_37	0.0636	16.2	0.00241	7.5	0.282383	0.0092	60.9	2.3	-12.49	0.97	1228	43
Obo_18	0.0390	16.3	0.00134	7.3	0.282416	0.0089	56.3	1.3	-11.38	0.91	1148	37
Obo_33	0.0257	16.1	0.00096	7.0	0.282382	0.0078	163.6	4.3	-10.19	0.85	1182	32
Obo_29	0.0511	16.1	0.00181	7.1	0.282424	0.0104	131.2	3.2	-9.50	1.09	1151	44
Obo_28	0.0354	16.2	0.00146	7.0	0.282327	0.0073	398.7	13.0	-7.05	0.99	1273	32
Obo_2	0.1036	8.1	0.00363	5.5	0.282622	0.0094	52.6	1.3	-4.24	0.97	923	44
Obo_34	0.0214	16.0	0.00076	6.9	0.282625	0.0086	46.6	1.0	-4.18	0.87	849	34
Obo_30	0.0525	16.2	0.00176	7.0	0.282222	0.0104	707.7	19.2	-4.10	1.37	1427	45
Obo_17	0.0345	9.0	0.00165	7.7	0.282692	0.0163	31.1	0.7	-2.16	1.64	777	66
Obo_32	0.0360	16.1	0.00167	7.6	0.282686	0.0076	71.4	1.7	-1.51	0.78	786	32
Obo_3	0.0365	11.7	0.00122	9.0	0.282700	0.0089	55.8	1.3	-1.33	0.93	757	37
Obo_36	0.0262	16.1	0.00100	7.9	0.282311	0.0107	723.5	19.0	-0.23	1.37	1279	43
Obo_11	0.0702	8.5	0.00274	7.7	0.282715	0.0122	99.7	2.4	0.06	1.28	768	54
Obo_25	0.0685	16.5	0.00243	8.1	0.282711	0.0104	117.2	2.6	0.30	1.08	767	46
Obo_35	0.0188	16.1	0.00066	6.9	0.282370	0.0129	689.9	15.1	1.27	1.42	1189	50
Obo_19	0.0519	16.4	0.00193	7.4	0.282811	0.0095	50.2	1.4	2.44	0.97	617	40
Obo_8	0.0175	8.3	0.00069	5.6	0.282845	0.0097	48.2	1.1	3.61	1.00	551	38
Obo_9	0.0227	8.1	0.00108	5.4	0.282984	0.0102	168.5	3.8	11.21	1.11	366	40
Obo_27	0.0203	16.1	0.00085	7.0	0.283051	0.0100	82.9	1.7	11.70	1.02	273	39
Obo_26	0.0342	16.5	0.00155	7.4	0.283069	0.0100	68.2	1.9	11.97	1.04	253	40
Obo_31	0.0264	16.3	0.00125	7.3	0.283078	0.0110	59.7	1.4	12.12	1.12	239	44
Obo_22	0.0257	16.0	0.00093	7.0	0.283112	0.0098	98.1	2.2	14.19	1.01	190	38

* $^{207}Pb/^{235}U$ age used

$\lambda Lu = 1.867 \times 10^{-11}$ yr-1 $\pm 8.0 \times 10^{-14}$, 2σ (Söderlund et al., 2004)

$\varepsilon Hf(t) = [(176Hf/177Hf)t\ sample / (176Hf/177Hf)t\ CHUR -1] \times 10^4$

$\varepsilon Hf(t) = ([((176Hf/177Hf)meas - (176Lu/177Hf)meas \times e^{\lambda T} -1))/((176Hf/177Hf)CHUR - (176Lu/177Hf)CHUR \times (e^{\lambda T} -1)) -1) \times 10^4$

$(176Lu/177Hf)CHUR,0 = 0.0332 \pm 2$ (Blichert-Toft and Albarede, 1997)

$(176Hf/177Hf)CHUR,0 = 0.282772 \pm 29$ (Blichert-Toft and Albarede, 1997)

$(176Lu/177Hf)DM = 0.0384$ (Blichert-Toft and Albarede, 1997)

$(176Hf/177Hf)DM = 0.28325$ (Griffin and others, 2000)

Table A5. Lu-Hf analysis of double dated (U-Pb, fission track) single grain detrital zircon (BIL)

Sample/ Grain	FT age (Ma)	error	U-Pb Age (Ma)	±1σ	ICPMS Lu/Hf ANALYSIS (JMC 475 corr) εHf_T	± 2σ	$^{176}Hf/^{177}Hf$	± 2σ	$^{176}Lu/^{177}Hf$	± 1σ	$^{176}Yb/^{177}Hf$	CHUR $^{176}Hf/^{177}Hf_T$
Pondaung 1												
Pond01_03	101.5	15.9	225.2	3.6	10.3	0.8	0.282939	0.000023	0.001044	0.000057	0.039275	0.282643
Pond01_04	66.5	8.8	79.5	1.6	11.6	0.7	0.283063	0.000021	0.000474	0.000014	0.014466	0.282735
Pond01_05	35.0	3.3	47.7	0.9	-2.1	0.7	0.282698	0.000020	0.001290	0.000049	0.050544	0.282755
Pond01_09	30.9	3.7	54.8	2.0	12.4	0.9	0.283102	0.000026	0.000830	0.000022	0.033855	0.282751
Pond01_10	24.1	4.7	35.0	1.2	9.4	1.0	0.283028	0.000029	0.000644	0.000004	0.021259	0.282763
Pond01_11	25.2	3.5	54.9	1.2	11.6	1.0	0.283080	0.000027	0.001445	0.000043	0.054801	0.282751
Pond01_13	41.4	6.0	83.3	1.9	12.6	0.8	0.283091	0.000022	0.000538	0.000003	0.019728	0.282733
Pond01_15	32.9	4.1	39.9	0.8	9.5	0.8	0.283030	0.000022	0.001005	0.000026	0.032340	0.282760
Pond01_18	21.7	5.3	44.8	1.8	12.4	0.9	0.283110	0.000025	0.000793	0.000013	0.028125	0.282757
Pond01_21	39.0	5.2	85.7	1.3	10.8	0.7	0.283038	0.000020	0.001169	0.000032	0.038089	0.282731
Pond01_23	60.4	10.5	61.8	1.4	10.8	0.9	0.283054	0.000025	0.001203	0.000033	0.039118	0.282746
Pond01_24	35.1	3.8	61.9	1.2	10.9	0.6	0.283056	0.000018	0.000621	0.000036	0.023044	0.282746
Pond01_27	23.4	2.2	90.3	1.4	-9.9	0.7	0.282451	0.000020	0.001562	0.000025	0.058494	0.282728
Pond01_28	77.7	15.3	86.0	2.4	11.2	0.7	0.283049	0.000020	0.000621	0.000019	0.022830	0.282731
Pond01_30	38.6	4.7	53.3	1.5	9.6	0.7	0.283024	0.000019	0.000494	0.000009	0.018872	0.282752
Pond01_31	56.4	7.6	78.2	1.5	9.3	0.9	0.282999	0.000025	0.000811	0.000006	0.032775	0.282736
Pond01_32	49.8	6.9	51.0	1.5	12.5	1.2	0.283107	0.000034	0.000473	0.000005	0.016751	0.282753
Pond01_33	37.1	5.4	55.2	1.2	10.0	0.9	0.283034	0.000026	0.000668	0.000015	0.024283	0.282750
Pond01_34	30.3	4.9	37.3	1.0	11.0	0.6	0.283074	0.000018	0.000927	0.000013	0.030133	0.282762
Pond01_37	208.7	41.5	1319.0	15.5	-1.7	1.1	0.281929	0.000031	0.001232	0.000020	0.051698	0.281947

Pond01_40	20.0	4.3	48.7	1.8	11.9	0.9	0.283091	0.000025	0.000842	0.000009	0.030266	0.282754
Pond01_42	16.9	2.3	69.6	1.4	-6.7	0.9	0.282554	0.000026	0.000566	0.000009	0.022928	0.282741
Pond01_43	45.0	6.9	54.6	1.2	10.9	0.7	0.283060	0.000020	0.000826	0.000029	0.031374	0.282751
Pond01_44	26.1	3.2	41.8	0.7	9.6	0.8	0.283031	0.000023	0.000979	0.000026	0.033339	0.282759
Pond01_45	35.3	5.9	65.4	1.6	11.1	1.1	0.283058	0.000030	0.000587	0.000025	0.020540	0.282744
Pond01_46	32.9	6.2	82.6	2.1	10.9	0.9	0.283043	0.000026	0.000583	0.000005	0.023414	0.282733
Pond01_47	34.3	5.7	75.7	1.8	10.8	0.8	0.283043	0.000022	0.000493	0.000011	0.019114	0.282737
Pond01_48	22.3	3.8	583.2	6.6	1.2	1.1	0.282458	0.000032	0.000792	0.000004	0.034231	0.282417
Pond01_06	313.3	54.8	52.2	1.4	11.0	0.7	0.283064	0.000020	0.000793	0.000002	0.032647	0.282752
Pond01_16	81.4	12.7	58.2	1.4	11.8	0.8	0.283083	0.000023	0.001954	0.000125	0.060235	0.282748
Pond01_25	83.3	15.3	61.4	1.3	11.8	0.7	0.283081	0.000020	0.001386	0.000048	0.047881	0.282746
Pondaung 2												
Pond02_03			69.0	4.1	12.3	1.0	0.000027	0.000014	0.001138	0.000015	0.031390	0.282742
Pond02_04	52.1	8.0	83.8	3.6	9.6	0.9	0.000025	0.000013	0.001008	0.000025	0.028106	0.282732
Pond02_08	30.3	4.5	71.4	4.2	13.6	0.8	0.000022	0.000011	0.000915	0.000007	0.030654	0.282740
Pond02_09	34.9	5.4	63.0	3.8	11.4	0.9	0.000027	0.000013	0.000407	0.000001	0.012806	0.282745
Pond02_10	28.2	3.9	64.8	3.6	10.6	0.9	0.000025	0.000012	0.000955	0.000026	0.031478	0.282744
Pond02_11	23.0	2.5	51.1	2.7	11.9	1.1	0.000031	0.000015	0.006715	0.000248	0.196685	0.282753
Pond02_12	34.1	4.6	41.6	2.7	10.0	0.8	0.000024	0.000012	0.001077	0.000006	0.034674	0.282759
Pond02_13	24.9	4.2	45.3	3.1	10.3	0.9	0.000024	0.000012	0.000800	0.000008	0.026304	0.282757
Pond02_14	23.2	3.0	65.2	3.7	11.0	0.8	0.000023	0.000011	0.000373	0.000010	0.011428	0.282744
Pond02_15	26.2	2.8	40.7	2.9	-4.2	1.0	0.000029	0.000014	0.000375	0.000002	0.012573	0.282759
Pond02_16	34.4	7.9	46.1	4.1	12.7	1.0	0.000029	0.000014	0.000489	0.000002	0.014795	0.282756
Pond02_17	34.2	3.8	44.3	2.9	10.9	0.9	0.000025	0.000012	0.000627	0.000013	0.016802	0.282757
Pond02_18	38.2	4.5	93.2	3.3	9.7	1.2	0.000034	0.000017	0.000904	0.000013	0.023932	0.282726
Pond02_19	57.6	7.0	68.7	4.3	10.6	0.8	0.000023	0.000012	0.000454	0.000004	0.012379	0.282742
Pond02_21	32.8	3.8	92.9	3.8	11.8	0.7	0.000021	0.000010	0.000383	0.000002	0.011457	0.282727
Pond02_22	34.4	4.4	49.8	4.0	10.9	0.9	0.000025	0.000013	0.000806	0.000003	0.025721	0.282754
Pond02_23	45.8	4.5	66.3	3.5	11.1	0.8	0.000024	0.000012	0.000879	0.000010	0.026953	0.282743

Pond02_24	35.7	5.4	74.9	3.6	11.0	0.8	0.000023	0.000011	0.000744	0.000011	0.017665	0.282738
Pond02_25	135.7	16.3	194.8	6.0	15.0	0.8	0.000023	0.000011	0.000588	0.000022	0.017822	0.282663
Pond02_26	77.7	11.3	76.8	4.1	10.8	0.9	0.000026	0.000013	0.000946	0.000028	0.028059	0.282737
Pond02_27	54.6	9.1	91.7	4.4	10.1	0.9	0.000027	0.000013	0.000488	0.000017	0.013965	0.282727
Pond02_28	32.2	3.6	37.0	2.7	-2.6	0.9	0.000024	0.000012	0.000242	0.000000	0.007851	0.282762
Pond02_29	30.7	4.2	71.7	4.1	12.2	0.8	0.000022	0.000011	0.000954	0.000018	0.030596	0.282740
Pond02_31	22.2	1.8	42.5	2.9	-5.0	0.7	0.000019	0.000010	0.000273	0.000000	0.008697	0.282758
Pond02_32	46.3	10.4	58.5	4.1	11.5	0.6	0.000018	0.000009	0.000648	0.000006	0.015648	0.282748
Pond02_33	36.7	7.4	59.2	3.8	11.7	0.9	0.000024	0.000012	0.000524	0.000002	0.016721	0.282748
Pond02_34	32.9	3.5	44.3	3.1	10.5	1.0	0.000028	0.000014	0.000851	0.000011	0.026274	0.282757
Pond02_35	67.1	7.1	78.4	3.4	12.6	0.8	0.000023	0.000011	0.000726	0.000005	0.019209	0.282736
Pond02_36	14.0	1.6	41.4	2.8	-4.9	1.0	0.000029	0.000014	0.000254	0.000003	0.007930	0.282759
Pond02_37	10.8	1.2	132.1	4.5	12.8	1.1	0.000031	0.000015	0.000658	0.000007	0.021832	0.282702
Pond02_39	26.7	3.0	90.5	4.0	10.5	0.9	0.000024	0.000012	0.000324	0.000001	0.010263	0.282728
Pond02_40	22.3	3.1	47.5	3.5	11.4	0.9	0.000024	0.000012	0.000766	0.000009	0.023296	0.282755
Pond02_38	–	–	138.8	5.3	9.4	1.0	0.000027	0.000014	0.000709	0.000006	0.024681	0.282698
Padaung 3												
Pad03_4	33.4	6.3	58.3	2.1	12.4	0.8	0.000022	0.000011	0.001101	0.000009	0.034758	0.282748
Pad03_10	17.4	3.8	40.1	1.9	10.3	0.8	0.000023	0.000012	0.000737	0.000033	0.023739	0.282760
Pad03_11	51.8	11.3	114.4	2.9	13.2	0.8	0.000022	0.000011	0.000757	0.000016	0.027062	0.282713
Pad03_12	22.2	4.6	52.3	1.9	13.0	0.9	0.000025	0.000012	0.000909	0.000024	0.026546	0.282752
Pad03_13	23.7	4.4	60.0	2.4	9.9	0.7	0.000020	0.000010	0.000441	0.000020	0.016061	0.282747
Pad03_14	31.1	4.6	46.9	1.8	3.5	0.8	0.000023	0.000012	0.003017	0.000095	0.098722	0.282756
Pad03_16	83.2	16.2	86.7	2.9	11.8	0.9	0.000026	0.000013	0.000628	0.000011	0.019128	0.282731
Pad03_20	28.9	6.9	57.7	1.9	10.9	0.8	0.000022	0.000011	0.000657	0.000004	0.023262	0.282749
Pad03_22	32.1	7.0	53.4	2.3	8.6	0.7	0.000019	0.000009	0.000448	0.000013	0.015978	0.282751
Pad03_21	–	–	56.5	1.9	7.9	0.8	0.000024	0.000012	0.001325	0.000091	0.047335	0.282750
Pad03_2	148.7	25.5	97.4	3.1	7.8	0.8	0.000022	0.000011	0.000498	0.000021	0.017655	0.282724
Pad03_7	93.2	15.3	72.0	2.9	10.6	0.6	0.000017	0.000009	0.000366	0.000003	0.010869	0.282740

Pad03_9	155.8	20.4	77.0	1.9	10.8	0.6	0.000016	0.000008	0.000767	0.000006	0.024807	0.282737
Pad03_5	*71.4*	*11.0*	*3072.6*	*10.1*	*79.0*	*0.6*	*0.000017*	*0.000009*	*0.000486*	*0.000015*	*0.015616*	0.280801
Pad03_6	*34.1*	*5.2*	*86.7*	*2.1*	*-62.1*	*0.7*	*0.000021*	*0.000010*	*0.000766*	*0.000003*	*0.027909*	0.282731
Pad03_8	*45.1*	*10.7*	*2755.7*	*13.9*	*49.3*	*0.8*	*0.000022*	*0.000011*	*0.000942*	*0.000015*	*0.041731*	0.281011
Pad03_1	*28.9*	*4.2*	*1786.1*	*9.8*	*42.3*	*0.9*	*0.000025*	*0.000012*	*0.001028*	*0.000032*	*0.039829*	0.281646
Pad03_3	*39.5*	*8.6*	*608.3*	*8.0*	*-55.2*	*0.7*	*0.000019*	*0.000010*	*0.000706*	*0.000017*	*0.024705*	0.282401
Pad03_17	*30.5*	*7.4*	*58.7*	*2.4*	*-44.4*	*0.9*	*0.000027*	*0.000013*	*0.000787*	*0.000030*	*0.025230*	0.282748
Pad03_18	*35.3*	*10.4*	*55.8*	*2.3*	*-39.9*	*0.7*	*0.000019*	*0.000009*	*0.000815*	*0.000005*	*0.029409*	0.282750
Pad03_19	*29.5*	*4.8*	*1829.0*	*12.6*	*52.0*	*1.1*	*0.000031*	*0.000015*	*0.001120*	*0.000004*	*0.041549*	0.281618
Pad03_15	–	–	*2800.4*	*10.0*	*72.7*	*0.8*	*0.000024*	*0.000012*	*0.000819*	*0.000006*	*0.025902*	0.280982
Shwetaung												
SHW_17	15.8	2.5	31.8	0.4	-0.8	0.6	0.282744	0.000018	0.001653	0.000090	0.053736	0.282765
SHW_03	20.3	3.1	35.5	0.4	-15.0	0.9	0.282339	0.000026	0.000937	0.000047	0.030155	0.282763
SHW_18	43.2	5.4	38.1	0.6	-0.9	0.7	0.282736	0.000021	0.000581	0.000005	0.016329	0.282761
SHW_16	21.1	3.6	44.4	0.7	-6.5	1.1	0.282574	0.000032	0.001671	0.000047	0.058719	0.282757
SHW_05	72.2	20.3	175.3	3.5	16.0	0.7	0.283137	0.000021	0.002552	0.000019	0.070400	0.282675
SHW_15	27.0	2.2	228.0	2.7	-5.3	1.0	0.282495	0.000028	0.000757	0.000015	0.023325	0.282642
SHW_06	25.1	4.4	995.0	10.9	0.4	0.7	0.282190	0.000020	0.001224	0.000050	0.041525	0.282155
SHW_19	*21.1*	*4.6*	*39.7*	*1.0*	*-65.2*	*0.8*	*0.280917*	*0.000023*	*0.000930*	*0.000014*	*0.032406*	0.282760
Taungtalon												
TA_17	26.8	2.4	34.5	2.2	1.7	0.8	0.282812	0.000023	0.002034	0.000012	0.070024	0.282763
TA201_14	38.5	6.2	37.6	2.0	-8.1	0.8	0.282532	0.000023	0.000439	0.000002	0.015417	0.282761
TA_12	24.6	2.6	38.8	1.7	-10.4	0.7	0.282467	0.000021	0.000190	0.000002	0.007667	0.282761
TA201_11	23.9	4.7	43.8	1.5	-5.5	0.9	0.282603	0.000027	0.000943	0.000010	0.031772	0.282758
TA_31	23.5	5.0	45.5	1.8	9.3	0.9	0.283019	0.000026	0.000648	0.000017	0.020065	0.282756
TA_09	31.7	3.8	46.2	2.3	11.0	0.9	0.283069	0.000024	0.001071	0.000180	0.034805	0.282756
TA_21	32.6	4.0	47.2	1.8	-9.5	0.7	0.282487	0.000020	0.000758	0.000003	0.027514	0.282755
TA201_20	14.2	2.3	47.9	1.2	-8.2	0.9	0.282524	0.000024	0.000803	0.000020	0.027802	0.282755

TA_08	14.8	3.9	50.3	0.6	12.7	0.8	0.283114	0.000024	0.001012	0.000008	0.038036	0.282753
TA_30	31.5	4.4	52.4	2.7	-5.9	0.8	0.282587	0.000023	0.000884	0.000006	0.033775	0.282752
TA_05	31.2	5.0	53.0	2.8	-11.8	0.9	0.282418	0.000024	0.000410	0.000004	0.016329	0.282752
TA_10	12.4	2.4	54.6	2.1	-7.3	1.0	0.282544	0.000027	0.000940	0.000025	0.034018	0.282751
TA_06	18.1	3.0	55.0	2.4	6.6	1.2	0.282940	0.000035	0.001354	0.000028	0.048845	0.282750
TA201_17	23.9	3.0	55.5	1.0	-12.1	0.8	0.282409	0.000021	0.001434	0.000022	0.045730	0.282750
TA201_15	25.3	2.7	57.8	0.6	-4.8	0.8	0.282613	0.000023	0.001001	0.000034	0.030104	0.282749
TA_11	18.3	3.0	58.7	2.8	11.7	0.8	0.283080	0.000022	0.000507	0.000003	0.015647	0.282748
TA201_04	36.1	4.7	60.2	1.1	-12.1	0.7	0.282407	0.000020	0.000736	0.000015	0.027342	0.282747
TA_14	14.7	2.7	62.2	2.1	-4.6	0.7	0.282618	0.000020	0.000657	0.000005	0.027005	0.282746
TA_18	33.2	5.2	62.8	2.4	10.5	0.8	0.283043	0.000024	0.000483	0.000021	0.014562	0.282746
TA201_19	24.3	4.1	63.8	1.6	12.7	0.8	0.283104	0.000023	0.000944	0.000010	0.029453	0.282745
TA_04	24.4	6.1	65.8	1.8	12.6	0.9	0.283100	0.000026	0.001067	0.000027	0.034973	0.282744
TA_01	20.0	1.5	66.2	2.7	10.4	0.8	0.283038	0.000022	0.000865	0.000034	0.030107	0.282743
TA201_22	22.6	3.7	67.1	1.5	8.7	0.8	0.282989	0.000022	0.000960	0.000054	0.028164	0.282743
TA201_16	36.1	8.0	67.3	1.3	11.9	0.7	0.283079	0.000019	0.000885	0.000012	0.032142	0.282743
TA_22	59.2	7.6	69.7	1.8	11.2	0.6	0.283060	0.000016	0.000894	0.000020	0.026893	0.282741
TA_16	35.3	4.3	70.0	3.6	-9.6	1.0	0.282471	0.000029	0.000490	0.000022	0.019428	0.282741
TA_02	19.3	3.0	70.8	6.7	-6.4	0.9	0.282560	0.000026	0.000830	0.000005	0.033610	0.282741
TA201_18	20.6	5.7	72.2	1.1	12.6	0.9	0.283096	0.000025	0.001045	0.000008	0.036985	0.282740
TA_15	26.6	2.7	74.6	5.3	-6.8	0.7	0.282547	0.000021	0.000532	0.000029	0.019541	0.282738
TA_33	9.0	2.7	78.2	4.1	-10.5	0.6	0.282439	0.000016	0.000395	0.000002	0.014233	0.282736
TA_23	62.4	5.3	85.2	1.3	11.9	0.9	0.283069	0.000024	0.000662	0.000011	0.018214	0.282732
TA201_10	22.3	3.9	87.5	2.2	11.5	1.0	0.283057	0.000027	0.000858	0.000057	0.029662	0.282730
TA201_07	39.3	7.6	87.7	0.5	13.1	0.6	0.283101	0.000018	0.000720	0.000007	0.023888	0.282730
TA_27	18.9	6.1	95.7	2.3	-7.8	0.9	0.282506	0.000025	0.000364	0.000005	0.013408	0.282725
TA_34	33.8	9.9	96.2	4.0	13.8	0.9	0.283115	0.000025	0.000320	0.000003	0.010981	0.282725
TA_13	23.1	3.9	105.1	1.8	14.3	0.7	0.283125	0.000021	0.000439	0.000003	0.016139	0.282719
TA_32	35.3	4.5	121.3	2.7	14.8	0.8	0.283127	0.000024	0.000590	0.000017	0.021655	0.282709
TA_26	20.1	4.0	167.0	0.7	15.6	0.8	0.283129	0.000024	0.002142	0.000031	0.062941	0.282680

TA_29	35.3	5.4	489.9	1.3	-1.3	0.7	0.282452	0.000021	0.001394	0.000024	0.045189	0.282476
TA_07	30.3	3.4	534.9	1.9	-17.9	0.7	0.281946	0.000021	0.000449	0.000016	0.019072	0.282448
TA_03	19.0	2.5	962.3	45.0	-2.2	0.8	0.282132	0.000022	0.000985	0.000048	0.041229	0.282176
TA_19	16.8	1.8	31.3	5.7	2.4	0.8	0.282833	0.000024	0.000725	0.000015	0.026017	0.282765
TA201_21	52.2	7.6	47.2	1.8	13.4	0.7	0.283135	0.000020	0.000643	0.000004	0.020098	0.282755
Obogon												
OB_03	54.0	10.7	795.0	12.2	2.4	1.0	0.282361	0.000029	0.000814	0.000023	0.025080	0.282283
OB_04	200.2	54.4	1168.1	14.4	-14.4	0.9	0.281649	0.000025	0.000557	0.000027	0.021659	0.282044
OB_07	9.3	2.0	48.4	3.9	-15.3	0.9	0.282323	0.000024	0.001030	0.000021	0.043216	0.282755
OB_08	44.4	6.4	62.2	4.1	9.9	0.7	0.283028	0.000019	0.000994	0.000021	0.032992	0.282746
OB_09	19.8	2.9	38.3	3.8	-8.8	0.7	0.282514	0.000018	0.000379	0.000003	0.011872	0.282761
OB_10	102.5	16.8	95.7	5.1	14.5	0.9	0.283137	0.000024	0.001257	0.000056	0.044320	0.282725
OB_12	26.5	2.9	23.8	3.5	-26.1	0.7	0.282032	0.000021	0.000508	0.000037	0.018447	0.282770
OB_13	15.4	2.2	113.7	4.6	-4.4	0.8	0.282592	0.000023	0.001657	0.000043	0.055869	0.282714
OB_14	16.9	3.2	28.2	3.7	-6.8	0.8	0.282577	0.000022	0.001046	0.000017	0.036544	0.282767
OB_15	18.2	2.9	112.9	4.9	-8.2	0.9	0.282484	0.000024	0.001002	0.000028	0.034060	0.282714
OB_16	12.5	1.9	51.0	3.8	-8.6	0.8	0.282511	0.000021	0.001229	0.000041	0.044215	0.282753
OB_17	18.4	2.2	36.0	3.8	-13.8	0.7	0.282372	0.000020	0.000297	0.000004	0.010834	0.282762
OB_18	68.4	19.9	105.2	5.7	15.2	0.7	0.283149	0.000019	0.000750	0.000018	0.025343	0.282719
OB_19	17.2	1.8	32.4	3.7	-12.3	0.6	0.282416	0.000016	0.000114	0.000002	0.003901	0.282765
OB_21	17.8	2.9	54.6	4.2	-11.1	0.7	0.282438	0.000021	0.000662	0.000005	0.024545	0.282751
OB_22	22.1	3.3	47.9	3.9	-8.4	0.9	0.282518	0.000025	0.001207	0.000039	0.038415	0.282755
OB_23	72.9	12.1	91.5	5.0	13.9	0.6	0.283122	0.000016	0.000336	0.000006	0.010562	0.282728
OB_26	27.2	5.5	59.7	4.0	11.2	0.6	0.283065	0.000016	0.000432	0.000017	0.013020	0.282748
OB_27	–	–	82.1	6.3	11.5	0.7	0.283060	0.000019	0.001050	0.000035	0.033855	0.282733
OB_20	*67.4*	*14.0*	*1331.0*	*17.0*	*39.1*	*0.8*	*0.283057*	*0.000022*	*0.000628*	*0.000002*	*0.020713*	0.281940

Lu-Hf analyses in italics are considered erronous and not included in interpretations.

$\lambda Lu = 1.867 \times 10^{-11}$ yr-1 ± 8.0×10^{-14}, 2σ (Söderlund et al., 2004)
$\varepsilon Hf(t) = [(176Hf/177Hf)t\ sample / (176Hf/177Hf)t\ CHUR -1] \times 10^4$
$\varepsilon Hf(t) = ([((176Hf/177Hf)meas - (176Lu/177Hf)meas \times e^{\lambda T} -1))/((176Hf/177Hf)CHUR - (176Lu/177Hf)CHUR \times (e^{\lambda T} -1)) -1) \times 10^4$
$(176Lu/177Hf)CHUR,0 = 0.0336 \pm 0.0001$, 2σ (Bouvier et al., 2008)
$(176Hf/177Hf)CHUR,0 = 0.282785 \pm 0.000011$, 2σ; (Bouvier et al., 2008)
(176Lu/177Hf)DM = 0.0384 (Blichert-Toft and Albarède, 1997)
(176Hf/177Hf)DM = 0.28325 (Griffin et al., 2000)

Table A6. $^{40}Ar/^{39}Ar$ total fusion analysis of single grain detrital white mica

	Relative Isotopic Abundances										$^{40}Ar^*/39Ar$		%	Age (Ma)	
Sample	^{40}Ar	±1σ	^{39}Ar	±1σ	^{38}Ar	±1σ	^{37}Ar	±1σ	^{36}Ar	±1σ	±1σ		40Ar*	±1σ	
Pondaung Formation 1 (Eocene); J-value = 0.000492 ± 0.000022															
PO1-01A	41.50	0.30	0.466	0.006	0.004	0.008	0.00	0.10	0.0031	0.0018	87.214	1.777	97.7	75.8	3.57
PO1-06A	4.81	0.09	0.101	0.006	0.000	0.008	0.10	0.10	0.0020	0.0020	41.996	7.209	87.9	37.0	6.47
PO1-08A	10.60	0.10	0.147	0.005	0.000	0.005	0.00	0.11	0.0000	0.0020	77.462	5.400	107.5	67.0	5.45
PO1-12A	99.99	0.16	1.274	0.008	0.016	0.006	0.00	0.10	0.0137	0.0015	75.270	0.601	95.9	65.6	2.86
PO1-13A	12.26	0.07	0.233	0.004	0.007	0.007	0.04	0.12	0.0030	0.0019	48.886	2.632	92.9	43.0	2.94
PO1-14A	25.10	0.15	0.300	0.004	0.002	0.006	0.13	0.10	0.0043	0.0015	79.582	1.964	95.0	69.3	3.41
PO1-16A	27.23	0.09	0.695	0.007	0.000	0.007	0.00	0.10	0.0034	0.0016	37.701	0.786	96.3	33.2	1.59
PO1-19A	5.98	0.07	0.100	0.005	0.001	0.007	0.16	0.10	0.0000	0.0015	60.727	5.352	101.5	53.0	5.15
PO1-26A	66.57	0.11	1.468	0.007	0.023	0.005	0.15	0.11	0.0307	0.0017	39.177	0.402	86.4	34.4	1.53
PO1-27A	71.29	0.13	0.105	0.003	0.047	0.006	0.16	0.13	0.2170	0.0030	67.486	9.331	10.0	59.0	8.41
PO1-30A	5.43	0.05	0.114	0.004	0.000	0.005	0.00	0.14	0.0000	0.0016	48.024	4.593	100.7	42.0	4.38
Pondaung Formation 2 (Eocene); J-value = 0.000500 ± 0.000021															
PO2-05A	140.00	0.40	2.794	0.013	0.012	0.017	0.09	0.11	0.0290	0.0030	47.029	0.412	93.8	42.0	1.81
PO2-07A	546.60	0.40	4.082	0.014	0.049	0.017	0.26	0.13	0.0180	0.0030	132.558	0.517	99.0	115.8	4.81
PO2-09A	401.90	0.30	1.026	0.013	0.040	0.020	0.00	0.13	0.0230	0.0030	385.139	5.078	98.3	318.0	13.03
PO2-15A	177.40	0.40	2.864	0.015	0.020	0.020	0.00	0.12	0.0000	0.0020	62.801	0.454	101.4	55.8	2.38
PO2-16A	203.00	0.40	1.461	0.013	0.000	0.019	0.00	0.12	0.0000	0.0014	139.524	1.377	100.5	121.7	5.16
PO2-17A	439.80	0.60	4.206	0.014	0.082	0.018	0.10	0.12	0.0527	0.0019	100.845	0.401	96.5	88.8	3.72
PO2-18A	180.10	0.40	2.852	0.012	0.068	0.017	0.00	0.11	0.0270	0.0020	60.337	0.370	95.6	53.6	2.28
PO2-22A	522.30	0.70	4.585	0.017	0.000	0.018	0.00	0.11	0.0330	0.0030	111.819	0.505	98.2	98.2	4.11

PO2-23A	168.60	0.50	2.670	0.016	0.000	0.016	0.10	0.12	0.0260	0.0030	60.336	0.521	95.5	53.6	2.30
PO2-28A	161.00	0.40	1.138	0.010	0.000	0.014	0.00	0.11	0.0000	0.0020	142.729	1.486	100.9	124.4	5.29
PO2-29A	196.20	0.50	0.844	0.011	0.026	0.014	0.06	0.14	0.0146	0.0014	227.402	3.162	97.8	194.0	8.28
PO2-30A	82.20	0.20	2.277	0.011	0.039	0.011	0.12	0.10	0.0051	0.0020	35.457	0.330	98.2	31.7	1.38
PO2-31A	94.60	0.30	0.676	0.008	0.020	0.009	0.00	0.09	0.0073	0.0017	136.730	1.784	97.7	119.4	5.16
PO2-34A	201.80	0.20	3.696	0.013	0.048	0.012	0.00	0.10	0.0543	0.0013	50.262	0.228	92.0	44.8	1.90
PO2-35A	207.10	0.30	5.378	0.014	0.079	0.011	0.00	0.13	0.0356	0.0018	36.557	0.152	94.9	32.7	1.39
PO2-40A	160.90	0.30	3.545	0.012	0.059	0.010	0.17	0.11	0.0497	0.0019	41.252	0.230	90.9	36.8	1.57
PO2-41A	166.12	0.20	2.752	0.011	0.057	0.009	0.11	0.11	0.0123	0.0019	59.052	0.324	97.8	52.5	2.23
PO2-42A	300.30	0.30	2.253	0.012	0.058	0.011	0.24	0.11	0.0990	0.0030	120.344	0.771	90.3	105.5	4.43
PO2-43A	142.40	0.40	1.924	0.011	0.042	0.010	0.00	0.11	0.0070	0.0020	72.938	0.615	98.6	64.6	2.77
PO2-44A	138.30	0.40	2.033	0.010	0.045	0.013	0.00	0.11	0.0120	0.0020	66.238	0.518	97.4	58.8	2.51
PO2-47A	228.40	0.30	3.001	0.011	0.061	0.012	0.00	0.12	0.0550	0.0030	70.653	0.399	92.8	62.7	2.65
PO2-50A	437.80	0.40	1.079	0.009	0.045	0.014	0.07	0.12	0.0307	0.0018	397.329	3.322	97.9	327.0	13.03
PO2-53A	18.32	0.12	0.479	0.005	0.017	0.005	0.01	0.19	0.0000	0.0016	38.973	1.077	101.9	34.8	1.76
PO2-54A	142.42	0.13	1.208	0.008	0.021	0.007	0.00	0.15	0.0065	0.0017	116.246	0.919	98.7	102.0	4.31
PO2-55A	113.05	0.18	0.835	0.007	0.034	0.006	0.00	0.13	0.0170	0.0020	129.255	1.301	95.5	113.0	4.81
PO2-56A	53.86	0.11	0.553	0.006	0.012	0.004	0.00	0.13	0.0029	0.0017	95.713	1.376	98.3	84.4	3.72
PO2-58A	83.45	0.14	0.612	0.006	0.000	0.005	0.00	0.12	0.0013	0.0007	135.571	1.386	99.5	118.4	5.03
PO2-59A	120.79	0.15	0.784	0.006	0.011	0.006	0.00	0.13	0.0050	0.0018	152.141	1.404	98.8	132.3	5.58
PO2-60A	51.37	0.10	1.267	0.008	0.020	0.006	0.00	0.14	0.0096	0.0019	38.284	0.503	94.4	34.2	1.52
PO2-61A	168.60	0.40	1.809	0.011	0.027	0.006	0.00	0.13	0.0180	0.0014	90.273	0.660	96.8	79.7	3.38
PO2-62A	39.00	0.20	0.551	0.006	0.008	0.005	0.12	0.14	0.0022	0.0018	69.642	1.281	98.3	61.8	2.83
PO2-63A	61.50	0.20	0.444	0.005	0.000	0.006	0.12	0.14	0.0028	0.0018	136.709	2.113	98.6	119.4	5.25
PO2-64A	59.39	0.12	1.366	0.008	0.021	0.007	0.15	0.13	0.0076	0.0015	41.848	0.425	96.2	37.4	1.63
PO2-65A	47.30	0.30	0.108	0.003	0.005	0.007	0.09	0.15	0.0021	0.0015	432.614	14.54	98.7	353.0	17.45
PO2-66A	77.20	0.12	0.527	0.005	0.008	0.006	0.15	0.14	0.0022	0.0012	145.236	1.657	99.2	126.5	5.41
PO2-67A	54.90	0.11	0.407	0.004	0.011	0.007	0.00	0.10	0.0007	0.0015	134.235	1.808	99.6	117.3	5.09
PO2-68A	29.88	0.13	0.198	0.004	0.004	0.006	0.12	0.13	0.0004	0.0011	150.393	3.294	99.6	131.0	6.06
PO2-70A	70.43	0.13	0.812	0.007	0.014	0.006	0.00	0.14	0.0029	0.0008	85.663	0.820	98.8	75.7	3.25

PO2-72A	105.78	0.12	0.312	0.005	0.010	0.005	0.21	0.13	0.0000	0.0015	341.287	5.528	100.6	284.0	12.02
PO2-73A	95.45	0.17	0.768	0.006	0.016	0.008	0.27	0.13	0.0008	0.0017	124.083	1.196	99.8	108.6	4.62
PO2-74A	74.48	0.12	1.553	0.009	0.031	0.006	0.00	0.16	0.0000	0.0018	47.958	0.457	100.0	42.8	1.85
PO2-75A	29.23	0.10	0.404	0.005	0.001	0.005	0.00	0.16	0.0000	0.0018	72.436	1.628	100.2	64.2	3.05
PO2-76A	25.80	0.20	0.578	0.006	0.007	0.006	0.00	0.17	0.0026	0.0018	43.358	1.098	97.0	38.7	1.90
PO2-77A	56.78	0.13	0.772	0.006	0.020	0.006	0.00	0.14	0.0074	0.0013	70.699	0.766	96.2	62.7	2.72
PO2-78A	59.74	0.14	0.440	0.004	0.010	0.005	0.00	0.16	0.0022	0.0012	134.184	1.638	98.9	117.2	5.04
PO2-80A	46.12	0.14	0.359	0.005	0.000	0.006	0.00	0.13	0.0005	0.0016	127.915	2.350	99.7	111.9	5.05
PO2-81A	33.41	0.15	0.700	0.005	0.003	0.007	0.00	0.11	0.0075	0.0016	44.521	0.774	93.4	39.7	1.81
PO2-82A	27.05	0.10	0.190	0.004	0.012	0.005	0.00	0.15	0.0010	0.0007	140.571	3.535	98.8	123.0	5.88
PO2-83A	91.66	0.13	0.642	0.005	0.007	0.005	0.00	0.12	0.0040	0.0013	140.762	1.350	98.7	122.8	5.20
PO2-84A	278.00	0.40	0.709	0.006	0.012	0.005	0.41	0.11	0.0039	0.0018	390.505	3.699	99.6	322.0	12.91
PO2-85A	27.02	0.09	0.397	0.005	0.011	0.007	0.14	0.14	0.0003	0.0017	67.839	1.570	99.7	60.2	2.88
PO2-86A	53.30	0.20	0.814	0.006	0.005	0.006	0.08	0.13	0.0043	0.0016	63.902	0.782	97.6	56.8	2.48
PO2-87A	105.47	0.18	0.810	0.006	0.019	0.006	0.11	0.15	0.0040	0.0015	128.726	1.195	98.9	112.6	4.77
PO2-88A	78.76	0.15	0.342	0.005	0.010	0.006	0.00	0.17	0.0008	0.0013	229.867	3.447	99.7	196.0	8.43
PO2-89A	170.80	0.40	0.500	0.006	0.003	0.006	0.00	0.19	0.0047	0.0015	338.271	4.377	99.2	282.0	11.66
PO2-90A	184.10	0.30	1.306	0.009	0.021	0.008	0.00	0.13	0.0488	0.0013	129.846	0.963	92.2	113.5	4.77
PO2-91A	56.05	0.14	0.580	0.005	0.013	0.006	0.00	0.14	0.0044	0.0008	94.295	0.952	97.7	83.2	3.57
PO2-92A	47.02	0.11	0.696	0.006	0.014	0.006	0.00	0.15	0.0059	0.0014	65.068	0.833	96.3	57.8	2.54
PO2-94A	36.04	0.10	0.249	0.004	0.019	0.006	0.12	0.16	0.0025	0.0008	142.028	2.656	97.9	124.0	5.58
PO2-95A	22.18	0.17	0.311	0.005	0.002	0.005	0.00	0.17	0.0046	0.0012	66.869	1.615	93.8	59.4	2.87
PO2-96A	57.10	0.12	0.618	0.005	0.008	0.006	0.00	0.12	0.0059	0.0007	89.586	0.868	97.0	79.1	3.39
PO2-99A	122.36	0.14	0.911	0.007	0.014	0.006	0.00	0.20	0.0077	0.0014	131.804	1.119	98.1	115.2	4.86
PO2-103A	90.03	0.13	1.225	0.007	0.023	0.006	0.20	0.20	0.0196	0.0013	68.816	0.502	93.6	61.1	2.60
PO2-104A	184.10	0.40	1.414	0.007	0.016	0.006	0.00	0.20	0.0081	0.0019	128.475	0.820	98.7	112.4	4.71
PO2-117A	92.88	0.19	0.799	0.006	0.004	0.006	0.00	0.20	0.0073	0.0013	113.528	1.001	97.7	99.7	4.23
PO2-118A	967.60	1.10	3.054	0.012	0.033	0.008	0.30	0.20	0.0160	0.0020	315.379	1.374	99.5	264.3	10.56
PO2-120A	80.43	0.17	0.527	0.006	0.000	0.006	0.00	0.20	0.0013	0.0015	151.768	1.877	99.5	132.0	5.66
PO2-121A	79.40	0.30	0.590	0.005	0.032	0.008	0.40	0.20	0.0055	0.0018	131.845	1.627	98.0	115.2	4.97

PO2-126A	44.14	0.15	0.682	0.005	0.013	0.008	0.00	0.19	0.0016	0.0012	64.076	0.766	98.9	56.9	2.49
PO2-128A	68.60	0.20	1.411	0.008	0.045	0.007	0.20	0.30	0.0160	0.0009	45.263	0.375	93.2	40.4	1.74
PO2-129A	651.60	0.90	1.910	0.010	0.036	0.009	0.00	0.20	0.0260	0.0020	337.143	1.923	98.8	281.2	11.23
PO2-130A	128.09	0.14	0.950	0.007	0.007	0.008	0.40	0.20	0.0036	0.0016	133.764	1.105	99.2	116.9	4.93
PO2-132A	44.90	0.20	1.088	0.006	0.046	0.009	0.50	0.30	0.0090	0.0020	38.972	0.642	94.4	34.8	1.58
PO2-136A	63.30	0.20	0.784	0.006	0.016	0.007	0.40	0.30	0.0106	0.0013	76.788	0.874	95.1	68.0	2.95
PO2-141A	50.50	0.20	1.193	0.008	0.015	0.007	0.00	0.20	0.0071	0.0018	40.570	0.564	95.8	36.2	1.61
PO2-144A	50.79	0.17	0.398	0.006	0.008	0.007	0.00	0.30	0.0033	0.0018	124.848	2.347	98.0	109.3	4.95
PO2-147A	31.07	0.14	0.242	0.004	0.007	0.005	0.00	0.20	0.0003	0.0016	127.544	2.792	99.6	112.0	5.20
PO2-149A	69.91	0.18	0.382	0.005	0.013	0.007	0.00	0.20	0.0119	0.0018	173.560	2.775	95.0	150.0	6.58
PO2-154A	170.61	0.17	0.425	0.005	0.000	0.006	0.00	0.20	0.0039	0.0018	398.173	4.742	99.3	328.0	13.29
PO2-155A	115.28	0.13	0.764	0.007	0.000	0.005	0.00	0.20	0.0158	0.0019	144.688	1.561	95.9	126.1	5.37
PO2-156A	48.13	0.16	0.384	0.005	0.001	0.007	0.30	0.20	0.0159	0.0008	113.133	1.647	90.3	99.3	4.36
PO2-160A	48.10	0.20	0.339	0.005	0.010	0.007	0.00	0.30	0.0066	0.0013	135.864	2.523	95.9	119.0	5.35
PO2-166A	145.20	0.20	0.971	0.007	0.017	0.006	0.00	0.18	0.0055	0.0019	147.724	1.237	98.8	128.6	5.41
Padaung Formation 3 (Oligocene); J-value = 0.000500 ± 0.000016															
PA3-01A	155.80	0.20	1.102	0.007	0.020	0.006	0.00	0.10	0.0065	0.0008	139.599	0.998	98.8	121.6	3.87
PA3-02A	75.02	0.15	0.888	0.006	0.014	0.006	0.00	0.11	0.0090	0.0009	81.412	0.695	96.4	71.9	2.34
PA3-04A	130.77	0.18	0.886	0.007	0.021	0.007	0.00	0.08	0.0120	0.0014	143.527	1.331	97.3	124.9	4.04
PA3-05A	115.80	0.20	1.373	0.009	0.013	0.006	0.01	0.07	0.0230	0.0014	79.426	0.653	94.1	70.2	2.28
PA3-06A	45.45	0.13	0.482	0.007	0.022	0.007	0.04	0.09	0.0048	0.0014	91.406	1.666	96.9	80.5	2.91
PA3-07A	25.70	0.12	0.350	0.006	0.006	0.007	0.00	0.09	0.0037	0.0013	70.234	1.753	95.7	62.2	2.49
PA3-09A	82.16	0.14	1.108	0.007	0.012	0.006	0.02	0.10	0.0068	0.0008	72.345	0.525	97.5	64.0	2.07
PA3-10A	32.60	0.09	0.351	0.005	0.000	0.005	0.22	0.08	0.0013	0.0008	91.956	1.525	98.9	81.0	2.87
PA3-11A	141.57	0.16	2.292	0.008	0.046	0.007	0.12	0.09	0.0208	0.0014	59.083	0.297	95.7	52.5	1.68
PA3-12A	35.40	0.10	0.443	0.005	0.015	0.006	0.01	0.08	0.0049	0.0013	76.589	1.325	95.9	67.7	2.43
PA3-13A	59.98	0.13	0.802	0.006	0.014	0.005	0.00	0.10	0.0055	0.0008	72.789	0.641	97.3	64.4	2.11
PA3-14A	43.40	0.13	0.259	0.005	0.016	0.007	0.00	0.10	0.0020	0.0008	165.147	3.549	98.6	143.0	5.32
PA3-15A	103.45	0.16	1.110	0.008	0.032	0.006	0.00	0.09	0.0034	0.0009	92.281	0.748	99.0	81.3	2.64

PA3-16A	114.19	0.14	1.342	0.008	0.034	0.007	0.00	0.10	0.0061	0.0014	83.738	0.594	98.4	73.9	2.38
PA3-17A	55.75	0.11	0.726	0.005	0.020	0.008	0.04	0.08	0.0152	0.0014	70.631	0.794	92.0	62.5	2.09
PA3-18A	110.66	0.18	1.397	0.006	0.019	0.007	0.07	0.08	0.0228	0.0014	74.391	0.482	93.9	65.8	2.12
PA3-19A	37.57	0.12	0.225	0.005	0.000	0.005	0.00	0.10	0.0021	0.0009	164.145	3.911	98.4	142.0	5.47
PA3-20A	48.79	0.12	0.692	0.006	0.015	0.007	0.00	0.10	0.0042	0.0010	68.633	0.782	97.4	60.8	2.04
PA3-21A	25.91	0.10	0.434	0.006	0.016	0.009	0.04	0.08	0.0063	0.0014	55.405	1.214	92.9	49.2	1.89
PA3-22A	65.85	0.13	0.746	0.006	0.014	0.008	0.00	0.10	0.0097	0.0014	84.364	0.933	95.6	74.4	2.48
PA3-23A	34.52	0.10	0.379	0.006	0.002	0.008	0.02	0.08	0.0031	0.0015	88.765	1.794	97.4	78.3	2.91
PA3-25A	67.60	0.11	1.079	0.008	0.004	0.007	0.04	0.08	0.0039	0.0015	61.593	0.603	98.3	54.7	1.81
PA3-26A	39.16	0.14	0.276	0.007	0.012	0.005	0.14	0.10	0.0017	0.0013	140.337	3.733	98.7	122.0	4.93
PA3-27A	22.52	0.10	0.350	0.006	0.014	0.007	0.00	0.10	0.0037	0.0009	61.285	1.330	95.1	54.4	2.08
PA3-28A	80.00	0.14	1.042	0.007	0.020	0.005	0.04	0.08	0.0046	0.0008	75.495	0.592	98.3	66.8	2.17
PA3-29A	41.61	0.10	0.530	0.006	0.007	0.006	0.00	0.08	0.0036	0.0009	76.501	1.030	97.4	67.6	2.31
PA3-30A	62.80	0.20	0.819	0.006	0.019	0.007	0.02	0.08	0.0048	0.0009	74.923	0.723	97.7	66.3	2.18
PA3-31A	34.91	0.08	0.344	0.004	0.013	0.007	0.05	0.10	0.0122	0.0015	90.897	1.646	89.7	80.1	2.89
PA3-32A	57.62	0.14	0.652	0.007	0.012	0.005	0.23	0.09	0.0109	0.0012	83.530	1.099	94.4	73.7	2.51
PA3-33A	57.52	0.14	0.782	0.007	0.013	0.006	0.14	0.07	0.0096	0.0013	69.944	0.836	95.1	61.9	2.09
PA3-34A	71.44	0.15	0.813	0.007	0.019	0.007	0.13	0.10	0.0037	0.0009	86.525	0.818	98.5	76.3	2.50
PA3-35A	19.21	0.09	0.216	0.005	0.000	0.008	0.00	0.10	0.0015	0.0014	86.880	2.753	97.7	77.0	3.39
PA3-36A	87.21	0.16	0.592	0.006	0.009	0.008	0.01	0.09	0.0043	0.0014	145.137	1.645	98.6	126.2	4.16
PA3-37A	35.64	0.15	0.475	0.006	0.015	0.006	0.05	0.10	0.0050	0.0013	71.937	1.280	95.8	63.7	2.30
PA3-39A	50.84	0.14	0.597	0.006	0.006	0.005	0.09	0.08	0.0060	0.0008	82.161	0.964	96.5	72.6	2.43
PA3-41A	35.38	0.11	0.436	0.006	0.000	0.005	0.02	0.09	0.0026	0.0007	79.306	1.225	97.9	70.1	2.45
PA3-42A	48.52	0.12	0.578	0.005	0.015	0.005	0.00	0.09	0.0009	0.0013	83.495	1.019	99.5	73.7	2.48
PA3-43A	19.79	0.07	0.232	0.006	0.003	0.005	0.00	0.10	0.0013	0.0008	83.470	2.436	98.0	74.0	3.13
PA3-45A	70.82	0.12	0.884	0.006	0.010	0.006	0.17	0.10	0.0037	0.0009	78.930	0.629	98.5	69.8	2.27
PA3-47A	54.98	0.10	0.621	0.006	0.001	0.004	0.01	0.08	0.0089	0.0009	84.303	0.946	95.2	74.4	2.48
PA3-48A	24.40	0.09	0.222	0.005	0.007	0.006	0.00	0.10	0.0068	0.0013	100.823	2.790	91.8	89.0	3.67
PA3-49A	53.13	0.12	0.649	0.004	0.018	0.006	0.02	0.09	0.0020	0.0012	80.926	0.825	98.9	71.5	2.36
PA3-50A	30.76	0.09	0.348	0.004	0.003	0.005	0.04	0.08	0.0004	0.0008	87.950	1.247	99.7	77.6	2.67

PA3-51A	52.80	0.12	0.760	0.005	0.016	0.007	0.27	0.09	0.0042	0.0007	67.832	0.565	97.7	60.1	1.96
PA3-52A	18.26	0.06	0.248	0.004	0.006	0.007	0.27	0.10	0.0007	0.0007	72.945	1.467	99.0	64.6	2.40
PA3-53A	36.50	0.10	0.194	0.004	0.013	0.005	0.27	0.14	0.0014	0.0009	186.129	3.766	98.9	160.0	5.83
PA3-56A	41.16	0.09	0.352	0.004	0.009	0.005	0.00	0.12	0.0138	0.0007	105.195	1.538	90.0	92.4	3.18
PA3-59A	32.71	0.07	0.257	0.004	0.004	0.004	0.06	0.11	0.0015	0.0007	125.519	2.063	98.7	109.7	3.84
PA3-60A	36.75	0.10	0.176	0.004	0.010	0.004	0.00	0.10	0.0025	0.0011	204.531	5.053	98.0	175.0	6.78
PA3-62A	24.61	0.09	0.353	0.005	0.006	0.005	0.00	0.11	0.0067	0.0011	63.934	1.294	91.9	56.7	2.12
PA3-63A	11.86	0.04	0.121	0.003	0.002	0.005	0.00	0.13	0.0011	0.0007	94.757	3.041	97.0	83.0	3.70
PA3-64A	36.07	0.09	0.541	0.006	0.009	0.005	0.00	0.17	0.0025	0.0007	65.211	0.865	97.9	57.8	1.98
PA3-65A	35.52	0.09	0.470	0.005	0.006	0.006	0.25	0.18	0.0025	0.0007	74.017	0.939	98.0	65.5	2.22
PA3-66A	45.30	0.09	0.600	0.006	0.005	0.005	0.00	0.17	0.0155	0.0007	67.712	0.751	89.8	60.0	2.01
PA3-68A	84.34	0.18	1.342	0.008	0.026	0.006	0.00	0.20	0.0088	0.0012	60.868	0.468	96.9	54.0	1.76
PA3-69A	21.85	0.09	0.246	0.004	0.000	0.004	0.02	0.19	0.0038	0.0011	84.323	1.936	94.9	74.4	2.88
PA3-70A	66.67	0.14	0.438	0.005	0.005	0.005	0.00	0.20	0.0053	0.0012	148.706	1.823	97.6	129.2	4.29
PA3-72A	28.19	0.07	0.352	0.004	0.007	0.005	0.00	0.17	0.0046	0.0011	76.325	1.368	95.2	67.5	2.44
PA3-73A	38.28	0.09	0.555	0.005	0.017	0.005	0.10	0.18	0.0060	0.0011	65.861	0.837	95.4	58.4	1.99
PA3-74A	50.18	0.11	0.338	0.004	0.000	0.005	0.36	0.15	0.0006	0.0011	148.071	2.228	99.7	128.7	4.41
PA3-75A	29.13	0.10	0.188	0.004	0.000	0.005	0.29	0.16	0.0001	0.0011	155.346	3.985	99.9	135.0	5.34
PA3-76A	29.36	0.08	0.190	0.004	0.014	0.005	0.50	0.20	0.0028	0.0012	150.350	3.683	97.4	131.0	5.09
PA3-77A	30.23	0.10	0.354	0.005	0.000	0.007	0.00	0.17	0.0017	0.0012	83.908	1.633	98.2	74.1	2.73
PA3-78A	55.17	0.10	0.630	0.005	0.001	0.005	0.06	0.17	0.0012	0.0012	86.949	0.968	99.4	76.7	2.55
PA3-79A	86.19	0.16	0.548	0.005	0.004	0.005	0.07	0.19	0.0030	0.0007	155.655	1.437	99.0	135.1	4.35
PA3-80A	59.61	0.11	0.726	0.006	0.011	0.005	0.00	0.16	0.0077	0.0012	78.902	0.819	96.1	69.7	2.31
PA3-81A	44.94	0.12	0.536	0.006	0.004	0.007	0.00	0.17	0.0065	0.0012	80.160	1.089	95.7	70.8	2.42
PA3-82A	51.51	0.10	0.342	0.004	0.006	0.004	0.00	0.19	0.0016	0.0008	149.084	2.141	99.1	129.6	4.40
PA3-83A	49.99	0.10	0.649	0.006	0.008	0.006	0.00	0.20	0.0046	0.0008	74.865	0.811	97.2	66.2	2.21
PA3-84A	35.77	0.09	0.505	0.006	0.004	0.005	0.24	0.17	0.0040	0.0012	68.548	1.168	96.8	60.7	2.17
PA3-85A	153.79	0.17	0.826	0.006	0.011	0.004	0.10	0.20	0.0122	0.0012	181.934	1.338	97.7	156.9	4.96
PA3-86A	43.83	0.11	0.503	0.006	0.012	0.005	0.07	0.18	0.0018	0.0011	86.013	1.212	98.8	75.9	2.61
PA3-87A	141.80	0.20	0.619	0.006	0.006	0.006	0.46	0.18	0.0009	0.0012	228.942	2.490	99.8	195.0	6.28

PA3-88A	28.24	0.09	0.620	0.006	0.000	0.005	0.00	0.20	0.0050	0.0013	43.092	0.783	94.7	38.4	1.40
PA3-89A	87.38	0.11	0.417	0.005	0.000	0.005	0.21	0.19	0.0020	0.0013	208.242	2.781	99.3	178.0	5.92
PA3-90A	26.79	0.08	0.350	0.004	0.006	0.005	0.06	0.18	0.0019	0.0012	75.059	1.414	98.0	66.4	2.43
PA3-91A	33.75	0.08	0.436	0.005	0.004	0.005	0.13	0.16	0.0013	0.0012	76.603	1.194	98.9	67.7	2.38
PA3-92A	56.97	0.12	0.773	0.006	0.008	0.005	0.13	0.20	0.0070	0.0008	71.052	0.679	96.4	62.9	2.07
PA3-93A	32.53	0.07	0.428	0.004	0.004	0.005	0.28	0.16	0.0071	0.0008	71.107	0.941	93.6	63.0	2.15
PA3-94A	91.94	0.13	0.521	0.005	0.008	0.007	0.10	0.17	0.0098	0.0007	171.099	1.642	96.9	147.9	4.77
PA3-95A	24.52	0.08	0.344	0.005	0.005	0.006	0.00	0.16	0.0037	0.0012	67.976	1.485	95.5	60.2	2.30
PA3-96A	52.37	0.11	0.588	0.006	0.008	0.005	0.00	0.18	0.0025	0.0012	87.608	1.156	98.5	77.3	2.63
PA3-98A	28.20	0.08	0.371	0.005	0.009	0.005	0.09	0.17	0.0022	0.0007	74.367	1.167	97.8	65.8	2.31
PA3-99A	29.76	0.10	0.365	0.006	0.011	0.005	0.28	0.19	0.0044	0.0014	78.104	1.668	95.7	69.0	2.61
PA3-100A	18.23	0.06	0.242	0.004	0.009	0.005	0.00	0.16	0.0015	0.0012	73.525	1.962	97.5	65.1	2.67
PA3-101A	23.54	0.08	0.343	0.005	0.006	0.004	0.50	0.30	0.0012	0.0011	67.803	1.388	98.6	60.1	2.25
PA3-102A	21.46	0.09	0.264	0.004	0.000	0.004	0.00	0.30	0.0060	0.0012	74.555	1.766	91.7	66.0	2.59
PA3-103A	26.35	0.08	0.166	0.005	0.008	0.006	0.00	0.20	0.0046	0.0012	150.040	5.070	94.7	130.0	5.87
PA3-104A	10.93	0.05	0.176	0.004	0.010	0.004	0.00	0.20	0.0024	0.0011	57.805	2.272	93.4	51.3	2.57
PA3-105A	33.23	0.07	0.402	0.004	0.011	0.004	0.60	0.20	0.0023	0.0011	81.119	1.235	98.1	71.6	2.50
PA3-108A	28.78	0.08	0.151	0.005	0.007	0.007	0.00	0.30	0.0002	0.0007	189.816	6.710	99.7	163.0	7.47
PA3-109A	54.71	0.12	0.308	0.004	0.007	0.005	0.00	0.30	0.0026	0.0011	174.917	2.695	98.5	151.0	5.17
PA3-111A	15.77	0.05	0.192	0.003	0.002	0.004	0.00	0.30	0.0014	0.0011	79.551	2.181	97.2	70.3	2.91
PA3-113A	44.93	0.12	0.228	0.005	0.013	0.004	0.40	0.30	0.0005	0.0011	196.959	4.748	99.7	169.0	6.49
PA3-115A	15.72	0.06	0.172	0.004	0.010	0.006	0.40	0.30	0.0032	0.0012	85.976	2.831	94.2	76.0	3.42
PA3-117A	76.03	0.11	0.370	0.004	0.014	0.005	0.00	0.30	0.0012	0.0008	204.233	2.596	99.5	175.0	5.77
PA3-118A	74.38	0.14	0.389	0.004	0.023	0.005	0.40	0.30	0.0011	0.0008	190.381	2.369	99.6	163.9	5.40
PA3-119A	13.89	0.05	0.152	0.004	0.009	0.005	0.00	0.30	0.0001	0.0007	90.952	2.808	99.7	80.0	3.49
PA3-120A	12.40	0.06	0.150	0.003	0.002	0.005	0.00	0.30	0.0026	0.0012	77.279	3.042	93.6	68.0	3.41
PA3-121A	14.27	0.05	0.174	0.004	0.007	0.005	0.00	0.30	0.0028	0.0012	76.930	2.646	93.8	68.0	3.14
PA3-122A	20.99	0.08	0.240	0.004	0.000	0.005	0.00	0.30	0.0041	0.0012	82.065	2.016	94.1	72.5	2.87
PA3-123A	14.26	0.04	0.220	0.004	0.005	0.006	0.00	0.30	0.0032	0.0012	60.470	1.960	93.2	53.7	2.41
PA3-125A	38.13	0.10	0.187	0.004	0.000	0.005	0.00	0.30	0.0020	0.0007	199.953	4.934	98.4	172.0	6.64

PA3-126A	46.70	0.11	0.520	0.005	0.005	0.005	0.10	0.30	0.0060	0.0007	86.512	0.983	96.2	76.3	2.55
PA3-127A	41.07	0.10	0.481	0.005	0.010	0.005	0.20	0.30	0.0038	0.0007	83.030	1.034	97.3	73.3	2.48
PA3-128A	22.68	0.07	0.258	0.004	0.005	0.006	0.50	0.30	0.0016	0.0012	86.189	2.006	98.1	76.0	2.96
PA3-129A	24.37	0.09	0.341	0.004	0.015	0.005	0.50	0.30	0.0023	0.0012	69.683	1.420	97.4	61.7	2.31
PA3-130A	39.94	0.10	0.478	0.006	0.006	0.006	0.00	0.30	0.0002	0.0007	83.320	1.121	99.8	73.6	2.51
PA3-131A	84.82	0.11	0.571	0.004	0.013	0.005	0.00	0.20	0.0010	0.0012	148.023	1.339	99.6	128.7	4.15
PA3-132A	14.90	0.06	0.152	0.003	0.003	0.005	0.00	0.20	0.0000	0.0012	98.424	3.147	100.4	86.0	3.83
PA3-133A	8.94	0.05	0.118	0.004	0.014	0.006	0.70	0.40	0.0035	0.0012	67.832	3.750	89.2	60.0	3.78
PA3-134A	16.62	0.06	0.195	0.003	0.001	0.005	0.00	0.30	0.0046	0.0012	78.084	2.370	91.7	69.0	2.99
PA3-135A	38.78	0.09	0.261	0.004	0.000	0.004	0.00	0.30	0.0044	0.0012	143.611	2.461	96.6	125.0	4.40
PA3-136A	22.39	0.07	0.242	0.004	0.008	0.006	0.60	0.20	0.0004	0.0010	92.474	2.006	99.7	81.4	3.09
PA3-137A	16.14	0.05	0.219	0.004	0.020	0.006	0.50	0.30	0.0000	0.0010	74.417	2.081	100.7	65.8	2.75
PA3-138A	45.82	0.10	0.568	0.005	0.011	0.005	0.00	0.20	0.0025	0.0012	79.368	0.951	98.4	70.1	2.36
PA3-139A	8.82	0.05	0.105	0.004	0.000	0.005	0.00	0.30	0.0023	0.0007	77.094	3.568	91.9	68.0	3.77
PA3-140A	22.17	0.08	0.258	0.005	0.000	0.006	0.00	0.30	0.0003	0.0008	85.401	1.837	99.5	75.4	2.85
PA3-141A	43.64	0.11	0.236	0.004	0.005	0.005	0.00	0.30	0.0023	0.0007	182.042	3.441	98.4	157.0	5.61
PA3-142A	52.96	0.10	0.452	0.005	0.000	0.006	0.00	0.30	0.0036	0.0012	114.640	1.543	97.9	100.4	3.41
PA3-143A	29.64	0.10	0.325	0.005	0.005	0.006	0.00	0.30	0.0005	0.0011	90.471	1.846	99.4	79.7	2.97
PA3-144A	34.33	0.10	0.605	0.006	0.015	0.006	0.40	0.20	0.0018	0.0008	55.947	0.675	98.6	49.7	1.68
PA3-145A	9.18	0.04	0.093	0.004	0.000	0.004	0.50	0.20	0.0000	0.0007	98.881	4.740	100.3	87.0	4.90
PA3-146A	36.58	0.10	0.502	0.005	0.002	0.006	0.00	0.30	0.0029	0.0011	71.002	0.973	97.6	62.9	2.16
PA3-147A	10.06	0.05	0.112	0.004	0.003	0.006	0.00	0.20	0.0023	0.0011	83.738	3.999	93.2	74.0	4.17
PA3-148A	18.68	0.06	0.222	0.004	0.000	0.006	0.00	0.20	0.0039	0.0011	78.902	1.956	93.9	69.7	2.78
PA3-149A	15.41	0.04	0.157	0.003	0.002	0.005	0.00	0.20	0.0005	0.0007	96.887	2.498	98.9	85.0	3.43
PA3-150A	39.34	0.10	0.248	0.005	0.000	0.005	0.20	0.30	0.0005	0.0012	157.946	3.665	99.7	137.0	5.23
PA3-151A	23.87	0.07	0.141	0.003	0.000	0.005	0.00	0.40	0.0013	0.0012	166.072	4.713	98.4	144.0	5.93
PA3-152A	28.74	0.07	0.350	0.004	0.006	0.006	0.00	0.30	0.0000	0.0011	82.345	1.433	100.2	72.7	2.61
PA3-154A	11.15	0.05	0.147	0.004	0.005	0.003	0.20	0.20	0.0009	0.0007	74.225	2.571	97.6	66.0	3.05
PA3-155A	27.12	0.08	0.130	0.004	0.006	0.006	0.10	0.20	0.0040	0.0011	200.045	6.341	95.6	172.0	7.40
PA3-156A	34.59	0.10	0.230	0.004	0.007	0.006	0.00	0.30	0.0028	0.0011	146.985	2.973	97.6	128.0	4.69

PA3-157A	17.66	0.06	0.199	0.003	0.000	0.004	0.00	0.30	0.0004	0.0007	87.588	1.912	99.1	77.2	2.94
PA3-158A	20.68	0.10	0.244	0.004	0.015	0.007	0.00	0.30	0.0027	0.0007	81.460	1.777	96.2	71.9	2.74
PA3-159A	20.78	0.09	0.255	0.004	0.003	0.005	0.00	0.30	0.0012	0.0007	79.868	1.722	98.2	70.6	2.68
PA3-160A	18.30	0.05	0.223	0.004	0.013	0.004	0.00	0.30	0.0010	0.0011	80.681	2.117	98.3	71.3	2.90
PA3-162A	14.87	0.03	0.198	0.004	0.007	0.005	0.80	0.30	0.0012	0.0006	73.756	1.777	98.2	65.3	2.58
PA3-163A	13.11	0.04	0.151	0.004	0.005	0.005	0.60	0.40	0.0016	0.0007	84.039	2.503	96.6	74.0	3.18
PA3-164A	27.84	0.09	0.340	0.004	0.012	0.004	0.00	0.30	0.0024	0.0007	79.634	1.219	97.4	70.4	2.46
PA3-165A	45.70	0.11	0.729	0.005	0.022	0.006	0.60	0.40	0.0048	0.0012	60.824	0.655	97.0	54.0	1.80
Padaung Formation 2 (Oligocene); J-value = 0.000503 ± 0.000020															
PA2-01A	87.50	0.20	1.164	0.006	0.006	0.010	0.00	0.09	0.0014	0.0017	74.828	0.636	99.5	66.7	2.69
PA2-02A	237.60	0.20	1.138	0.007	0.012	0.008	0.02	0.09	0.0012	0.0015	208.491	1.469	99.8	180.0	6.99
PA2-03A	123.77	0.20	0.816	0.006	0.024	0.006	0.02	0.10	0.0000	0.0020	153.478	1.479	101.1	134.2	5.35
PA2-04A	126.40	0.17	0.640	0.007	0.000	0.008	0.10	0.07	0.0029	0.0014	196.038	2.436	99.3	170.0	6.81
PA2-07A	27.09	0.12	0.116	0.004	0.000	0.007	0.20	0.12	0.0072	0.0016	214.989	9.325	92.2	185.0	10.42
PA2-08A	343.60	0.30	0.859	0.006	0.027	0.010	0.06	0.11	0.0054	0.0016	398.166	2.916	99.5	330.0	12.30
PA2-09A	91.54	0.14	0.992	0.008	0.009	0.006	0.00	0.08	0.0010	0.0008	91.893	0.786	99.6	81.6	3.28
PA2-13A	82.64	0.14	0.897	0.006	0.014	0.006	0.00	0.10	0.0029	0.0018	91.130	0.908	99.0	80.9	3.28
PA2-15A	83.45	0.18	0.883	0.006	0.018	0.008	0.12	0.09	0.0030	0.0008	93.553	0.776	99.0	83.0	3.33
PA2-16A	62.16	0.14	0.838	0.007	0.022	0.008	0.00	0.09	0.0065	0.0009	71.859	0.736	96.9	64.1	2.61
PA2-17A	90.90	0.20	0.906	0.006	0.019	0.006	0.00	0.08	0.0033	0.0014	99.202	0.854	98.9	87.9	3.53
PA2-18A	39.20	0.20	0.480	0.005	0.000	0.009	0.02	0.09	0.0023	0.0020	80.194	1.567	98.2	71.4	3.13
PA2-19A	38.70	0.10	0.649	0.006	0.000	0.007	0.00	0.09	0.0024	0.0019	58.510	1.045	98.1	52.4	2.27
PA2-20A	58.11	0.18	0.427	0.004	0.012	0.007	0.00	0.09	0.0020	0.0011	134.738	1.642	99.0	118.4	4.81
PA2-21A	56.78	0.13	0.494	0.006	0.014	0.006	0.00	0.09	0.0027	0.0009	113.186	1.443	98.6	100.0	4.10
PA2-22A	20.78	0.14	0.238	0.004	0.000	0.005	0.00	0.08	0.0025	0.0009	84.061	2.019	96.5	74.8	3.43
PA2-23A	56.83	0.14	0.731	0.006	0.016	0.006	0.13	0.10	0.0019	0.0008	77.034	0.706	99.0	68.6	2.78
PA2-24A	11.17	0.08	0.123	0.004	0.009	0.008	0.18	0.08	0.0019	0.0008	86.098	3.790	95.0	76.0	4.47
PA2-25A	94.41	0.16	0.849	0.007	0.033	0.005	0.00	0.08	0.0011	0.0016	110.784	1.107	99.7	97.9	3.95
PA2-26A	28.17	0.15	0.273	0.005	0.011	0.006	0.00	0.08	0.0000	0.0011	105.340	2.261	102.1	93.2	4.14

PA2-28A	15.46	0.08	0.297	0.005	0.004	0.004	0.07	0.07	0.0000	0.0013	52.830	1.596	101.4	47.3	2.35
PA2-29A	6.75	0.06	0.103	0.004	0.000	0.005	0.06	0.08	0.0000	0.0011	66.288	4.371	100.8	59.0	4.50
PA2-30A	87.78	0.12	0.453	0.004	0.002	0.006	0.09	0.10	0.0000	0.0015	194.300	2.196	100.3	168.3	6.71
PA2-32A	57.76	0.15	0.771	0.006	0.005	0.007	0.00	0.09	0.0019	0.0007	74.151	0.666	99.0	66.1	2.67
PA2-33A	65.30	0.20	0.694	0.006	0.007	0.006	0.04	0.09	0.0014	0.0008	93.539	0.961	99.4	83.0	3.36
PA2-35A	70.06	0.12	0.800	0.007	0.019	0.005	0.00	0.08	0.0075	0.0014	84.819	0.923	96.8	75.4	3.07
PA2-38A	24.52	0.17	0.360	0.006	0.000	0.006	0.00	0.09	0.0050	0.0020	64.287	2.033	94.3	57.4	2.89
PA2-41A	23.69	0.16	0.223	0.004	0.000	0.004	0.08	0.10	0.0015	0.0016	104.251	3.104	98.1	92.0	4.50
PA2-42A	37.00	0.20	0.417	0.006	0.010	0.007	0.00	0.09	0.0033	0.0013	86.366	1.645	97.3	76.8	3.34
PA2-45A	54.95	0.12	0.306	0.005	0.000	0.006	0.00	0.08	0.0038	0.0014	175.848	3.105	98.0	153.0	6.44
PA2-46A	112.83	0.17	0.638	0.006	0.018	0.006	0.00	0.08	0.0070	0.0020	173.271	2.083	98.0	150.9	6.07
PA2-48A	23.21	0.16	0.386	0.005	0.008	0.005	0.00	0.09	0.0049	0.0012	56.388	1.203	93.7	50.5	2.26
PA2-49A	35.44	0.08	0.373	0.005	0.000	0.005	0.14	0.08	0.0018	0.0007	93.533	1.425	98.5	83.0	3.49
PA2-50A	27.53	0.16	0.326	0.005	0.012	0.005	0.16	0.08	0.0034	0.0014	81.497	1.896	96.4	72.5	3.30
PA2-51A	64.98	0.12	0.379	0.004	0.009	0.006	0.00	0.10	0.0015	0.0008	170.224	2.026	99.3	148.3	5.97
PA2-52A	53.20	0.12	0.770	0.007	0.014	0.005	0.00	0.09	0.0029	0.0015	67.945	0.876	98.4	60.7	2.52
PA2-53A	16.41	0.08	0.183	0.004	0.007	0.004	0.10	0.19	0.0020	0.0016	86.552	3.181	96.5	77.0	4.10
PA2-54A	9.08	0.06	0.163	0.004	0.003	0.004	0.00	0.18	0.0032	0.0015	49.891	2.953	89.6	45.0	3.16
PA2-55A	10.28	0.07	0.167	0.004	0.011	0.004	0.00	0.16	0.0017	0.0012	58.604	2.617	95.0	52.0	3.11
PA2-56A	22.09	0.16	0.308	0.004	0.002	0.005	0.00	0.19	0.0022	0.0013	69.552	1.672	97.0	62.1	2.86
PA2-57A	98.20	0.30	1.279	0.008	0.020	0.005	0.00	0.17	0.0048	0.0014	75.697	0.622	98.6	67.5	2.72
PA2-58A	23.41	0.19	0.353	0.005	0.003	0.005	0.28	0.12	0.0023	0.0012	64.422	1.452	97.1	57.6	2.61
PA2-59A	29.24	0.19	0.186	0.004	0.000	0.005	0.15	0.16	0.0026	0.0011	153.322	3.796	97.4	134.0	6.10
PA2-61A	30.94	0.10	0.458	0.005	0.016	0.007	0.00	0.19	0.0030	0.0012	65.410	1.147	97.0	58.4	2.52
PA2-62A	51.81	0.11	0.356	0.004	0.017	0.005	0.15	0.17	0.0034	0.0012	142.680	2.091	98.1	125.1	5.17
PA2-63A	39.19	0.09	0.498	0.004	0.004	0.003	0.30	0.18	0.0000	0.0010	78.751	0.917	100.1	70.1	2.88
PA2-64A	34.93	0.13	0.236	0.004	0.009	0.005	0.48	0.12	0.0000	0.0010	149.391	3.005	100.9	131.0	5.67
PA2-65A	45.06	0.10	0.437	0.006	0.005	0.006	0.00	0.20	0.0036	0.0012	100.630	1.607	97.6	89.1	3.76
PA2-66A	12.23	0.09	0.228	0.004	0.001	0.005	0.00	0.18	0.0004	0.0016	53.130	2.311	99.1	48.0	2.78
PA2-68A	42.44	0.19	0.462	0.005	0.008	0.006	0.25	0.13	0.0047	0.0012	88.839	1.392	96.8	78.9	3.33

PA2-69A	26.89	0.15	0.330	0.003	0.000	0.006	0.00	0.17	0.0000	0.0011	81.752	1.419	100.4	72.8	3.12
PA2-71A	20.38	0.12	0.315	0.005	0.009	0.006	0.10	0.15	0.0025	0.0016	62.291	1.799	96.4	55.7	2.71
PA2-72A	17.19	0.07	0.355	0.004	0.001	0.005	0.00	0.16	0.0008	0.0014	47.738	1.311	98.6	42.8	2.06
PA2-73A	57.41	0.10	0.230	0.004	0.007	0.006	0.40	0.16	0.0023	0.0016	246.760	4.988	98.9	211.0	8.96
PA2-74A	16.24	0.08	0.239	0.005	0.001	0.005	0.00	0.19	0.0015	0.0016	66.158	2.405	97.3	59.0	3.15
PA2-76A	36.17	0.14	0.639	0.006	0.005	0.005	0.00	0.16	0.0003	0.0010	56.449	0.745	99.7	50.5	2.11
PA2-77A	32.18	0.14	0.387	0.005	0.004	0.006	0.00	0.18	0.0015	0.0016	81.985	1.650	98.6	73.0	3.21
PA2-78A	59.50	0.16	0.324	0.005	0.000	0.005	0.04	0.15	0.0000	0.0015	184.335	3.228	100.3	160.0	6.71
PA2-82A	39.30	0.20	0.473	0.004	0.018	0.006	0.10	0.17	0.0043	0.0014	80.535	1.245	96.8	71.7	3.03
PA2-83A	17.19	0.08	0.306	0.004	0.010	0.006	0.00	0.18	0.0031	0.0016	53.288	1.680	94.7	47.8	2.41
PA2-86A	16.71	0.07	0.115	0.003	0.000	0.004	0.00	0.19	0.0009	0.0016	143.160	5.981	98.3	126.0	7.03
PA2-87A	14.47	0.08	0.160	0.004	0.000	0.006	0.57	0.19	0.0036	0.0007	84.203	2.378	92.9	75.0	3.60
PA2-88A	46.13	0.17	0.292	0.004	0.001	0.006	0.10	0.20	0.0000	0.0014	159.178	2.649	100.9	139.0	5.82
PA2-89A	66.85	0.14	0.396	0.005	0.015	0.006	0.00	0.15	0.0019	0.0007	167.307	2.331	99.1	145.9	5.96
PA2-90A	34.88	0.17	0.483	0.005	0.005	0.006	0.28	0.15	0.0045	0.0011	69.537	1.115	96.2	62.1	2.64
PA2-91A	12.19	0.05	0.169	0.004	0.006	0.006	0.30	0.14	0.0036	0.0011	66.150	2.595	91.4	59.0	3.26
PA2-93A	17.87	0.08	0.309	0.005	0.005	0.005	0.00	0.17	0.0039	0.0012	54.164	1.491	93.6	48.5	2.33
PA2-95A	9.46	0.07	0.107	0.003	0.009	0.004	0.09	0.20	0.0000	0.0011	88.869	4.041	100.5	79.0	4.69
PA2-96A	30.14	0.10	0.430	0.005	0.012	0.005	0.32	0.19	0.0018	0.0016	69.016	1.406	98.3	61.6	2.73
PA2-97A	11.75	0.07	0.191	0.004	0.010	0.005	0.00	0.18	0.0025	0.0012	57.357	2.273	93.5	51.0	2.86
PA2-101A	28.96	0.08	0.139	0.003	0.002	0.004	0.20	0.30	0.0012	0.0012	206.020	5.441	98.9	178.0	8.15
PA2-102A	12.62	0.08	0.159	0.003	0.000	0.005	0.00	0.30	0.0000	0.0012	79.862	2.884	100.4	71.0	3.77
PA2-103A	112.32	0.17	0.572	0.004	0.008	0.006	0.00	0.20	0.0066	0.0011	193.069	1.680	98.3	167.3	6.57
PA2-104A	36.45	0.08	0.254	0.004	0.006	0.004	0.00	0.30	0.0017	0.0016	141.131	2.728	98.6	124.0	5.33
PA2-108A	9.50	0.06	0.132	0.004	0.000	0.003	0.40	0.30	0.0031	0.0012	65.308	3.245	90.8	58.0	3.67
PA2-111A	5.98	0.05	0.120	0.003	0.002	0.005	0.10	0.30	0.0007	0.0016	48.037	4.062	96.8	43.0	3.99
Padaung Formation 1 (Oligocene); J-value = 0.000497 ± 0.000020															
PA1-01A	226.50	0.60	1.009	0.015	0.026	0.005	0.32	0.07	0.0220	0.0020	218.186	3.432	97.2	186.0	7.73
PA1-02A	108.90	0.40	1.457	0.019	0.033	0.006	0.07	0.08	0.0260	0.0020	69.434	1.055	92.9	61.2	2.62

PA1-03A	539.60	0.70	5.776	0.016	0.098	0.009	2.43	0.11	0.0410	0.0020	91.373	0.322	97.8	80.1	3.21
PA1-05A	68.20	0.20	0.416	0.008	0.008	0.006	2.40	0.12	0.0147	0.0017	154.634	3.461	93.9	133.0	6.00
PA1-06A	56.10	0.30	0.848	0.014	0.012	0.007	0.96	0.09	0.0160	0.0020	60.660	1.331	91.6	53.5	2.45
PA1-08A	85.10	0.20	0.918	0.006	0.023	0.007	2.45	0.11	0.0211	0.0018	86.254	0.870	92.9	75.7	3.12
PA1-09A	55.61	0.16	0.661	0.005	0.007	0.007	0.34	0.08	0.0109	0.0017	79.375	1.062	94.3	69.8	2.94
PA1-10A	67.20	0.30	0.846	0.008	0.022	0.009	0.09	0.08	0.0190	0.0020	72.806	1.087	91.6	64.1	2.74
PA1-11A	36.51	0.19	0.377	0.007	0.000	0.007	0.12	0.07	0.0088	0.0014	90.037	2.112	92.9	78.9	3.64
PA1-12A	72.10	0.30	0.786	0.007	0.016	0.007	0.63	0.07	0.0190	0.0020	84.615	1.166	92.2	74.3	3.14
PA1-13A	54.63	0.18	0.748	0.006	0.005	0.007	0.13	0.09	0.0088	0.0016	69.575	0.936	95.2	61.3	2.59
PA1-14A	140.50	0.20	1.103	0.007	0.015	0.008	0.51	0.10	0.0180	0.0020	122.681	0.978	96.3	106.7	4.32
PA1-17A	152.20	0.40	0.996	0.007	0.017	0.008	0.57	0.10	0.0284	0.0017	144.402	1.264	94.5	125.0	5.05
PA1-18A	120.75	0.18	0.787	0.008	0.017	0.009	0.02	0.10	0.0131	0.0016	148.465	1.583	96.8	128.4	5.23
PA1-19A	77.70	0.20	0.791	0.006	0.011	0.009	0.20	0.12	0.0060	0.0020	96.144	1.096	97.8	84.2	3.49
PA1-20A	117.31	0.20	0.850	0.007	0.016	0.008	0.63	0.09	0.0121	0.0016	133.863	1.308	97.0	116.1	4.73
PA1-21A	119.40	0.30	0.790	0.008	0.012	0.008	0.43	0.08	0.0060	0.0020	149.129	1.698	98.6	128.9	5.28
PA1-23A	136.70	0.30	0.869	0.006	0.006	0.006	0.82	0.09	0.0269	0.0017	148.248	1.272	94.2	128.2	5.17
PA1-24A	54.00	0.30	0.666	0.006	0.004	0.006	0.00	0.08	0.0200	0.0020	72.011	1.216	89.0	63.4	2.76
PA1-25A	67.00	0.20	0.427	0.005	0.000	0.007	0.00	0.10	0.0062	0.0018	152.533	2.373	97.3	131.7	5.56
PA1-26A	55.80	0.20	0.752	0.006	0.016	0.007	0.06	0.08	0.0086	0.0010	70.805	0.752	95.4	62.4	2.59
PA1-27A	53.50	0.20	0.458	0.005	0.015	0.006	0.07	0.09	0.0007	0.0016	116.263	1.818	99.6	101.3	4.31
PA1-28A	85.80	0.40	0.518	0.006	0.019	0.007	0.68	0.11	0.0067	0.0018	162.031	2.243	97.8	139.6	5.80
PA1-29A	75.60	0.30	0.740	0.007	0.021	0.007	0.00	0.09	0.0162	0.0019	95.652	1.255	93.7	83.7	3.51
PA1-30A	42.19	0.19	0.262	0.005	0.000	0.007	0.00	0.10	0.0055	0.0018	154.759	3.785	96.2	134.0	6.13
PA1-31A	67.61	0.14	0.762	0.006	0.025	0.008	1.44	0.11	0.0115	0.0018	84.576	0.973	95.1	74.2	3.09
PA1-32A	30.44	0.13	0.402	0.006	0.005	0.006	0.45	0.10	0.0090	0.0017	69.233	1.671	91.4	61.0	2.85
PA1-33A	90.00	0.30	0.615	0.005	0.017	0.007	0.00	0.08	0.0075	0.0020	142.822	1.653	97.5	123.6	5.08
PA1-34A	127.19	0.16	0.683	0.007	0.006	0.006	0.00	0.09	0.0109	0.0016	181.360	2.014	97.5	155.6	6.32
PA1-36A	176.70	0.30	2.198	0.009	0.014	0.008	0.00	0.09	0.0101	0.0014	79.014	0.414	98.3	69.4	2.81
PA1-37A	67.00	0.20	0.447	0.006	0.010	0.009	0.18	0.09	0.0055	0.0015	146.256	2.451	97.6	126.0	5.40
PA1-38A	89.20	0.30	0.440	0.006	0.006	0.009	0.06	0.11	0.0110	0.0020	195.263	3.395	96.2	167.0	7.09

PA1-39A	41.30	0.20	0.405	0.007	0.010	0.009	0.08	0.08	0.0050	0.0020	98.341	2.411	96.4	86.0	4.00
PA1-40A	103.70	0.30	1.077	0.008	0.011	0.010	0.00	0.08	0.0018	0.0018	95.836	0.918	99.5	83.9	3.44
PA1-41A	81.00	0.20	0.913	0.006	0.020	0.009	0.00	0.08	0.0031	0.0017	87.795	0.884	98.9	77.0	3.17
PA1-42A	20.13	0.16	0.443	0.006	0.017	0.007	0.25	0.08	0.0070	0.0020	40.736	1.515	89.7	36.1	1.98
PA1-43A	55.22	0.18	0.578	0.005	0.012	0.006	0.20	0.08	0.0056	0.0015	92.705	1.199	97.0	81.2	3.41
PA1-45A	116.59	0.16	0.787	0.006	0.036	0.007	0.32	0.06	0.0092	0.0020	144.713	1.389	97.7	125.2	5.08
PA1-46A	32.14	0.14	0.331	0.005	0.012	0.008	0.28	0.10	0.0064	0.0017	91.593	2.171	94.2	80.2	3.71
PA1-50A	38.20	0.20	0.241	0.006	0.004	0.006	0.24	0.09	0.0068	0.0014	150.387	4.564	94.8	130.0	6.38
PA1-51A	41.70	0.20	0.456	0.006	0.003	0.006	0.03	0.08	0.0050	0.0020	88.611	1.831	96.7	77.7	3.48
PA1-52A	47.92	0.18	0.593	0.006	0.005	0.008	0.10	0.09	0.0042	0.0014	78.698	1.173	97.4	69.2	2.95
PA1-54A	44.43	0.10	0.633	0.005	0.016	0.005	0.34	0.19	0.0101	0.0015	65.582	0.920	93.4	57.8	2.46
PA1-55A	41.23	0.10	0.385	0.005	0.007	0.006	0.00	0.20	0.0015	0.0014	105.961	1.697	98.9	92.5	3.96
PA1-56A	49.26	0.09	0.553	0.006	0.011	0.005	0.45	0.17	0.0024	0.0015	87.963	1.234	98.7	77.1	3.26
PA1-57A	27.63	0.15	0.392	0.005	0.002	0.005	0.27	0.14	0.0020	0.0014	68.949	1.462	97.9	60.7	2.75
PA1-58A	28.89	0.07	0.175	0.003	0.000	0.004	0.00	0.20	0.0010	0.0012	163.606	3.807	99.0	141.0	6.38
PA1-59A	24.37	0.10	0.298	0.004	0.003	0.005	0.70	0.20	0.0064	0.0009	75.615	1.451	92.4	66.5	2.95
PA1-60A	17.31	0.08	0.225	0.004	0.003	0.005	0.38	0.17	0.0002	0.0012	76.946	2.117	99.9	67.6	3.27
PA1-61A	59.42	0.11	0.720	0.006	0.016	0.006	0.00	0.18	0.0048	0.0009	80.525	0.791	97.6	70.7	2.92
PA1-62A	23.56	0.09	0.303	0.004	0.007	0.006	0.15	0.19	0.0030	0.0015	74.949	1.860	96.3	65.9	3.10
PA1-64A	35.02	0.09	0.474	0.005	0.011	0.005	0.00	0.20	0.0026	0.0014	72.243	1.195	97.8	63.6	2.76
PA1-65A	29.21	0.08	0.367	0.005	0.016	0.005	0.22	0.17	0.0011	0.0012	78.871	1.427	99.0	69.3	3.04
PA1-66A	16.33	0.05	0.180	0.004	0.010	0.004	0.28	0.17	0.0019	0.0016	87.783	3.216	96.7	77.0	4.14
PA1-68A	60.14	0.12	0.728	0.006	0.022	0.005	0.26	0.17	0.0032	0.0012	81.380	0.893	98.5	71.5	2.97
PA1-69A	27.18	0.09	0.368	0.006	0.003	0.006	1.47	0.20	0.0100	0.0016	66.306	1.668	89.6	58.4	2.76
PA1-70A	56.44	0.10	0.593	0.005	0.012	0.005	0.42	0.15	0.0027	0.0014	94.024	1.104	98.7	82.3	3.42
PA1-71A	25.79	0.08	0.275	0.004	0.005	0.006	0.60	0.16	0.0040	0.0011	89.828	1.938	95.6	78.7	3.56
PA1-73A	28.79	0.17	0.425	0.005	0.020	0.005	0.02	0.18	0.0041	0.0009	64.907	1.095	95.8	57.2	2.49
PA1-74A	38.53	0.14	0.426	0.004	0.014	0.006	0.09	0.15	0.0026	0.0011	88.648	1.188	98.0	77.7	3.27
PA1-75A	52.76	0.10	0.296	0.004	0.011	0.005	0.00	0.15	0.0078	0.0012	170.343	2.623	95.6	146.0	6.15
PA1-76A	22.92	0.07	0.286	0.004	0.010	0.006	0.06	0.19	0.0043	0.0010	75.770	1.549	94.4	66.6	2.99

PA1-77A	14.66	0.06	0.160	0.004	0.000	0.006	0.02	0.17	0.0000	0.0014	93.436	3.524	102.2	82.0	4.45
PA1-78A	26.60	0.20	0.378	0.005	0.000	0.005	0.00	0.18	0.0050	0.0008	66.455	1.278	94.4	58.6	2.60
PA1-79A	27.99	0.09	0.357	0.004	0.011	0.006	0.00	0.16	0.0024	0.0014	76.340	1.519	97.3	67.1	3.00
PA1-80A	42.77	0.10	0.162	0.004	0.003	0.005	0.00	0.20	0.0015	0.0014	261.975	6.738	99.0	221.0	10.03
PA1-83A	14.27	0.07	0.210	0.003	0.009	0.006	0.05	0.19	0.0018	0.0010	65.371	1.838	96.3	57.6	2.81
PA1-84A	64.89	0.10	0.837	0.006	0.010	0.004	0.22	0.19	0.0024	0.0014	76.680	0.785	98.9	67.4	2.79
PA1-85A	14.31	0.07	0.230	0.004	0.012	0.004	0.04	0.19	0.0024	0.0011	59.000	1.777	95.0	52.1	2.61
PA1-93A	49.79	0.13	0.330	0.005	0.005	0.005	0.00	0.20	0.0047	0.0009	146.602	2.378	97.2	126.8	5.39
PA1-100A	28.76	0.15	0.228	0.005	0.003	0.003	0.00	0.18	0.0013	0.0014	124.290	3.278	98.6	108.0	5.10
PA1-101A	37.14	0.15	0.354	0.004	0.011	0.004	0.40	0.20	0.0026	0.0015	103.009	1.814	98.0	90.0	3.91
PA1-102A	47.24	0.16	0.322	0.004	0.004	0.005	0.50	0.20	0.0040	0.0011	143.349	2.173	97.5	124.1	5.23
PA1-104A	20.04	0.08	0.093	0.004	0.003	0.007	0.00	0.30	0.0014	0.0018	210.585	10.985	97.9	179.0	11.32
PA1-105A	14.11	0.08	0.257	0.005	0.009	0.007	0.90	0.20	0.0017	0.0008	53.398	1.413	97.0	47.2	2.27
PA1-108A	12.56	0.09	0.161	0.003	0.005	0.005	0.10	0.20	0.0023	0.0012	73.658	2.857	94.5	65.0	3.59
PA1-117A	22.28	0.08	0.114	0.004	0.021	0.006	0.00	0.20	0.0037	0.0013	185.375	7.435	95.0	159.0	8.71
PA1-118A	26.61	0.16	0.143	0.003	0.004	0.004	0.00	0.20	0.0047	0.0007	176.480	4.687	94.8	152.0	7.09
PA1-120A	22.66	0.14	0.221	0.004	0.007	0.005	0.10	0.20	0.0042	0.0014	96.955	2.844	94.5	85.0	4.17
PA1-121A	14.20	0.08	0.090	0.003	0.000	0.005	0.50	0.30	0.0000	0.0017	160.969	7.896	101.9	139.0	8.53
PA1-122A	9.16	0.08	0.057	0.003	0.003	0.005	0.20	0.20	0.0015	0.0016	152.047	11.445	95.3	131.0	10.85
PA1-125A	9.51	0.07	0.046	0.003	0.000	0.004	0.20	0.20	0.0039	0.0012	180.933	14.493	88.1	155.0	13.38
PA1-129A	17.04	0.06	0.298	0.005	0.003	0.006	0.00	0.20	0.0024	0.0012	54.702	1.549	95.8	48.4	2.37
PA1-131A	83.70	0.20	0.158	0.004	0.007	0.004	0.00	0.20	0.0007	0.0013	528.217	13.502	99.7	420.0	18.08
PA1-132A	26.27	0.08	0.341	0.005	0.005	0.005	0.00	0.30	0.0029	0.0009	74.404	1.327	96.7	65.5	2.87
PA1-133A	27.00	0.20	0.169	0.004	0.002	0.005	0.00	0.20	0.0018	0.0016	156.467	4.805	98.0	135.0	6.65
PA1-135A	14.96	0.07	0.222	0.004	0.000	0.003	0.00	0.20	0.0005	0.0009	66.376	1.774	98.8	58.5	2.81
PA1-136A	41.86	0.16	0.549	0.005	0.003	0.004	0.00	0.20	0.0010	0.0014	75.659	1.065	99.3	66.5	2.83
PA1-137A	18.73	0.12	0.205	0.004	0.012	0.005	0.70	0.20	0.0034	0.0016	86.955	2.978	94.9	76.0	3.98
PA1-138A	49.18	0.10	0.317	0.004	0.013	0.005	0.00	0.20	0.0069	0.0010	148.381	2.010	95.8	128.3	5.33
PA1-140A	12.91	0.08	0.149	0.003	0.000	0.006	0.20	0.30	0.0049	0.0014	77.156	3.313	88.9	68.0	3.95
PA1-141A	29.32	0.14	0.190	0.004	0.000	0.006	0.50	0.20	0.0028	0.0014	150.114	3.774	97.3	130.0	6.01

PA1-143A	37.73	0.08	0.248	0.004	0.000	0.005	0.40	0.30	0.0045	0.0012	147.171	2.628	96.6	127.0	5.48
PA1-144A	308.70	0.60	5.519	0.015	0.078	0.008	0.10	0.30	0.0284	0.0015	54.416	0.205	97.3	48.1	1.95
PA1-145A	75.96	0.15	0.480	0.005	0.007	0.006	0.00	0.20	0.0095	0.0015	152.125	1.992	96.2	131.4	5.44
PA1-146A	36.71	0.09	0.478	0.004	0.015	0.006	0.30	0.20	0.0000	0.0009	77.288	0.955	100.5	68.0	2.85
PA1-147A	10.14	0.06	0.137	0.003	0.008	0.005	0.00	0.30	0.0002	0.0009	73.427	2.662	99.4	65.0	3.47
PA1-149A	14.01	0.08	0.167	0.003	0.001	0.005	0.60	0.30	0.0052	0.0013	75.090	2.817	89.4	66.0	3.60
PA1-152A	32.77	0.09	0.220	0.004	0.007	0.006	0.20	0.30	0.0049	0.0017	142.375	3.417	95.6	123.0	5.65
PA1-154A	8.80	0.06	0.112	0.004	0.002	0.006	0.10	0.20	0.0009	0.0014	76.296	4.437	97.0	67.0	4.68
PA1-156A	25.16	0.10	0.296	0.004	0.004	0.006	0.00	0.30	0.0036	0.0009	81.301	1.507	95.7	71.4	3.14
Shwetaung Formation (Early Miocene); J-value = 0.000490 ± 0.000014															
SHW-03A	107.17	0.15	2.343	0.011	0.041	0.005	0.48	0.11	0.0380	0.0020	40.944	0.342	89.5	35.8	1.06
SHW-04A	101.64	0.14	2.268	0.007	0.035	0.006	0.18	0.08	0.0114	0.0013	43.329	0.230	96.7	37.9	1.10
SHW-05A	43.46	0.10	0.914	0.007	0.025	0.006	0.00	0.10	0.0118	0.0018	43.715	0.681	92.0	38.2	1.24
SHW-07A	47.14	0.16	1.433	0.007	0.020	0.007	0.19	0.08	0.0051	0.0012	31.873	0.319	96.8	28.0	0.84
SHW-08A	105.94	0.18	3.142	0.011	0.044	0.007	0.18	0.10	0.0052	0.0015	33.234	0.197	98.6	29.1	0.85
SHW-13A	44.80	0.20	1.188	0.008	0.020	0.007	0.00	0.12	0.0084	0.0017	35.560	0.521	94.4	31.2	1.00
SHW-14A	112.31	0.20	2.405	0.010	0.046	0.008	0.00	0.13	0.0080	0.0020	45.641	0.326	97.8	39.9	1.17
SHW-18A	99.00	0.30	2.396	0.011	0.031	0.008	0.00	0.13	0.0070	0.0020	40.424	0.361	97.8	35.4	1.05
SHW-19A	75.60	0.20	1.646	0.009	0.014	0.006	0.00	0.08	0.0150	0.0010	43.225	0.328	94.1	37.8	1.11
SHW-21A	60.59	0.20	1.724	0.008	0.023	0.008	0.22	0.09	0.0186	0.0018	31.966	0.373	91.0	28.0	0.86
SHW-22A	119.00	0.30	2.615	0.010	0.031	0.007	0.16	0.08	0.0155	0.0019	43.738	0.301	96.2	38.2	1.12
SHW-23A	51.45	0.20	1.155	0.008	0.022	0.010	0.25	0.09	0.0118	0.0015	41.574	0.502	93.3	36.4	1.12
SHW-24A	279.00	0.70	2.382	0.012	0.033	0.009	0.00	0.07	0.0140	0.0020	115.332	0.730	98.5	99.2	2.84
SHW-27A	149.59	0.18	2.158	0.010	0.031	0.012	0.46	0.10	0.0226	0.0015	66.263	0.405	95.6	57.6	1.67
SHW-29A	48.00	0.20	1.267	0.007	0.021	0.008	0.05	0.09	0.0040	0.0020	37.105	0.561	97.8	32.5	1.05
SHW-30A	32.81	0.14	0.724	0.006	0.010	0.008	0.13	0.09	0.0100	0.0015	41.243	0.733	91.1	36.1	1.21
SHW-31A	60.40	0.20	1.134	0.008	0.017	0.008	0.13	0.11	0.0003	0.0014	53.184	0.553	99.9	46.4	1.40
SHW-32A	68.99	0.15	1.546	0.010	0.024	0.008	0.21	0.10	0.0240	0.0019	40.055	0.457	89.7	35.0	1.07
SHW-33A	53.10	0.30	1.902	0.009	0.031	0.008	0.00	0.10	0.0062	0.0018	26.962	0.345	96.5	23.7	0.74

SHW-34A	14.28	0.12	0.301	0.005	0.000	0.008	0.00	0.11	0.0000	0.0019	48.958	2.107	103.2	42.8	2.19
SHW-35A	98.90	0.30	2.356	0.010	0.018	0.009	0.00	0.09	0.0065	0.0018	41.159	0.314	98.0	36.0	1.06
SHW-36A	103.30	0.20	3.438	0.010	0.042	0.008	0.31	0.09	0.0098	0.0020	29.228	0.205	97.2	25.7	0.75
SHW-37A	77.60	0.20	0.879	0.006	0.022	0.007	0.30	0.08	0.0100	0.0017	84.869	0.908	96.2	73.5	2.21
SHW-38A	57.75	0.13	0.731	0.006	0.017	0.006	0.10	0.10	0.0040	0.0016	77.346	0.905	97.9	67.1	2.04
SHW-39A	113.52	0.15	2.617	0.012	0.043	0.008	0.26	0.12	0.0062	0.0016	42.688	0.281	98.4	37.3	1.09
SHW-40A	77.59	0.15	1.844	0.008	0.017	0.007	0.19	0.10	0.0126	0.0018	40.059	0.351	95.2	35.0	1.04
SHW-44A	60.80	0.20	0.801	0.007	0.029	0.008	0.17	0.09	0.0100	0.0020	72.418	1.097	95.4	62.9	2.01
SHW-45A	60.60	0.30	1.515	0.009	0.020	0.008	0.31	0.09	0.0130	0.0020	37.561	0.528	93.8	32.9	1.04
SHW-47A	59.10	0.20	1.212	0.007	0.009	0.008	0.14	0.10	0.0019	0.0017	48.329	0.538	99.1	42.2	1.29
SHW-48A	64.37	0.15	1.357	0.008	0.017	0.006	0.27	0.11	0.0039	0.0017	46.616	0.493	98.2	40.7	1.23
SHW-49A	19.66	0.18	0.551	0.007	0.008	0.008	0.00	0.13	0.0018	0.0020	34.666	1.203	97.1	30.4	1.36
SHW-50A	34.79	0.19	0.778	0.008	0.008	0.007	0.00	0.10	0.0012	0.0017	44.260	0.836	99.0	38.7	1.32
SHW-51A	30.73	0.14	0.711	0.006	0.006	0.005	0.16	0.09	0.0012	0.0013	42.711	0.691	98.9	37.4	1.22
SHW-52A	31.99	0.18	1.064	0.006	0.008	0.007	0.27	0.10	0.0076	0.0008	27.975	0.328	93.1	24.6	0.76
SHW-53A	39.33	0.08	1.349	0.006	0.004	0.006	0.24	0.14	0.0084	0.0014	27.321	0.339	93.7	24.0	0.75
SHW-54A	41.96	0.11	0.999	0.007	0.001	0.005	0.05	0.13	0.0067	0.0017	40.023	0.585	95.3	35.0	1.12
SHW-55A	162.90	0.40	3.160	0.013	0.037	0.006	0.00	0.11	0.0072	0.0014	50.870	0.280	98.7	44.4	1.28
SHW-57A	38.31	0.09	0.865	0.006	0.007	0.005	0.00	0.13	0.0052	0.0012	42.512	0.520	96.0	37.2	1.15
SHW-58A	32.24	0.18	1.383	0.006	0.016	0.005	0.00	0.14	0.0031	0.0017	22.650	0.403	97.1	19.9	0.67
SHW-59A	47.42	0.10	1.069	0.007	0.016	0.004	0.01	0.13	0.0050	0.0012	42.974	0.455	96.8	37.6	1.14
SHW-60A	25.68	0.07	0.546	0.005	0.004	0.005	0.00	0.12	0.0023	0.0007	45.764	0.580	97.4	40.0	1.24
SHW-61A	62.92	0.11	1.404	0.008	0.026	0.005	0.00	0.13	0.0016	0.0011	44.471	0.362	99.2	38.9	1.15
SHW-62A	47.64	0.16	1.092	0.006	0.019	0.005	0.09	0.13	0.0057	0.0011	42.084	0.413	96.5	36.8	1.11
SHW-64A	31.22	0.08	0.672	0.005	0.009	0.004	0.09	0.11	0.0028	0.0007	45.279	0.467	97.4	39.6	1.20
SHW-65A	22.13	0.08	0.506	0.005	0.008	0.006	0.02	0.12	0.0013	0.0016	43.017	1.076	98.3	37.6	1.42
SHW-66A	45.82	0.09	1.090	0.007	0.014	0.005	0.00	0.11	0.0000	0.0016	42.290	0.518	100.7	37.0	1.14
SHW-67A	67.00	0.20	1.244	0.007	0.018	0.006	0.00	0.12	0.0036	0.0017	53.063	0.546	98.4	46.3	1.40
SHW-68A	52.15	0.10	1.254	0.007	0.019	0.004	0.40	0.13	0.0031	0.0007	40.881	0.298	98.3	35.8	1.05
SHW-69A	22.91	0.13	0.962	0.006	0.012	0.005	0.17	0.15	0.0021	0.0015	23.184	0.505	97.3	20.4	0.73

SHW-70A	222.00	0.50	1.073	0.007	0.027	0.005	0.04	0.14	0.0164	0.0020	202.341	1.505	97.8	170.5	4.83
SHW-71A	35.55	0.08	0.701	0.006	0.000	0.006	0.18	0.16	0.0002	0.0016	50.646	0.791	99.9	44.2	1.43
SHW-72A	94.32	0.17	0.671	0.005	0.004	0.006	0.10	0.16	0.0000	0.0015	140.848	1.215	100.3	120.4	3.50
SHW-73A	25.61	0.09	0.680	0.005	0.007	0.006	0.04	0.13	0.0052	0.0014	35.401	0.691	94.0	31.0	1.07
SHW-74A	34.87	0.10	0.422	0.005	0.009	0.006	0.00	0.13	0.0025	0.0008	80.889	1.100	97.9	70.1	2.19
SHW-75A	10.56	0.06	0.196	0.003	0.000	0.005	0.00	0.13	0.0000	0.0014	54.455	2.331	101.4	47.0	2.42
SHW-76A	34.56	0.10	0.913	0.008	0.023	0.004	0.00	0.13	0.0096	0.0018	34.730	0.661	91.7	30.4	1.04
SHW-77A	22.93	0.14	0.329	0.004	0.010	0.004	0.00	0.15	0.0003	0.0012	69.290	1.434	99.6	60.2	2.10
SHW-78A	19.06	0.10	0.434	0.004	0.000	0.005	0.22	0.14	0.0000	0.0010	44.937	0.858	102.2	39.3	1.34
SHW-79A	38.54	0.08	0.952	0.005	0.007	0.006	0.00	0.11	0.0042	0.0012	39.185	0.454	96.8	34.3	1.05
SHW-82A	58.37	0.12	1.083	0.008	0.015	0.005	0.65	0.14	0.0059	0.0014	52.353	0.551	97.1	45.7	1.38
SHW-84A	14.98	0.09	0.371	0.005	0.008	0.006	0.00	0.11	0.0001	0.0012	40.254	1.150	99.8	35.2	1.41
SHW-85A	21.23	0.16	0.514	0.005	0.003	0.006	0.00	0.11	0.0039	0.0015	39.054	0.989	94.6	34.2	1.30
SHW-86A	14.52	0.09	0.316	0.005	0.001	0.005	0.16	0.15	0.0022	0.0013	43.851	1.439	95.5	38.3	1.66
SHW-87A	39.90	0.20	0.970	0.007	0.027	0.006	0.13	0.14	0.0078	0.0012	38.755	0.537	94.2	33.9	1.07
SHW-88A	313.20	0.60	0.916	0.007	0.021	0.006	0.00	0.16	0.0033	0.0013	340.882	2.673	99.7	278.0	7.69
SHW-90A	27.62	0.10	0.598	0.006	0.008	0.005	0.00	0.14	0.0012	0.0017	45.527	0.960	98.6	39.8	1.40
SHW-91A	22.28	0.07	0.567	0.006	0.008	0.006	0.24	0.14	0.0035	0.0017	37.532	0.979	95.4	32.9	1.26
SHW-92A	42.70	0.12	0.955	0.008	0.009	0.008	0.00	0.15	0.0022	0.0018	44.033	0.707	98.5	38.5	1.25
SHW-93A	22.21	0.14	0.529	0.006	0.010	0.007	0.33	0.13	0.0030	0.0018	40.363	1.149	96.2	35.3	1.42
SHW-95A	32.61	0.08	0.804	0.007	0.017	0.005	0.11	0.12	0.0063	0.0018	38.232	0.743	94.3	33.5	1.15
SHW-96A	28.29	0.08	0.565	0.006	0.015	0.005	0.00	0.12	0.0062	0.0018	46.787	1.055	93.5	40.9	1.48
SHW-97A	27.15	0.07	0.702	0.006	0.000	0.006	0.00	0.13	0.0018	0.0008	37.876	0.472	97.9	33.2	1.03
SHW-98A	10.94	0.09	0.246	0.004	0.000	0.005	0.05	0.12	0.0018	0.0012	42.293	1.712	95.1	37.0	1.82
SHW-99A	42.92	0.10	1.051	0.008	0.023	0.004	0.10	0.13	0.0049	0.0012	39.459	0.479	96.6	34.5	1.07
SHW-100A	6.09	0.05	0.161	0.003	0.000	0.005	0.13	0.11	0.0006	0.0014	36.719	2.777	97.2	32.0	2.58
SHW-101A	29.92	0.09	0.669	0.005	0.006	0.005	0.00	0.20	0.0000	0.0014	45.158	0.732	101.0	39.5	1.29
SHW-102A	141.52	0.15	3.094	0.010	0.061	0.008	0.00	0.20	0.0351	0.0016	42.397	0.215	92.7	37.1	1.07
SHW-103A	30.89	0.13	0.715	0.006	0.017	0.005	0.00	0.20	0.0019	0.0011	42.369	0.615	98.1	37.1	1.18
SHW-104A	22.04	0.14	0.619	0.005	0.015	0.006	0.00	0.30	0.0020	0.0015	34.600	0.817	97.2	30.3	1.12

SHW-106A	21.80	0.15	0.507	0.006	0.002	0.006	0.00	0.20	0.0033	0.0012	41.053	0.902	95.5	35.9	1.29
SHW-107A	52.71	0.11	0.920	0.007	0.005	0.007	0.00	0.18	0.0010	0.0017	56.911	0.709	99.4	49.6	1.53
SHW-108A	40.67	0.10	0.643	0.006	0.006	0.007	0.40	0.20	0.0083	0.0011	59.547	0.775	94.1	51.9	1.61
SHW-109A	19.74	0.13	0.715	0.005	0.017	0.008	0.20	0.30	0.0052	0.0016	25.496	0.719	92.3	22.4	0.90
SHW-110A	73.17	0.11	1.708	0.008	0.037	0.005	0.10	0.20	0.0065	0.0012	41.730	0.303	97.4	36.5	1.07
SHW-111A	55.72	0.11	1.385	0.009	0.022	0.006	0.10	0.20	0.0072	0.0012	38.681	0.372	96.2	33.9	1.02
SHW-112A	27.45	0.17	0.716	0.007	0.012	0.006	0.00	0.20	0.0086	0.0017	34.755	0.823	90.7	30.4	1.13
SHW-113A	19.46	0.09	0.475	0.005	0.000	0.008	0.00	0.20	0.0003	0.0016	40.781	1.129	99.5	35.7	1.41
SHW-115A	72.09	0.12	1.617	0.006	0.017	0.005	0.15	0.19	0.0053	0.0011	43.619	0.278	97.8	38.1	1.11
SHW-116A	48.34	0.18	1.135	0.008	0.016	0.007	0.50	0.19	0.0164	0.0012	38.367	0.453	90.0	33.6	1.03
SHW-118A	45.65	0.08	0.997	0.007	0.018	0.006	0.20	0.20	0.0034	0.0017	44.820	0.597	97.8	39.2	1.23
SHW-119A	12.27	0.07	0.310	0.004	0.002	0.006	0.00	0.20	0.0000	0.0015	40.651	1.545	102.8	35.6	1.68
SHW-120A	11.61	0.08	0.274	0.004	0.002	0.006	0.00	0.20	0.0010	0.0016	41.132	1.823	97.2	36.0	1.88
SHW-121A	35.30	0.12	0.793	0.007	0.018	0.005	0.00	0.20	0.0013	0.0014	43.990	0.667	98.9	38.5	1.24
SHW-122A	75.65	0.13	1.069	0.006	0.028	0.006	0.00	0.20	0.0040	0.0012	69.669	0.563	98.4	60.5	1.78
SHW-123A	21.53	0.15	0.462	0.005	0.010	0.006	0.00	0.20	0.0008	0.0012	46.080	0.996	98.9	40.3	1.43
SHW-124A	16.36	0.08	0.329	0.004	0.001	0.005	0.00	0.20	0.0035	0.0013	46.546	1.343	93.6	40.7	1.64
SHW-125A	50.47	0.12	1.102	0.008	0.017	0.006	0.00	0.30	0.0042	0.0015	44.613	0.527	97.5	39.0	1.20
SHW-126A	255.60	0.70	1.115	0.008	0.019	0.005	0.30	0.20	0.0058	0.0012	227.832	1.887	99.3	190.9	5.42
SHW-127A	49.60	0.10	0.876	0.006	0.007	0.005	0.80	0.20	0.0033	0.0006	55.611	0.464	98.2	48.5	1.43
SHW-128A	45.76	0.16	0.761	0.006	0.004	0.005	0.53	0.20	0.0025	0.0011	59.275	0.673	98.5	51.6	1.57
SHW-129A	47.88	0.10	0.595	0.005	0.019	0.004	0.00	0.19	0.0034	0.0017	78.755	1.088	97.9	68.3	2.14
SHW-130A	51.24	0.12	1.184	0.006	0.017	0.005	0.30	0.30	0.0039	0.0007	42.322	0.309	97.8	37.0	1.09
SHW-131A	20.28	0.07	0.422	0.005	0.002	0.006	0.10	0.20	0.0060	0.0008	43.942	0.775	91.4	38.4	1.28
SHW-133A	165.10	0.30	0.957	0.007	0.017	0.005	0.40	0.20	0.0172	0.0019	167.219	1.363	96.9	142.0	4.08
SHW-134A	47.32	0.10	1.359	0.007	0.014	0.005	0.00	0.30	0.0082	0.0016	33.045	0.394	94.9	29.0	0.89
SHW-136A	27.43	0.11	0.627	0.005	0.003	0.006	0.00	0.20	0.0020	0.0007	42.733	0.522	97.7	37.4	1.16
SHW-138A	75.79	0.11	0.842	0.006	0.016	0.006	0.00	0.20	0.0024	0.0011	89.124	0.786	99.0	77.1	2.27
SHW-140A	35.76	0.09	0.688	0.006	0.010	0.005	0.00	0.20	0.0022	0.0013	50.862	0.742	98.0	44.4	1.41
SHW-141A	98.52	0.14	1.319	0.007	0.015	0.006	0.00	0.20	0.0069	0.0013	73.104	0.513	97.9	63.5	1.85

SHW-142A	32.29	0.15	0.713	0.006	0.009	0.008	0.10	0.30	0.0003	0.0016	45.203	0.817	99.8	39.5	1.33
SHW-143A	31.89	0.08	0.555	0.004	0.000	0.005	0.00	0.20	0.0044	0.0007	55.034	0.562	95.9	48.0	1.44
SHW-144A	13.18	0.07	0.376	0.004	0.006	0.005	0.00	0.20	0.0030	0.0007	32.657	0.691	93.2	28.6	1.01
SHW-145A	31.85	0.16	0.733	0.007	0.004	0.004	0.00	0.20	0.0005	0.0015	43.189	0.754	99.5	37.8	1.26
SHW-146A	111.19	0.18	0.847	0.007	0.024	0.005	1.13	0.19	0.0024	0.0014	130.718	1.193	99.5	112.0	3.28
SHW-148A	21.63	0.08	0.500	0.006	0.013	0.006	0.30	0.20	0.0029	0.0015	41.620	1.026	96.2	36.4	1.37
SHW-149A	35.34	0.10	0.878	0.006	0.015	0.004	0.00	0.20	0.0038	0.0006	38.937	0.372	96.8	34.1	1.02
SHW-150A	25.70	0.07	0.527	0.005	0.008	0.005	0.40	0.20	0.0064	0.0016	45.200	0.992	92.7	39.5	1.41
SHW-152A	16.67	0.08	0.485	0.005	0.007	0.004	0.00	0.20	0.0040	0.0014	31.866	0.953	92.7	27.9	1.15
SHW-153A	80.33	0.16	1.293	0.008	0.017	0.005	0.10	0.20	0.0110	0.0017	59.633	0.552	96.0	51.9	1.55
SHW-154A	16.38	0.08	0.428	0.005	0.006	0.006	0.10	0.20	0.0047	0.0015	35.093	1.105	91.6	30.8	1.30
SHW-155A	40.47	0.10	0.874	0.007	0.019	0.004	0.00	0.18	0.0053	0.0006	44.476	0.418	96.1	38.9	1.16
SHW-156A	20.40	0.20	0.434	0.005	0.012	0.004	0.00	0.30	0.0071	0.0013	42.053	1.161	89.6	36.8	1.45
SHW-157A	38.32	0.12	0.905	0.005	0.013	0.004	0.00	0.20	0.0000	0.0015	42.936	0.554	101.5	37.6	1.17
SHW-159A	46.82	0.14	0.769	0.006	0.042	0.006	0.15	0.16	0.0150	0.0010	55.190	0.584	90.6	48.1	1.45
SHW-160A	136.94	0.15	0.637	0.006	0.016	0.006	0.00	0.20	0.0114	0.0007	209.587	1.919	97.5	176.3	5.07
SHW-161A	98.20	0.13	0.342	0.004	0.007	0.004	0.10	0.20	0.0006	0.0010	286.517	3.292	99.8	237.0	6.87
SHW-162A	70.20	0.10	0.823	0.006	0.014	0.005	0.00	0.20	0.0020	0.0011	84.523	0.767	99.1	73.2	2.16
SHW-163A	79.28	0.11	0.917	0.005	0.011	0.005	0.24	0.18	0.0000	0.0010	86.747	0.641	100.3	75.1	2.18
SHW-164A	13.71	0.10	0.311	0.004	0.009	0.006	0.00	0.30	0.0000	0.0007	44.017	0.953	99.8	38.5	1.37
SHW-165A	84.06	0.16	1.986	0.008	0.031	0.008	0.00	0.30	0.0019	0.0007	41.987	0.226	99.3	36.7	1.06
SHW-166A	39.94	0.18	0.563	0.005	0.008	0.004	0.00	0.20	0.0056	0.0011	68.002	0.891	95.8	59.1	1.84
SHW-167A	30.06	0.12	0.650	0.005	0.009	0.004	0.00	0.20	0.0036	0.0013	44.555	0.724	96.4	39.0	1.27
SHW-168A	43.70	0.20	1.044	0.007	0.015	0.005	0.00	0.20	0.0050	0.0012	40.429	0.489	96.6	35.4	1.09
SHW-169A	21.48	0.14	0.482	0.005	0.004	0.006	0.00	0.20	0.0000	0.0016	44.656	1.119	100.1	39.0	1.47
Taungtalon Formation (Early-Mid Miocene); J-value = 0.000496 ± 0.000019															
TA-01A	332.40	0.30	7.690	0.020	0.094	0.008	0.00	0.11	0.0536	0.0012	41.180	0.131	95.2	36.5	1.35
TA-02A	134.03	0.18	5.319	0.014	0.072	0.010	0.36	0.11	0.0210	0.0015	24.039	0.112	95.4	21.4	0.80
TA-03A	127.32	0.15	3.243	0.013	0.056	0.010	0.00	0.11	0.0261	0.0015	36.878	0.210	93.9	32.7	1.22

TA-05A	272.40	0.30	6.795	0.017	0.126	0.010	0.08	0.12	0.0163	0.0011	39.376	0.125	98.2	34.9	1.29
TA-06A	303.90	0.30	3.944	0.014	0.092	0.008	0.20	0.12	0.0139	0.0010	76.012	0.312	98.7	66.8	2.45
TA-07A	154.00	0.20	5.872	0.016	0.060	0.012	0.15	0.14	0.0247	0.0019	24.992	0.127	95.3	22.2	0.83
TA-08A	98.30	0.30	3.347	0.014	0.042	0.011	0.04	0.15	0.0191	0.0019	27.697	0.231	94.3	24.6	0.93
TA-09A	138.40	0.30	3.865	0.013	0.045	0.013	0.22	0.11	0.0089	0.0020	35.123	0.207	98.1	31.2	1.16
TA-10A	150.90	0.30	2.760	0.013	0.031	0.012	0.17	0.11	0.0110	0.0020	53.459	0.353	97.8	47.2	1.76
TA-11A	329.10	0.30	6.706	0.016	0.105	0.015	0.18	0.13	0.0460	0.0020	47.032	0.159	95.8	41.6	1.54
TA-12A	232.80	0.30	2.601	0.013	0.032	0.014	0.00	0.09	0.0180	0.0020	87.397	0.533	97.6	76.6	2.83
TA-13A	114.70	0.20	3.166	0.014	0.054	0.013	0.25	0.10	0.0310	0.0020	33.312	0.254	92.0	29.6	1.11
TA-14A	192.00	0.30	4.394	0.014	0.087	0.013	0.10	0.10	0.0182	0.0018	42.469	0.200	97.2	37.6	1.40
TA-15A	72.60	0.20	2.620	0.013	0.049	0.012	0.13	0.10	0.0213	0.0019	25.302	0.265	91.3	22.5	0.86
TA-16A	498.80	0.40	3.213	0.010	0.058	0.013	0.12	0.09	0.0236	0.0018	153.087	0.541	98.6	132.0	4.76
TA-17A	159.20	0.20	3.225	0.013	0.024	0.011	0.18	0.12	0.0207	0.0017	47.462	0.264	96.2	42.0	1.56
TA-18A	144.40	0.20	3.611	0.017	0.052	0.011	0.12	0.12	0.0332	0.0018	37.270	0.242	93.2	33.0	1.24
TA-19A	157.60	0.20	3.594	0.014	0.052	0.014	0.15	0.13	0.0228	0.0017	41.974	0.230	95.7	37.2	1.38
TA-21A	101.40	0.40	3.061	0.014	0.069	0.014	0.03	0.15	0.0234	0.0018	30.877	0.253	93.2	27.4	1.04
TA-22A	286.30	0.30	3.505	0.016	0.044	0.015	0.00	0.10	0.0130	0.0020	80.570	0.424	98.6	70.7	2.61
TA-23A	278.00	0.30	6.187	0.018	0.110	0.014	0.08	0.12	0.0210	0.0020	43.939	0.172	97.8	38.9	1.44
TA-24A	434.20	0.40	5.785	0.019	0.068	0.012	0.09	0.10	0.0450	0.0020	72.777	0.275	97.0	64.0	2.35
TA-25A	227.30	0.20	5.458	0.016	0.074	0.017	0.01	0.13	0.0110	0.0020	41.044	0.174	98.5	36.4	1.35
TA-26A	125.20	0.40	2.877	0.012	0.072	0.013	0.00	0.10	0.0100	0.0020	42.515	0.318	97.7	37.6	1.41
TA-27A	217.90	0.30	3.729	0.014	0.049	0.015	0.03	0.11	0.0182	0.0020	56.979	0.283	97.5	50.3	1.86
TA-28A	106.20	0.20	2.370	0.011	0.028	0.012	0.00	0.10	0.0340	0.0020	40.500	0.338	90.4	35.9	1.36
TA-29A	95.40	0.30	2.234	0.012	0.022	0.013	0.13	0.13	0.0133	0.0011	40.953	0.297	95.9	36.3	1.36
TA-30A	326.50	0.30	4.004	0.016	0.064	0.015	0.22	0.11	0.0322	0.0012	79.182	0.346	97.1	69.5	2.56
TA-31A	71.60	0.20	1.855	0.010	0.036	0.015	0.00	0.13	0.0095	0.0012	37.101	0.307	96.1	32.9	1.24
TA-32A	105.67	0.20	2.477	0.012	0.022	0.011	0.29	0.11	0.0130	0.0019	41.119	0.316	96.4	36.4	1.37
TA-33A	258.60	0.20	3.887	0.015	0.044	0.010	0.00	0.10	0.0235	0.0020	64.737	0.304	97.3	57.0	2.11
TA-34A	131.70	0.30	2.409	0.012	0.026	0.008	0.06	0.12	0.0123	0.0011	53.155	0.335	97.3	47.0	1.75
TA-35A	283.40	0.40	4.465	0.016	0.069	0.013	0.22	0.12	0.0513	0.0015	60.086	0.255	94.7	53.0	1.96

TA-36A	291.70	0.30	3.468	0.014	0.053	0.009	0.02	0.11	0.0085	0.0012	83.381	0.367	99.1	73.1	2.69
TA-38A	71.40	0.30	1.987	0.008	0.027	0.014	0.00	0.11	0.0236	0.0019	32.409	0.362	90.2	28.8	1.11
TA-39A	96.60	0.20	1.673	0.011	0.008	0.012	0.06	0.11	0.0069	0.0018	56.547	0.502	97.9	49.9	1.88
TA-40A	247.50	0.30	3.990	0.013	0.046	0.012	0.00	0.09	0.0315	0.0018	59.685	0.254	96.2	52.6	1.94
TA-41A	63.40	0.30	1.596	0.008	0.023	0.010	0.00	0.09	0.0068	0.0018	38.484	0.450	96.8	34.1	1.32
TA-42A	130.00	0.20	3.063	0.013	0.040	0.009	0.06	0.14	0.0166	0.0020	40.833	0.269	96.2	36.2	1.35
TA-43A	128.42	0.19	3.502	0.014	0.051	0.012	0.47	0.14	0.0400	0.0020	33.305	0.232	90.8	29.6	1.11
TA-44A	482.60	0.40	2.294	0.011	0.051	0.012	0.08	0.12	0.0154	0.0019	208.448	1.056	99.1	177.5	6.35
TA-45A	64.20	0.20	1.794	0.010	0.059	0.010	0.06	0.10	0.0152	0.0019	33.316	0.395	93.0	29.6	1.15
TA-46A	116.70	0.20	3.086	0.013	0.072	0.009	0.00	0.11	0.0156	0.0019	36.312	0.256	96.0	32.2	1.21
TA-47A	127.30	0.20	2.608	0.012	0.054	0.013	0.22	0.11	0.0062	0.0011	48.120	0.272	98.6	42.6	1.58
TA-49A	79.50	0.20	1.867	0.010	0.029	0.011	0.00	0.13	0.0166	0.0019	39.973	0.392	93.8	35.4	1.35
TA-50A	85.80	0.30	2.330	0.012	0.042	0.009	0.03	0.12	0.0148	0.0019	34.974	0.330	94.9	31.0	1.18
TA-51A	147.20	0.20	2.337	0.010	0.028	0.012	0.00	0.11	0.0101	0.0019	61.721	0.371	98.0	54.4	2.02
TA-52A	86.96	0.20	1.518	0.009	0.015	0.011	0.00	0.10	0.0091	0.0018	55.493	0.507	96.9	49.0	1.85
TA-53A	78.92	0.13	1.362	0.008	0.014	0.006	0.12	0.13	0.0082	0.0011	56.164	0.431	96.9	49.6	1.86
TA-54A	60.50	0.10	0.908	0.006	0.019	0.005	0.16	0.13	0.0017	0.0008	66.051	0.540	99.2	58.2	2.18
TA-55A	93.38	0.17	2.196	0.008	0.039	0.008	0.00	0.10	0.0124	0.0014	40.842	0.253	96.1	36.2	1.35
TA-56A	41.26	0.10	1.056	0.007	0.010	0.007	0.19	0.10	0.0074	0.0014	37.019	0.470	94.8	32.8	1.28
TA-57A	107.30	0.15	1.207	0.006	0.020	0.004	0.04	0.16	0.0031	0.0011	88.155	0.527	99.2	77.2	2.85
TA-58A	98.26	0.11	2.217	0.007	0.031	0.007	0.00	0.11	0.0113	0.0012	42.822	0.221	96.6	37.9	1.41
TA-59A	303.90	0.30	0.851	0.006	0.018	0.007	0.00	0.12	0.0028	0.0012	356.239	2.513	99.7	293.6	10.26
TA-60A	70.21	0.14	1.908	0.010	0.033	0.006	0.19	0.14	0.0078	0.0013	35.590	0.285	96.7	31.6	1.19
TA-61A	232.50	0.30	1.550	0.009	0.034	0.005	0.00	0.15	0.0186	0.0013	146.383	0.904	97.6	126.5	4.61
TA-63A	72.20	0.11	1.050	0.006	0.017	0.005	0.00	0.12	0.0096	0.0008	66.064	0.465	96.1	58.2	2.17
TA-65A	31.63	0.09	0.929	0.006	0.010	0.006	0.03	0.14	0.0076	0.0012	31.622	0.454	92.9	28.1	1.11
TA-66A	39.66	0.10	0.869	0.008	0.016	0.008	0.00	0.13	0.0033	0.0008	44.492	0.511	97.5	39.4	1.52
TA-67A	64.86	0.12	1.669	0.010	0.024	0.007	0.00	0.16	0.0034	0.0008	38.253	0.278	98.5	33.9	1.27
TA-69A	16.84	0.06	0.407	0.005	0.006	0.005	0.11	0.15	0.0038	0.0013	38.590	1.064	93.3	34.2	1.57
TA-70A	101.28	0.17	1.235	0.007	0.020	0.007	0.14	0.15	0.0043	0.0013	81.020	0.571	98.8	71.1	2.64

TA-71A	195.10	0.20	0.816	0.006	0.010	0.006	0.05	0.14	0.0051	0.0012	237.376	2.017	99.2	200.8	7.26
TA-72A	779.90	0.60	3.465	0.012	0.062	0.008	0.23	0.13	0.0368	0.0014	221.975	0.843	98.6	188.5	6.69
TA-73A	143.03	0.16	3.212	0.013	0.042	0.007	0.42	0.18	0.0170	0.0014	42.986	0.231	96.5	38.1	1.42
TA-75A	173.10	0.20	1.559	0.010	0.027	0.006	0.00	0.14	0.0194	0.0010	107.351	0.711	96.7	93.6	3.45
TA-76A	174.16	0.19	1.580	0.010	0.031	0.007	0.00	0.16	0.0158	0.0009	107.253	0.702	97.3	93.5	3.44
TA-77A	156.80	0.17	4.544	0.013	0.086	0.008	0.00	0.16	0.0102	0.0009	33.839	0.126	98.1	30.0	1.11
TA-78A	241.70	0.30	2.583	0.011	0.032	0.008	0.34	0.15	0.0114	0.0015	92.271	0.466	98.6	80.7	2.97
TA-79A	44.74	0.14	1.233	0.007	0.005	0.008	0.00	0.14	0.0038	0.0014	35.381	0.404	97.5	31.4	1.21
TA-80A	42.56	0.18	0.888	0.006	0.010	0.007	0.15	0.12	0.0105	0.0014	44.424	0.595	92.7	39.3	1.54
TA-83A	71.10	0.15	1.806	0.010	0.030	0.005	0.00	0.14	0.0087	0.0014	37.939	0.333	96.4	33.6	1.27
TA-84A	128.68	0.20	1.410	0.008	0.019	0.007	0.02	0.13	0.0027	0.0013	90.671	0.612	99.4	79.4	2.94
TA-85A	27.11	0.10	0.583	0.007	0.005	0.007	0.00	0.14	0.0037	0.0014	44.638	0.899	95.9	39.5	1.65
TA-87A	40.67	0.09	1.002	0.007	0.007	0.006	0.00	0.14	0.0014	0.0013	40.180	0.503	98.9	35.6	1.38
TA-88A	89.91	0.16	1.039	0.008	0.016	0.008	0.12	0.14	0.0015	0.0013	86.154	0.766	99.5	75.5	2.83
TA-89A	62.18	0.12	1.037	0.007	0.011	0.008	0.00	0.12	0.0094	0.0016	57.240	0.619	95.5	50.5	1.93
TA-90A	74.95	0.14	1.940	0.010	0.020	0.007	0.00	0.17	0.0200	0.0015	35.569	0.298	92.1	31.6	1.19
TA-92A	94.24	0.14	1.299	0.008	0.018	0.005	0.00	0.13	0.0147	0.0014	69.177	0.535	95.4	60.9	2.28
TA-93A	13.83	0.07	0.326	0.004	0.008	0.005	0.00	0.13	0.0042	0.0013	38.529	1.315	90.9	34.2	1.71
TA-94A	43.36	0.12	0.590	0.006	0.012	0.006	0.00	0.16	0.0046	0.0013	71.149	0.965	96.8	62.6	2.44
TA-95A	58.49	0.11	1.290	0.007	0.025	0.006	0.00	0.15	0.0126	0.0013	42.452	0.392	93.6	37.6	1.43
TA-96A	24.42	0.10	0.632	0.006	0.016	0.005	0.00	0.14	0.0047	0.0013	36.423	0.704	94.3	32.3	1.34
TA-97A	63.26	0.14	0.284	0.004	0.012	0.007	0.00	0.14	0.0004	0.0014	221.729	3.751	99.8	188.0	7.31
TA-98A	32.12	0.10	1.015	0.009	0.014	0.008	0.00	0.14	0.0050	0.0008	30.139	0.378	95.3	26.8	1.04
TA-99A	71.68	0.12	1.589	0.009	0.016	0.007	0.00	0.12	0.0137	0.0017	42.549	0.402	94.3	37.7	1.43
TA-101	249.40	0.30	2.831	0.012	0.050	0.005	0.00	0.18	0.0157	0.0011	86.426	0.412	98.1	75.7	2.78
TA-104A	38.88	0.12	1.100	0.008	0.020	0.005	0.10	0.20	0.0058	0.0010	33.807	0.375	95.6	30.0	1.16
TA-109A	56.17	0.10	1.354	0.007	0.022	0.005	0.16	0.16	0.0081	0.0007	39.743	0.265	95.8	35.2	1.32
TA-110A	73.09	0.13	1.542	0.008	0.022	0.004	0.56	0.17	0.0170	0.0008	44.189	0.293	93.2	39.1	1.46
TA-111A	57.79	0.11	1.785	0.011	0.021	0.004	0.41	0.18	0.0112	0.0007	30.552	0.238	94.3	27.1	1.02
TA-113A	173.00	0.20	3.397	0.010	0.051	0.006	0.00	0.20	0.0080	0.0010	50.220	0.196	98.6	44.4	1.64

TA-114A	72.63	0.13	1.715	0.009	0.028	0.005	0.30	0.20	0.0134	0.0010	40.070	0.298	94.6	35.5	1.33
TA-116A	81.29	0.12	1.215	0.005	0.020	0.005	0.26	0.18	0.0111	0.0007	64.215	0.352	96.0	56.6	2.10
TA-117A	167.00	0.20	1.806	0.008	0.034	0.006	0.40	0.20	0.0109	0.0007	90.752	0.430	98.1	79.4	2.92
TA-118A	71.88	0.10	1.602	0.008	0.024	0.006	0.30	0.20	0.0035	0.0006	44.231	0.257	98.6	39.2	1.46
TA-119A	30.20	0.11	0.744	0.005	0.004	0.005	0.00	0.20	0.0034	0.0010	39.190	0.518	96.6	34.7	1.36
TA-120A	32.08	0.10	0.898	0.007	0.019	0.005	0.20	0.20	0.0051	0.0011	34.046	0.477	95.3	30.2	1.19
TA-121A	44.77	0.09	0.916	0.006	0.018	0.004	0.00	0.20	0.0074	0.0012	46.465	0.488	95.1	41.1	1.57
TA-122A	59.72	0.11	1.480	0.006	0.034	0.006	0.10	0.20	0.0063	0.0011	39.094	0.296	96.9	34.6	1.30
TA-123A	84.84	0.14	2.387	0.010	0.042	0.006	0.00	0.20	0.0207	0.0012	32.974	0.211	92.8	29.3	1.10
TA-124A	93.14	0.17	2.128	0.008	0.030	0.005	0.00	0.19	0.0176	0.0011	41.326	0.235	94.4	36.6	1.36
TA-125A	47.89	0.10	0.739	0.005	0.000	0.005	0.00	0.20	0.0038	0.0010	63.284	0.634	97.6	55.8	2.12
TA-126A	69.61	0.13	1.680	0.008	0.018	0.005	0.00	0.20	0.0160	0.0011	38.597	0.285	93.2	34.2	1.29
TA-127A	137.46	0.13	2.486	0.009	0.035	0.006	0.70	0.20	0.0164	0.0008	53.368	0.220	96.5	47.1	1.74
TA-128A	71.83	0.14	1.706	0.008	0.029	0.004	0.00	0.20	0.0129	0.0012	39.822	0.297	94.6	35.3	1.33
TA-130A	283.70	0.20	1.371	0.007	0.019	0.005	0.00	0.20	0.0029	0.0011	206.319	1.153	99.7	175.8	6.30
TA-131A	36.93	0.12	1.014	0.006	0.022	0.006	0.00	0.20	0.0046	0.0011	35.048	0.416	96.2	31.1	1.20
TA-132A	355.80	0.40	1.799	0.009	0.035	0.007	0.00	0.20	0.0046	0.0008	196.973	1.035	99.6	168.2	6.04
TA-133A	45.25	0.10	1.039	0.007	0.016	0.006	0.00	0.20	0.0066	0.0013	41.643	0.473	95.6	36.9	1.42
TA-134A	39.33	0.08	0.944	0.006	0.010	0.007	0.00	0.20	0.0044	0.0013	40.229	0.481	96.6	35.6	1.38
TA-135A	113.68	0.17	1.398	0.007	0.024	0.004	0.00	0.20	0.0033	0.0008	80.583	0.475	99.1	70.7	2.61
TA-137A	62.02	0.14	1.561	0.010	0.031	0.006	0.00	0.20	0.0098	0.0013	37.862	0.358	95.3	33.6	1.28
TA-138A	33.37	0.14	0.820	0.006	0.002	0.005	0.00	0.20	0.0037	0.0011	39.347	0.508	96.7	34.9	1.36
TA-139A	259.80	0.20	1.598	0.009	0.023	0.007	0.30	0.20	0.0091	0.0012	160.916	0.955	99.0	138.6	5.03
TA-140A	120.24	0.17	1.535	0.007	0.033	0.005	0.41	0.17	0.0044	0.0011	77.513	0.435	99.0	68.1	2.51
TA-141A	77.85	0.13	1.280	0.007	0.030	0.005	1.06	0.19	0.0174	0.0011	56.896	0.438	93.5	50.2	1.88
TA-142A	42.29	0.11	0.724	0.007	0.033	0.006	0.50	0.20	0.0109	0.0011	54.026	0.720	92.5	47.7	1.86
TA-143A	123.02	0.15	1.939	0.010	0.034	0.006	0.00	0.20	0.0353	0.0013	58.022	0.376	91.5	51.2	1.91
TA-144A	37.04	0.09	0.848	0.006	0.020	0.008	0.20	0.20	0.0098	0.0013	40.265	0.537	92.2	35.7	1.40
TA-145A	41.89	0.10	1.218	0.008	0.009	0.006	0.30	0.20	0.0056	0.0012	33.070	0.394	96.1	29.4	1.14
TA-146A	17.10	0.06	0.638	0.006	0.001	0.007	0.00	0.20	0.0029	0.0011	25.423	0.589	94.8	22.6	0.98

TA-147A	36.42	0.10	1.012	0.006	0.010	0.005	0.00	0.20	0.0129	0.0011	32.192	0.408	89.5	28.6	1.11
TA-148A	39.74	0.11	0.850	0.006	0.016	0.006	0.00	0.20	0.0043	0.0007	45.225	0.439	96.8	40.0	1.52
TA-149A	12.22	0.06	0.315	0.004	0.000	0.004	0.60	0.20	0.0031	0.0012	36.127	1.235	92.9	32.0	1.61
TA-150A	65.02	0.14	1.564	0.006	0.026	0.004	0.30	0.20	0.0132	0.0013	39.093	0.312	94.0	34.6	1.31
TA-151A	8.73	0.05	0.349	0.005	0.007	0.005	0.30	0.20	0.0000	0.0011	25.175	1.012	100.5	22.4	1.22
TA-152A	76.25	0.13	2.086	0.008	0.052	0.007	0.30	0.20	0.0136	0.0011	34.649	0.215	94.8	30.7	1.15
TA-153A	25.85	0.09	0.431	0.005	0.021	0.006	0.00	0.30	0.0032	0.0011	57.702	1.068	96.3	50.9	2.09
TA-154A	21.17	0.11	0.585	0.007	0.016	0.007	0.00	0.19	0.0024	0.0012	34.994	0.755	96.6	31.0	1.32
TA-156A	32.37	0.08	0.754	0.008	0.006	0.006	0.20	0.20	0.0038	0.0008	41.478	0.556	96.6	36.7	1.44
TA-157A	33.63	0.10	0.679	0.005	0.013	0.006	0.00	0.18	0.0022	0.0011	48.474	0.644	98.0	42.9	1.67
TA-158A	92.59	0.13	2.093	0.010	0.029	0.007	0.00	0.20	0.0012	0.0011	44.068	0.269	99.6	39.0	1.46
TA-160A	50.34	0.10	1.370	0.008	0.011	0.006	0.00	0.20	0.0015	0.0007	36.386	0.266	99.1	32.3	1.21
TA-161A	44.21	0.08	1.095	0.006	0.002	0.005	0.00	0.20	0.0036	0.0007	39.347	0.305	97.5	34.9	1.31
TA-162A	37.76	0.13	0.825	0.007	0.021	0.006	0.00	0.20	0.0019	0.0012	45.043	0.579	98.4	39.9	1.55
TA-163A	74.40	0.14	1.293	0.009	0.032	0.007	0.00	0.20	0.0042	0.0012	56.537	0.490	98.3	49.9	1.88
TA-164A	45.87	0.11	1.111	0.006	0.025	0.006	0.00	0.20	0.0022	0.0008	40.642	0.336	98.5	36.0	1.36
TA-165A	358.20	0.40	1.994	0.009	0.022	0.009	0.27	0.20	0.0092	0.0013	178.299	0.898	99.2	152.9	5.51
TA-166A	61.46	0.13	1.904	0.008	0.018	0.008	0.30	0.20	0.0117	0.0013	30.473	0.249	94.4	27.1	1.02
TA-167A	345.30	0.40	1.657	0.010	0.034	0.006	0.10	0.20	0.0080	0.0013	206.990	1.277	99.3	176.3	6.34
TA-168A	69.88	0.14	1.616	0.009	0.028	0.005	0.40	0.20	0.0055	0.0008	42.257	0.295	97.7	37.4	1.40
TA-169A	127.54	0.19	1.487	0.008	0.027	0.007	0.07	0.20	0.0017	0.0008	85.417	0.520	99.6	74.9	2.77
TA-170A	57.68	0.12	1.424	0.007	0.026	0.005	0.00	0.20	0.0102	0.0008	38.397	0.276	94.8	34.0	1.28
Kyaukkok Formation (Early-Mid Miocene); J-value = 0.000493 ± 0.000018															
KK-04A	87.01	0.12	0.345	0.005	0.012	0.005	0.00	0.10	0.0020	0.0008	250.388	3.781	99.3	210.0	8.00
KK-05A	10.25	0.06	0.278	0.004	0.012	0.004	0.00	0.09	0.0025	0.0008	34.110	1.021	92.7	30.1	1.43
KK-07A	27.90	0.10	0.646	0.006	0.012	0.005	0.00	0.07	0.0017	0.0013	42.406	0.728	98.2	37.3	1.52
KK-09A	27.43	0.08	0.615	0.006	0.015	0.006	0.11	0.09	0.0039	0.0008	42.749	0.597	95.8	37.6	1.49
KK-10A	86.57	0.11	0.489	0.005	0.013	0.006	0.00	0.08	0.0172	0.0009	166.614	1.812	94.1	142.4	5.34
KK-12A	17.21	0.06	0.389	0.005	0.009	0.005	0.00	0.10	0.0006	0.0012	43.739	1.107	98.9	38.5	1.72

KK-15A	17.86	0.06	0.374	0.004	0.000	0.005	0.02	0.09	0.0014	0.0012	46.657	1.141	97.6	41.0	1.81
KK-18A	13.92	0.06	0.323	0.004	0.008	0.005	0.06	0.11	0.0002	0.0013	42.978	1.368	99.7	37.8	1.84
KK-20A	23.75	0.06	0.400	0.005	0.005	0.005	0.00	0.10	0.0016	0.0008	58.192	0.940	98.0	51.0	2.05
KK-24A	46.19	0.12	0.523	0.004	0.010	0.008	0.00	0.09	0.0036	0.0013	86.349	1.093	97.7	75.2	2.91
KK-28A	18.56	0.06	0.402	0.004	0.001	0.006	0.00	0.08	0.0017	0.0011	44.905	0.971	97.3	39.5	1.69
KK-29A	85.46	0.11	0.393	0.005	0.004	0.006	0.05	0.06	0.0041	0.0011	214.526	2.908	98.6	181.0	6.87
KK-30A	17.62	0.07	0.302	0.005	0.017	0.005	0.00	0.10	0.0013	0.0007	57.101	1.211	97.8	50.1	2.12
KK-31A	34.98	0.08	0.415	0.005	0.000	0.008	0.00	0.09	0.0022	0.0008	82.783	1.208	98.2	72.2	2.84
KK-34A	44.84	0.11	0.216	0.005	0.013	0.006	0.00	0.08	0.0000	0.0008	207.687	4.760	100.1	176.0	7.35
KK-35A	6.26	0.05	0.177	0.004	0.002	0.005	0.00	0.09	0.0001	0.0008	35.237	1.571	99.7	31.1	1.79
KK-36A	10.26	0.04	0.308	0.004	0.004	0.004	0.00	0.10	0.0032	0.0012	30.135	1.266	90.6	26.6	1.49
KK-41A	29.38	0.08	0.337	0.004	0.009	0.005	0.16	0.06	0.0006	0.0012	86.837	1.554	99.5	75.6	3.07
KK-42A	16.04	0.07	0.317	0.004	0.000	0.005	0.06	0.06	0.0033	0.0012	47.650	1.313	94.0	41.9	1.92
KK-44A	39.62	0.09	0.448	0.004	0.006	0.007	0.00	0.09	0.0020	0.0011	87.108	1.108	98.5	75.8	2.94
KK-45A	22.34	0.08	0.284	0.004	0.010	0.006	0.00	0.09	0.0010	0.0012	77.655	1.726	98.7	67.8	2.89
KK-46A	10.66	0.05	0.303	0.005	0.013	0.004	0.07	0.10	0.0007	0.0008	34.461	0.961	98.0	30.4	1.41
KK-48A	16.21	0.06	0.358	0.004	0.004	0.006	0.20	0.13	0.0006	0.0008	44.815	0.867	99.1	39.4	1.64
KK-51A	10.68	0.05	0.226	0.004	0.004	0.004	0.00	0.08	0.0001	0.0007	47.095	1.368	99.8	41.4	1.94
KK-52A	18.91	0.06	0.427	0.005	0.007	0.004	0.11	0.09	0.0033	0.0007	42.027	0.677	95.0	37.0	1.49
KK-53A	27.07	0.09	0.328	0.004	0.011	0.004	0.00	0.11	0.0018	0.0007	80.840	1.255	98.0	70.5	2.80
KK-54A	18.93	0.04	0.399	0.004	0.006	0.004	0.40	0.09	0.0008	0.0010	46.897	0.896	98.8	41.2	1.71
KK-55A	14.50	0.05	0.235	0.004	0.005	0.004	0.00	0.13	0.0008	0.0006	60.567	1.391	98.2	53.1	2.30
KK-56A	11.55	0.05	0.276	0.004	0.007	0.005	0.00	0.12	0.0009	0.0006	40.661	0.943	97.3	35.8	1.56
KK-57A	12.24	0.05	0.197	0.004	0.003	0.005	0.08	0.11	0.0033	0.0011	57.126	2.106	92.1	50.1	2.60
KK-58A	60.11	0.11	0.259	0.004	0.003	0.004	0.00	0.13	0.0030	0.0011	228.748	4.217	98.5	193.0	7.63
KK-59A	13.84	0.05	0.196	0.004	0.003	0.004	0.02	0.14	0.0034	0.0011	65.478	2.280	92.8	57.3	2.88
KK-60A	10.08	0.04	0.231	0.004	0.003	0.004	0.04	0.12	0.0000	0.0011	43.936	1.614	100.7	38.6	2.01
KK-62A	55.19	0.11	0.280	0.004	0.005	0.005	0.00	0.12	0.0014	0.0007	195.260	2.969	99.2	166.0	6.40
KK-63A	5.57	0.04	0.134	0.003	0.002	0.004	0.00	0.14	0.0019	0.0011	37.166	2.573	89.6	33.0	2.55
KK-64A	43.42	0.11	0.188	0.003	0.000	0.005	0.00	0.12	0.0007	0.0011	229.255	4.320	99.4	193.0	7.67

KK-65A	20.11	0.09	0.250	0.007	0.004	0.007	0.07	0.14	0.0029	0.0012	77.065	2.586	95.8	67.0	3.32
KK-66A	13.58	0.04	0.292	0.005	0.004	0.004	0.00	0.13	0.0029	0.0011	43.597	1.382	93.6	38.4	1.86
KK-67A	26.67	0.07	0.235	0.005	0.015	0.004	0.15	0.13	0.0019	0.0011	111.067	2.960	98.0	96.0	4.30
KK-68A	13.21	0.05	0.299	0.004	0.006	0.005	0.10	0.16	0.0013	0.0011	42.969	1.253	97.2	37.8	1.78
KK-71A	15.34	0.05	0.369	0.006	0.000	0.005	0.08	0.14	0.0019	0.0007	40.091	0.875	96.3	35.3	1.51
KK-72A	83.60	0.14	0.265	0.004	0.000	0.004	0.00	0.11	0.0016	0.0007	313.351	4.623	99.4	259.0	9.71
KK-73A	15.04	0.05	0.335	0.004	0.014	0.004	0.03	0.11	0.0008	0.0007	44.203	0.874	98.4	38.9	1.63
KK-75A	16.28	0.05	0.207	0.004	0.007	0.005	0.22	0.11	0.0028	0.0012	74.582	2.263	95.0	65.1	3.08
KK-76A	19.57	0.07	0.276	0.003	0.008	0.005	0.00	0.13	0.0021	0.0010	68.599	1.412	96.9	60.0	2.52
KK-78A	16.00	0.06	0.194	0.004	0.000	0.004	0.04	0.14	0.0000	0.0012	82.834	2.461	100.3	72.0	3.38
KK-79A	15.25	0.04	0.353	0.004	0.013	0.005	0.09	0.11	0.0020	0.0011	41.546	1.091	96.2	36.6	1.66
KK-80A	9.88	0.04	0.239	0.004	0.017	0.004	0.02	0.12	0.0014	0.0011	39.599	1.553	95.8	34.9	1.87
KK-81A	40.96	0.12	0.685	0.008	0.025	0.005	0.00	0.13	0.0004	0.0011	59.569	0.911	99.7	52.2	2.08
KK-82A	17.75	0.05	0.279	0.004	0.003	0.006	0.00	0.12	0.0003	0.0011	63.217	1.524	99.5	55.4	2.43
KK-83A	10.73	0.03	0.327	0.004	0.000	0.005	0.14	0.15	0.0020	0.0011	31.015	1.095	94.6	27.4	1.40
KK-84A	17.83	0.05	0.391	0.005	0.005	0.004	0.00	0.10	0.0009	0.0010	44.729	0.960	98.2	39.3	1.68
KK-85A	10.65	0.04	0.215	0.004	0.002	0.004	0.00	0.12	0.0020	0.0009	46.720	1.512	94.4	41.1	2.01
KK-86A	47.70	0.09	1.192	0.007	0.021	0.005	0.28	0.14	0.0023	0.0007	39.455	0.310	98.6	34.8	1.32
KK-89A	62.22	0.14	0.548	0.005	0.010	0.004	0.15	0.09	0.0000	0.0007	113.611	1.102	100.0	98.3	3.70
KK-90A	18.26	0.04	0.246	0.005	0.000	0.004	0.00	0.13	0.0004	0.0007	73.620	1.704	99.3	64.3	2.78
KK-92A	49.91	0.11	0.412	0.005	0.006	0.005	0.06	0.16	0.0040	0.0007	118.463	1.562	97.7	102.4	3.95
KK-93A	21.90	0.09	0.314	0.004	0.000	0.005	0.04	0.16	0.0033	0.0007	66.590	1.233	95.5	58.3	2.39
KK-94A	7.84	0.04	0.174	0.005	0.015	0.005	0.00	0.12	0.0012	0.0012	43.083	2.443	95.6	38.0	2.55
KK-97A	8.73	0.04	0.191	0.004	0.009	0.004	0.00	0.15	0.0000	0.0006	46.054	1.403	100.7	40.5	1.93
KK-100	40.88	0.08	0.748	0.005	0.007	0.005	0.46	0.13	0.0058	0.0011	52.391	0.584	95.9	46.0	1.77
KK-103A	14.24	0.06	0.211	0.003	0.002	0.003	0.20	0.30	0.0000	0.0012	67.827	2.046	100.4	59.3	2.81
KK-105A	10.38	0.05	0.230	0.004	0.005	0.003	0.20	0.40	0.0025	0.0011	42.058	1.632	93.0	37.0	1.98
KK-106A	38.29	0.10	0.263	0.004	0.006	0.006	0.00	0.30	0.0006	0.0007	144.891	2.388	99.5	124.5	4.92
KK-108A	13.37	0.04	0.281	0.004	0.002	0.004	0.00	0.40	0.0015	0.0010	45.925	1.212	96.5	40.4	1.83
KK-110A	12.96	0.04	0.313	0.004	0.009	0.004	0.00	0.40	0.0020	0.0010	39.468	1.061	95.4	34.8	1.59

KK-111A	12.23	0.05	0.178	0.003	0.012	0.004	0.00	0.40	0.0044	0.0010	61.243	2.031	89.4	53.7	2.64
KK-117A	7.57	0.04	0.224	0.003	0.005	0.005	0.40	0.30	0.0002	0.0008	33.712	1.231	99.4	29.7	1.54
KK-120A	11.16	0.04	0.182	0.003	0.008	0.005	0.50	0.30	0.0025	0.0006	57.620	1.453	93.8	50.5	2.25
KK-121A	11.98	0.04	0.275	0.003	0.001	0.004	1.40	0.40	0.0008	0.0007	43.263	0.926	99.0	38.1	1.62
KK-124A	37.75	0.11	0.164	0.003	0.004	0.004	0.00	0.30	0.0013	0.0011	227.792	5.144	99.0	192.0	7.96
KK-125A	10.73	0.04	0.257	0.004	0.002	0.005	0.00	0.30	0.0018	0.0007	39.479	1.053	94.7	34.8	1.58
KK-130A	7.11	0.03	0.182	0.003	0.009	0.004	0.00	0.40	0.0013	0.0006	36.306	1.269	93.4	32.0	1.62
KK-131A	8.49	0.05	0.195	0.004	0.000	0.005	0.00	0.40	0.0005	0.0012	42.619	2.033	98.0	37.5	2.25
KK-135A	8.03	0.04	0.161	0.003	0.001	0.004	0.50	0.30	0.0020	0.0011	46.569	2.206	93.2	40.9	2.44
KK-137A	9.83	0.04	0.209	0.004	0.005	0.005	0.20	0.30	0.0006	0.0007	46.262	1.271	98.2	40.7	1.87
KK-138A	15.55	0.04	0.341	0.004	0.001	0.004	0.00	0.30	0.0047	0.0010	41.282	1.040	90.7	36.3	1.62
KK-143A	41.32	0.09	0.252	0.004	0.002	0.004	0.50	0.30	0.0037	0.0011	159.914	2.753	97.5	137.0	5.43
KK-148A	5.90	0.04	0.190	0.004	0.009	0.004	0.00	0.30	0.0004	0.0007	29.809	1.248	96.5	26.3	1.47
KK-153A	6.01	0.04	0.143	0.003	0.002	0.004	0.00	0.30	0.0002	0.0007	41.087	1.750	98.2	36.2	2.03
KK-157A	28.90	0.09	0.174	0.004	0.003	0.003	0.00	0.30	0.0011	0.0006	163.883	3.914	98.8	140.0	5.99

Lower Moza Formation (Middle Miocene); J-value = 0.000504 ± 0.000001

LM-01A	37.16	0.10	0.852	0.006	0.001	0.005	0.00	0.12	0.0071	0.0011	41.123	0.520	94.4	37.0	0.47
LM-02A	358.00	0.30	1.732	0.009	0.018	0.007	0.01	0.12	0.0162	0.0013	203.896	1.084	98.7	176.3	0.93
LM-03A	45.61	0.09	1.029	0.006	0.008	0.005	0.00	0.12	0.0126	0.0012	40.674	0.453	91.8	36.6	0.41
LM-04A	248.60	0.30	0.817	0.006	0.016	0.007	0.00	0.12	0.0056	0.0013	302.245	2.567	99.3	256.0	2.06
LM-05A	54.90	0.11	1.202	0.009	0.018	0.005	0.00	0.15	0.0035	0.0008	44.772	0.397	98.1	40.2	0.36
LM-07A	61.92	0.10	0.671	0.005	0.010	0.006	0.00	0.13	0.0078	0.0007	88.857	0.750	96.3	79.0	0.66
LM-08A	65.15	0.11	1.516	0.008	0.032	0.005	0.00	0.15	0.0116	0.0007	40.720	0.283	94.7	36.6	0.26
LM-09A	37.37	0.10	0.852	0.007	0.006	0.004	0.00	0.16	0.0031	0.0007	42.764	0.440	97.5	38.4	0.40
LM-10A	267.60	0.30	1.771	0.010	0.022	0.005	0.06	0.13	0.0094	0.0007	149.549	0.909	99.0	131.0	0.80
LM-11A	42.98	0.10	0.969	0.006	0.019	0.005	0.00	0.15	0.0045	0.0010	42.935	0.405	96.9	38.6	0.37
LM-12A	1401.4	0.90	2.768	0.012	0.051	0.006	0.00	0.16	0.0093	0.0011	505.197	2.312	99.8	408.9	1.78
LM-13A	86.86	0.14	2.046	0.010	0.025	0.007	0.53	0.15	0.0090	0.0013	41.184	0.291	97.0	37.0	0.27
LM-14A	61.65	0.12	1.464	0.008	0.015	0.007	0.12	0.16	0.0065	0.0013	40.817	0.354	96.9	36.7	0.32

LM-15A	105.54	0.17	1.047	0.006	0.018	0.005	0.00	0.14	0.0007	0.0011	100.568	0.734	99.8	89.1	0.65
LM-16A	23.98	0.07	0.508	0.006	0.010	0.006	0.14	0.15	0.0020	0.0012	46.106	0.896	97.6	41.4	0.80
LM-18A	106.34	0.18	0.781	0.007	0.011	0.006	0.32	0.17	0.0050	0.0011	134.406	1.361	98.6	118.2	1.17
LM-19A	23.94	0.09	0.598	0.005	0.006	0.005	0.00	0.17	0.0018	0.0012	39.153	0.724	97.8	35.2	0.65
LM-20A	37.20	0.09	0.864	0.006	0.006	0.006	0.00	0.17	0.0054	0.0012	41.161	0.519	95.7	37.0	0.47
LM-21A	29.86	0.09	0.702	0.005	0.013	0.005	0.00	0.15	0.0038	0.0007	40.888	0.458	96.2	36.8	0.41
LM-22A	65.22	0.11	0.518	0.005	0.007	0.005	0.00	0.15	0.0021	0.0007	124.705	1.368	99.0	109.9	1.18
LM-24A	22.60	0.08	0.888	0.007	0.015	0.005	0.00	0.16	0.0084	0.0011	22.656	0.409	89.0	20.5	0.37
LM-25A	70.20	0.12	0.664	0.005	0.017	0.005	0.28	0.16	0.0074	0.0010	102.538	0.940	96.9	90.8	0.83
LM-26A	47.38	0.09	0.836	0.006	0.000	0.004	0.00	0.14	0.0025	0.0007	55.789	0.529	98.4	50.0	0.47
LM-27A	14.08	0.04	0.304	0.004	0.004	0.005	0.18	0.17	0.0042	0.0007	42.299	0.956	91.2	38.0	0.85
LM-28A	14.59	0.05	0.314	0.005	0.001	0.004	0.00	0.18	0.0018	0.0007	44.750	0.966	96.3	40.2	0.86
LM-29A	85.31	0.14	0.488	0.005	0.015	0.006	0.00	0.16	0.0119	0.0012	167.411	1.928	95.9	146.0	1.63
LM-30A	36.01	0.09	0.414	0.005	0.014	0.005	0.00	0.16	0.0072	0.0011	81.797	1.364	94.0	72.8	1.20
LM-31A	35.75	0.10	0.880	0.006	0.013	0.005	0.19	0.13	0.0048	0.0007	39.030	0.397	96.1	35.1	0.36
LM-32A	16.55	0.05	0.470	0.004	0.006	0.004	0.34	0.12	0.0022	0.0006	33.850	0.527	96.2	30.5	0.47
LM-33A	45.96	0.11	1.045	0.007	0.015	0.005	0.15	0.13	0.0024	0.0007	43.311	0.377	98.5	38.9	0.34
LM-34A	29.08	0.08	0.762	0.006	0.010	0.006	0.00	0.17	0.0006	0.0007	37.928	0.418	99.4	34.1	0.38
LM-35A	31.30	0.08	0.722	0.006	0.006	0.005	0.00	0.17	0.0030	0.0012	42.043	0.620	97.0	37.8	0.56
LM-36A	35.31	0.09	0.773	0.004	0.013	0.006	0.12	0.15	0.0055	0.0012	43.599	0.531	95.4	39.2	0.48
LM-38A	73.15	0.12	0.824	0.006	0.014	0.006	0.00	0.19	0.0082	0.0011	85.758	0.778	96.7	76.3	0.69
LM-39A	28.59	0.09	0.632	0.005	0.016	0.006	0.00	0.14	0.0026	0.0010	43.945	0.621	97.3	39.5	0.56
LM-40A	118.53	0.18	0.436	0.004	0.008	0.004	0.00	0.18	0.0033	0.0009	269.458	2.960	99.2	230.0	2.39
LM-41A	13.76	0.04	0.355	0.004	0.012	0.003	0.15	0.17	0.0030	0.0009	36.231	0.894	93.6	32.6	0.80
LM-42A	71.34	0.12	0.996	0.006	0.017	0.005	0.08	0.14	0.0179	0.0008	66.293	0.522	92.6	59.2	0.47
LM-43A	14.98	0.05	0.339	0.004	0.000	0.004	0.00	0.15	0.0022	0.0007	42.127	0.809	95.3	37.9	0.72
LM-44A	21.12	0.08	0.656	0.006	0.013	0.005	0.00	0.19	0.0050	0.0010	29.846	0.568	92.8	26.9	0.51
LM-45A	25.41	0.08	0.622	0.006	0.008	0.006	0.00	0.18	0.0023	0.0011	39.696	0.651	97.3	35.7	0.58
LM-46A	23.98	0.09	0.547	0.006	0.014	0.004	0.34	0.17	0.0022	0.0011	42.739	0.764	97.4	38.4	0.68
LM-47A	48.35	0.12	1.036	0.006	0.012	0.004	0.00	0.18	0.0044	0.0007	45.411	0.346	97.3	40.8	0.31

LM-48A	39.42	0.12	0.609	0.008	0.010	0.005	0.00	0.11	0.0000	0.0007	65.342	0.959	100.9	58.4	0.85
LM-49A	31.32	0.08	0.713	0.006	0.000	0.004	0.14	0.12	0.0032	0.0007	42.606	0.482	97.0	38.3	0.43
LM-50A	63.05	0.12	0.939	0.007	0.024	0.004	0.32	0.13	0.0032	0.0007	66.165	0.568	98.5	59.1	0.51
LM-51A	35.93	0.12	0.662	0.005	0.012	0.005	0.00	0.30	0.0036	0.0011	52.613	0.687	97.0	47.2	0.61
LM-53A	179.20	0.20	0.502	0.005	0.008	0.005	0.50	0.30	0.0053	0.0011	354.416	3.852	99.1	296.0	3.00
LM-54A	43.28	0.12	0.988	0.006	0.022	0.005	0.00	0.20	0.0035	0.0007	42.671	0.381	97.4	38.4	0.34
LM-55A	204.80	0.20	0.467	0.006	0.016	0.006	0.00	0.30	0.0021	0.0007	436.302	5.317	99.7	358.0	4.00
LM-57A	25.13	0.10	0.590	0.006	0.009	0.004	0.00	0.30	0.0030	0.0008	41.031	0.576	96.3	36.9	0.52
LM-58A	29.57	0.09	0.711	0.006	0.011	0.006	0.00	0.30	0.0028	0.0007	40.392	0.479	97.1	36.3	0.43
LM-59A	39.48	0.08	0.865	0.005	0.013	0.004	0.20	0.20	0.0037	0.0007	44.385	0.371	97.3	39.9	0.34
LM-60A	23.89	0.08	0.528	0.004	0.014	0.006	0.25	0.19	0.0050	0.0007	42.463	0.552	93.9	38.2	0.50
LM-61A	88.01	0.16	0.725	0.005	0.008	0.004	0.00	0.30	0.0049	0.0012	119.401	1.064	98.4	105.3	0.93
LM-62A	29.68	0.09	0.713	0.005	0.014	0.006	0.20	0.20	0.0013	0.0012	41.137	0.591	98.7	37.0	0.53
LM-63A	21.48	0.07	0.504	0.005	0.003	0.006	0.40	0.20	0.0027	0.0011	41.114	0.801	96.4	37.0	0.72
LM-64A	36.14	0.10	0.879	0.006	0.023	0.006	0.00	0.20	0.0046	0.0008	39.540	0.396	96.2	35.6	0.36
LM-65A	16.99	0.06	0.405	0.005	0.001	0.006	0.00	0.30	0.0000	0.0011	42.046	0.956	100.4	37.8	0.85
LM-66A	30.40	0.10	0.713	0.007	0.001	0.006	0.00	0.30	0.0010	0.0011	42.217	0.655	99.0	38.0	0.59
LM-67A	38.93	0.10	0.568	0.006	0.009	0.005	0.00	0.30	0.0059	0.0012	65.327	0.962	95.4	58.4	0.85
LM-68A	24.16	0.08	0.634	0.007	0.006	0.007	0.00	0.30	0.0044	0.0012	36.023	0.710	94.5	32.4	0.64
LM-71A	49.62	0.11	1.159	0.008	0.014	0.005	0.20	0.30	0.0053	0.0012	41.465	0.440	96.9	37.3	0.40
LM-73A	327.60	0.30	1.601	0.009	0.018	0.007	0.00	0.30	0.0091	0.0008	202.807	1.158	99.2	175.4	0.99
LM-74A	15.99	0.06	0.364	0.005	0.006	0.006	0.20	0.20	0.0005	0.0007	43.571	0.858	99.2	39.2	0.77
LM-75A	32.07	0.09	0.748	0.006	0.008	0.006	0.20	0.30	0.0025	0.0011	41.925	0.564	97.8	37.7	0.51
LM-77A	13.02	0.05	0.281	0.005	0.001	0.004	0.70	0.30	0.0000	0.0010	46.815	1.394	100.7	42.0	1.24
LM-78A	16.17	0.06	0.340	0.004	0.008	0.006	0.00	0.30	0.0021	0.0012	45.573	1.247	95.9	40.9	1.11
LM-79A	13.04	0.05	0.323	0.004	0.002	0.005	0.00	0.30	0.0000	0.0012	40.374	1.219	100.1	36.3	1.09
LM-80A	31.92	0.10	0.485	0.006	0.000	0.006	0.00	0.30	0.0035	0.0008	63.631	0.924	96.8	56.9	0.82
LM-81A	18.84	0.06	0.408	0.005	0.002	0.007	0.30	0.20	0.0034	0.0007	43.782	0.770	94.8	39.3	0.69
LM-82A	26.08	0.08	0.127	0.003	0.000	0.006	0.20	0.20	0.0016	0.0007	201.250	5.807	98.2	174.0	4.80
LM-83A	19.85	0.07	0.428	0.005	0.023	0.006	0.00	0.30	0.0034	0.0012	43.985	0.978	95.0	39.5	0.87

LM-84A	63.95	0.11	0.309	0.004	0.010	0.006	0.20	0.30	0.0022	0.0011	205.102	3.187	99.0	177.0	2.64
LM-85A	20.66	0.09	0.722	0.008	0.023	0.007	0.60	0.30	0.0003	0.0013	28.589	0.643	99.9	25.8	0.58
LM-86A	10.69	0.05	0.210	0.004	0.000	0.005	0.00	0.20	0.0029	0.0012	46.989	1.915	92.1	42.2	1.70
LM-89A	164.20	0.17	0.848	0.006	0.017	0.005	0.10	0.30	0.0020	0.0006	193.048	1.329	99.6	167.4	1.13
LM-90A	22.18	0.07	0.526	0.005	0.017	0.004	0.40	0.30	0.0005	0.0008	41.972	0.629	99.4	37.7	0.56
LM-91A	37.40	0.10	0.965	0.007	0.015	0.005	0.00	0.30	0.0029	0.0007	37.831	0.372	97.6	34.0	0.34
LM-92A	17.58	0.06	0.383	0.005	0.005	0.004	0.00	0.30	0.0012	0.0007	44.829	0.864	97.8	40.3	0.77
LM-93A	32.17	0.09	0.746	0.006	0.007	0.006	0.00	0.30	0.0028	0.0006	42.013	0.420	97.4	37.8	0.38
LM-94A	34.23	0.08	0.839	0.006	0.005	0.006	0.00	0.30	0.0004	0.0008	40.677	0.419	99.7	36.6	0.38
LM-95A	23.60	0.07	0.567	0.006	0.006	0.008	0.00	0.30	0.0031	0.0008	40.004	0.612	96.1	36.0	0.55
LM-96A	20.30	0.09	0.496	0.006	0.013	0.007	0.00	0.40	0.0012	0.0008	40.100	0.739	98.1	36.1	0.66
LM-97A	19.09	0.07	0.432	0.005	0.008	0.007	0.00	0.20	0.0024	0.0011	42.451	0.917	96.2	38.2	0.82
LM-98A	17.08	0.04	0.473	0.004	0.005	0.006	0.30	0.20	0.0000	0.0012	36.319	0.808	100.4	32.7	0.72
LM-99A	22.44	0.07	0.559	0.005	0.006	0.005	0.20	0.30	0.0013	0.0015	39.504	0.897	98.4	35.5	0.80
LM-100A	60.49	0.11	0.636	0.005	0.010	0.004	0.10	0.20	0.0023	0.0010	94.154	0.952	98.9	83.6	0.84
LM-103A	22.20	0.08	0.527	0.005	0.005	0.005	0.00	0.30	0.0051	0.0011	39.094	0.746	92.9	35.2	0.67
LM-104A	26.20	0.08	0.661	0.006	0.014	0.005	0.50	0.30	0.0038	0.0008	38.035	0.497	95.9	34.2	0.45
LM-105A	31.65	0.10	0.704	0.005	0.011	0.004	0.10	0.30	0.0030	0.0012	43.713	0.632	97.3	39.3	0.57
LM-106A	14.79	0.05	0.242	0.004	0.004	0.004	0.40	0.30	0.0007	0.0012	60.514	1.772	98.9	54.2	1.56
LM-107A	122.38	0.13	0.638	0.006	0.009	0.004	0.70	0.30	0.0063	0.0011	189.264	1.838	98.5	164.2	1.55
LM-108A	135.92	0.12	0.612	0.005	0.008	0.005	0.10	0.30	0.0016	0.0011	221.363	1.848	99.7	190.7	1.54
LM-109A	28.66	0.09	0.640	0.006	0.004	0.004	0.00	0.30	0.0025	0.0011	43.553	0.673	97.4	39.1	0.60
LM-110A	120.12	0.19	0.642	0.006	0.018	0.005	0.40	0.30	0.0000	0.0011	187.761	1.800	100.3	163.0	1.52
LM-111A	16.02	0.05	0.485	0.005	0.009	0.006	0.10	0.30	0.0000	0.0011	33.177	0.793	100.5	29.9	0.71
LM-113A	9.78	0.04	0.229	0.004	0.000	0.006	0.10	0.20	0.0000	0.0007	42.900	1.215	100.4	38.6	1.08
LM-114A	29.23	0.10	0.689	0.005	0.012	0.006	0.80	0.30	0.0018	0.0008	41.770	0.489	98.4	37.6	0.44
LM-116A	35.10	0.10	0.832	0.006	0.008	0.007	0.00	0.30	0.0004	0.0012	41.976	0.531	99.6	37.7	0.48
LM-117A	12.98	0.05	0.306	0.004	0.002	0.006	0.00	0.30	0.0000	0.0010	42.539	1.186	100.4	38.2	1.06
LM-119A	18.97	0.07	0.462	0.005	0.005	0.005	0.10	0.30	0.0024	0.0006	39.601	0.608	96.4	35.6	0.54
LM-120A	16.94	0.05	0.420	0.004	0.008	0.006	0.00	0.30	0.0008	0.0012	39.585	0.914	98.2	35.6	0.82

LM-121A	14.32	0.05	0.316	0.004	0.000	0.005	0.00	0.30	0.0009	0.0007	44.277	0.914	98.0	39.8	0.81
LM-122A	38.50	0.09	0.805	0.006	0.006	0.006	0.00	0.30	0.0009	0.0006	47.523	0.447	99.3	42.7	0.40
LM-123A	9.63	0.05	0.228	0.004	0.000	0.005	0.50	0.30	0.0006	0.0007	41.596	1.219	98.5	37.4	1.09
LM-124A	19.25	0.06	0.387	0.004	0.003	0.004	0.30	0.20	0.0063	0.0007	45.006	0.780	90.4	40.4	0.70
LM-126A	21.90	0.09	0.488	0.006	0.018	0.005	0.00	0.30	0.0042	0.0007	42.339	0.685	94.4	38.1	0.61
LM-127A	25.44	0.06	0.583	0.006	0.012	0.005	0.40	0.30	0.0030	0.0007	42.192	0.567	96.7	37.9	0.51
LM-128A	39.00	0.11	0.203	0.005	0.000	0.005	0.10	0.30	0.0018	0.0007	189.598	4.746	98.7	164.0	3.94
LM-130A	14.24	0.05	0.439	0.004	0.009	0.004	0.00	0.40	0.0047	0.0011	29.281	0.816	90.3	26.4	0.73
LM-131A	10.03	0.05	0.255	0.004	0.008	0.004	0.00	0.30	0.0028	0.0011	35.932	1.383	91.5	32.4	1.23
LM-132A	112.24	0.15	0.585	0.005	0.013	0.004	0.00	0.30	0.0014	0.0011	191.111	1.668	99.6	165.8	1.41
LM-134A	18.56	0.05	0.424	0.004	0.010	0.005	0.00	0.30	0.0019	0.0011	42.364	0.904	96.9	38.1	0.81
LM-137A	62.88	0.11	0.452	0.004	0.000	0.005	0.00	0.30	0.0021	0.0007	137.539	1.371	99.0	120.8	1.18
LM-138A	7.00	0.04	0.143	0.004	0.002	0.005	0.00	0.20	0.0010	0.0007	46.351	1.982	95.1	41.6	1.76
LM-139A	8.07	0.04	0.203	0.004	0.000	0.004	0.00	0.30	0.0010	0.0011	37.988	1.765	95.6	34.2	1.57
Obogon Formation (Mid-Late Miocene); J-value = 0.000490 ± 0.000016															
OB-02A	96.00	0.12	2.134	0.007	0.042	0.005	0.04	0.11	0.0249	0.0018	41.549	0.290	92.3	36.4	1.19
OB-03A	40.07	0.11	0.829	0.005	0.023	0.006	0.32	0.10	0.0120	0.0013	44.068	0.564	91.2	38.6	1.33
OB-04A	32.69	0.11	0.751	0.005	0.012	0.005	0.07	0.09	0.0026	0.0007	42.508	0.442	97.7	37.2	1.25
OB-07A	67.09	0.12	1.139	0.007	0.013	0.006	0.00	0.10	0.0016	0.0017	58.452	0.587	99.2	51.0	1.70
OB-08A	30.88	0.10	0.790	0.005	0.007	0.007	0.00	0.12	0.0000	0.0016	39.154	0.681	100.2	34.3	1.25
OB-09A	215.00	0.60	0.707	0.007	0.000	0.008	0.00	0.09	0.0098	0.0013	299.773	3.207	98.7	247.0	7.87
OB-10A	25.04	0.09	0.636	0.006	0.000	0.006	0.00	0.11	0.0032	0.0012	37.843	0.708	96.2	33.2	1.23
OB-12A	202.60	0.40	0.866	0.006	0.011	0.006	0.04	0.09	0.0670	0.0020	210.980	1.654	90.2	177.6	5.63
OB-13A	21.90	0.09	0.487	0.005	0.006	0.007	0.18	0.10	0.0052	0.0013	41.879	0.947	93.1	36.7	1.43
OB-14A	33.70	0.15	0.803	0.006	0.016	0.006	0.00	0.11	0.0055	0.0013	39.933	0.601	95.2	35.0	1.24
OB-15A	23.48	0.15	0.698	0.005	0.015	0.007	0.04	0.11	0.0021	0.0013	32.748	0.657	97.3	28.7	1.09
OB-17A	24.40	0.19	0.572	0.004	0.009	0.006	0.08	0.10	0.0000	0.0015	42.680	0.919	100.1	37.4	1.44
OB-19A	44.23	0.13	0.615	0.006	0.016	0.006	0.09	0.10	0.0006	0.0011	71.653	0.901	99.6	62.3	2.12
OB-22A	14.90	0.08	0.344	0.005	0.006	0.006	0.00	0.13	0.0030	0.0013	40.651	1.290	93.9	35.6	1.60

OB-24A	15.23	0.09	0.239	0.004	0.000	0.005	0.09	0.12	0.0008	0.0013	62.691	2.046	98.4	54.6	2.47
OB-25A	35.78	0.09	0.339	0.004	0.014	0.007	0.00	0.11	0.0022	0.0019	103.486	2.163	98.1	89.3	3.35
OB-27A	31.11	0.16	0.458	0.005	0.013	0.004	0.07	0.20	0.0039	0.0015	65.539	1.289	96.4	57.1	2.13
OB-28A	74.20	0.20	0.422	0.004	0.016	0.004	0.12	0.18	0.0001	0.0011	175.836	1.965	100.0	149.2	4.90
OB-29A	13.17	0.05	0.318	0.004	0.006	0.005	0.00	0.17	0.0000	0.0013	41.345	1.335	99.8	36.2	1.64
OB-30A	25.42	0.10	0.326	0.004	0.011	0.005	0.24	0.18	0.0026	0.0012	75.740	1.475	97.1	65.8	2.44
OB-32A	23.53	0.09	0.606	0.006	0.009	0.005	0.00	0.20	0.0026	0.0011	37.557	0.669	96.7	32.9	1.20
OB-33A	27.88	0.08	0.451	0.005	0.014	0.004	0.00	0.20	0.0031	0.0012	59.671	1.063	96.6	52.0	1.89
OB-34A	21.78	0.07	0.572	0.005	0.013	0.004	0.01	0.17	0.0000	0.0010	38.166	0.654	100.2	33.4	1.21
OB-37A	23.21	0.07	0.418	0.004	0.011	0.004	0.21	0.16	0.0001	0.0011	55.597	0.997	100.0	48.5	1.77
OB-38A	21.98	0.09	0.513	0.005	0.013	0.005	0.01	0.18	0.0000	0.0011	43.200	0.795	100.8	37.8	1.39
OB-39A	23.73	0.08	0.571	0.006	0.014	0.005	0.00	0.19	0.0006	0.0015	41.235	0.896	99.3	36.1	1.39
OB-40A	30.06	0.10	0.498	0.006	0.008	0.005	0.28	0.16	0.0005	0.0007	60.215	0.840	99.6	52.5	1.82
OB-41A	16.37	0.05	0.581	0.005	0.008	0.006	0.00	0.15	0.0000	0.0012	28.279	0.667	100.4	24.8	0.99
OB-42A	35.56	0.09	0.852	0.006	0.010	0.004	0.32	0.16	0.0040	0.0012	40.389	0.521	96.7	35.4	1.22
OB-43A	18.01	0.09	0.505	0.005	0.008	0.003	0.20	0.20	0.0032	0.0016	33.842	1.033	94.9	29.7	1.31
OB-44A	19.26	0.06	0.430	0.004	0.011	0.004	0.00	0.18	0.0025	0.0012	43.095	0.948	96.2	37.7	1.46
OB-45A	37.38	0.10	0.826	0.007	0.022	0.004	0.00	0.17	0.0060	0.0016	43.093	0.687	95.2	37.7	1.35
OB-46A	10.44	0.04	0.350	0.004	0.005	0.004	0.00	0.17	0.0024	0.0010	27.859	0.930	93.3	24.5	1.13
OB-47A	21.72	0.16	0.536	0.005	0.000	0.005	0.00	0.15	0.0030	0.0007	38.882	0.603	95.9	34.1	1.21
OB-48A	34.27	0.10	0.850	0.007	0.005	0.005	0.24	0.17	0.0066	0.0017	38.070	0.686	94.4	33.4	1.22
OB-49A	52.26	0.09	0.702	0.006	0.002	0.005	0.15	0.14	0.0046	0.0016	72.462	0.917	97.4	63.0	2.15
OB-50A	22.05	0.08	0.411	0.005	0.000	0.005	0.04	0.18	0.0033	0.0012	51.271	1.099	95.6	44.8	1.72
OB-51A	31.82	0.07	0.760	0.005	0.013	0.005	0.20	0.30	0.0019	0.0014	41.132	0.612	98.2	36.0	1.27
OB-52A	40.88	0.09	0.952	0.006	0.019	0.004	0.40	0.40	0.0013	0.0011	42.577	0.437	99.1	37.3	1.25
OB-54A	33.77	0.09	0.655	0.006	0.015	0.005	0.30	0.30	0.0015	0.0013	50.919	0.783	98.8	44.5	1.57
OB-55A	23.82	0.16	0.564	0.004	0.009	0.005	0.10	0.40	0.0014	0.0016	41.546	0.954	98.3	36.4	1.43
OB-56A	13.82	0.04	0.363	0.004	0.004	0.005	0.20	0.30	0.0029	0.0009	35.838	0.886	94.0	31.4	1.27
OB-57A	8.68	0.05	0.206	0.003	0.005	0.005	0.00	0.30	0.0013	0.0006	40.264	1.163	95.6	35.3	1.51
OB-59A	9.84	0.07	0.288	0.004	0.009	0.006	0.00	0.40	0.0011	0.0011	32.996	1.252	96.5	29.0	1.43

OB-60A	38.35	0.08	0.818	0.006	0.011	0.006	0.00	0.40	0.0030	0.0014	45.726	0.607	97.6	40.0	1.38
OB-61A	44.98	0.13	0.606	0.005	0.015	0.004	0.00	0.40	0.0031	0.0014	72.524	0.983	97.8	63.0	2.17
OB-62A	25.70	0.08	0.491	0.006	0.006	0.005	0.10	0.40	0.0015	0.0012	51.482	0.966	98.4	45.0	1.66
OB-65A	32.21	0.16	0.714	0.004	0.015	0.004	0.00	0.30	0.0061	0.0006	42.567	0.448	94.4	37.3	1.25
OB-67A	15.80	0.05	0.420	0.005	0.005	0.005	0.00	0.40	0.0000	0.0006	37.993	0.659	101.0	33.3	1.21
OB-68A	31.12	0.09	0.712	0.006	0.006	0.006	0.00	0.40	0.0047	0.0015	41.624	0.755	95.4	36.4	1.34
OB-69A	54.12	0.09	0.293	0.004	0.008	0.005	0.00	0.40	0.0017	0.0010	182.612	2.721	99.0	155.0	5.28
OB-70A	12.33	0.04	0.381	0.004	0.012	0.003	0.00	0.30	0.0033	0.0007	29.784	0.660	92.0	26.2	1.02
OB-71A	104.89	0.16	0.623	0.006	0.007	0.005	0.00	0.40	0.0041	0.0008	166.266	1.593	98.8	141.4	4.59
OB-74A	57.81	0.14	1.364	0.007	0.012	0.004	0.00	0.40	0.0008	0.0014	42.191	0.391	99.6	36.9	1.23
OB-75A	18.63	0.11	0.722	0.005	0.008	0.004	0.10	0.40	0.0048	0.0010	23.828	0.478	92.4	21.0	0.79
OB-76A	55.92	0.12	0.890	0.006	0.014	0.004	0.10	0.30	0.0002	0.0016	62.787	0.729	99.9	54.7	1.85
OB-79A	75.61	0.14	0.366	0.005	0.003	0.005	0.00	0.40	0.0000	0.0017	207.069	3.284	100.2	174.0	5.99
OB-80A	17.88	0.08	0.454	0.005	0.003	0.005	0.00	0.30	0.0035	0.0012	37.017	0.926	94.1	32.4	1.32
OB-81A	16.34	0.09	0.353	0.004	0.000	0.005	0.00	0.40	0.0023	0.0011	44.354	1.128	95.8	38.8	1.58
OB-82A	22.50	0.09	0.444	0.005	0.008	0.004	0.00	0.40	0.0015	0.0012	49.665	1.051	98.0	43.4	1.66
OB-83A	62.50	0.20	0.751	0.006	0.016	0.005	0.00	0.40	0.0018	0.0012	82.589	0.906	99.2	71.6	2.40

NOTES:
Samples were irradiated for 1.92 hours in the Oregon State University CLICIT (cadmium lined) facility. Sanidine from the Fish Canyon Tuff was used as the neutron fluence monitor with a reference age of 28.201 Ma (Kuiper *et al.*, 2008).

Nucleogenic production ratios:

$(^{36}Ar/^{37}Ar)_{Ca}$	2.64×10^{-4}
$(^{39}Ar/^{37}Ar)_{Ca}$	6.5×10^{-4}
$(^{38}Ar/^{37}Ar)_{Ca}$	$0.196 \pm 0.00816\times 10^{-4}$
$(^{40}Ar/^{39}Ar)_{K}$	8.5×10^{-3}
$(^{38}Ar/^{39}Ar)_{K}$	$1.22 \pm 0.0027 \times 10^{-2}$
$(^{36}Ar/^{38}Ar)_{Cl}$	$2.629 \pm 0.011 \times 10^{2}$
$^{37}Ar/^{39}Ar$ to Ca/K	1.96
$^{38}Ar/^{39}Ar$ to Cl/K	2.9

Isotopic constants and decay rates:

$\lambda(^{40}K_{\varepsilon})$ /yr	$5.81\pm 0.17\times 10^{-11}$
$\lambda(^{40}K_{\beta-})$ /yr	$4.962\pm 0.086\times 10$
$\lambda(^{37}Ar)$ /d	1.975×10^{-2}
$\lambda(^{39}Ar)$ /d	7.068×10^{-6}
$\lambda(^{36}Cl)$ /d	6.308×10^{-9}
$(^{40}Ar/^{36}Ar)_{Atm}$	295.5 ± 0.5
$(^{40}Ar/^{38}Ar)_{Atm}$	1575 ± 2
$^{40}K/K_{Total}$	0.01167